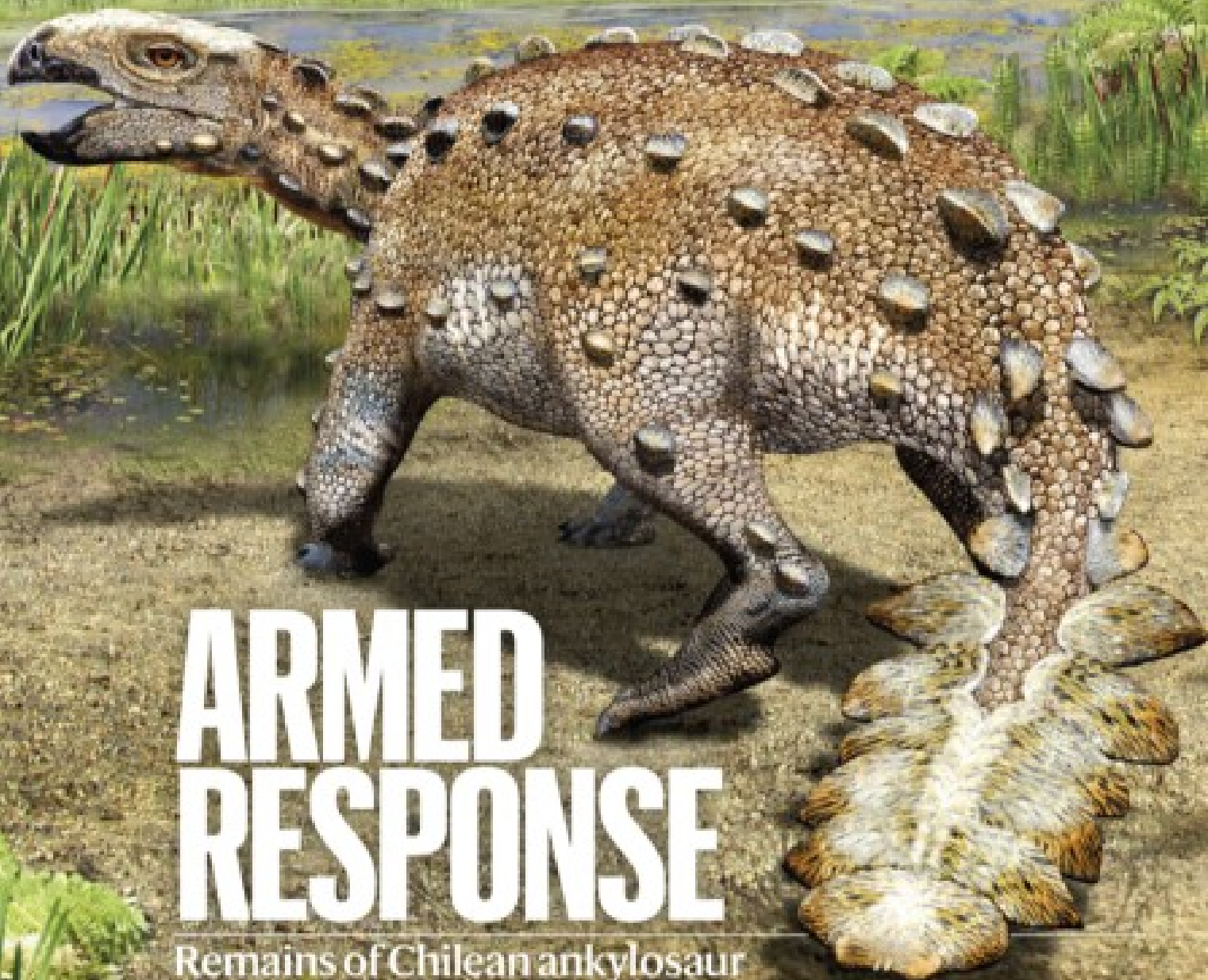


# nature



## ARMED RESPONSE

Remains of Chilean ankylosaur display unique tail weaponry

### Coronavirus

The rise of Omicron and what's next for SARS-CoV-2 evolution

### Webb wonder

Inside the telescope that aims to unlock the early Universe

### Going green

Rising levels of CO<sub>2</sub> drive increase in global photosynthesis

# Nature.2021.12.11

[Sat, 11 Dec 2021]

- [This Week](#)
- [News in Focus](#)
- [Books & Arts](#)
- [Opinion](#)
- [Work](#)
- [Research](#)

# This Week

- **[The UN must get on with appointing its new science board](#)** [ 08 December 2021]  
Editorial • The decision to appoint a board of advisors is welcome — and urgent, given the twin challenges of COVID and climate change.
- **[Omicron: the global response is making it worse](#)** [ 07 December 2021]  
Editorial • The pandemic will not end while vaccine equity keeps getting pushed to the margins.
- **[Understand the real reasons reproducibility reform fails](#)** [ 06 December 2021]  
World View • Lack of rigour is often blamed on pressure to publish. But ethnographers can find out what truly keeps science from upping its game.
- **[Does police outreach cut crime? Efforts in six nations give a bleak answer](#)** [ 02 December 2021]  
Research Highlight • Community policing in the global south fails to reduce crime rates or public mistrust.
- **[This enormous eagle could have killed you, probably](#)** [ 01 December 2021]  
Research Highlight • The extinct Haast's eagle — known from fossils found in New Zealand — hunted like its modern relatives, but also had habits of a scavenger.
- **[Shutting ‘super-polluters’ slashes greenhouse gases — and deaths](#)** [ 01 December 2021]  
Research Highlight • Early retirement for climate-damaging power plants would also cut emissions of air pollution that endanger human health.
- **[Famous space family has a surprisingly peaceful history](#)** [ 02 December 2021]  
Research Highlight • The seven planets orbiting the star TRAPPIST-1 were largely spared cosmic collisions, raising questions about where these worlds got their water.
- **[What fuelled an ancient empire’s rise? Potatoes and quinoa](#)** [ 06 December 2021]  
Research Highlight • The Andean superpower Tiwanaku developed with the help of a stable source of nutrients, including llama meat.

- **Across the Sahara in a day: swifts zip across the desert at amazing rates** [ 30 November 2021]

Research Highlight • A species of swift lives up to its name as it migrates from southern Europe to central Africa.

- **Super jelly springs back from a squashing** [ 06 December 2021]

Research Highlight • This fabricated gel doesn't crack under pressure.

- EDITORIAL
- 08 December 2021

# The UN must get on with appointing its new science board

The decision to appoint a board of advisors is welcome — and urgent, given the twin challenges of COVID and climate change.



UN secretary-general António Guterres announced plans for a new science board in September, but is yet to release further details. Credit: Juancho Torres/Anadolu Agency/Getty

Scientists helped to create the United Nations system. Today, people look to UN agencies — such as the UN Environment Programme or the World Health Organization — for reliable data and evidence on, say, climate

change or the pandemic. And yet, shockingly, the UN leader's office has not had a department for science advice for most of its 76-year history. That is about to change.

UN secretary-general António Guterres is planning to appoint a board of scientific advisers, reporting to his office. The decision was announced in September in Our Common Agenda (see [go.nature.com/3y1g3hp](https://go.nature.com/3y1g3hp)), which lays out the organization's vision for the next 25 years, but few other details have been released.

Representatives of the scientific community are excited about the potential for science to have a position at the centre of the UN, but are rightly anxious for rapid action, given the twin challenges of COVID-19 and climate change, which should be urgent priorities for the board. The International Science Council (ISC), the Paris-based non-governmental body representing many of the world's scientists, recommended such a board in its own report on science and the intergovernmental system, published last week (see [go.nature.com/3rjdjos](https://go.nature.com/3rjdjos)). Council president Peter Gluckman, former chief science adviser to New Zealand's prime minister, has written to Guterres to say the ISC is ready to help.



[COP26 didn't solve everything — but researchers must stay engaged](#)

But it's been more than two months since the announcement, and the UN has not yet revealed the names of the board members. *Nature* spoke to a number of serving and former UN science advisers who said they know little about the UN chief's plans. So far, there are no terms of reference and there is no timeline.

*Nature* understands that the idea is still being developed, and that Guterres is leaning towards creating a board that would draw on UN agencies' existing science networks. Guterres is also aware of the need to take into account that both the UN and the world have changed since the last such board was put in place. All the same, the UN chief needs to end the suspense and set out his plans. Time is of the essence.

Guterres's predecessor, Ban Ki-moon, had a science advisory board between 2014 and 2016. Its members were tasked with providing advice to the secretary-general on science, technology and innovation for sustainable development. But COVID-19 and climate change have pushed science much higher up the international agenda. Moreover, global challenges are worsening — the pandemic has put back progress towards the UN's flagship Sustainable Development Goals (SDGs), a plan to end poverty and achieve sustainability by 2030. There is now widespread recognition that science has an important part to play in addressing these and other challenges.



[How science can put the Sustainable Development Goals back on track](#)

Research underpins almost everything we know about the nature of the virus SARS-CoV-2 and the disease it causes. All countries have access to similar sets of findings, but many are coming to different decisions on how to act on those data — for example, when to mandate mask-wearing or introduce travel restrictions. The UN's central office needs advice that takes this socio-cultural-political dimension of science into account. It needs advice from experts who study how science is applied and perceived by different constituencies and in different regions.

Science advice from the heart of the UN system could also help with another problem highlighted by the pandemic — how to reinvigorate the idea that it is essential for countries to cooperate on solving global problems.

Climate change is one example. Advice given by the Intergovernmental Panel on Climate Change (IPCC) is being read and applied in most countries, albeit to varying degrees. But climate is also an area in which states are at odds. Despite Guterres's calls for solidarity, there were times during last month's climate conference in Glasgow when the atmosphere was combative. Science advisers could help the secretary-general's office to find innovative ways to encourage cooperation between countries in efforts to meet the targets of the 2015 Paris climate agreement.



[Reset Sustainable Development Goals for a pandemic world](#)

The SDGs are also, to some extent, impeded by competition within the UN system. To tackle climate change, manage land and forests, and protect biodiversity, researchers and policymakers need to work collegially. But the UN's scientific bodies, such as the IPCC, are set up along disciplinary lines with their own objectives, work programmes and rules, all guided by their own institutional histories. The IPCC and the Intergovernmental Science-Policy Platform on Biodiversity and Ecosystem Services (IPBES), for example, have only begun to collaborate in the past few years .

Independence will be key for an advisory role to be credible. Guterres needs to consider an organizational architecture through which UN agencies are represented, and funding could come from outside the UN. But all of those involved would have to accept that their contributions were for common goals — not to promote their own organization's interests.

Leadership matters, as do communication and support. Guterres should ensure that his scientific advisers are chosen carefully to represent individuals from diverse disciplines and across career stages, and to ensure good representation from low-income countries. The board needs to be well staffed and have a direct line to his office. And it will need a decent budget. Guterres should quickly publish the terms of reference so that the research community has time to provide input and critique.

At its most ambitious, a scientific advisory board to the secretary-general could help to break the culture of individualism that beleaguers efforts to reach collective, global goals, and bring some coherence to the current marketplace of disciplines, ideas and outcomes. This will be a monumental task, requiring significant resources and the will to change. But if the advisers succeed, there will also be valuable lessons for the practice of science, which, as we know all too well, still largely rewards individual effort.

*Nature* **600**, 189-190 (2021)

doi: <https://doi.org/10.1038/d41586-021-03615-y>

| [Section menu](#) | [Main menu](#) |

- EDITORIAL
- 07 December 2021

# Omicron: the global response is making it worse

The pandemic will not end while vaccine equity keeps getting pushed to the margins.



The COVAX scheme for delivering vaccines to low-income countries needs some star power. Credit: Jaafar Ashtiyeh/AFP/Getty

The arrival of Omicron — a newly discovered, highly mutated coronavirus variant that seems to be highly transmissible — is creating unease, uncertainty and disruption. The response from world leaders, especially those from high-income countries, is making things worse.

Travel restrictions are back, even though some have [questionable efficacy when transmission of the virus is high](#). Countries with many fully vaccinated people are placing new vaccine orders — but only 6% of people in low-income countries have had one dose. Tulio de Oliveira at South Africa's Centre for Epidemic Response and Innovation in Stellenbosch, who leads the team that alerted the world to Omicron, [tweeted that African researchers had shared their COVID-19 data](#). Vaccines and diagnostics will come, but high-income countries will be the first to benefit.

Scientists know that this cycle will prolong the pandemic — but world leaders are still failing to choose the fastest path out. European Union member states are instead focusing their energies on [drafting a new international accord](#), or possibly a legally binding treaty. It would create rules to facilitate cooperation between countries during a pandemic, so that the next crisis can be better handled and no country will be left behind when it comes to diagnostics and treatment. That project passed a huge milestone last week: the World Health Assembly, a meeting of health ministers from around the world, formally agreed to begin talks.



### [Omicron-variant border bans ignore the evidence, say scientists](#)

The World Health Organization (WHO) has voiced its strong support for a treaty, accord or other international instrument that might push leaders to follow the organization's public-health recommendations on sharing data

and vaccines. But in the timeline laid out at the assembly, this pact wouldn't be up for adoption until 2024 — and its passing is not a given.

That is why more than 100 countries (including both China and the United States) and hundreds of organizations, including *Nature*, are supporting a campaign, led by India and South Africa and backed by the WHO, to temporarily waive intellectual-property (IP) rights to COVID-19 vaccines and drugs. The design and development of such therapies is concentrated in a [relatively small number of companies that hold key patents, along with the US government](#). IP scholars such as Luke McDonagh at the London School of Economics and Political Science say IP relief for the duration of the pandemic will kick-start vaccine manufacturing around the world. But the EU is resisting, partly because of the strength of opposition from European pharmaceutical companies that fear they will lose their market share if their competitors are allowed to use their designs. But another way is possible.

The COVID-19 Vaccines Global Access (COVAX) scheme for providing vaccines to low-income countries needs a shot in the arm. When donor countries, philanthropic foundations and the WHO established COVAX at the start of the pandemic, they had a vision captured in the slogan “no one is safe until everyone is safe”. The plan was for the world to be vaccinated step by step, starting with the most vulnerable populations.



[What the Moderna–NIH COVID vaccine patent fight means for research](#)

This never happened. Donor governments promised vaccines to COVAX while conducting parallel negotiations with companies, in some cases ordering many more doses than they needed. COVAX was not the priority, and it showed: the scheme had promised to provide 2 billion doses by the end of this year, but by July it had delivered only 95 million.

With populations in high-income nations largely vaccinated, COVAX looks to be turning a corner and will have delivered around 600 million vaccines by the end of the month. But these green shoots could be short-lived now that Omicron is prompting high-income nations to once more place large vaccine orders, especially for Omicron-specific vaccines based on messenger RNA. So long as this cycle continues, low- and lower-middle-income countries will always be at the back of the vaccines queue.

David Heymann, a long-standing science adviser to the WHO, says COVAX needs a high-profile global figure — someone of the stature of a leader of one of the G7 group of wealthy nations — to head it. Someone with the contacts, heft, star power and skills to knock heads together to hammer out a global solution to vaccinating the world, including compelling pharmaceutical company executives to agree that IP has to be shared, as happened with HIV drugs. This is not a criticism of COVAX's present leadership, Heymann emphasized — but adjustments are needed.

For a short while this year, researchers were optimistic that the pandemic might end at the end of 2022. But Andrea Taylor, who leads a COVID-19 data team at the Duke Global Health Innovation Center in Durham, North Carolina, says that will be pushed back until 2023 or even 2024, so long as wealthy nations insist on buying up most of the available vaccine stock without agreeing to provide more manufacturing capacity, and as new variants such as Omicron continue to arise. “We are taking the least efficient pathway out of the pandemic,” she laments.

It’s an inescapable reality and an almost iron-clad law: the pandemic will not end while vaccine equity is pushed to the margins.

*Nature* **600**, 190 (2021)

doi: <https://doi.org/10.1038/d41586-021-03616-x>

---

This article was downloaded by **calibre** from <https://www.nature.com/articles/d41586-021-03616-x>

| [Section menu](#) | [Main menu](#) |

- WORLD VIEW
- 06 December 2021

# Understand the real reasons reproducibility reform fails



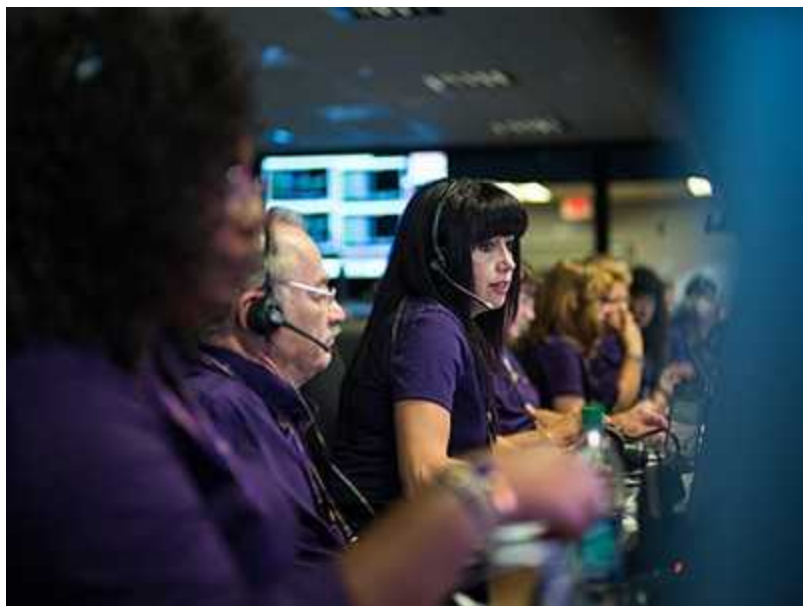
Lack of rigour is often blamed on pressure to publish. But ethnographers can find out what truly keeps science from upping its game.

- [Nicole C. Nelson](#) 0

A decade ago, the US National Institute of Neurological Disorders and Stroke convened a workshop on how to improve the rigour of preclinical research. Its recommendations were surprisingly straightforward: scientists should mask (or ‘blind’) their studies; randomize; estimate appropriate sample sizes; and specify rules for data handling ([S. C. Landis et al. \*Nature\* 490, 187–191; 2012](#)). Ten years on, many preclinical scientists still do not take these basic steps.

Ask most advocates of rigorous science why this is, and they will answer with two words: perverse incentives. Scientists are rewarded for getting things published, not for getting things right, and so they tend to favour speed and ease over robustness. But as an ethnographer, this explanation has never sat well with me. I've spent more than 15 years studying biomedical research cultures, and scientists' behaviours are rarely so transactional. So I decided to knock on a few doors at my institution, the University of Wisconsin–Madison, to ask researchers who work with animals why they were using the methods they were.

They explained that their decisions were based not on publication pressures, but on maintaining the integrity of experiments and respecting facility routines. For example, techniques to mask which treatment groups animals are in risk causing misidentification or cross-infection.



### What NASA missions can teach us about teamwork

One scientist told me how years of tedious mouse breeding had gone off the rails when animals' ear tags fell out, cage cards were swapped or spreadsheets had errors. The risk of mix-ups caused by masking seemed too great, especially in experiments where effects were so pronounced that there was no risk of bias. "You'd have to be fooling yourself pretty hard to see tumours where there are none," he laughed. Yet he did think masking was important if the effects of an intervention were small. As we spoke, he

realized that he had been so focused on avoiding the ‘horrors of misidentification’ that he might have dismissed other risks. In his case, one set of fears crowded out another.

Labour structures also make masking fraught. An investigator in a collaborative clinical project can pass tissue samples to a pathologist without explaining the sample numbering system. But in preclinical research, lab members are expected to take projects from beginning to end, providing few natural opportunities for masking. One graduate student didn’t want to ‘beg’ for labour from fellow students to allow her to mask her studies. She also worried that colleagues might be less conscientious about tasks that were important for her progress but not their projects.



### The replication crisis won’t be solved with broad brushstrokes

Efforts to implement masking often run counter to policies at animal facilities. US guidelines state that genotype information should be listed on cage cards, which effectively unmasks many studies. Other policies pose similar conundrums. Segregating mice treated with a viral vector prevents cross-contamination, but also reveals the treatment group. Many scientists were reluctant to ask facilities to alter their routines or make exceptions.

The main considerations I found for whether to mask were integrity, collegiality and animal welfare. Dig deeper on failures to adopt other

reproducibility reforms, and I'm confident that you'll find more than perverse incentives.

Ethnography excels as a tool for disrupting oversimplified stories about decisions. Sociological expertise was key to understanding how the culture at NASA led to the 1986 *Challenger* disaster, in which a Space Shuttle exploded shortly after launch. More recent ethnographic work at the agency has shown how [the administrative structure of a mission affects the science it produces](#). This work enables more-informed choices on research culture and other issues.

I've experienced this first-hand. As the embedded ethnographer in an early cancer-genomics trial, I helped the team to understand problems in implementing this new type of study. These came down to conflicting beliefs about what constitutes high-quality data. Bench scientists wanted regular technology upgrades to get ever more accurate genomic information; clinical researchers wanted set protocols that rarely changed. Understanding this conflict helped the team to work through it.

Unearthing assumptions, fears and social relations does not have to mean leaving scientific practice unchallenged. In the 1990s, scientists assumed that the effect of knocking out a gene in an organism would be so pronounced that there was no need for controls — until failures to replicate started popping up. But challenging experimental designs is best done after asking what's behind them. And it's worth considering that, in some situations, the net benefit of making practices more rigorous might be minimal.

Scientific values can drive change. Reproducible workflows can be implemented in ways that assuage fears rather than stoking them. One scientist had an elaborate system of masking, involving colour-coded sample tubes and cage cards, and often had to fight the animal core facility to use it. “I just know that we’re human,” she told me, “and humans are always going to be biased.” Her commitment to an ideal of good science overruled her concerns about the costs.

Yes, perverse incentives exist, but their role as a barrier to reform should be assessed, not assumed. Ethnography’s open-ended methods, comparative

frameworks and holistic explanations can capture overlooked variables and open up new avenues for action. Instead of solely blaming foot-dragging senior scientists, bring in the ethnographers.

*Nature* **600**, 191 (2021)

doi: <https://doi.org/10.1038/d41586-021-03617-w>

---

This article was downloaded by **calibre** from <https://www.nature.com/articles/d41586-021-03617-w>

| [Section menu](#) | [Main menu](#) |

- RESEARCH HIGHLIGHT
- 02 December 2021

# Does police outreach cut crime? Efforts in six nations give a bleak answer

Community policing in the global south fails to reduce crime rates or public mistrust.



Police officers in the Philippines took part in the study on the impact of community-policing efforts. Credit: Evidence in Governance and Politics

Involving the public in crime-fighting efforts does not always improve trust in the police or reduce the crime rates, at least in the global south<sup>1</sup>.

## Access options

Subscribe to Journal

Get full journal access for 1 year

\$199.00

only \$3.90 per issue

[Subscribe](#)

All prices are NET prices.

VAT will be added later in the checkout.

Tax calculation will be finalised during checkout.

Rent or Buy article

Get time limited or full article access on ReadCube.

from \$8.99

[Rent or Buy](#)

All prices are NET prices.

### **Additional access options:**

- [Log in](#)
- [Learn about institutional subscriptions](#)

*Nature* **600**, 192 (2021)

doi: <https://doi.org/10.1038/d41586-021-03580-6>

## **References**

1. 1.

Blair, G. *et al.* *Science* **374**, eabd3446 (2021).

---

This article was downloaded by **calibre** from <https://www.nature.com/articles/d41586-021-03580-6>

- RESEARCH HIGHLIGHT
- 01 December 2021

# This enormous eagle could have killed you, probably

The extinct Haast's eagle — known from fossils found in New Zealand — hunted like its modern relatives, but also had habits of a scavenger.



An artist's illustration of the Haast's eagle on the hunt shows it with a feathered head, but new analysis suggests that it might have been bald, like modern-day vultures. Credit: Jaime Chirinos/Science Photo Library

You might see the gigantic Haast's eagle in your nightmares, but never aloft in the New Zealand skies, because it went extinct centuries ago. But was this largest known eagle of all time — weighing as much as 15 kilograms — a fearsome hunter or simply a scavenger?

## Access options

Subscribe to Journal

Get full journal access for 1 year

\$199.00

only \$3.90 per issue

[Subscribe](#)

All prices are NET prices.  
VAT will be added later in the checkout.

Tax calculation will be finalised during checkout.

## Rent or Buy article

Get time limited or full article access on ReadCube.

from \$8.99

[Rent or Buy](#)

All prices are NET prices.

## Additional access options:

- [Log in](#)
- [Learn about institutional subscriptions](#)

*Nature* **600**, 192 (2021)

doi: <https://doi.org/10.1038/d41586-021-03585-1>

## References

1. 1.

van Heteren, A. H. *et al.* *Proc. R. Soc. B* **288**, 20211913 (2021).

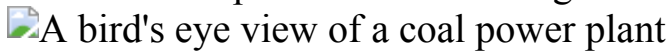
---

This article was downloaded by **calibre** from <https://www.nature.com/articles/d41586-021-03585-1>

- RESEARCH HIGHLIGHT
- 01 December 2021

# Shutting ‘super-polluters’ slashes greenhouse gases — and deaths

Early retirement for climate-damaging power plants would also cut emissions of air pollution that endanger human health.



A coal-fired power plant in Shandong province, China. Such plants produce vast quantities of greenhouse gases and can emit high levels of hazardous air pollutants, as well. Credit: Andrea Verdelli/Getty

Retiring ‘super polluting’ power plants to aid the climate could have another benefit: saving millions of lives<sup>1</sup>.

## Access options

Subscribe to Journal

Get full journal access for 1 year

\$199.00

only \$3.90 per issue

[Subscribe](#)

All prices are NET prices.

VAT will be added later in the checkout.

Tax calculation will be finalised during checkout.

Rent or Buy article

Get time limited or full article access on ReadCube.

from \$8.99

[Rent or Buy](#)

All prices are NET prices.

### **Additional access options:**

- [Log in](#)
- [Learn about institutional subscriptions](#)

*Nature* **600**, 192 (2021)

doi: <https://doi.org/10.1038/d41586-021-03581-5>

## **References**

1. 1.

Tong, D. et al. *Nature Clim. Change* <https://doi.org/10.1038/s41558-021-01216-1> (2021).

---

This article was downloaded by **calibre** from <https://www.nature.com/articles/d41586-021-03581-5>

- RESEARCH HIGHLIGHT
- 02 December 2021

# Famous space family has a surprisingly peaceful history

The seven planets orbiting the star TRAPPIST-1 were largely spared cosmic collisions, raising questions about where these worlds got their water.

An illustration showing what the TRAPPIST-1 system might look like from a vantage point near planet TRAPPIST-1f

The star named TRAPPIST-1 (left; artist's illustration) is circled by seven rocky, Earth-sized planets that had a tranquil early existence. Credit: NASA/JPL-Caltech

Comets and asteroids have bombarded many planets — including Earth in its youth. But the seven Earth-sized worlds in an iconic planetary system have enjoyed a relatively quiet and undisturbed life, research shows<sup>1</sup>.

## Access options

Subscribe to Journal

Get full journal access for 1 year

\$199.00

only \$3.90 per issue

[Subscribe](#)

All prices are NET prices.  
VAT will be added later in the checkout.

Tax calculation will be finalised during checkout.

Rent or Buy article

Get time limited or full article access on ReadCube.

from \$8.99

[Rent or Buy](#)

All prices are NET prices.

### **Additional access options:**

- [Log in](#)
- [Learn about institutional subscriptions](#)

*Nature* **600**, 192 (2021)

doi: <https://doi.org/10.1038/d41586-021-03584-2>

## **References**

1. 1.

Raymond, S. N. *et al.* *Nature Astron.* <https://doi.org/10.1038/s41550-021-01518-6> (2021).

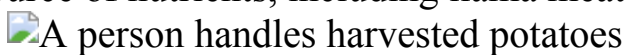
---

This article was downloaded by **calibre** from <https://www.nature.com/articles/d41586-021-03584-2>

- RESEARCH HIGHLIGHT
- 06 December 2021

# What fuelled an ancient empire's rise? Potatoes and quinoa

The Andean superpower Tiwanaku developed with the help of a stable source of nutrients, including llama meat.



The Tiwanaku culture rose to dominance millennia ago thanks in part to potato power, which people in the region still rely on today. Credit: Aizar Raldes/AFP/Getty

Hailed a superfood, quinoa has seen its popularity soar in the past decade. But the grain-like seed was already prized some 3,000 years ago: researchers have found that it helped to fuel an ancient Andean civilization in an inhospitable climate through centuries of political upheaval<sup>1</sup>.

## Access options

Subscribe to Journal

Get full journal access for 1 year

\$199.00

only \$3.90 per issue

[Subscribe](#)

All prices are NET prices.  
VAT will be added later in the checkout.

Tax calculation will be finalised during checkout.

Rent or Buy article

Get time limited or full article access on ReadCube.

from \$8.99

[Rent or Buy](#)

All prices are NET prices.

### **Additional access options:**

- [Log in](#)
- [Learn about institutional subscriptions](#)

*Nature* **600**, 193 (2021)

doi: <https://doi.org/10.1038/d41586-021-03583-3>

## **References**

1. 1.

Miller, M. J. *et al.* *Proc. Natl Acad. Sci. USA* **118**, e2113395118 (2021).

---

This article was downloaded by **calibre** from <https://www.nature.com/articles/d41586-021-03583-3>

- RESEARCH HIGHLIGHT
- 30 November 2021

# Across the Sahara in a day: swifts zip across the desert at amazing rates

A species of swift lives up to its name as it migrates from southern Europe to central Africa.



Pallid swifts live life on the wing, spending day and night in the air. Credit: Frank McClintock/Shutterstock

Pallid swifts are the marathoners of the sky, spending most of their lives in flight. Tracking devices now show that pallid swifts have not only endurance but also speed: some cross the Sahara Desert at an average pace of 400 kilometres per day<sup>1</sup>.

## Access options

Subscribe to Journal

Get full journal access for 1 year

\$199.00

only \$3.90 per issue

[Subscribe](#)

All prices are NET prices.  
VAT will be added later in the checkout.  
Tax calculation will be finalised during checkout.

Rent or Buy article

Get time limited or full article access on ReadCube.

from \$8.99

[Rent or Buy](#)

All prices are NET prices.

### **Additional access options:**

- [Log in](#)
- [Learn about institutional subscriptions](#)

*Nature* **600**, 193 (2021)

doi: <https://doi.org/10.1038/d41586-021-03582-4>

## **References**

1. 1.

Finlayson, S. *et al.* *PLoS ONE*  
<https://doi.org/10.1371/journal.pone.0259656> (2021).

---

This article was downloaded by **calibre** from <https://www.nature.com/articles/d41586-021-03582-4>

- RESEARCH HIGHLIGHT
- 06 December 2021

# Super jelly springs back from a squashing

This fabricated gel doesn't crack under pressure.



An unassuming gel can return to its original shape even after being run over by a car. Credit: Z. Huang *et al./Nature Mater.*

After being flattened by a 4,000-kilogram weight, a puck-shaped sample of a wobbly, gummy-like material can spring back to its original shape within 2 minutes<sup>1</sup>.

## Access options

Subscribe to Journal

Get full journal access for 1 year

\$199.00

only \$3.90 per issue

[Subscribe](#)

All prices are NET prices.

VAT will be added later in the checkout.

Tax calculation will be finalised during checkout.

Rent or Buy article

Get time limited or full article access on ReadCube.

from \$8.99

[Rent or Buy](#)

All prices are NET prices.

### **Additional access options:**

- [Log in](#)
- [Learn about institutional subscriptions](#)

*Nature* **600**, 193 (2021)

doi: <https://doi.org/10.1038/d41586-021-03586-0>

## **References**

1. 1.

Huang, Z. *et al.* *Nature Mater.* <https://doi.org/10.1038/s41563-021-01124-x> (2021).

---

This article was downloaded by **calibre** from <https://www.nature.com/articles/d41586-021-03586-0>

| [Section menu](#) | [Main menu](#) |

# News in Focus

- [\*\*Metal planet, COVID pact and Hubble telescope time\*\*](#) [ 08 December 2021]  
News Round-Up • The latest science news, in brief.
- [\*\*How bad is Omicron? What scientists know so far\*\*](#) [ 02 December 2021]  
News • COVID researchers are working at breakneck speed to learn about the variant's transmissibility, severity and ability to evade vaccines.
- [\*\*Omicron-variant border bans ignore the evidence, say scientists\*\*](#) [ 02 December 2021]  
News • Researchers say travel restrictions in response to the newly detected coronavirus variant come too late and could even slow studies of Omicron.
- [\*\*What the Moderna–NIH COVID vaccine patent fight means for research\*\*](#) [ 30 November 2021]  
News Explainer • Collaborators are locked in a high-stakes dispute over which researchers should be named as inventors on a key vaccine patent application.
- [\*\*DeepMind's AI helps untangle the mathematics of knots\*\*](#) [ 01 December 2021]  
News • The machine-learning techniques could benefit other areas of maths that involve large data sets.
- [\*\*China's Mars rover has amassed reams of novel geological data\*\*](#) [ 30 November 2021]  
News • Data collected by the Tianwen-1 mission and Zhurong Mars rover are offering insights into a previously unexplored region of Mars's northern hemisphere.
- [\*\*Beyond Omicron: what's next for COVID's viral evolution\*\*](#) [ 07 December 2021]  
News Feature • The rapid spread of new variants offers clues to how SARS-CoV-2 is adapting and how the pandemic will play out over the next several months.
- [\*\*The \\$11-billion Webb telescope aims to probe the early Universe\*\*](#) [ 08 December 2021]  
News Feature • Three decades after it was conceived, Hubble's successor is set for launch. Here's why astronomers around the world can't wait.

---

| [Next section](#) | [Main menu](#) | [Previous section](#) |

- NEWS ROUND-UP
- 08 December 2021

# Metal planet, COVID pact and Hubble telescope time

The latest science news, in brief.



During the day, the exoplanet GJ 367b (shown here in an artist's rendering) is so hot, the iron it holds could almost begin to melt.Credit: SPP 1992 (Patricia Klein)

**This tiny iron-rich planet is super metal**

Astronomers have spotted the [tiniest, most metal-based planet yet](#) — an iron-rich world that is light years away from Earth and zips around its star once every eight hours.

The planet, known as GJ 367b, is three-quarters the size of Earth, but much denser. It's more like Mercury, in that it is made mostly of iron and is superheated by blazing radiation from its star. GJ 367b is a searing 1,500 °C during the day — nearly hot enough for its iron to begin to melt.

GJ 367b is the smallest planet outside the Solar System for which scientists have been able to determine the composition, says Kristine Lam, an astronomer at the German Aerospace Center in Berlin. She and her colleagues reported the finding on 2 December ([K. W. F. Lam et al. Science 374, 1271–1275; 2021](#)).

Astronomers have discovered more than a dozen ‘ultrashort-period’ planets, which are so close to their stars that they make a complete orbit in less than a day. The GJ 367b discovery “showcases our ability to measure the mass of tiny, sub-Earth planets”, says David Armstrong, an astronomer at the University of Warwick in Coventry, UK. “Being able to observe such planets is fascinating and promises many Earth-like planet discoveries in the future.”

## World commits to pandemic-response pact

As researchers scrambled last week to learn more about Omicron, the latest SARS-CoV-2 coronavirus variant of concern, world leaders met to negotiate a way of ensuring that a crisis on the scale of the COVID-19 pandemic won’t happen again. Initially on the table was a legally binding pandemic treaty that would dictate how nations should respond to future outbreaks. [A fuzzier form of that proposal is now moving forwards](#), to be sharpened in the months and years to come.

“Omicron demonstrates just why the world needs a new accord on pandemics,” said Tedros Adhanom Ghebreyesus, director-general of the World Health Organization (WHO), at the special session of the World

Health Assembly, which was held from 29 November to 1 December in Geneva, Switzerland.

The original proposal, driven largely by the president of the European Council, Charles Michel, contained strong terms such as ‘legally binding’ and ‘treaty’. Backing off from the more rigid terminology seems to have coaxed all 194 of the WHO’s member states to reach a final consensus to move forwards. Countries that are particularly defensive about their sovereignty, such as the United States, often oppose treaties.

Michel has said that a treaty would be a good way to ensure the equitable distribution of vaccines and other medical countermeasures, such as protective equipment and diagnostic tests.

International accords typically take years to become reality, and the process for this one is expected to continue until at least 2024.

## Hubble Telescope’s first-time user numbers soar

An unprecedented number of first-time investigators have secured viewing time on NASA’s Hubble Space Telescope in the years since the agency overhauled the application process to reduce bias.

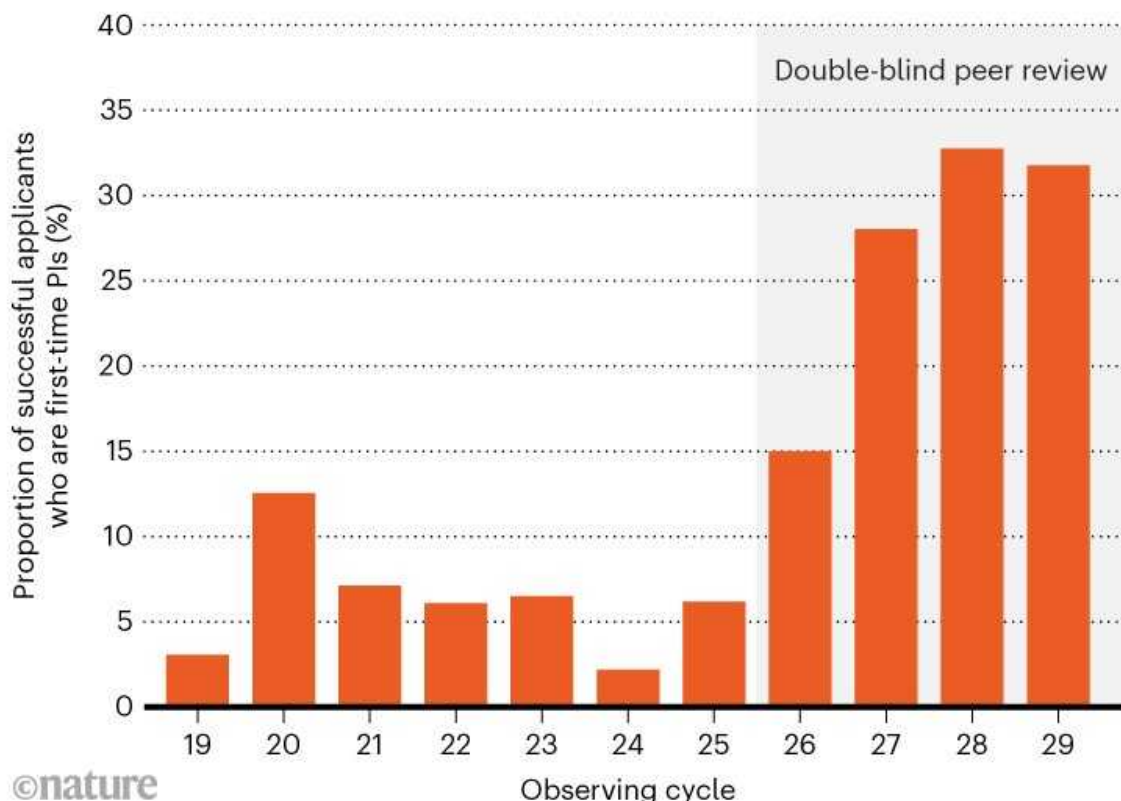
In 2018, NASA changed the way it evaluates requests for observing time on Hubble by introducing a ‘double-blind’ system, in which neither the applicants nor the reviewers assessing their proposals know each other’s identities. All the agency’s other telescopes followed suit the next year.

The move was intended to reduce gender and other biases, including discrimination against scientists who are at small research institutions, or who haven’t received NASA grants before.

Data from the Space Telescope Science Institute (STScI) show that since the change was introduced, [more first-time principal investigators have been securing viewing time on Hubble](#). In 2018, a record-breaking 15% of successful proposals came from applicants who hadn’t been awarded observation time before. That proportion rose to just under 32% in 2021 (see ‘First-time observers’).

## FIRST-TIME OBSERVERS

Since the introduction of double-blind peer review for proposals in 2018 (cycle 26), higher numbers of new principal investigators have won observing time on the Hubble Space Telescope.



Source: STScI

Increasing numbers of female researchers have also secured Hubble observing time in recent years, according to STScI data. This year, just over 29% of successful applications were from female principal investigators. And in 2018, women had a higher application success rate than men for the first time.

Double-blind review has the potential to level the playing field for under-represented groups, says Priyamvada Natarajan, an astrophysicist at Yale University in New Haven, Connecticut. “This is a first step in mitigating biases,” she says.

NASA has rolled out double-blind review to all of its upcoming programmes, and some other organizations have adopted similar systems for allocating telescope time and research grants. These include the European Southern Observatory in Garching, Germany, and the Atacama Large Millimeter/submillimeter Array in Chile's Atacama Desert.

*Nature* **600**, 195 (2021)

doi: <https://doi.org/10.1038/d41586-021-03618-9>

---

This article was downloaded by **calibre** from <https://www.nature.com/articles/d41586-021-03618-9>

| [Section menu](#) | [Main menu](#) |

- NEWS
- 02 December 2021
- Correction [07 December 2021](#)

# How bad is Omicron? What scientists know so far

COVID researchers are working at breakneck speed to learn about the variant's transmissibility, severity and ability to evade vaccines.

- [Ewen Callaway](#) &
- [Heidi Ledford](#)



South Africa is dealing with a large uptick in COVID cases, driven by a new, heavily mutated variant called Omicron. Credit: Guillem

Sartorio/AFP/Getty

Barely a week has elapsed since scientists in Botswana and South Africa alerted the world to a fast-spreading [SARS-CoV-2 variant now known as Omicron](#). Researchers worldwide are racing to understand the threat that the variant — now confirmed in more than 20 countries — poses to the world. Yet it might take scientists weeks to paint a more complete picture of Omicron, and to gain an understanding of its transmissibility and severity, as well as its potential to evade vaccines and cause reinfections.



### [Heavily mutated Omicron variant puts scientists on alert](#)

“Wherever I go, everyone says: tell us more about Omicron,” says Senjuti Saha, a molecular microbiologist and director of the Child Health Research Foundation in Dhaka, Bangladesh. “There is so little understanding of what’s going on, and that’s true, even for scientists.”

*Nature* rounds up what scientists know so far about the Omicron variant.

## **How fast is Omicron spreading?**

Omicron’s rapid rise in South Africa is what worries researchers most, because it suggests the variant could spark explosive increases in COVID-19 cases elsewhere. On 1 December, South Africa recorded 8,561 cases, up from the 3,402 reported on 26 November and several hundred per day in

mid-November, with much of the growth occurring in Gauteng Province, home to Johannesburg.

Epidemiologists measure an epidemic's growth using  $R$ , the average number of new cases spawned by each infection. In late November, South Africa's National Institute for Communicable Diseases (NICD) in Johannesburg determined that  $R$  was above 2 in Gauteng. That level of growth was last observed in the early days of the pandemic, Richard Lessells, an infectious-disease physician at University of KwaZulu-Natal in Durban, South Africa, told a press briefing last week.

Gauteng's  $R$  value was well below 1 in September — when Delta was the predominant variant and cases were falling — suggesting that Omicron has the potential to spread much faster and infect vastly more people than Delta, says Tom Wenseleers, an evolutionary biologist at the Catholic University of Leuven in Belgium. Based on the rise in COVID-19 cases and on sequencing data, Wenseleers estimates that Omicron can infect three to six times as many people as Delta, over the same time period. "That's a huge advantage for the virus — but not for us," he adds.

Researchers will be watching how Omicron spreads in other parts of South Africa and globally to get a better read on its transmissibility, says Christian Althaus, a computational epidemiologist at the University of Bern, Switzerland. Heightened surveillance in South Africa could cause researchers to overestimate Omicron's fast growth. But if this pattern is repeated in other countries, it would be very strong evidence that Omicron has a transmission advantage, adds Althaus. "If it doesn't happen, for example, in European countries, it means things are a bit more complex and strongly depend on the immunological landscape. So we have to wait."

Although genome sequencing is needed to confirm Omicron cases, some PCR tests can pick up a hallmark of the variant that distinguishes it from Delta. On the basis of this signal, there are preliminary indications that cases, although extremely low in number, are rising in the United Kingdom. "That's certainly not what we want to see right now and suggests that Omicron could indeed also have a transmission advantage in the UK," Althaus adds.

# Can Omicron overcome immunity from vaccines or infection?

The variant's swift rise in South Africa hints that it has some capacity to evade immunity. Around one-quarter of South Africans are fully vaccinated, and it's likely that a large fraction of the population was infected with SARS-CoV-2 in earlier waves, says Wenseleers, based on heightened death rates since the start of the pandemic.

In this context, Omicron's success in southern Africa might be due largely to its capacity to infect people who recovered from COVID-19 caused by Delta and other variants, as well as those who've been vaccinated. A 2 December preprint<sup>1</sup> from researchers at the NICD found that reinfections in South Africa have increased as Omicron has spread. "Unfortunately, this is the perfect environment for immune-escape variants to develop," says Althaus.

How well the variant spreads elsewhere might depend on factors such as vaccination and previous infection rates, says Aris Katzourakis, who researches viral evolution at the University of Oxford, UK. "If you throw it into the mix in a highly vaccinated population that has given up on other control measures, it might have the edge there."



## Omicron-variant border bans ignore the evidence, say scientists

Researchers want to measure Omicron's ability to evade immune responses and the protection they offer. For instance, a team led by Penny Moore, a

virologist at the NICD and the University of the Witwatersrand in Johannesburg, is measuring the ability of neutralizing, or virus-blocking, antibodies triggered by previous infection and vaccination to stop Omicron from infecting cells. To test this in the laboratory, her team is making ‘pseudovirus’ particles — an engineered version of HIV that uses SARS-CoV-2’s spike protein to infect cells — that match Omicron, which harbours as many as 32 changes to spike.

Another South Africa-based team, led by virologist Alex Sigal at the Africa Health Research Institute in Durban, is conducting similar tests of virus-neutralizing antibodies using infectious SARS-CoV-2 particles. So is a team led by Pei-Yong Shi, a virologist at the University of Texas Medical Branch in Galveston, who is collaborating with the makers of the Pfizer–BioNTech vaccine to determine how it holds up against Omicron. “I was really very concerned when I saw the constellation of mutations in the spike,” he says. “We just have to wait for the results.”

Previous studies of Omicron’s spike mutations — particularly in the region that recognizes receptors on human cells — suggest that the variant will blunt the potency of neutralizing antibodies. For instance, in a September 2021 *Nature* paper<sup>2</sup>, a team co-led by Paul Bieniasz, a virologist at Rockefeller University in New York City, engineered a highly mutated version of spike — in a virus incapable of causing COVID-19 — that shares numerous mutations with Omicron. The ‘polymutant spike’ proved fully resistant to neutralizing antibodies from most of the people they tested, who had either received two doses of an mRNA vaccine or recovered from COVID-19. With Omicron, “we expect there to be a significant hit”, says Bieniasz.



Vaccines' potency against the Omicron variant could be blunted, early analyses suggest.Credit: Horacio Villalobos/Corbis/Getty

## How will vaccines fare against Omicron?

If Omicron can dodge neutralizing antibodies, it does not mean that immune responses triggered by vaccination and prior infection will offer no protection against the variant. Immunity studies suggest that modest levels of neutralizing antibodies may protect people from severe forms of COVID-19, says Miles Davenport, an immunologist at the University of New South Wales in Sydney, Australia.

Other aspects of the immune system, particularly T cells, may be less affected by Omicron's mutations than are antibody responses. Researchers in South Africa plan to measure the activity of T cells and another immune player called natural killer cells, which might be especially important for protection against severe COVID-19, says Shabir Madhi, a vaccinologist at the University of the Witwatersrand.

Madhi, who has led COVID-19 vaccine trials in South Africa, is also part of efforts to conduct epidemiological studies of vaccines' effectiveness against Omicron. There are anecdotal reports of breakthrough infections involving all three vaccines that have been administered in South Africa — Johnson & Johnson, Pfizer–BioNTech and Oxford–AstraZeneca. But Madhi says researchers will want to quantify the level of protection against Omicron provided by vaccines, as well as by previous infection.

He suspects that the results will be reminiscent of how the AstraZeneca–Oxford vaccine performed against the Beta variant, an immune-evasive variant that was identified in South Africa in late 2020. A trial led by Madhi found that the vaccine offered little protection against mild and moderate disease, while a real-world analysis in Canada showed greater than 80% protection against hospitalization.

If Omicron behaves similarly, Madhi says, “we’re going to see a surge of cases. We’re going to see lots of breakthrough infections, lots of reinfections. But there’s going to be this unhinging of the case rate in the community compared to the hospitalization rate”. Early reports suggest that most breakthrough infections with Omicron have been mild, says Madhi. “For me, that is a positive signal.”

## **Will current boosters improve protection against Omicron?**

The threat of Omicron has prompted some rich countries, such as the United Kingdom, to accelerate and broaden the roll-out of COVID vaccine booster doses. But it’s not yet clear how effective these doses will be against this variant.

Third doses supercharge neutralizing-antibody levels, and it’s likely that this will provide a bulwark against Omicron’s ability to evade these antibodies, says Bieniasz. His team’s work on the polymutant spike found that people who had recovered from COVID-19 months before receiving their jabs had antibodies capable of blocking the mutant spike. To Bieniasz, those results suggest that people with repeated exposure to SARS-CoV-2’s spike protein,

be it through infection or a booster dose, are “quite likely to have neutralizing activity against Omicron”.

## **Does Omicron cause milder or more severe disease than previous variants?**

Early reports linked Omicron with mild disease, raising hopes that the variant might be less severe than some of its predecessors. But these reports — which are often based on anecdotes or scant scraps of data — can be misleading, cautions Müge Çevik, an infectious-disease specialist at the University of St Andrews, UK. “Everyone is trying to find some data that could guide us,” she says. “But it’s very difficult at the moment.”

A major challenge when assessing a variant’s severity is how to control for the many confounding variables that can influence the course of disease, particularly when outbreaks are geographically localized. For example, reports of mild disease from Omicron infection in South Africa could reflect the fact that the country has a relatively young population, many of whom have already been exposed to SARS-CoV-2.

During the early days of the Delta outbreak, there were reports that the variant was causing more serious illness in children than did other variants — an association that dissolved once more data were collected, Çevik says.

Researchers will be looking for data on Omicron infections in other countries. This geographical spread, and a larger sample size as cases accrue, will give researchers a better idea of how generalizable the early reports of mild disease might be. Ultimately, researchers will want to conduct case-controlled studies, in which two groups of participants are matched in terms of important factors such as age, vaccination status and health conditions. Data from both groups will need to be collected at the same time, because the number of hospitalizations can be influenced by overall hospital capacity in a region.

And, crucially, researchers will need to control for the level of economic deprivation. A rapidly spreading new variant may reach vulnerable groups

more rapidly, Çevik says, by nature of their work or living conditions. And such groups often experience more severe disease.

All of this will take time. “I think the severity question will be one of the last bits that we’ll be able to untangle,” she says. “That’s how it happened with Delta.”

## Where has Omicron spread and how are scientists tracking it?

More countries are detecting the Omicron variant, but the capacity to rapidly sequence viruses from positive COVID-19 tests is concentrated in wealthy countries, meaning that early data on Omicron’s spread will be skewed.

Surveillance efforts in Brazil and some other countries are taking advantage of a distinctive result on a particular PCR test that could allow them to pinpoint potential Omicron cases for sequencing, says virologist Renato Santana at the Federal University of Minas Gerais in Brazil. The test looks for segments of three viral genes, one of which is the gene that encodes for the spike protein. Mutations in Omicron’s spike gene prevent its detection in the test, meaning that samples containing the variant will test positive for only two of the genes.

Even so, not everyone uses that test and it could take some time before Omicron’s spread is fully mapped. Despite some guidelines urging countries to sequence 5% of their samples that test positive for SARS-CoV-2, few can afford to do so, says computational virologist Anderson Brito at the All for Health Institute in São Paulo, Brazil. And Brito worries that the [travel bans](#) enacted by some countries against South Africa, and other southern African nations, in the wake of its Omicron discovery could discourage governments from sharing genomic surveillance data. “We are punishing those who did a good job,” he says.

In Bangladesh, which sequences about 0.2% of positive coronavirus samples, researchers would be eager to ramp up sequencing to keep tabs on Omicron and other emerging variants, says Saha. But resources are limited. Bangladesh is recovering from a large dengue outbreak, she adds. “In the

global south, we are all worried about COVID, but let's not forget our endemic diseases," Saha says. "We can only do so many."

*Nature* **600**, 197-199 (2021)

doi: <https://doi.org/10.1038/d41586-021-03614-z>

## Updates & Corrections

- **Correction 07 December 2021:** An earlier version of this story misspelt Richard Lessells' name.

## References

1. 1.

Pulliam, J. R. C. *et al.* Preprint at medRxiv  
<https://doi.org/10.1101/2021.11.11.21266068> (2021).

2. 2.

Schmidt, F. *et al.* *Nature* <https://doi.org/10.1038/s41586-021-04005-0> (2021).

---

This article was downloaded by **calibre** from <https://www.nature.com/articles/d41586-021-03614-z>

- NEWS
- 02 December 2021

# Omicron-variant border bans ignore the evidence, say scientists

Researchers say travel restrictions in response to the newly detected coronavirus variant come too late and could even slow studies of Omicron.

- [Smriti Mallapaty](#)



Passengers in a largely empty terminal wait for a flight in Cape Town, South Africa. Credit: David Silverman/Getty

More than 50 countries have stepped up border controls to slow the spread of Omicron, a [highly mutated](#) SARS-CoV-2 variant of concern that is sweeping through South Africa. But researchers say many of the restrictions — especially those targeting only travellers from a handful of countries —

are unlikely to keep Omicron out, and come at significant cost to the countries concerned.

Scientists in some of the affected countries also say that travel bans risk slowing down urgent research on Omicron, by limiting the arrival of imported lab supplies.

“I’m not that optimistic that the way in which these measures are being rolled out right now will have an impact,” says Karen Grépin, a health economist at the University of Hong Kong, who studies border-control measures.

“It’s too late. The variant is circulating globally,” agrees Kelley Lee, who studies global health at Simon Fraser University in Burnaby, Canada.

## Dangerous deterrent

Most travel bans target South Africa, which raised the alarm about Omicron on 24 November, and Botswana, which also reported early cases. Many nations are also banning visitors from neighbouring Lesotho, Eswatini, Zimbabwe and Namibia.

In South Africa’s most populous province, Gauteng, Omicron accounts for the majority of virus samples sequenced in the past few weeks. The World Health Organization (WHO) has designated Omicron a variant of concern because it has numerous mutations in its spike protein, some of which could make it more infectious or improve its ability to evade antibodies.



### [Heavily mutated Omicron variant puts scientists on alert](#)

The extent of travel restrictions varies. The United States is preventing only non-US citizens who have been in selected countries from entering; Australia is also requiring 14 days of quarantine for its own citizens and residents who have visited those countries in the past two weeks.

Researchers say border restrictions might deter nations from alerting the world to future variants. They will also slow down urgent research, because few planes carrying cargo — including lab supplies needed for sequencing — are now arriving in South Africa. Researchers are racing to understand how Omicron's transmissibility and ability to evade immunity created by vaccines differ from those of pre-existing variants of SARS CoV-2. They're also investigating the relative severity of the illness Omicron causes.

“The travel ban will paradoxically affect the speed at which scientists are able to investigate,” says Shabir Madhi, a vaccinologist at the University of the Witwatersrand in Johannesburg, South Africa. Researchers might also struggle to share samples with global collaborators.

## **Threat to genomic surveillance**

Tulio de Oliveira, a bioinformatician at the University of KwaZulu-Natal in Durban, South Africa, says the slashing of commercial flights could threaten crucial genomic surveillance efforts by a network of institutions in the

country. “By next week, if nothing changes, we will run out of sequencing reagents,” he says.

Earlier this week, in response to the border restrictions, the WHO published guidance that recommended against travel bans to control viral spread. The advice includes specific recommendations for measures that would be useful, including quarantining new arrivals, and testing travellers for SARS-CoV-2 before and after they make their journeys.

The WHO guidance represents [a clear shift](#) in researchers’ understanding of the effectiveness of travel restrictions over the course of the pandemic. Before COVID-19, scattered data led many public-health agencies to denounce border restrictions — although almost every country imposed them in early 2020 anyway. But the pandemic has revealed that restrictions can be useful in certain contexts<sup>1</sup>, especially for relatively geographically isolated nations such as Australia<sup>2</sup> and New Zealand.

However, more rigorous studies are needed to flesh out when and how restrictions work best, in particular for countries with more porous borders, says Steven Hoffman, an international lawyer and epidemiologist at York University in Toronto, Canada.

## Buying time

One clear lesson has been that restrictions are most effective when they are implemented rapidly, but the Omicron-related border closures were too late, says Grépin.

The variant has now been detected on every populated continent and in more than 20 countries and territories, including the Netherlands, the United Kingdom, Australia and Japan. Some nations acquired the infection even before South Africa reported the variant to the WHO. “As soon as countries start looking for it, they’re finding it, so the advantage of time is probably gone,” says Grépin.



## What the data say about border closures and COVID spread

Restrictions are also probably most effective at slowing the number of initial cases in a country when they reduce the total volume of international arrivals, rather than when they pick and choose specific countries, says Lee.

For example, one modelling study<sup>3</sup> from the Canadian province of Newfoundland and Labrador, which closed its borders to non-residents on 4 May 2020, found that the restrictions helped to reduce the average number of COVID-19 cases by 92% in the 9 weeks after they were imposed.

For border-control measures to be effective, they also need to be comprehensive, including regular testing and at least a week of quarantine<sup>4,5</sup> for those travellers who do arrive, says Catherine Worsnop, who studies international cooperation during global health emergencies at the University of Maryland in College Park. But this, she says, is something “most countries have not done”.

Border-control measures should be used alongside efforts to strengthen public-health interventions such as social distancing, mask wearing and vaccination, says Grépin, because genomic studies<sup>6</sup> have shown that cases will eventually slip through.

Ultimately, travel restrictions are intended to buy countries time to prepare their health systems for Omicron’s potential impact. But unless they

implement domestic measures, it's hard to know what "we're buying time for", adds Worsnop.

*Nature* **600**, 199 (2021)

doi: <https://doi.org/10.1038/d41586-021-03608-x>

## References

1. 1.

Grépin K. A. *et al.* *BMJ Glob. Health* **6**, e004537 (2021).

2. 2.

Chang, S. L. *et al.* *Nature Commun.* **11**, 5710 (2020).

3. 3.

Hurford, A., Rahman, P. & Loredo-Osti, J. C. *R. Soc. Open Sci.* **8**, 202266 (2021).

4. 4.

Tu, H. *et al.* *BMJ* **375**, e066121 (2021).

5. 5.

Yang, B. *et al.* *Lancet Reg. Health West. Pac.* **13**, 100184 (2021).

6. 6.

McLaughlin, A. *et al.* Preprint at medRxiv  
<https://doi.org/10.1101/2021.04.09.21255131> (2021).

| [Section menu](#) | [Main menu](#) |

- NEWS EXPLAINER
- 30 November 2021

# What the Moderna–NIH COVID vaccine patent fight means for research

Collaborators are locked in a high-stakes dispute over which researchers should be named as inventors on a key vaccine patent application.

- [Heidi Ledford](#)



Moderna's COVID-19 vaccine is at the centre of a patent dispute that could potentially affect future public-private collaborations. Credit: Moch Farabi

Wardana/Pacific Press/LightRocket/Getty

It was a testament to the power of collaboration: scientists at the biotechnology firm Moderna Therapeutics teamed up with government researchers at the US National Institutes of Health (NIH) to [swiftly produce one of the world's first successful COVID-19 vaccines.](#)

But a boiling patent dispute between the collaborators also showcases the complexities of teamwork, as the two groups battle over whether NIH researchers were unfairly left off as co-inventors on a pivotal vaccine patent application.

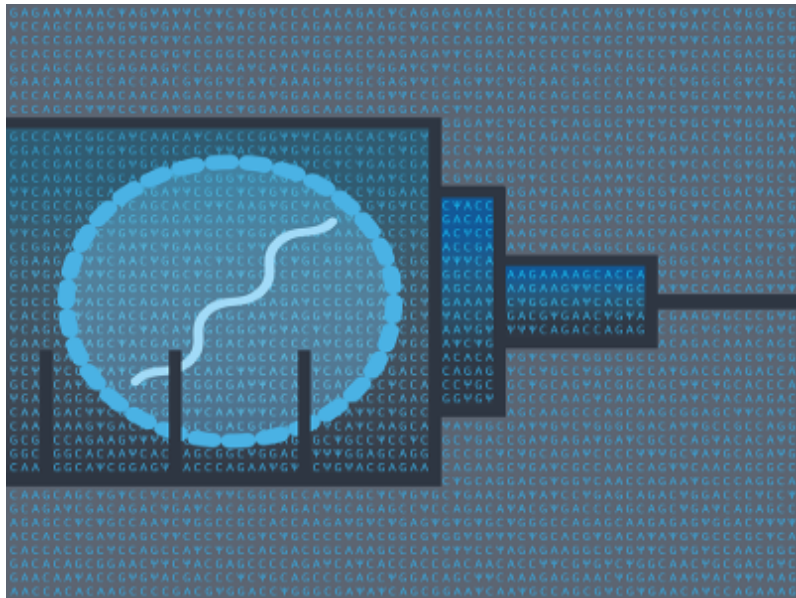
The stakes are high. Moderna, which is based in Cambridge, Massachusetts, has projected that it will make up to US\$18 billion on its COVID-19 vaccine this year. Inventor status could enable the NIH to collect royalties — potentially recouping some of its investment of taxpayer money — and to license the patent as it sees fit, including to competing vaccine makers in low- and middle-income countries, where vaccines are still painfully scarce.

*Nature* looks at four key questions about the patent spat and its potential ripple effects on collaborations between government and industry.

## What are Moderna and the NIH fighting about?

Before the COVID-19 pandemic struck, the NIH and Moderna collaborated on the development of vaccines for other coronaviruses. So, when the news of the SARS-CoV-2 outbreak reached them, it was only natural that they work together on producing a vaccine.

The vaccine they created contains mRNA that encodes a modified form of the SARS-CoV-2 spike protein. The modifications were intended to hold the protein in a stable conformation that was deemed likely to trigger an immune response. The NIH has stated in the past that these modifications were developed by researchers at its National Institute of Allergy and Infectious Diseases and other collaborators, and it published analogous modifications in another coronavirus in 2017<sup>1</sup>.



## The tangled history of mRNA vaccines

In drug and vaccine development, it is common for inventors to file multiple patents — often dozens or more — to cover different aspects of a single product. Moderna has filed several patent applications on its COVID-19 vaccine that name NIH investigators as co-inventors.

But some of its patent applications do not, including at least one that claims the mRNA sequence used in the vaccine. In an August statement to the US Patent and Trademark Office, Moderna acknowledged that the NIH had submitted three of its researchers as co-inventors, but stood by its decision to exclude them from the application.

The company argues that its researchers independently developed the mRNA sequence for the vaccine. NIH researchers, however, have said that they developed the sequence and shared it with the company.

The patent in question could be particularly critical because it covers the principal component of the vaccine, says Christopher Morten, who specializes in intellectual-property law at Columbia Law School in New York City: “A claim on the active ingredient in a pharmaceutical product is important, because it can be impossible for competitors to design around it.”

## Is it unusual for collaborators to fight over inventor status on a patent?

Disputes over who deserves to be credited on a patent are common, particularly in collaborations between institutions, says Rebecca Eisenberg, who studies patent law and biopharmaceutical regulation at the University of Michigan Law School in Ann Arbor. There can be different ways of defining an invention, for example, or patents can be structured such that they only include one group's contribution. "Whoever drafts the application tends to draft around what they've done," she says.



### In shock move, US backs waiving patents on COVID vaccines

An inventor is defined by US patent law as someone who aids in the conception of the invention. Individual inventors in universities, government agencies and company laboratories often assign their patent rights to the institution that they work for. But when it comes to collaborations, it can be difficult to agree up front who will be named as an inventor on the patent. "You can address in advance who's going to own the patent rights, but you can't necessarily specify who is going to be an inventor," says Eisenberg.

In the 1990s, the NIH was involved in a patent dispute with industry collaborators over the development of the HIV drug AZT. Two generics

makers that wanted to challenge AZT patents argued that NIH researchers had been unfairly omitted from some of them — in which case, the patents could have been rendered invalid, or the NIH would have had the right to license them. But the court sided with the pharmaceutical companies, which argued that they had already prepared their patent application before using the NIH's assay. The analysis, they said, simply confirmed the value of something that they had already invented.

The NIH lost the AZT case, but that does not mean it is at a disadvantage in this one, says Eisenberg: "Every case is idiosyncratic."

## Will the patent snub affect future public–private partnerships?

The US government has a reputation for not aggressively enforcing its patent rights, says Chad Landmon, a patent attorney at the law firm Axinn, Veltrop & Harkrider in Hartford, Connecticut. Instead, the government often funds early-stage research, and then largely leaves it to industry partners to manage intellectual property on later stages of an invention. Pharmaceutical companies often invest heavily — sometimes in the order of hundreds of millions of dollars — in the final development of a therapy; the government has generally considered the potential benefit to taxpayers as the main reward for funding early research.

But political sentiment on this could be shifting, Landmon says. Several of the Democratic presidential candidates in the 2020 election — including Kamala Harris, now vice-president — pushed for the government to become more assertive about intellectual property, particularly if by doing so it could rein in the prices of prescription drugs. And in 2019, the government took the unusual step of suing Gilead Sciences in Foster City, California, for infringing government patents in the production of HIV-prevention drugs.

Then came the pandemic, and concerns that patents could restrict vaccine production. At a meeting of the World Trade Association in May, the United States made a surprise announcement that it supported [waiving patent protection on COVID-19 vaccines](#).



## COVID vaccine boosters: the most important questions

This, plus the NIH's outcry over its exclusion from the Moderna patent, could suggest that the government will take a more active stance in managing intellectual property, Landmon says: "My general sense is that it's pointing in that direction."

In 2020, Morten and a collaborator analysed patents on the antiviral drug remdesivir, which has been used as a treatment for COVID-19. They determined that government researchers had probably contributed to the drug's development but been left off the patents. A subsequent government investigation, however, concluded that the scientists' work had not contributed to the inventions in the patents.

If the government does become tougher about licensing patents, "it might lead companies to be pickier in terms of deciding if they are going to collaborate with the government", says Landmon.

Any change in government policy is unlikely to happen rapidly, says Ana Santos Rutschman, who specializes in health law at Saint Louis University in Missouri. But she thinks that a change could be on the horizon. "At the end of the day, it's not just about this particular patent," she says. "Public scrutiny is as important as legal scrutiny."

## **What happens now?**

In November, NIH chief Francis Collins was quoted by Reuters news agency as saying that the patent dispute was not yet over. “Clearly this is something that legal authorities are going to have to figure out,” he said.

Moderna has said that it offered the NIH co-ownership of the patent in September, and that the agency could then license the patent “as they see fit”. But this is different from inventor status: terms of co-ownership would need to be negotiated, and could come with strings attached, says Morten. The NIH might also want its scientists on the patent for scientific credit or political reasons, says Lisa Ouellette, who specializes in vaccine production and patent law at Stanford Law School in California.



### The fight to manufacture COVID vaccines in lower-income countries

The NIH could choose to bring a lawsuit and argue in court that Moderna inappropriately left off NIH researchers. If the court determines that the NIH is correct, and that the omission was an unintentional oversight, the patent might be corrected. But if the court finds that Moderna knowingly deceived the patent office about NIH’s contribution, the patent would no longer be valid.

Such a case could involve poring over lab notebooks to investigate when Moderna investigators determined the mRNA sequence used in the vaccine, and whether this pre-dated the NIH team sharing its mRNA sequence with the company, says Morten.

The potential impact of the case on vaccine production is uncertain. Moderna has already said that it would not enforce its patents on its COVID vaccine during the pandemic, and patents are generally not the key hurdle to vaccine production, says Ouellette.

Still, given the unusually high stakes in this dispute, it is likely that any decision would prompt an appeal — potentially all the way to the US Supreme Court — and the battle could drag out for years. “With this patent, you could imagine the magnitude of the importance of making sure it is correct,” says Joy Goswami, a technology-transfer officer at the University of Delaware in Newark. “This is probably going to be a long run.”

*Nature* **600**, 200-201 (2021)

doi: <https://doi.org/10.1038/d41586-021-03535-x>

## References

1. 1.

Pallesen, J. *et al.* *Proc. Natl Acad. Sci. USA* **114**, E7348–e7357 (2017).

---

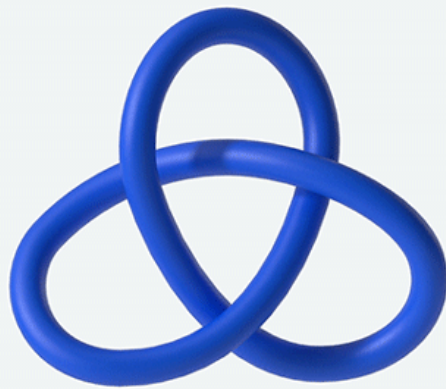
This article was downloaded by **calibre** from <https://www.nature.com/articles/d41586-021-03535-x>

- NEWS
- 01 December 2021

# DeepMind's AI helps untangle the mathematics of knots

The machine-learning techniques could benefit other areas of maths that involve large data sets.

- [Davide Castelvecchi](#)



Knot theorists proved the validity of a mathematical formula about knots after using machine learning to guess what the formula should be. Credit: DeepMind

For the first time, machine learning has spotted mathematical connections that humans had missed. Researchers at artificial-intelligence powerhouse DeepMind, based in London, teamed up with mathematicians to tackle two

separate problems — one in the theory of knots and the other in the study of symmetries. In both cases, AI techniques helped the researchers discover new patterns that could then be investigated using conventional methods.

“I was very struck at just how useful the machine-learning tools could be as a guide for intuition,” says Marc Lackenby at the University of Oxford, UK, one of the mathematicians who took part in the study. “I was not expecting to have some of my preconceptions turned on their head.”



### [AI maths whiz creates tough new problems for humans to solve](#)

Computer simulations and visualizations of knots and other objects have long helped mathematicians to look for patterns and develop their intuition, says Jeffrey Weeks, a mathematician based in Canton, New York, who has pioneered some of those techniques since the 1980s. But, he adds, “Getting the computer to seek out patterns takes the research process to a qualitatively different level.”

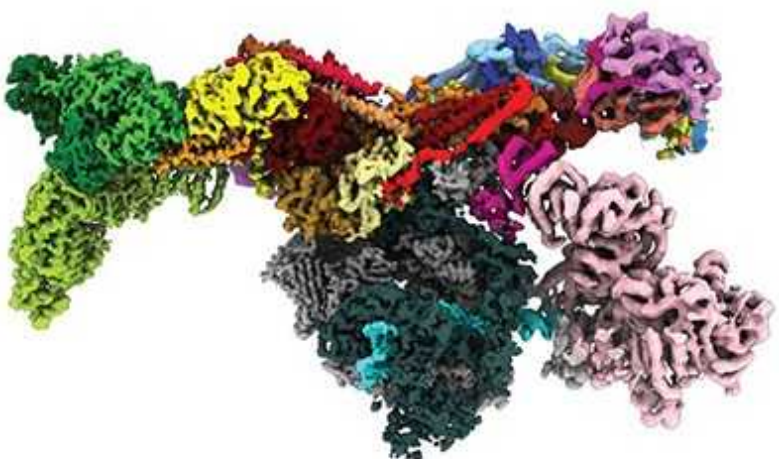
The authors say the approach, described in a paper in the 2 December issue of *Nature*<sup>1</sup>, could benefit other areas of maths that involve large data sets.

## **Maths versus machine**

DeepMind, a sister company of Google, has made headlines with breakthroughs such as cracking the game Go, but its long-term focus has been scientific applications such as [predicting how proteins fold](#).

The idea for a maths collaboration was sparked by a casual conversation in 2019 between mathematician Geordie Williamson at the University of Sydney in Australia and DeepMind's chief executive, neuroscientist Demis Hassabis. Lackenby and a colleague at Oxford, András Juhász, both knot theorists, soon joined the project.

Initially, the work focused on identifying mathematical problems that could be attacked using DeepMind's technology. Machine learning enables computers to feed on large data sets and make guesses, such as matching a surveillance-camera image to a known face from a database of photographs. But its answers are inherently probabilistic, and mathematical proofs require certainty.



### [DeepMind's AI predicts structures for a vast trove of proteins](#)

But the team reasoned that machine learning could help to detect patterns, such as the relationship between two types of object. Mathematicians could then try to work out the precise relationship by formulating what they call a conjecture, and then attempting to write a rigorous proof that turns that statement into a certainty.

Because machine learning requires lots of data to train on, one requirement was to be able to calculate properties for large numbers of objects: in the

case of knots, the team calculated several properties, called invariants, for millions of different knots.

The researchers then moved on to working out which AI technique would be most helpful for finding a pattern that linked two properties. One technique in particular, called saliency maps, turned out to be especially helpful. It is often used in computer vision to identify which parts of an image carry the most-relevant information. Saliency maps pointed to knot properties that were likely to be linked to each other, and generated a formula that seemed to be correct in all cases that could be tested. Lackenby and Juhász then provided a rigorous proof that the formula applied to a very large class of knots<sup>2</sup>.

“The fact that the authors have proven that these invariants are related, and in a remarkably direct way, shows us that there is something very fundamental that we in the field have yet to fully understand,” says Mark Brittenham, a knot theorist at the University of Nebraska–Lincoln who frequently uses computational techniques. Brittenham adds that although machine learning has been used in knot theory before, the authors’ technique is novel in its ability to discover surprising connections.

## Solving symmetries

Williamson focused on a separate problem, regarding symmetries. Symmetries that switch around finite sets of objects have an important role in several branches of maths, and mathematicians have long studied them using various tools, including graphs — large abstract networks linking thousands of nodes — and algebraic expressions called polynomials. For decades, researchers have suspected that it would be possible to calculate the polynomials from the networks, but guessing how to do it seemed like a hopeless task, Williamson says. “Very quickly, the graph becomes beyond human comprehension.”

### [AI Copernicus ‘discovers’ that Earth orbits the Sun](#)

With the computer’s help, he and the rest of the team noticed that it should be possible to break down the graph into smaller, more-manageable parts,

one of which has the structure of a higher-dimensional cube. This gave Williamson a solid conjecture to work on for the first time.

“I was just blown away by how powerful this stuff is,” says Williamson. Once the algorithm zeroed in on a pattern, it was able to guess very precisely which graphs and polynomials came from the same symmetries. “How quickly the models were getting accuracy — that for me was just shocking,” he says. “I think I spent basically a year in the darkness just feeling the computers knew something that I didn’t.”

Whether Williamson’s conjecture will prove true is still an open question. Conjectures sometimes take a long time for the mathematical community to crack, but they can help to shape entire fields.

## Wider applications

Throughout the project, the researchers had to tailor the AI techniques to the two different mathematical problems, says Alex Davies, a computer scientist at DeepMind. “We did not originally expect these to be the most useful techniques,” he says.

“Any area of mathematics where sufficiently large data sets can be generated could benefit from this approach,” says Juhász, adding that the techniques they demonstrated could also find applications in fields such as biology or economics.



[Abel Prize celebrates union of mathematics and computer science](#)

Adam Zsolt Wagner, a mathematician at Tel Aviv University, Israel, who has used machine learning, says that the authors' methods could prove valuable for certain kinds of problems. "Without this tool, the mathematician might waste weeks or months trying to prove a formula or theorem that would ultimately turn out to be false." But he adds that it is unclear how broad its impact will be.

At a press conference, Davies told reporters that the project has given him a "real appreciation" for the nature of mathematical research. Learning maths at school is akin to playing scales on a piano, he added, whereas real mathematicians' work is more like jazz improvisations.

Williamson agrees that the work highlights a more exciting aspect of maths than people normally see. "As mathematical researchers, we live in a world that is rich with intuition and imaginations," he says. "Computers so far have served the dry side. The reason I love this work so much is that they are helping with the other side."

"My personal guess is that computer-generated conjectures will become ever more useful in 'filling in the details', but will never replace human intuition and creativity," says Weeks.

*Nature* **600**, 202 (2021)

doi: <https://doi.org/10.1038/d41586-021-03593-1>

## References

1. 1.

Davies, A. *et al.* *Nature* **600**, 70–74 (2021).

2. 2.

Davies, A., Juhász, A., Lackenby, M. & Tomasev, N. Preprint at <https://arxiv.org/abs/2111.15323> (2021).

---

This article was downloaded by **calibre** from <https://www.nature.com/articles/d41586-021-03593-1>

| [Section menu](#) | [Main menu](#) |

- NEWS
- 30 November 2021

# China's Mars rover has amassed reams of novel geological data

Data collected by the Tianwen-1 mission and Zhurong Mars rover are offering insights into a previously unexplored region of Mars's northern hemisphere.

- [Smriti Mallapaty](#)



In July, Zhurong took this image of the landing site of the parachute and part of the capsule that had carried it safely to the surface. Credit: CNSA

More than 30 scientists across the Chinese mainland, Hong Kong and Macau are rushing to process data collected by China's Mars rover, Zhurong, and

by the nation's Tianwen-1 spacecraft, which is in orbit around the planet. Several studies have trickled out, but researchers say that more are coming in the next weeks and months, offering insights on the climate, geology and history of Mars's northern hemisphere.

Since September, the National Astronomical Observatories of the Chinese Academy of Sciences (NAOC), which has been receiving the data from space, has released nearly 200 gigabytes of information that was collected from eight instruments on the rover and orbiter between February and June. These instruments include cameras, a radar system, climate sensors and a laser spectrometer.



### Why the China Mars rover's landing site has geologists excited

Some surface features, such as possible sedimentary material and [potential mud volcanoes](#), hint at the historical flow of water, so scientists are looking for any clues that there was once water or ice below the surface. This is "of great scientific interest" because it might provide evidence of an ancient ocean, says Bo Wu, a planetary scientist at the Hong Kong Polytechnic University, who is analysing some of the data.

Tianwen-1 arrived at Mars [in February](#). In May, it [dropped](#) a lander containing Zhurong onto a vast basin known as Utopia Planitia. The rover's initial mission was intended to be only about three months long, but it has exceeded expectations. Over a period of four months, the rover travelled more than 1,000 metres, visiting features of interest and even investigating

part of the capsule that brought it to the surface, along with the remains of the descent parachute.

## Pause in communications

In September, Zhurong was powered down into hibernation by the China National Space Administration (CNSA) because Mars had passed behind the Sun, relative to Earth, meaning that communication was lost. However, in October it was powered up again, and it has traversed another 200 metres in the direction of what might once have been the coastline of an ancient ocean.

The month-long break offered mission scientists at research institutes across China a chance to start analysing data. Some researchers had already received images of Mars from the orbiter's cameras in March, and the CNSA had previously shared with the public images and videos taken by the rover during its descent and from the surface. But now researchers are studying the much larger volume of data released in September.

This data set includes images from Zhurong's navigation camera; climatic data on temperature, pressure and wind speed; information on the chemical composition of rocks, soil and sand dunes from a laser spectrometer; and clues from below the surface from its ground-penetrating radar.

Apart from the [handful of images](#) and [videos](#) released by the CNSA, few scientific insights about the mission have been released or published until now. Researchers say this is because it has taken time to process and clean up the data.

Doing this ensures that the data are reliable and removes noise produced by the instruments, says Lu Pan, a planetary scientist at the University of Copenhagen. The fact that this mission is China's first to the surface of another planet might also have slowed things down compared with NASA's recent Mars missions. "If this is the first time you do it, there's a learning process," she says.

David Flannery, an astrobiologist at Queensland University of Technology in Brisbane, Australia, who is in communication with scientists in China, says that the team's approach to managing data could also have contributed to the

delay in releasing new insights. With NASA's Perseverance mission, which Flannery is involved in, each instrument on the rover is designed by a different team, which has exclusive access to data from that instrument for a few months before the data become available to all.

But under the CNSA model, the data generated for all the instruments on Zhurong and Tianwen-1 are processed by the NAOC, before making the information available to multiple teams of scientists linked to the mission.



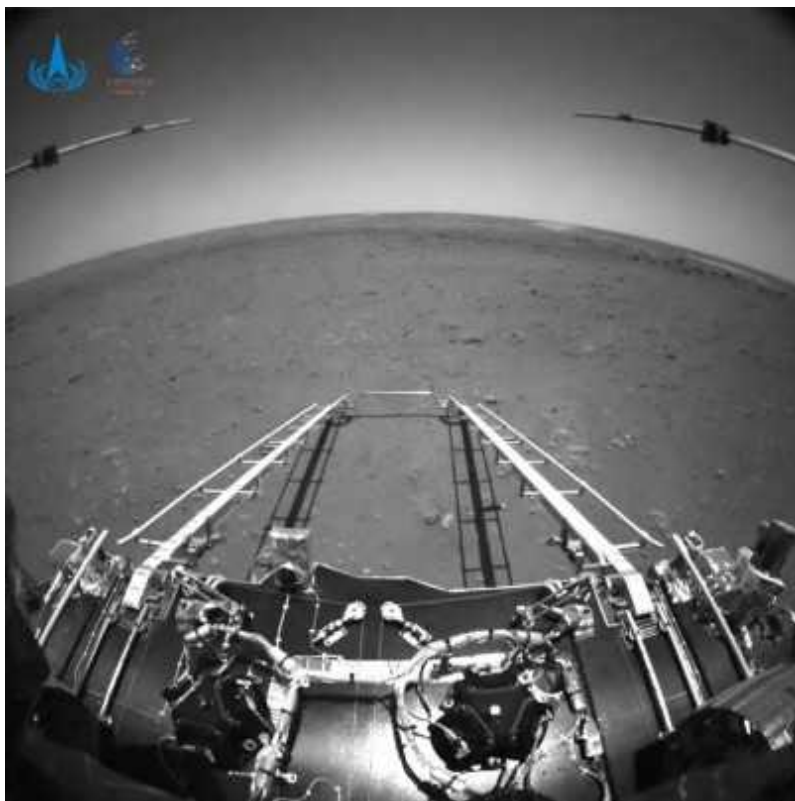
The CNSA released this image in July of the view from the lander up towards the parachute as it drifted down to the surface of Mars. Credit:

CNSA

## Speeding up the analysis

Two publications have already emerged. One study<sup>1</sup>, posted as a preprint in late September, analysed images and information on friction that were gleaned from the movement of Zhurong's wheels. The results show that regions of Mars that the rover trundled over have properties similar to those of compact, sandy soil on Earth.

The study "provides useful data about surface soil properties", says Xiao Long, a planetary geologist at the China University of Geosciences in Wuhan. This might be helpful for understanding how soil and dust on the surface formed, says Long, who is also conducting his own analysis.



[China's Mars rover returns first images — scientists say the view is promising](#)

A second study<sup>2</sup>, published in August, used high-resolution images from the orbiter to pinpoint the rover's precise coordinates on Mars. But researchers say that many more studies are expected soon, including some on the region's topography.

So far, the data have been shared only with researchers directly involved with the mission, but Wu says that the NAOC will at some point release them to the public and the international community.

That could help to speed up the analysis. Scientists with more experience of Mars might be able to recognize features of interest and their significance more quickly, says Flannery. "Mars is peculiar in some ways, and geologists are only as good as the rocks they have seen in the past," he adds.

## Next phase of the mission

Zhurong will now continue to explore, potentially for years, as some of NASA's Mars rovers have.

Tianwen-1 has also been busy. The spacecraft recently adjusted its orbit and switched from acting mainly as a communications relay between Zhurong and Earth to also conducting its own observations of Mars. Wenzhe Fa, a planetary scientist at Peking University, Beijing, who is analysing Zhurong's radar data, says that on 11 November, the CNSA deployed and began to test the antenna for the orbiter's radar.

Also earlier this month, the CNSA and the European Space Agency (ESA) trialled whether ESA's Mars Express orbiter could be used to relay Zhurong's data to Earth — an exercise that Pan says is an "amazing step" towards increased international collaboration with China.

As Zhurong resumes its journey, Bo says that he and his team are providing "suggestions for future data collection" that take in surface features of particular scientific interest.

*Nature* **600**, 203 (2021)

doi: <https://doi.org/10.1038/d41586-021-03554-8>

# References

1. 1.

Ding, L. *et al.* Preprint at Research Square  
<https://doi.org/10.21203/rs.3.rs-836162/v1> (2021).

2. 2.

Wan, W. *et al.* *Remote Sens.* **13**, 3439 (2021).

---

This article was downloaded by **calibre** from <https://www.nature.com/articles/d41586-021-03554-8>

| [Section menu](#) | [Main menu](#) |

- NEWS FEATURE
- 07 December 2021

# Beyond Omicron: what's next for COVID's viral evolution

The rapid spread of new variants offers clues to how SARS-CoV-2 is adapting and how the pandemic will play out over the next several months.

- [Ewen Callaway](#)

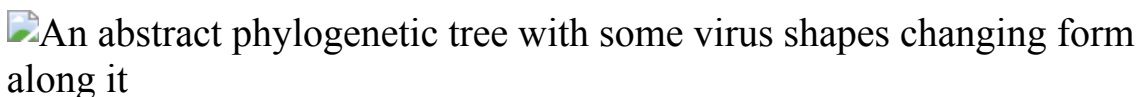


Illustration by Ana Kova

As the world sped towards a pandemic in early 2020, evolutionary biologist Jesse Bloom gazed into the future of SARS-CoV-2. Like many virus specialists at the time, he predicted that the new pathogen would not be eradicated. Rather, it would become endemic — the fifth coronavirus to permanently establish itself in humans, alongside four ‘seasonal’ coronaviruses that cause relatively mild colds and have been circulating in humans for decades or more.

Bloom, who is based at the Fred Hutchinson Cancer Research Center in Seattle, Washington, saw these seasonal coronaviruses as potentially providing a roadmap for how SARS-CoV-2 might evolve and for the future of the pandemic. But little is known about how these other viruses continue to thrive. One of the best-studied examples — a seasonal coronavirus called 229E — infects people repeatedly throughout their lives. But it’s not clear whether these reinfections are the result of fading immune responses in their human hosts or whether changes in the virus help it to dodge immunity. To find out, Bloom got hold of decades-old blood samples from

people probably exposed to 229E, and tested them for antibodies against different versions of the virus going back to the 1980s.

The results were striking<sup>1</sup>. Blood samples from the 1980s contained high levels of infection-blocking antibodies against a 1984 version of 229E. But they had much less capacity to neutralize a 1990s version of the virus. They were even less effective against 229E variants from the 2000s and 2010s. The same held true for blood samples from the 1990s: people had immunity to viruses from the recent past, but not to those from the future, suggesting that the virus was evolving to evade immunity.

“Now that we’ve had almost two years to see how SARS-CoV-2 evolves, I think there are clear parallels with 229E,” says Bloom. Variants such as Omicron and Delta carry mutations that blunt the potency of antibodies raised against past versions of SARS-CoV-2. And the forces propelling this ‘antigenic change’ are likely to grow stronger as most of the planet gains immunity to the virus through infection, vaccination or both. Researchers are racing to characterize the [highly mutated Omicron variant](#). But its rapid rise in South Africa suggests that it has already found a way to dodge human immunity.



[How bad is Omicron? What scientists know so far](#)

How SARS-CoV-2 evolves over the next several months and years will determine what the end of this global crisis looks like — whether the virus morphs into another common cold or into something more threatening such as influenza or worse. A global vaccination push that has delivered nearly 8 billion doses is shifting the evolutionary landscape, and it's not clear how the virus will meet this challenge. Meanwhile, as some countries lift restrictions to control viral spread, opportunities increase for SARS-CoV-2 to make significant evolutionary leaps.

Scientists are searching for ways to predict the virus's next moves, looking to other pathogens for clues. They are tracking the effects of the mutations in the variants that have arisen so far, while watching out for new ones. They expect SARS-CoV-2 eventually to evolve more predictably and become like other respiratory viruses — but when this shift will occur, and which infection it might resemble is not clear.

Researchers are learning as they go, says Andrew Rambaut, an evolutionary biologist at the University of Edinburgh, UK. "We haven't had much to go on."

## An early plateau

Scientists tracking the evolution of SARS-CoV-2 are looking out for two broad categories of changes to the virus. One makes it more infectious or transmissible, for instance by replicating more quickly so that it spreads more easily through coughs, sneezes and wheezes. The other enables it to overcome a host's immune response. When a virus first starts spreading in a new host, the lack of pre-existing immunity means that there is little advantage to be gained by evading immunity. So, the first — and biggest — gains a new virus will make tend to come through enhancements to infectivity or transmissibility.

"I was thoroughly expecting that this new coronavirus would adapt to humans in a meaningful way — and that would probably mean increased transmissibility," says Wendy Barclay, a virologist at Imperial College London.

Genome sequencing early in the pandemic showed the virus diversifying and [picking up about two single-letter mutations per month](#). This rate of change is about half that of influenza and one-quarter that of HIV, thanks to an error-correcting enzyme coronaviruses possess that is rare among other RNA viruses. But few of these early changes seemed to have any effect on the behaviour of SARS-CoV-2, or show signs of being favoured under natural selection.

An early mutation called D614G within the gene encoding the virus's spike protein — the protein responsible for recognizing and penetrating host cells — seemed to offer a slight transmissibility boost<sup>2</sup>. But this gain was nothing like the leaps in transmissibility that researchers would later observe with the variants Delta and Alpha, says Sarah Otto, an evolutionary biologist at the University of British Columbia in Vancouver, Canada.



### [Omicron is supercharging the COVID vaccine booster debate](#)

Otto sees the virus's evolution as like walking in a landscape, where higher elevations equate to improved transmissibility. The way she sees it, when SARS-CoV-2 began spreading in humans it seemed to be on a 'fitness plateau' surrounded by a landscape of many possible evolutionary outcomes. In any given infection, there were probably thousands of viral particles each with unique single-letter mutations, but Otto suspects that

few, if any, of these made the virus more infectious. Most changes probably reduced transmissibility.

“If the virus entered at a reasonably high point, any one-step mutation would take it downhill,” Otto says. Summiting higher peaks required the combinations of several mutations to make more-significant gains in its ability to spread.

## Reaching new heights

In late 2020 and early 2021, there were signs that SARS-CoV-2 had scaled some distant peaks. Researchers in the United Kingdom spotted a variant called B.1.1.7 that contained numerous mutations in its spike protein. “It was a bit unusual because it seemed to come out of nowhere,” says Francois Balloux, a computational biologist at University College London.

That variant — since renamed Alpha — spread at least 50% faster than earlier circulating lineages. UK public-health officials linked it to a mysterious rise in cases in southeast England during a national lockdown in November 2020. Around the same time, virus hunters in South Africa linked another mutation-laden variant called B.1.351 — now known as Beta — to a second wave of infections there. Not long after, a highly transmissible variant, now called Gamma, was tracked to Amazonas state in Brazil.

These three ‘variants of concern’ share some mutations, particularly in key regions of the spike protein involved in recognizing the host-cell ACE2 receptors that the virus uses to enter cells. They also carried mutations similar or identical to those spotted in SARS-CoV-2 in people with compromised immune systems whose infections lasted for months. This led researchers to speculate that long-term infections might allow the virus to explore different combinations of mutations to find ones that are successful. Typical infections lasting days offer fewer opportunities. Super-spreading events, where large numbers of people are infected, might also explain why some variants flourished and others fizzled out.

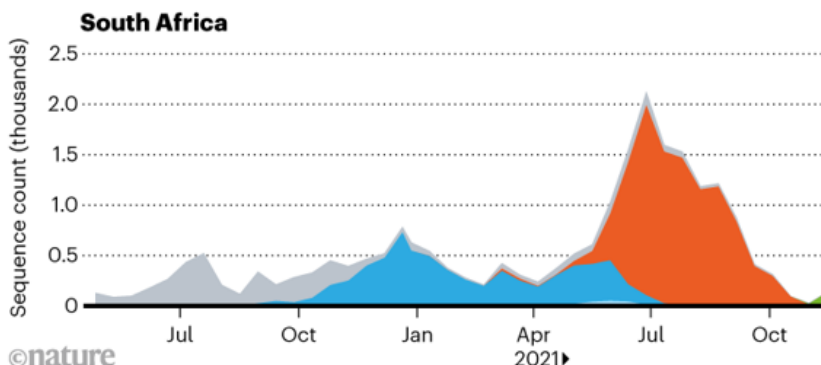
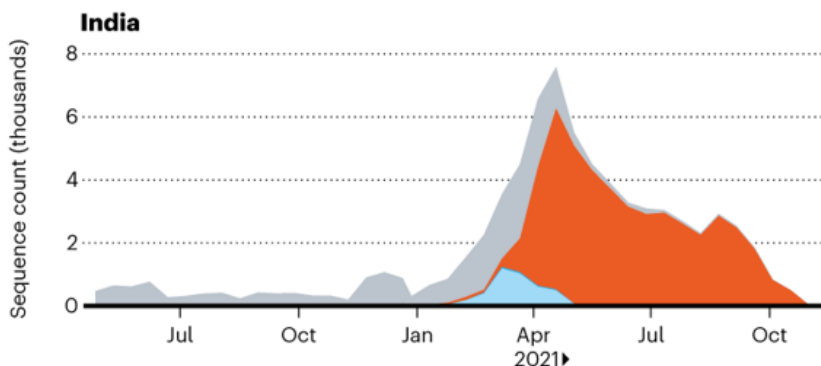
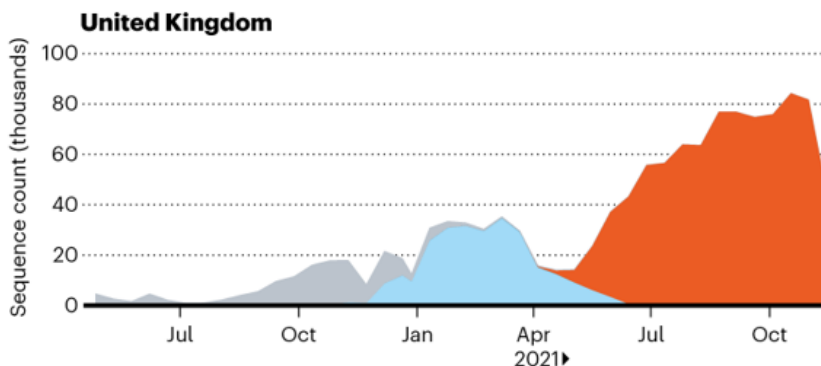
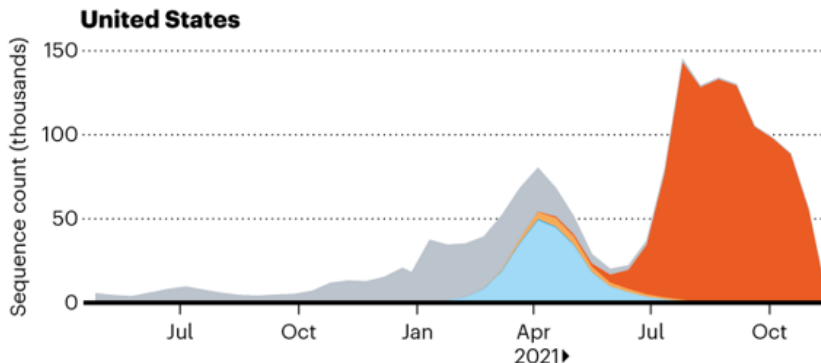
Whatever their origins, all three variants seemed to be more infectious than the strains they displaced. But Beta and Gamma also contained mutations that blunted the potency of infection-blocking ‘neutralizing’ antibodies triggered by previous infection or vaccination. This raised the possibility that the virus was beginning to behave in the ways predicted by Bloom’s studies of 229E.

The three variants spread around the world, particularly Alpha, which sparked new waves of COVID-19 as it came to dominate in Europe, North America, the Middle East and beyond (see ‘Variant waves’). Many researchers expected that a descendant of Alpha — which seemed to be the most infectious of the bunch — would pick up additional mutations, such as those that evade immune responses, to make it even more successful. “That absolutely proved not to be the case,” says Paul Bieniasz, a virologist at Rockefeller University in New York City. “Delta came out of left field.”

## VARIANT WAVES

Although SARS-CoV-2 sequences captured within a country might not be representative of the overall disease burden, they do help to show how different variants have become dominant.

■ Alpha ■ Beta ■ Delta ■ Gamma ■ Omicron ■ Other



Source: [Covariants.org](https://covariants.org)

## The Delta dilemma

The Delta variant was identified in India's Maharashtra state during a ferocious wave of COVID-19 that hit the country in the spring of 2021, and researchers are still taking stock of its consequences for the pandemic. Once it arrived in the United Kingdom, the variant spread quickly and epidemiologists determined that it was about 60% more transmissible than Alpha, making it several times as infectious as the first circulating strains of SARS-CoV-2. "Delta is kind of a super-Alpha," says Barclay. "I think the virus is still looking for solutions to adapt to the human host."

Studies from Barclay's laboratory and others suggest that [Delta made significant gains in its fitness](#) by improving its ability to infect human cells and spread between people<sup>3,4</sup>. Compared with other variants, including Alpha, Delta multiplies faster and to higher levels in the airways of infected individuals, potentially outpacing initial immune responses against the virus.

Yet researchers expect such gains to become ever smaller. Scientists measure a virus's inherent ability to spread in an immunologically naive population (that is, unvaccinated and not exposed to the virus previously) by a number called  $R_0$ , which is the average number of people an infected person infects. Since the start of the pandemic this figure has jumped as much as threefold. "At some point, I would expect that increased transmissibility will stop happening," says Bloom. "It's not going to become infinitely transmissible." Delta's  $R_0$  is higher than seasonal coronaviruses and influenza, but still lower than that of polio or measles.



## Omicron-variant border bans ignore the evidence, say scientists

Other established human viruses do not make the leaps in infectivity that SARS-CoV-2 has in the past two years, and Bloom and other scientists expect the virus to eventually behave in the same way. Trevor Bedford, an evolutionary biologist at the Fred Hutchinson, says the virus must balance its ability to replicate to high levels in people's airways with the need to keep them healthy enough to infect new hosts. "The virus doesn't want to put someone in bed and make them sick enough that they're not encountering a number of other people," he says. One way for the virus to thread this needle would be to evolve to grow to lower levels in people's airways, but maintain infections for a longer period of time, increasing the number of new hosts exposed to the virus, says Rambaut. "Ultimately there's going to be trade-off between how much virus you can produce and how quickly you elicit the immune system." By lying low, SARS-CoV-2 could ensure its continued spread.

If the virus evolved in this way, it might become less severe, but that outcome is far from certain. "There's this assumption that something more transmissible becomes less virulent. I don't think that's the position we should take," says Balloux. Variants including Alpha, Beta and Delta have been linked to heightened rates of hospitalization and death — potentially because they grow to such high levels in people's airways. The assertion

that viruses evolve to become milder “is a bit of a myth”, says Rambaut. “The reality is far more complex.”

## The rise of Omicron

Delta and its descendants now account for the vast majority of COVID-19 cases worldwide. Most researchers expected these Delta lineages to eventually outcompete the last holdouts. But Omicron has undermined those predictions. “A lot of us were expecting the next weird variant to be a child of Delta, and this is a bit of a wild card,” says Aris Katzourakis, a specialist in viral evolution at the University of Oxford, UK. Teams in Botswana and South Africa identified the variant in late November — although researchers say it is unlikely to have originated in either country — and health officials have linked it to a rapidly growing outbreak centred in South Africa’s Gauteng province. The variant harbours around 30 changes to spike, many shared with the other variants of concern, and scientists worldwide are working to gauge the threat it poses.

The swift rise in cases of Omicron in South Africa suggests that the new variant has a fitness advantage over Delta, says Tom Wenseleers, an evolutionary biologist and biostatistician at the Catholic University of Leuven in Belgium. Omicron carries some of the mutations associated with Delta’s sky-high infectivity. But if increased infectivity were the sole reason for its rapid growth, it would translate to an  $R_0$  in the 30s, Wenseleers says. “That’s very implausible.”

Instead, he and other researchers suspect that Omicron’s rise may be largely due to its ability to infect people who are immune to Delta through vaccination or previous infection.



## [COVID vaccine makers brace for a variant worse than Delta](#)

Scientists' portrait of Omicron is still blurry and it will take weeks before they can fully assess its properties. But if the variant is spreading, in part, because of its ability to evade immunity, it fits in with theoretical predictions about how SARS-CoV-2 is likely to evolve, says Sarah Cobey, an evolutionary biologist at the University of Chicago in Illinois.

As gains in SARS-CoV-2's infectivity start to slow, the virus will have to maintain its fitness through overcoming immune responses, says Cobey. For instance, if a mutation or set of mutations halved a vaccine's ability to block transmission, this could vastly increase the number of available hosts in a population. Cobey says it's hard to imagine that any future gains in infectivity could provide the same boost.

That evolutionary path, towards immune evasion and away from gains in infectivity, is common among established respiratory viruses such as influenza says Adam Kucharski, a mathematical epidemiologist at the London School of Hygiene and Tropical Medicine. "The easiest way for the virus to cause new epidemics is to evade immunity over time. That's similar to what we see with the seasonal coronaviruses."

Lab experiments and sequencing of circulating variants have identified a smorgasbord of mutations in the spike protein that [weaken the potency of](#)

neutralizing antibodies triggered by infection and vaccination. Variants carrying these mutations, such as Beta, have blunted the effectiveness of vaccines. But they have not obliterated the protection that the shots offer, particularly against severe disease.

Compared with other variants, Omicron contains many more of these mutations, particularly in the region of spike that recognizes host cells. Preliminary analysis from Bloom suggests that these mutations might render some portions of spike unrecognizable to the antibodies raised by vaccines and previous infection with other strains. But lab experiments and epidemiological studies will be needed to fully appreciate the effects of these mutations.



### How the Delta variant achieves its ultrafast spread

Evolving to evade immune responses such as antibodies could also carry some evolutionary costs. A spike mutation that dodges antibodies might reduce the virus's ability to recognize and bind to host cells. The receptor-binding region of spike — the major target for neutralizing antibodies — is relatively small, says Jason McLellan, a structural biologist at the University of Texas at Austin, and the region might be able to tolerate only so much change and still perform its main job of attaching itself to host cells' ACE2 receptors.

It's also possible that repeated exposure to different versions of spike — through infection with different virus strains, vaccine updates or both — could eventually build up a wall of immunity that SARS-CoV-2 will have difficulty overcoming. Mutations that overcome some people's antibody responses are unlikely to foil responses across an entire population, and T-cell-mediated immunity, another arm of the immune response, seems to be more resilient to changes in the viral genome.

Such constraints might slow SARS-CoV-2's evasion of immunity, but they are unlikely to stop it, says Bloom. There is clear evidence that some antibody-dodging mutations do not carry large evolutionary costs, says McLellan. "The virus will always be able to mutate parts of the spike."

## A virus in transition

How SARS-CoV-2 evolves in response to immunity has implications for its transition to an endemic virus. There wouldn't be a steady baseline level of infections, says Kucharski. "A lot of people have a flat horizontal line in their head, which is not what endemic infections do." Instead, the virus is likely to cause outbreaks and epidemics of varying size, like influenza and most other common respiratory infections do.

To predict what these outbreaks will look like, scientists are investigating how quickly a population becomes newly susceptible to infection, says Kucharski, and whether that happens mostly through viral evolution, waning immune responses, or the birth of new children without immunity to the virus. "My feeling is that small changes that open up a certain fraction of the previously exposed population to reinfection may be the most likely evolutionary trajectory," says Rambaut.

The most hopeful — but probably least likely — future for SARS-CoV-2 would be to follow the path of measles. Infection or vaccination provides lifetime protection, and the virus circulates largely on the basis of new births. "Even a virus like measles, which has essentially no ability to evolve to evade immunity, is still around," says Bloom.



### [Closest known relatives of virus behind COVID-19 found in Laos](#)

A more likely, but still relatively hopeful, parallel for SARS-CoV-2 is a pathogen called respiratory syncytial virus (RSV). Most people get infected in their first two years of life. RSV is a leading cause of hospitalization of infants, but most childhood cases are mild. Waning immunity and viral evolution together allow new strains of RSV to sweep across the planet each year, infecting adults in large numbers, but with mild symptoms thanks to childhood exposure. If SARS-CoV-2 follows this path — aided by vaccines that provide strong protection against severe disease — “it becomes essentially a virus of kids,” says Rambaut.

Influenza offers another scenario — in fact two. The influenza A virus, which drives global seasonal influenza epidemics each year, is characterized by the rapid evolution and spread of new variants able to escape the immunity elicited by past strains. The result is seasonal epidemics, propelled largely by spread in adults, who can still develop severe symptoms. Flu jabs reduce disease severity and slow transmission, but influenza A’s fast evolution means the vaccines aren’t always well matched to circulating strains.

But if SARS-CoV-2 evolves to evade immunity more sluggishly, it might come to resemble influenza B. That virus’s slower rate of change, compared

with influenza A, means that its transmission is driven largely by infections in children, who have less immunity than adults.

How quickly SARS-CoV-2 evolves in response to immunity will also determine whether — and how often — vaccines need to be updated. The current offerings will probably need to be updated at some point, says Bedford. In a preprint<sup>5</sup> published in September, his team found signs that SARS-CoV-2 was evolving much faster than seasonal coronaviruses and even outpacing influenza A, whose major circulating form is called H3N2. Bedford expects SARS-CoV-2 to eventually slow down to a steadier state of change. “Whether it’s H3N2-like, where you need to update the vaccine every year or two, or where you need to update the vaccine every five years, or if it’s something worse, I don’t quite know,” he says.

Although other respiratory viruses, including seasonal coronaviruses such as 229E, offer several potential futures for SARS-CoV-2, the virus may go in a different direction entirely, say Rambaut and others. The sky-high circulation of the Delta variant and the rise of Omicron — aided by inequitable vaccine roll-outs to lower-income countries and minimal control measures in some wealthy countries such as the United States and the United Kingdom — offer fertile ground for SARS-CoV-2 to take additional surprising evolutionary leaps.

For instance, a [document prepared by a UK government science advisory group in July](#) raised the possibility that SARS-CoV-2 could become more severe or evade current vaccines by recombining with other coronaviruses. Continued circulation in animal reservoirs, such as mink or white-tailed deer, brings more potential for surprising changes, such as immune escape or heightened severity.

It may be that the future of SARS-CoV-2 is still in human hands. Vaccinating as many people as possible, while the jabs are still highly effective, could stop the virus from unlocking changes that drive a new wave. “There may be multiple directions that the virus can go in,” Rambaut says, “and the virus hasn’t committed.”

*doi: <https://doi.org/10.1038/d41586-021-03619-8>*

## References

1. 1.

Eguia, R. T. *et al.* *PLoS Pathog.* **17**, e1009453 (2021).

2. 2.

Volz, E. *et al.* *Cell* **184**, 64–75 (2021).

3. 3.

Peacock, T. P. *et al.* Preprint at bioRxiv  
<https://doi.org/10.1101/2021.05.28.446163> (2021).

4. 4.

Liu, Y. *et al.* Preprint at bioRxiv  
<https://doi.org/10.1101/2021.08.12.456173> (2021).

5. 5.

Kistler, K. E., Juddleston, J. & Bedford, T. Preprint at bioRxiv  
<https://doi.org/10.1101/2021.09.11.459844> (2021).

---

This article was downloaded by **calibre** from <https://www.nature.com/articles/d41586-021-03619-8>

- NEWS FEATURE
- 08 December 2021

# The \$11-billion Webb telescope aims to probe the early Universe

Three decades after it was conceived, Hubble's successor is set for launch. Here's why astronomers around the world can't wait.

- [Alexandra Witze](#)



The 6.5-metre-wide primary mirror of the James Webb Space Telescope is folded up for launch. Credit: NASA/Chris Gunn

Lisa Dang wasn't even born when astronomers started planning the most ambitious and complex space observatory ever built. Now, three decades later, NASA's James Webb Space Telescope (JWST) is finally about to launch, and Dang has scored some of its first observing time — in a research area that didn't even exist when it was being designed.

Dang, an astrophysicist and graduate student at McGill University in Montreal, Canada, will be using the telescope, known as Webb for short, to stare at a planet beyond the Solar System. Called K2-141b, it is a world so hot that its surface is partly molten rock. She is one of dozens of astronomers who learnt in March that they had won observing time on the telescope. The long-awaited Webb — a partnership involving NASA, the European Space Agency (ESA) and the Canadian Space Agency (CSA) — is slated to lift off from a launch pad in Kourou, French Guiana, no earlier than 22 December.

If everything goes to plan, Webb will remake astronomy by peering at cosmic phenomena such as the most distant galaxies ever seen, the atmospheres of far-off planets and the hearts of star-forming regions swaddled in dust. Roughly 100 times more powerful than its predecessor, the Hubble Space Telescope, which has transformed our understanding of the cosmos over the past 31 years, Webb will reveal previously hidden aspects of the Universe.



The Webb telescope will spend hundreds of hours surveying this patch of sky, seen here in an image from the Hubble Space Telescope that captures 7,500 galaxies, some more than 13 billion years old. Credit: NASA, ESA, Rogier Windhorst (ASU), S. Cohen (ASU), M. Mechtley (ASU), M. Rutkowski (ASU), Robert O'Connell (UVA), P. McCarthy (OCIW), N. Hathi (UC Riverside), R. Ryan (UC Davis), Haojing Yan (OSU), Anton M. Koekemoer (STScI)

“Webb has such transformative capabilities that — to me — it’s going to be the ‘before’ times and the ‘after’ times,” says Jane Rigby, an astrophysicist at NASA’s Goddard Space Flight Center in Greenbelt, Maryland, who serves as Webb’s operations project scientist.

But if anything goes wrong, it will be an ignominious setback to what is already the most expensive astronomical gamble in history. The telescope took decades and more than US\$10 billion to develop, and frequent delays repeatedly ate into NASA’s astrophysics budget. Just this year, the telescope has been enveloped in controversy over whether it ought to remain named

after James Webb, who headed NASA in the 1960s when a NASA employee was fired on suspicion of being gay. Webb also held a high-ranking position in the US Department of State in the late 1940s and early 1950s, at a time when that department was systematically rooting out and firing gay and lesbian people because of their sexual orientation.

When the telescope lifts off after so many delays and so much debate, it will carry with it the hopes of thousands of astronomers around the world.

“There aren’t many times in your life when you’re on the cusp of such a big thing,” says Heidi Hammel, an astronomer and vice-president for science at the Association of Universities for Research in Astronomy in Washington DC, who has worked on Webb for decades. “There are a lot of emotions.”

## Decades of development

The first glimmers of what would become Webb arose at a workshop at the Space Telescope Science Institute in Baltimore, Maryland, in 1989. It was the year before the launch of the Hubble Space Telescope, and scientists were already thinking about how to follow up that transformative observatory. What ultimately emerged were plans for a space telescope with a 6.5-metre-wide primary mirror, nearly three times the size of Hubble’s, and made up of 18 hexagonal segments. The mirror is so large that it must be folded up like origami during launch and unfurled once in space. Shading it will be a kite-shaped sunshield the size of a tennis court, made of five aluminium-coated layers that block the Sun’s heat and keep the telescope cool enough to operate.

Webb’s overall cost was originally estimated at \$1 billion — an appraisal few believed even then — and has since ballooned. NASA provided US\$9.7 billion, including funds to cover operating costs in space; €700 million (US\$810 million) came from ESA; and the CSA contributed Can\$200 million (US\$160 million). The project’s skyrocketing costs drew intense scrutiny from government auditors as well as perennial questions as to whether it would be worth its unprecedented price tag. “To be truly transformational in a field, you have to build the tool you need,” says Hammel. “This is what it costs to do this.”

Plagued by repeated cancellations and design changes, the telescope finally took shape in laboratories around the world and was then assembled at Goddard. It was later combined with the rest of the observatory at Northrop Grumman Aerospace Systems in Redondo Beach, California. There, Webb ran into even more trouble when technicians damaged it by using the wrong solvent to clean propulsion valves. Later, screws literally came loose during testing.

Now, 32 years after its conception, Webb is finally sitting at the spaceport in Kourou in preparation for launch. It is destined for a point in space 1.5 million kilometres from Earth — too far away for astronauts to visit and fix the telescope if something goes wrong. Hubble required an after-launch repair in 1993, when astronauts used the space shuttle to get to the Earth-orbiting observatory and install corrective optics for its primary mirror, which had been improperly ground.

If it launches successfully, Webb will probe the cosmos in the near- to mid-infrared wavelengths, most of which are longer than Hubble can see. That means Webb can study light that has travelled from faraway galaxies and been stretched to redder wavelengths by the expansion of the Universe. Webb will also be able to study dust that enshrouds star-forming regions as well as the gas between the stars, both of which are not as visible at shorter wavelengths. Like Hubble, it will be able to take spectra of astronomical objects, meaning it can split their light into components to determine what they are made of.

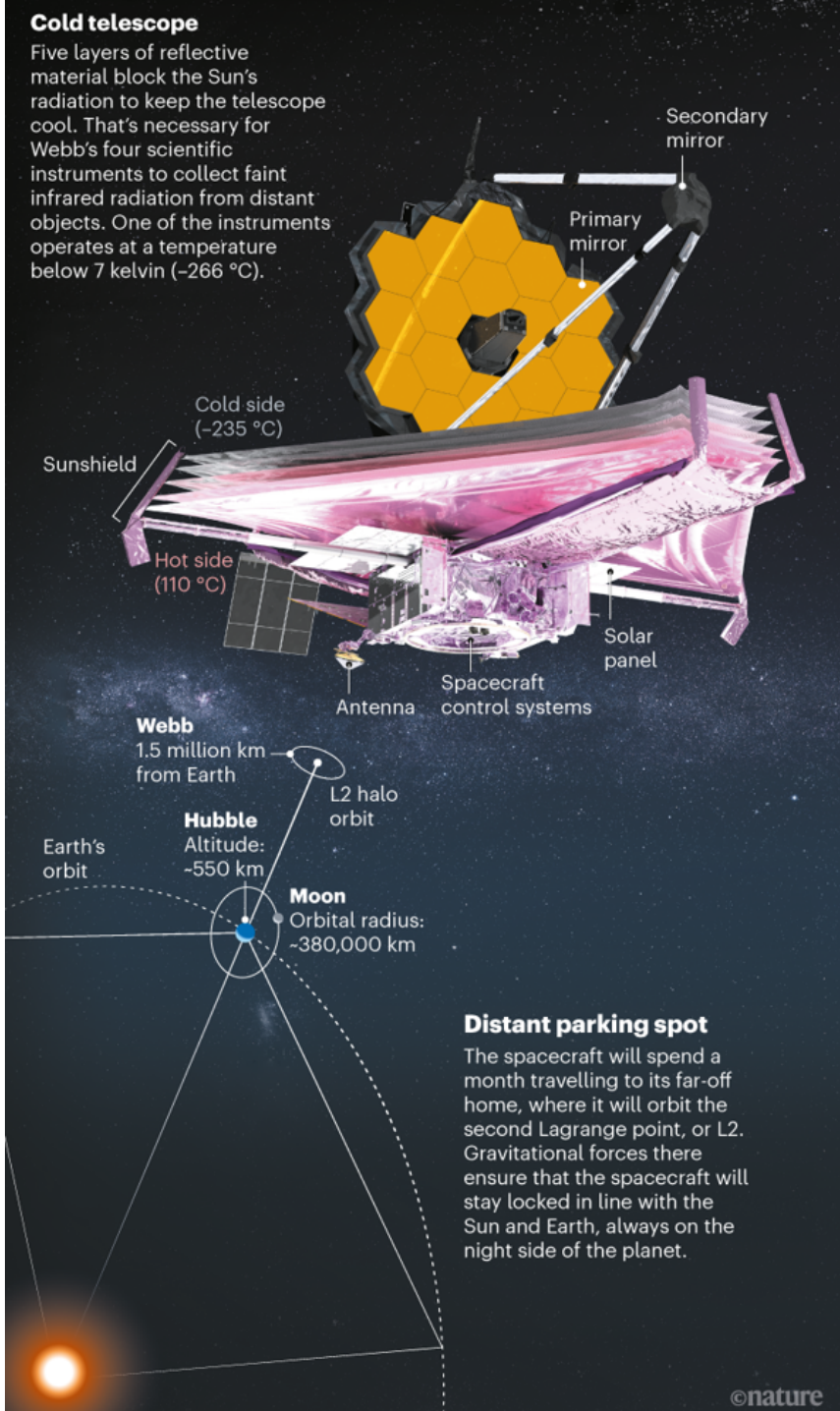
Earth's atmosphere interferes with most ground-based infrared astronomical studies. Space-based telescopes, such as ESA's Herschel Space Observatory, which operated between 2009 and 2013, have explored the Universe in infrared light before. But Webb's enormous mirror and suite of sensitive instruments (see 'New eye in the sky') mean that its discoveries will surpass those of any previous infrared space telescope, scientists say. "It's going to change a lot of what we know about a lot of areas of astronomy," says Jeyhan Kartaltepe, an astronomer at the Rochester Institute of Technology in New York.

# NEW EYE IN THE SKY

NASA's next space telescope, known as Webb, will capture infrared light from some of the first stars and galaxies, which have never been seen before. From its orbit 1.5 million kilometres from Earth, the observatory will also peer at the atmospheres of planets orbiting other stars, looking for hints of life.

## Cold telescope

Five layers of reflective material block the Sun's radiation to keep the telescope cool. That's necessary for Webb's four scientific instruments to collect faint infrared radiation from distant objects. One of the instruments operates at a temperature below 7 kelvin (-266 °C).



## Distant parking spot

The spacecraft will spend a month travelling to its far-off home, where it will orbit the second Lagrange point, or L2. Gravitational forces there ensure that the spacecraft will stay locked in line with the Sun and Earth, always on the night side of the planet.

Graphic: Nik Spencer/*Nature*; ‘Cold telescope’ main image: NASA GSFC/CIL/Adriana Manrique Gutierrez

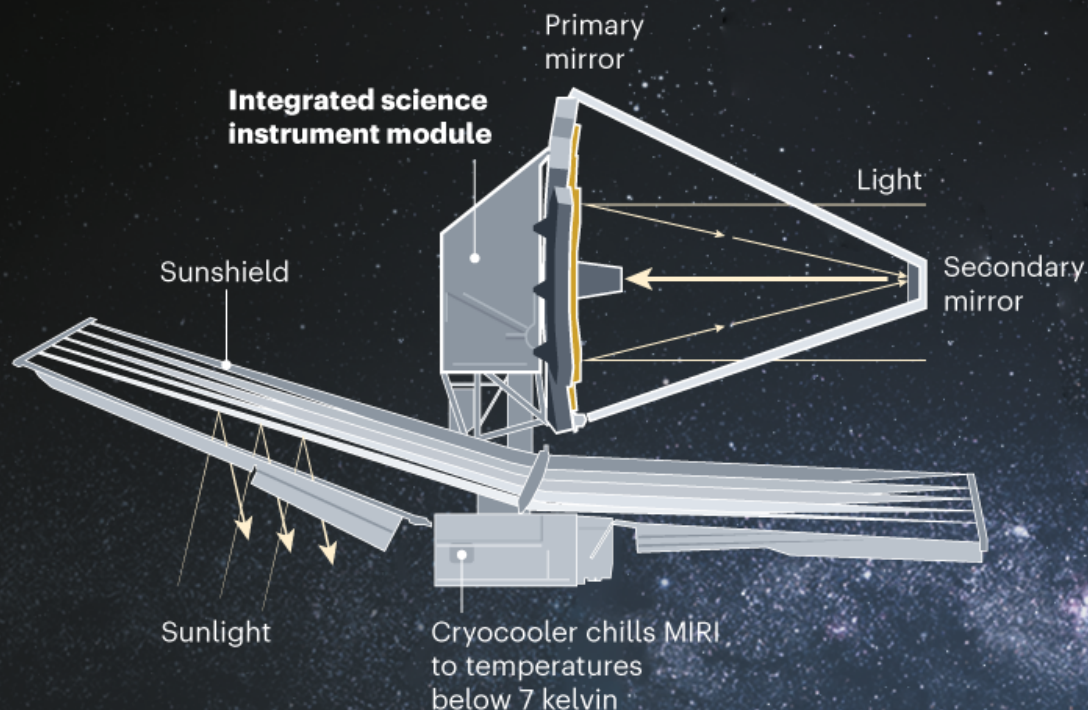
Because it can spot faint red objects, Webb is primed to observe some of the first stars and galaxies to form after the Big Bang created the Universe 13.8 billion years ago. Webb will almost certainly shatter the record for the most distant galaxy ever observed, which is currently held by an unassuming galaxy named GN-z11 that lies 13.4 billion light years from Earth<sup>1,2</sup>.

One large study will look at a region of sky that is the size of three full Moons, aiming to capture half a million galaxies in it. This survey, known as COSMOS-Webb, builds on an ongoing project that has used nearly every major ground- and space-based telescope to study the same patch of sky, which lies along the celestial equator and can be seen from both the Northern and Southern hemispheres. Webb will look at this field for more than 200 hours, making it the biggest project for the observatory’s first year of science and creating a rich data set for astronomers to mine for discoveries. Webb’s infrared view will probe, for instance, the period from around 400,000 years to 1 billion years after the Big Bang, when the first stars and galaxies lit up the Universe. This epoch, known as the cosmic reionization era, set the stage for today’s galaxies to evolve. “There’s a lot we don’t know about that time period,” says Kartaltepe, who co-leads COSMOS-Webb.

By observing these extremely distant astronomical objects, scientists can answer questions such as how the first stars assembled into galaxies and how those galaxies evolved over time. Getting a better picture of galaxy formation in the early Universe will help astronomers to understand how the modern cosmos came to be.<sup>1,2</sup> Mariska Kriek, an astronomer at Leiden Observatory in the Netherlands, plans to use Webb to study distant galaxies that are no longer forming stars. The observations will reveal the chemical composition of stars in those galaxies and the velocities at which they are moving. Those data, in turn, will help Kriek to unravel the mystery of how and why these galaxies stopped forming stars at some point in their history, unlike galaxies that did not stop<sup>3</sup>. “We’re looking for a very, very faint signal,” she says. “This is really what James Webb is going to open up.”

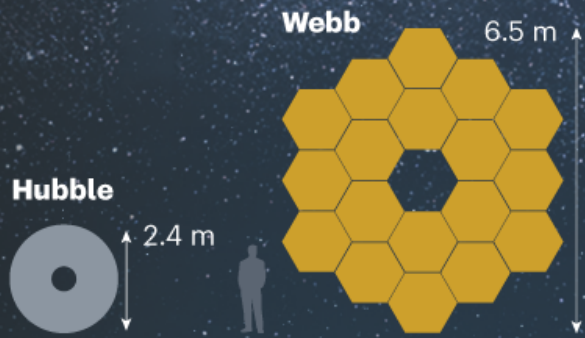
# SCIENCE CENTRE

The instrument package consists of the Near-Infrared Camera (NIRCam), Near-Infrared Spectrograph (NIRSpec), Mid-Infrared Instrument (MIRI) and Near-Infrared Imager and Slitless Spectrograph (NIRISS). The instruments include spectrographs that break down light from distant objects into different wavelengths, revealing clues about the source of the radiation.



## More mirrors

The telescope's primary mirror has a diameter of 6.5 metres and is made of 18 segments that are folded up for launch. It is almost three times the size of the Hubble Space Telescope's mirror.



©nature

Graphic: Nik Spencer/*Nature*

## Peering at distant planets

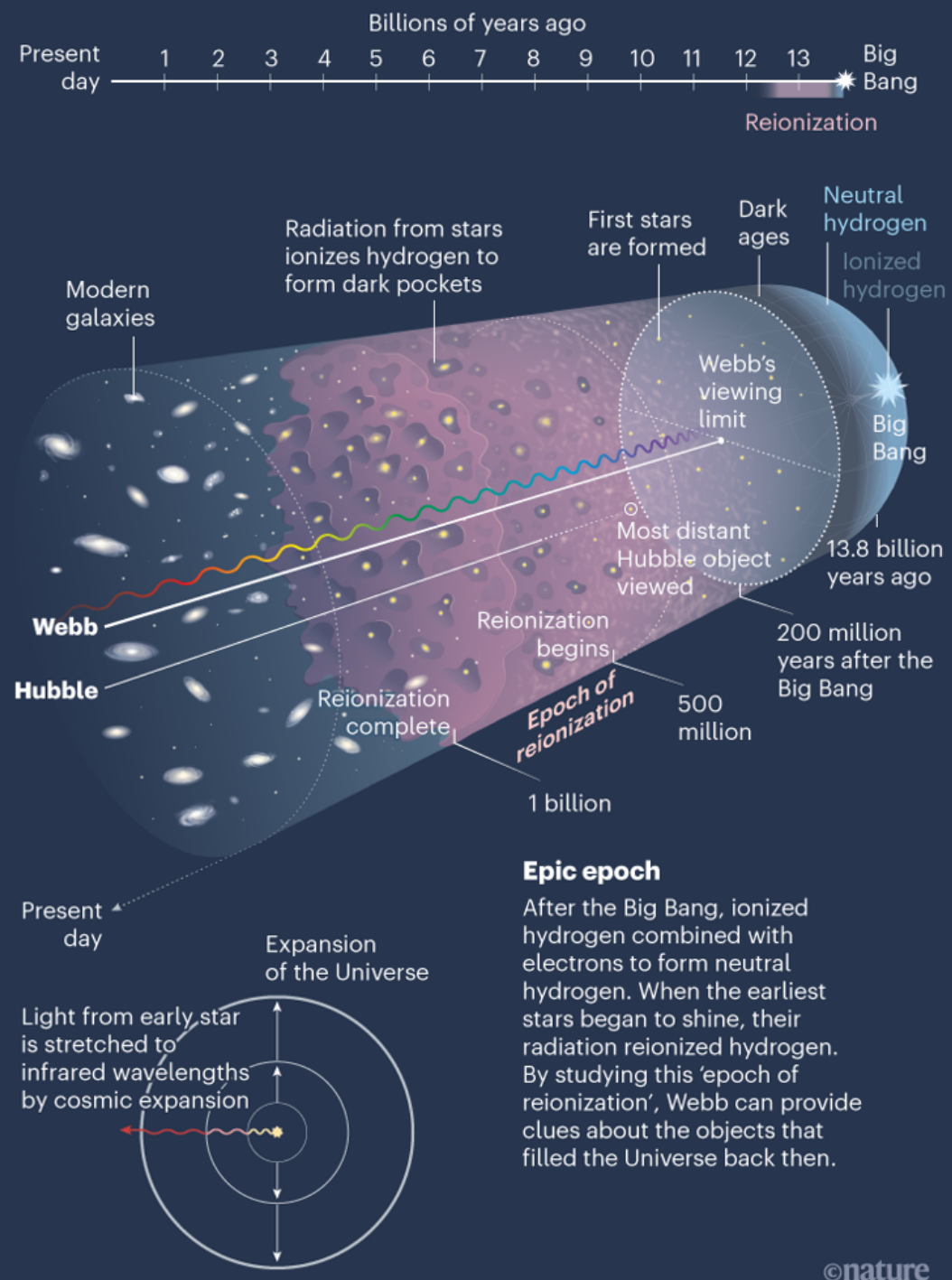
When not looking at stars and galaxies, Webb will spend a lot of its time scrutinizing planets, particularly some of the thousands that have been discovered beyond the Solar System. It can watch as a planet slips across the face of a star and the star's light briefly shines through the planet's atmosphere. Webb's spectral analysis can reveal the composition of planetary atmospheres in greater detail than ever before — and astronomers are particularly keen to find molecules such as methane and water, which signal conditions that could support life. In its first year, Webb will study some of the most famous exoplanets, including the seven Earth-sized worlds that orbit the star TRAPPIST-1.

Dang will observe several exoplanets using Webb, but the project she is leading will explore the world K2-141b, which is just 1.5 times the size of Earth and travels so close to its star that part of it is molten. It is an example of a rare 'lava planet' with a geology unlike anything known in the Solar System. Webb's infrared vision might detect minerals in K2-141b's atmosphere that have been vaporized off its surface, and the observatory might even map temperatures across the planet. "Webb is opening a lot of avenues for exoplanet science that didn't exist before," says Dang.

The repeated delays in developing and building Webb actually worked to the benefit of exoplanet scientists, says Néstor Espinoza, an astronomer at the Space Telescope Science Institute. At one point, Webb was scheduled to launch in 2011, but astronomers didn't confirm the first atmosphere around an exoplanet until 2005<sup>4,5</sup>. Webb's delays gave them more time to tweak its instruments to suit the study of exoplanet atmospheres. "We are much better poised now than if JWST were launched in 2011," says Espinoza.

# ORIGIN STORIES

A few hundred million years after the Big Bang, matter in the Universe coalesced and ignited to form the first stars. Webb's infrared-sensing instruments will give astronomers a first look at those earliest stars and galaxies as far back perhaps as 13.6 billion years ago. The most distant object seen by the Hubble Space Telescope hails from around 200 million years later.



Graphic: Nik Spencer/*Nature*

Webb will target a wide range of exoplanets, including gas giants and the class of planets that are larger than Earth but smaller than Neptune, which are the most common type of exoplanet discovered so far.

Closer to home, Webb will have plenty of objects to look at. Astronomers hope to use its wide range of wavelengths to reveal previously unseen details of the Solar System's residents. The colour and surface chemistry of the icy worlds in orbits near Pluto and beyond, for example, could help to reveal secrets of the Solar System's origins. Hammel and others plan to use the telescope to study the upper atmospheres of the ice giants Neptune and Uranus, the chemical make-ups of which are best seen in the infrared. By linking studies of the upper atmosphere with those of the lower atmosphere, seen at other wavelengths by other telescopes, scientists can obtain a 3D picture of how a planet's atmosphere behaves. This, in turn, can illuminate the workings of similar giant planets beyond the Solar System.

## Final hurdles

Although some scientists see benefits in the delays, many more have criticized NASA and its contractors over the years for the numerous problems in developing Webb. The telescope was strongly endorsed in a 2001 report setting out a road map for US astronomy, but NASA struggled, particularly between 2002 and 2008, to develop the many technologies required for such a complex observatory, such as the sunshield. A scathing report from an independent review in 2010 noted that key problems stemmed from NASA underestimating the time and money required: "This resulted in a project that was simply not executable within the budgeted resources," it concluded.

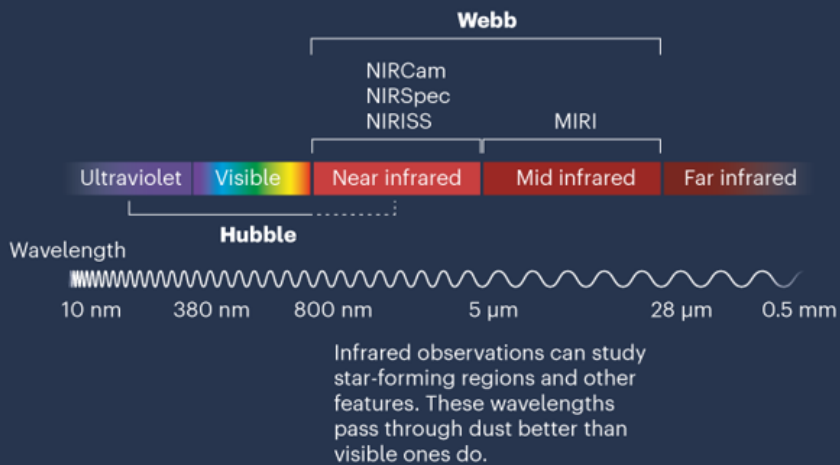
NASA restructured the management of the project in response, but in 2018, another independent review again slammed the agency for insufficient oversight. Costs were forecast to rise by another \$800 million, and the launch was delayed by nearly a year — and was then further held up because of problems at Northrop Grumman and challenges stemming from the COVID-19 pandemic. Earlier this year, the controversy over the telescope's

naming broke out; NASA announced in October that it had no plans to change the name, following a historical investigation into James Webb's actions. Many astronomers, however, have expressed unhappiness with the limited information that NASA has released about the scope of that investigation.

Then, less than a month before a scheduled launch date of 18 December, Webb hit yet another hurdle. At the facility in Kourou, a band that clamped the telescope to the launch vehicle released unexpectedly, causing vibrations. NASA investigated and concluded that the vibration did not cause any damage.

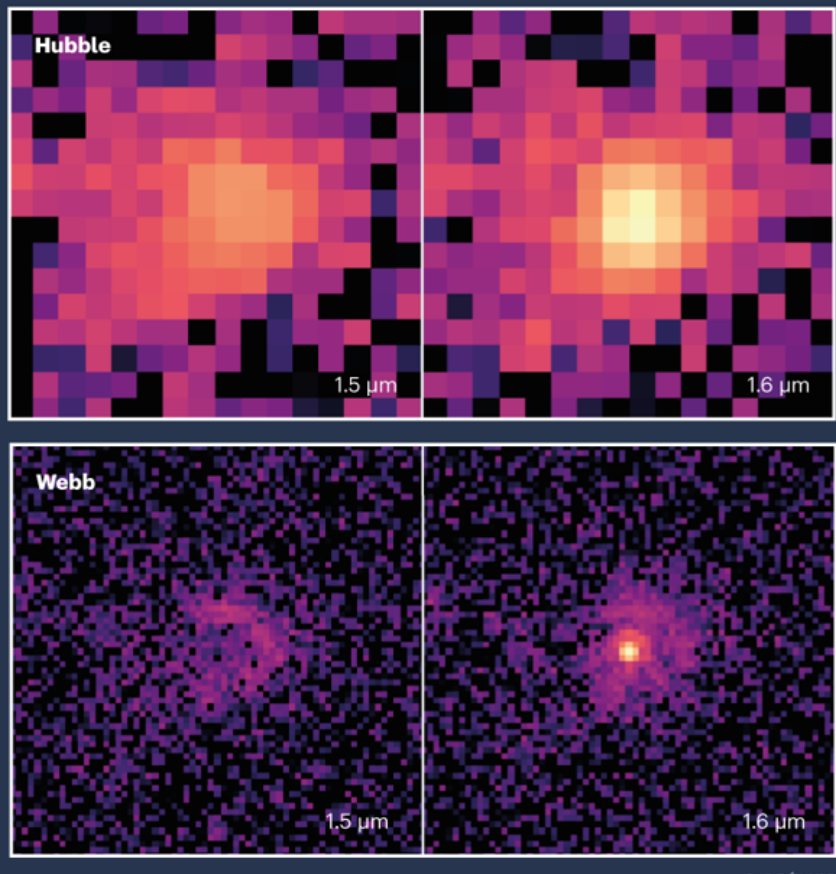
## IN THE RED

Webb's instruments are designed to collect light in the near-infrared and mid-infrared parts of the spectrum, whereas Hubble's vision centres on shorter wavelengths.



## Better vision

During years of waiting for Webb's launch, astronomers have prepared by planning their observations and modelling what they might see. Simulated images show how a quasar and its host galaxy might look in data collected by Hubble and Webb at infrared wavelengths.



©nature

Graphic: Nik Spencer/*Nature*; Infrared simulations: Madeline Marshall (Univ. Melbourne)

If and when Webb finally lifts off, which is always a risky procedure, the telescope faces a carefully choreographed six-month sequence of events that starts with unfolding and deploying the sunshield, then unfolding and deploying the primary and secondary mirrors. The telescope will begin cooling down as it travels towards its final orbit around the gravitationally stable point in space known as L2, or the second Lagrange point. At this location, Webb will always be pointed away from the Sun with Earth at its back, allowing it to see distant objects while the sunshield keeps it cool.

Then come two months of synchronizing and aligning the mirrors and telescope optics, and a month of calibrating the instruments. By June 2022, if all goes well, Webb will finally be ready for science.

Astronomers have planned the next steps carefully. “We have to hit the ground running and work very quickly,” says Kartaltepe. First will come a set of ‘early release’ observations. Their contents are closely guarded but will probably involve a series of jaw-dropping images chosen to show off the telescope’s capabilities. After that will come a series of general observations, the data from which NASA will release immediately to the astronomical community. One such project will look at infrared galaxies that formed as a result of violent galactic collisions. “We are the first guinea pigs to see what data will come off JWST and how we will analyse that data,” says Vivian U, an astronomer at the University of California, Irvine, who works on the project. “I know I’m standing on the shoulders of giants.”

Astronomers who spent years working to build Webb’s instruments have been guaranteed observing time, as have six scientists, including Hammel, who are tasked with pursuing research of interdisciplinary interest. After that come the proposals led by principal investigators. Astronomers in Europe will get at least 15% of the observing time, and ones in Canada will have at least 5%, for their space agencies’ contributions to Webb. Proposals are assessed using dual-anonymous peer review, in which reviewers and proposers do not know each other’s names — a practice that has been shown to reduce gender bias in allocating telescope time<sup>6</sup>.

Webb is expected to operate for at least five years and perhaps up to ten, a lifetime dictated by the amount of fuel that it uses to orient itself in space. In the meantime, the ageing Hubble continues to limp along. It was last upgraded by astronauts in 2009, and has been slowly degrading since then. A computer failure knocked it offline in June, and engineers had to switch to a back-up system before getting it working again in July. Hubble's science instruments also went offline in October owing to internal communications problems. Engineers restored all of the instruments to operation in early December.

After many years of waiting, astronomers are more than ready for Webb to pick up the baton of discovery from Hubble. "I'm probably most excited for the things we don't know yet," says Kriek.

*Nature* **600**, 208–212 (2021)

doi: <https://doi.org/10.1038/d41586-021-03620-1>

## References

1. 1.

Oesch, P. A. *et al. Astrophys. J.* **819**, 129 (2016).

2. 2.

Jiang, L. *et al. Nature Astron.* **5**, 256–261 (2021).

3. 3.

Kriek, M. *et al. Nature* **540**, 248–251 (2016).

4. 4.

Charbonneau, D., Brown, T. M., Noyes, R. W. & Gilliland, R. L. *Astrophys. J.* **568**, 377 (2002).

5. 5.

Deming, D., Seager, S., Richardson, L. J. & Harrington, J. *Nature* **434**, 740–743 (2005).

## 6. 6.

Strolger, L. & Natarajan, P. *Phys. Today*  
<https://doi.org/10.1063/PT.6.3.20190301a> (2019).

---

This article was downloaded by **calibre** from <https://www.nature.com/articles/d41586-021-03620-1>

| [Section menu](#) | [Main menu](#) |

## Books & Arts

- **Has Eric Kandel rested on his laurels? No** [ 06 December 2021]  
Book Review • The Nobel-winning neuroscientist has been studying connections on an ever-grander scale.
- **Climate adaptation, and the next great extinction: Books in brief** [ 06 December 2021]  
Book Review • Andrew Robinson reviews five of the week's best science picks.

- BOOK REVIEW
- 06 December 2021

# Has Eric Kandel rested on his laurels? No

The Nobel-winning neuroscientist has been studying connections on an ever-grander scale.

- [Alison Abbott](#) 0



Eric Kandel at a ceremony in Vienna in November 2019.Credit: APA-PictureDesk GmbH/Shutterstock

**There Is Life After the Nobel Prize** *Eric Kandel* Columbia Univ. Press (2021)

In 1996, Denise Kandel warned her husband that were he to win the Nobel prize for his pioneering work on memory, then it should be later rather than sooner. Laureates too often turn into socialites, she warned, and stop contributing to the intellectual life of science.

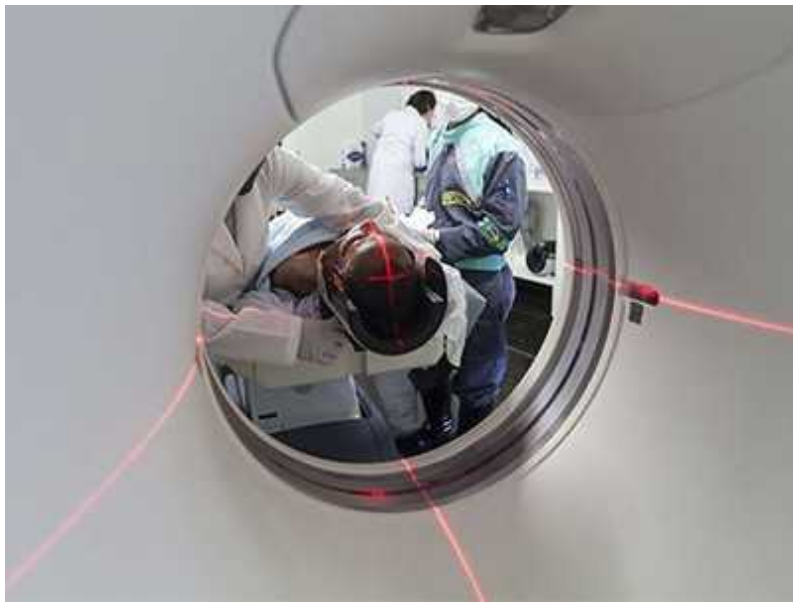
Just four years later, Eric Kandel shared the 2000 Nobel Prize in Physiology or Medicine. He was then 71, an age when he could legitimately have rested on his laurels. But resting is not among Kandel's many strengths. His new book, *There Is Life After the Nobel Prize*, outlines his achievements of the past couple of decades — numerous enough to dispel Denise's fears, he writes. It is hard to disagree.

The volume adds to Kandel's respected literary oeuvre, which ranges from neuroscience textbooks to highly original popular science. But it is slight, and feels like a coda. In it, he summarises his post-Nobel research (on learning and memory deficits in addiction, schizophrenia and ageing), writing and public outreach. And he acknowledges colleagues and sponsors of his long career, particularly the Howard Hughes Medical Institute in Chevy Chase, Maryland, and Columbia University in New York City, where he remains a professor and institute director. A fuller and more poignant autobiography can be found in Kandel's 2006 book *In Search of Memory*. There, he explains why his traumatic childhood in Austria drew him to study the mechanisms of memory. That book also presents a marvellous history of neuroscience.

## Making sense

Kandel was born in 1929 in Vienna. His family was Jewish and owned a toy shop. When Hitler annexed Austria in 1938, his parents began their year-long effort to emigrate. They finally arrived in New York shortly before the outbreak of World War II, physically unharmed but psychologically traumatized.

Incidents from that final year in Vienna etched themselves into Kandel's brain: the burning of synagogues on Kristallnacht in November 1938, eviction from the family apartment just days after his ninth birthday, being shunned by his school friends and roughed up by neighbourhood bullies. Such memories would flash unannounced into his consciousness years later.



### Probing the genetics of the mind

His desire to make sense of his experience led him to study history at Harvard University in Cambridge, Massachusetts, to which he won a scholarship. There, a girlfriend introduced him to psychoanalysis. Thinking that this new way of analysing the patterns of mind and memory could bring him the understanding he sought, he entered medical school at New York University.

Disillusionment with the non-empirical nature of psychoanalysis soon set in. Kandel realized that progress required a return to basics. In the 1950s, he joined the avant-garde neuroscientists studying the physiology of the brain, such as the electrical properties of neurons. Kandel went a radical step further. Unpicking exactly how neurons facilitated learning and memory required study in a very simple organism, and a very simple learning-dependent behaviour, he decided.

The reductionist approach he chose — the protective reflex of gill withdrawal in the sea slug *Aplysia* — raised eyebrows. Most neuroscientists thought that simple invertebrates could never elucidate the complexities of mammalian memory systems. In fact, Kandel discovered that as the slug learnt which environmental conditions required it to suck in its gills for protection, its synapses — structures that allow electrical or chemical signals to transmit between neurons — were altered.

He went on to describe the neural circuitry and molecular biology involved in short- and long-term memory in the slugs. Determining these principles won him the Nobel prize, and they have proved true for all creatures, humans included. Post-Nobel, he has studied memory in higher organisms including mice, turning out high-profile papers well into his eighties.



### [Documentary follows implosion of billion-euro brain project](#)

The Nobel experience widened Kandel's horizons beyond experimental science. The success of *In Search of Memory* awakened in him the desire for broader communication. I met him in Vienna in 2008, when a German-language documentary based on this book was about to have its premiere ([Nature 453, 985; 2008](#)). Radiating energy, he had started to make peace with the city of his birth.

His new book relates how, following the prize, Austria's president, Thomas Klestil, made overtures. Kandel initially rebuffed them, saying that he considered himself a Jewish American scientist. But then he proposed that Klestil honour him by setting up a symposium at the University of Vienna on Austria's response to the Nazi doctrine of National Socialism, and its implications for science and the humanities. Since that symposium, in 2003, Kandel has acted as an adviser to a couple of Austrian neuroscience organizations. "My relationship with Austria is becoming more comfortable, although it's got a way to go," he writes.

Since the 1960s, he has collected twentieth-century German and Austrian expressionist art, an interest that led to his 2012 book *The Age of Insight: The Quest to Understand the Unconscious in Art, Mind and Brain, from Vienna 1900 to the Present*. This superb volume illuminates the period when modernists of all shades were engaging with the internal workings of the mind. Sigmund Freud was developing psychoanalysis; novelist Arthur Schnitzler was pioneering the interior-monologue mode of narration; expressionist artists including Gustav Klimt, Oskar Kokoschka and Egon Schiele were portraying subjective emotions. Kandel guides readers through this cultural history and describes how the neuroscience of perception explains so much of our intuitive understanding of art. It epitomizes Kandel's breadth of vision. There has indeed been life after the Nobel prize.

*Nature* **600**, 213-214 (2021)

doi: <https://doi.org/10.1038/d41586-021-03623-y>

---

This article was downloaded by **calibre** from <https://www.nature.com/articles/d41586-021-03623-y>

- BOOK REVIEW
- 06 December 2021

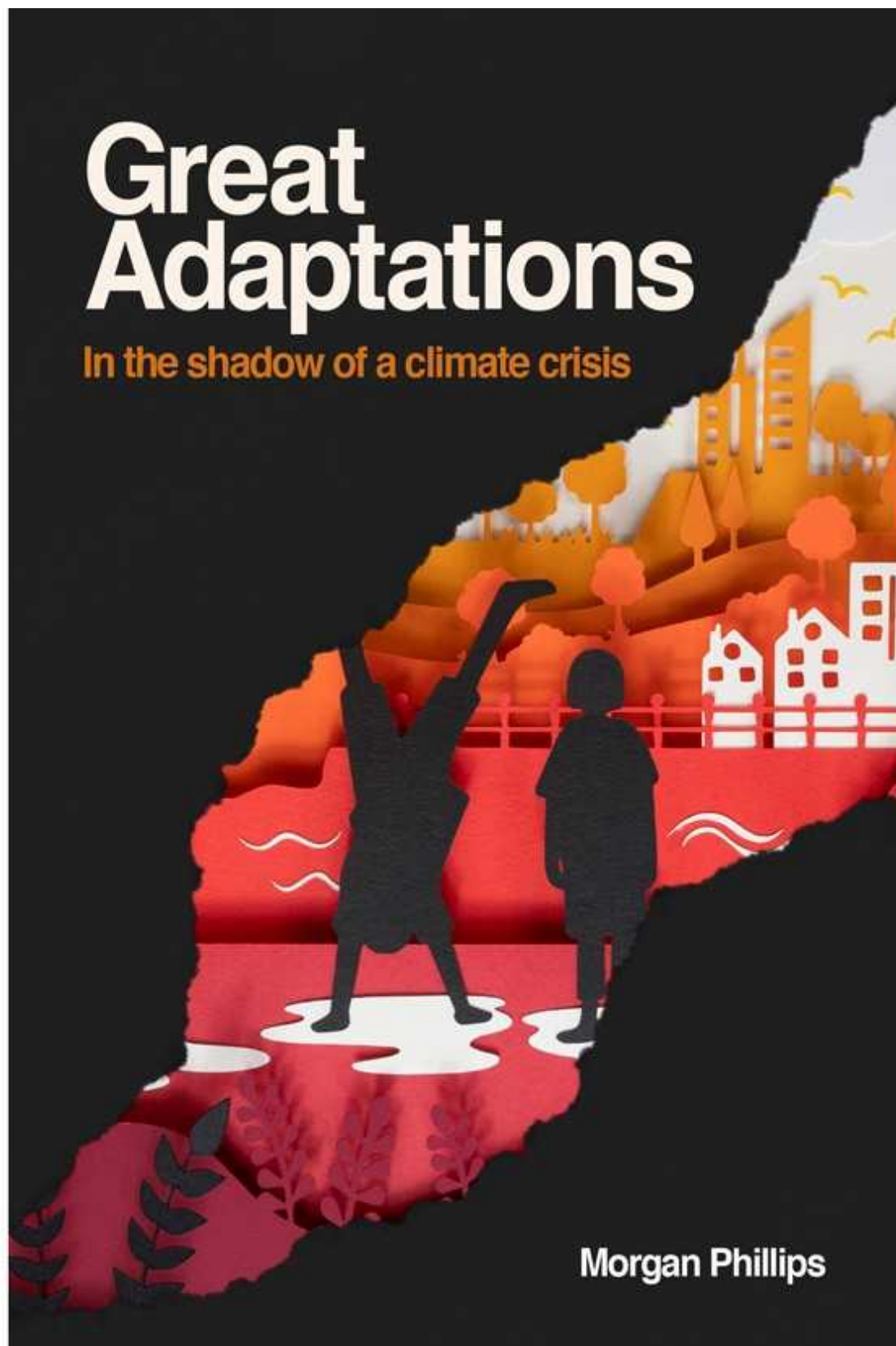
# Climate adaptation, and the next great extinction: Books in brief

Andrew Robinson reviews five of the week's best science picks.

- [Andrew Robinson](#) 0

# Great Adaptations

In the shadow of a climate crisis



Morgan Phillips

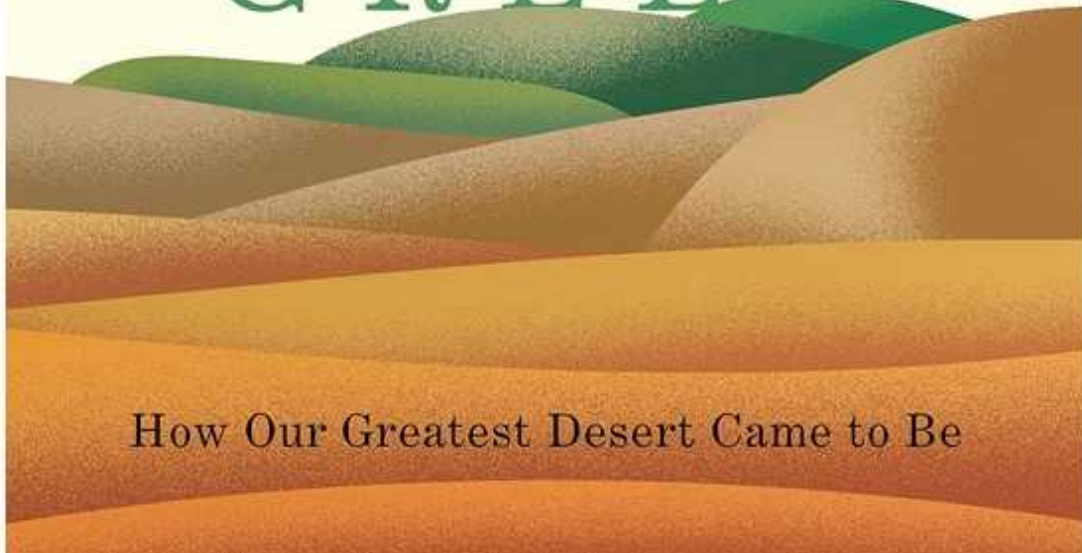
Great Adaptations

Morgan Phillips *Arkbound* (2021)

Until recently, climate-change activists advocated mitigation of rising global carbon dioxide levels — adapting to them was considered inappropriate or defeatist. Morgan Phillips disagrees. As the UK-based director of the Glacier Trust, which works with remote Nepalese mountain communities, he pragmatically supports mitigation and adaptation. He advocates that “Western civilization” be urgently but carefully “disassembled” to avoid climate catastrophe. His proposed adaptations seem mostly feasible and humane — if challenging.

M A R T I N   W I L L I A M S

W H E N  
T H E  
S A H A R A  
W A S  
G R E E N



How Our Greatest Desert Came to Be

**When the Sahara Was Green**

Martin Williams *Princeton Univ. Press* (2021)

On Saharan desert rock, prehistoric artists engraved or painted scenes of cattle camps and herds of giraffes and elephants. Even hippos flourished by lakes. Some 15,000–5,000 years ago, the region was green: the tropics received more solar radiation than they do now, which strengthened the monsoon and brought both summer and winter rains. This vivid historical survey by Earth scientist Martin Williams is the result of a lifetime's work. Are humans responsible for the region's current aridity? No, says Williams.



MICHAEL HANNAH

# EXTINCTIONS

Living and Dying in the Margin of Error

'... an exuberant road trip through the history of life on Earth'

MARCIA BJORNERUD

Author of *Timefulness* and *Reading the Rocks*

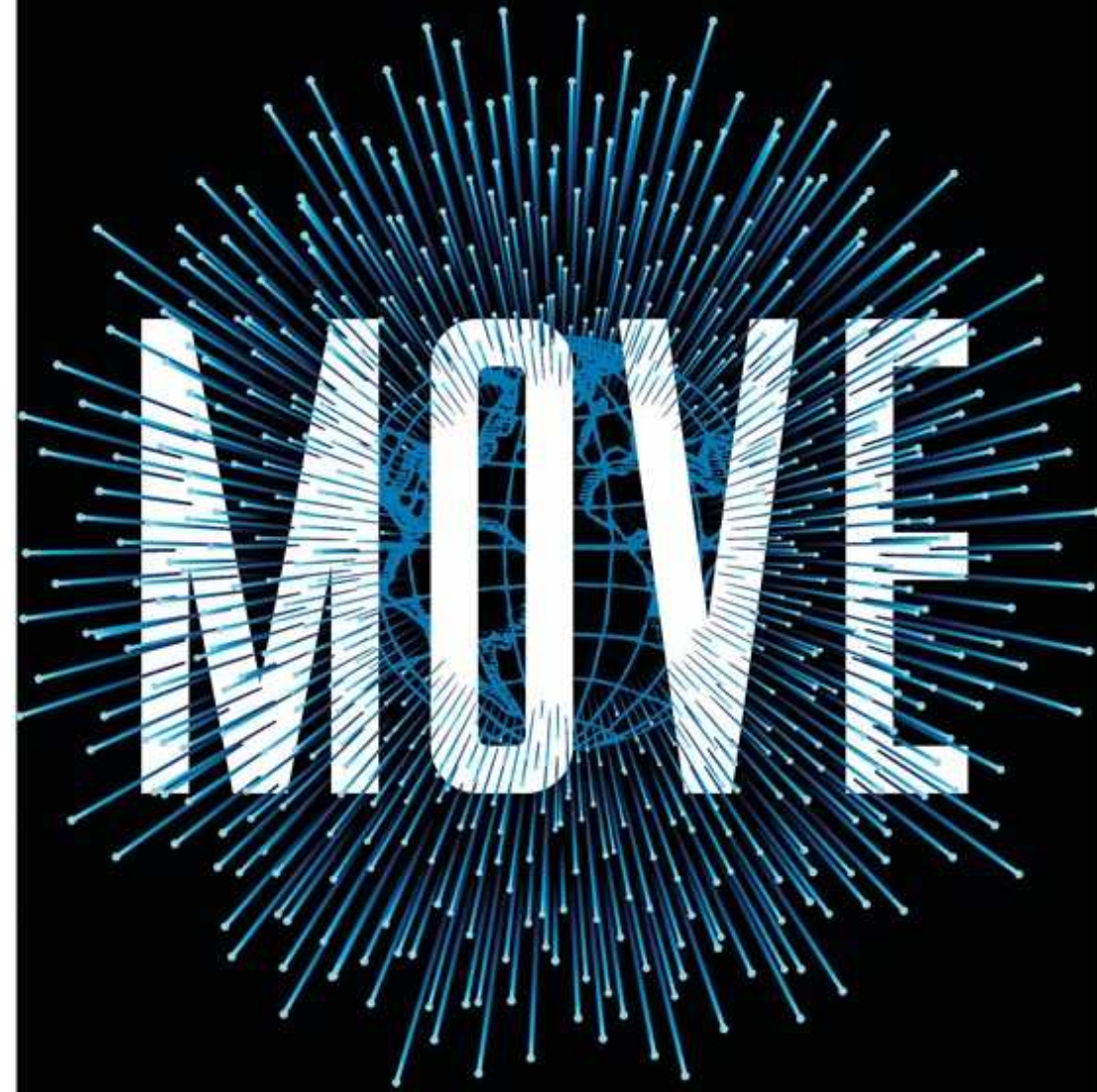


**Extinctions**

Michael Hannah *Cambridge Univ. Press* (2021)

One well-documented estimate puts the number of living species at 8.7 million, excluding bacteria and archaea. If correct, this represents less than 1% of species that have evolved and gone extinct since the first appearance of life 3.7 billion years ago, notes palaeontologist Michael Hannah in his measured, thought-provoking analysis. He says the cause of past mass extinctions is a “fraught subject” and has no doubt that humans will cause another, possibly in “as little as 240 years”, unless we stop damaging the biosphere and the atmosphere.

HOW MASS MIGRATION WILL RESHAPE THE WORLD  
- AND WHAT IT MEANS FOR YOU



PARAG KHANNA

INTERNATIONALLY BESTSELLING AUTHOR OF *CONNECTOGRAPHY*

Move

Parag Khanna *Weidenfeld & Nicolson* (2021)

“Mobility is destiny,” says entrepreneur Parag Khanna. Born in India, educated in the United States and United Kingdom, and now US-based, he has been to more than 150 countries. His timely, contentious study of mass migration observes that nearly 40% of US scientists are foreign-born, along with more than two-thirds of US tech-company employees, who come mostly from India and China. Yet he makes little attempt to analyse the complexities of migration in these cosmopolitan occupations; his index includes neither ‘research’ nor ‘science’.

CHRIS BEGLEY

# THE NEXT APOCALYPSE



THE ART AND SCIENCE  
OF SURVIVAL

The Next Apocalypse

## Chris Begley *Basic Books* (2021)

Underwater archaeologist and survival coach Chris Begley is intrigued by apocalypses, such as the collapse of the ancient Maya culture in Central America. His intriguing book begins in Honduras, with a campfire discussion about a ‘lost city’ with an Indigenous Pech man, who believes it inhabited by gods that fled Spanish colonial invaders. However, “this is not a doomsday book”. Surviving apocalypse, he says, depends not on lone heroes and escape, but on communities rebuilding with new structures and systems.

*Nature* **600**, 214 (2021)

doi: <https://doi.org/10.1038/d41586-021-03624-x>

---

This article was downloaded by **calibre** from <https://www.nature.com/articles/d41586-021-03624-x>

| [Section menu](#) | [Main menu](#) |

# Opinion

- **[Build solar-energy systems to last — save billions](#)** [ 07  
December 2021]  
Comment • To withstand extreme weather, rapid innovation and rock-bottom prices, solar installations need tighter quality control, standards and testing.
- **[Brazil is in water crisis — it needs a drought plan](#)** [ 08  
December 2021]  
Comment • To avoid crop failures and soaring power costs, Brazil needs to diversify sources, monitor soil moisture, model local hydroclimate dynamics and treat water as a national security priority.
- **[Call to join the decentralized science movement](#)** [ 07  
December 2021]  
Correspondence •
- **[Portugal: female science leaders could speed up change](#)** [ 07  
December 2021]  
Correspondence •
- **[Are female science leaders judged more harshly than men?  
Study it](#)** [ 07 December 2021]  
Correspondence •

- COMMENT
- 07 December 2021

# Build solar-energy systems to last — save billions

To withstand extreme weather, rapid innovation and rock-bottom prices, solar installations need tighter quality control, standards and testing.

- [Dirk Jordan](#) <sup>0</sup>,
- [Teresa Barnes](#) <sup>1</sup>,
- [Nancy Haegel](#) <sup>2</sup> &
- [Ingrid Repins](#) <sup>3</sup>



Only solar panels remain intact after a bush fire burnt down a property in Torrington, Australia, in 2019. Credit: Brook Mitchell/Getty

Solar energy is being adopted the world over. Prices have plunged 100-fold since 1980. By 2023, the installed capacity of photovoltaics globally is expected to surpass 1 terawatt — 30–100 TW will be required by 2050. Yet colliding trends mean that many of the technologies being installed today might not last until then if quality is not assured.

To displace fossil fuels, solar energy needs to be dependable. Photovoltaic technologies must function as well in the steamy tropics as at the icy poles — working through storms, hail, heatwaves and snow. Until now, solar energy has been very reliable. Most modules have warranties that last 25–35 years (see ‘Solar trends’), and less than 1% of those in the United States fail within the first 5 years<sup>1</sup>. Intact solar panels were crucial, for example, in helping small island states to recover after devastating hurricanes in the Caribbean in 2017.

Yet, reliability challenges loom. Solar energy systems are being installed in more diverse settings. New cell designs, materials, packaging and racking technologies are advancing to market within months. Durability testing needs to keep up. Some components that passed quality tests a decade ago have since turned out to be defective.

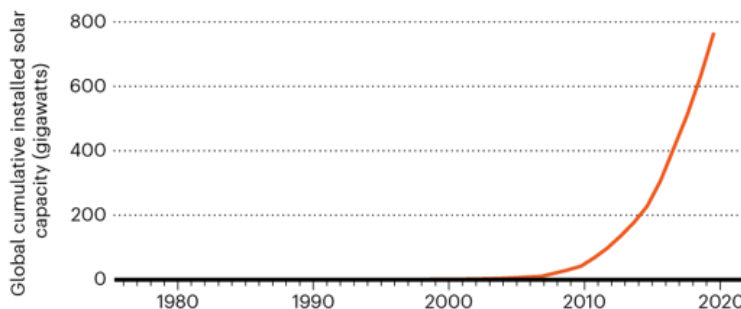
Today’s sophisticated systems are more efficient, but there is also little room for error. Manufacturers striving for higher energy yields and lower costs are making modules larger and thinner. They are connecting many cells together to boost power and speed up production. The electronics are more complex. Disruptions to supply chains might tempt some makers to use cheap, substandard or counterfeit components (see [go.nature.com/3kptewj](https://go.nature.com/3kptewj)). Poor installation, operations and maintenance practices cost utility firms tens of millions of dollars a year in lost power generation (see [go.nature.com/3xnyfef](https://go.nature.com/3xnyfef)). Over decades, that could amount to billions.

## SOLAR TRENDS

Photovoltaics technologies are advancing so fast that quality testing can't keep up. Defects might slip through, worsened by damage from extreme weather.

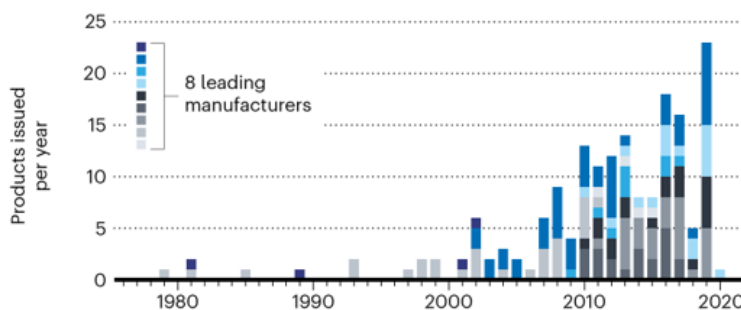
### More power

Solar energy generation is rising by 30% per year.



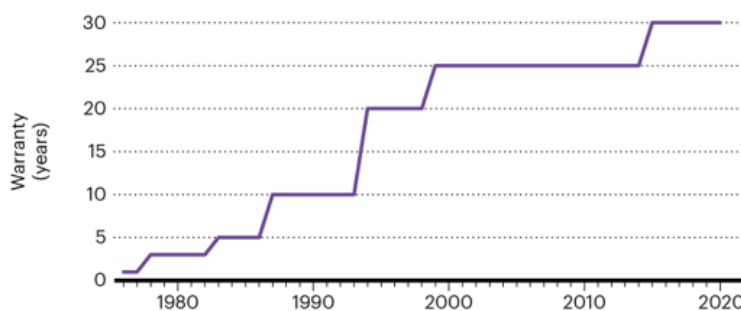
### Faster innovation

Manufacturers are releasing more products every year.



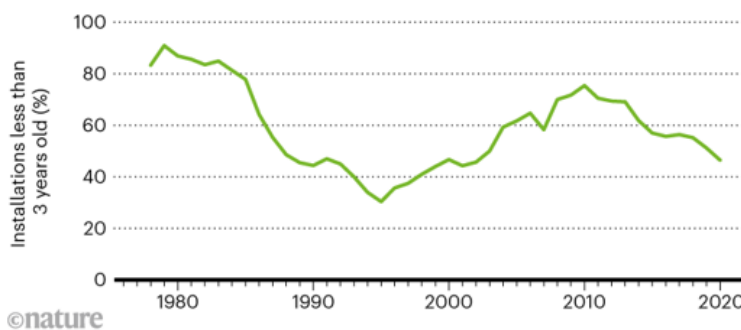
### Longer warranties

Makers now guarantee systems for decades.



### Early days

Installation rates fluctuate. Roughly half of modules involve technologies too new to assess longevity.



Sources: Power, *VDMA 2020 International Technology Roadmap*, 11th edn; Warranties, Updated from D. C. Jordan & S. R. Kurtz *Prog. Photovolt.* **21**, 12–29 (2011); Innovation & early days, D. Jordan

Solar panels are also increasingly exposed to extreme weather whipped up by climate change. During a storm in Texas in 2019, hailstones nearly 7 centimetres across shattered modules powering around 20,000 homes. Insurance losses exceeded US\$75 million.

Unaddressed, such vulnerabilities will slow the roll out of solar energy. Key climate milestones could be missed. The sector will face higher insurance claims, lost revenue and financial and safety risks. Grid operators will be reluctant to switch to solar. Carbon-neutral targets will be missed.

And in the short term, solar power could save lives. For example, when 10 million people lost electricity during Texas's big freeze in February, at least 111 people died and the damage in the state amounted to \$130 billion. Thermal generation crashed and wind generation underperformed, but solar power production was largely unaffected<sup>2</sup> and continued to generate 2% of the state's energy.

Here, we set out five steps the solar sector needs to take to assure the dependability of solar energy — including installation checks and training, basic research on materials and system failures and more robust operations and standards. Solar-energy scientists and engineers, investors, consumers and governing bodies all have a role.

## Boost science

Laboratory tests and computer models need to be advanced to assess how well the next generation of modules will perform in the field.

Researchers need to better understand the physics and chemistry of degradation. One challenge is the acceleration of subtle processes involving diffusion and reactions of chemical species. Heating samples or amplifying stresses by, for instance, exposing the samples to 100% humidity or intense ultraviolet light, can produce misleading results if reactions are triggered

that don't occur in the field. Once-popular 'pressure cooker' tests of panels can give the wrong impressions for this reason. Tests need to expose faults in a more realistic way. They should, for example, apply many stressors at once, in naturalistic sequences, and include more extreme conditions.



### [Eight priorities for calculating the social cost of carbon](#)

Failure mechanisms need to be identified, as do strategies for minimizing them. For example, solar modules at the ends of strings connected in series experience higher voltages than do those in the middle. Those voltages could be high enough to free sodium ions in the glass cover, which might then drift into the solar cell and overwhelm it. Similarly, researchers must understand why and how light and heat degrade various types of cell in different ways; hydrogen is thought to have a role.

Larger and more-complex testing facilities are needed. These must deliver uniform levels of light, heat and other stressors to panels that now cover several square metres and take two or more people to position. Panels in the 1980s spanned only around  $0.5 \text{ m}^2$  and were easier to handle. Multiple panels need to be tested at once, to ensure the statistical significance of conclusions. Many national and top-tier testing labs, including ours in the United States and others in Europe and Asia, have these capabilities. Few small buyers or testers in low-income countries have such access.

## **Strengthen standards**

Quality standards are widely used to verify individual components, such as a panel, diode or junction box. None covers an entire solar energy system. Poor assembly practices, differences in components between batches and the inclusion of even one unqualified component can all ruin performance.

To guide more holistic standards, the durability of whole systems needs to be tested. As a first step, in 2014, the International Electrotechnical Commission (IEC) began to form a global certification system for renewable-energy applications (IECRE), which reported its first photovoltaics certificate in 2016. It needs to be expanded. Oversight must extend beyond factory and product inspections. Random sampling and compliance testing must be introduced at every stage of the supply chain, as happens in the food industry. Customers should demand certified products and methods when they buy.

Standards need to be updated continually to address the latest technologies and failure modes. The current development cycle, which relies on reaching consensus in international teams of volunteer experts, is too slow and often takes years. Full-time technical support is needed in every member country of the IEC.



A pile of solar panels blown out of place during Hurricane Irma in the US Virgin Islands in 2017.Credit: Jessica Rinaldi/The Boston Globe/Getty

Harsher test conditions also need to be considered, to predict failures over longer periods and to account for increasingly severe weather. Current IEC standards require modules to withstand hailstones 25 millimetres across. Certifications involving larger ice balls are being developed, but researchers still need to establish a realistic range of conditions to be tested, while keeping product costs low and avoiding overdesign. One solution is to introduce specialized certifications of systems that are tailored to harsh conditions in specific regions.

Components such as modules, inverters and connectors must be exposed to a range of stressors at the same time in tests, as they would be outdoors. Otherwise, defects could be missed. For example, when 6.5 million modules were sampled from more than 350 international sites in 2019, 14% had degraded backsheets, with problems ranging from discolouration to

cracking<sup>3</sup>. Unforeseen issues with one type of backsheet (made of a type of AAA polyamide) illustrate the wider problem. Introduced to the market in 2010, these components became popular because they were relatively cheap, and conventional backsheets were facing supply-chain problems. AAA panels passed standard tests for exposure to damp heat and ultraviolet light. But five to ten years later, many began to crack, causing short circuits. Thermomechanical stresses from manufacturing and outdoor exposure, not previously part of standard tests, were eventually found to be the culprit<sup>4</sup>. These factors are now being incorporated into testing.

Researchers must develop tests and standards for unexpected failures. For example, new forms of low-temperature solder degrade through a different mechanism from conventional solders and thus require a different testing protocol<sup>5</sup>. Floating photovoltaics, installed on water, will need more corrosion-resistant materials for connectors and brackets, and wave motion could speed up wear and tear. Tests are needed to define when it is acceptable to mix and match components: fires can occur when installers plug together connector parts from different manufacturers.

## Monitor changes

Early identification of faults using sensors and monitoring needs to be routine in the solar industry, as it is for conventional energy generators and wind turbines. Some operators of large solar arrays already use infrared or visible cameras flown on drones and aircraft to spot faults. However, they need better analytical methods to interpret data quickly, and then respond rapidly to mitigate production losses and damage. Machine-learning algorithms are a promising way to detect slight underperformances that could be masked by larger diurnal and seasonal changes.



### Net-zero emissions targets are vague: three ways to fix

More comprehensive technologies are needed — these would track meteorological predictions along with data from on-site wind sensors, accelerometers and video, for example. Many large solar-power systems have a dedicated weather station, measuring solar irradiance, temperature and wind. Some also follow weather forecasts. Operators sometimes stow arrays when hail or high winds threaten. Attaching vibration sensors would allow them to make finer adjustments to reduce the impacts of ice, high winds or snow. On a smaller scale, sensors could be integrated into modules to reveal physical or chemical changes that might warn of reliability concerns later; some versions have been demonstrated<sup>6</sup>.

Adding sensors and monitoring systems to solar arrays will increase costs. But over decades, these investments will be recouped by lowering maintenance needs and downtime.

## Track materials

Content information is typically not shared in the competitive, low-margin solar market. Few producers, if any, report how a panel has been manufactured, or list what it is made of. Supply-chain bottlenecks — such as those stemming from the COVID-19 pandemic for backsheets, polysilicon

and glass— are hitting the photovoltaics industry hard. Consumers have no way of knowing whether manufacturers have made last-minute substitutions with untested components. Buyers with strict contract deadlines could turn a blind eye to avoid penalties. Such uncertainties also cloud the conclusions that scientists draw from lab tests.



### Protect global supply chains for low-carbon technologies

Developers, buyers and testers should request accurate information on module content — the bill of materials. Manufacturers should provide it as a customer service. For example, when operators at a large utility site in New Jersey investigated the 12% of modules that were underperforming, they found that the problem stemmed from variations in the silver paste top contact on different cells in the same module<sup>7</sup>. Transparency would also facilitate recycling and rebuilding of old solar panels, opening markets and reducing landfill.

The solar sector should look to other industries in which reliability is key. For example, aviation insists on rigorous inspection, maintenance and materials control. Data on materials degradation or failure are shared openly, because the entire industry depends on safety.

Regulation of labelling requirements should also be considered, as it is for foods. International organizations such as the IEC System of Conformity

Assessment Schemes for Electrotechnical Equipment and Components (IECEE) could assist — they already monitor consistency of manufacturing for some certified solar equipment.

## Educate community

Although electrical-safety requirements are common in developed countries, many parts of the world don't have or abide by them. There are also inconsistencies that affect reliability. Best practices need to be communicated and adopted worldwide. For example, in hurricane-prone regions, simple steps can increase the likelihood of a system surviving. These include: using strong support structures rated for storm wind speeds; through-bolting frames or using more mounting clips per solar panel; using vibration-resistant bolts; mounting brackets into the rafters and not just into the roof; and avoiding locating the system close to the roof edge, to minimize uplift.<sup>8</sup>

Proper handling and shipping are essential. Walking on modules that are not designed for it, resting the soft backsheet underside of a solar panel on a hard hat, shipping horizontally, twisting panels or other rough handling can cause invisible damage.

Other common problems include improper wiring, and issues with fuses, breakers and connectors. Inverters, which convert direct current to alternating current, are what most often fail. Exposure to heat is often the reason. There's a simple remedy: lengthen connectors and install the inverters on a shady side of the building, rather than in full sun.

Commitment to the quality of photovoltaic systems is essential across the value chain. It must include rigorous training for solar installers and state of the art maintenance and operation. Certifications should be provided that solar consumers can recognize. The North America Board of Certified Energy Practitioners (NABCEP) offers certifications and training for solar installers and has recently expanded internationally. Similar organizations are needed globally. A digested form of the IECRE quality certification system should be provided for consumers and homeowners.

All these quality-assurance measures are cost-effective, compared with the price of climate change. Power outages in the United States from hurricanes in 2018 alone cost \$150 billion and this year's flooding in Germany in excess of €10 billion (US\$11.3 billion). Investment in quality control now will assure decades of affordable clean electricity to come.

*Nature* **600**, 215–217 (2021)

doi: <https://doi.org/10.1038/d41586-021-03626-9>

The views expressed in the article do not necessarily represent the views of the Department of Energy or the US government.

## References

1. 1.

Jordan, D. C., Marion, B., Deline, C., Barnes, T. & Bolinger, M. *Prog. Photovolt.* **28**, 739–754 (2020).

2. 2.

Busby, J. W. *et al.* *Energy Res. Soc. Sci.* **77**, 102106 (2021).

3. 3.

Tracy, J. *et al.* in *IEEE 46th Photovolt. Spec. Conf* 874–879 (2019).

4. 4.

Eder G. C. *et al.* *Sol. Energy Mat. Sol. Cells* **203**, 110194 (2019).

5. 5.

Spinella, L. *et al.* in *IEEE 48th Photovolt. Spec. Conf* 108–111 (2021)

6. 6.

Beinert, A. J. *et al.* *Prog. Photovolt.* **28**, 717–724 (2020).

7. 7.

Gaulding, A. E. *et al.* in *IEEE 48th Photovolt. Spec. Conf* 1735–1736 (2021).

8. 8.

Burgess, C., Detweiler, S., Needham, C. & Oudheusden, F. *Solar Under Storm Part II: Select Best Practices for Resilient RoofMount PV Systems with Hurricane Exposure* (Clinton Foundation, FCX Solar & Rocky Mountain Inst., 2020).

---

This article was downloaded by **calibre** from <https://www.nature.com/articles/d41586-021-03626-9>

| [Section menu](#) | [Main menu](#) |

- COMMENT
- 08 December 2021

# Brazil is in water crisis — it needs a drought plan

To avoid crop failures and soaring power costs, Brazil needs to diversify sources, monitor soil moisture, model local hydroclimate dynamics and treat water as a national security priority.

- [Augusto Getirana](#)<sup>0</sup>,
- [Renata Libonati](#)<sup>1</sup> &
- [Marcio Cataldi](#)<sup>2</sup>



Jaguari dam is part of the Cantareira system that supplies water to São Paulo, Brazil. Credit: Paulo Fridman/Bloomberg/Getty

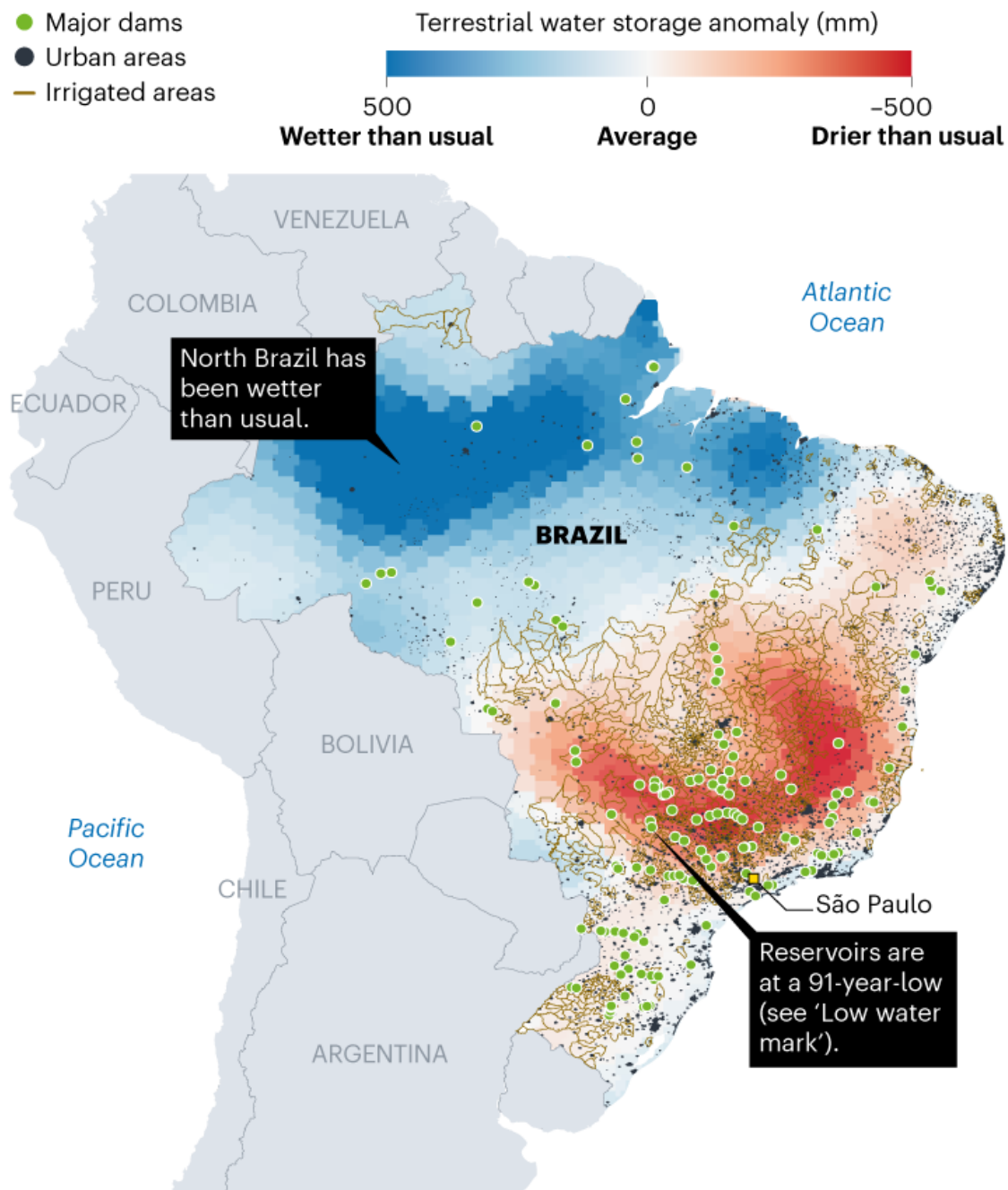
Brazil has the largest amount of fresh water in the world. Two-thirds of what flows in the Amazon River alone could supply the world's demand. Yet much of the nation now faces drought.

It's the worst in many decades in a nation that grows more than one-third of the world's sugar crops and produces almost 15% of the world's beef.

This year, between March and May, dry weather in Brazil's south-central region led to a 267 km<sup>3</sup> shortage of water held in rivers, lakes, soil and aquifers, compared with the seasonal average for the past 20 years (see 'Brazil dries out' and 'Low water mark'). The result? Many major reservoirs have reached less than 20% capacity. Farming and energy generation have been hit. Since July, coffee prices have risen by 30% — Brazil accounts for one-third of global exports. Soya bean prices rose by 67% from June 2020 to May this year. And electricity bills have soared by 130%. Many cities face imminent water rationing.

## BRAZIL DRIES OUT

The worst drought since satellite records began hit Brazil's south-central region (red) in 2021. Almost one-quarter of the nation's gross domestic product (GDP) comes from agriculture, including crops such as soya and sugar cane.



Data from NASA's GRACE satellite mission show the 2021 Terrestrial Water Storage (TWS) anomaly against historic trends. TWS measures integrated changes in the surface water across rivers, lakes, wetlands, soil moisture, groundwater and snow (see H. Save et al. *J. Geophys. Res. Solid Earth* **121**, 7547–7569; 2016).

Source: H. Save *et al.* *J. Geophys. Res. Solid Earth* **121**, 7547–7569 (2016)

How has this happened? And what needs to be done?

Worldwide climate change is making droughts more intense and more frequent. Deforestation in the Amazon is a contributor locally and globally. The hydroclimate in the south-central region — the engine of 70% of Brazil's gross domestic product (GDP) — is partly controlled by moisture transfer from the rainforest. Atmospheric fluxes caused by tree transpiration — also known as ‘flying rivers’ — might contribute as much water per day in rainfall as the Amazon River itself carries. Cutting down these trees reduces precipitation over those areas, as well as eroding a crucial global carbon sink.

For decades there has been a governmental failure to recognize drought as a matter of national and international security. Brazil's water crisis is a world crisis. What's needed is a coordinated nationwide drought-mitigation plan crafted by researchers, policymakers, industry, the public sector and civil society. Here are some key points that such a plan should address; these points are supported by 95 Brazilian and international water and climate scientists (see Supplementary information for list of co-signatories).

## Vast reserves

About 20% of all global inland water flowing to the oceans is generated in Brazilian territory<sup>1</sup>. This fuels the country's welfare and economic growth. About 85% of the nation's fresh water needs are supplied by surface waters — rivers and lakes<sup>2</sup>. In the United States, that figure is 75%; in India, it is 60%.

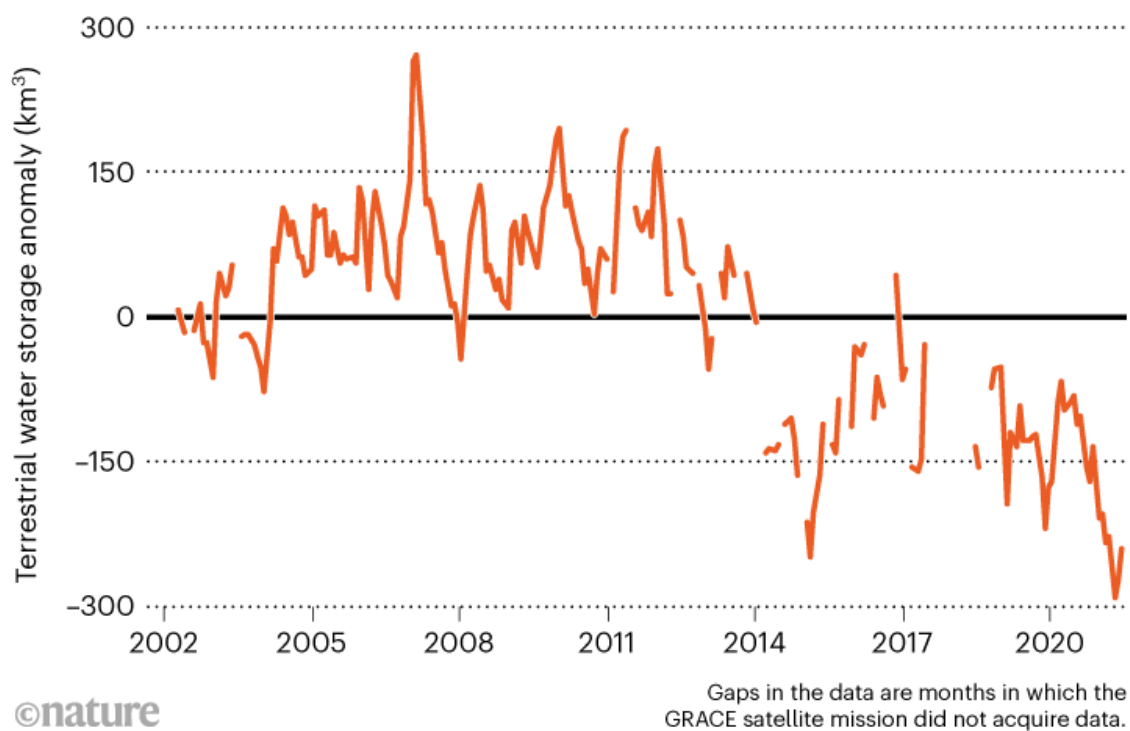
Brazil has the world's second-largest installed hydropower capacity, at 107.4 gigawatts (GW); it produces 65% of the country's electricity. Two-fifths of this is generated in the Paraná River Basin, where river discharges have fallen to their lowest levels in 91 years. The country has had to revert to burning fossil fuels and biofuel, passing the higher costs onto consumers. Thermal power produced 13.2% of the nation's electricity in July 2021, the highest in its history.

In a nation dependent on agriculture for almost one-quarter of its GDP, crops such as soya, coffee and sugar cane, and livestock use much of the water. Irrigation feeds about 13% of the cultivated land<sup>3</sup>, drawing down 68% of total water consumption — some 68.4 billion litres per day<sup>4</sup>.

But water is not equally available across the country, nor over time.

## LOW WATER MARK

Water storage levels are at their lowest across south-central Brazil since satellite records began.



Source: H. Save *et al.* *J. Geophys. Res. Solid Earth* **121**, 7547–7569 (2016)

## Different droughts

Water crises can originate from many types of drought: meteorological, hydrological, agricultural and socio-economic.

Meteorological droughts are dry weather patterns due to periods of little rainfall or high temperatures, which increase evaporation rates. These can

cause hydrological droughts, water shortages on land surfaces such as rivers and lakes.

Agricultural droughts — a decline in soil moisture levels — can result. These can jeopardize crop yield and increase food insecurity. Shortages to the domestic and industrial supply — socio-economic droughts — can also follow. This might lead to rationing, disease, conflict and migration. It could also bring water-intensive processes such as concrete and steel production to a halt.

These different droughts can interact in complex and non-linear ways. Hydrological droughts, for example, are intensified when prolonged periods of low soil moisture begin to dry out shallow aquifers. This can drop their levels below riverbed elevations, interrupting river–groundwater connectivity. Depleted rivers or lakes can then have a knock-on effect on reservoir levels, triggering a socio-economic drought.

## Human fingerprint

The 2021 Intergovernmental Panel on Climate Change (IPCC) report highlighted that unabated regional land-cover change and global warming are causing a cascade of persistent dry conditions around the globe<sup>5</sup>. Studies suggest an extended dry season in most of central South America under an extreme, but not unlikely, scenario<sup>6</sup>.

Decades of deforestation of the Amazon has led to vast knock-on effects. Cutting down trees, as well as slashing the amount of moisture transported from the rainforest towards central-southern Brazil<sup>7</sup>, is the main driver of fire<sup>8</sup>. The particulate matter released into the upper air alters the formation of rain clouds<sup>9</sup>.



## End the drought in drought research

Improper land use can worsen droughts, too, and even cause rivers to run dry. Intensive cattle farming leads to unvegetated land and compacted soils. As well as decreasing the amount of moisture given off by plants, it limits the soil's capacity to retain water and recharge aquifers.

But droughts alone don't explain the recurrence of water crises in Brazil. Failure to treat water as an essential national resource has led Brazil to a long history of mismanagement. Science denialism is now promoted at the highest levels around the country<sup>10,11</sup>. And national policies have driven increasingly erratic land occupation by agribusiness and mining interests, increasing deforestation and wildfires and undermining climate mitigation<sup>12–14</sup>.

As the country plunged into severe water shortages in 2014 and 2015, the Brazilian Academy of Sciences upbraided state authorities for failure to take swift, bold actions and for a lack of transparency about the gravity of the situation<sup>15</sup>.

Six years have passed and not much has changed. This time around, the country's economy is recovering to pre-pandemic levels. Economic growth requires extra energy to power production. With the current hydropower situation, this demand might have to be met by burning biofuel or fossil fuel.

## Research priorities

The nation's groundwater and meteorological monitoring is sparse and insufficient to properly track water variability and availability across the country. Brazil monitors groundwater at 409 sites nationwide; to put that into perspective, the North American and Indian networks have more than 16,000 and 22,000 sites, respectively. There are no nationwide systems in place to track soil moisture in Brazil, and monitoring of water use is patchy.



### [Rescue Brazil's burning Pantanal wetlands](#)

Governance of these networks must be strengthened, and more effective guidance on how to respond to future crises is needed. Monitoring networks are currently operated across different national agencies and departments, often leading to duplicated efforts and inefficient data access. Drought monitoring initiatives developed in Brazil through international partnerships, such as the Monitor de Secas, have been emerging in recent years. However, reducing delays to the availability of data, and improving accuracy and accessibility for end-users, such as farmers and local water departments, would make these initiatives more useful.

There needs to be more investment into high-quality, readily available data and computing power — the key ingredients for multidisciplinary drought

research. Tupã — Brazil's most powerful supercomputer at the Brazilian National Institute for Space Research (INPE) is nearing the end of its life. Funds from the United Nations have provided temporary access to alternative computers, but these are not powerful enough to perform hydrometeorological forecasts and climate predictions. US\$20 million of federal funds should be put aside for a new supercomputer. Instead, the science and technology ministry's budget for 2022 has been reduced by 87% ( see [Nature https://doi.org/g77w](https://doi.org/g77w); 2021).

Many processes that affect south-central Brazil's water availability are not well understood. These need more research to best inform policy. They include:

**Climate feedbacks.** Deforestation, land use, biomass burning and global warming interact to determine water availability. Fresh approaches should exploit emerging knowledge and computational tools to better incorporate small-scale and fast processes, such as vegetation, land cover, clouds and aerosol feedback effects in climate models. This will need higher-resolution simulations, more computational power and reliable *in situ* and satellite-based observations.



[Policy, drought and fires combine to affect biodiversity in the Amazon basin](#)

**Compound events.** Hazards such as droughts, heatwaves and fires can have devastating impacts beyond an area related to an isolated event. Risk-assessment approaches should consider how the co-occurrence of multiple and dependent hazards affect models. Climate, health and social scientists, as well as engineers and modellers, should work to improve predictions.

**Groundwater.** Intensive pumping, especially combined with droughts, has led to severe depletion in regions such as the western and central United States, northern India and the Middle East<sup>16</sup>. More research, along with groundwater and soil-moisture monitoring, is needed to understand how Brazilian aquifers respond to pumping, as well as climate variability and change.

**Migration and health.** Climate change could intensify migration from the northeast, Brazil's driest and poorest region, to the southeast. Other movements of people could be triggered across the country as longer, more frequent and severe droughts arise. Massive climate migrations might result in an increase of water insecurity, as well as unemployment and poverty in major Brazilian cities. Social, political and economic scientists should work to identify the drivers of climate migration to guide policymaking. Research initiatives should also consider the long-term effects of drought on human health, such as malnutrition and mental health.

## Diversify sources

Stable, long-term investment is needed to upgrade the nation's water and power system. Hydropower has a small carbon footprint once installed, despite its initial high environmental and social impacts. When there isn't enough water to generate electricity, however, expensive and more-polluting fossil-fuel-based thermal power currently picks up the slack.

Instead, Brazil could diversify by amplifying wind and solar capacity. This could be supported by an existing system of contract auctions, providing a mechanism to gather funds for clean energy. The success of such a mechanism in Brazil is demonstrated by recent investments totalling nearly \$8 billion over the past 5 years, mostly from the private sector. An estimated

300 GW could be generated from clean energy sources by 2050 — 3 times the nation's current demand<sup>[17](#)</sup>.

Brazil lies on major aquifers — valuable and underused resources. The agricultural sector should build climate resilience by using this groundwater, especially during extreme hydrological droughts. This needs to be done sustainably, to avoid the depletion experienced by other countries<sup>[16](#)</sup>. A clear picture of the spatial distribution and temporal variability of aquifers could guide farmers towards appropriate locations and rates of extraction.

In November, Brazil promised to end illegal deforestation and cut emissions from 2005 levels by 50% by 2030 at the 2021 United Nations Climate Change Conference (COP26) in Glasgow, UK. However, such measures are not ambitious enough and would not bring the country in line with green policies, such as the European Green Deal and the US Green New Deal.

There might be short-term economic harm from stemming deforestation, especially among farmers and landowners. But the costs of doing nothing are too extreme to ignore. The World Economic Forum has classed water crises as a top global risk, owing to their impact on food production, human health, conflict, ecosystem function and extreme weather (see [go.nature.com/3lwow7x](https://go.nature.com/3lwow7x)).

Brazil has the expertise and motivation to mitigate this risk. The research community must work with governments to craft laws, policies and investments that enforce optimal water practice — preventive and adaptive. With political willpower, funding and infrastructure to match, the country could become a world leader in hydroclimate resilience.

*Nature* **600**, 218-220 (2021)

doi: <https://doi.org/10.1038/d41586-021-03625-w>

A.G. writes in their personal capacity and not on behalf of NASA Goddard Space Flight Center or Science Applications International Corporation.

## References

1. 1.  
Getirana, A. *J. Hydrometeorol.* **17**, 591–599 (2016).
2. 2.  
National Water and Basic Sanitation Agency. *Report on the Situation of Water Resources in Brazil 2020* (ANA, 2020).
3. 3.  
National Water and Basic Sanitation Agency. *Atlas Irrigation 2021: Water Use in Irrigated Agriculture* 2nd edn (ANA, 2021).
4. 4.  
National Water and Basic Sanitation Agency. *Manual of Consumptive Uses of Water in Brazil* (ANA, 2019).
5. 5.  
Intergovernmental Panel on Climate Change. *Assessment Report 6 Climate Change 2021: The Physical Science Basis* (IPCC, 2021).
6. 6.  
Gomes, G. D., Nunes, A. M. B., Libonati, R. & Ambrizzi, T. *Clim. Dyn.* <https://doi.org/10.1007/s00382-021-05955-x> (2021).
7. 7.  
Khanna, J., Medvigy, D., Fueglistaler, S. & Walko, R. *Nature Clim. Change* **7**, 200–204 (2017).
8. 8.  
Libonati, R. *et al. Sci. Rep.* **11**, 4400 (2021).
9. 9.

Correia, A. L., Sena, E. T., Silva Dias, M. A. F. & Koren, I. *Commun. Earth Environ.* **2**, 168 (2021).

10. 10.

Escobar, H. *Science* <https://doi.org/10.1126/science.aay9857> (2019).

11. 11.

Diele-Viegas, L. M., Hipólito, J. & Ferrante, L. *Science* **374**, 948–949 (2021).

12. 12.

Feng, X. *et al.* *Nature* **597**, 516–521 (2021).

13. 13.

da Silva, C. A. *et al.* *Sci. Rep.* **10**, 16246 (2020).

14. 14.

Abessa, D., Famá, A. & Buruaem, L. *Nature Ecol. Evol.* **3**, 510–511 (2019).

15. 15.

de Mattos Bicudo, C. E. *et al.* *Rev. USP* **106**, 11–20 (2015).

16. 16.

Rodell, M. *et al.* *Nature* **557**, 651–659 (2018).

17. 17.

Ministry of Mines and Energy. *National Energy Plan 2050* (MME, 2020).

| [Section menu](#) | [Main menu](#) |

- CORRESPONDENCE
- 07 December 2021

# Call to join the decentralized science movement

- [Sarah Hamburg](#)   [ORCID: http://orcid.org/0000-0002-8142-3253](#) 9

The decentralized science (DeSci) movement aims to harness new technologies such as blockchain and ‘Web3’ to address some important research pain points, silos and bottlenecks. However, it is happening with little input from established academic communities.

## Access options

Subscribe to Journal

Get full journal access for 1 year

\$199.00

only \$3.90 per issue

[Subscribe](#)

All prices are NET prices.

VAT will be added later in the checkout.

Tax calculation will be finalised during checkout.

Rent or Buy article

Get time limited or full article access on ReadCube.

from \$8.99

Rent or Buy

All prices are NET prices.

### **Additional access options:**

- [Log in](#)
- [Learn about institutional subscriptions](#)

*Nature* **600**, 221 (2021)

doi: <https://doi.org/10.1038/d41586-021-03642-9>

---

This article was downloaded by **calibre** from <https://www.nature.com/articles/d41586-021-03642-9>

| [Section menu](#) | [Main menu](#) |

- CORRESPONDENCE
- 07 December 2021

# Portugal: female science leaders could speed up change

- [Paulo Cartaxana](#) 0

Faculty members at Portuguese universities have not unanimously welcomed the government's programmes to attract young researchers and provide them with more stable employment opportunities. These funding schemes, including the Foundation for Science and Technology's investigator programme and its Individual Call to Scientific Employment Stimulus, are allowing early-career scientists to build strong research teams and to acquire international funding.

## Access options

Subscribe to Journal

Get full journal access for 1 year

\$199.00

only \$3.90 per issue

[Subscribe](#)

All prices are NET prices.

VAT will be added later in the checkout.

Tax calculation will be finalised during checkout.

Rent or Buy article

Get time limited or full article access on ReadCube.

from \$8.99

[Rent or Buy](#)

All prices are NET prices.

### **Additional access options:**

- [Log in](#)
- [Learn about institutional subscriptions](#)

*Nature* **600**, 221 (2021)

*doi:* <https://doi.org/10.1038/d41586-021-03641-w>

---

This article was downloaded by **calibre** from <https://www.nature.com/articles/d41586-021-03641-w>

| [Section menu](#) | [Main menu](#) |

- CORRESPONDENCE
- 07 December 2021

# Are female science leaders judged more harshly than men? Study it

- [Martina Schraudner](#) ORCID: <http://orcid.org/0000-0001-7227-3022><sup>0</sup>  
&
- [Elizabeth Pollitzer](#) ORCID: <http://orcid.org/0000-0002-9608-5517><sup>1</sup>

The open letter from 145 leading female scientists calling on Germany's Max Planck Society to identify and address issues that might have contributed to the sanctioning or downgrading of highly successful female directors (see [Nature 600, 20; 2021](#)) raises an important question. Are there systemic biases at play in many such institutions that affect even those women who make it to the end of the leaky pipeline?

## Access options

Subscribe to Journal

Get full journal access for 1 year

\$199.00

only \$3.90 per issue

[Subscribe](#)

All prices are NET prices.

VAT will be added later in the checkout.

Tax calculation will be finalised during checkout.

Rent or Buy article

Get time limited or full article access on ReadCube.

from \$8.99

[Rent or Buy](#)

All prices are NET prices.

### **Additional access options:**

- [Log in](#)
- [Learn about institutional subscriptions](#)

*Nature* **600**, 221 (2021)

doi: <https://doi.org/10.1038/d41586-021-03643-8>

---

This article was downloaded by **calibre** from <https://www.nature.com/articles/d41586-021-03643-8>

| [Section menu](#) | [Main menu](#) |

# Work

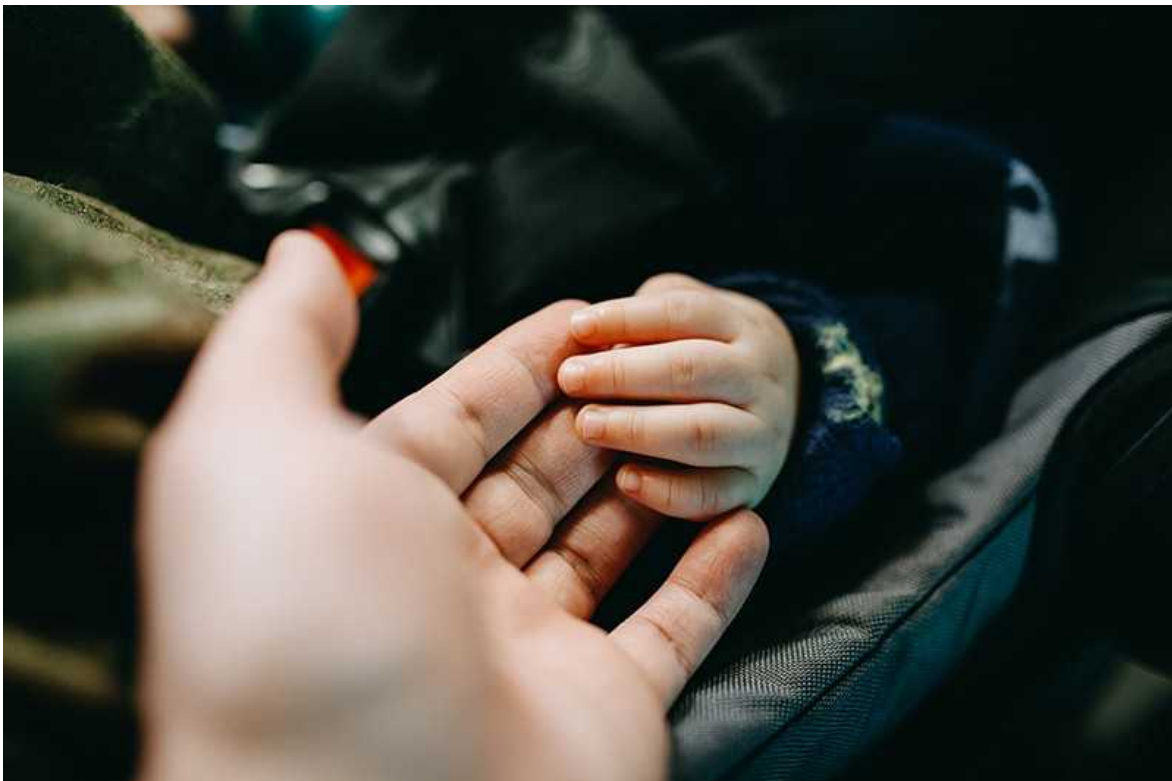
- **[Adopting as academics: what we learnt](#)** [ 18 November 2021]  
Career Column • Our quest to bring a child into our family led us to confront academic working practices, say Tony Ly and Nathan W. Bailey.
- **[Python power-up: new image tool visualizes complex data](#)**  
[ 06 December 2021]  
Technology Feature • The image viewing and analysis software napari has filled a gap in the programming language's scientific ecosystem.
- **[How remouldable computer hardware is speeding up science](#)** [ 07 December 2021]  
Technology Feature • Field-programmable gate arrays can speed up applications ranging from genomic alignment to deep learning.
- **[Handling snakes for science](#)** [ 06 December 2021]  
Where I Work • Eletra de Souza's research aims to help decrease lethal strikes in Brazil.

- CAREER COLUMN
- 18 November 2021

# Adopting as academics: what we learnt

Our quest to bring a child into our family led us to confront academic working practices, say Tony Ly and Nathan W. Bailey.

- [Tony Ly](#)<sup>0</sup> &
- [Nathan W. Bailey](#)<sup>1</sup>



The demands of academia can make it difficult to welcome a child into a family. Credit: Getty

This month, we're celebrating an important milestone: one year since a court issued the legal order that made us adoptive parents to our son. In 2016, we took the first step towards adoption when we contacted our local government council in Scotland. In our subsequent journey to becoming adoptive parents, we discovered that the process has unique challenges for academics, arising from common preconceptions around work-life balance and pressures in academia.

All people who plan to adopt a child in the United Kingdom go through an extensive evaluation process. This is very intrusive by design, because social workers have a responsibility to put children's needs first. That means ensuring that prospective parents are resilient — a key asset when facing the considerable pressure and uncertainty of the adoption process. The evaluation culminates in a formal panel hearing, in which prospective adoptive parents are asked questions by social workers, doctors, lawyers and community volunteers. Leading up to our own adoption panel, our life stories and personalities were forensically dissected by social workers. We anticipated some topics, such as our marriage and our support network, but others took us by surprise.

## Parenting priorities

We were warned by social workers, for example, that our academic backgrounds could disadvantage us with the adoption panel. This was because members might have preconceived ideas that academic workloads are not family friendly, or that academics are 'tiger parents' who demand unrealistic achievement from their children. We were asked whether we would be willing to prioritize our child over our careers if circumstances demanded it — a question asked of all adoptive parents. But as academics who have invested heavily in our careers, it was a major reality check for us to produce contingency plans such as being prepared to take an extended career break to deal with unexpected health or welfare issues that might emerge after the adoption. By notable contrast, our ethnicities (we have different ethnic backgrounds), our sexual orientation (we are gay men) and our nationalities (neither of us was a UK citizen at the time) were not raised as barriers.



### Collection: Careers toolkit

It is safe to say that academia does not have a widespread reputation for supporting work-life balance — owing to both stereotypes about the personalities of academics, and perceptions of the demands and competitiveness of their careers. Two things helped us to address this concern with our social workers. The first was to challenge some of those stereotypes: we pointed to examples of highly respected colleagues who have children, some with significant additional support needs. There is no lack of nurturing parents in academia. We also noted the relative flexibility of an academic schedule, compared with the more rigid working days typical of other professions.

But we also tried to take the question on board, and we examined our own ways of working. We realized that changes were in order. We had to convey to our social workers that we would be able to put reasonable boundaries around our work commitments, and that meant developing assertiveness and self-discipline when it came to managing our workloads. We had to change ourselves and our relationship with work: no more staying in the office until 10 p.m. and then grabbing a takeaway meal.

Although adjustments to working life are inevitable for all new parents, what surprised us was that we had to walk through every scenario in detail and explain them to our social workers, all while still being unsure whether any

child would ever be placed with us. What would we do if our child experienced a difficult transition to our home and could not be looked after by childcare providers when we returned to work? Could one of us leave academia to home-school the child? If you are an academic thinking of adopting, it is helpful to examine every aspect of your work–life balance — research schedules, conferences, fieldwork, commitments to your research group — well in advance, and be prepared to explain how you will set healthy limits so that you can support your child.

## Institutional attitude

Before our son was placed with us two years ago, we researched policies for adoption and shared parental leave (SPL) across a variety of UK higher-education institutions. We discovered striking differences; some institutions were more adoption-friendly than others. Some SPL policies require that paid leave at full salary be taken in the first 16 weeks after a child is placed, or the entitlement is lost. Others give the parent the freedom to decide when to take their allotment of full-salary leave over the course of 12 months. Flexible policies enable academic parents to share leave in a way that permits more one-on-one time with their children, lessens any negative impact on their research and teaching careers, and helps institutions to hire teaching replacements more efficiently, bolstering reputation and retention of faculty members.



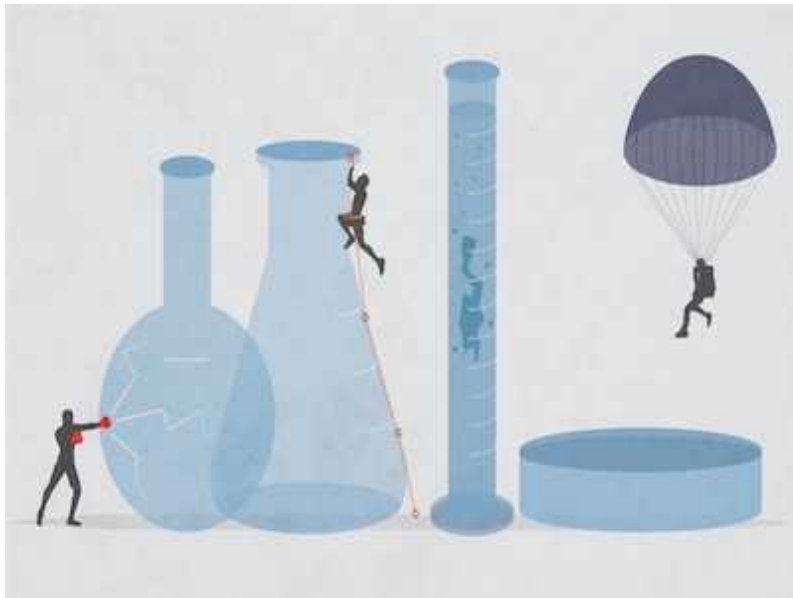
Tony Ly, Nathan Bailey and their son created art together during the COVID-19 lockdowns in 2020.Credit: Nathan W. Bailey & son

Flexibility is crucial for adoptive parents for another reason. There is an enormous amount of uncertainty regarding the timing of a child's placement. Although we were able to inform our employers that we had been approved for adoption, there was no way to predict whether a child would be placed with us in one month, three months, two years or never. That made it tricky to plan teaching replacements and contingencies for research supervision. Our placement was eventually confirmed through a matching panel in June 2019, and our son was placed with us in August 2019, giving us and our employers less than three months to prepare the practicalities of running our research and teaching in absentia before our son's arrival.

Furthermore, when we were first approved to adopt, in 2017, we were told that the child might be a newborn or as old as three years. By as late as March 2019 — nearly two years later — we still had no idea where the child might be in that range. The adoption process might be slow to start, but it crystallizes very quickly, which makes it difficult to plan ahead. This uncertainty is what makes flexible work and leave policies so important.

## **Love and support**

We received immense personal support from our academic colleagues, which was incredibly helpful. Official policy goes only so far: workplaces that are generally family-friendly are likely to be friendly to adopters, so we advocate that academics considering adopting should cautiously gauge the social environments of their departments, and that institutions should cultivate good social environments.



## Collection: Work–life balance

Every adoption is unique, and there can be striking differences across countries and regions. We are originally from the United States, where adoptions routinely cost many tens of thousands of dollars. Our colleagues there are often surprised to discover that not only was our adoption free, but the local council provided a £500 (US\$670) start-up package to cover parenting essentials such as nappies, infant formula, clothing and car seats, to ensure that children have the best possible start with their family. The situation will differ elsewhere, and in many countries, including some in the European Union, we would not even be allowed to adopt because we are gay.

Adopting our son has brought so much love into our lives. He is three now, and the star of our show. Our friends, family and colleagues have been supportive. And, at the end of the day, academia allows flexibility in juggling family commitments that simply does not exist in a lot of other jobs. If you are considering adopting, we wish you the most positive experience possible.

*Nature* **600**, 345-346 (2021)

doi: <https://doi.org/10.1038/d41586-021-03482-7>

This is an article from the Nature Careers Community, a place for *Nature* readers to share their professional experiences and advice. [Guest posts are encouraged.](#)

---

This article was downloaded by **calibre** from <https://www.nature.com/articles/d41586-021-03482-7>

| [Section menu](#) | [Main menu](#) |

- TECHNOLOGY FEATURE
- 06 December 2021

# Python power-up: new image tool visualizes complex data

The image viewing and analysis software napari has filled a gap in the programming language’s scientific ecosystem.

- [Jeffrey M. Perkel](#)

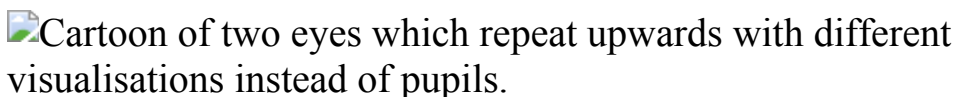


Illustration by The Project Twins

Josh Dorrington has become adept at viewing the jet streams. He plots fast-moving rivers of air at different atmospheric altitudes and positions the charts side by side. “You get pretty good at looking at all these cross-sections and working out what it implies,” says Dorrington, an atmospheric physicist at the University of Oxford, UK. But compared with computerized visualizations, this ‘manual’ method is slower and “it’s not as interactive”.

So when it came to visualizing atmospheric blocking events, in which stationary air masses of high pressure deflect the jet stream and lead to extreme weather events, Dorrington tried an alternative approach. Using the image viewer napari, he animated the streams in 3D as they flowed over the Northern Hemisphere — usually, but not always, in sync with each other. “One afternoon spent hacking stuff together and I already have a short visualisation of the lower and upper level Atlantic jet streams!” he tweeted in August.

napari is a free, open-source and extensible image viewer for arbitrarily complex ('*n*-dimensional') data that is tightly coupled to the Python programming language (see napari.org). It is the brainchild of microscopist Loïc Royer, at the Chan Zuckerberg Biohub in San Francisco, California; Juan Nunez-Iglesias, who develops image analysis at Monash University in Melbourne, Australia; and Nicholas Sofroniew, who leads the imaging-technology team at the Chan Zuckerberg Initiative (CZI) in Redwood City, California.

The team created the software in 2018 to fill a gap in the Python scientific ecosystem. Although Python is the lingua franca of scientific computing, it had no visualization tools that could handle *n*-dimensional data sets. As a result, data analysis usually required a tedious back and forth between Python and other tools (such as the Java-based image-analysis package ImageJ) as researchers alternately manipulated their data and then visualized them to see what had happened.



### Ten computer codes that transformed science

napari — the name refers to a Pacific island village midway between the developers' bases in San Francisco and Melbourne — features a simple graphical interface with a built-in Python console in which images can be rendered, rotated and manipulated in 2D or 3D, with additional dimensions, such as the succession of temporal 'slices' in a time series, accessible using

sliders beneath the image window. If available, graphics-processing units can be used to accelerate the software. “We make sure that we actually use the computer to its full capacity,” Royer explains. (ImageJ users can also work in Python using PyImageJ; see [pypi.org/project/pyimagej](https://pypi.org/project/pyimagej)).

Adobe Photoshop-like layers allow users to overlay points, vectors, tracks, surfaces, polygons, annotations or other images. A researcher could, for instance, open an image of a tissue in napari, identify cell nuclei with a click of the mouse, retrieve those points in Python and use them to ‘seed’ a cell-segmentation algorithm, which identifies cell boundaries. By then pushing the results to napari as a new layer on the original image, they can assess how well the segmentation process worked.

Xavier Casas Moreno, an applied physicist at the Royal Institute of Technology in Stockholm, has embedded napari in an instrument-control system, called ImSwitch, that he built to control his lab’s super-resolution microscopes. Using layers, researchers can overlay images taken from different angles by multiple cameras and sensors. “That’s a challenge that we couldn’t solve before,” Moreno says. A custom napari control panel, or ‘widget’, built into ImSwitch, allows users to move one image relative to the other to align them.

Users can also extend napari using plug-ins: more than 100 are available on the napari hub (see [napari-hub.org](https://napari-hub.org)). These include plug-ins for reading and writing files, microscope control and cell segmentation. Carsen Stringer, a computational neuroscientist at the Howard Hughes Medical Institute’s Janelia Research Campus near Ashburn, Virginia, created a cell-segmentation plug-in called CellPose, which makes the power of Python deep-learning algorithms available through a simple graphical interface. Stringer and her colleagues use CellPose to measure gene expression and calcium signalling cell by cell in neural tissue.

Robert Haase, who develops biological image analysis at Dresden University of Technology in Germany, has built several plug-ins for napari. These include one for his py-clEsperanto assistant, which aims to accelerate image processing and remove programming-language barriers between different image-viewing systems, and one called natari — a portmanteau of

napari and Atari (the videogame developer) — in which users play a game that involves removing cells from a field of view by shooting them.



### NatureTech hub

Nunez-Iglesias has even written a plug-in that allows users to control napari through a music instrument digital interface (MIDI) board, which typically would be used to tailor digital audio output. In a video demonstration, Nunez-Iglesias combines a MIDI controller and Apple iPad to manually segment cells by drawing on the image on the tablet with an Apple Pen, and moving from layer to layer in napari by turning a dial on the MIDI controller. “I just like hardware controllers and physical feedback more than virtual user interfaces,” he explains.

At version 0.4.12, napari is still in development, with support from the CZI science imaging programme, which hosts the napari hub and provides several staff members to the project, and code contributed by many developers in the scientific community. CZI has also earmarked US\$1 million to support the napari Plugin Accelerator grant programme: [41 awards were announced last month](#).

Key development goals include improving installation, documentation, the plug-in interface and the handling of large 3D data sets. Some experiments, such as neural connectomics studies, produce data sets so massive that the

software slows to a crawl, says Nunez-Iglesias. A ‘lazy-loading’ scheme, in which data are loaded on demand, should alleviate that bottleneck, he says.

Nunez-Iglesias estimates that napari’s user base is “in the thousands”. And it’s growing fast, even among non-microscopists. Users have demonstrated applications in geophysics and structural biology, for instance. And DeepLabCut, a popular tool for capturing the poses of animals as they move, has announced plans to replace its viewer with napari.

Hung-Yi Wu, a systems biologist then at Harvard Medical School in Boston, Massachusetts, summed up the excitement the project is generating in a tweet in 2020. “@napari\_imaging is awesome,” he wrote: “I felt like [I was] using the first iPhone”.

*Nature* **600**, 347-348 (2021)

doi: <https://doi.org/10.1038/d41586-021-03628-7>

---

This article was downloaded by **calibre** from <https://www.nature.com/articles/d41586-021-03628-7>

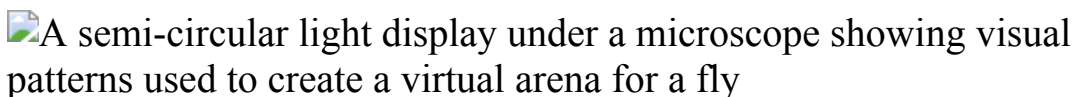
| [Section menu](#) | [Main menu](#) |

- TECHNOLOGY FEATURE
- 07 December 2021

# How remouldable computer hardware is speeding up science

Field-programmable gate arrays can speed up applications ranging from genomic alignment to deep learning.

- [Jeffrey M. Perkel](#)



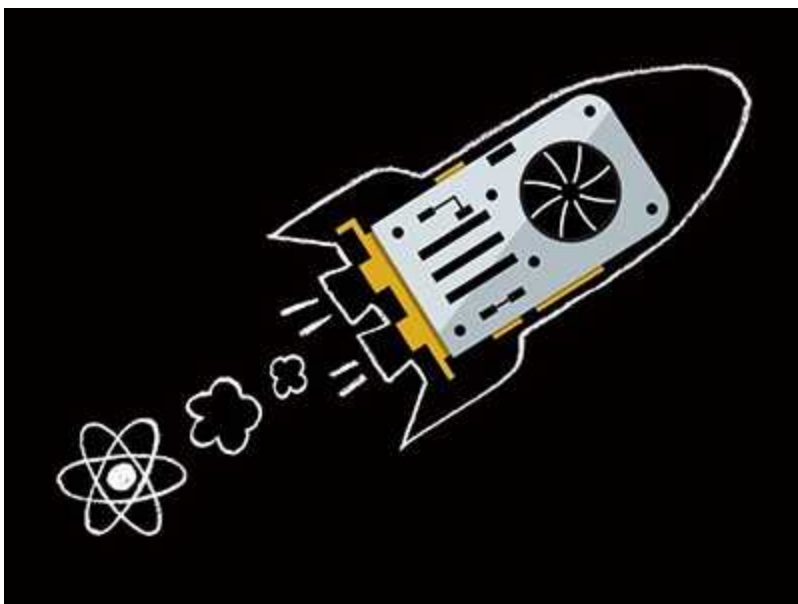
This virtual-reality arena for flies tests the insects' reaction times. Credit: Matthew Isaacson

Michael Reiser is, as he puts it, “fanatical about timing”. A neuroscientist at the Howard Hughes Medical Institute’s Janelia Research Campus in Ashburn, Virginia, Reiser studies fly vision. Some of his experiments involve placing flies in an immersive virtual-reality arena and seamlessly redrawing the scene while tracking how the insects respond. Modern PCs, with their complex operating systems and multitasking central processing units (CPUs), cannot guarantee the temporal precision required. So Reiser, together with engineers at Sciotex, a technology firm in Newtown Square, Pennsylvania, found a piece of computing hardware that could: an FPGA.

An FPGA, or field-programmable gate array, is basically “electronic mud”, says Bruno Levy, a computer scientist and director of the Inria Nancy Grand-Est research centre in Villers-lès-Nancy, France. It is a collection of hundreds or even millions of unconfigured logic elements on a silicon chip that, like clay, can be ‘moulded’ — and even re-moulded — to accelerate

applications ranging from genomic alignment to image processing to deep learning.

Suppose that a researcher needs to quickly process data streaming off a camera in chunks of 1,000 bits. Most modern CPUs have 64-bit processors and would have to break the problem into smaller pieces. But it's possible to configure an FPGA to do that calculation in a single step, says Inria Nancy computer scientist Sylvain Lefebvre. Even if each FPGA step is slower than its CPU counterpart, "it's actually a win, you're going faster", he says, because the problem isn't broken down. FPGAs excel at applications requiring precise timing, speed-critical algorithms or low energy consumption, he adds.



### [Supercharge your data wrangling with a graphics card](#)

Javier Serrano, manager of electronics design and low-level software at CERN, Europe's particle-physics laboratory near Geneva, Switzerland, and his colleagues used FPGAs, plus White Rabbit — a bespoke extension to the Ethernet networking protocol — to create a system that can capture instabilities in the Large Hadron Collider particle beam with nanosecond precision.

At Queens University Belfast, UK, computer hardware specialist Roger Woods is building a fibre-optic camera system that uses FPGAs to process

multispectral images of coronary arteries fast enough for use during surgery. And at Janelia, senior scientist Chuntao Dan has created a closed-loop imaging system that can interpret and respond to the positioning of fly wings as they beat every 5 milliseconds. Microsoft's Windows operating system introduces a timing jitter of up to 30 milliseconds, Dan says. But using an FPGA, "we achieved all the analysis in 145 microseconds", meaning temporal resolution is never an issue despite the limitations of a conventional computer.

FPGAs are configured using a hardware-description language (HDL), such as VHDL or Verilog, with which researchers can implement anything from blinking LEDs to a full-blown CPU. Another option is Silice, a language with C-like syntax that Lefebvre, who developed it, has bolted on to Verilog. Whichever HDL is used, a synthesis tool translates it into a list of logic elements, and a place-and-route tool matches those to the physical chip. The resulting bitstream is then flashed to the FPGA.



## [NatureTech hub](#)

The configuration code, or gateware, as Serrano calls it, isn't necessarily difficult to write. But it does require a different mindset to traditional programming, says Olof Kindgren, a director and co-founder of the UK-based Free and Open Source Silicon Foundation. Whereas software code is procedural, gateware is descriptive. "You describe how the data moves

between the registers in your design each clock cycle, which is not how most software developers think,” says Kindgren. As a result, even computationally savvy researchers might want to consult a specialist to squeeze the most speed from their designs.

FPGA technology dates to the mid-1980s, but improvements in design software have made it increasingly accessible. Xilinx (owned by the chipmaker AMD) and Altera (owned by chipmaker Intel) dominate the market, and both offer development tools and chips of varying complexity and cost. A handful of open-source tools also exist, including Yosys (a synthesis tool) and nextpnr (place-and-route), both developed by computer scientist Claire Wolf, who is chief technology officer at the Vienna-based software company YosysHQ. Lefebvre advises starting with a ready-to-use FPGA board that includes memory and peripherals, such as USB and HDMI ports. The Xilinx PYNQ, which can be programmed using Python, and the open-hardware iCEBreaker and ULX3S, are good options.

Reiser’s collaborators at Sciotex used an FPGA from National Instruments, based in Austin, Texas, which they programmed using the company’s graphical LabVIEW coding environment. The hardware, including components for data acquisition, cost about US\$5,000, Reiser says. But with it, he got his answer: flies can react to moving objects in their field of view about twice as fast as people can, he found. Proving that limit required a display that his team could refresh ten times faster than the reactions they were probing. “We like temporal precision,” Reiser says. “It makes our lives so much easier.”

*Nature* **600**, 348–349 (2021)

doi: <https://doi.org/10.1038/d41586-021-03627-8>

---

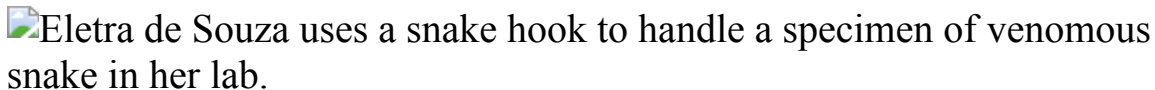
This article was downloaded by **calibre** from <https://www.nature.com/articles/d41586-021-03627-8>

- WHERE I WORK
- 06 December 2021
- Correction [08 December 2021](#)

# Handling snakes for science

Eletra de Souza's research aims to help decrease lethal strikes in Brazil.

- [Virginia Gewin](#) <sup>0</sup>



Eletra de Souza is a PhD student at the University of São Paulo, Brazil.  
Credit: Pablo Albarenga for *Nature*

I study snakes in Brazil's Ribeira Valley, an area where snake bites are very common. I focus mainly on the venomous lancehead (*Bothrops jararaca*), which I am holding here. It is responsible for most of the 26,000 recorded snake bites in Brazil each year.

After my undergraduate biology degree at the Federal University of São Carlos, I spent two years at the Butantan Institute in São Paulo, studying snakes that live in São Paulo's rivers and urban parks. I then did a master's degree at São Paulo State University, researching the reproductive biology of the bushmaster (*Lachesis muta*) — one of the largest venomous snakes in the Americas and one of the few snakes that show a form of parental care. It lays its eggs in underground burrows and remains curled around them for long periods of time to keep them warm and protected.

When I was 12 years old, I visited the Acqua Mundo aquarium on the coast of São Paulo and fell in love with a beautiful, giant, albino ball python (*Python regius*). Brazil has more than 400 snake species. At first, I just thought that snakes were pretty, but as I learnt about and worked with them,

I became curious about how their environment influences their movement and activities.

I'm now planning to attach accelerometers to snakes. These small data loggers can monitor fine-scale body movements and postures. Because many of the snakes are venomous, it is dangerous to work with them. But we learn to respect them and understand their defence behaviours, and two people always work together when handling them.

One goal of my project is to learn more about interactions with humans, aiming to inform policies to mitigate snake bites. The biggest threat to snakes is habitat loss, which has been made worse by Brazil's current environment policies, which encourage the clearing of land for farming.

*Nature* **600**, 352 (2021)

doi: <https://doi.org/10.1038/d41586-021-03629-6>

## Updates & Corrections

- **Correction 08 December 2021:** An earlier version of this article erroneously named the snake pictured as a juvenile red-tailed boa (*Boa constrictor*). In fact, the image is of the venomous lancehead (*Bothrops jararaca*).

---

This article was downloaded by **calibre** from <https://www.nature.com/articles/d41586-021-03629-6>

# Research

- [\*\*A peek into the black box of human embryology\*\*](#) [ 17

November 2021]

News & Views • The molecular mechanisms involved in human gastrulation, a crucial stage in early embryonic development, have been largely elusive. Gene-expression data from a gastrulating human embryo shed light on this process.

- [\*\*Constraints on estimating the CO<sub>2</sub> fertilization effect emerge\*\*](#) [ 08 December 2021]

News & Views • Plants offset a large fraction of Earth's carbon dioxide emissions, but estimating the size of this carbon sink relies on differing terrestrial-biosphere models. Combining multiple models with data has now reduced the uncertainty.

- [\*\*Clues that natural killer cells help to control COVID\*\*](#) [ 25 October 2021]

News & Views • Natural killer cells can destroy cells infected by SARS-CoV-2, but this immune-system defence malfunctions in people with severe COVID-19. Will this finding drive a search for ways to reinvigorate natural killer cells in such cases?

- [\*\*Giant planet imaged orbiting two massive stars\*\*](#) [ 08 December 2021]

News & Views • Direct imaging has revealed the existence of a large planet orbiting a binary system that contains the most massive planet-hosting stars detected so far. The discovery challenges existing models for how planets and stars form.

- [\*\*From the archive\*\*](#) [ 07 December 2021]

News & Views • Nature's pages feature changes in the number of topics a science lecturer might cover, and official rules about who can be called a chemist.

- [\*\*Cerebellar neurons that curb food consumption\*\*](#) [ 17 November 2021]

News & Views • Artificial activation of neurons identified in a brain region called the cerebellum reduces food intake in mice. The findings could have implications for people with appetite disorders.

- [\*\*A wide-orbit giant planet in the high-mass b Centauri binary system\*\*](#) [ 08 December 2021]

Article • A direct imaging study demonstrates the existence of a giant planet in a wide orbit around the high-mass b Centauri binary system, and uses measurements of the orbital properties to discuss its formation mechanism.

- **Giant modulation of optical nonlinearity by Floquet engineering** [ 08 December 2021]  
Article • Coherent control and giant modulation of optical nonlinearity in a van der Waals layered magnetic insulator is demonstrated using Floquet engineering.
- **Evidence for unconventional superconductivity in twisted bilayer graphene** [ 20 October 2021]  
Article • A study combining tunnelling and Andreev reflection spectroscopy with a scanning tunnelling microscope provides evidence for unconventional superconductivity in magic-angle twisted bilayer graphene.
- **High-frequency and intrinsically stretchable polymer diodes** [ 08 December 2021]  
Article • A stretchable anode, cathode, semiconductor and current collector have been developed to create stretchable diodes that can operate at megahertz frequencies for use in wirelessly operated, skin-like wearable electronics.
- **A constraint on historic growth in global photosynthesis due to increasing CO<sub>2</sub>** [ 08 December 2021]  
Article • An emergent constraint combining biosphere models and carbon budget estimates suggests that the increase in the global terrestrial carbon sink is caused largely by a CO<sub>2</sub>-induced increase in photosynthesis.
- **Bizarre tail weaponry in a transitional ankylosaur from subantarctic Chile** [ 01 December 2021]  
Article • Stegouros elengassen, an ankylosaur from the late Cretaceous of Chile, has a large tail weapon, named a macuahuitl after the Aztec club, with a frond-like structure formed by seven pairs of laterally projecting osteoderms encasing the distal half of the tail.
- **Quantifying social organization and political polarization in online platforms** [ 01 December 2021]  
Article • A new method quantifies the social makeup of online communities, and applying it to 14 years of commenting patterns on Reddit shows increased polarization in 2016, driven by new users to the platform.
- **Reverse-translational identification of a cerebellar satiation network** [ 17 November 2021]  
Article • Activity in anterior deep cerebellar nuclei reduces food consumption in mice without reducing metabolic rate, potentially identifying a therapeutic target for disorders involving excessive eating.
- **Allometric rules for mammalian cortical layer 5 neuron biophysics** [ 10 November 2021]

Article • Analyses of layer 5 cortical pyramidal neurons in 10 mammalian species show that human neurons are distinct in that they do not follow the expected allometric relationship between neuron size and membrane conductance.

- [\*\*Multiview confocal super-resolution microscopy\*\*](#) [ 26 November 2021]

Article • A combination of multiview imaging, structured illumination, reconstruction algorithms and deep-learning predictions realizes spatial- and temporal-resolution improvements in fluorescence microscopy to produce super-resolution images from diffraction-limited input images.

- [\*\*Single-cell transcriptomic characterization of a gastrulating human embryo\*\*](#) [ 17 November 2021]

Article • The single-cell transcriptional profile of a human embryo between 16 and 19 days after fertilization reveals parallels and differences in gastrulation in humans as compared with mouse and non-human primate models.

- [\*\*Observation of universal ageing dynamics in antibiotic persistence\*\*](#) [ 17 November 2021]

Article • Characterizations of bacteria under acute stress reveal features that can be predicted using a conceptual model of physical ageing.

- [\*\*Untimely TGF \$\beta\$  responses in COVID-19 limit antiviral functions of NK cells\*\*](#) [ 25 October 2021]

Article • The improper timing of transforming growth factor- $\beta$  production is a hallmark of severe COVID-19 that may impede natural killer cell function and early control of infection.

- [\*\*Host immunomodulatory lipids created by symbionts from dietary amino acids\*\*](#) [ 10 November 2021]

Article • The symbiotic gut bacterium *Bacteroides fragilis* produces unique  $\alpha$ -galactosylceramides from host dietary branched-chain amino acids, which are presented as CD1d ligands and immunomodulate natural killer T cells.

- [\*\*CRISPR screens unveil signal hubs for nutrient licensing of T cell immunity\*\*](#) [ 18 November 2021]

Article • CRISPR screening and protein–protein interaction networks identify components and mechanisms of nutrient-dependent mTORC1 signalling in regulatory T cells and reveal how mTORC1 integrates immunological cues and nutrient signals for adaptive immunity.

- [\*\*IL-27 signalling promotes adipocyte thermogenesis and energy expenditure\*\*](#) [ 24 November 2021]

Article • Therapeutic administration of IL-27—serum levels of which are decreased in individuals with obesity—improves thermogenesis, protects against diet-induced obesity and ameliorates insulin resistance in mouse models of obesity.

- **The CLIP1–LTK fusion is an oncogenic driver in non-small-cell lung cancer** [ 24 November 2021]  
Article • Whole-transcriptome sequencing of a subset of 75 non-small-cell lung cancer specimens in a multi-institutional genome screening study identified a fusion of the CLIP1 and LTK genes with transformational potential due to constitutive LTK kinase activity.
- **FAM72A antagonizes UNG2 to promote mutagenic repair during antibody maturation** [ 24 November 2021]  
Article • FAM72A differentially controls mutation rates by regulating uracil processing at different stages of the cell cycle, thereby regulating somatic hypermutation and class-switch recombination in B cells.
- **Fam72a enforces error-prone DNA repair during antibody diversification** [ 24 November 2021]  
Article • FAM72A interacts with UNG2 to regulate the balance between error-prone and error-free DNA repair.
- **Structural insights into Ubr1-mediated N-degron polyubiquitination** [ 17 November 2021]  
Article • Structures of Ubr1 in complex with Ubc2, ubiquitin and two N-degron peptides reveal a Ubc2-binding region and an acceptor ubiquitin-binding loop on Ubr1, providing mechanistic insights into the initiation and elongation steps of ubiquitination catalysed by Ubr1.
- **Structures of the HER2–HER3–NRG1 $\beta$  complex reveal a dynamic dimer interface** [ 10 November 2021]  
Article • Cryo-electron microscopy structures of the HER2–HER3–NRG1 $\beta$  complex reveal a dynamic HER2–HER3 interface and explain the mechanism for the activating HER2 cancer mutations.

- NEWS AND VIEWS
- 17 November 2021

# A peek into the black box of human embryology

The molecular mechanisms involved in human gastrulation, a crucial stage in early embryonic development, have been largely elusive. Gene-expression data from a gastrulating human embryo shed light on this process.

- [Alexander Goedel](#)<sup>0</sup> &
- [Fredrik Lanner](#)<sup>1</sup>

Even for embryology researchers, it is difficult to grasp that the entire human body is derived from a single cell. In the first weeks of life, this cell divides, building all the embryonic as well as the supportive tissues, such as the placenta. Advances in technologies to study individual cells have provided unprecedented mechanistic insights into the initial ‘decisions’ that determine the fate and lineages of cells in the early embryo, before it implants into the wall of the uterus<sup>1,2</sup>. However, the events that follow implantation have remained a ‘black box’, with knowledge based mostly on limited historical histological collections, or on experimental work performed on model organisms or *in vitro* model systems<sup>3–6</sup>. [Writing in \*Nature\*](#), Tyser *et al.*<sup>7</sup> provide a glimpse into this black box by profiling gene expression in individual cells in a post-implantation human embryo, using a method called single-cell RNA sequencing.

## Access options

[Subscribe to Journal](#)

Get full journal access for 1 year

\$199.00

only \$3.90 per issue

[Subscribe](#)

All prices are NET prices.

VAT will be added later in the checkout.

Tax calculation will be finalised during checkout.

Rent or Buy article

Get time limited or full article access on ReadCube.

from \$8.99

[Rent or Buy](#)

All prices are NET prices.

### **Additional access options:**

- [Log in](#)
- [Learn about institutional subscriptions](#)

*Nature* **600**, 223-224 (2021)

doi: <https://doi.org/10.1038/d41586-021-03381-x>

## **References**

1. 1.

Petropoulos, S. *et al.* *Cell* **165**, 1012–1026 (2016).

2. 2.

Yan, L. *et al.* *Nature Struct. Mol. Biol.* **20**, 1131–1139 (2013).

3. 3.

Ghimire, S., Mantziou, V., Moris, N. & Martinez Arias, A. *Dev. Biol.* **474**, 100–108 (2021).

4. 4.

Nakamura, T. *et al.* *Nature* **537**, 57–62 (2016).

5. 5.

Ma, H. *et al.* *Science* **366**, eaax7890 (2019).

6. 6.

Zhou, F. *et al.* *Nature* **572**, 660–664 (2019).

7. 7.

Tyser, R. C. V. *et al.* *Nature* **600**, 285–289 (2021).

8. 8.

Jarvis, G. E. *F1000Res.* **5**, 2765 (2016).

9. 9.

Chen, D. *et al.* *Cell Rep.* **29**, 4568–4582 (2019).

10. 10.

Tavian, M., Hallais, M. F. & Péault, B. *Development* **126**, 793–803 (1999).

11. 11.

Yang, R. *et al.* *Nature Commun.* **12**, 5126 (2021).

12. 12.

Minn, K. T., Dietmann, S., Waye, S. E., Morris, S. A. & Solnica-Krezel, L. *Stem Cell Rep.* **16**, 1210–1227 (2021).

---

This article was downloaded by **calibre** from <https://www.nature.com/articles/d41586-021-03381-x>

| [Section menu](#) | [Main menu](#) |

- NEWS AND VIEWS
- 08 December 2021

# Constraints on estimating the CO<sub>2</sub> fertilization effect emerge

Plants offset a large fraction of Earth's carbon dioxide emissions, but estimating the size of this carbon sink relies on differing terrestrial-biosphere models. Combining multiple models with data has now reduced the uncertainty.

- [Chris Huntingford](#) <sup>0</sup> &
- [Rebecca J. Oliver](#) <sup>1</sup>

The goal of mitigating climate change requires a global commitment to reducing greenhouse-gas emissions to avoid substantial temperature increases. However, achieving this objective is complicated by uncertainty over how much carbon dioxide will be absorbed naturally by trees and other plants. [Writing in Nature](#), Keenan *et al.*<sup>1</sup> have constrained estimates of this uncertainty by drawing empirical links between observations of the current climate and multi-model predictions of the land-carbon sink. The relationships between these observations and predictions are known as emergent constraints.

## Access options

Subscribe to Journal

Get full journal access for 1 year

\$199.00

only \$3.90 per issue

## Subscribe

All prices are NET prices.

VAT will be added later in the checkout.

Tax calculation will be finalised during checkout.

Rent or Buy article

Get time limited or full article access on ReadCube.

from \$8.99

## Rent or Buy

All prices are NET prices.

## **Additional access options:**

- [Log in](#)
- [Learn about institutional subscriptions](#)

*Nature* **600**, 224–225 (2021)

doi: <https://doi.org/10.1038/d41586-021-03560-w>

## **References**

1. 1.

Keenan, T. F. *et al.* *Nature* **600**, 253–258 (2021).

2. 2.

Etheridge, D. M. *et al.* *J. Geophys. Res. Atmos.* **101**, 4115–4128 (1996).

3. 3.

Ainsworth, E. A. & Long, S. P. *Glob. Change Biol.* **27**, 27–49 (2021).

4. 4.

Friedlingstein, P. *et al. Earth Syst. Sci. Data* **12**, 3269–3340 (2020).

5. 5.

Ryu, Y., Berry, J. A. & Baldocchi, D. D. *Remote Sens. Environ.* **223**, 95–114 (2019).

6. 6.

Hall, A., Cox, P., Huntingford, C. & Klein, S. *Nature Clim. Change* **9**, 269–278 (2019).

7. 7.

Williamson, M. S. *et al. Rev. Mod. Phys.* **93**, 025004 (2021).

8. 8.

Hungate, B. A., Dukes, J. S., Shaw, M. R., Luo, Y. & Field, C. B. *Science* **302**, 1512–1513 (2003).

9. 9.

Arora, V. K. *et al. Biogeosciences* **17**, 4173–4222 (2020).

10. 10.

Fleischer, K. *et al. Nature Geosci.* **12**, 736–741 (2019).

11. 11.

Mercado, L. M. *et al. N. Phytol.* **218**, 1462–1477 (2018).

12. 12.

Xia, J., Yuan, W., Wang, Y.-P. & Zhang, Q. *Sci. Rep.* **7**, 3341 (2017).

---

This article was downloaded by **calibre** from <https://www.nature.com/articles/d41586-021-03560-w>

| [Section menu](#) | [Main menu](#) |

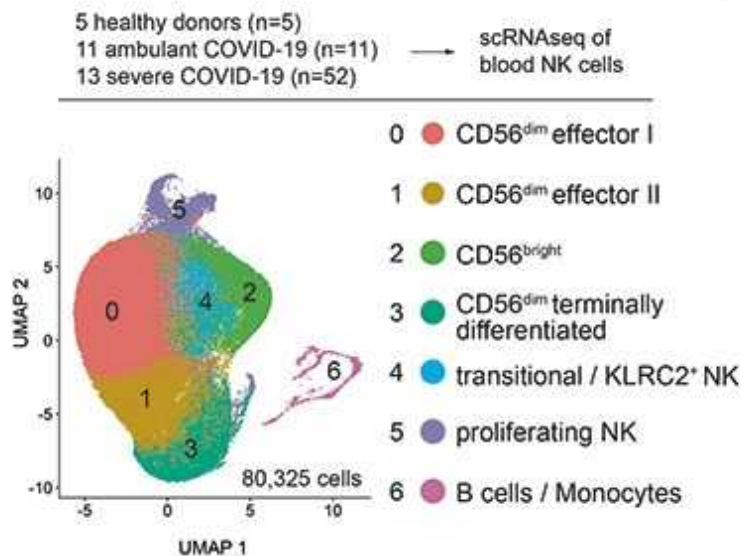
- NEWS AND VIEWS
- 25 October 2021

# Clues that natural killer cells help to control COVID

Natural killer cells can destroy cells infected by SARS-CoV-2, but this immune-system defence malfunctions in people with severe COVID-19. Will this finding drive a search for ways to reinvigorate natural killer cells in such cases?

- [Emilie Narni-Mancinelli](#) <sup>0</sup> &
- [Eric Vivier](#) <sup>1</sup>

Most cases of SARS-CoV-2 infection are mild, but a proportion of people progress to severe COVID-19 for reasons that are not entirely clear. Some factors associated with the severe illness are known. For example, people with severe COVID-19 often have other pre-existing conditions, such as coronary artery disease, hypertension and diabetes<sup>1</sup>. Unsurprisingly, compromised antiviral defences can also lead to life-threatening illness, as is the case for around 15% of people with severe COVID-19 who have a deficiency in what is called the type I interferon pathway<sup>2</sup>. Indeed, it has been known since the discovery of this pathway in 1957 that it directly interferes with viral replication in an infected cell<sup>3</sup>.



### [Read the paper: Untimely TGF \$\beta\$ responses in COVID-19 limit antiviral functions of NK cells](#)

There might also be other mechanisms at play in antiviral defences, such as a role for the natural killer (NK) cells of the immune system. [Writing in Nature](#), Witkowski *et al.*<sup>4</sup> report that people with severe COVID-19 have higher than normal levels of an anti-inflammatory molecule, transforming growth factor- $\beta$ 1 (TGF- $\beta$ 1), in their bloodstream, and that this is associated with impaired antiviral defence by NK cells and defective immune-system control of SARS-CoV-2.

Natural killer cells are white blood cells that are part of the innate branch of the immune system. They make key contributions to tackling viral infections, and their rapid activation is linked to the efficient control of several types of virus<sup>5</sup>. NK cells can eliminate virus-infected cells in various ways — by releasing cytotoxic granules (termed degranulation) that directly kill the virus-infected cells, or by shaping both the innate and adaptive branches of immune defence by producing molecules called cytokines and chemokines, which can modulate the behaviour of other immune cells. Previous studies<sup>6–10</sup> monitored the responses of NK cells in individuals with COVID-19, and reported lower than normal levels of NK cells in people with the disease, but the precise role of these cells in severe COVID-19 was unclear.

Witkowski *et al.* analysed clinical samples, and found a correlation between a rapid decline in the level of virus (the viral load) and high levels of NK cells in the bloodstream at the beginning of the infection. This correlation was not observed for the T cells or B cells of the immune system. The drastic decrease in NK cells in the bloodstream over the course of infection might be due to their death by a process called apoptosis<sup>7</sup>, or their recruitment from the bloodstream to the lungs.

Crucially, Witkowski *et al.* report that NK cells from healthy individuals can directly kill SARS-CoV-2-infected cells *in vitro*, but that NK cells from people with moderate or severe COVID-19 had impaired cell-killing activity (Fig. 1). These defective NK cells express higher-than-normal levels of the cytotoxic molecules that kill cells, but are impaired in their ability to bind to target cells and to export their cytotoxic granules at the cell surface. In addition, NK cells from people with severe COVID-19 were less able to produce cytokines and chemokines than were such cells from healthy donors or from infected people who have no or minimal COVID-19 symptoms.

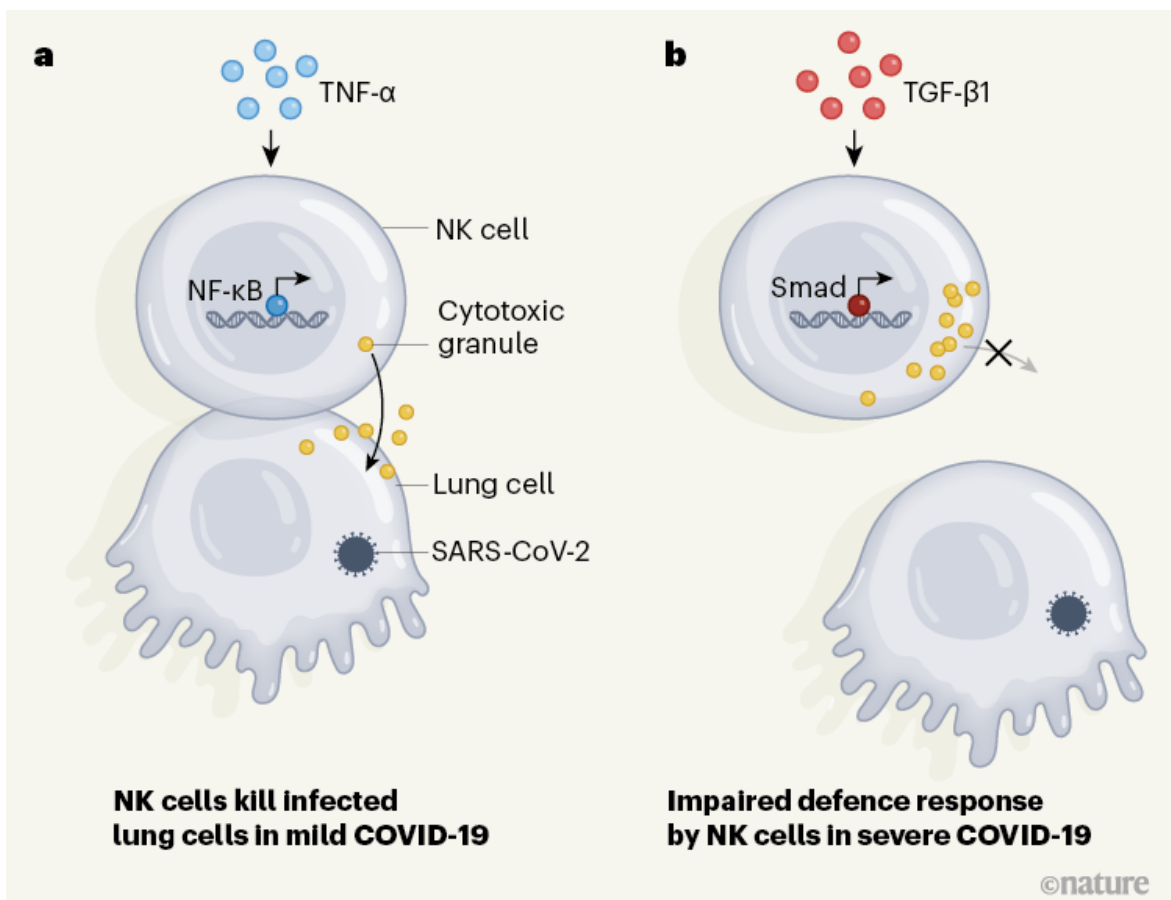
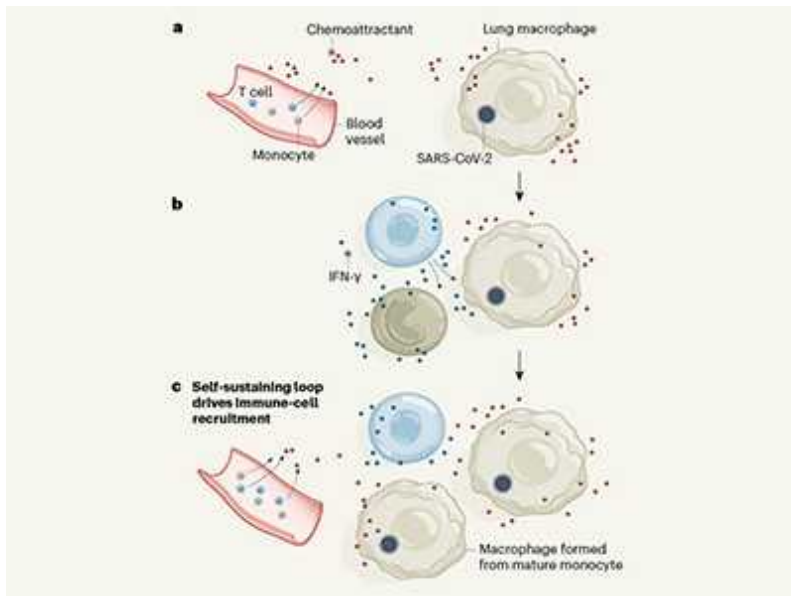


**Figure 1 | Characterizing immune responses associated with COVID-19.** Immune cells called natural killer (NK) cells can help to tackle viral infections by releasing cytotoxic granules that can kill infected cells. **a**, Previous work<sup>7</sup> indicates that, in cases of mild COVID-19, NK cells express genes that are typically induced through the protein TNF- $\alpha$  pathway. This type of gene-expression profile arises through the action of transcription factors such as the protein NF- $\kappa$ B, and it aids the recovery of function of NK cells<sup>7</sup>. **b**, Witkowski *et al.*<sup>4</sup> analysed samples of NK cells from individuals with severe COVID-19, and report that these cells had a gene-expression pattern characteristic of that driven by the protein TGF- $\beta$ 1. Gene expression mediated by this pathway depends on transcription factors that include Smad proteins. The authors report that NK cells from people with severe COVID-19 are impaired in their ability to bind to infected cells and to release cytotoxic granules. This finding provides insights into the factors driving severe COVID-19.

To dissect the mechanisms underlying the dysfunction of NK cells, Witkowski *et al.* assessed gene expression by carrying out single-cell RNA sequencing of these cells from people with COVID-19 of differing degrees of severity. The authors found, consistently with another study<sup>7</sup> reporting a similar transcriptional analysis of NK cells from people with COVID-19, that the cells had a gene-expression pattern characteristic of that driven by type I interferons. This gene-expression signature was more prominent in NK cells from people with severe rather than milder forms of COVID-19. Moreover, a pattern of gene expression characteristic of that driven by the protein TNF- $\alpha$  in NK cells has been described<sup>7</sup> for mild cases of COVID-19. Witkowski *et al.* also reveal an increase in the expression of genes controlled by TGF- $\beta$ 1 in NK cells purified from either the blood or the lungs of people infected with SARS-CoV-2. This increase seems to correlate with the patients' symptoms, with a higher prevalence of TGF- $\beta$ 1-driven gene expression corresponding to more severe illness.

TGF- $\beta$ 1 is a cytokine with a central role in tissue remodelling, but it also suppresses the functioning of NK cells<sup>11</sup>. TGF- $\beta$ 1 limits the ability of NK cells to control SARS-CoV-2 replication as tested *in vitro*. When NK cells from healthy individuals were treated with TGF- $\beta$ 1 *in vitro*, the cells were

less able to form connections with infected target cells and were less able to degranulate and produce cytokines.

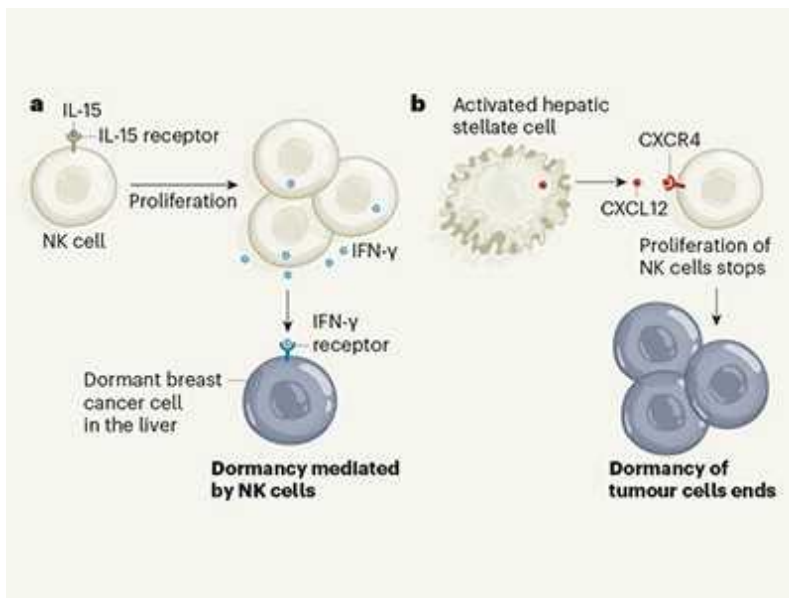


### Signs of self-sustained inflammatory circuits in severe COVID pneumonia

Witkowski and colleagues report high levels of TGF- $\beta$ 1 in the blood of people with severe COVID-19, but not in those with no or minimal signs of the disease. Notably, the authors reveal that serum from people with severe COVID-19 can limit, to some extent, the *in vitro* degranulation and control of viral replication mediated by NK cells from healthy donors, and that this effect can be prevented by adding an antibody that blocks TGF- $\beta$ 1. Together, these findings indicate a correlation between severe COVID-19, the presence of a high level of TGF- $\beta$ 1 in the bloodstream and an impaired defensive response by NK cells.

Several questions remain. The first is whether NK cells are necessary to fight SARS-CoV-2 infection. Several studies of mouse models of respiratory viral infections, such as influenza A virus, respiratory syncytial virus and Sendai virus, have shown that NK cells contribute to virus control and aid host survival<sup>5</sup>. Consistent with this, the only characteristic shared by people with various types of NK-cell deficiency is a predisposition to viral infections, especially of herpesvirus<sup>12</sup>. The fact that type I interferons are strong activators of NK cells also suggests a link between deficiencies in type I interferons and impaired NK-cell-mediated antiviral immunity. All

these findings, together with the inverse correlation between the number of functional NK cells and the severity of COVID-19, support a role for these cells in controlling SARS-CoV-2 infection, but formal proof of this hypothesis remains to be obtained.



### Natural killer cells lull tumours into dormancy

A second question to be addressed is, what are the mechanisms underlying the high production of TGF- $\beta$ 1 during COVID-19? SARS-CoV-2 contains a spike protein that interacts with the ACE2 receptor on human cells<sup>1</sup>. This receptor is an enzyme that converts the protein angiotensin II (AngII) to a peptide called Ang1-7. The enzymatic activity of ACE2 is disturbed during SARS-CoV-2 infection, resulting in a rise in AngII levels that promotes TGF- $\beta$ 1 expression<sup>1</sup>. Thus, excessive damage to lung tissue caused by a high viral load might induce a high level of TGF- $\beta$ 1, which could affect NK cells. Moreover, TGF- $\beta$ 1 is known to promote a type of tissue damage called fibrosis, which is a hallmark of severe COVID-19. A rise in the level of AngII is a common feature of coronary artery disease, hypertension and diabetes<sup>13</sup>, and high levels of TGF- $\beta$ 1 are observed in obesity<sup>14</sup>. It will therefore be interesting to investigate whether the association of such conditions with severe COVID-19 involves defective functioning of NK cells mediated by TGF- $\beta$ 1.

Ways of manipulating NK cells are of increasing interest in anticancer therapy, using approaches such as immune-checkpoint inhibitors, NK-cell ‘engagers’ and off-the-shelf infusions of NK cells<sup>15</sup>. The importance of NK cells in the control of viruses should similarly prompt the design of innovative treatments based on harnessing these cells to fight viral infections. In the case of severe COVID-19, the high levels of TGF- $\beta$ 1 present might compromise strategies to boost the activity of NK cells. Instead, the use of TGF- $\beta$ 1 blockers<sup>16</sup> might be a way to promote NK-cell-mediated antiviral defence and prevent lung fibrosis, although the safety of such treatment in this context is a concern that should be addressed. In addition, monitoring TGF- $\beta$ 1 levels in plasma, along with TNF- $\alpha$ -mediated gene expression in NK cells from the bloodstream<sup>7</sup>, might help to predict the outcome of infection and to guide a patient’s care appropriately.

*Nature* **600**, 226–227 (2021)

doi: <https://doi.org/10.1038/d41586-021-02778-y>

## References

1. 1.

Delpino, M. V. & Quarleri, J. *Front. Cell. Infect. Microbiol.* **10**, 340 (2020).

2. 2.

Bastard, P. *et al.* *Sci. Immunol.* **6**, eabl4340 (2021).

3. 3.

Hoffmann H.-H., Schneider W. M. & Rice C. M. *Trends Immunol.* **36**, 124–138 (2015).

4. 4.

Witkowski, M. *et al.* *Nature* **600**, 295–301 (2021).

5. 5.

Waggoner, S. N. *et al.* *Curr. Opin. Virol.* **16**, 15–23 (2016).

6. 6.

Jiang, Y. *et al.* *Clin. Immunol.* **218**, 108516 (2020).

7. 7.

Kramer, B. *et al.* *Immunity*  
<https://doi.org/10.1016/j.jimmuni.2021.09.002> (2021).

8. 8.

Maucourant, C. *et al.* *Sci. Immunol.* **5**, eabd6832 (2020).

9. 9.

Wilk, A. J. *et al.* *Nature Med.* **26**, 1070–1076 (2020).

10. 10.

Demaria, O. *et al.* *Cell. Mol. Immunol.* **17**, 995–997 (2020).

11. 11.

Viel, S. *et al.* *Sci. Signal.* **9**, ra19 (2016).

12. 12.

Jouanguy, E. *et al.* *Curr. Opin. Allergy Clin. Immunol.* **13**, 589–595 (2013).

13. 13.

Liu, L.-P., Zhang, X.-L. & Li, J. *World J. Diabetes* **12**, 839–854 (2021).

14. 14.

Fain, J. N. Tichansky, D. S. & Madan, A. K. *Metabolism* **54**, 1546–1551 (2005).

15. 15.

Myers, J. A. & Miller, J. S. *Nature Rev. Clin. Oncol.* **18**, 85–100 (2021).

16. 16.

Huang, C. Y. *et al.* *Biomed. Pharmacother.* **134**, 111046 (2021).

---

This article was downloaded by **calibre** from <https://www.nature.com/articles/d41586-021-02778-y>.

| [Section menu](#) | [Main menu](#) |

- NEWS AND VIEWS
- 08 December 2021

# Giant planet imaged orbiting two massive stars

Direct imaging has revealed the existence of a large planet orbiting a binary system that contains the most massive planet-hosting stars detected so far. The discovery challenges existing models for how planets and stars form.

- [Kaitlin Kratter](#) <sup>0</sup>

If a child had been asked to draw a planet 30 years ago, they would have had a relatively straightforward task. Perhaps they would draw Earth in orbit around the Sun, or maybe Saturn with its beautiful ring system. Now, the options are dizzying: as detection techniques have become more powerful, myriad planetary systems have been discovered, hosting planets with a range of masses, charting varied orbits around a diverse population of stars. [Writing in Nature](#), Janson *et al.*<sup>1</sup> have further stretched our collective imagination of what a planetary system looks like, by directly imaging a planet of roughly ten times the mass of Jupiter, orbiting not one, but two stars, whose combined mass is nearly ten times that of the Sun.

## Access options

Subscribe to Journal

Get full journal access for 1 year

\$199.00

only \$3.90 per issue

## Subscribe

All prices are NET prices.  
VAT will be added later in the checkout.  
Tax calculation will be finalised during checkout.

Rent or Buy article

Get time limited or full article access on ReadCube.

from \$8.99

## Rent or Buy

All prices are NET prices.

## **Additional access options:**

- [Log in](#)
- [Learn about institutional subscriptions](#)

*Nature* **600**, 227–228 (2021)

doi: <https://doi.org/10.1038/d41586-021-03607-y>

## **References**

1. 1.

Janson, M. *et al.* *Nature* **600**, 231–234 (2021).

2. 2.

Wolszczan, A. & Frail, D. *Nature* **355**, 145–147 (1992).

3. 3.

Mayor, M. & Queloz, D. *Nature* **378**, 355–359 (1995).

4. 4.

Youdin, A. N. *Astrophys. J.* **742**, 38 (2011).

5. 5.

Marois, C. *et al. Science* **322**, 1348 (2008).

6. 6.

Gaudi, B. *et al. Nature* **546**, 514–518 (2017).

7. 7.

Doyle, L.-R. *et al. Science* **333**, 1602–1606 (2011).

8. 8.

Nesvorný, D., Li, R., Youdin, A. N., Simon, J. B. & Grundy, W. M. *Nature Astron.* **3**, 808–812 (2019).

9. 9.

Kratter, K. & Lodato, G. *Annu. Rev. Astron. Astrophys.* **54**, 271–311 (2016).

10. 10.

Moe, M. & Di Stefano, R. *Astrophys. J. Suppl. Ser.* **230**, 15 (2017).

---

This article was downloaded by **calibre** from <https://www.nature.com/articles/d41586-021-03607-y>.

- NEWS AND VIEWS
- 07 December 2021

## From the archive

*Nature's* pages feature changes in the number of topics a science lecturer might cover, and official rules about who can be called a chemist.

**100 years ago**

### Access options

Subscribe to Journal

Get full journal access for 1 year

\$199.00

only \$3.90 per issue

[Subscribe](#)

All prices are NET prices.

VAT will be added later in the checkout.

Tax calculation will be finalised during checkout.

Rent or Buy article

Get time limited or full article access on ReadCube.

from \$8.99

[Rent or Buy](#)

All prices are NET prices.

## **Additional access options:**

- [Log in](#)
- [Learn about institutional subscriptions](#)

*Nature* **600**, 229 (2021)

*doi:* <https://doi.org/10.1038/d41586-021-03561-9>

---

This article was downloaded by **calibre** from <https://www.nature.com/articles/d41586-021-03561-9>

| [Section menu](#) | [Main menu](#) |

- NEWS AND VIEWS
- 17 November 2021

# Cerebellar neurons that curb food consumption

Artificial activation of neurons identified in a brain region called the cerebellum reduces food intake in mice. The findings could have implications for people with appetite disorders.

- [Richard Simerly](#) <sup>0</sup> &
- [Ralph DiLeone](#) <sup>1</sup>

The desire to consume food is one of the strongest drives in nature, and its opposition by inhibitory signals is required to maintain an optimal energy balance. In calorie-rich environments, how much we eat is jointly influenced by our internal state (for example, how hungry we feel) and the effect of environmental cues, such as the aroma or visual appeal of food. When we are hungry and see or smell a meal, we initiate a series of actions that will lead to us consuming the food. If we feel full or lack an appetite, we would probably push the plate away and end the meal. [Writing in Nature](#), Low *et al.*<sup>1</sup> show that neuronal cells in a brain region called the cerebellum have a key role in regulating satiety and meal termination.

## Access options

Subscribe to Journal

Get full journal access for 1 year

\$199.00

only \$3.90 per issue

## Subscribe

All prices are NET prices.  
VAT will be added later in the checkout.  
Tax calculation will be finalised during checkout.

Rent or Buy article

Get time limited or full article access on ReadCube.

from \$8.99

## Rent or Buy

All prices are NET prices.

## **Additional access options:**

- [Log in](#)
- [Learn about institutional subscriptions](#)

*Nature* **600**, 229–230 (2021)

doi: <https://doi.org/10.1038/d41586-021-03383-9>

## **References**

1. 1.

Low, A. Y. T. *et al.* *Nature* **600**, 269–273 (2021).

2. 2.

Angulo, M. A., Butler, M. G. & Cataletto, M. E. *J. Endocrinol. Invest.* **38**, 1249–1263 (2015).

3. 3.

Berthoud, H.-R. & Morrison, C. *Annu. Rev. Psychol.* **59**, 55–92 (2008).

4. 4.

Castro, D. C., Cole, S. L. & Berridge, K. C. *Front. Syst. Neurosci.* **9**, 90 (2015).

5. 5.

Williams, K. W. & Elmquist, J. K. *Nature Neurosci.* **15**, 1350–1355 (2012).

6. 6.

Sternson, S. M. & Eiselt, A.-K. *Annu. Rev. Physiol.* **79**, 401–423 (2017).

7. 7.

Andermann, M. L. & Lowell, B. B. *Neuron* **95**, 757–778 (2017).

8. 8.

Zhu, J.-N., Yung, W.-H., Chow, B. K.-C., Chan, Y.-S. & Wang, J.-J. *Brain Res. Rev.* **52**, 93–106 (2006).

9. 9.

McCutcheon, J. E., Beeler, J. A. & Roitman, M. F. *Synapse* **66**, 346–351 (2012).

10. 10.

Robinson, J. E. *et al.* *eLife* **8**, e48983 (2019).

11. 11.

Beeler, J. A., Frazier, C. R. M. & Zhuang, X. *Eur. J. Neurosci.* **35**, 146–159 (2012).

12. 12.

Wang, G. J. *et al. Lancet* **357**, 354–357 (2001).

13. 13.

Engelhard, B. *et al. Nature* **570**, 509–513 (2019).

14. 14.

Beeler, J. A., Frazier, C. R. M. & Zhuang, X. *Front. Integr. Neurosci.* **6**, 49 (2012).

15. 15.

Chung, M. S., Langouët, M., Chamberlain, S. J. & Carmichael, G. G. *Open Biol.* **10**, 200195 (2020).

16. 16.

Krakauer, J. W. & Mazzoni, P. *Curr. Opin. Neurobiol.* **21**, 636–644 (2011).

17. 17.

Ohyama, T., Nores, W. L., Murphy, M. & Mauk, M. D. *Trends Neurosci.* **26**, 222–227 (2003).

18. 18.

Requarth, T. & Sawtell, N. B. *Curr. Opin. Neurobiol.* **21**, 602–608 (2011).

---

This article was downloaded by **calibre** from <https://www.nature.com/articles/d41586-021-03383-9>

- Article
- [Published: 08 December 2021](#)

# A wide-orbit giant planet in the high-mass b Centauri binary system

- [Markus Janson](#)<sup>1</sup>,
- [Raffaele Gratton](#)<sup>2</sup>,
- [Laetitia Rodet](#) [ORCID: orcid.org/0000-0002-1259-3312](#)<sup>3</sup>,
- [Arthur Vigan](#) [ORCID: orcid.org/0000-0002-5902-7828](#)<sup>4</sup>,
- [Mickaël Bonnefoy](#)<sup>5</sup>,
- [Philippe Delorme](#) [ORCID: orcid.org/0000-0002-2279-410X](#)<sup>5</sup>,
- [Eric E. Mamajek](#)<sup>6</sup>,
- [Sabine Reffert](#) [ORCID: orcid.org/0000-0002-0460-8289](#)<sup>7</sup>,
- [Lukas Stock](#)<sup>7</sup>,
- [Gabriel-Dominique Marleau](#)<sup>8,9,10</sup>,
- [Maud Langlois](#) [ORCID: orcid.org/0000-0003-3574-9903](#)<sup>11</sup>,
- [Gaël Chauvin](#)<sup>5,12</sup>,
- [Silvano Desidera](#)<sup>2</sup>,
- [Simon Ringqvist](#) [ORCID: orcid.org/0000-0001-6377-8272](#)<sup>1</sup>,
- [Lucio Mayer](#)<sup>13</sup>,
- [Gayathri Viswanath](#) [ORCID: orcid.org/0000-0003-3250-6236](#)<sup>1</sup>,
- [Vito Squicciarini](#) [ORCID: orcid.org/0000-0002-3122-6809](#)<sup>2,14</sup>,
- [Michael R. Meyer](#) [ORCID: orcid.org/0000-0003-1227-3084](#)<sup>15</sup>,
- [Matthias Samland](#)<sup>1</sup>,
- [Simon Petrus](#)<sup>5</sup>,
- [Ravit Helled](#) [ORCID: orcid.org/0000-0001-5555-2652](#)<sup>13</sup>,
- [Matthew A. Kenworthy](#) [ORCID: orcid.org/0000-0002-7064-8270](#)<sup>16</sup>,
- [Sascha P. Quanz](#) [ORCID: orcid.org/0000-0003-3829-7412](#)<sup>17</sup>,

- [Beth Biller<sup>18</sup>](#),
- [Thomas Henning](#) [ORCID: orcid.org/0000-0002-1493-300X<sup>10</sup>](#),
- [Dino Mesa<sup>2</sup>](#),
- [Natalia Engler<sup>17</sup>](#) &
- [Joseph C. Carson<sup>19</sup>](#)

[\*Nature\*](#) volume **600**, pages 231–234 (2021)

- 1253 Accesses
- 878 Altmetric
- [Metrics details](#)

## Subjects

- [Exoplanets](#)
- [Stars](#)

## Abstract

Planet formation occurs around a wide range of stellar masses and stellar system architectures<sup>1</sup>. An improved understanding of the formation process can be achieved by studying it across the full parameter space, particularly towards the extremes. Earlier studies of planets in close-in orbits around high-mass stars have revealed an increase in giant planet frequency with increasing stellar mass<sup>2</sup> until a turnover point at 1.9 solar masses ( $M_{\odot}$ ), above which the frequency rapidly decreases<sup>3</sup>. This could potentially imply that planet formation is impeded around more massive stars, and that giant planets around stars exceeding  $3 M_{\odot}$  may be rare or non-existent. However, the methods used to detect planets in small orbits are insensitive to planets in wide orbits. Here we demonstrate the existence of a planet at 560 times the Sun–Earth distance from the 6- to  $10 M_{\odot}$  binary b Centauri through direct imaging. The planet-to-star mass ratio of 0.10–0.17% is similar to the Jupiter–Sun ratio, but the separation of the detected planet is about 100 times wider than that of Jupiter. Our results show that planets can reside in

much more massive stellar systems than what would be expected from extrapolation of previous results. The planet is unlikely to have formed in situ through the conventional core accretion mechanism<sup>4</sup>, but might have formed elsewhere and arrived to its present location through dynamical interactions, or might have formed via gravitational instability.

This is a preview of subscription content

## Access options

Subscribe to Journal

Get full journal access for 1 year

\$199.00

only \$3.90 per issue

[Subscribe](#)

All prices are NET prices.

VAT will be added later in the checkout.

Tax calculation will be finalised during checkout.

Rent or Buy article

Get time limited or full article access on ReadCube.

from \$8.99

[Rent or Buy](#)

All prices are NET prices.

### Additional access options:

- [Log in](#)
- [Learn about institutional subscriptions](#)

**Fig. 1: Image of b Cen (AB)b.**

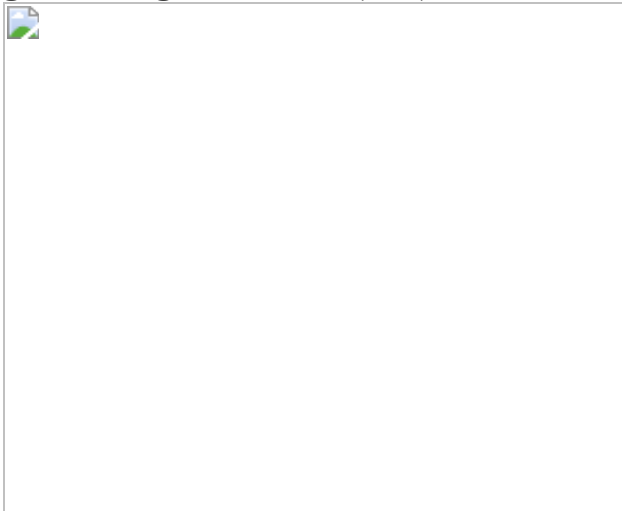
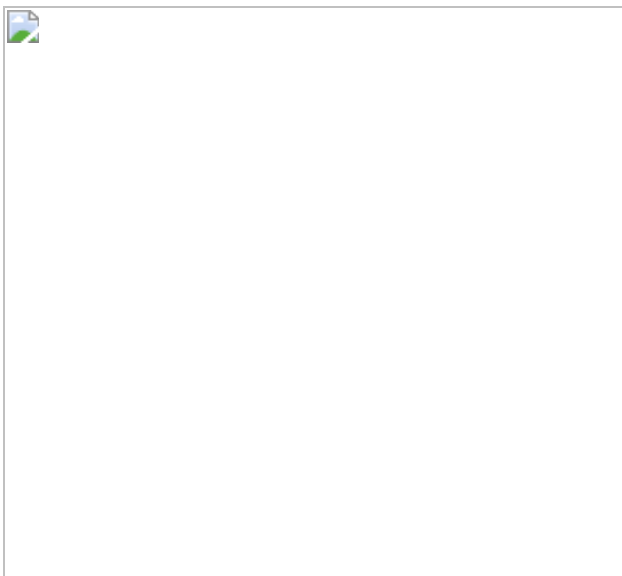


**Fig. 2: The planet-to-star mass ratio of b Cen (AB)b in an exoplanetary context.**



## Data availability

All the raw data used in this study are available at the European Southern Observatories archive (<http://archive.eso.org/cms.html>) under programme ID 1101.C-0258, by default after a proprietary time of 1 yr after each respective dataset was acquired, but earlier access can be provided upon reasonable request to the corresponding author. Processed data are available from the Data Center by following the instructions at <https://sphere.osug.fr/spip.php?article74&lang=en>.

# Code availability

Data were processed using recipes at the SPHERE Data Center. Access to the Data Center is available by following the instructions at  
<https://sphere.osug.fr/spip.php?article47&lang=en>.

# References

1. 1.

Winn, J. N. & Fabrycky, D. C. The occurrence and architecture of exoplanetary systems. *Annu. Rev. Astron. Astrophys.* **53**, 409–447 (2015).

2. 2.

Johnson, J. A., Aller, K. M., Howard, A. W. & Crepp, J. R. Giant planet occurrence in the stellar mass-metallicity plane. *Publ. Astron. Soc. Pac.* **122**, 905 (2010).

3. 3.

Reffert, S., Bergmann, C., Quirrenbach, A., Trifonov, T. & Künstler, A. Precise radial velocities of giant stars. VII. Occurrence rate of giant extrasolar planets as a function of mass and metallicity. *Astron. Astrophys.* **574**, A116 (2015).

4. 4.

Mordasini, C., Alibert, Y., Benz, W., Klahr, H. & Henning, T. Extrasolar planet population synthesis. IV. Correlations with disk metallicity, mass, and lifetime. *Astron. Astrophys.* **541**, A97 (2012).

5. 5.

Janson, M. et al. BEAST begins: sample characteristics and survey performance of the B-star Exoplanet Abundance Study. *Astron.*

*Astrophys.* **646**, A164 (2021).

6. 6.

Shatsky, N. & Tokovinin, A. The mass ratio distribution of B-type visual binaries in the Sco OB2 association. *Astron. Astrophys.* **382**, 92–103 (2002).

7. 7.

Houk, N. *Michigan Catalogue of Two-dimensional Spectral Types for the HD stars. Volume 3 (p. 8). Declinations -40 to -26* (Dept. of Astronomy, Univ. of Michigan, 1982).

8. 8.

Gutierrez-Moreno, A. & Moreno, H. A photometric investigation of the Scorpio-Centaurus association. *Astrophys. J. Suppl.* **15**, 459 (1968).

9. 9.

Bressan, A. et al. PARSEC: stellar tracks and isochrones with the PAdova and TRieste Stellar Evolution Code. *Mon. Not. R. Astron. Soc.* **427**, 127–145 (2012).

10. 10.

Gaia Collaboration. *Gaia* Early Data Release 3. Summary of the contents and survey properties. *Astron. Astrophys.* **649**, A1 (2021).

11. 11.

Nguyen, M. M., De Rosa, R. J. & Kalas, P. First detection of orbital motion for HD 106906 b: a wide-separation exoplanet on a Planet Nine-like orbit. *Astron. J.* **161**, 22 (2021).

12. 12.

Marleau, G.-D. & Cumming, A. Constraining the initial entropy of directly detected exoplanets. *Mon. Not. R. Astron. Soc.* **437**, 1378–1399 (2014).

13. 13.

Marleau, G.-D., Coleman, G. A. L., Leleu, A. & Mordasini, C. Exploring the formation by core accretion and the luminosity evolution of directly imaged planets. The case of HIP 65426 b. *Astron. Astrophys.* **624**, A20 (2019).

14. 14.

Reggiani, M. & Meyer, M. R. Universality of the companion mass-ratio distribution. *Astron. Astrophys.* **553**, A124 (2013).

15. 15.

Blunt, S. et al. Orbits for the impatient: a Bayesian rejection-sampling method for quickly fitting the orbits of long-period exoplanets. *Astron. J.* **153**, 229 (2017).

16. 16.

Nielsen, E. L. et al. The Gemini Planet Imager Exoplanet Survey: giant planet and brown dwarf demographics from 10 to 100 au. *Astron. J.* **158**, 13 (2019).

17. 17.

Vigan, A. et al. The SPHERE infrared survey for exoplanets (SHINE). III. The demographics of young giant exoplanets below 300 au with SPHERE. *Astron. Astrophys.* **651**, 72 (2021).

18. 18.

Yao, Y., Meyer, M. R., Covey, K. R., Tan, J. C. & Da Rio, N. IN SYNC. VIII. Primordial disk frequencies in NGC 1333, IC 348, and the Orion A molecular cloud. *Astrophys. J.* **869**, 72 (2018).

19. 19.

Adams, F. C., Meyer, M. R. & Adams, A. D. A theoretical framework for the mass distribution of gas giant planets forming through the core accretion paradigm. *Astrophys. J.* **909**, 1 (2021).

20. 20.

Kennedy, G. M. & Kenyon, S. J. Planet formation around stars of various masses: the snow line and the frequency of giant planets. *Astrophys. J.* **673**, 502–512 (2008).

21. 21.

Beltrán, M. T. & de Wit, W. J. Accretion disks in luminous young stellar objects. *Astron. Astrophys. Rev.* **24**, 6 (2016).

22. 22.

Pollack, J. B. et al. Formation of the giant planets by concurrent accretion of solids and gas. *Icarus* **124**, 62–85 (1996).

23. 23.

Lambrechts, M. & Johansen, A. Rapid growth of gas-giant cores by pebble accretion. *Astron. Astrophys.* **544**, A32 (2012).

24. 24.

Holman, M. J. & Wiegert, P. A. Long-term stability of planets in binary systems. *Astron. J.* **117**, 621–628 (1999).

25. 25.

Mudryk, L. R. & Wu, Y. Resonance overlap is responsible for ejecting planets in binary systems. *Astrophys. J.* **639**, 423–431 (2006).

26. 26.

Asensio-Torres, R. et al. SPOTS: The Search for Planets Orbiting Two Stars. III. Complete sample and statistical analysis. *Astron. Astrophys.* **619**, A43 (2018).

27. 27.

Boss, A. P. Giant planet formation by gravitational instability. *Science* **276**, 1836–1839 (1997).

28. 28.

Szulágyi, J., Mayer, L. & Quinn, T. Circumplanetary discs around young giant planets: a comparison between core-accretion and disc instability. *Mon. Not. R. Astron. Soc.* **464**, 3158–3168 (2017).

29. 29.

Baruteau, C., Bai, X., Mordasini, C. & Mollière, P. Formation, orbital and internal evolutions of young planetary systems. *Space Sci. Rev.* **205**, 77–124 (2016).

30. 30.

Kratter, K. M. & Matzner, C. D. Fragmentation of massive protostellar discs. *Mon. Not. R. Astron. Soc.* **373**, 1563–1576 (2006).

31. 31.

Parker, R. J. & Quanz, S. P. The effects of dynamical interactions on planets in young substructured star clusters. *Mon. Not. R. Astron. Soc.* **419**, 2448–2458 (2012).

32. 32.

Perets, H. B. & Kouwenhoven, M. B. N. On the origin of planets at very wide orbits from the recapture of free floating planets. *Astrophys. J.* **750**, 83 (2012).

33. 33.

Ambartsumian, V. A. On the statistics of double stars. *Astron. Zh.* **14**, 207–219 (1937).

34. 34.

Marois, C., Zuckerman, B., Konopacky, Q. M., Macintosh, B. & Barman, T. Images of a fourth planet orbiting HR 8799. *Nature* **468**, 1080–1083 (2010).

35. 35.

Bailey, V. et al. HD 106906 b: a planetary-mass companion outside a massive debris disk. *Astrophys. J. Lett.* **780**, L4 (2014).

36. 36.

Beuzit, J.-L. et al. SPHERE: the exoplanet imager for the Very Large Telescope. *Astron. Astrophys.* **631**, A155 (2019).

37. 37.

Zurlo, A. et al. Performance of the VLT Planet Finder SPHERE. I. Photometry and astrometry precision with IRDIS and IFS in laboratory. *Astron. Astrophys.* **572**, A85 (2014).

38. 38.

Vigan, A. et al. Photometric characterization of exoplanets using angular and spectral differential imaging. *Mon. Not. R. Astron. Soc.* **407**, 71–82 (2010).

39. 39.

Delorme, P. et al. The SPHERE Data Center: a reference for high contrast imaging processing. In *SF2A-2017: Proc Annual Meeting of the French Society of Astronomy and Astrophysics* 347–361 (2017).

40. 40.

Galicher, R. et al. Astrometric and photometric accuracies in high contrast imaging: the SPHERE speckle calibration tool (SpeCal). *Astron. Astrophys.* **615**, A92 (2018).

41. 41.

Marois, C., Lafrenière, D., Doyon, R., Macintosh, B. & Nadeau, D. Angular differential imaging: a powerful high-contrast imaging technique. *Astrophys. J.* **641**, 556–564 (2006).

42. 42.

Lafrenière, D., Marois, C., Doyon, R., Nadeau, D. & Artigau, É. A new algorithm for point-spread function subtraction in high-contrast imaging: a demonstration with angular differential imaging. *Astrophys. J.* **660**, 770–780 (2007).

43. 43.

Maire, A.-L. et al. SPHERE IRDIS and IFS astrometric strategy and calibration. In *Proc. Ground-based and Airborne Instrumentation for Astronomy VI* Vol. 9908, 990834 (2016).

44. 44.

van Leeuwen, F. Validation of the new Hipparcos reduction. *Astron. Astrophys.* **474**, 653–664 (2007).

45. 45.

de Zeeuw, P. T., Hoogerwerf, R., de Bruijne, J. H. J., Brown, A. G. A. & Blaauw, A. A HIPPARCOS census of the nearby OB associations. *Astron. J.* **117**, 354–399 (1999).

46. 46.

Gagné, J. et al. BANYAN. XI. The BANYAN  $\Sigma$  multivariate Bayesian algorithm to identify members of young associations with 150 pc. *Astrophys. J.* **856**, 23 (2018).

47. 47.

Pecaut, M. J. & Mamajek, E. E. The star formation history and accretion-disc fraction among the K-type members of the Scorpius-Centaurus OB association. *Mon. Not. R. Astron. Soc.* **461**, 794–815 (2016).

48. 48.

Fitzpatrick, E. L. & Massa, D. Determining the physical properties of the B Stars. II. Calibration of synthetic photometry. *Astron. J.* **129**, 1642–1662 (2005).

49. 49.

Niemczura, E. Metallicities of the SPB stars from the IUE ultraviolet spectra. *Astron. Astrophys.* **404**, 689–700 (2003).

50. 50.

Kervella, P., Arenou, F., Mignard, F. & Thévenin, F. Stellar and substellar companions of nearby stars from Gaia DR2. Binarity from proper motion anomaly. *Astron. Astrophys.* **623**, A72 (2019).

51. 51.

Leike, R. H., Glatzle, M. & Enßlin, T. A. Resolving nearby dust clouds. *Astron. Astrophys.* **639**, A138 (2020).

52. 52.

Rizzuto, A. C. et al. Long-baseline interferometric multiplicity survey of the Sco-Cen OB association. *Mon. Not. R. Astron. Soc.* **436**, 1694–1707 (2013).

53. 53.

Wolff, S. C., Strom, S. E., Dror, D. & Venn, K. Rotational velocities for B0-B3 stars in seven young clusters: further study of the

relationship between rotation speed and density in star-forming regions. *Astron. J.* **133**, 1092–1103 (2007).

54. 54.

Janson, M. et al. The B-Star Exoplanet Abundance Study: a co-moving 16–25 M<sub>Jup</sub> companion to the young binary system HIP 79098. *Astron. Astrophys.* **626**, A99 (2019).

55. 55.

Blunt, S. et al. orbitize! : a comprehensive orbit-fitting software package for the high-contrast imaging community. *Astron. J.* **159**, 89 (2020).

56. 56.

Rodet, L. et al. Dynamical masses of M-dwarf binaries in young moving groups. I. The case of TWA 22 and GJ 2060. *Astron. Astrophys.* **618**, A23 (2018).

57. 57.

Skrutskie, M. F. et al. The Two Micron All Sky Survey (2MASS). *Astron. J.* **131**, 1163–1183 (2006).

58. 58.

Baraffe, I., Chabrier, G., Barman, T. S., Allard, F. & Hauschildt, P. H. Evolutionary models for cool brown dwarfs and extrasolar giant planets. The case of HD 209458. *Astron. Astrophys.* **402**, 701–712 (2003).

59. 59.

Chabrier, G., Baraffe, I., Allard, F. & Hauschildt, P. Evolutionary models for very low-mass stars and brown dwarfs with dusty atmospheres. *Astrophys. J.* **542**, 464–472 (2000).

60. 60.

Müller, S. & Helled, R. Synthetic evolution tracks of giant planets. *Mon. Not. R. Astron. Soc.* **507**, 2094–2102 (2021).

61. 61.

Öberg, K. I., Murray-Clay, R. & Bergin, E. A. The effects of snowlines on C/O in planetary atmospheres. *Astrophys. J. Lett.* **743**, L16 (2011).

62. 62.

Bowler, B. P. Imaging extrasolar giant planets. *Publ. Astron. Soc. Pac.* **128**, 102001 (2016).

63. 63.

Chauvin, G. et al. Discovery of a warm, dusty giant planet around HIP 65426. *Astron. Astrophys.* **605**, L9 (2017).

64. 64.

Keppler, M. et al. Discovery of a planetary-mass companion within the gap of the transition disk around PDS 70. *Astron. Astrophys.* **617**, A44 (2018).

65. 65.

Bohn, A. J. et al. Two directly imaged, wide-orbit giant planets around the young, solar analog TYC 8998-760-1. *Astrophys. J. Lett.* **898**, L16 (2020).

66. 66.

Wagner, K., Apai, D. & Kratter, K. M. On the mass function, multiplicity, and origins of wide-orbit giant planets. *Astrophys. J.* **877**, 46 (2019).

67. 67.

Schlaufman, K. C. Evidence of an upper bound on the masses of planets and its implications for giant planet formation. *Astrophys. J.* **853**, 37 (2018).

68. 68.

Delorme, P. et al. Direct-imaging discovery of a 12–14 Jupiter-mass object orbiting a young binary system of very low-mass stars. *Astron. Astrophys.* **553**, L5 (2013).

69. 69.

Macintosh, B. et al. Discovery and spectroscopy of the young jovian planet 51 Eri b with the Gemini Planet Imager. *Science* **350**, 64–67 (2015).

70. 70.

Moe, M. & Di Stefano, R. Mind your Ps and Qs: the interrelation between period (P) and mass-ratio (Q) distributions of binary stars. *Astrophys. J. Suppl.* **230**, 15 (2017).

71. 71.

De Rosa, R. J. et al. The VAST Survey - III. The multiplicity of A-type stars within 75 pc. *Mon. Not. R. Astron. Soc.* **437**, 1216–1240 (2014).

72. 72.

Bowler, B. P. et al. Retired A stars and their companions. III. Comparing the mass-period distributions of planets around A-type stars and Sun-like stars. *Astrophys. J.* **709**, 396–410 (2010).

73. 73.

Jones, M. I. et al. Four new planets around giant stars and the mass-metallicity correlation of planet-hosting stars. *Astron. Astrophys.* **590**, A38 (2016).

74. 74.

Vigan, A. et al. The International Deep Planet Survey. I. The frequency of wide-orbit massive planets around A-stars. *Astron. Astrophys.* **544**, A9 (2012).

75. 75.

Rameau, J. et al. A survey of young, nearby, and dusty stars conducted to understand the formation of wide-orbit giant planets. VLT/NaCo adaptive optics thermal and angular differential imaging. *Astron. Astrophys.* **553**, A60 (2013).

76. 76.

Rafikov, R. R. Can giant planets form by direct gravitational instability? *Astrophys. J. Lett.* **621**, L69–L72 (2005).

77. 77.

Kratter, K. M., Murray-Clay, R. A. & Youdin, A. N. The runts of the litter: why planets formed through gravitational instability can only be failed binary stars. *Astrophys. J.* **710**, 1375–1386 (2010).

78. 78.

Forgan, D. & Rice, K. Towards a population synthesis model of objects formed by self-gravitating disc fragmentation and tidal downsizing. *Mon. Not. R. Astron. Soc.* **432**, 3168–3185 (2013).

79. 79.

Boley, A. C., Hayfield, T., Mayer, L. & Durisen, R. H. Clumps in the outer disk by disk instability: why they are initially gas giants and the legacy of disruption. *Icarus* **207**, 509–516 (2010).

80. 80.

Nayakshin, S. Formation of planets by tidal downsizing of giant planet embryos. *Mon. Not. R. Astron. Soc. Lett.* **408**, L36–L40 (2010).

81. 81.

Mordasini, C., Marleau, G.-D. & Mollière, P. Characterization of exoplanets from their formation. III. The statistics of planetary luminosities. *Astron. Astrophys.* **608**, A72 (2017).

## Acknowledgements

We thank M. Ireland for input regarding SUSI interferometry. The results presented here are based on observations collected at the European Organisation for Astronomical Research in the Southern Hemisphere under ESO programme 1101.C-0258. The work has made use of the SPHERE Data Centre, jointly operated by OSUG/IPAG (Grenoble), PYTHEAS/LAM/CeSAM (Marseille), OCA/Lagrange (Nice), Observatoire de Paris/LESIA (Paris) and Observatoire de Lyon/CRAL, and supported by a grant from Labex OSUG@2020 (Investissements d’avenir – ANR10 LABX56). The study made use of CDS and NASA-ADS services. M.J. acknowledges support from the Knut and Alice Wallenberg Foundation (KAW). G.-D.M. acknowledges the support of the DFG priority programme SPP 1992 “Exploring the Diversity of Extrasolar Planets” (MA 9185/1-1) and from the Swiss National Science Foundation under grant BSSGI0\_155816 “PlanetsInTime”. Parts of this work have been carried out within the framework of the NCCR PlanetS supported by the Swiss National Science Foundation. A.V. acknowledges funding from the European Research Council (ERC) under the European Union’s Horizon 2020 research and innovation programme (grant agreement no. 757561). Part of this research was carried out at the Jet Propulsion Laboratory, California Institute of Technology, under a contract with the National Aeronautics and Space Administration (80NM0018D0004).

## Author information

### Affiliations

1. Department of Astronomy, Stockholm University, Stockholm, Sweden

Markus Janson, Simon Ringqvist, Gayathri Viswanath & Matthias Samland

2. INAF Osservatorio Astronomico di Padova, Padova, Italy

Raffaele Gratton, Silvano Desidera, Vito Squicciarini & Dino Mesa

3. Cornell Center for Astrophysics and Planetary Science, Department of Astronomy, Cornell University, Ithaca, NY, USA

Laetitia Rodet

4. Aix-Marseille Université, CNRS, CNES, LAM (Laboratoire d’Astrophysique de Marseille), UMR 7326, Marseille, France

Arthur Vigan

5. Université Grenoble Alpes, CNRS, IPAG, Grenoble, France

Mickaël Bonnefoy, Philippe Delorme, Gaël Chauvin & Simon Petrus

6. Jet Propulsion Laboratory, California Institute of Technology, Pasadena, CA, USA

Eric E. Mamajek

7. Landessternwarte, Zentrum für Astronomie der Universität Heidelberg, Heidelberg, Germany

Sabine Reffert & Lukas Stock

8. Institut für Astronomie und Astrophysik, Universität Tübingen, Tübingen, Germany

Gabriel-Dominique Marleau

9. Physikalisches Institut, Universität Bern, Bern, Switzerland

Gabriel-Dominique Marleau

10. Max-Planck-Institut für Astronomie, Heidelberg, Germany

Gabriel-Dominique Marleau & Thomas Henning

11. CRAL, UMR 5574, CNRS, Université Lyon 1, Saint Genis Laval, France

Maud Langlois

12. Unidad Mixta Internacional Franco-Chilena de Astronomía, CNRS/INSU UMI 3386 and Departamento de Astronomía, Universidad de Chile, Santiago, Chile

Gaël Chauvin

13. Center for Theoretical Physics and Cosmology, Institute for Computational Science, University of Zurich, Zurich, Switzerland

Lucio Mayer & Ravit Helled

14. Department of Physics and Astronomy “Galileo Galilei”, University of Padova, Padova, Italy

Vito Squicciarini

15. Department of Astronomy, University of Michigan, Ann Arbor, MI, USA

Michael R. Meyer

16. Leiden Observatory, Leiden University, Leiden, The Netherlands

Matthew A. Kenworthy

17. ETH Zurich, Institute for Particle Physics and Astrophysics, Zurich, Switzerland

Sascha P. Quanz & Natalia Engler

18. SUPA, Institute for Astronomy, Royal Observatory, University of Edinburgh, Edinburgh, UK

Beth Biller

19. College of Charleston, Department of Physics & Astronomy, Charleston, SC, USA

Joseph C. Carson

## Contributions

M.J. is the principal investigator for the BEAST survey and led the management, observation preparations, analysis and manuscript writing. R.G., A.V., M.B., G.-D.M., S. S. Ringqvist, G.V., V.S. and S.P contributed to the data analysis and plots. L.R. led the orbital fitting. P.D. led the data reduction. R.G., E.E.M., S. Reffert, L.S., G.-D.M. and S.D. contributed to the stellar and planetary characterization. M.L. contributed to the observation preparations. G.C. assisted with the project management. L.M., M.R.M. and R.H. contributed to the formation discussion. All co-authors assisted with the manuscript writing.

## Corresponding author

Correspondence to [Markus Janson](#).

## Ethics declarations

## Competing interests

The authors declare no competing interests.

## Additional information

**Peer review information** *Nature* thanks Katherine Follete and the other, anonymous, reviewer(s) for their contribution to the peer review of this work. Peer reviewer reports are available.

**Publisher's note** Springer Nature remains neutral with regard to jurisdictional claims in published maps and institutional affiliations.

## Extended data figures and tables

### [Extended Data Fig. 1 J2-band image of b Cen \(AB\)b.](#)

The image reduction is performed with classical angular differential imaging. The planet is denoted ‘b’ and the brighter of the background stars is denoted ‘bg’. The fainter background star cannot be easily seen at the contrast/saturation of this display, which is chosen to optimize visibility of other image elements.

### [Extended Data Fig. 2 Astrometric motion of b Cen \(AB\)b and the background stars.](#)

The image shows the astrometric motion of the three point sources detected around b Cen, in the reference frame of b Cen itself. Squares show the locations of background star 1 at epochs 2019 (purple) and 2021 (blue). Circles show the locations of background star 2 at the same epochs. Diamonds show the locations of b Cen (AB)b, both at the 2019 and 2021 epochs, but also in the 2000 epoch (green) where it could additionally be retrieved. Gray tracks show a representative collection of orbits that fit the observed motion of b Cen (AB)b. The insets zoom in on the locations around background star 1 (upper left inset), background star 2 (upper right inset), and the confirmed planet b Cen (AB)b (lower left inset). The filled symbols are the measured locations, while the open symbols show the projected motion expected for a static background object (which would follow the dashed trajectories over time), where 2021 is chosen as the reference epoch.

### [Extended Data Fig. 3 Orbital parameters of b Cen \(AB\)b.](#)

Prior (in orange) and posterior (in blue) distributions for the full set of orbital parameters: Orbital period  $P$ , eccentricity  $e$ , inclination  $i$ , ascending node  $\Omega$ , argument of periapsis  $\omega$ , and time of periapsis  $T_p$ .

### [Extended Data Fig. 4 Colour-magnitude diagrams for b Cen \(AB\)b.](#)

**a**, J2-J3 colour versus absolute J2 magnitude. **b**, K1-K2 colour versus absolute K1 magnitude. The planet b Cen (AB)b is plotted as a blue-green star, and follows the same colour trends as are generally observed for young planetary and substellar companions to stars, plotted as purple and black symbols with error bars. Symbols without error bars are young and field brown dwarfs.

### [Extended Data Fig. 5 Constraints on mass and initial entropy for b Cen \(AB\)b.](#)

Posterior probability distribution for the mass and initial entropy of b Cen (AB)b based on its brightness and age. The BEX-Cond models are used in this MCMC exploration, but the results are not very sensitive to the choice of the atmospheric model since the bolometric luminosity (and not a magnitude) is used. The red dotted (blue dashed) lines show for reference the approximate minimum and maximum of the hot-start (cold-start) planets in the Bern population synthesis<sup>81</sup>. A subset of the models is shown for plotting purposes.

**Extended Data Table 1 Astrometric values for point sources around b Cen**

**Extended Data Table 2 Photometric values for point sources around b Cen**

## Supplementary information

[Peer Review File](#)

# Rights and permissions

[Reprints and Permissions](#)

## About this article

### Cite this article

Janson, M., Gratton, R., Rodet, L. *et al.* A wide-orbit giant planet in the high-mass b Centauri binary system. *Nature* **600**, 231–234 (2021).  
<https://doi.org/10.1038/s41586-021-04124-8>

- Received: 23 July 2021
- Accepted: 12 October 2021
- Published: 08 December 2021
- Issue Date: 09 December 2021
- DOI: <https://doi.org/10.1038/s41586-021-04124-8>

### Share this article

Anyone you share the following link with will be able to read this content:

[Get shareable link](#)

Sorry, a shareable link is not currently available for this article.

[Copy to clipboard](#)

Provided by the Springer Nature SharedIt content-sharing initiative

## [Giant planet imaged orbiting two massive stars](#)

- Kaitlin Kratter

# News & Views 08 Dec 2021

---

This article was downloaded by **calibre** from <https://www.nature.com/articles/s41586-021-04124-8>

| [Section menu](#) | [Main menu](#) |

- Article
- [Published: 08 December 2021](#)

# Giant modulation of optical nonlinearity by Floquet engineering

- [Jun-Yi Shan](#) [ORCID: orcid.org/0000-0001-7665-2169<sup>1,2</sup>](#),
- [M. Ye<sup>3</sup>](#),
- [H. Chu<sup>1,2</sup>](#),
- [Sungmin Lee<sup>4</sup>](#),
- [Je-Geun Park](#) [ORCID: orcid.org/0000-0002-3930-4226<sup>4,5,6</sup>](#),
- [L. Balents<sup>3</sup>](#) &
- [D. Hsieh](#) [ORCID: orcid.org/0000-0002-0812-955X<sup>1,2</sup>](#)

[Nature](#) volume **600**, pages 235–239 (2021)

- 1733 Accesses
- 96 Altmetric
- [Metrics details](#)

## Subjects

- [Electronic properties and materials](#)
- [Nonlinear optics](#)
- [Ultrafast photonics](#)

## Abstract

Strong periodic driving with light offers the potential to coherently manipulate the properties of quantum materials on ultrafast timescales. Recently, strategies have emerged to drastically alter electronic and magnetic properties by optically inducing non-trivial band topologies<sup>1,2,3,4,5,6</sup>, emergent spin interactions<sup>7,8,9,10,11</sup> and even superconductivity<sup>12</sup>. However, the prospects and methods of coherently engineering optical properties on demand are far less understood<sup>13</sup>. Here we demonstrate coherent control and giant modulation of optical nonlinearity in a van der Waals layered magnetic insulator, manganese phosphorus trisulfide ( $\text{MnPS}_3$ ). By driving far off-resonance from the lowest on-site manganese  $d-d$  transition, we observe a coherent on–off switching of its optical second harmonic generation efficiency on the timescale of 100 femtoseconds with no measurable dissipation. At driving electric fields of the order of  $10^9$  volts per metre, the on–off ratio exceeds 10, which is limited only by the sample damage threshold. Floquet theory calculations<sup>14</sup> based on a single-ion model of  $\text{MnPS}_3$  are able to reproduce the measured driving field amplitude and polarization dependence of the effect. Our approach can be applied to a broad range of insulating materials and could lead to dynamically designed nonlinear optical elements.

This is a preview of subscription content

## Access options

Subscribe to Journal

Get full journal access for 1 year

\$199.00

only \$3.90 per issue

[Subscribe](#)

All prices are NET prices.

VAT will be added later in the checkout.

Tax calculation will be finalised during checkout.

Rent or Buy article

Get time limited or full article access on ReadCube.

from \$8.99

[Rent or Buy](#)

All prices are NET prices.

### **Additional access options:**

- [Log in](#)
- [Learn about institutional subscriptions](#)

**Fig. 1: Static SHG from MnPS<sub>3</sub>.**

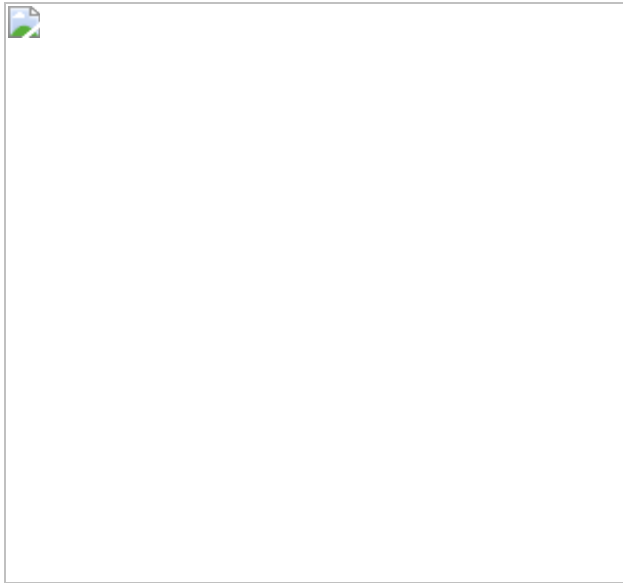


**Fig. 2: Coherent drive-induced state modification.**



**Fig. 3: Driving photon energy dependence of RA SHG transients.**

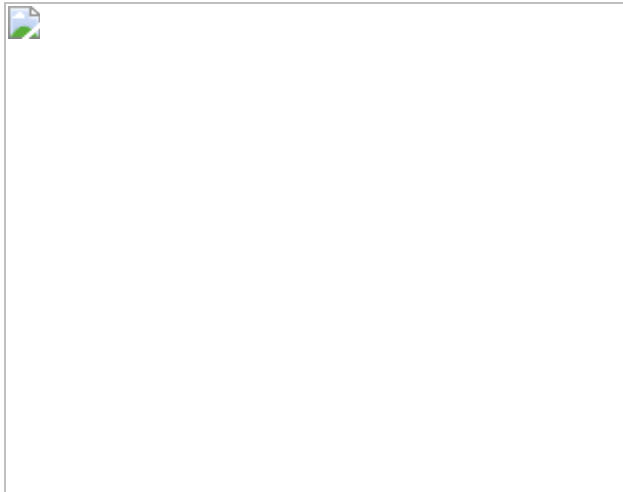
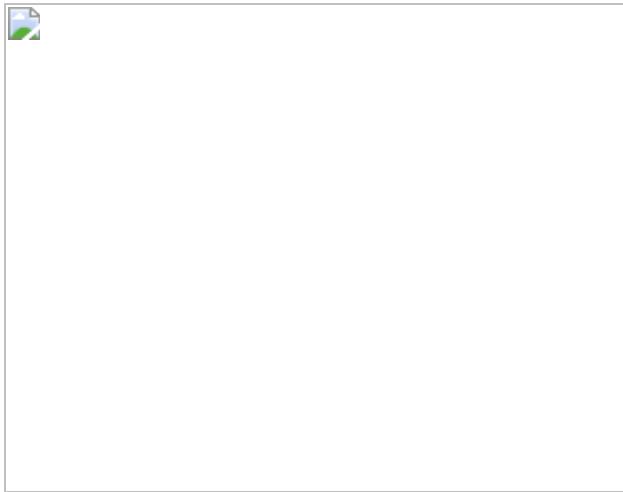


**Fig. 4: Driving field amplitude and polarization dependence of SHG modulation.**



## Data availability

All other data that support the findings of this study are available from the corresponding author on reasonable request. [Source data](#) are provided with this paper.

## References

1. 1.

- Oka, T. & Aoki, H. Photovoltaic Hall effect in graphene. *Phys. Rev. B* **79**, 081406 (2009).

2. 2.

Kitagawa, T., Oka, T., Brataas, A., Fu, L. & Demler, E. Transport properties of nonequilibrium systems under the application of light: photoinduced quantum Hall insulators without Landau levels. *Phys. Rev. B* **84**, 235108 (2011).

3. 3.

Rudner, M. S. & Lindner, N. H. Band structure engineering and non-equilibrium dynamics in Floquet topological insulators. *Nat. Rev. Phys.* **2**, 229–244 (2020).

4. 4.

Hübener, H., Sentef, M. A., De Giovannini, U., Kemper, A. F. & Rubio, A. Creating stable Floquet–Weyl semimetals by laser-driving of 3D Dirac materials. *Nat. Commun.* **8**, 13940 (2017).

5. 5.

McIver, J. W. et al. Light-induced anomalous Hall effect in graphene. *Nat. Phys.* **16**, 38–41 (2020).

6. 6.

Wang, Y. H., Steinberg, H., Jarillo-Herrero, P. & Gedik, N. Observation of Floquet–Bloch states on the surface of a topological insulator. *Science* **342**, 453–457 (2013).

7. 7.

Mentink, J. H., Balzer, K. & Eckstein, M. Ultrafast and reversible control of the exchange interaction in Mott insulators. *Nat. Commun.* **6**, 6708 (2015).

8. 8.

Claassen, M., Jiang, H. C., Moritz, B. & Devereaux, T. P. Dynamical time-reversal symmetry breaking and photo-induced chiral spin liquids in frustrated Mott insulators. *Nat. Commun.* **8**, 1192 (2017).

9. 9.

Liu, J., Hejazi, K. & Balents, L. Floquet engineering of multiorbital Mott insulators: applications to orthorhombic titanates. *Phys. Rev. Lett.* **121**, 107201 (2018).

10. 10.

Mikhaylovskiy, R. V. et al. Ultrafast optical modification of exchange interactions in iron oxides. *Nat. Commun.* **6**, 8190 (2015).

11. 11.

Chaudhary, S., Hsieh, D. & Refael, G. Orbital Floquet engineering of exchange interactions in magnetic materials. *Phys. Rev. B* **100**, 220403 (2019).

12. 12.

Mitrano, M. et al. Possible light-induced superconductivity in  $K_3C_{60}$  at high temperature. *Nature* **530**, 461–464 (2016).

13. 13.

Gu, B. & Franco, I. Optical absorption properties of laser-driven matter. *Phys. Rev. A* **98**, 063412 (2018).

14. 14.

Shirley, J. H. Solution of the Schrödinger equation with a Hamiltonian periodic in time. *Phys. Rev.* **138**, B979–B987 (1965).

15. 15.

Bayarjargal, L. & Winkler, B. Pressure-induced magnetic phase transition in Cr<sub>2</sub>O<sub>3</sub> determined by second harmonic generation measurements. *Appl. Phys. Lett.* **102**, 182403 (2013).

16. 16.

Terhune, R. W., Maker, P. D. & Savage, C. M. Optical harmonic generation in calcite. *Phys. Rev. Lett.* **8**, 404–406 (1962).

17. 17.

An, Y. Q., Nelson, F., Lee, J. U. & Diebold, A. C. Enhanced optical second-harmonic generation from the current-biased graphene/SiO<sub>2</sub>/Si(001) structure. *Nano Lett.* **13**, 2104–2109 (2013).

18. 18.

Ruzicka, B. A. et al. Second-harmonic generation induced by electric currents in GaAs. *Phys. Rev. Lett.* **108**, 077403 (2012).

19. 19.

Seyler, K. L. et al. Electrical control of second-harmonic generation in a WSe<sub>2</sub> monolayer transistor. *Nat. Nanotechnol.* **10**, 407–411 (2015).

20. 20.

Soavi, G. et al. Broad-band, electrically tunable third-harmonic generation in graphene. *Nat. Nanotechnol.* **13**, 583–588 (2018).

21. 21.

Satoh, T., Van Aken, B. B., Duong, N. P., Lottermoser, T. & Fiebig, M. Ultrafast spin and lattice dynamics in antiferromagnetic Cr<sub>2</sub>O<sub>3</sub>. *Phys. Rev. B* **75**, 155406 (2007).

22. 22.

Zhang, M. Y. et al. Light-induced subpicosecond lattice symmetry switch in MoTe<sub>2</sub>. *Phys. Rev. X* **9**, 021036 (2019).

23. 23.

Sartorello, G. et al. Ultrafast optical modulation of second- and third-harmonic generation from cut-disk-based metasurfaces. *ACS Photon.* **3**, 1517–1522 (2016).

24. 24.

Piryatinskaya, V. G., Kachur, I. S., Slavin, V. V., Yeremenko, A. V. & Vysochanskii, Y. M. Temperature behavior of the fundamental optical absorption band in quasi-two-dimensional crystalline MnPS<sub>3</sub>. *Low Temp. Phys.* **38**, 870–873 (2012).

25. 25.

Chu, H. et al. Linear magnetoelectric phase in ultrathin MnPS<sub>3</sub> probed by optical second harmonic generation. *Phys. Rev. Lett.* **124**, 027601 (2020).

26. 26.

Vaclavkova, D. et al. Magnetoelastic interaction in the two-dimensional magnetic material MnPS<sub>3</sub> studied by first principles calculations and Raman experiments. *2D Mater.* **7**, 035030 (2020).

27. 27.

Kurosawa, K., Saito, S. & Yamaguchi, Y. Neutron diffraction study on MnPS<sub>3</sub> and FePS<sub>3</sub>. *J. Phys. Soc. Jpn* **52**, 3919–3926 (1983).

28. 28.

Grasso, V., Neri, F., Perillo, P., Silipigni, L. & Piacentini, M. Optical-absorption spectra of crystal-field transitions in MnPS<sub>3</sub> at low temperatures. *Phys. Rev. B* **44**, 11060–11066 (1991).

29. 29.

Fiebig, M., PavlovV. V. & Pisarev, R. V. Second-harmonic generation as a tool for studying electronic and magnetic structures of crystals: review. *J. Opt. Soc. Am. B* **22**, 96–118 (2005).

30. 30.

Boyd, R. W. *Nonlinear Optics* (Academic Press, 2003).

31. 31.

Muthukumar, V. N., Valentí, R. & Gros, C. Microscopic model of nonreciprocal optical effects in Cr<sub>2</sub>O<sub>3</sub>. *Phys. Rev. Lett.* **75**, 2766–2769 (1995).

32. 32.

Harter, J. W., Niu, L., Woss, A. J. & Hsieh, D. High-speed measurement of rotational anisotropy nonlinear optical harmonic generation using position-sensitive detection. *Opt. Lett.* **40**, 4671–4674 (2015).

33. 33.

Wildes, A. R., Rønnow, H. M., Roessli, B., Harris, M. J. & Godfrey, K. W. Static and dynamic critical properties of the quasi-two-dimensional antiferromagnet MnPS<sub>3</sub>. *Phys. Rev. B* **74**, 094422 (2006).

34. 34.

Autler, S. H. & Townes, C. H. Stark effect in rapidly varying fields. *Phys. Rev.* **100**, 703–722 (1955).

35. 35.

Sie, E. J. et al. Valley-selective optical Stark effect in monolayer WS<sub>2</sub>. *Nat. Mater.* **14**, 290–294 (2015).

36. 36.

Bloch, F. & Siegert, A. Magnetic resonance for nonrotating fields. *Phys. Rev.* **57**, 522–527 (1940).

37. 37.

Sentef, M. A., Li, J., Künzel, F. & Eckstein, M. Quantum to classical crossover of Floquet engineering in correlated quantum systems. *Phys. Rev. Res.* **2**, 033033 (2020).

38. 38.

Long, G. et al. Isolation and characterization of few-layer manganese thiophosphite. *ACS Nano* **11**, 11330–11336 (2017).

39. 39.

Yang, J., Zhou, Y., Guo, Q., Dedkov, Y. & Voloshina, E. Electronic, magnetic and optical properties of MnPX<sub>3</sub> (X = S, Se) monolayers with and without chalcogen defects: a first-principles study. *RSC Adv.* **10**, 851–864 (2020).

40. 40.

Shklovskii, B. I. & Efros, A. L. *Electronic Properties of Doped Semiconductors* (Springer-Verlag, 1984).

41. 41.

Bloembergen, N. & Pershan, P. S. Light waves at the boundary of nonlinear media. *Phys. Rev.* **128**, 606–622 (1962).

42. 42.

Dang, W., Chen, Y., Gong, M. & Chen, X. Competition between SFG and two SHGs in broadband type-I QPM. *Appl. Phys. B* **110**, 477–482 (2013).

43. 43.

Choge, D. K., Chen, H., Guo, L., Li, G. & Liang, W. Simultaneous second-harmonic, sum-frequency generation and stimulated Raman scattering in MgO:PPLN. *Materials* **11**, 2266 (2018).

44. 44.

Takano, Y. et al. Magnetic properties and specific heat of  $MPS_3$  ( $M=Mn, Fe, Zn$ ). *J. Magn. Magn. Mater.* **272–276**, E593–E595 (2004).

45. 45.

Gnatchenko, S. L., Kachur, I. S., Piryatinskaya, V. G., Vysochanskii, Y. M. & Gurzan, M. I. Exciton-magnon structure of the optical absorption spectrum of antiferromagnetic  $MnPS_3$ . *Low Temp. Phys.* **37**, 144–148 (2011).

46. 46.

Kargar, F. et al. Phonon and thermal properties of quasi-two-dimensional  $FePS_3$  and  $MnPS_3$  antiferromagnetic semiconductors. *ACS Nano* **14**, 2424–2435 (2020).

47. 47.

Villars, P. *Pauling file. Inorganic Solid Phases*, SpringerMaterials (Springer, 2016);  
[https://materials.springer.com/isp/crystallographic/docs/sd\\_0558101](https://materials.springer.com/isp/crystallographic/docs/sd_0558101)

## Acknowledgements

We acknowledge discussions with X. Li, S. Chaudhary and G. Refael. This work was supported by ARO MURI grant number W911NF-16-1-0361. D.H. also acknowledges support for instrumentation from the David and Lucile Packard Foundation and from the Institute for Quantum Information and Matter, an NSF Physics Frontiers Center (PHY-1733907). M.Y.

acknowledges support by the Gordon and Betty Moore Foundation through grant GBMF8690 to UCSB and by the National Science Foundation under grant number NSF PHY-1748958. J.-G.P. was supported by the Leading Researcher Program of the National Research Foundation of Korea (grant number 2020R1A3B2079375).

## Author information

### Affiliations

1. Department of Physics, California Institute of Technology, Pasadena, CA, USA

Jun-Yi Shan, H. Chu & D. Hsieh

2. Institute for Quantum Information and Matter, California Institute of Technology, Pasadena, CA, USA

Jun-Yi Shan, H. Chu & D. Hsieh

3. Kavli Institute for Theoretical Physics, University of California, Santa Barbara, CA, USA

M. Ye & L. Balents

4. Department of Physics and Astronomy, Seoul National University, Seoul, Republic of Korea

Sungmin Lee & Je-Geun Park

5. Center for Quantum Materials, Seoul National University, Seoul, Republic of Korea

Je-Geun Park

6. Institute of Applied Physics, Seoul National University, Seoul, Republic of Korea

Je-Geun Park

## Contributions

S.L. and J.-G.P. synthesized and characterized the MnPS<sub>3</sub> crystals. J.-Y.S. and H.C. performed the optical measurements. M.Y., J.-Y.S. and L.B. performed the single-ion model based static and Floquet dynamical calculations. J.-Y.S., M.Y. and D.H. wrote the paper with input from all authors.

## Corresponding author

Correspondence to [D. Hsieh](#).

## Ethics declarations

## Competing interests

The authors declare no competing interests.

## Additional information

**Peer review information** *Nature* thanks Liang Wu and the other, anonymous, reviewer(s) for their contribution to the peer review of this work. Peer reviewer reports are available.

**Publisher's note** Springer Nature remains neutral with regard to jurisdictional claims in published maps and institutional affiliations.

## Extended data figures and tables

### [Extended Data Fig. 1 EDX measurements.](#)

The EDX spectrum and the calculated atomic percentage measured at three different spots.

## Extended Data Fig. 2 Magnetic susceptibility measurements.

The magnetic susceptibility measured with the magnetic field parallel to the  $ab$  plane and to the  $c^*$  axis, which is the out-of-plane direction.

## Extended Data Fig. 3 Optical absorption data.

The relationship between  $(KE)^2$  and  $E$  is plotted (green circles) to facilitate the linear fit (black curve). Inset shows the DOS of in-gap impurity states.

## Extended Data Fig. 4 Linear coupling between SHG susceptibility and AFM order parameter.

The log-log plot of the critical behavior of  $\chi_{ijk}^{\rm ED}(c)$  (squares). Linear fits within two different temperature ranges are overlaid (lines).

## Extended Data Fig. 5 Linear reflectivity transients.

$\Delta R/R$  with 1.55 eV probe and  $\hbar\Omega = 0.66$  eV taken at various driving **a**, amplitudes and **b**, polarizations.

## Extended Data Fig. 6 Ruling out competition between SHG and SFG as the source of SHG suppression.

Driving field amplitude dependence of SFG intensity at various probe fluences.

## Extended Data Fig. 7 SHG transients at higher temperatures.

Time-resolved SHG measured at **a**, 70 K and **b**, 90 K with  $\hbar\Omega = 0.66$  eV driving.  $E_{\max} = 10^9$  V/m,  $\theta = 90^\circ$  and  $\varphi = 60^\circ$ .

## Extended Data Fig. 8 Comparisons between RA patterns induced by resonant driving and static RA patterns at higher temperatures.

Upper panels show the time-resolved RA patterns taken at 10 K, and lower panels show the static RA patterns taken at higher temperatures. Identical fits to the crystal point group for each column are overlaid (black lines).

## Extended Data Fig. 9 Drive amplitude dependence of long time SHG suppression.

The calculated (black) and experimental (blue) driving amplitude ( $\hbar\Omega = 2.07$  eV) dependence of  $\Delta I^{\text{mag}}/I^{\text{mag}}$  plateau values. Experimental data are taken at  $t = 200$  ps.

## Supplementary information

### Supplementary Information

### Peer Review File

## Source data

### Source Data Fig. 1

### Source Data Fig. 2

### Source Data Fig. 3

### Source Data Fig. 4

## Rights and permissions

## [Reprints and Permissions](#)

## About this article

### Cite this article

Shan, JY., Ye, M., Chu, H. *et al.* Giant modulation of optical nonlinearity by Floquet engineering. *Nature* **600**, 235–239 (2021).  
<https://doi.org/10.1038/s41586-021-04051-8>

- Received: 27 April 2021
- Accepted: 23 September 2021
- Published: 08 December 2021
- Issue Date: 09 December 2021
- DOI: <https://doi.org/10.1038/s41586-021-04051-8>

### Share this article

Anyone you share the following link with will be able to read this content:

[Get shareable link](#)

Sorry, a shareable link is not currently available for this article.

[Copy to clipboard](#)

Provided by the Springer Nature SharedIt content-sharing initiative

---

This article was downloaded by **calibre** from <https://www.nature.com/articles/s41586-021-04051-8>

- Article
- [Published: 20 October 2021](#)

# Evidence for unconventional superconductivity in twisted bilayer graphene

- [Myungchul Oh](#) ORCID: [orcid.org/0000-0003-0477-1390<sup>1 na1</sup>](https://orcid.org/0000-0003-0477-1390),
- [Kevin P. Nuckolls](#) ORCID: [orcid.org/0000-0002-1078-7113<sup>1 na1</sup>](https://orcid.org/0000-0002-1078-7113),
- [Dillon Wong<sup>1 na1</sup>](#),
- [Ryan L. Lee<sup>1</sup>](#),
- [Xiaomeng Liu](#) ORCID: [orcid.org/0000-0002-0039-7090<sup>1</sup>](https://orcid.org/0000-0002-0039-7090),
- [Kenji Watanabe](#) ORCID: [orcid.org/0000-0003-3701-8119<sup>2</sup>](https://orcid.org/0000-0003-3701-8119),
- [Takashi Taniguchi](#) ORCID: [orcid.org/0000-0002-1467-3105<sup>3</sup>](https://orcid.org/0000-0002-1467-3105) &
- [Ali Yazdani](#) ORCID: [orcid.org/0000-0003-4996-8904<sup>1</sup>](https://orcid.org/0000-0003-4996-8904)

[Nature](#) volume 600, pages 240–245 (2021)

- 8242 Accesses
- 57 Altmetric
- [Metrics details](#)

## Subjects

- [Electronic properties and materials](#)
- [Superconducting properties and materials](#)

## Abstract

The emergence of superconductivity and correlated insulators in magic-angle twisted bilayer graphene (MATBG) has raised the intriguing possibility that its pairing mechanism is distinct from that of conventional superconductors<sup>1,2,3,4</sup>, as described by the Bardeen–Cooper–Schrieffer (BCS) theory. However, recent studies have shown that superconductivity persists even when Coulomb interactions are partially screened<sup>5,6</sup>. This suggests that pairing in MATBG might be conventional in nature and a consequence of the large density of states of its flat bands. Here we combine tunnelling and Andreev reflection spectroscopy with a scanning tunnelling microscope to observe several key experimental signatures of unconventional superconductivity in MATBG. We show that the tunnelling spectra below the transition temperature  $T_c$  are inconsistent with those of a conventional  $s$ -wave superconductor, but rather resemble those of a nodal superconductor with an anisotropic pairing mechanism. We observe a large discrepancy between the tunnelling gap  $\Delta_T$ , which far exceeds the mean-field BCS ratio (with  $2\Delta_T/k_B T_c \sim 25$ ), and the gap  $\Delta_{AR}$  extracted from Andreev reflection spectroscopy ( $2\Delta_{AR}/k_B T_c \sim 6$ ). The tunnelling gap persists even when superconductivity is suppressed, indicating its emergence from a pseudogap phase. Moreover, the pseudogap and superconductivity are both absent when MATBG is aligned with hexagonal boron nitride. These findings and other observations reported here provide a preponderance of evidence for a non-BCS mechanism for superconductivity in MATBG.

This is a preview of subscription content

## Access options

Subscribe to Journal

Get full journal access for 1 year

\$199.00

only \$3.90 per issue

[Subscribe](#)

All prices are NET prices.  
VAT will be added later in the checkout.  
Tax calculation will be finalised during checkout.

Rent or Buy article

Get time limited or full article access on ReadCube.

from \$8.99

[Rent or Buy](#)

All prices are NET prices.

### **Additional access options:**

- [Log in](#)
- [Learn about institutional subscriptions](#)

**Fig. 1: STS of the tunnelling gap of superconducting MATBG.**



**Fig. 2: PCS and Andreev reflection for MATBG.**

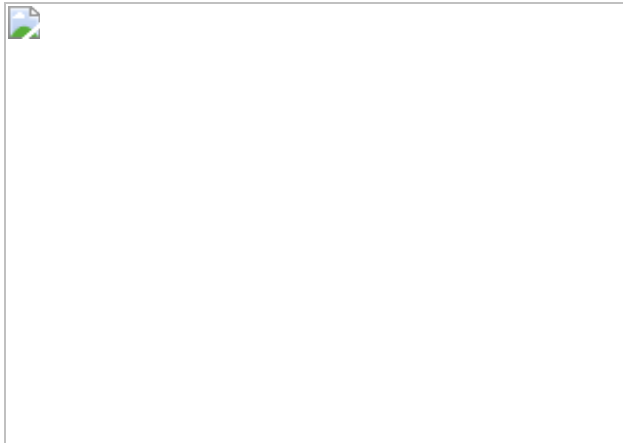


**Fig. 3: Tunnelling and Andreev reflection spectra curve fits.**

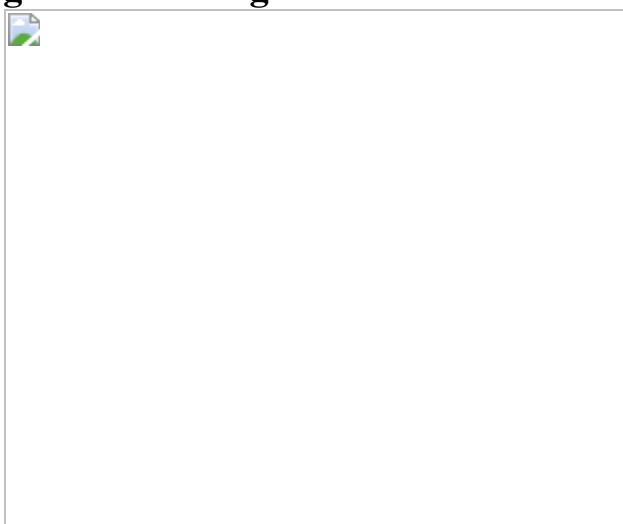


**Fig. 4: Pseudogap regime and phase diagram of hole-doped MATBG.**

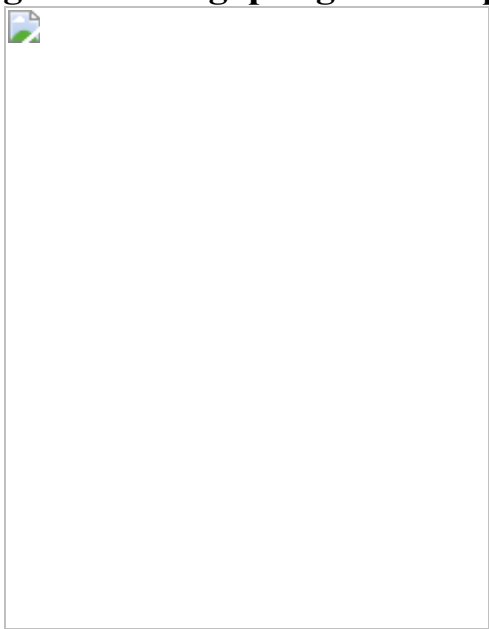
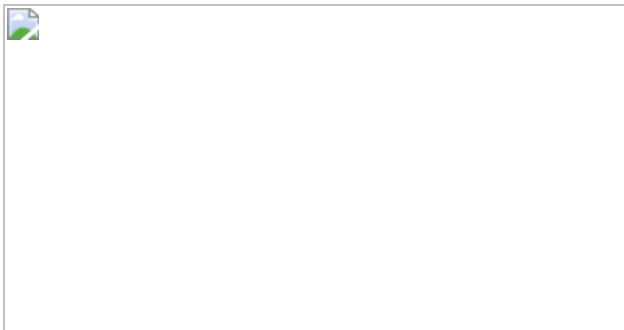


**Fig. 5: DT-STS and DT-PCS on non-superconducting MATBG aligned to hBN.**



## Data availability

The data that support the findings of this study are available at  
<https://doi.org/10.5281/zenodo.5722484>.

## References

1. 1.  
Cao, Y. et al. Unconventional superconductivity in magic-angle graphene superlattices. *Nature* **556**, 43–50 (2018).
2. 2.  
Yankowitz, M. et al. Tuning superconductivity in twisted bilayer graphene. *Science* **363**, 1059–1064 (2019).
3. 3.  
Lu, X. et al. Superconductors, orbital magnets and correlated states in magic-angle bilayer graphene. *Nature* **574**, 653–657 (2019).
4. 4.  
Cao, Y. et al. Correlated insulator behaviour at half-filling in magic-angle graphene superlattices. *Nature* **556**, 80–84 (2018).

5. 5.

Saito, Y., Ge, J., Watanabe, K., Taniguchi, T. & Young, A. F. Independent superconductors and correlated insulators in twisted bilayer graphene. *Nat. Phys.* **16**, 926–930 (2020).

6. 6.

Stepanov, P. et al. Untying the insulating and superconducting orders in magic-angle graphene. *Nature* **583**, 375–378 (2020).

7. 7.

Bardeen, J. Electron-phonon interactions and superconductivity. *Science* **181**, 1209–1214 (1973).

8. 8.

Damascelli, A., Hussain, Z. & Shen, Z.-X. Angle-resolved photoemission studies of the cuprate superconductors. *Rev. Mod. Phys.* **75**, 473–541 (2003).

9. 9.

Fischer, Ø., Kugler, M., Maggio-Aprile, I., Berthod, C. & Renner, C. Scanning tunneling spectroscopy of high-temperature superconductors. *Rev. Mod. Phys.* **79**, 353–419 (2007).

10. 10.

Isobe, H., Yuan, N. F. Q. & Fu, L. Unconventional superconductivity and density waves in twisted bilayer graphene. *Phys. Rev. X* **8**, 041041 (2018).

11. 11.

Liu, C.-C., Zhang, L.-D., Chen, W.-Q. & Yang, F. Chiral spin density wave and  $d + id$  superconductivity in the magic-angle-twisted bilayer graphene. *Phys. Rev. Lett.* **121**, 217001 (2018).

12. 12.

Kennes, D. M., Lischner, J. & Karrasch, C. Strong correlations and  $d + id$  superconductivity in twisted bilayer graphene. *Phys. Rev. B* **98**, 241407 (2018).

13. 13.

Wu, F., MacDonald, A. H. & Martin, I. Theory of phonon-mediated superconductivity in twisted bilayer graphene. *Phys. Rev. Lett.* **121**, 257001 (2018).

14. 14.

Lian, B., Wang, Z. & Bernevig, B. A. Twisted bilayer graphene: a phonon-driven superconductor. *Phys. Rev. Lett.* **122**, 257002 (2019).

15. 15.

Wong, D. et al. A modular ultra-high vacuum millikelvin scanning tunneling microscope. *Rev. Sci. Instrum.* **91**, 023703 (2020).

16. 16.

Kerelsky, A. et al. Maximized electron interactions at the magic angle in twisted bilayer graphene. *Nature* **572**, 95–100 (2019).

17. 17.

Choi, Y. et al. Electronic correlations in twisted bilayer graphene near the magic angle. *Nat. Phys.* **15**, 1174–1180 (2019).

18. 18.

Jiang, Y. et al. Charge order and broken rotational symmetry in magic-angle twisted bilayer graphene. *Nature* **573**, 91–95 (2019).

19. 19.

Xie, Y. et al. Spectroscopic signatures of many-body correlations in magic-angle twisted bilayer graphene. *Nature* **572**, 101–105 (2019).

20. 20.

Wong, D. et al. Cascade of electronic transitions in magic-angle twisted bilayer graphene. *Nature* **582**, 198–202 (2020).

21. 21.

Zondiner, U. et al. Cascade of phase transitions and Dirac revivals in magic-angle graphene. *Nature* **582**, 203–208 (2020).

22. 22.

Nuckolls, K. P. et al. Strongly correlated Chern insulators in magic-angle twisted bilayer graphene. *Nature* **588**, 610–615 (2020).

23. 23.

Choi, Y. et al. Interaction-driven band flattening and correlated phases in twisted bilayer graphene. *Nat. Phys.* <https://doi.org/10.1038/s41567-021-01359-0> (2021).

24. 24.

Saito, Y. et al. Isospin Pomeranchuk effect in twisted bilayer graphene. *Nature* **592**, 220–224 (2021).

25. 25.

Rozen, A. et al. Entropic evidence for a Pomeranchuk effect in magic-angle graphene. *Nature* **592**, 214–219 (2021).

26. 26.

Rodan-Legrain, D. et al. Highly tunable junctions and non-local Josephson effect in magic-angle graphene tunnelling devices. *Nat. Nanotechnol.* **16**, 769–775 **16**, 769–775 (2021).

27. 27.

Deutscher, G. Andreev–Saint-James reflections: a probe of cuprate superconductors. *Rev. Mod. Phys.* **77**, 109–135 (2005).

28. 28.

Dubouchet, T. et al. Collective energy gap of preformed Cooper pairs in disordered superconductors. *Nat. Phys.* **15**, 233–236 (2019).

29. 29.

Blonder, G. E., Tinkham, M. & Klapwijk, T. M. Transition from metallic to tunneling regimes in superconducting microconstrictions: excess current, charge imbalance, and supercurrent conversion. *Phys. Rev. B* **25**, 4515–4532 (1982).

30. 30.

Randeria, M., Trivedi, N., Moreo, A. & Scalettar, R. T. Pairing and spin gap in the normal state of short coherence length superconductors. *Phys. Rev. Lett.* **69**, 2001–2004 (1992).

31. 31.

Serlin, M. et al. Intrinsic quantized anomalous Hall effect in a moiré heterostructure. *Science* **367**, 900–903 (2020).

32. 32.

Sharpe, A. L. et al. Emergent ferromagnetism near three-quarters filling in twisted bilayer graphene. *Science* **365**, 605–608 (2019).

33. 33.

Hunt, B. et al. Massive Dirac fermions and Hofstadter butterfly in a van der Waals heterostructure. *Science* **340**, 1427–1430 (2013).

34. 34.

Shi, J., Zhu, J. & MacDonald, A. H. Moiré commensurability and the quantum anomalous Hall effect in twisted bilayer graphene on hexagonal boron nitride. *Phys. Rev. B* **103**, 075122 (2021).

35. 35.

Zhang, Y.-H., Mao, D. & Senthil, T. Twisted bilayer graphene aligned with hexagonal boron nitride: anomalous Hall effect and a lattice model. *Phys. Rev. Res.* **1**, 033126 (2019).

36. 36.

He, M. et al. Symmetry breaking in twisted double bilayer graphene. *Nat. Phys.* **17**, 26–30 (2021).

37. 37.

Khalaf, E., Chatterjee, S., Bultinck, N., Zaletel, M. P. & Vishwanath, A. Charged skyrmions and topological origin of superconductivity in magic-angle graphene. *Sci. Adv.* **7**, eabf5299 (2021).

38. 38.

Park, J. M., Cao, Y., Watanabe, K., Taniguchi, T. & Jarillo-Herrero, P. Tunable strongly coupled superconductivity in magic-angle twisted trilayer graphene. *Nature* **590**, 249–255 (2021).

39. 39.

Hao, Z. et al. Electric field–tunable superconductivity in alternating-twist magic-angle trilayer graphene. *Science* **371**, 1133–1138 (2021).

40. 40.

Goll, G., Löhneysen, H. V., Yanson, I. K. & Taillefer, L. Anisotropy of point-contact spectra in the heavy-fermion superconductor UPt<sub>3</sub>. *Phys. Rev. Lett.* **70**, 2008–2011 (1993).

41. 41.

Laube, F., Goll, G., Eschrig, M., Fogelström, M. & Werner, R. Excess current in superconducting  $\text{Sr}_2\text{RuO}_4$ . *Phys. Rev. B* **69**, 014516 (2004).

42. 42.

Khalaf, E., Bultinck, N., Vishwanath, A. & Zaletel, M. P. Soft modes in magic angle twisted bilayer graphene. Preprint at <https://arxiv.org/abs/2009.14827v2> (2020).

43. 43.

Millis, A. J., Sachdev, S. & Varma, C. M. Inelastic scattering and pair breaking in anisotropic and isotropic superconductors. *Phys. Rev. B* **37**, 4975–4986 (1988).

44. 44.

Zhang, Y. et al. Giant phonon-induced conductance in scanning tunnelling spectroscopy of gate-tunable graphene. *Nat. Phys.* **4**, 627–630 (2008).

45. 45.

Hapala, P. et al. Mechanism of high-resolution STM/AFM imaging with functionalized tips. *Phys. Rev. B* **90**, 085421 (2014).

46. 46.

Stroscio, J. A. & Celotta, R. J. Controlling the dynamics of a single atom in lateral atom manipulation. *Science* **306**, 242–247 (2004).

47. 47.

Wolter, B. et al. Spin friction observed on the atomic scale. *Phys. Rev. Lett.* **109**, 116102 (2012).

48. 48.

Daghero, D. & Gonnelli, R. S. Probing multiband superconductivity by point-contact spectroscopy. *Supercond. Sci. Technol.* **23**, 043001 (2010).

49. 49.

Kim, K. et al. Van der Waals heterostructures with high accuracy rotational alignment. *Nano Lett.* **16**, 1989–1995 (2016).

## Acknowledgements

We thank P. Jarillo-Herrero, A. H. MacDonald and S. A. Kivelson for helpful discussions. We thank C.-L. Chiu, G. Farahi and H. Ding for helpful technical discussions. This work was primarily supported by the Gordon and Betty Moore Foundation’s EPiQS initiative grant GBMF9469 and DOE-BES grant DE-FG02-07ER46419 to A.Y. Other support for the experimental work was provided by NSF-MRSEC through the Princeton Center for Complex Materials NSF-DMR- 2011750 and NSF-DMR-1904442, ExxonMobil through the Andlinger Center for Energy and the Environment at Princeton, and the Princeton Catalysis Initiative. A.Y. acknowledges the hospitality of the Aspen Center for Physics, which is supported by the National Science Foundation grant PHY-1607611, and Trinity College, Cambridge, UK, where part of this work was carried out with the support of, in part, a QuantEmX grant from ICAM and the Gordon and Betty Moore Foundation through the grant GBMF9616. K.W. and T.T. acknowledge support from the Elemental Strategy Initiative conducted by the MEXT, Japan, grant JPMXP0112101001, and JSPS KAKENHI grants 19H05790 and JP20H00354.

## Author information

### Author notes

1. These authors contributed equally: Myungchul Oh, Kevin P. Nuckolls, Dillon Wong

## Affiliations

1. Joseph Henry Laboratories and Department of Physics, Princeton University, Princeton, NJ, USA

Myungchul Oh, Kevin P. Nuckolls, Dillon Wong, Ryan L. Lee, Xiaomeng Liu & Ali Yazdani

2. Research Center for Functional Materials, National Institute for Materials Science, Tsukuba, Japan

Kenji Watanabe

3. International Center for Materials Nanoarchitectonics, National Institute for Materials Science, Tsukuba, Japan

Takashi Taniguchi

## Contributions

M.O., K.P.N., D.W. and A.Y. designed the experiment. M.O., D.W. and K.P.N. fabricated the devices used for the study. M.O., K.P.N., D.W. and R.L.L. carried out STM/STS and PCS measurements, with invaluable input from X.L. on the latter. M.O., D.W. and K.P.N. performed the data analysis. K.W. and T.T. synthesized the hBN crystals. All authors discussed the results and contributed to the writing of the manuscript.

## Corresponding author

Correspondence to [Ali Yazdani](#).

## Ethics declarations

## Competing interests

The authors declare no competing interests.

# Additional information

**Peer review information** *Nature* thanks Dante Kennes and the other, anonymous, reviewer(s) for their contribution to the peer review of this work.

**Publisher's note** Springer Nature remains neutral with regard to jurisdictional claims in published maps and institutional affiliations.

## Supplementary information

### Supplementary Information

This file contains Supplementary Sections A–L, including text and data, tables and Supplementary Figs. 1–16. See contents page for details.

## Rights and permissions

### Reprints and Permissions

## About this article

### Cite this article

Oh, M., Nuckolls, K.P., Wong, D. *et al.* Evidence for unconventional superconductivity in twisted bilayer graphene. *Nature* **600**, 240–245 (2021). <https://doi.org/10.1038/s41586-021-04121-x>

- Received: 16 June 2021
- Accepted: 11 October 2021
- Published: 20 October 2021
- Issue Date: 09 December 2021

- DOI: <https://doi.org/10.1038/s41586-021-04121-x>

## Share this article

Anyone you share the following link with will be able to read this content:

[Get shareable link](#)

Sorry, a shareable link is not currently available for this article.

[Copy to clipboard](#)

Provided by the Springer Nature SharedIt content-sharing initiative

---

This article was downloaded by **calibre** from <https://www.nature.com/articles/s41586-021-04121-x>

| [Section menu](#) | [Main menu](#) |

- Article
- [Published: 08 December 2021](#)

# High-frequency and intrinsically stretchable polymer diodes

- [Naoji Matsuhsia](#) ORCID: [orcid.org/0000-0002-5978-2778](https://orcid.org/0000-0002-5978-2778)<sup>1,2,3,4 na1</sup>,
- [Simiao Niu](#) ORCID: [orcid.org/0000-0003-1973-2204](https://orcid.org/0000-0003-1973-2204)<sup>1 na1</sup>,
- [Stephen J. K. O'Neill](#)<sup>1</sup>,
- [Jiheong Kang](#)<sup>1</sup>,
- [Yuto Ochiai](#) ORCID: [orcid.org/0000-0002-7785-9628](https://orcid.org/0000-0002-7785-9628)<sup>1</sup>,
- [Toru Katsumata](#)<sup>1,5</sup>,
- [Hung-Chin Wu](#) ORCID: [orcid.org/0000-0001-6492-0525](https://orcid.org/0000-0001-6492-0525)<sup>1</sup>,
- [Minoru Ashizawa](#)<sup>1,6</sup>,
- [Ging-Ji Nathan Wang](#) ORCID: [orcid.org/0000-0002-5432-3046](https://orcid.org/0000-0002-5432-3046)<sup>1</sup>,
- [Donglai Zhong](#) ORCID: [orcid.org/0000-0002-0876-414X](https://orcid.org/0000-0002-0876-414X)<sup>1</sup>,
- [Xuelin Wang](#)<sup>1,7</sup>,
- [Xiwen Gong](#) ORCID: [orcid.org/0000-0003-4004-1299](https://orcid.org/0000-0003-4004-1299)<sup>1</sup>,
- [Rui Ning](#)<sup>8</sup>,
- [Huixin Gong](#)<sup>1</sup>,
- [Insang You](#)<sup>1</sup>,
- [Yu Zheng](#)<sup>1</sup>,
- [Zhitao Zhang](#)<sup>1</sup>,
- [Jeffrey B.-H. Tok](#) ORCID: [orcid.org/0000-0002-2794-0663](https://orcid.org/0000-0002-2794-0663)<sup>1</sup>,
- [Xiaodong Chen](#) ORCID: [orcid.org/0000-0002-3312-1664](https://orcid.org/0000-0002-3312-1664)<sup>2</sup> &
- [Zhenan Bao](#) ORCID: [orcid.org/0000-0002-0972-1715](https://orcid.org/0000-0002-0972-1715)<sup>1</sup>

*Nature* volume 600, pages 246–252 (2021)

- 3510 Accesses

- 32 Altmetric
- [Metrics details](#)

## Subjects

- [Electrical and electronic engineering](#)
- [Organic molecules in materials science](#)

## Abstract

Skin-like intrinsically stretchable soft electronic devices are essential to realize next-generation remote and preventative medicine for advanced personal healthcare<sup>1,2,3,4</sup>. The recent development of intrinsically stretchable conductors and semiconductors has enabled highly mechanically robust and skin-conformable electronic circuits or optoelectronic devices<sup>2,5,6,7,8,9,10</sup>. However, their operating frequencies have been limited to less than 100 hertz, which is much lower than that required for many applications. Here we report intrinsically stretchable diodes—based on stretchable organic and nanomaterials—capable of operating at a frequency as high as 13.56 megahertz. This operating frequency is high enough for the wireless operation of soft sensors and electrochromic display pixels using radiofrequency identification in which the base-carrier frequency is 6.78 megahertz or 13.56 megahertz. This was achieved through a combination of rational material design and device engineering. Specifically, we developed a stretchable anode, cathode, semiconductor and current collector that can satisfy the strict requirements for high-frequency operation. Finally, we show the operational feasibility of our diode by integrating it with a stretchable sensor, electrochromic display pixel and antenna to realize a stretchable wireless tag. This work is an important step towards enabling enhanced functionalities and capabilities for skin-like wearable electronics.

This is a preview of subscription content

## Access options

[Subscribe to Journal](#)

Get full journal access for 1 year

\$199.00

only \$3.90 per issue

[Subscribe](#)

All prices are NET prices.

VAT will be added later in the checkout.

Tax calculation will be finalised during checkout.

Rent or Buy article

Get time limited or full article access on ReadCube.

from \$8.99

[Rent or Buy](#)

All prices are NET prices.

### **Additional access options:**

- [Log in](#)
- [Learn about institutional subscriptions](#)

**Fig. 1: A high-frequency stretchable diode.**

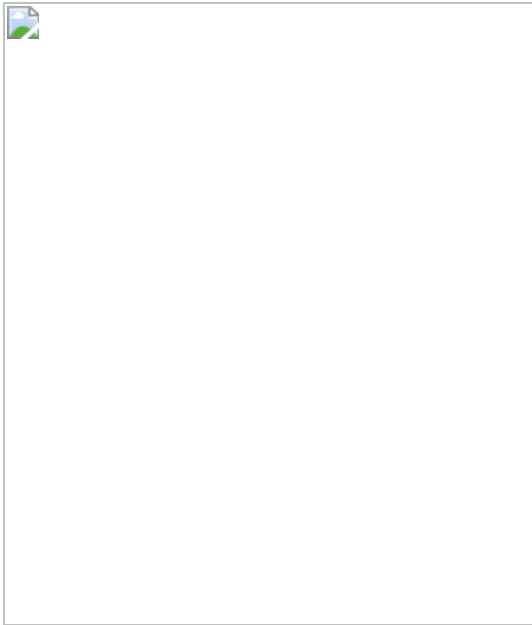


**Fig. 2: Characterization of stretchable current collectors based on AgNWs.**



**Fig. 3: High-frequency operation of the stretchable diodes.**

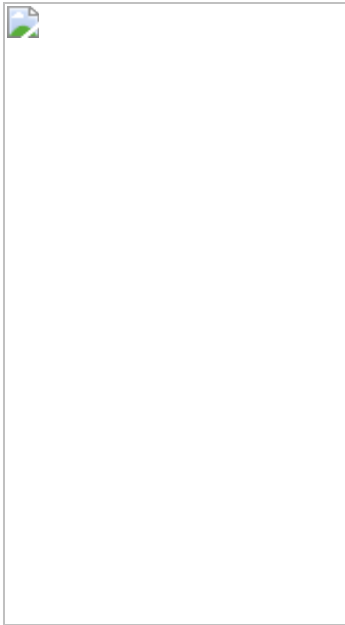
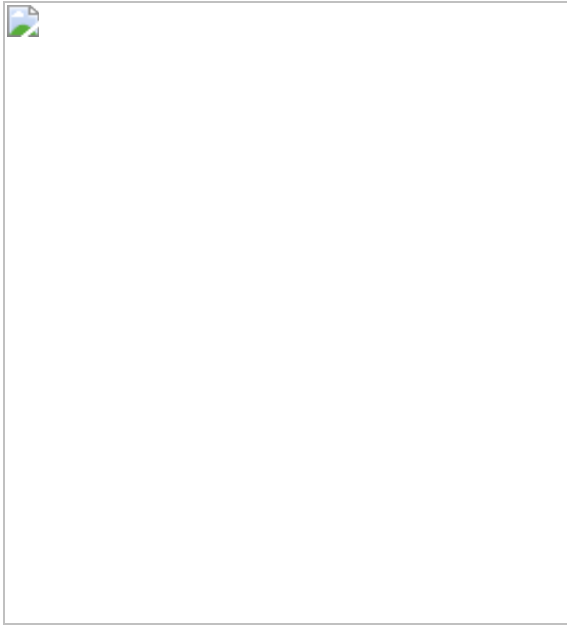


**Fig. 4: A wireless stretchable sensor and display system.**



## Data availability

[Source data](#) are provided with this paper.

## References

1. 1.

Sim, K. et al. An epicardial bioelectronic patch made from soft rubbery materials and capable of spatiotemporal mapping of electrophysiological activity. *Nat. Electron.* **3**, 775–784 (2020).

2. 2.

Wang, S. et al. Skin electronics from scalable fabrication of an intrinsically stretchable transistor array. *Nature* **555**, 83–88 (2018).

3. 3.

Miyamoto, A. et al. Inflammation-free, gas-permeable, lightweight, stretchable on-skin electronics with nanomeshes. *Nat. Nanotechnol.* **12**, 907–913 (2017).

4. 4.

Kim, D.-H. et al. Epidermal electronics. *Science* **333**, 838–843 (2011).

5. 5.

Zheng, Y. et al. Monolithic optical microlithography of high-density elastic circuits. *Science* **373**, 88–94 (2021).

6. 6.

Liang, J., Li, L., Niu, X., Yu, Z. & Pei, Q. Elastomeric polymer light-emitting devices and displays. *Nat. Photon.* **7**, 817–824 (2013).

7. 7.

Kim, H., Sim, K., Thukral, A. & Yu, C. Rubbery electronics and sensors from intrinsically stretchable elastomeric composites of semiconductors and conductors. *Sci. Adv.* **3**, e1701114 (2017).

8. 8.

Kim, J.-H. & Park, J.-W. Intrinsically stretchable organic light-emitting diodes. *Sci. Adv.* **7**, eabd9715 (2021).

9. 9.

Wang, Z. et al. Intrinsically stretchable organic solar cells beyond 10% power conversion efficiency enabled by transfer printing method. *Adv. Funct. Mater.* **31**, 2103534 (2021).

10. 10.

Noh, J. et al. Intrinsically stretchable organic solar cells with efficiencies of over 11%. *ACS Energy Lett.* **6**, 2512–2518 (2021).

11. 11.

Kaltenbrunner, M. et al. An ultra-lightweight design for imperceptible plastic electronics. *Nature* **499**, 458–463 (2013).

12. 12.

Minev, I. R. et al. Electronic dura mater for long-term multimodal neural interfaces. *Science* **347**, 159–163 (2015).

13. 13.

Khodagholy, D. et al. NeuroGrid: recording action potentials from the surface of the brain. *Nat. Neurosci.* **18**, 310–315 (2015).

14. 14.

Wang, C., Wang, C., Huang, Z. & Xu, S. Materials and structures toward soft electronics. *Adv. Mater.* **30**, 1801368 (2018).

15. 15.

Kim, D.-H. et al. Dissolvable films of silk fibroin for ultrathin conformal bio-integrated electronics. *Nat. Mater.* **9**, 511–517 (2010).

16. 16.

Gao, W. et al. Fully integrated wearable sensor arrays for multiplexed in situ perspiration analysis. *Nature* **529**, 509–514 (2016).

17. 17.

Matsuhisa, N., Chen, X., Bao, Z. & Someya, T. Materials and structural designs of stretchable conductors. *Chem. Soc. Rev.* **48**, 2946–2966 (2019).

18. 18.

Wang, S., Oh, J. Y., Xu, J., Tran, H. & Bao, Z. Skin-inspired electronics: an emerging paradigm. *Acc. Chem. Res.* **51**, 1033–1045 (2018).

19. 19.

Kim, H., Thukral, A., Sharma, S. & Yu, C. Biaxially stretchable fully elastic transistors based on rubbery semiconductor nanocomposites. *Adv. Mater. Technol.* **3**, 1800043 (2018).

20. 20.

Sim, K. et al. Fully rubbery integrated electronics from high effective mobility intrinsically stretchable semiconductors. *Sci. Adv.* **5**, 14 (2019).

21. 21.

Niu, S. et al. A wireless body area sensor network based on stretchable passive tags. *Nat. Electron.* **2**, 361–368 (2019).

22. 22.

Huang, Z. et al. Three-dimensional integrated stretchable electronics. *Nat. Electron.* **1**, 473–480 (2018).

23. 23.

Bandodkar, A. J. et al. Battery-free, skin-interfaced microfluidic/electronic systems for simultaneous electrochemical, colorimetric, and volumetric analysis of sweat. *Sci. Adv.* **5**, 587 (2019).

24. 24.

Steudel, S. et al. Comparison of organic diode structures regarding high-frequency rectification behavior in radio-frequency identification tags. *J. Appl. Phys.* **99**, 114519 (2006).

25. 25.

Viola, F. A. et al. A 13.56 MHz rectifier based on fully inkjet printed organic diodes. *Adv. Mater.* **32**, 2002329 (2020).

26. 26.

Higgins, S. G., Agostinelli, T., Markham, S., Whiteman, R. & Sirringhaus, H. Organic diode rectifiers based on a high-performance conjugated polymer for a near-field energy-harvesting circuit. *Adv. Mater.* **29**, 1703782 (2017).

27. 27.

Zhou, X., Yang, D. & Ma, D. Extremely low dark current, high responsivity, all-polymer photodetectors with spectral response from 300 nm to 1000 nm. *Adv. Opt. Mater.* **3**, 1570–1576 (2015).

28. 28.

Huang, J. et al. A high-performance solution-processed organic photodetector for near-infrared sensing. *Adv. Mater.* **32**, 1906027 (2020).

29. 29.

Heljo, P. S., Schmidt, C., Klengel, R., Majumdar, H. S. & Lupo, D. Electrical and thermal analysis of frequency dependent filamentary

switching in printed rectifying diodes. *Org. Electron.* **20**, 69–75 (2015).

30. 30.

Bose, I., Tetzner, K., Borner, K. & Bock, K. Air-stable, high current density, solution-processable, amorphous organic rectifying diodes (ORDs) for low-cost fabrication of flexible passive low frequency RFID tags. *Microelectron. Reliab.* **54**, 1643–1647 (2014).

31. 31.

Lee, Y. et al. Standalone real-time health monitoring patch based on a stretchable organic optoelectronic system. *Sci. Adv.* **7**, eabg9180 (2021).

32. 32.

Gao, H., Chen, S., Liang, J. & Pei, Q. Elastomeric light emitting polymer enhanced by interpenetrating networks. *ACS Appl. Mater. Interfaces* **8**, 32504–32511 (2016).

33. 33.

Li, L. et al. A solid-state intrinsically stretchable polymer solar cell. *ACS Appl. Mater. Interfaces* **9**, 40523–40532 (2017).

34. 34.

Hsieh, Y. T. et al. Realization of intrinsically stretchable organic solar cells enabled by charge-extraction layer and photoactive material engineering. *ACS Appl. Mater. Interfaces* **10**, 21712–21720 (2018).

35. 35.

Liu, N. et al. Ultratransparent and stretchable graphene electrodes. *Sci. Adv.* **3**, e1700159 (2017).

36. 36.

Matsuhsia, N. et al. High-transconductance stretchable transistors achieved by controlled gold microcrack morphology. *Adv. Electron. Mater.* **5**, 1900347 (2019).

37. 37.

Zhou, Y. et al. A universal method to produce low-work function electrodes for organic electronics. *Science* **336**, 327–332 (2012).

38. 38.

Wang, Y. et al. A highly stretchable, transparent, and conductive polymer. *Sci. Adv.* **3**, e1602076 (2017).

39. 39.

Lipomi, D. J., Tee, B. C.-K., Vosgueritchian, M. & Bao, Z. Stretchable organic solar cells. *Adv. Mater.* **23**, 1771–1775 (2011).

40. 40.

Steudel, S. et al. 50 MHz rectifier based on an organic diode. *Nat. Mater.* **4**, 597–600 (2005).

41. 41.

Kang, C. et al. 1 GHz pentacene diode rectifiers enabled by controlled film deposition on SAM-treated Au anodes. *Adv. Electron. Mater.* **2**, 1500282 (2016).

42. 42.

Matsuhsia, N. et al. A mechanically durable and flexible organic rectifying diode with a polyethylenimine ethoxylated cathode. *Adv. Electron. Mater.* **2**, 1600259 (2016).

43. 43.

Borchert, J. W. et al. Flexible low-voltage high-frequency organic thin-film transistors. *Sci. Adv.* **6**, 1–9 (2020).

44. 44.

Yamamura, A. et al. Wafer-scale, layer-controlled organic single crystals for high-speed circuit operation. *Sci. Adv.* **4**, 21 (2018).

45. 45.

Wang, X. et al. Printed conformable liquid metal e-skin-enabled spatiotemporally controlled bioelectromagnetics for wireless multisite tumor therapy. *Adv. Funct. Mater.* **29**, 1907063 (2019).

46. 46.

Liu, Z. et al. Thickness-gradient films for high gauge factor stretchable strain sensors. *Adv. Mater.* **27**, 6230–6237 (2015).

47. 47.

JK O'Neill, S. et al. A carbon flower based flexible pressure sensor made from large-area coating. *Adv. Mater. Interfaces* **7**, 2000875 (2020).

48. 48.

Jeon, J., Lee, H.-B.-R. & Bao, Z. Flexible wireless temperature sensors based on Ni microparticle-filled binary polymer composites. *Adv. Mater.* **25**, 850–855 (2013).

49. 49.

Wang, C. et al. Thiophene-diketopyrrolopyrrole-based quinoidal small molecules as solution-processable and air-stable organic semiconductors: tuning of the length and branching position of the alkyl side chain toward a high-performance n-channel organic field-effect tran. *ACS Appl. Mater. Interfaces* **7**, 15978–15987 (2015).

50. 50.

Ito, Y. et al. Crystalline ultrasmooth self-assembled monolayers of alkylsilanes for organic field-effect transistors. *J. Am. Chem. Soc.* **131**, 9396–9404 (2009).

51. 51.

Tahk, D., Lee, H. H. & Khang, D.-Y. Elastic moduli of organic electronic materials by the buckling method. *Macromolecules* **42**, 7079–7083 (2009).

52. 52.

Kawahara, J., Ersman, P. A., Engquist, I. & Berggren, M. Improving the color switch contrast in PEDOT:PSS-based electrochromic displays. *Org. Electron.* **13**, 469–474 (2012).

## Acknowledgements

This work was partially supported by SAIT, Samsung Electronics Co., Ltd., and the Agency for Science, Technology and Research (A\*STAR) under its Advanced Manufacturing and Engineering (AME) Programmatic Scheme (no. A18A1b0045). N.M. was partially supported by a Japan Society for the Promotion of Science (JSPS) overseas research fellowship. Part of this work was performed at the Stanford Nano Shared Facilities (SNSF), supported by the National Science Foundation under award ECCS-1542152. Grazing incidence X-ray diffraction measurements were carried out at the Stanford Synchrotron Radiation Laboratory (SSRL), a national user facility operated by Stanford University on behalf of the US Department of Energy, Office of Basic Energy Sciences. Experiments performed during revision were carried out in Keio University and was supported by JST, PRESTO Grant Number JPMJPR20B7, Japan.

## Author information

### Author notes

1. These authors contributed equally: Naoji Matsuhisa, Simiao Niu

## Affiliations

1. Department of Chemical Engineering, Stanford University, Stanford, CA, USA

Naoji Matsuhisa, Simiao Niu, Stephen J. K. O'Neill, Jiheong Kang, Yuto Ochiai, Toru Katsumata, Hung-Chin Wu, Minoru Ashizawa, Ging-Ji Nathan Wang, Donglai Zhong, Xuelin Wang, Xiwen Gong, Huaxin Gong, Insang You, Yu Zheng, Zhitao Zhang, Jeffrey B.-H. Tok & Zhenan Bao

2. Innovative Center for Flexible Devices (iFLEX), School of Materials Science and Engineering, Nanyang Technological University, Singapore, Singapore

Naoji Matsuhisa & Xiaodong Chen

3. Department of Electronics and Electrical Engineering, Keio University, Yokohama, Japan

Naoji Matsuhisa

4. Japan Science and Technology Agency, PRESTO, Kawaguchi, Japan

Naoji Matsuhisa

5. Corporate Research and Development, Performance Materials Technology Center, Asahi Kasei Corporation, Fuji, Japan

Toru Katsumata

6. Department of Materials Science and Engineering, Tokyo Institute of Technology, Tokyo, Japan

Minoru Ashizawa

7. School of Medical Science and Engineering, Beihang University,  
Beijing, China

Xuelin Wang

8. Department of Materials Science and Engineering, Stanford  
University, Stanford, CA, USA

Rui Ning

## Contributions

N.M., S.N., X.C. and Z.B. designed the project and experiments. S.N. and D.Z. performed the simulation of a diode, circuit and wireless communication. T.K. designed DPP4T-oSi10. Y.O., T.K., M.A., G.-J.N.W. and Y.Z. synthesized DPP4T-oSi10. N.M., Y.O., T.K. and H.-C.W. characterized DPP4T-oSi10. J.K. synthesized ION E. N.M., S.J.K.O., H.-C.W. and R.N. developed stretchable PEDOT:PSS. H.G. performed XPS. N.M., S.J.K.O., R.N., I.Y. and Z.Z. developed stretchable AgNWs. N.M., S.J.K.O., R.N. and X.G. developed the fabrication process of stretchable diodes. N.M. and X.W. fabricated O-GaIn. N.M., S.N. and X.C. developed CNT strain sensors. N.M. and S.J.K.O. developed stretchable ECDs. S.N. developed the flexible power-supply circuit. N.M., S.N., J.B.-H.T. and Z.B. wrote the manuscript.

## Corresponding author

Correspondence to [Zhenan Bao](#).

## Ethics declarations

## Competing interests

The authors declare no competing interests.

## Additional information

**Peer review information** *Nature* thanks the anonymous reviewers for their contribution to the peer review of this work.

**Publisher's note** Springer Nature remains neutral with regard to jurisdictional claims in published maps and institutional affiliations.

## Supplementary information

### Supplementary Information

This file contains Supplementary Figs. 1–50, Tables 1–60 and Notes I–XIV.

### Supplementary Data

This file contains the source data of the plots in the Supplementary Information.

### Supplementary Video 1

Operation of the stretchable ECD under 0% strain. The ECD showed a fast response up to 10 Hz.

### Supplementary Video 2

Operation of the stretchable ECD under 20% strain. The ECD showed a fast response up to 10 Hz.

### Supplementary Video 3

Operation of the stretchable ECD under 50% strain. The ECD showed a fast response up to 10 Hz.

### Supplementary Video 4

Wireless operation of the stretchable sensor and display system. Strain larger than 20% increased the resistance of the integrated strain sensor, and

a clear colour change of the ECD was observed.

## Source data

[Source Data Fig. 1](#)

[Source Data Fig. 2](#)

[Source Data Fig. 3](#)

[Source Data Fig. 4](#)

## Rights and permissions

[Reprints and Permissions](#)

## About this article

### Cite this article

Matsuhsia, N., Niu, S., O'Neill, S.J.K. *et al.* High-frequency and intrinsically stretchable polymer diodes. *Nature* **600**, 246–252 (2021). <https://doi.org/10.1038/s41586-021-04053-6>

- Received: 07 February 2021
- Accepted: 24 September 2021
- Published: 08 December 2021
- Issue Date: 09 December 2021
- DOI: <https://doi.org/10.1038/s41586-021-04053-6>

### Share this article

Anyone you share the following link with will be able to read this content:

[Get shareable link](#)

Sorry, a shareable link is not currently available for this article.

[Copy to clipboard](#)

Provided by the Springer Nature SharedIt content-sharing initiative

---

This article was downloaded by **calibre** from <https://www.nature.com/articles/s41586-021-04053-6>

| [Section menu](#) | [Main menu](#) |

- Article
- [Published: 08 December 2021](#)

# A constraint on historic growth in global photosynthesis due to increasing CO<sub>2</sub>

- [T. F. Keenan](#) ORCID: [orcid.org/0000-0002-3347-0258](#)<sup>1,2</sup>,
- [X. Luo](#) ORCID: [orcid.org/0000-0002-9546-0960](#)<sup>1,2,3</sup>,
- [M. G. De Kauwe](#) ORCID: [orcid.org/0000-0002-3399-9098](#)<sup>4,5,6</sup>,
- [B. E. Medlyn](#) ORCID: [orcid.org/0000-0001-5728-9827](#)<sup>7</sup>,
- [I. C. Prentice](#) ORCID: [orcid.org/0000-0002-1296-6764](#)<sup>8,9,10</sup>,
- [B. D. Stocker](#)<sup>11,12</sup>,
- [N. G. Smith](#) ORCID: [orcid.org/0000-0001-7048-4387](#)<sup>13</sup>,
- [C. Terrer](#) ORCID: [orcid.org/0000-0002-5479-3486](#)<sup>14,15</sup>,
- [H. Wang](#) ORCID: [orcid.org/0000-0003-2482-1818](#)<sup>10</sup>,
- [Y. Zhang](#) ORCID: [orcid.org/0000-0002-7468-2409](#)<sup>1,2,16</sup> &
- [S. Zhou](#)<sup>1,2,17,18,19,20</sup>

[Nature](#) volume 600, pages 253–258 (2021)

- 3727 Accesses
- 589 Altmetric
- [Metrics details](#)

## Subjects

- [Carbon cycle](#)
- [Climate-change ecology](#)

- [Ecophysiology](#)
- [Ecosystem ecology](#)

## Abstract

The global terrestrial carbon sink is increasing<sup>1,2,3</sup>, offsetting roughly a third of anthropogenic CO<sub>2</sub> released into the atmosphere each decade<sup>1</sup>, and thus serving to slow<sup>4</sup> the growth of atmospheric CO<sub>2</sub>. It has been suggested that a CO<sub>2</sub>-induced long-term increase in global photosynthesis, a process known as CO<sub>2</sub> fertilization, is responsible for a large proportion of the current terrestrial carbon sink<sup>4,5,6,7</sup>. The estimated magnitude of the historic increase in photosynthesis as result of increasing atmospheric CO<sub>2</sub> concentrations, however, differs by an order of magnitude between long-term proxies and terrestrial biosphere models<sup>7,8,9,10,11,12,13</sup>. Here we quantify the historic effect of CO<sub>2</sub> on global photosynthesis by identifying an emergent constraint<sup>14,15,16</sup> that combines terrestrial biosphere models with global carbon budget estimates. Our analysis suggests that CO<sub>2</sub> fertilization increased global annual photosynthesis by  $11.85 \pm 1.4\%$ , or  $13.98 \pm 1.63$  petagrams carbon (mean  $\pm$  95% confidence interval) between 1981 and 2020. Our results help resolve conflicting estimates of the historic sensitivity of global photosynthesis to CO<sub>2</sub>, and highlight the large impact anthropogenic emissions have had on ecosystems worldwide.

This is a preview of subscription content

## Access options

Subscribe to Journal

Get full journal access for 1 year

\$199.00

only \$3.90 per issue

## Subscribe

All prices are NET prices.  
VAT will be added later in the checkout.  
Tax calculation will be finalised during checkout.

Rent or Buy article

Get time limited or full article access on ReadCube.

from \$8.99

## Rent or Buy

All prices are NET prices.

### **Additional access options:**

- [Log in](#)
- [Learn about institutional subscriptions](#)

**Fig. 1: A constraint on the sensitivity of global photosynthesis to CO<sub>2</sub>.**

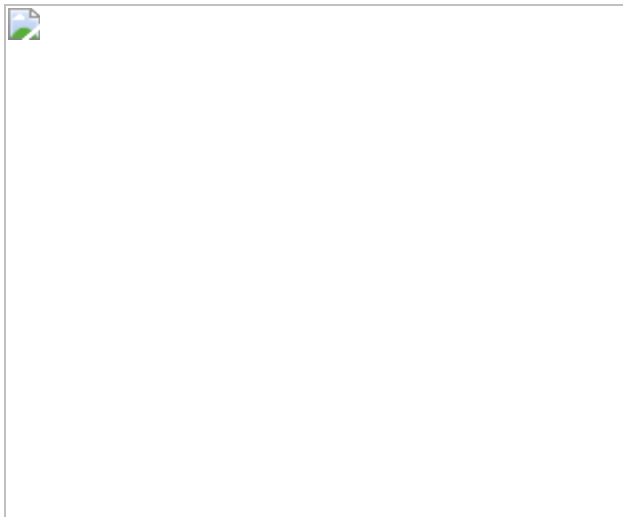


**Fig. 2: Long-term changes in global annual photosynthesis from TBMs and multiple satellite observations.**

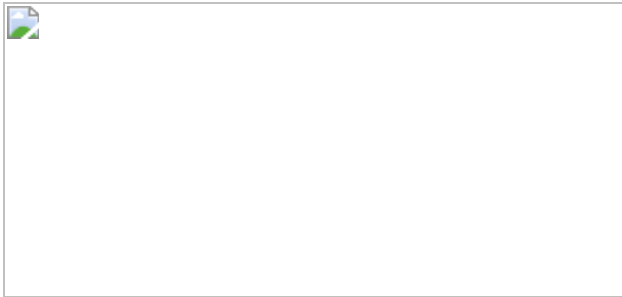
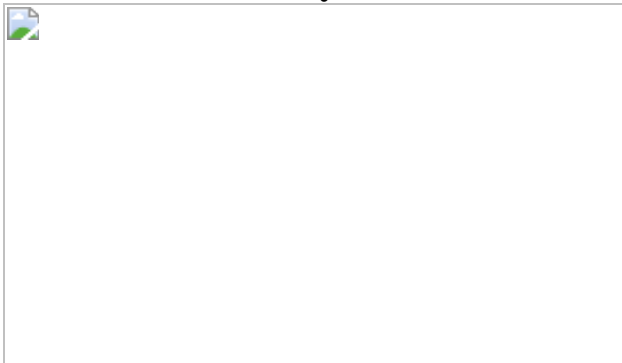


**Fig. 3: Spatial differences in the estimated long-term changes in global photosynthesis from LUE theory, TBMs and satellite observations combined with theory.**



## Data availability

All data used to support the findings of this study are publicly available. TRENDY model simulations are available on request from TRENDY coordinator S. Sitch ([s.a.sitch@exeter.ac.uk](mailto:s.a.sitch@exeter.ac.uk); <https://blogs.exeter.ac.uk/trendy/>). The Multivariate ENSO Index is available from <https://psl.noaa.gov/enso/mei/>. The GIMMS fAPAR data are available on request from R. Myneni ([rmyneni@bu.edu](mailto:rmyneni@bu.edu)). Climate forcings used are available from the Climate Research Unit at East Anglia University (<https://crudata.uea.ac.uk/cru/data/hrg/>). Upscaled GPP data are available from the Max Planck Institute for Biogeochemistry (<https://www.bgc-jena.mpg.de/geodb/projects/Home.php>). Locations for FLUXNET tower sites are available at [www.fluxnet.org](http://www.fluxnet.org).

## Code availability

Code used to support the findings of this study is publicly available at [www.github.com/trevorkeenan/gpp-co2](https://www.github.com/trevorkeenan/gpp-co2).

# References

1. 1.

Friedlingstein, P. et al. Global carbon budget 2019. *Earth Syst. Sci. Data* **11**, 1783–1838 (2019).

2. 2.

Ballantyne, A. P., Alden, C. B., Miller, J. B., Tans, P. P. & White, J. W. C. Increase in observed net carbon dioxide uptake by land and oceans during the past 50 years. *Nature* **488**, 70–72 (2012).

3. 3.

Sitch, S. et al. Recent trends and drivers of regional sources and sinks of carbon dioxide. *Biogeosciences* **12**, 653–679 (2015).

4. 4.

Keenan, T. F. et al. Recent pause in the growth rate of atmospheric CO<sub>2</sub> due to enhanced terrestrial carbon uptake. *Nat. Commun.* **7**, 13428 (2016).

5. 5.

Schimel, D., Stephens, B. B. & Fisher, J. B. Effect of increasing CO<sub>2</sub> on the terrestrial carbon cycle. *Proc. Natl Acad. Sci. USA* **112**, 436–441 (2015).

6. 6.

Huntzinger, D. N. et al. Uncertainty in the response of terrestrial carbon sink to environmental drivers undermines carbon-climate feedback predictions. *Sci. Rep.* **7**, 4765 (2017).

7. 7.

Walker, A. P. et al. Integrating the evidence for a terrestrial carbon sink caused by increasing atmospheric CO<sub>2</sub>. *New Phytol.* **229**, 2383–2385 (2020).

8. 8.

Sun, Z. et al. Evaluating and comparing remote sensing terrestrial GPP models for their response to climate variability and CO<sub>2</sub> trends. *Sci. Total Environ.* **668**, 696–713 (2019).

9. 9.

Smith, W. K. et al. Large divergence of satellite and Earth system model estimates of global terrestrial CO<sub>2</sub> fertilization. *Nat. Clim. Change* **6**, 306–310 (2016).

10. 10.

Li, W. et al. Recent changes in global photosynthesis and terrestrial ecosystem respiration constrained from multiple observations. *Geophys. Res. Lett.* **45**, 1058–1068 (2018).

11. 11.

Wenzel, S., Cox, P. M., Eyring, V. & Friedlingstein, P. Projected land photosynthesis constrained by changes in the seasonal cycle of atmospheric CO<sub>2</sub>. *Nature* **538**, 499–501 (2016).

12. 12.

Ehlers, I. et al Detecting long-term metabolic shifts using isotopomers: CO<sub>2</sub>-driven suppression of photorespiration in C<sub>3</sub> plants over the 20th century. *Proc. Natl Acad. Sci. USA* **112**, 15585–15590 (2015).

13. 13.

Campbell, J. E. et al. Large historical growth in global terrestrial gross primary production. *Nature* **544**, 84–87 (2017).

14. 14.

Eyring, V. et al. Taking climate model evaluation to the next level. *Nat. Clim. Change* **9**, 102–110 (2019).

15. 15.

Winkler, A. J., Myneni, R. B. & Brovkin, V. Investigating the applicability of emergent constraints. *Earth Syst. Dyn.* **10**, 501–523 (2019).

16. 16.

Hall, A., Cox, P., Huntingford, C. & Klein, S. Progressing emergent constraints on future climate change. *Nat. Clim. Change* **9**, 269–278 (2019).

17. 17.

Keenan, T. F. & Williams, C. A. The terrestrial carbon sink. *Annu. Rev. Environ. Resour.* **43**, 219–243 (2018).

18. 18.

Ryu, Y., Berry, J. A. & Baldocchi, D. D. What is global photosynthesis? History, uncertainties and opportunities. *Remote Sens. Environ.* **223**, 95–114 (2019).

19. 19.

Winkler, A. J., Myneni, R. B., Alexandrov, G. A. & Brovkin, V. Earth system models underestimate carbon fixation by plants in the high latitudes. *Nat. Commun.* **10**, 95 (2019).

20. 20.

Ainsworth, E. A. & Long, S. P. What have we learned from 15 years of free-air CO<sub>2</sub> enrichment (FACE)? A meta-analytic review of the

responses of photosynthesis, canopy properties and plant production to rising CO<sub>2</sub>. *New Phytol.* **165**, 351–372 (2005).

21. 21.

De Kauwe, M. G., Keenan, T. F., Medlyn, B. E., Prentice, I. C. & Terrer, C. Satellite based estimates underestimate the effect of CO<sub>2</sub> fertilization on net primary productivity. *Nat Clim. Change* **6**, 892–893 (2016).

22. 22.

Cernusak, L. A. et al Robust response of terrestrial plants to rising CO<sub>2</sub>. *Trends Plant Sci.* **24**, 578–586 (2019).

23. 23.

Piao, S. et al. Evaluation of terrestrial carbon cycle models for their response to climate variability and to CO<sub>2</sub> trends. *Glob. Change Biol.* **19**, 2117–2132 (2013).

24. 24.

Haverd, V. et al. Higher than expected CO<sub>2</sub> fertilization inferred from leaf to global observations. *Glob. Change Biol.* **26**, 2390–2402 (2020).

25. 25.

Friedlingstein, P. et al. Uncertainties in CMIP5 climate projections due to carbon cycle feedbacks. *J. Clim.* **27**, 511–526 (2014).

26. 26.

Zhao, F. et al. Role of CO<sub>2</sub>, climate and land use in regulating the seasonal amplitude increase of carbon fluxes in terrestrial ecosystems: a multimodel analysis. *Biogeosciences* **13**, 5121–5137 (2016).

27. 27.

Le Quéré, C. et al. Global carbon budget 2017. *Earth Syst. Sci. Data* **10**, 405–448 (2018).

28. 28.

Running, S. W. & Zhao, M. *Daily GPP and Annual NPP (MOD17A2/A3) Products NASA Earth Observing System MODIS Land Algorithm User's Guide* v. 3 (MODIS Land Team, 2015).

29. 29.

Jung, M. et al. Global patterns of land-atmosphere fluxes of carbon dioxide, latent heat, and sensible heat derived from eddy covariance, satellite, and meteorological observations. *J. Geophys. Res.* **116**, <https://doi.org/10.1029/2010JG001566> (2011).

30. 30.

Zeng, N. et al. Agricultural Green Revolution as a driver of increasing atmospheric CO<sub>2</sub> seasonal amplitude. *Nature* **515**, 394–397 (2014).

31. 31.

Long, S. P. Modification of the response of photosynthetic productivity to rising temperature by atmospheric CO<sub>2</sub> concentrations: has its importance been underestimated? *Plant Cell Environ.* **14**, 729–739 (1991).

32. 32.

Stevens, N., Lehmann, C. E. R., Murphy, B. P. & Durigan, G. Savanna woody encroachment is widespread across three continents. *Glob. Change Biol.* **23**, 235–244 (2017).

33. 33.

Fleischer, K. et al. Amazon forest response to CO<sub>2</sub> fertilization dependent on plant phosphorus acquisition. *Nat. Geosci.* **12**, 736–741

(2019).

34. 34.

Myneni, R. B. et al. Global products of vegetation leaf area and fraction absorbed PAR from year one of MODIS data. *Remote Sens. Environ.* **83**, 214–231 (2002).

35. 35.

Cernusak, L. A. et al. Tropical forest responses to increasing atmospheric CO<sub>2</sub>: current knowledge and opportunities for future research. *Funct. Plant Biol.* **40**, 531–551 (2013).

36. 36.

Ainsworth, E. A. & Rogers, A. The response of photosynthesis and stomatal conductance to rising [CO<sub>2</sub>]: mechanisms and environmental interactions. *Plant Cell Environ.* **30**, 258–270 (2007).

37. 37.

Braig, S., Medlyn, B. E., Mercado, L. M. & Zaehle, S. Does the growth response of woody plants to elevated CO<sub>2</sub> increase with temperature? A model-oriented meta-analysis. *Glob. Change Biol.* **21**, 4303–4319 (2015).

38. 38.

Yang, J. et al. Low sensitivity of gross primary production to elevated CO<sub>2</sub> in a mature eucalypt woodland. *Biogeosciences* **17**, 265–279 (2020).

39. 39.

McMurtrie, R. E., Comins, H. N., Kirschbaum, M. U. F. & Wang, Y. P. Modifying existing forest growth models to take account of effects of elevated CO<sub>2</sub>. *Aust. J. Bot.* **40**, 657–677 (1992).

40. 40.

Luo, Y., Sims, D. A., Thomas, R. B., Tissue, D. T. & Ball, J. T. Sensitivity of leaf photosynthesis to CO<sub>2</sub> concentration is an invariant function for C3 plants: a test with experimental data and global applications. *Global Biogeochem. Cycles* **10**, 209–222 (1996).

41. 41.

Li, Q. et al. Leaf area index identified as a major source of variability in modeled CO<sub>2</sub> fertilization. *Biogeosciences* **15**, 6909–6925 (2018).

42. 42.

Graven, H. D. et al. Enhanced seasonal exchange of CO<sub>2</sub> by northern ecosystems since 1960. *Science* **341**, 1085–1089 (2013).

43. 43.

Zaehle, S. et al. Evaluation of 11 terrestrial carbon-nitrogen cycle models against observations from two temperate free-air CO<sub>2</sub> enrichment studies. *New Phytol.* **202**, 803–822 (2014).

44. 44.

De Kauwe, M. G. et al. Where does the carbon go? A model-data intercomparison of vegetation carbon allocation and turnover processes at two temperate forest free-air CO<sub>2</sub> enrichment sites. *New Phytol.* **203**, 883–899 (2014).

45. 45.

Stocker, B. D. et al Drought impacts on terrestrial primary production underestimated by satellite monitoring. *Nat. Geosci.* **12**, 264–270 (2019).

46. 46.

Williamson, M. S. et al Emergent constraints on climate sensitivities. *Rev. Mod. Phys.* **93**, 025004 (2021).

47. 47.

Sanderson, B. et al. On structural errors in emergent constraints. *Earth Syst. Dyn. Discuss.* <https://doi.org/10.5194/esd-2020-85> (2021).

48. 48.

Fisher, J. B., Huntzinger, D. N., Schwalm, C. R. & Sitch, S. Modeling the terrestrial biosphere. *Annu. Rev. Environ. Resour.* **39**, 91–123 (2014).

49. 49.

Arora, V. K. et al. Carbon-concentration and carbon-climate feedbacks in CMIP5 earth system models. *J. Clim.* **26**, 5289–5314 (2013).

50. 50.

Ballantyne, A. et al. Accelerating net terrestrial carbon uptake during the warming hiatus due to reduced respiration. *Nat. Clim. Change* **7**, 148–152 (2017).

51. 51.

Forkel, M. et al. Enhanced seasonal CO<sub>2</sub> exchange caused by amplified plant productivity in northern ecosystems. *Science* **351**, 696–699 (2016).

52. 52.

Friedlingstein, P. et al. On the contribution of CO<sub>2</sub> fertilization to the missing biospheric sink. *Global Biogeochem. Cycles* **9**, 541–556 (1995).

53. 53.

Farquhar, G. D., von Caemmerer, S. & Berry, J. A. A biochemical model of photosynthetic CO<sub>2</sub> assimilation in leaves of C<sub>3</sub> species. *Planta* **149**, 78–90 (1980).

54. 54.

Myneni, R. B., Keeling, C. D., Tucker, C. J., Asrar, G. & Nemani, R. R. Increased plant growth in the northern high latitudes from 1981 to 1991. *Nature* **386**, 698–702 (1997).

55. 55.

Zhu, Z. et al. Greening of the Earth and its drivers. *Nat. Clim. Change* **6**, 791–795 (2016).

56. 56.

Keenan, T. F. et al. Increase in forest water-use efficiency as atmospheric carbon dioxide concentrations rise. *Nature* **499**, 324–327 (2013).

57. 57.

Ukkola, A. M., Keenan, T. F., Kelley, D. I. & Prentice, I. C. Vegetation plays an important role in mediating future water resources. *Environ. Res. Lett.* **11**, 094022 (2016).

58. 58.

Donohue, R. J., Roderick, M. L., McVicar, T. R. & Farquhar, G. D. Impact of CO<sub>2</sub> fertilization on maximum foliage cover across the globe's warm, arid environments. *Geophys. Res. Lett.* **40**, 3031–3035 (2013).

59. 59.

Smith, N. G. & Dukes, J. S. Plant respiration and photosynthesis in global-scale models: incorporating acclimation to temperature and

$\text{CO}_2$ . *Glob. Change Biol.* **19**, 45–63 (2013).

60. 60.

De Kauwe, M. G. et al. A test of the ‘one-point method’ for estimating maximum carboxylation capacity from field-measured, light-saturated photosynthesis. *New Phytol.* **210**, 1130–1144 (2016).

61. 61.

Maire, V. et al. The coordination of leaf photosynthesis links C and N fluxes in  $\text{C}_3$  plant species. *PLoS ONE* **7**, e0038345 (2012).

62. 62.

Smith, N. G. & Keenan, T. F. Mechanisms underlying leaf photosynthetic acclimation to warming and elevated  $\text{CO}_2$  as inferred from least-cost optimality theory. *Glob. Change Biol.* **26**, 806–834 (2020).

63. 63.

Lloyd, J. & Farquhar, G. The  $\text{CO}_2$  dependence of photosynthesis, plant growth responses to elevated atmospheric  $\text{CO}_2$  concentrations and their interaction with soil nutrient status. I. General principles and forest ecosystems. *Funct. Ecol.* **10**, 4–32 (1996).

64. 64.

Ehleringer, J. & Björkman, O. Quantum yields for  $\text{CO}_2$  uptake in  $\text{C}_3$  and  $\text{C}_4$  plants: dependence on temperature,  $\text{CO}_2$ , and  $\text{O}_2$  concentration. *Plant Physiol.* **59**, 86–90 (1997).

65. 65.

Bernacchi, C. J., Singsaas, E. L., Pimentel, C., Portis, A. R. Jr & Long, SP. Improved temperature response functions for models of Rubisco-

limited photosynthesis. *Plant, Cell Environ.* **24**, 253–259 (2001).

66. 66.

Prentice, I. C., Dong, N., Gleason, S. M., Maire, V. & Wright, I. J. Balancing the costs of carbon gain and water transport: testing a new theoretical framework for plant functional ecology. *Ecol. Lett.* **17**, 82–91 (2014).

67. 67.

Wang, H. et al. Towards a universal model for carbon dioxide uptake by plants. *Nat. Plants* **3**, 734–741 (2017).

68. 68.

Huber, M. L. et al. New international formulation for the viscosity of H<sub>2</sub>O. *J. Phys. Chem. Ref Data* **38**, 101–125 (2009).

69. 69.

Still, C. J., Berry, J. A., Collatz, G. J. & DeFries, R. S. Global distribution of C<sub>3</sub> and C<sub>4</sub> vegetation: carbon cycle implications. *Global Biogeochem. Cycles* **17**, 6-1–6-14 (2003).

70. 70.

Zhu, Z. et al. Global data sets of vegetation leaf area index (LAI)3g and fraction of photosynthetically active radiation (FPAR)3g derived from global inventory modeling and mapping studies (GIMMS) normalized difference vegetation index (NDVI3g) for the period 1981 to 2. *Remote Sens.* **5**, 927–948 (2013).

71. 71.

Zhao, M. & Running, S. W. Drought-induced reduction in global terrestrial net primary production from 2000 through 2009. *Science* **329**, 940–943 (2010).

72. 72.

Gallego-Sala, A. et al. Bioclimatic envelope model of climate change impacts on blanket peatland distribution in Great Britain. *Clim. Res.* **45**, 151–162 (2010).

73. 73.

Veroustraete, F. On the use of a simple deciduous forest model for the interpretation of climate change effects at the level of carbon dynamics. *Ecol. Modell.* **75–76**, 221–237 (1994).

74. 74.

Jiang, C. & Ryu, Y. Multi-scale evaluation of global gross primary productivity and evapotranspiration products derived from Breathing Earth System Simulator (BESS). *Remote Sens. Environ.* **186**, 528–547 (2016).

75. 75.

Zhang, S. et al. Evaluation and improvement of the daily boreal ecosystem productivity simulator in simulating gross primary productivity at 41 flux sites across Europe. *Ecol. Modell.* **368**, 205–232 (2018).

76. 76.

Liu, Y., Hejazi, M., Li, H., Zhang, X. & Leng, G. A hydrological emulator for global applications-HE v1.0.0. *Geosci. Model Dev.* **11**, 1077–1092 (2018).

77. 77.

Yuan, W. et al. Increased atmospheric vapor pressure deficit reduces global vegetation growth. *Sci. Adv.* **5**, aax1396 (2019).

78. 78.

Haverd, V. et al. A new version of the CABLE land surface model (Subversion revision r4601) incorporating land use and land cover change, woody vegetation demography, and a novel optimisation-based approach to plant coordination of photosynthesis. *Geosci. Model Dev.* **11**, 2995–3026 (2018).

79. 79.

Melton, J. R. & Arora, V. K. Competition between plant functional types in the Canadian Terrestrial Ecosystem Model (CTEM) v. 2.0. *Geosci. Model Dev.* **9**, 323–361 (2016).

80. 80.

Oleson, K. W. et al. *Technical Description of Version 4.0 of the Community Land Model (CLM)* (National Center for Atmospheric Research, 2013).

81. 81.

Tian, H. et al. North American terrestrial CO<sub>2</sub> uptake largely offset by CH<sub>4</sub> and N<sub>2</sub>O emissions: toward a full accounting of the greenhouse gas budget. *Clim. Change* **129**, 413–426 (2015).

82. 82.

Jain, A. K., Meiyappan, P., Song, Y. & House, J. I. CO<sub>2</sub> emissions from land-use change affected more by nitrogen cycle, than by the choice of land-cover data. *Glob. Change Biol.* **19**, 2893–2906 (2013).

83. 83.

Reick, C. H., Raddatz, T., Brovkin, V. & Gayler, V. Representation of natural and anthropogenic land cover change in MPI-ESM. *J. Adv. Model Earth Syst.* **5**, 459–482 (2013).

84. 84.

Clark, D. B. et al. The Joint UK Land Environment Simulator (JULES), model description—Part 2: Carbon fluxes and vegetation dynamics. *Geosci. Model Dev.* **4**, 701–722 (2011).

85. 85.

Smith, B. et al. Implications of incorporating N cycling and N limitations on primary production in an individual-based dynamic vegetation model. *Biogeosciences* **11**, 2027–2054 (2014).

86. 86.

Sitch, S. et al. Evaluation of ecosystem dynamics, plant geography and terrestrial carbon cycling in the LPJ dynamic global vegetation model. *Glob. Chang. Biol.* **9**, 161–185 (2003).

87. 87.

Keller, K. M. et al. 20th century changes in carbon isotopes and water-use efficiency: tree-ring-based evaluation of the CLM4.5 and LPX-Bern models. *Biogeosciences* **14**, 2641–2673 (2017).

88. 88.

Krinner, G. et al. A dynamic global vegetation model for studies of the coupled atmosphere-biosphere system. *Global Biogeochem. Cycles* **19**, GB1015 (2005).

89. 89.

Guimbertea, M. et al. ORCHIDEE-MICT (v8.4.1), a land surface model for the high latitudes: model description and validation. *Geosci. Model Dev.* **11**, 121–163 (2018).

90. 90.

Zeng, N., Mariotti, A. & Wetzel, P. Terrestrial mechanisms of interannual CO<sub>2</sub> variability. *Global Biogeochem. Cycles* **19**,

<https://doi.org/10.1029/2004GB002273> (2005).

91. 91.

Kato, E., Kinoshita, T., Ito, A., Kawamiya, M. & Yamagata, Y. Evaluation of spatially explicit emission scenario of land-use change and biomass burning using a process-based biogeochemical model. *J. Land Use Sci.* **8**, 104–122 (2013).

92. 92.

Fernández-Martínez, M. et al. Atmospheric deposition, CO<sub>2</sub>, and change in the land carbon sink. *Sci. Rep.* **7**, 9632 (2017).

93. 93.

Ciais, P. et al. Large inert carbon pool in the terrestrial biosphere during the Last Glacial Maximum. *Nat. Geosci.* **5**, 74–79 (2012).

94. 94.

Cheng, L. et al. Recent increases in terrestrial carbon uptake at little cost to the water cycle. *Nat. Commun.* **8**, 110 (2017).

95. 95.

Ueyama, M. et al. Inferring CO<sub>2</sub> fertilization effect based on global monitoring land-atmosphere exchange with a theoretical model. *Environ. Res. Lett.* **15**, 084009 (2020).

96. 96.

Pastorello, G. et al. The FLUXNET2015 dataset and the ONEFlux processing pipeline for eddy covariance data. *Sci. Data* **7**, 225 (2020).

## Acknowledgements

T.F.K., X.L. and Y.Z. acknowledge primary support from the NASA IDS Award NNN17AE86I. T.F.K. acknowledges additional support from NASA award 80NSSC21K1705 and by the Director, Office of Science, Office of Biological and Environmental Research of the US Department of Energy (DOE) under Contract DE-AC02-05CH11231 as part of the RUBISCO SFA and a DOE ECRP Award DE-SC0021023. M.G.D.K. acknowledges support from the Australian Research Council (ARC) Centre of Excellence for Climate Extremes (CE170100023), the ARC Discovery Grant (DP190101823) and the NSW Research Attraction and Acceleration Program. I.C.P. acknowledges the Imperial College initiative on Grand Challenges in Ecosystems and the Environment and the European Research Council (ERC) under the European Union's Horizon 2020 Research and Innovation Programme (grant agreement no. 787203 REALM). N.G.S. acknowledges support from NSF DEB-2045968 and Texas Tech University. B.D.S. was funded by the Swiss National Science Foundation grant no. PCEFP2\_181115. C.T. was supported by a Lawrence Fellow award through Lawrence Livermore National Laboratory (LLNL), the DOE LLNL contract DE-AC52-07NA27344, and the LLNL-LDRD Program project 20-ERD-055. We thank R. Myneni and Z. Zhu for the provision of the fAPAR dataset, the Max Planck Institute for Biogeochemistry Department of Biogeochemical Integration for the provision of the upscaled GPP data. We thank the TRENDY team for the provision of the DGVM simulations, and the researchers of the Global Carbon Project for making their data publicly available. We thank A. Walker for useful discussions on interpreting the deuterium isotopomer results, and acknowledge the stimulating discussions during the Integrating CO<sub>2</sub> Fertilization Evidence Streams and Theory (ICOFEST) meeting September 2018, part of the FACE model Data-Synthesis project funded by the US Department of Energy, Office of Science, Office of Biological and Environmental Research.

## Author information

### Affiliations

1. Department of Environmental Science, Policy and Management, UC Berkeley, Berkeley, CA, USA

T. F. Keenan, X. Luo, Y. Zhang & S. Zhou

2. Climate and Ecosystem Sciences Division, Lawrence Berkeley National Laboratory, Berkeley, CA, USA

T. F. Keenan, X. Luo, Y. Zhang & S. Zhou

3. Department of Geography, National University of, Singapore, Singapore

X. Luo

4. ARC Centre of Excellence for Climate Extremes, Sydney, New South Wales, Australia

M. G. De Kauwe

5. Climate Change Research Centre, University of New South Wales, Sydney, New South Wales, Australia

M. G. De Kauwe

6. School of Biological Sciences, University of Bristol, Bristol, UK

M. G. De Kauwe

7. Hawkesbury Institute for the Environment, Western Sydney University, Penrith, New South Wales, Australia

B. E. Medlyn

8. Department of Life Sciences, Imperial College London, Ascot, UK

I. C. Prentice

9. Department of Biological Sciences, Macquarie University, North Ryde, New South Wales, Australia

I. C. Prentice

10. Department of Earth System Science, Tsinghua University, Haidian, Beijing, China

I. C. Prentice & H. Wang

11. Department of Environmental Systems Science, ETH, Zurich, Switzerland

B. D. Stocker

12. Swiss Federal Institute for Forest, Snow and Landscape Research WSL, Birmensdorf, Switzerland

B. D. Stocker

13. Department of Biological Sciences, Texas Tech University, Lubbock, TX, USA

N. G. Smith

14. Physical and Life Sciences Directorate, Lawrence Livermore National Laboratory, Livermore, CA, USA

C. Terrer

15. Department of Civil and Environmental Engineering, Massachusetts Institute of Technology, Boston, MA, USA

C. Terrer

16. Sino-French Institute for Earth System Science, College of Urban and Environmental Sciences, Peking University, Beijing, China

Y. Zhang

17. Lamont-Doherty Earth Observatory of Columbia University, Palisades, NY, USA

S. Zhou

18. Earth Institute, Columbia University, New York, NY, USA

S. Zhou

19. Department of Earth and Environmental Engineering, Columbia University, New York, NY, USA

S. Zhou

20. State Key Laboratory of Earth Surface Processes and Resources Ecology, Faculty of Geographical Science, Beijing Normal University, Beijing, China

S. Zhou

## Contributions

T.F.K. designed the study, performed the analysis and wrote the manuscript. X.L. aided in the regridding of the TRENDY model data. M.G.D.K., B.D.S., I.C.P., H.W., N.G.S., B.E.M., X.L. and S.Z. provided feedback on the remote sensing implementation. S.Z. and Y.Z. provided feedback on the emergent constraint implementation. B.S. provided feedback on the TRENDY model data interpretation. All authors discussed and commented on the results and the manuscript.

## Corresponding author

Correspondence to [T. F. Keenan](#).

## Ethics declarations

## Competing interests

The authors declare no competing interests.

## Additional information

**Peer review information** *Nature* thanks Peter Cox, Alexander Winkler and the other, anonymous, reviewer(s) for their contribution to the peer review of this work. Peer reviewer reports are available.

**Publisher's note** Springer Nature remains neutral with regard to jurisdictional claims in published maps and institutional affiliations.

## Extended data figures and tables

[Extended Data Fig. 1 The relationship between the sensitivity of global primary photosynthesis \(GPP\) to CO<sub>2</sub>\\(\beta\\)\ and the terrestrial carbon sink \( \$S\_{LAND}\$ , PgC y<sup>-1</sup>\).](#)

The emergent constraint on  $\beta_R \cdot GPP$  is comparable to that derived using the normalized  $S_{LAND}$ , though the associated uncertainty is considerably higher due to the unexplained variance in the  $\beta_R \cdot GPP \sim S_{LAND}$  relationship. The red line and shaded area show the best linear fit across models, and the associated 95% prediction intervals.

[Extended Data Fig. 2 A multiple linear model of the terrestrial biosphere model predictions of the global carbon sink.](#)

**a**, The terrestrial biosphere model (TBM) predictions of the global carbon sink are predicted as a function of the modeled sensitivity of photosynthesis to CO<sub>2</sub> ( $\beta_R \cdot GPP$ ), the modeled sensitivity of respiration to CO<sub>2</sub> ( $\beta_R \cdot Reco$ ) and the magnitude of the modeled non-respired carbon flux ( $\gamma$ ) (Extended Data Table 2). The red line and shaded area show the best linear fit across models, and the associated 95% prediction intervals. **b**, the effect size of each of the terms included in the model (mean, 95% CI), which estimates main effect on the response from changing each predictor value, averaging out the effects of the other predictors. TBM names and details are

provided in Extended Data Table 1. Details of the linear model used are provided in Extended Data Table 2.

### Extended Data Fig. 3 An emergent constraint on the sensitivity of global photosynthesis to CO<sub>2</sub>.

**a**, The relationship between the sensitivity of global primary photosynthesis (GPP) to CO<sub>2</sub> and the modeled terrestrial carbon sink (PgC y<sup>-1</sup>), in relative terms ( $\Delta$ GPP (%)). The vertical gray shading shows the range of the observed terrestrial residual carbon sink over the period of 1982 to 2012, as estimated by the Global Carbon Project. The red line and shaded area show the best linear fit across models, and the associated 95% prediction intervals, and the horizontal dashed line shows the implied emergent constraint on the sensitivity of GPP to CO<sub>2</sub>. This figure reproduces Fig. 1a, but includes model names, which correspond to labels given in Extended Data Table 1. See Extended Data Fig. 1 for the underlying relationship between the sensitivity of GPP to CO<sub>2</sub> and the terrestrial carbon sink. **b**, Uncertainty contributions to the constrained sensitivity of global photosynthesis to CO<sub>2</sub>. The unconstrained probability density function (PDF) distribution of  $(\beta_{R,GPP})$  across models (black line, gray bars), which assumes that all of the TRENDY models are equally likely conditional to be correct and that they come from a Gaussian distribution. The orange area represents the probability distribution derived by applying the constraint from (a) to the across model relationship, with dashed and dotted lines in the orange area indicating the relative contribution of different sources of uncertainty (see [methods](#)).

### Extended Data Fig. 4 Assessment of the effect of choice of period on the sensitivity of global primary photosynthesis (GPP) to CO<sub>2</sub> $(\beta_{R,GPP})$ .

Estimates of the residual terrestrial sink ( $S_{LAND}$ ) from the Global Carbon Project (GCP) used in this study were split into two 15-year periods (1982–1997 (**a, b**) and 1998–2012 (**c, d**)) and the emergent constraint approach

(see [methods](#)) was applied to each independently, using GCP estimates of the land sink for those periods to estimate a constrained value of  $\beta \{ \rm{R} \}^{\gamma \{ \rm{GPP} \}}$  from the TRENDY dynamic global vegetation models (Extended Data Table 1). Estimated  $S_{\text{LAND}}$  in panel **a** and **c** is  $S_{\text{LAND}} \sim 1 + \beta \{ \rm{R} \}^{\gamma \{ \rm{GPP} \}} + \beta \{ \rm{R} \}^{\gamma \{ \rm{Reco} \}}$  +  $\gamma \{ \rm{R} \}^{\gamma \{ \rm{Reco} \}}$ . The vertical dashed lines in **a** and **c** indicate the GCP estimate of the mean residual sink for that period. The red lines and shaded areas in **a** and **c** show the best linear fit across models, and the associated 95% prediction intervals.

### [Extended Data Fig. 5 Long-term changes in annual gross primary production \(GPP\) of global tropical forests.](#)

GPP estimated by terrestrial biosphere models (TBMs) in the TRENDY model ensemble considers either temporally dynamic CO<sub>2</sub> and fixed climate and land use (orange, experiment S1), temporally dynamic CO<sub>2</sub> and climate, and fixed land use (red, experiment S2), or temporally dynamic CO<sub>2</sub>, climate, and land use (purple, experiment S3). Shaded areas represent the mean and standard error of the annual estimate across the TRENDY ensemble. Remote sensing (RS) GPP considers temporally dynamic climate and land use, and either fixed (blue) or varying (red) CO<sub>2</sub>. Tropical forests represent the Evergreen Broadleaf Forest classification within tropical latitudes (23.5°N: 23.5°S).

### [Extended Data Fig. 6 Assessment of the effect of CO<sub>2</sub> on global primary photosynthesis \(GPP\) at sites included in the FLUXNET 2015 dataset.](#)

**(a)** The distribution of the length of the observational record at each of the 206 sites in the FLUXNET 2015 open access database. The vertical red line indicates the median site record length (5 years). **(b)** The expected effect of CO<sub>2</sub> on GPP at all sites, demonstrated by comparing the GPP predicted by the original (x-axis) and updated (y-axis) remote sensing-based methods for

all site months of observations in the FLUXNET 2015 database<sup>96</sup>. The mean expected difference across sites is 2.39%.

## **Extended Data Fig. 7 Global and high latitude changes in the terrestrial carbon cycle.**

Both the global (**a, b, c**) and northern land (high latitude, > 45°N) (**d, e, f**) contribution of CO<sub>2</sub> (orange shaded area, derived from TRENDYv6 CO<sub>2</sub>-only simulations (S1)) and climate (red shaded area, derived from the difference between TRENDYv6 CO<sub>2</sub>-only simulations and CO<sub>2</sub> + Climate simulations (S2-S1)), to long term (1900-2016) changes in annual net ecosystem productivity (NEP), gross primary production (GPP) and ecosystem respiration (RECO). The shaded areas represent the annual mean and standard error across the TRENDY model ensemble. The impact of climate change is large in high latitude ecosystems, increasing both GPP (**e**) and RECO (**f**). This does not however translate to a large impact on the global carbon cycle (**a–c**).

**Extended Data Table 1** The terrestrial biosphere models (TBMs) used

**Extended Data Table 2** Linear models of the land sink as estimated from terrestrial biosphere models

**Extended Data Table 3** Calculation of  $\beta_{R,GPP}$  from existing proxies

## **Supplementary information**

[Peer Review File](#)

## **Rights and permissions**

[Reprints and Permissions](#)

## **About this article**

[Cite this article](#)

Keenan, T.F., Luo, X., De Kauwe, M.G. *et al.* A constraint on historic growth in global photosynthesis due to increasing CO<sub>2</sub>. *Nature* **600**, 253–258 (2021). <https://doi.org/10.1038/s41586-021-04096-9>

- Received: 09 July 2020
- Accepted: 05 October 2021
- Published: 08 December 2021
- Issue Date: 09 December 2021
- DOI: <https://doi.org/10.1038/s41586-021-04096-9>

## Share this article

Anyone you share the following link with will be able to read this content:

[Get shareable link](#)

Sorry, a shareable link is not currently available for this article.

[Copy to clipboard](#)

Provided by the Springer Nature SharedIt content-sharing initiative

## [Constraints on estimating the CO<sub>2</sub> fertilization effect emerge](#)

- Chris Huntingford
- Rebecca J. Oliver

News & Views 08 Dec 2021

---

This article was downloaded by **calibre** from <https://www.nature.com/articles/s41586-021-04096-9>

- Article
- [Published: 01 December 2021](#)

# Bizarre tail weaponry in a transitional ankylosaur from subantarctic Chile

- [Sergio Soto-Acuña](#) [ORCID: orcid.org/0000-0002-9311-9355<sup>1,2</sup>](#),
- [Alexander O. Vargas](#) [ORCID: orcid.org/0000-0002-2009-7116<sup>1</sup>](#),
- [Jonatan Kaluza<sup>1,3,4</sup>](#),
- [Marcelo A. Leppe](#) [ORCID: orcid.org/0000-0002-1545-8167<sup>1,5</sup>](#),
- [Joao F. Botelho<sup>1,6</sup>](#),
- [José Palma-Liberona<sup>1,6</sup>](#),
- [Carolina Simon-Gutstein<sup>1</sup>](#),
- [Roy A. Fernández<sup>1,7</sup>](#),
- [Héctor Ortiz](#) [ORCID: orcid.org/0000-0001-6010-3990<sup>1,8</sup>](#),
- [Verónica Milla](#) [ORCID: orcid.org/0000-0002-9849-0428<sup>1,7</sup>](#),
- [Bárbara Aravena<sup>1</sup>](#),
- [Leslie M. E. Manríquez](#) [ORCID: orcid.org/0000-0002-0797-0355<sup>1,9</sup>](#),
- [Jhonatan Alarcón-Muñoz<sup>1,2</sup>](#),
- [Juan Pablo Pino<sup>1,2</sup>](#),
- [Cristine Trevisan<sup>1,5</sup>](#),
- [Héctor Mansilla<sup>1,5</sup>](#),
- [Luis Felipe Hinojosa<sup>1,2</sup>](#),
- [Vicente Muñoz-Walther<sup>1</sup>](#) &
- [David Rubilar-Rogers<sup>1,10</sup>](#)

*Nature* volume 600, pages 259–263 (2021)

- 5634 Accesses

- 1289 Altmetric
- [Metrics details](#)

## Subjects

- [Herpetology](#)
- [Palaeontology](#)

## Abstract

Armoured dinosaurs are well known for their evolution of specialized tail weapons—paired tail spikes in stegosaurs and heavy tail clubs in advanced ankylosaurs<sup>1</sup>. Armoured dinosaurs from southern Gondwana are rare and enigmatic, but probably include the earliest branches of Ankylosauria<sup>2,3,4</sup>. Here we describe a mostly complete, semi-articulated skeleton of a small (approximately 2 m) armoured dinosaur from the late Cretaceous period of Magallanes in southernmost Chile, a region that is biogeographically related to West Antarctica<sup>5</sup>. *Stegouros elengassen* gen. et sp. nov. evolved a large tail weapon unlike any dinosaur: a flat, frond-like structure formed by seven pairs of laterally projecting osteoderms encasing the distal half of the tail. *Stegouros* shows ankylosaurian cranial characters, but a largely ancestral postcranial skeleton, with some stegosaur-like characters. Phylogenetic analyses placed *Stegouros* in Ankylosauria; specifically, it is related to *Kunbarsaurus* from Australia<sup>6</sup> and *Antarctopelta* from Antarctica<sup>7</sup>, forming a clade of Gondwanan ankylosaurs that split earliest from all other ankylosaurs. The large osteoderms and specialized tail vertebrae in *Antarctopelta* suggest that it had a tail weapon similar to *Stegouros*. We propose a new clade, the Parankylosauria, to include the first ancestor of *Stegouros*—but not *Ankylosaurus*—and all descendants of that ancestor.

This is a preview of subscription content

## Access options

## Subscribe to Journal

Get full journal access for 1 year

\$199.00

only \$3.90 per issue

[Subscribe](#)

All prices are NET prices.

VAT will be added later in the checkout.

Tax calculation will be finalised during checkout.

## Rent or Buy article

Get time limited or full article access on ReadCube.

from \$8.99

[Rent or Buy](#)

All prices are NET prices.

## **Additional access options:**

- [Log in](#)
- [Learn about institutional subscriptions](#)

**Fig. 1: Skeletal anatomy of the *S. elongassen* holotype (CPAP-3165).**

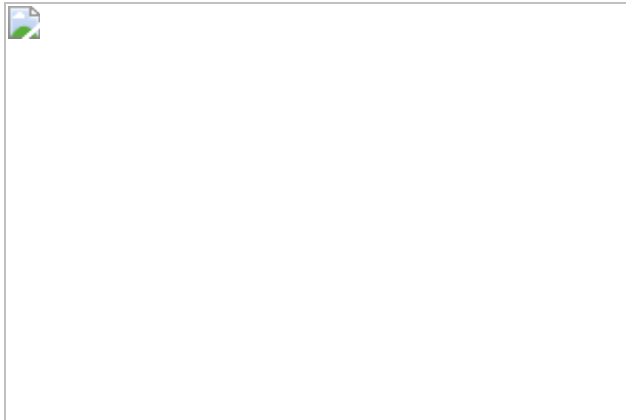


**Fig. 2: Caudal weapon of *S. elongasseri* holotype (CPAP-3165).**

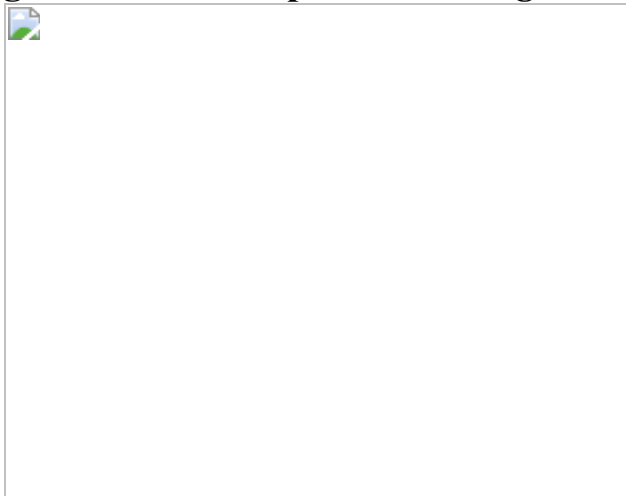


**Fig. 3: Evolution of armoured dinosaurs and their tail weaponry.**

## Data availability

All data supporting the findings of this study are available in the paper and its [Supplementary Information](#). Raw data from all CT scans are available online

([https://www.morphosource.org/concern/biological\\_specimens/000382748](https://www.morphosource.org/concern/biological_specimens/000382748)).

The LSID for this publication is urn:lsid:zoobank.org:pub:4D3ABFEE-5F21-4632-96F9-FE8C1542ACF7. The LSID ZooBank code for the new genus (*Stegouros*) is: urn:lsid:zoobank.org:act:5306DD47-2130-4866-8DB4-09092C632A4A. The LSID ZooBank code for the new species (*Stegouros elengassen*) is: urn:lsid:zoobank.org:act:992A259B-75EE-4206-89FB-6666FBCBDF6A6. TNT files for phylogenetic analysis are provided on Zenodo (<https://zenodo.org/record/5706422#.YZQ7Kr3Q8-R>).

## References

1. 1.

Arbour, V. M. & Zanno, L. E. The evolution of tail weaponization in amniotes. *Proc. R. Soc. B* **285**, 20172299 (2018).

2. 2.

Thompson, R. S., Parish, J. C., Maidment, S. C. & Barrett, P. M. Phylogeny of the ankylosaurian dinosaurs (Ornithischia: Thyreophora). *J. Syst. Palaeontol.* **10**, 301–312 (2012).

3. 3.

Arbour, V. M. & Currie, P. J. Systematics, phylogeny and palaeobiogeography of the ankylosaurid dinosaurs. *J. Syst. Palaeontol.* **14**, 385–444 (2016).

4. 4.

Wiersma, J. P. & Irmis, R. B. A new southern Laramidian ankylosaurid, *Akainacephalus johnsoni* gen. et sp. nov., from the upper Campanian Kaiparowits Formation of southern Utah, USA. *PeerJ* **6**, e5016 (2018).

5. 5.

Reguero, M. A. & Goin, F. J. Paleogeography and biogeography of the Gondwanan final breakup and its terrestrial vertebrates: new insights from southern South America and the “double Noah’s Ark” Antarctic Peninsula. *J. South Am. Earth Sci.* **108**, 103358 (2021).

6. 6.

Leahey, L. G., Molnar, R. E., Carpenter, K., Witmer, L. M. & Salisbury, S. W. Cranial osteology of the ankylosaurian dinosaur formerly known as *Minmi* sp. (Ornithischia: Thyreophora) from the Lower Cretaceous Allaru Mudstone of Richmond, Queensland, Australia. *PeerJ* **3**, e1475 (2015).

7. 7.

Salgado, L. & Gasparini, Z. Reappraisal of an ankylosaurian dinosaur from the Upper Cretaceous of James Ross Island (Antarctica). *Geodiversitas* **28**, 119–135 (2006).

8. 8.

Claraz, J. *Diario de Viaje de Exploración al Chubut, 1865-1866* (Ediciones Marymar, 1988).

9. 9.

Hone, D. W. E., Farke, A. A. & Wedel, M. J. Ontogeny and the fossil record: what, if anything, is an adult dinosaur? *Biol. Lett.* **12**, 20150947 (2016).

10. 10.

Gutiérrez, N. M. et al. Tectonic events reflected by palaeocurrents, zircon geochronology, and palaeobotany in the Sierra Baguales of Chilean Patagonia. *Tectonophysics* **695**, 76–99 (2017).

11. 11.

Manríquez, L. M., Lavina, E. L., Fernández, R. A., Trevisan, C. & Leppe, M. A. Campanian-Maastrichtian and Eocene stratigraphic architecture, facies analysis, and paleoenvironmental evolution of the northern Magallanes Basin (Chilean Patagonia). *J. South Am. Earth Sci.* **93**, 102–118 (2019).

12. 12.

Raven, T. J. & Maidment, S. C. The systematic position of the enigmatic thyreophoran dinosaur *Paranthodon africanus*, and the use of basal exemplifiers in phylogenetic analysis. *PeerJ* **6**, e4529 (2018).

13. 13.

Vickaryous, M. V., Maryańska, T. & Weishampel, D. B. in *The Dinosauria* (eds Weishampel, D. B. et al.) 464–477 (Univ. California Press, 2004).

14. 14.

Coombs Jr W. P. in *Dinosaur Systematics: Approaches and Perspectives* (eds Carpenter, K. & Currie, P. J.) 269–279 (Cambridge Univ. Press, 1990).

15. 15.

Pereda-Suberbiola, X., Galton, P. M., Mallison, H. & Novas, F. A plated dinosaur (Ornithischia, Stegosauria) from the Early Cretaceous of Argentina, South America: an evaluation. *Alcheringa* **37**, 65–78 (2013).

16. 16.

Norman, D. B. *Scelidosaurus harrisonii* from the Early Jurassic of Dorset, England: postcranial skeleton. *Zool. J.* **189**, 47–157 (2020).

17. 17.

Sereno, P. C. The evolution of dinosaurs. *Science* **284**, 2137–2147 (1999).

18. 18.

Maidment, S. C., Norman, D. B., Barrett, P. M. & Upchurch, P. Systematics and phylogeny of Stegosauria (Dinosauria: Ornithischia). *J. Syst. Palaeontol.* **6**, 367–407 (2008).

19. 19.

Carpenter, K., DiCroce, T., Kinneer, B. & Simon, R. Pelvis of *Gargoyleosaurus* (Dinosauria: Ankylosauria) and the origin and evolution of the ankylosaur pelvis. *PLoS ONE* **8**, e79887 (2013).

20. 20.

Norman, D. B. *Scelidosaurus harrisonii* from the Early Jurassic of Dorset, England: the dermal skeleton. *Zool. J.* **190**, 1–53 (2020).

21. 21.

Burns, M. E. & Currie, P. J. External and internal structure of ankylosaur (Dinosauria, Ornithischia) osteoderms and their systematic relevance. *J. Vertebr. Paleontol.* **34**, 835–851 (2014).

22. 22.

Han, F., Forster, C. A., Xu, X. & Clark, J. M. Postcranial anatomy of *Yinlong downsi* (Dinosauria: Ceratopsia) from the Upper Jurassic Shishugou Formation of China and the phylogeny of basal ornithischians. *J. Syst. Palaeontol.* **16**, 1159–1187 (2018).

23. 23.

Norman, D. B. *Scelidosaurus harrisonii* (Dinosauria: Ornithischia) from the Early Jurassic of Dorset, England: biology and phylogenetic relationships. *Zool. J.* **191**, 1–86 (2021).

24. 24.

Raven, T. J. & Maidment, S. C. A new phylogeny of Stegosauria (Dinosauria, Ornithischia). *Palaeontology* **60**, 401–408 (2017).

25. 25.

Loewen, M. A. & Kirkland, J. I. The evolution and biogeographic distribution of Ankylosauria: new insights from a comprehensive phylogenetic analysis. *J. Vertebr. Paleontol (Program and Abstracts)*. **2013**, 163-164A (2013).

26. 26.

Molnar, R. E. Preliminary report a new ankylosaur from the Early Cretaceous of Queensland, Australia. *Mem. Queensland Mus.* **39**, 653–668 (1996).

27. 27.

Molnar, R. E. in *The Armored Dinosaurs* (ed. Carpenter, K.) 341–362 (Indiana Univ. Press, 2001).

28. 28.

Arbour, V. M., Burns, M. E. & Currie, P. J. A review of pelvic shield morphology in ankylosaurs (Dinosauria: Ornithischia). *J. Paleontol.* **85**, 298–302 (2011).

29. 29.

Lamanna, M. C. et al. Late Cretaceous non-avian dinosaurs from the James Ross Basin, Antarctica: description of new material, updated synthesis, biostratigraphy, and paleobiogeography. *Adv. Polar Sci.* **30**, 228–250 (2019).

30. 30.

de Ricqlès, A., Suberbiola, X. P., Gasparini, Z. & Olivero, E. Histology of dermal ossifications in an ankylosaurian dinosaur from the Late Cretaceous of Antarctica. *Asoc. Paleontol. Argent.* **7**, 171–174 (2001).

31. 31.

Arbour, V. M. & Currie, P. J. Ankylosaurid dinosaur tail clubs evolved through stepwise acquisition of key features. *J. Anat.* **227**, 514–523 (2015).

32. 32.

Arbour, V. M. & Zanno, L. E. Tail weaponry in ankylosaurs and glyptodonts: an example of a rare but strongly convergent phenotype. *Anat. Rec.* **303**, 988–998 (2020).

33. 33.

Maidment, S. C., Raven, T. J., Ouarhache, D. & Barrett, P. M. North Africa's first stegosaur: implications for Gondwanan thyreophoran dinosaur diversity. *Gondwana Res.* **77**, 82–97 (2020).

34. 34.

Goloboff, P. A. & Catalano, S. A. TNT version 1.5, including a full implementation of phylogenetic morphometrics. *Cladistics* **32**, 221–238 (2016).

35. 35.

Arbour, V. M., Zanno, L. E. & Gates, T. Ankylosaurian dinosaur palaeoenvironmental associations were influenced by extirpation, sea-level fluctuation, and geodispersal. *Palaeogeogr. Palaeoclimatol. Palaeoecol.* **449**, 289–299 (2016).

36. 36.

Goloboff, P. A., Farris, J. S. & Nixon, K. C. TNT, a free program for phylogenetic analysis. *Cladistics* **24**, 774–786 (2008).

37. 37.

Siddall, M. E. Stratigraphic fit to phylogenies: a proposed solution. *Cladistics* **14**, 201–208 (1998).

38. 38.

Wills, M. A. Congruence between phylogeny and stratigraphy: randomization tests and the gap excess ratio. *Syst. Biol.* **48**, 559–580 (1999).

39. 39.

Pol, D. & Norell, M. A. Comments on the Manhattan stratigraphic measure. *Cladistics* **17**, 285–289 (2001).

40. 40.

Pol, D., Norell, M. A. & Siddall, M. E. Measures of stratigraphic fit to phylogeny and their sensitivity to tree size, tree shape, and scale. *Cladistics* **20**, 64–75 (2004).

41. 41.

Pol, D. & Norell, M. A. Uncertainty in the age of fossils and the stratigraphic fit to phylogenies. *Syst. Biol.* **55**, 512–521 (2006).

## Acknowledgements

We thank F. Suazo, E. Nuñez, D. Bajor, J. P. Guevara, D. Flores, S. Jiménez, I. Meyer-Navia, S. Davis and members of the J. Clark team for help in the field and/or fossil preparation; Estancia Cerro Guido and especially the Matetic, Simunovic and Reyes families for granting access and important logistical support in the field; the Consejo de Monumentos Nacionales (National Monuments Council) of the Chilean Ministry of

Culture, Arts and Heritage for fieldwork permits; M. Reguero for access and help with the *Antarctopelta* holotype; J. Vidal for technical support in the acquisition of CT images; and staff at the Willi Hennig society for free distribution of TNT software. This research was supported by the Agencia Nacional de Investigación y Desarrollo ANID (National Agency for Research and Development) of the Chilean Ministry of Science, Technology, Knowledge and Innovation through grants PIA Anillo ACT172099 (to A.O.V.), FONDECYT 1190891 (to A.O.V.), FONDECYT 1151389 (to M.A.L.), and PhD scholarships for S.S.-A., J.A.-M., J.P.-L. and J.P.P.

## Author information

### Affiliations

1. Red Paleontológica U-Chile, Departamento de Biología, Facultad de Ciencias, Universidad de Chile, Santiago, Chile

Sergio Soto-Acuña, Alexander O. Vargas, Jonatan Kaluza, Marcelo A. Leppe, Joao F. Botelho, José Palma-Liberona, Carolina Simon-Gutstein, Roy A. Fernández, Héctor Ortiz, Verónica Milla, Bárbara Aravena, Leslie M. E. Manríquez, Jhonatan Alarcón-Muñoz, Juan Pablo Pino, Cristine Trevisan, Héctor Mansilla, Luis Felipe Hinojosa, Vicente Muñoz-Walther & David Rubilar-Rogers

2. Departamento de Ecología, Facultad de Ciencias, Universidad de Chile, Santiago, Chile

Sergio Soto-Acuña, Jhonatan Alarcón-Muñoz, Juan Pablo Pino & Luis Felipe Hinojosa

3. Fundación de Historia Natural Félix de Azara, Universidad Maimónides, Buenos Aires, Argentina

Jonatan Kaluza

4. CONICET, Buenos Aires, Argentina

Jonatan Kaluza

5. Laboratorio de Paleobiología, Instituto Nacional Antártico Chileno,  
Punta Arenas, Chile

Marcelo A. Leppe, Cristine Trevisan & Héctor Mansilla

6. Escuela de Medicina Veterinaria, Pontificia Universidad Católica de  
Chile, Santiago, Chile

Joao F. Botelho & José Palma-Liberona

7. Universidad de Concepción, Concepción, Chile

Roy A. Fernández & Verónica Milla

8. Universidad de Magallanes, Punta Arenas, Chile

Héctor Ortiz

9. Universidade do Vale do Rio do Sinos, São Leopoldo, Brazil

Leslie M. E. Manríquez

10. Área Paleontología, Museo Nacional de Historia Natural de Chile,  
Santiago, Chile

David Rubilar-Rogers

## Contributions

J.K., S.S.-A., H.O., B.A., J.A.-M., J.P.P. and V.M. extracted the fossil. J.K., S.S.-A., B.A. and J.A.-M. carried out laboratory preparation. J.P.-L., J.F.B., S.S.-A. and V.M.-W. processed and sampled CT and  $\mu$ CT data. S.S.-A. and A.O.V. described the material. S.S.-A. and A.O.V. scored phylogenetic matrices. S.S.-A. conducted the maximum-parsimony analyses. C.S.-G. and V.M. carried out taphonomic studies. M.A.L., L.M.E.M., R.A.F., J.P.P., H.M., C.T., D.R. and L.F.H. carried out geological and palaeoenvironmental studies. A.O.V. and S.S.-A. wrote the bulk of the manuscript; S.S.-A., C.S.-

G., V.M. and J.P.P. made figures. All of the authors collected data and contributed to the writing, discussion and conclusions.

## Corresponding authors

Correspondence to [Sergio Soto-Acuña](#) or [Alexander O. Vargas](#).

## Ethics declarations

### Competing interests

The authors declare no competing interests.

## Additional information

**Peer review information** *Nature* thanks James Kirkland and the other, anonymous, reviewer(s) for their contribution to the peer review of this work. Peer reviewer reports are available.

**Publisher's note** Springer Nature remains neutral with regard to jurisdictional claims in published maps and institutional affiliations.

## Extended data figures and tables

### [Extended Data Fig. 1 Cranial bones of \*S. elongassen\* holotype \(CPAP-3165\).](#)

**a**, skull in lateral view (with left? supraorbital reversed). **b**, posterior skull in dorsal view. **c**, premaxilla in ventral view. **d**, left maxilla lateral view. **e**, **f**, both maxillae in ventral view. **g**, left? supraorbital dorsal view. **h**, **i**, predentary in occlusal and ventral views. **j**, basisphenoid in palatal view. **k**, right dentary in lingual view. Scale bars, 10 cm.

### [Extended Data Fig. 2 Postcranial axial skeleton of \*S. elongassen\* holotype \(CPAP-3165\).](#)

**a-c** axis in anterior and right lateral views. **d-f**, anterior cervical vertebra in anterior, right lateral and ventral views. **g-i**, posterior cervical vertebra in anterior, right lateral and dorsal views. **j-l**, anterior dorsal vertebra in anterior, right lateral and dorsal views. **m, n**, posterior dorsal vertebra in anterior and right lateral views. **o**, synsacral vertebrae in right lateral view. **p**, anterior caudal vertebrae in right lateral view. **q**, posterior caudal vertebrae in right lateral view. Scale bar 10 cm.

**Extended Data Fig. 3 Sternal, pectoral girdle and forelimb bones of *S. elongassen* holotype (CPAP-3165).**

**a, b**, sternal plates in ventral view. **c-e**, right coracoid in lateral, medial and glenoideal views. **f-i** left humerus in anterior, posterior, proximal and distal views. **j**, left radius in lateral view. **k**, left ulna in anterior view. **l, m**, left hand in proximal and dorsal views. **n**, originally semiarticulated right hand in dorsal view. **o**, fully prepared right hand in dorsal view. Scale bars, 10 cm.

**Extended Data Fig. 4 Pelvic girdle, hindlimbs and dermal armour of *S. elongassen* holotype (CPAP-3165).**

**a**, right ilium in lateral view. **b**, pelvis in ventral view. **c, d**, left pubis in lateral and medial views. **e-h**, left femur in proximal, distal and posterior views. **i**, right femur in lateral view. **j**, left foot in dorsal view. **k**, right foot in lateral view. **l, m**, isolated mid-sized ovalate keeled osteoderm in dorsal and lateral views. **n, o**, sacral covering in dorsal and ventral views. **p**, keeled osteoderm with deeply excavated inner surface associated with right ulna in ventrolateral view. **q**, flat osteoderm associated with right radius in dorsal view. Scale bars, 10 cm (a-k, n, o) 2 cm (l, m, p, q).

**Extended Data Fig. 5 Paired comparisons of the axial skeleton between *S. elongassen* holotype CPAP-3165 (left) and *A. oliveroi* holotype MLP 86-X-28-1 (right).**

Synsacral complex in **a, b**, anterior, **c, d**, posterior and **e, f**, ventral views; anterior caudal vertebrae (6th in *Stegouros elongassen*) in **g, h**, posterior and

**j, k**, right lateral views; posterior caudal vertebrae (17th in *Stegouros elengassen*) in **l, m**, dorsal and **n, o**, posterior views. Scale bars, 2 cm (a, c, e, h, j, l, n), 5 cm (b, d, f, g, i, k, m, o).

**Extended Data Fig. 6 Anatomy of caudal weapon osteoderms in *S. elengassen* holotype (CPAP-3165) and *A. oliveroi* holotype (MLP 86-X-28-1).**

**a**, digital reconstruction and **b**, photograph of *Stegouros elengassen* caudal weapon cross section (at level of first osteoderm pair and 14th caudal vertebra) in anterior and left lateral views. **c, d**, *Antarctopelta oliveroi* dorsal osteoderm of the first pair in left lateral and anterior views. **e**, *Stegouros elengassen*, 3D reconstruction of the left second osteoderm in dorsal and internal views. **f**, *Antarctopelta oliveroi* left second osteoderm fragment in dorsal and internal views. **g, h**, *Stegouros elengassen*, digital reconstruction of the caudal weapon cross section (at level of second pair and 17th caudal vertebra) in anterior and posterior views. **i, j**, proposed configuration of the caudal weapon of *Antarctopelta oliveroi* in anterior and posterior views. Scale bars 10 cm.

**Extended Data Fig. 7 Comparison of cervical and pedal bones between *S. elengassen* holotype (CPAP-3165) and *A. oliveroi* holotype (MLP 86-X-28-1).**

**a–d**, *Stegouros elengassen* posterior cervical vertebra in anterior, right lateral, posterior, and dorsal views. **e–h**, *Antarctopelta oliveroi* posterior cervical vertebra in anterior, right lateral, posterior, and dorsal views. **i, j**, *Stegouros elengassen* right foot in dorsal and ventral views. **k, l**, *Antarctopelta oliveroi* right metatarsal in dorsal and ventral views. **m**, *Antarctopelta oliveroi* isolated pedal phalanx in dorsal, proximal and ventral views. Scale bars 5 cm.

**Extended Data Fig. 8 Comparison of dermal skeleton between *S. elengassen* holotype (CPAP-3165) and *A. oliveroi* holotype (MLP 86-X-28-1).**

**a**, *Stegouros elengassen* dermal ossicles in internal view. **b**, *Antarctopelta oliveroi* disarticulated dermal ossicles. **c**, *Antarctopelta oliveroi* dermal ossicle close-up exposed in internal view. **d–f**, sacral covering fragments of *Antarctopelta oliveroi*. Scale bars, 5 mm (1, b), 1 mm (c), 10 cm (d-f).

### [Extended Data Fig. 9 Comparison of teeth and dentary of \*S. elengassen\* holotype \(CPAP-3165\) and \*A. oliveroi\* holotype \(MLP 86-X-28-1\).](#)

**a–d**, *Stegouros elengassen* digital reconstruction of cheek tooth in labial, mesial, lingual, and distal views. **e–h**, *Antarctopelta oliveroi* tooth (reversed) in labial, mesial, lingual, and distal views. **i–k**, *Stegouros elengassen* right dentary (mirrored for better comparison) in labial, lingual and occlusal views. **l–n** *Antarctopelta oliveroi* right dentary fragment in labial, lingual and occlusal views. Scale bars 5 mm (a-d), 10 mm (e-h), 10 cm (i-n).

### **Extended Data Table 1 Results of phylogenetic analysis**

## **Supplementary information**

### [Supplementary Information](#)

(1) Taphonomical aspects of the holotype. (2) Geological and Palaeoenvironmental context. (3) Additional comparisons to *Antarctopelta oliveroi*. (4) Results of the phylogenetic analyses. (5) References.

### [Reporting Summary](#)

### [Peer Review File](#)

### [Supplementary Video 1](#)

3D reconstruction of the tail weapon of *Stegouros* based on the digital segmentation of a CT scan volume.

## Supplementary Video 2

Transversal view of the segmented volume for the tail weapon of *Stegouros*.

## Supplementary Video 3

Digital endocast of the tail weapon of *Stegouros*.

## Rights and permissions

### Reprints and Permissions

## About this article

### Cite this article

Soto-Acuña, S., Vargas, A.O., Kaluza, J. *et al.* Bizarre tail weaponry in a transitional ankylosaur from subantarctic Chile. *Nature* **600**, 259–263 (2021). <https://doi.org/10.1038/s41586-021-04147-1>

- Received: 17 August 2021
- Accepted: 14 October 2021
- Published: 01 December 2021
- Issue Date: 09 December 2021
- DOI: <https://doi.org/10.1038/s41586-021-04147-1>

### Share this article

Anyone you share the following link with will be able to read this content:

[Get shareable link](#)

Sorry, a shareable link is not currently available for this article.

[Copy to clipboard](#)

Provided by the Springer Nature SharedIt content-sharing initiative

## Armoured dinosaurs of the Southern Hemisphere

Research Briefing 01 Dec 2021

---

This article was downloaded by **calibre** from <https://www.nature.com/articles/s41586-021-04147-1>

| [Section menu](#) | [Main menu](#) |

- Article
- [Published: 01 December 2021](#)

# Quantifying social organization and political polarization in online platforms

- [Isaac Waller ORCID: orcid.org/0000-0003-4283-2502<sup>1</sup>](#) &
- [Ashton Anderson ORCID: orcid.org/0000-0003-3089-6883<sup>1</sup>](#)

[Nature](#) volume **600**, pages 264–268 (2021)

- 6396 Accesses
- 399 Altmetric
- [Metrics details](#)

## Subjects

- [Computer science](#)
- [Interdisciplinary studies](#)
- [Sociology](#)

## Abstract

Mass selection into groups of like-minded individuals may be fragmenting and polarizing online society, particularly with respect to partisan differences<sup>1,2,3,4</sup>. However, our ability to measure the social makeup of online communities and in turn, to understand the social organization of online platforms, is limited by the pseudonymous, unstructured and large-

scale nature of digital discussion. Here we develop a neural-embedding methodology to quantify the positioning of online communities along social dimensions by leveraging large-scale patterns of aggregate behaviour. Applying our methodology to 5.1 billion comments made in 10,000 communities over 14 years on Reddit, we measure how the macroscale community structure is organized with respect to age, gender and US political partisanship. Examining political content, we find that Reddit underwent a significant polarization event around the 2016 US presidential election. Contrary to conventional wisdom, however, individual-level polarization is rare; the system-level shift in 2016 was disproportionately driven by the arrival of new users. Political polarization on Reddit is unrelated to previous activity on the platform and is instead temporally aligned with external events. We also observe a stark ideological asymmetry, with the sharp increase in polarization in 2016 being entirely attributable to changes in right-wing activity. This methodology is broadly applicable to the study of online interaction, and our findings have implications for the design of online platforms, understanding the social contexts of online behaviour, and quantifying the dynamics and mechanisms of online polarization.

This is a preview of subscription content

## Access options

Subscribe to Journal

Get full journal access for 1 year

\$199.00

only \$3.90 per issue

[Subscribe](#)

All prices are NET prices.

VAT will be added later in the checkout.

Tax calculation will be finalised during checkout.

Rent or Buy article

Get time limited or full article access on ReadCube.

from \$8.99

[Rent or Buy](#)

All prices are NET prices.

### **Additional access options:**

- [Log in](#)
- [Learn about institutional subscriptions](#)

**Fig. 1: Quantifying social dimensions on Reddit.**



**Fig. 2: Macroscale social organization of Reddit communities.**

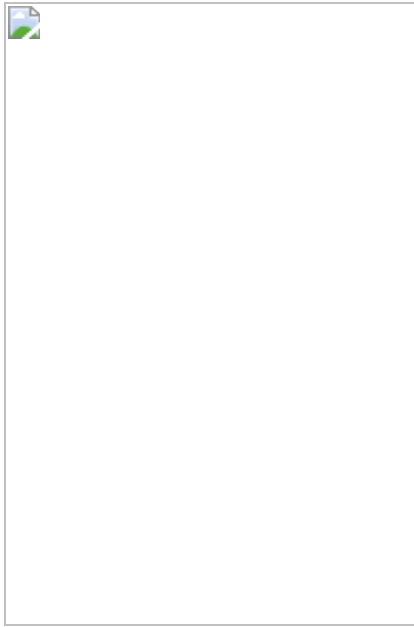


**Fig. 3: Distribution of political activity on Reddit.**

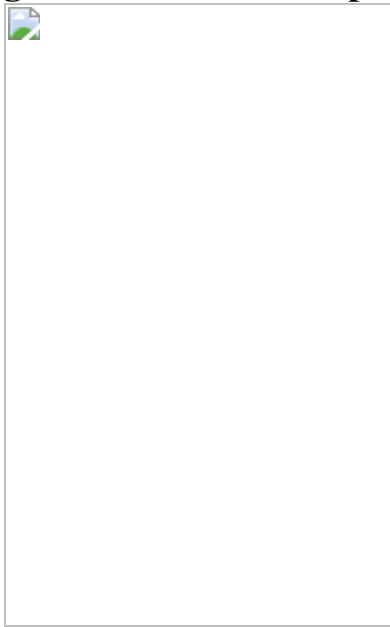


**Fig. 4: Political polarization of new and existing users.**

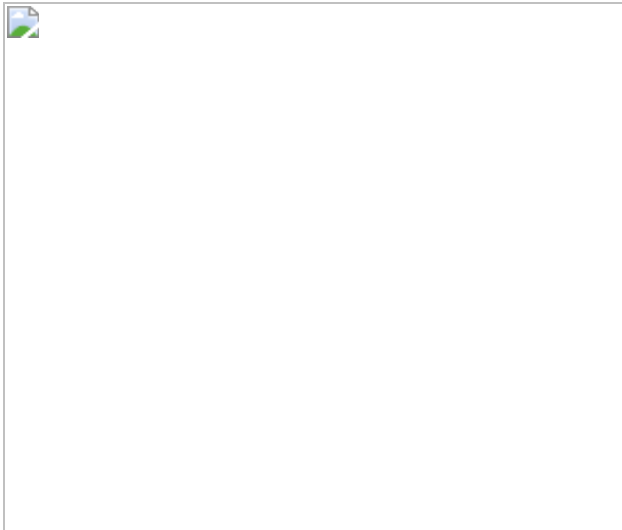
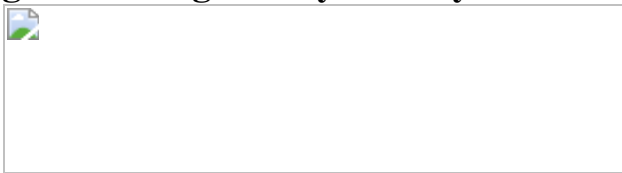


**Fig. 5: Ideological asymmetry in online polarization.**



## Data availability

All data are available from the pushshift.io Reddit archive<sup>28</sup> at <http://files.pushshift.io/reddit/>. [Source data](#) are provided with this paper. Reddit community embedding, social dimension vectors and community scores are available at <https://github.com/CSSLab/social-dimensions>.

## Code availability

All code is available at <https://github.com/CSSLab/social-dimensions>. Analyses were performed with Python v3.7, pandas v1.3.3 and Spark v3.0.

## References

1. 1.

Sunstein, C. #*Republic: Divided Democracy in the Age of Social Media* (Princeton Univ. Press, 2018).

2. 2.

Iyengar, S. & Hahn, K. S. Red media, blue media: evidence of ideological selectivity in media use. *J. Commun.* **59**, 19–39 (2009).

3. 3.

van Alstyne, M. & Brynjolfsson, E. Electronic communities: global villages or cyberbalkanization? In *Proc. International Conference on Information Systems 5* <https://aisel.aisnet.org/icis1996/5> (1996).

4. 4.

van Dijck, J. *The Culture of Connectivity: A Critical History of Social Media* (Oxford Univ. Press, 2013).

5. 5.

McLuhan, M. *The Gutenberg Galaxy: The Making of Typographic Man* (Univ. of Toronto Press, 1962).

6. 6.

Farrell, H. The consequences of the internet for politics. *Ann. Rev. Pol. Sci.* **15**, 35–52 (2012).

7. 7.

Conover, M. D. et al. Political polarization on Twitter. *Proc. Intl AAAI Conf Web Soc. Media* **133**, 89–96 (2011).

8. 8.

Bail, C. A. et al. Exposure to opposing views on social media can increase political polarization. *Proc. Natl Acad. Sci. USA* **115**, 9216–9221 (2018).

9. 9.

Martin, T. community2vec: vector representations of online communities encode semantic relationships. In *Proc. 2nd Workshop on NLP and Computational Social Science* 27–31 (2017).

10. 10.

Garg, N., Schiebinger, L., Jurafsky, D. & Zou, J. Word embeddings quantify 100 years of gender and ethnic stereotypes. *Proc. Natl Acad. Sci. USA* **115**, E3635–E3644 (2018).

11. 11.

Bolukbasi, T., Chang, K.-W., Zou, J. Y., Saligrama, V. & Kalai, A. T. Man is to computer programmer as woman is to homemaker? Debiasing word embeddings. *Adv. Neural Inf Process. Syst.* **29**, 4349–4357 (2016).

12. 12.

Caliskan, A., Bryson, J. J. & Narayanan, A. Semantics derived automatically from language corpora contain human-like biases. *Science* **356**, 183–186 (2017).

13. 13.

Kozlowski, A. C., Taddy, M. & Evans, J. A. The geometry of culture: analyzing the meanings of class through word embeddings. *Am. Soc. Rev.* **84**, 905–949 (2019).

14. 14.

Shi, F., Shi, Y., Dokshin, F. A., Evans, J. A. & Macy, M. W. Millions of online book co-purchases reveal partisan differences in the consumption of science. *Nat. Hum. Behav.* **1**, 0079 (2017).

15. 15.

Del Vicario, M. et al. Echo chambers: emotional contagion and group polarization on Facebook. *Sci. Rep.* **6**, 37825 (2016).

16. 16.

Pariser, E. *The Filter Bubble: What the Internet is Hiding from You* (Penguin, 2011).

17. 17.

Flaxman, S., Goel, S. & Rao, J. M. Filter bubbles, echo chambers, and online news consumption. *Public Opin. Q.* **80**, 298–320 (2016).

18. 18.

Bakshy, E., Messing, S. & Adamic, L. A. Exposure to ideologically diverse news and opinion on Facebook. *Science* **348**, 1130–1132 (2015).

19. 19.

DiMaggio, P., Evans, J. & Bryson, B. Have American's social attitudes become more polarized? *Am. J. Sociol.* **102**, 690–755 (1996).

20. 20.

Barberá, P., Jost, J. T., Nagler, J., Tucker, J. A. & Bonneau, R. Tweeting from left to right: is online political communication more than an echo chamber? *Psychol. Sci.* **26**, 1531–1542 (2015).

21. 21.

Adamic, L. A. & Glance, N. The political blogosphere and the 2004 US election: divided they blog. In *Proc. 3rd International Workshop on Link Discovery* 36–43 (2005).

22. 22.

*An Examination of the 2016 Electorate, Based on Validated Voters*  
<https://www.pewresearch.org/politics/2018/08/09/an-examination-of-the-2016-electorate-based-on-validated-voters/> (Pew Research Center, 2018).

23. 23.

Hawley, G. *Making Sense of the Alt-Right* (Columbia Univ. Press, 2017).

24. 24.

Simmel, G. *Conflict and the Web of Group Affiliations* (Free Press, 1955).

25. 25.

Breiger, R. L. The duality of persons and groups. *Social Forces* **53**, 181–190 (1974).

26. 26.

Bourdieu, P. *Distinction: A Social Critique of the Judgement of Taste* (Routledge, 1984).

27. 27.

Crenshaw, K. W. *On Intersectionality: Essential Writings* (The New Press, 2017).

28. 28.

Baumgartner, J., Zannettou, S., Keegan, B., Squire, M. & Blackburn, J. The Pushshift Reddit dataset. In *Proc. International AAAI Conference on Web and Social Media* **14**, 830–839 (2020).

29. 29.

Reddit privacy policy *Reddit*  
<https://www.redditinc.com/policies/privacy-policy> (2021).

30. 30.

Kumar, S., Hamilton, W. L., Leskovec, J. & Jurafsky, D. Community interaction and conflict on the web. In *Proc. 2018 World Wide Web Conference* 933–943 (2018).

31. 31.

Waller, I. & Anderson, A. Generalists and specialists: using community embeddings to quantify activity diversity in online platforms. In *Proc. 2019 World Wide Web Conference* 1954–1964 (2019).

32. 32.

Levy, O. & Goldberg, Y. Dependency-based word embeddings. In *Proc. 52nd Annual Meeting of the Association for Computational Linguistics* **2**, 302–308 (2014).

33. 33.

Levy, O. & Goldberg, Y. Neural word embedding as implicit matrix factorization. *Adv. Neural Inf. Process. Syst.* **27**, 2177–2185 (2014).

34. 34.

Schlechtweg, D., Oguz, C. & im Walde, S. S., Second-order co-occurrence sensitivity of skip-gram with negative sampling. Preprint at <https://arxiv.org/abs/1906.02479> (2019).

## Acknowledgements

This research was supported by the National Sciences and Engineering Research Council of Canada (NSERC), the Canada Foundation for Innovation (CFI) and the Ontario Research Fund (ORF).

# Author information

## Affiliations

1. Department of Computer Science, University of Toronto, Toronto, Ontario, Canada

Isaac Waller & Ashton Anderson

## Contributions

I.W. performed the computational analysis. A.A. and I.W. designed the research, analysed the results and wrote the paper.

## Corresponding author

Correspondence to [Ashton Anderson](#).

## Ethics declarations

## Competing interests

The authors declare no competing interests.

## Additional information

**Peer review information** *Nature* thanks Kenneth Benoit, Kate Starbird and the other, anonymous, reviewer(s) for their contribution to the peer review of this work. Peer reviewer reports are available.

**Publisher's note** Springer Nature remains neutral with regard to jurisdictional claims in published maps and institutional affiliations.

## Extended data figures and tables

## Extended Data Fig. 1 Distribution of community scores.

Left: distributions of communities on the age, gender, partisan, and affluence dimensions. Right: the most extreme communities and words on those dimensions. Word scores are calculated by averaging community scores weighted by the number of occurrences of the word in the community in 2017. Community descriptions can be found in the glossary (Supplementary Table 1).

## Extended Data Fig. 2 External validations of social dimensions.

Scatter plots of the external validations of the gender, partisan, and affluence axes. The gender scores for occupational communities are plotted against the percentage of women in that occupation from the 2018 American Community Survey. The partisan scores for city communities are plotted against the Republican vote differential for that metropolitan area in the 2016 presidential election. The affluence scores of city communities are plotted against the median household income for that metropolitan area from the 2016 US Census. The blue line is the best-fit linear regression for the data; the shaded area represents a 95% confidence interval for the regression estimated using a bootstrap.  $\backslash(p\backslash)$ -values for correlation coefficients computed using two-sided test of Pearson correlation assuming joint normality.

## Extended Data Fig. 3 Further validations of social dimensions.

Clockwise from left: The gap between university and city communities on the age dimension. The distribution of university and city communities on the age dimension; age is strongly related to label ( $(r=0.91)$ , two-sided  $\backslash(p < \{ 10 \} ^\{ -58 \})$ ,  $\backslash(n=150)$ ), Cohen's  $\backslash(d=4.37)$ ). The distribution of left and right wing labelled communities on the partisan dimension; partisan is strongly related to label ( $(r=0.92)$ , two-sided  $\backslash(p < \{ 10 \} ^\{ -21 \})$ ,  $\backslash(n=50)$ ), Cohen's  $\backslash(d=4.89)$ ). The distribution of explicitly labelled left- and right-wing communities on the partisan-ness axis as compared to the general distribution; there is a large difference in their means (Cohen's  $\backslash(d=3.27)$ ). For violin plots, white dot represents median; box represents 25th to 75th percentile; whiskers represent 1.5 times the inter-quartile range; and density

estimate ('violin') extends to the minima and maxima of the data.  $\langle p \rangle$ -values for correlation coefficients computed using two-sided test of Pearson correlation assuming joint normality.

### **Extended Data Fig. 4 Distributions of age, gender and partisan scores by cluster.**

Distributions of raw age, gender and partisan scores, separated by cluster. Outlier communities that lie more than two standard deviations from the mean are annotated. Dashed lines represent the global mean on each dimension. Community descriptions can be found in the glossary (Supplementary Table 1).

### **Extended Data Fig. 5 Distributions of affluence, time, sociality and edgy scores by cluster.**

Outlier communities that lie more than two standard deviations from the mean are annotated. Dashed lines represent the global mean on each dimension. Community descriptions can be found in the glossary (Supplementary Table 1).

### **Extended Data Fig. 6 Relationships between online social dimensions.**

The relationships between the partisan dimension and (a) gender, (b) age, (c) partisan-ness. Every bar represents a bin of communities with partisan scores a given number of standard deviations from the mean, and the distribution illustrates the scores on the secondary dimension (e.g. gender in (a)). From left to right, the bars represent highly left-wing, leaning left-wing, center, leaning right-wing, highly right-wing communities. The leftmost and rightmost bars are annotated with the number of communities, and examples of the largest communities, in each group. The hex-plot in (c) illustrates the joint distribution of partisan and partisan-ness scores. Labels correspond to the categorizations used in the polarization analysis.

### **Extended Data Fig. 7 Polarization robustness checks.**

**(a)** The partisan distribution of deleted and non-deleted comments in political communities. **(b)** The proportion of activity that took place in very left-wing ( $(z < -3)$ ) and very right-wing ( $(z > 3)$ ) communities over time. **(c)** Alternate version of Fig. 3a generated using a dataset in which the authorship of all comments was randomly shuffled. Each individual bin distribution is extremely similar to the overall activity distribution, showing that the overall activity distribution is a useful reference point for what bin distributions would look like if there were no tendency for users to comment in ideologically homogeneous communities. **(d)** Average distributions of political activity for authors of comments in the 25 largest political communities on Reddit (by number of comments). **(e)** Correlation of users' average partisan scores over time. Each  $(\text{left}(x,y)\text{right})$  cell represents the correlation between scores of a user in month  $(\{t\}_{x})$  and that same user in month  $(\{t\}_{y})$ , for all users active in both time periods. A user is only considered active if they make at least  $(10)$  comments in a month. **(f)** The relationship between the proportion of users who polarize and the polarization threshold. The polarization threshold is the number of standard deviations a user must increase in polarization to be considered polarized. Three lines are plotted corresponding to three pairs of months; the pairs of months with the minimum (blue), maximum (orange), and median (green) proportion of users polarized when using a threshold of  $(1)$ . A threshold of  $(1)$  is used in all other calculations. **(g)** The relationship between the proportion of users who polarize and the comment threshold. The comment threshold is the value used to filter inactive users from the calculation. Users must have at least  $(x)$  comments in each of the two months to be included in the calculation of the proportion of users who polarize. The same three month pairs are plotted as in part (e). There are minimal differences between different thresholds. A threshold of  $(10)$  is used in all other calculations.

### [Extended Data Fig. 8 Distribution of political activity by user group.](#)

The distribution of political activity on Reddit over time by partisan score. Each bar represents one month of comment activity in political communities on Reddit, and is coloured according to the distribution of partisan scores of comments posted during the month (the partisan score of

a comment is simply the partisan score of the community in which it was posted.) The top plot includes all activity as in Fig. 3b, while the four following plots decompose this into the subsets of activity authored by particular groups of users. Users are classified based on the average partisan score of their activity in the month 12 months prior—into left-wing (having a score at least one standard deviation to the left), right-wing (one standard deviation to the right), or center. Users with no political activity in the month 12 months prior use the label of the most recent month more than 12 months prior in which they had political activity; if they have never had political activity before, they fall into the new / newly political category (bottom).

### Extended Data Fig. 9 Additional measures of ideological asymmetry.

**(a)** Average polarization (absolute  $\langle z \rangle$ -score) of activity in different ideological categories over time. **(b)** Volume of activity (number of comments) in different ideological categories over time. **(c, d)** Annual change in polarization in the two partisan activity categories, decomposed into the change attributable to new ( $\langle \varDelta n \rangle$ ) and existing ( $\langle \varDelta e \rangle$ ) users as done in Fig. 4.

### Extended Data Fig. 10 Implicit polarization.

The relationship between explicitly partisan and implicitly partisan activity (left: left-wing activity; right: right-wing activity.) Of users who were first active in an explicitly partisan community at time  $\langle m \rangle_E$ , the proportion of them who were first active in an implicitly partisan community at time  $\langle m \rangle_I$  is denoted by the colour in cell  $\langle \text{left}(\langle m \rangle_E, \langle m \rangle_I) \rangle_{\text{right}}$ . The line graphs at the top show the total proportion of users who were active in implicitly partisan communities before they were active in an explicitly partisan community (i.e. the sum of each column below the diagonal back to 2005, or the total proportion of users for whom  $\langle m \rangle_I < \langle m \rangle_E$ )).

### **Extended Data Table 1 Social dimension seeds**

# **Supplementary information**

## **Supplementary Information**

This file contains Supplementary Tables 1 and 2.

## **Reporting Summary**

## **Peer Review File**

## **Source data**

### **Source Data Fig. 1**

### **Source Data Fig. 2**

### **Source Data Fig. 3**

### **Source Data Fig. 4**

### **Source Data Fig. 5**

## **Rights and permissions**

### **Reprints and Permissions**

## **About this article**

### **Cite this article**

Waller, I., Anderson, A. Quantifying social organization and political polarization in online platforms. *Nature* **600**, 264–268 (2021).  
<https://doi.org/10.1038/s41586-021-04167-x>

- Received: 30 September 2020
- Accepted: 19 October 2021
- Published: 01 December 2021
- Issue Date: 09 December 2021
- DOI: <https://doi.org/10.1038/s41586-021-04167-x>

## Share this article

Anyone you share the following link with will be able to read this content:

[Get shareable link](#)

Sorry, a shareable link is not currently available for this article.

[Copy to clipboard](#)

Provided by the Springer Nature SharedIt content-sharing initiative

---

This article was downloaded by **calibre** from <https://www.nature.com/articles/s41586-021-04167-x>

| [Section menu](#) | [Main menu](#) |

- Article
- [Published: 17 November 2021](#)

# Reverse-translational identification of a cerebellar satiation network

- [Aloysius Y. T. Low<sup>1</sup>](#),
- [Nitsan Goldstein<sup>1</sup>](#),
- [Jessica R. Gaunt<sup>2</sup>](#),
- [Kuei-Pin Huang<sup>3</sup>](#),
- [Norliyana Zainolabidin<sup>4</sup>](#),
- [Alaric K. K. Yip<sup>2</sup>](#),
- [Jamie R. E. Carty<sup>1</sup>](#),
- [Ju Y. Choi<sup>1</sup>](#),
- [Alekso M. Miller<sup>1</sup>](#),
- [Helen S. T. Ho<sup>4</sup>](#),
- [Clara Lenherr<sup>1,5</sup>](#),
- [Nicholas Baltar<sup>6</sup>](#),
- [Eiman Azim ORCID: orcid.org/0000-0002-1015-1772<sup>6</sup>](#),
- [October M. Sessions<sup>7</sup>](#),
- [Toh Hean Ch'ng<sup>2</sup>](#),
- [Amanda S. Bruce<sup>8</sup>](#),
- [Laura E. Martin<sup>9</sup>](#),
- [Mark A. Halko ORCID: orcid.org/0000-0002-7427-0789<sup>10,11</sup>](#),
- [Roscoe O. Brady Jr ORCID: orcid.org/0000-0002-2692-6755<sup>11,12</sup>](#),
- [Laura M. Holsen<sup>11,13</sup>](#),
- [Amber L. Alhadeff ORCID: orcid.org/0000-0001-5355-024X<sup>3,14</sup>](#),
- [Albert I. Chen<sup>15</sup>](#) &
- [J. Nicholas Betley ORCID: orcid.org/0000-0002-4014-9147<sup>1,14</sup>](#)

*Nature* volume **600**, pages 269–273 (2021)

- 8580 Accesses
- 1 Citations
- 291 Altmetric
- [Metrics details](#)

## Subjects

- [Feeding behaviour](#)
- [Neural circuits](#)
- [Reward](#)

## Abstract

The brain is the seat of body weight homeostasis. However, our inability to control the increasing prevalence of obesity highlights a need to look beyond canonical feeding pathways to broaden our understanding of body weight control<sup>1,2,3</sup>. Here we used a reverse-translational approach to identify and anatomically, molecularly and functionally characterize a neural ensemble that promotes satiation. Unbiased, task-based functional magnetic resonance imaging revealed marked differences in cerebellar responses to food in people with a genetic disorder characterized by insatiable appetite. Transcriptomic analyses in mice revealed molecularly and topographically -distinct neurons in the anterior deep cerebellar nuclei (aDCN) that are activated by feeding or nutrient infusion in the gut. Selective activation of aDCN neurons substantially decreased food intake by reducing meal size without compensatory changes to metabolic rate. We found that aDCN activity terminates food intake by increasing striatal dopamine levels and attenuating the phasic dopamine response to subsequent food consumption. Our study defines a conserved satiation centre that may represent a novel therapeutic target for the management of excessive eating, and underscores the utility of a ‘bedside-to-bench’ approach for the identification of neural circuits that influence behaviour.

This is a preview of subscription content

## **Access options**

Subscribe to Journal

Get full journal access for 1 year

\$199.00

only \$3.90 per issue

[Subscribe](#)

All prices are NET prices.

VAT will be added later in the checkout.

Tax calculation will be finalised during checkout.

Rent or Buy article

Get time limited or full article access on ReadCube.

from \$8.99

[Rent or Buy](#)

All prices are NET prices.

### **Additional access options:**

- [Log in](#)
- [Learn about institutional subscriptions](#)

**Fig. 1: The deep cerebellum is activated by food.**

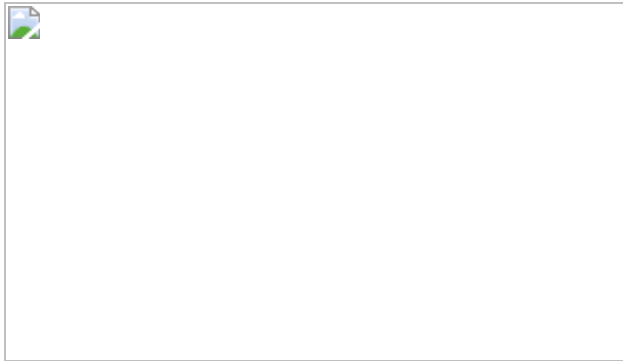


**Fig. 2: Activation of aDCN suppresses food intake without metabolic compensation.**



**Fig. 3: Molecular and topographical organization of nutrient-sensing DCN neurons.**

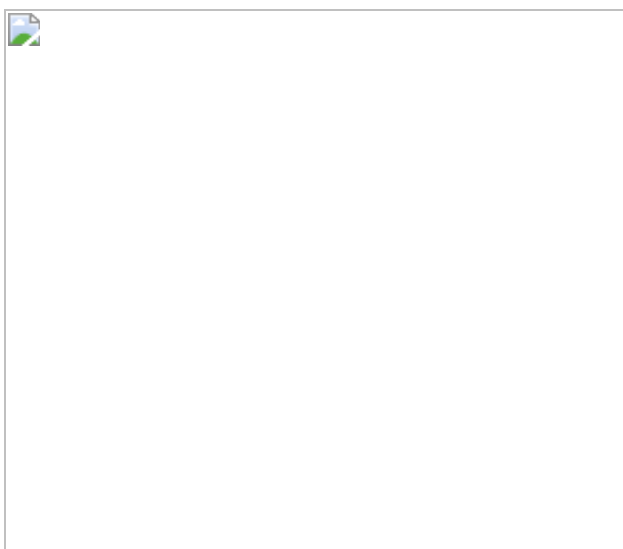
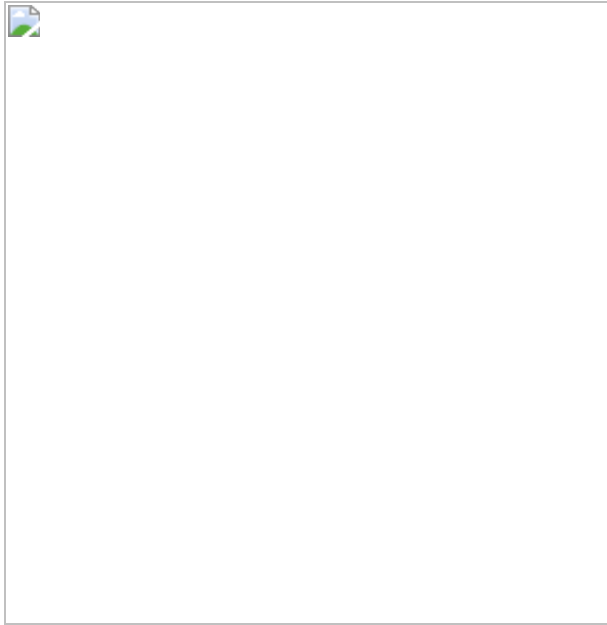


**Fig. 4: aDCN suppresses food intake via hedonic, but not homeostatic, signaling.**



## Materials availability

This study did not generate any new unique reagents. Mouse lines used in this study are on deposit at Jackson Laboratories and are listed under ‘Mice’.

## Data and code availability

The sequencing datasets generated in this study are accessible at Gene Expression Omnibus under accession [GSE184385](#). This manuscript contains all other datasets except the processed sequencing data, raw fibre photometry datasets and codes for analysis which have been uploaded to Mendeley Data (<https://data.mendeley.com//datasets/j2mgy5486k/2>). [Source data](#) are provided with this paper.

## References

1. 1.

Berthoud, H. R. & Morrison, C. The brain, appetite, and obesity. *Annu. Rev. Psychol.* **59**, 55–92 (2008).

2. 2.

Speakman, J. R. A nonadaptive scenario explaining the genetic predisposition to obesity: the “predation release” hypothesis. *Cell Metab.* **6**, 5–12 (2007).

3. 3.

Rossi, M. A. & Stuber, G. D. Overlapping brain circuits for homeostatic and hedonic feeding. *Cell Metab.* **27**, 42–56 (2018).

4. 4.

Woods, S. C. & Ramsay, D. S. Food intake, metabolism and homeostasis. *Physiol. Behav.* **104**, 4–7 (2011).

5. 5.

Berthoud, H. R. The neurobiology of food intake in an obesogenic environment. *Proc. Nutr. Soc.* **71**, 478–487 (2012).

6. 6.

Gautron, L., Elmquist, J. K. & Williams, K. W. Neural control of energy balance: translating circuits to therapies. *Cell* **161**, 133–145 (2015).

7. 7.

Angulo, M. A., Butler, M. G. & Cataletto, M. E. Prader–Willi syndrome: a review of clinical, genetic, and endocrine findings. *J. Endocrinol. Invest.* **38**, 1249–1263 (2015).

8. 8.

Holsen, L. M. et al. Importance of reward and prefrontal circuitry in hunger and satiety: Prader-Willi syndrome vs simple obesity. *Int. J. Obes.* **36**, 638–647 (2012).

9. 9.

Barrachina, M. D., Martinez, V., Wang, L., Wei, J. Y. & Tache, Y. Synergistic interaction between leptin and cholecystokinin to reduce short-term food intake in lean mice. *Proc. Natl Acad. Sci. USA* **94**, 10455–10460 (1997).

10. 10.

Kebschull, J. M. et al. Cerebellar nuclei evolved by repeatedly duplicating a conserved cell-type set. *Science* **370**, eabd5059 (2020).

11. 11.

Betley, J. N., Cao, Z. F., Ritola, K. D. & Sternson, S. M. Parallel, redundant circuit organization for homeostatic control of feeding behavior. *Cell* **155**, 1337–1350 (2013).

12. 12.

Carta, I., Chen, C. H., Schott, A. L., Dorizan, S. & Khodakhah, K. Cerebellar modulation of the reward circuitry and social behavior. *Science* **363**, eaav0581 (2019).

13. 13.

Salamone, J. D., Correa, M., Mingote, S. & Weber, S. M. Nucleus accumbens dopamine and the regulation of effort in food-seeking behavior: implications for studies of natural motivation, psychiatry, and drug abuse. *J. Pharmacol. Exp. Ther.* **305**, 1–8 (2003).

14. 14.

Palmiter, R. D. Is dopamine a physiologically relevant mediator of feeding behavior? *Trends Neurosci.* **30**, 375–381 (2007).

15. 15.

Hinton, E. C. et al. Neural representations of hunger and satiety in Prader–Willi syndrome. *Int. J. Obes.* **30**, 313–321 (2006).

16. 16.

Chen, Y., Lin, Y. C., Kuo, T. W. & Knight, Z. A. Sensory detection of food rapidly modulates arcuate feeding circuits. *Cell* **160**, 829–841 (2015).

17. 17.

Betley, J. N. et al. Neurons for hunger and thirst transmit a negative-valence teaching signal. *Nature* **521**, 180–185 (2015).

18. 18.

Alhadeff, A. L. et al. Natural and drug rewards engage distinct pathways that converge on coordinated hypothalamic and reward circuits. *Neuron* **103**, 891–908.e896 (2019).

19. 19.

Somana, R. & Walberg, F. Cerebellar afferents from the nucleus of the solitary tract. *Neurosci. Lett.* **11**, 41–47 (1979).

20. 20.

Zhu, J. N. & Wang, J. J. The cerebellum in feeding control: possible function and mechanism. *Cell Mol. Neurobiol.* **28**, 469–478 (2008).

21. 21.

Sodersten, P., Bergh, C., Leon, M. & Zandian, M. Dopamine and anorexia nervosa. *Neurosci. Biobehav. Rev.* **60**, 26–30 (2016).

22. 22.

Daberkow, D. P. et al. Amphetamine paradoxically augments exocytotic dopamine release and phasic dopamine signals. *J. Neurosci.* **33**, 452–463 (2013).

23. 23.

Alhadeff, A. L., Rupprecht, L. E. & Hayes, M. R. GLP-1 neurons in the nucleus of the solitary tract project directly to the ventral tegmental area and nucleus accumbens to control for food intake. *Endocrinology* **153**, 647–658 (2012).

24. 24.

Keiflin, R., Pribut, H. J., Shah, N. B. & Janak, P. H. Ventral tegmental dopamine neurons participate in reward identity predictions. *Curr. Biol.* **29**, 93–103.e103 (2019).

25. 25.

Butler, M. G., Bittel, D. C., Kibiryeva, N., Talebizadeh, Z. & Thompson, T. Behavioral differences among subjects with Prader–Willi syndrome and type I or type II deletion and maternal disomy. *Pediatrics* **113**, 565–573 (2004).

26. 26.

Holsen, L. M. et al. Neural mechanisms underlying food motivation in children and adolescents. *Neuroimage* **27**, 669–676 (2005).

27. 27.

Holsen, L. M. et al. Neural mechanisms underlying hyperphagia in Prader–Willi syndrome. *Obesity* **14**, 1028–1037 (2006).

28. 28.

Holsen, L. M. et al. Genetic subtype differences in neural circuitry of food motivation in Prader-Willi syndrome. *Int. J. Obes.* **33**, 273–283 (2009).

29. 29.

LaBar, K. S. et al. Hunger selectively modulates corticolimbic activation to food stimuli in humans. *Behav. Neurosci.* **115**, 493–500 (2001).

30. 30.

Gelman, N. et al. MR imaging of human brain at 3.0 T: preliminary report on transverse relaxation rates and relation to estimated iron content. *Radiology* **210**, 759–767 (1999).

31. 31.

Whitfield-Gabrieli, S. Region of interest extraction (REX) toolbox (Boston, MA). p497 (2009).

32. 32.

Holmes, C. J. et al. Enhancement of MR images using registration for signal averaging. *J. Comp. Assist. Tomography* **22**, 324–333 (1998).

33. 33.

Vong, L. et al. Leptin action on GABAergic neurons prevents obesity and reduces inhibitory tone to POMC neurons. *Neuron* **71**, 142–154 (2011).

34. 34.

Backman, C. M. et al. Characterization of a mouse strain expressing Cre recombinase from the 3' untranslated region of the dopamine transporter locus. *Genesis* **44**, 383–390 (2006).

35. 35.

Allen, W. E. et al. Thirst-associated preoptic neurons encode an aversive motivational drive. *Science* **357**, 1149–1155 (2017).

36. 36.

Madisen, L. et al. A toolbox of Cre-dependent optogenetic transgenic mice for light-induced activation and silencing. *Nat. Neurosci.* **15**, 793–802 (2012).

37. 37.

Borgius, L., Restrepo, C. E., Leao, R. N., Saleh, N. & Kiehn, O. A transgenic mouse line for molecular genetic analysis of excitatory glutamatergic neurons. *Mol. Cell Neurosci.* **45**, 245–257 (2010).

38. 38.

Tong, Q., Ye, C. P., Jones, J. E., Elmquist, J. K. & Lowell, B. B. Synaptic release of GABA by AgRP neurons is required for normal regulation of energy balance. *Nat. Neurosci.* **11**, 998–1000 (2008).

39. 39.

Su, Z., Alhadeff, A. L. & Betley, J. N. Nutritive, post-ingestive signals are the primary regulators of AgRP neuron activity. *Cell Rep.* **21**, 2724–2736 (2017).

40. 40.

Alhadeff, A. L., Park, O., Hernandez, E. & Betley, J. N. Inhibition of itch by hunger and AgRP neuron activity. *Neuroscience* **450**, 126–134 (2020).

41. 41.

Sun, F. et al. A genetically encoded fluorescent sensor enables rapid and specific detection of dopamine in flies, fish, and mice. *Cell* **174**, 481–496.e419 (2018).

42. 42.

Goebel, M., Stengel, A., Wang, L. & Tache, Y. Central nesfatin-1 reduces the nocturnal food intake in mice by reducing meal size and increasing inter-meal intervals. *Peptides* **32**, 36–43 (2011).

43. 43.

Lerner, T. N. et al. Intact-brain analyses reveal distinct information carried by SNc dopamine subcircuits. *Cell* **162**, 635–647 (2015).

44. 44.

Zalocusky, K. A. et al. Nucleus accumbens D2R cells signal prior outcomes and control risky decision-making. *Nature* **531**, 642–646 (2016).

45. 45.

Weir, J. B. New methods for calculating metabolic rate with special reference to protein metabolism. 1949. *Nutrition* **6**, 213–221 (1990).

46. 46.

Betley, J. N. et al. Stringent specificity in the construction of a GABAergic presynaptic inhibitory circuit. *Cell* **139**, 161–174 (2009).

47. 47.

Young, M. D. & Behjati, S. SoupX removes ambient RNA contamination from droplet-based single-cell RNA sequencing data. *Gigascience* **9**, giaa151 (2020).

48. 48.

Stuart, T. et al. Comprehensive integration of single-cell data. *Cell* **177**, 1888–1902.e1821 (2019).

49. 49.

Wolf, F. A., Angerer, P. & Theis, F. J. SCANPY: large-scale single-cell gene expression data analysis. *Genome Biol.* **19**, 15 (2018).

50. 50.

Levine, J. H. et al. Data-driven phenotypic dissection of AML reveals progenitor-like cells that correlate with prognosis. *Cell* **162**, 184–197 (2015).

51. 51.

McGinnis, C. S., Murrow, L. M. & Gartner, Z. J. DoubletFinder: doublet detection in single-cell RNA sequencing data using artificial nearest neighbors. *Cell Syst.* **8**, 329–337.e324 (2019).

52. 52.

Hafemeister, C. & Satija, R. Normalization and variance stabilization of single-cell RNA-seq data using regularized negative binomial regression. *Genome Biol.* **20**, 296 (2019).

53. 53.

Becht, E. et al. Dimensionality reduction for visualizing single-cell data using UMAP. *Nat Biotechnol* **37**, 38–44 (2019).

54. 54.

Marques, S. et al. Oligodendrocyte heterogeneity in the mouse juvenile and adult central nervous system. *Science* **352**, 1326–1329 (2016).

55. 55.

Saunders, A. et al. Molecular diversity and specializations among the cells of the adult mouse brain. *Cell* **174**, 1015–1030.e1016 (2018).

56. 56.

Vanlandewijck, M. et al. A molecular atlas of cell types and zonation in the brain vasculature. *Nature* **554**, 475–480 (2018).

57. 57.

Zeisel, A. et al. Molecular architecture of the mouse nervous system. *Cell* **174**, 999–1014.e1022 (2018).

58. 58.

Carter, R. A. et al. A single-cell transcriptional atlas of the developing murine cerebellum. *Curr. Biol.* **28**, 2910–2920.e2912 (2018).

59. 59.

Wizeman, J. W., Guo, Q., Wilion, E. M. & Li, J. Y. Specification of diverse cell types during early neurogenesis of the mouse cerebellum. *eLife* **8**, e42388 (2019).

60. 60.

Wang, F. et al. RNAscope: a novel in situ RNA analysis platform for formalin-fixed, paraffin-embedded tissues. *14*, 22–29 (2012).

61. 61.

Goldstein, N. et al. Hypothalamic detection of macronutrients via multiple gut–brain pathways. *Cell Metab.* **33**, 676–687.e5 (2021).

62. 62.

Andermann, M. L. & Lowell, B. B. Toward a wiring diagram understanding of appetite control. *Neuron* **95**, 757–778 (2017).

63. 63.

Brakeman, P. R. et al. Homer: a protein that selectively binds metabotropic glutamate receptors. *Nature* **386**, 284–288 (1997).

64. 64.

Berridge, K. C. 'Liking' and 'wanting' food rewards: brain substrates and roles in eating disorders. *Physiol. Behav.* **97**, 537–550 (2009).

65. 65.

Wise, R. A. Role of brain dopamine in food reward and reinforcement. *Philos. Trans. R. Soc. B* **361**, 1149–1158 (2006).

66. 66.

Becker, M. I. & Person, A. L. Cerebellar control of reach kinematics for endpoint precision. *Neuron* **103**, 335–348.e335 (2019).

67. 67.

Dacre, J. et al. A cerebellar-thalamocortical pathway drives behavioral context-dependent movement initiation. *Neuron* **109**, 2326–2338.e2328 (2021).

68. 68.

Darmohray, D. M., Jacobs, J. R., Marques, H. G. & Carey, M. R. Spatial and temporal locomotor learning in mouse cerebellum. *Neuron* **102**, 217–231.e214 (2019).

69. 69.

Frontera, J. L. et al. Bidirectional control of fear memories by cerebellar neurons projecting to the ventrolateral periaqueductal grey. *Nat. Commun.* **11**, 5207 (2020).

70. 70.

Gao, Z. et al. A cortico-cerebellar loop for motor planning. *Nature* **563**, 113–116 (2018).

71. 71.

Kelly, E. et al. Regulation of autism-relevant behaviors by cerebellar-prefrontal cortical circuits. *Nat. Neurosci.* **23**, 1102–1110 (2020).

72. 72.

Xiao, L., Bornmann, C., Hatstatt-Burkle, L. & Scheiffele, P. Regulation of striatal cells and goal-directed behavior by cerebellar outputs. *Nat. Commun.* **9**, 3133 (2018).

73. 73.

Giovannucci, A. et al. Cerebellar granule cells acquire a widespread predictive feedback signal during motor learning. *Nat. Neurosci.* **20**, 727–734 (2017).

74. 74.

Locke, T. M. et al. Dopamine D1 receptor-positive neurons in the lateral nucleus of the cerebellum contribute to cognitive behavior. *Biol. Psychiatry* **84**, 401–412 (2018).

75. 75.

Fujita, H., Kodama, T. & du Lac, S. Modular output circuits of the fastigial nucleus mediate diverse motor and nonmotor functions of the cerebellar vermis. *eLife* **9**, e58613 (2020).

76. 76.

DiFeliceantonio, A. G. et al. Supra-additive effects of combining fat and carbohydrate on food reward. *Cell Metab.* **28**, 33–44.e33 (2018).

77. 77.

Kralj-Hans, I., Baizer, J. S., Swales, C. & Glickstein, M. Independent roles for the dorsal paraflocculus and vermal lobule VII of the cerebellum in visuomotor coordination. *Exp. Brain Res.* **177**, 209–222 (2007).

78. 78.

Sobel, N. et al. Odorant-induced and sniff-induced activation in the cerebellum of the human. *J. Neurosci.* **18**, 8990–9001 (1998).

79. 79.

Wagner, M. J., Kim, T. H., Savall, J., Schnitzer, M. J. & Luo, L. Cerebellar granule cells encode the expectation of reward. *Nature* **544**, 96–100 (2017).

80. 80.

Nieoullon, A., Cheramy, A. & Glowinski, J. Release of dopamine in both caudate nuclei and both substantia nigrae in response to unilateral stimulation of cerebellar nuclei in the cat. *Brain Res.* **148**, 143–152 (1978).

81. 81.

Miller, J. L. et al. Enhanced activation of reward mediating prefrontal regions in response to food stimuli in Prader–Willi syndrome. *J. Neurol. Neurosurg. Psychiatry* **78**, 615–619 (2007).

82. 82.

Shapira, N. A. et al. Satiety dysfunction in Prader–Willi syndrome demonstrated by fMRI. *J. Neurol. Neurosurg. Psychiatry* **76**, 260–262 (2005).

83. 83.

Brady, R. O., Jr et al. Cerebellar-prefrontal network connectivity and negative symptoms in schizophrenia. *Am. J. Psychiatry* **176**, 512–520 (2019).

84. 84.

Halko, M. A., Farzan, F., Eldaief, M. C., Schmahmann, J. D. & Pascual-Leone, A. Intermittent theta-burst stimulation of the lateral cerebellum increases functional connectivity of the default network. *J. Neurosci.* **34**, 12049–12056 (2014).

85. 85.

Miterko, L. N. et al. Neuromodulation of the cerebellum rescues movement in a mouse model of ataxia. *Nat. Commun.* **12**, 1295 (2021).

86. 86.

Stoodley, C. J. et al. Altered cerebellar connectivity in autism and cerebellar-mediated rescue of autism-related behaviors in mice. *Nat. Neurosci.* **20**, 1744–1751 (2017).

## Acknowledgements

We thank H. Fujita, K. Gallagher and A. Thanawalla for comments on the manuscript. N.G. is supported by the National Science Foundation Graduate Research Fellowship Program (DGE-1845298). E.A. is supported by the National Institutes of Health (NIH) (DP2NS105555, R01NS111479 and U19NS112959), the Searle Scholars Program, The Pew Charitable Trusts, and the McKnight Foundation. O.M.S. is supported by the National University of Singapore. M.A.H. is supported by the NIH (R01MH111868; R56MH125995). R.O.B. is supported by the NIH (R01MH116170). L.M.H. is supported by the NIH (R01DK104772). A.L.A. is supported by the Monell Chemical Senses Center, NIH (R00DK119574), the Klingenstein-Simons Fellowship Award, the American Heart Association (857082) and the Penn Institute for Diabetes, Obesity, and Metabolism. J.N.B. is supported by the University of Pennsylvania School of Arts and Sciences, the American Diabetes Association (118IBS116), the American Heart Association (AHA 17SDG33400158), the Whitehall Foundation, the Klingenstein-Simons Fellowship Award and the NIH (1R01DK114104). A.I.C. and A.Y.T.L. were supported by the Warwick-NTU Neuroscience Programme. A.I.C., O.M.S. and T.H.C. are supported by the Singapore Ministry of Education (MOE2018-T2-1-065). A.I.C. and T.H.C. are

supported by the Singapore Ministry of Education (MOE2017-T3-1-002). J.N.B. and A.I.C. are supported by the NIH (1R01DK124801).

## Author information

### Affiliations

1. Department of Biology, University of Pennsylvania, Philadelphia, PA, USA

Aloysius Y. T. Low, Nitsan Goldstein, Jamie R. E. Carty, Ju Y. Choi, Alekso M. Miller, Clara Lenherr & J. Nicholas Betley

2. LKC School of Medicine, Nanyang Technological University, Singapore, Singapore

Jessica R. Gaunt, Alaric K. K. Yip & Toh Hean Ch'ng

3. Monell Chemical Senses Center, Philadelphia, PA, USA

Kuei-Pin Huang & Amber L. Alhadeff

4. School of Biological Sciences, Nanyang Technological University, Singapore, Singapore

Norliyana Zainolabidin & Helen S. T. Ho

5. Division of Neuroscience, King's College London, London, UK

Clara Lenherr

6. Molecular Neurobiology Laboratory, Salk Institute, San Diego, CA, USA

Nicholas Baltar & Eiman Azim

7. School of Public Health, National University of Singapore, Singapore, Singapore

October M. Sessions

8. Department of Pediatrics, University of Kansas Medical Center, Kansas City, KS, USA

Amanda S. Bruce

9. Department of Population Health, University of Kansas Medical Center, Kansas City, KS, USA

Laura E. Martin

10. Schizophrenia and Bipolar Disorder Research Program, McLean Hospital, Belmont, MA, USA

Mark A. Halko

11. Harvard Medical School, Boston, MA, USA

Mark A. Halko, Roscoe O. Brady Jr & Laura M. Holsen

12. Beth Israel Deaconess Medical Center, Boston, MA, USA

Roscoe O. Brady Jr

13. Division of Women's Health, Department of Medicine, Department of Psychiatry, Brigham and Women's Hospital, Boston, MA, USA

Laura M. Holsen

14. Department of Neuroscience, University of Pennsylvania, Philadelphia, PA, USA

Amber L. Alhadeff & J. Nicholas Betley

15. Center for Aging Research, Scintillon Institute, San Diego, CA, USA

Albert I. Chen

## Contributions

A.Y.T.L., A.I.C. and J.N.B. initiated the project and prepared the manuscript with comments from all authors. A.Y.T.L., N.G., J.R.G., K.-P.H., N.Z., A.K.K.Y., J.R.E.C., J.Y.C., A.M.M., H.S.T.H., C.L., L.M.H. and A.L.A. performed experiments. A.Y.T.L., N.G., J.R.G., E.A., O.M.S., T.H.C., A.S.B., L.E.M., M.A.H., R.O.B., L.M.H., A.L.A., A.I.C. and J.N.B. designed experiments and analysed data.

## Corresponding authors

Correspondence to [Albert I. Chen](#) or [J. Nicholas Betley](#).

## Ethics declarations

## Competing interests

The authors declare no competing interests.

## Additional information

**Peer review information** *Nature* thanks Dana Small, Larry Zweifel and the other, anonymous, reviewer(s) for their contribution to the peer review of this work. Peer reviewer reports are available.

**Publisher's note** Springer Nature remains neutral with regard to jurisdictional claims in published maps and institutional affiliations.

## Extended data figures and tables

### [Extended Data Fig. 1 fMRI paradigm for response to food cue.](#)

Subjects with Prader-Willi syndrome (PWS) and controls underwent two separate scanning sessions (top left, group): either during fasting or post-meal (bottom left, session). During each scanning session, participants were

presented with visual cues that alternate between food (muffin) and non-food (dog) categories (right, stimulus)<sup>8</sup>.

## **Extended Data Fig. 2 Neural activation pattern following food infusion and refeeding in mice.**

(a-c) Experimental design for Targeted Recombination of Activated Populations (TRAP) labelling of neurons activated by water infusion (IG water), Ensure infusion (IG Ensure) or refeeding (Refed) in *Fos2A::iCreER; Ai9* mice. (d-i) tdTomato expression in the DCN after water infusion (d; e, magnified of box in d), 1 kcal Ensure infusion (f; g, magnified of box in f), and chow refeeding (h; i, magnified of box in h). Scale bar, 500 µm (d, f, h), 100 µm (e, g, i). (j) Heatmap depicting the activated cells recombined in DCN subregions following infusion and refeeding (n = 9). (k-m) tdTomato expression in the nucleus tractus solitarius (NTS) 3 weeks after water infusion (k), 1 kcal Ensure infusion (l), and chow refeeding (m). Scale bar, 500 µm. (n-p) tdTomato expression in the paraventricular hypothalamic nucleus (PVH) 3 weeks after water infusion (n), 1 kcal Ensure infusion (o), and chow refeeding (p). Scale bar, 250 µm. (q-s) tdTomato expression in the arcuate hypothalamic nuclei (ARC) 3 weeks after water infusion (q), 1 kcal Ensure infusion (r), and chow refeeding (s). Scale bar, 250 µm. (t-v) tdTomato expression in the lateral parabrachial nucleus (LPBN) 3 weeks after water infusion (t), 1 kcal Ensure infusion (u), and chow refeeding (v). Scale bar, 250 µm. (w-y) tdTomato expression in the central amygdaloid nucleus (CEA) 3 weeks after water infusion (w), 1 kcal Ensure infusion (x), and chow refeeding (y). Scale bar, 500 µm. (z-bb) tdTomato expression in the bed nucleus of the stria terminalis (BNST) 3 weeks after water infusion (z), 1 kcal Ensure infusion (aa), and chow refeeding (bb). Scale bar, 250 µm. (cc) Heatmap depicting relative density of cells recombined following water and calorie intake (top), and 1 kcal Ensure infusion and refeeding (bottom, n = 9). (dd) Schematic depicting the DCN and key feeding brain regions that sense food cues and nutrients<sup>62</sup>. Statistical analysis in [Supplementary Table 1](#)

[Source data](#).

## Extended Data Fig. 3 Mapping the DCN subregions that suppress food intake.

(a) Schematic of the deep cerebellar nuclei. The lateral subnuclei of the anterior deep cerebellar nuclei (aDCN) are depicted in maroon (aDCN-LAT, consisting of Lat and LatPC, bregma -5.68 to -5.88 mm), interposed subnuclei of the aDCN are depicted in pink (aDCN-INT, consisting of IntA, IntDL, IntP, and IntPPC, bregma -6.00 to -6.35 mm). The posterior DCN is in grey (pDCN, consisting of IntP, IntPPC, Med, MedDL, and MedL, bregma -6.36 to -6.64 mm, see also e and g). (b) Distribution of cells expressing hM3D(Gq) across 9 DCN subnuclei in mice with hM3D(Gq) targeted to the lateral nucleus (aDCN-LAT) and mice with hM3D(Gq) targeted to the interposed nucleus (aDCN-INT). Mice with targeting to the LAT show a reduction in food intake following DREADD activation (aDCN-LAT in maroon, n = 5 mice, and aDCN-INT in pink, n=3 mice). (c) Schematised serial coronal sections depicting regions where hM3D expression results in food intake reduction (magenta). (d) Representative images of the entire DCN in a aDCN-LAT hM3D(Gq) mouse with hM3D(Gq) expression in the lateral nucleus. Scale bar, 2000  $\mu$ m. (e) Expression of mCherry (as control viral vector) in the aDCN (red: mCherry). Scale bar, 500  $\mu$ m. (f) Chow intake in mice with mCherry expression in the aDCN following vehicle or CNO treatment (n = 8, paired t-test,  $P = 0.539$ ). (g) hM3D(Gq) expression in the pDCN (red: hM3D(Gq)). Scale bar, 500  $\mu$ m. (h) Chow intake in mice with hM3D(Gq) expression in the pDCN following vehicle or CNO treatment (n = 12, paired t-test,  $P = 0.548$ ). (i) Chow intake in mice with mCherry expression in the pDCN following vehicle or CNO treatment (n=8, paired t-test,  $P = 0.722$ ). Data are expressed as mean  $\pm$  SEM. Lat, lateral; LatPC, lateral parvicellular; IntDL, interposed dorsolateral; IntA, interposed anterior nucleus; IntP, interposed posterior; IntPPC, interposed posterior parvicellular; MedDL, medial dorsolateral; Med, medial; MedL, medial lateral. Statistical analysis in [Supplementary Table 1](#)

[Source data](#).

## Extended Data Fig. 4 Neural activity in the aDCN suppresses food intake independent of hunger state with no compensatory

## metabolic changes.

(a) Experimental design: meal pattern measurements of 24-h food-deprived mice following vehicle or CNO i.p. administration. (b) Latency to first bite in food-deprived mice with hM3D(Gq) expression in the aDCN-LAT ( $n = 9$ ), aDCN-INT ( $n = 16$ ) or mCherry control in the aDCN ( $n = 8$ ) following vehicle or CNO treatment (two-way ANOVA interaction  $P < 0.001$ , main effect  $P = 0.005$ ; Holm-Sidak's,  $P < 0.001$ ). (c) Average meal duration during a 1-h chow intake assay following 24-h food deprivation in mice with hM3D(Gq) expression in the aDCN-LAT ( $n = 9$ ), aDCN-INT ( $n = 16$  mice), or control mCherry expression in the aDCN ( $n = 8$ ) following vehicle or CNO treatment (two-way ANOVA interaction  $P = 0.005$ , main effect  $P < 0.001$ ; Holm-Sidak's,  $P < 0.001$ ). (d) Rate of food intake during a 1-h chow intake assay following 24-h food deprivation in mice with hM3D expression in the aDCN-LAT ( $n = 9$ ), aDCN-INT ( $n = 16$ ), or control mCherry expression in the aDCN ( $n = 8$ ) following vehicle or CNO treatment (two-way ANOVA interaction  $P = 0.748$ ). (e) Experimental design: meal pattern measurements of *ad libitum* fed mice following vehicle or CNO i.p. administration. (f) Chow intake in *ad libitum* fed mice with hM3D(Gq) expression following vehicle or CNO treatment (aDCN-LAT:  $n = 9$ , aDCN-INT:  $n = 16$ , mCherry control:  $n = 8$ ; two-way ANOVA, interaction  $P = 0.001$ , main effect  $P = 0.006$ ; Holm-Sidak's,  $P < 0.001$ ). (g) Latency to first bite in *ad libitum* fed mice with hM3D(Gq) expression following vehicle or CNO treatment (aDCN-LAT:  $n = 9$ , aDCN-INT:  $n = 16$ , mCherry control:  $n = 8$ ; two-way ANOVA interaction  $P < 0.001$ , main effect  $P < 0.001$ ; Holm-Sidak's,  $P < 0.001$ ). (h) Chow intake in *ad libitum* fed mice with mCherry control or hM3D(Gq) expression in the pDCN following vehicle or CNO treatment (pDCN mCherry:  $n = 8$ , pDCN hM3D(Gq):  $n = 12$ ; two-way ANOVA interaction  $P = 0.358$ ). (i) Schematic of the metabolic monitoring experiment. (j) Energy expenditure (kcal) over a 48-h period in mice with mCherry control ( $n = 8$ ) or hM3D(Gq) ( $n = 7$ ) expression in the aDCN-LAT (unpaired t-test,  $P = 0.004$ ). (k) Energy intake (EI) and energy expenditure (EE) over 48-h period in mice with mCherry control or hM3D(Gq) expression in the aDCN-LAT following CNO treatment normalized to vehicle treatment ( $n = 7$  control, 8 aDCN-LAT-hM3D(Gq), repeated measures two-way ANOVA interaction  $P < 0.001$ , main effect  $P < 0.001$ ; Holm-Sidak's,  $P < 0.001$ ,  $P = 0.009$  (EE);  $P < 0.001$ ,  $P < 0.001$ ,  $P$

$< 0.001$ ,  $P = 0.006$  (EI)). Data are expressed as mean  $\pm$  SEM, two-sided  $P$  values, t-tests and post-hoc comparisons: \*\* $P < 0.01$ , \*\*\* $P < 0.001$ , ANOVA interaction:  $\infty\infty P < 0.01$ ,  $\infty\infty P < 0.001$ ; ANOVA main effect of group:  $\square P < 0.01$ ,  $\square\square P < 0.001$ . Statistical analysis in [Supplementary Table 1](#)

[Source data](#).

[Extended Data Fig. 5 aDCN activity suppresses food intake regardless of hedonic value of food.](#)

(a) Experimental timeline: 24-h food deprivation followed by measurements of chow intake over 12-h (top). Cumulative kcal of chow intake in food-deprived mice with hM3D(Gq) expression in the aDCN-LAT following vehicle or CNO treatment (bottom;  $n = 9$  hM3D(Gq); repeated measures two-way ANOVA interaction  $P < 0.001$ , main effect  $P < 0.001$ ; Holm-Sidak's,  $P = 0.094$  (30 min),  $P = 0.008$  (1 h),  $P < 0.001$  (2 h),  $P < 0.001$  (4h),  $P < 0.001$  (6h),  $P < 0.001$  (8 h),  $P < 0.001$  (10 h),  $P < 0.001$  (12 h)). (b) 12-h food intake in food-deprived mice expressing hM3D(Gq) in the aDCN-LAT ( $n = 9$  mice, paired t-test,  $P = 0.008$ ). (c) 12-h food intake in food-deprived mice expressing mCherry in the aDCN-LAT ( $n = 8$  mice, paired t-test,  $P = 0.391$ ). (d) Food intake during the first 2-h of refeeding in food-deprived mice expressing hM3D(Gq) in the aDCN-LAT ( $n = 9$  mice, paired t-test,  $P < 0.001$ ). (e) Food intake during the first 2-h of refeeding in food-deprived mice expressing mCherry in the aDCN-LAT ( $n = 8$  mice, paired t-test,  $P = 0.223$ ). (f) Experimental timeline: 24-h food deprivation followed by measurement of high fat high sugar (HFHS) diet intake over 12 h (top). Cumulative kcal of HFHS diet intake in food-deprived mice with hM3D(Gq) expression in the aDCN-LAT following vehicle or CNO treatment (bottom;  $n = 9$  hM3D(Gq) mice; two-way repeated measures ANOVA interaction  $P < 0.001$ , main effect  $P < 0.001$ ; Holm-Sidak's,  $P < 0.001$  (30-min),  $P < 0.001$  (1-h),  $P < 0.001$  (2-h),  $P < 0.001$  (4-h),  $P < 0.001$  (6-h),  $P < 0.001$  (8-h),  $P < 0.001$  (10-h),  $P < 0.001$  (12-h)). (g) 12-h HFHS diet intake in food-deprived mice expressing hM3D(Gq) in the aDCN-LAT ( $n = 9$  mice, paired t-test,  $P < 0.001$ ). (h) 12-h HFHS diet intake in food-deprived mice expressing mCherry in the aDCN-LAT ( $n = 8$  mice, paired t-test,  $P = 0.527$ ). (i) Calorie intake during the first 2-h of HFHS diet refeeding in food-deprived mice expressing hM3D(Gq) in the aDCN-LAT

(n = 9 mice, paired t-test,  $P < 0.001$ ). (j) Calorie intake during the first 2-h of HFHS diet refeeding in food-deprived mice expressing mCherry in the aDCN-LAT (n=9 mice, paired t-test,  $P = 0.686$ ). Data are expressed as mean  $\pm$  SEM, two-sided  $P$  values, t-tests and post-hoc comparisons: \*\* $P < 0.01$ , \*\*\* $P < 0.001$ , ANOVA interaction:  $\infty\infty P < 0.001$ ; ANOVA main effect of group:  $\alpha\alpha\alpha P < 0.001$ . Statistical analysis in [Supplementary Table 1](#)

[Source data](#).

### [Extended Data Fig. 6 Glutamatergic neurons in the DCN are activated by food intake.](#)

(a-h) Fluorescent *In Situ* Hybridization (FISH) histochemistry in the lateral nucleus of the DCN in food-deprived (a, b, e, f) and chow-refed mice (c, d, g, h) (red, *Homer1a*; green, *vGlut2*; blue, *vGAT* in b and d, *GlyT2* in f and h). Scale bars, 20  $\mu$ m. (i) *Homer1a* expression in excitatory (*vGlut2* $^+$ ) and inhibitory (*vGAT* $^+$  or *GlyT2* $^+$ ) DCN neurons following food deprivation or refeeding (n = 3 mice per group, two-way ANOVA main effect  $P < 0.001$ ; Holm-Sidak's,  $P = 0.034$ ). (j) Number of excitatory (*vGlut2* $^+$ ) and inhibitory (*vGAT* $^+$  or *GlyT2* $^+$ ) DCN neurons that express *Homer1a* following food deprivation or refeeding (n = 3 mice per group, two-way ANOVA main effect  $P = 0.009$ ; Holm-Sidak's,  $P = 0.023$ ). (k, l) Expression level (k) and number (l) of *Homer1a* $^+$  *vGlut2* $^+$  neurons within the 3 major cerebellar nuclei following food deprivation or refeeding (n = 3 mice per group, two-way ANOVA, expression level main effect  $P = 0.013$ , number main effect  $P = 0.010$ ; Holm-Sidak's, expression level,  $P = 0.006$ , number,  $P = 0.025$ ). Data are expressed as mean  $\pm$  SEM, two-sided  $P$  values, t-tests and post-hoc comparisons: \* $P < 0.05$ , \*\* $P < 0.01$ , ANOVA interaction:  $\infty\infty P < 0.001$ ; ANOVA main effect of group:  $\alpha P < 0.05$ ,  $\alpha\alpha\alpha P < 0.001$ . Statistical analysis in [Supplementary Table 1](#)

[Source data](#).

### [Extended Data Fig. 7 Gene expression gradient along the anterior-posterior axis of the DCN.](#)

(a) Experimental design of single nucleus RNA sequencing of DCN neurons. (b) Uniform Manifold Approximation and Projection for Dimension Reduction (UMAP) plot of cerebellar cell types derived from microdissection of the DCN and surrounding tissues. (c) Principal component (PC) 1 loadings of select class I and class II defining genes expressed by *vGluT2*<sup>+</sup> DCN neurons. (d) *Celʃ* (red) and *Spp1* (blue) expression level in *vGluT2*<sup>+</sup> neurons in the DCN, 492 neurons (two-way ANOVA interaction  $P < 0.001$ ; Holm-Sidak's,  $P < 0.001$ ,  $P < 0.001$ ,  $P < 0.001$ ,  $P < 0.001$ ). (e, f) *vGluT2* (red, e, f), *Spp1* (green, e) and *Celʃ* (green, f) expression in the aDCN. Scale bar, 25  $\mu\text{m}$ . (g) PC embedding of *Miat* expression, fluorescent in situ hybridization (FISH) and quantification of *Miat* levels in *vGluT2*<sup>+</sup> neurons in the three major cerebellar nuclei ( $n = 1,434$  neurons, one-way ANOVA  $P < 0.001$ ; Holm-Sidak's,  $P = 0.165$ ,  $P < 0.001$ ,  $P < 0.001$ ). (h) PC embedding of *Crhr1* expression, FISH, and quantification of *Crhr1* levels in *Miat*<sup>+</sup> neurons in the three major cerebellar nuclei ( $n = 1,434$  neurons, one-way ANOVA  $P < 0.001$ ; Holm-Sidak's,  $P = 0.003$ ,  $P = 0.006$ ,  $P < 0.001$ ). (i) PC embedding of *Dpp10* expression, FISH, and quantification of *Dpp10* levels in *Celʃ*<sup>+</sup> neurons in the three major cerebellar nuclei ( $n = 2,261$  neurons, one-way ANOVA  $P < 0.001$ ; Holm-Sidak's,  $P < 0.001$ ,  $P < 0.001$ ,  $P < 0.001$ ). (j) PC embedding of *Unc5d* expression, FISH, and quantification of *Unc5d* levels in *Celʃ*<sup>+</sup> neurons in the three major cerebellar nuclei ( $n = 2,261$  neurons, one-way ANOVA  $P < 0.001$ ; Holm-Sidak's,  $P < 0.001$ ,  $P < 0.001$ ,  $P < 0.001$ ). Scale bar, 100  $\mu\text{m}$ . (k) FISH of *Spp1* and *Celʃ* expression in *vGluT2*<sup>+</sup> neurons of the interposed nucleus (left image: red, *vGluT2*; green, *Spp1*; right image: red, *vGluT2*; green, *Celʃ*;  $n = 3$ , unpaired t-test,  $P < 0.001$ ). Scale bar, 100  $\mu\text{m}$ . (l) FISH of *Spp1* and *Celʃ* expression in *vGluT2*<sup>+</sup> neurons in the medial nucleus (left image: red, *vGluT2*; green, *Spp1*; right image: red, *vGluT2*; green, *Celʃ*;  $n = 3$ , unpaired t-test,  $P < 0.001$ ). Scale bar, 100  $\mu\text{m}$ . (m) *Spp1* expression levels in *vGluT2*<sup>+</sup> neurons across the three major cerebellar nuclei ( $n = 3$ , one-way ANOVA  $P < 0.001$ ; Holm-Sidak's,  $P = 0.946$ ,  $P < 0.001$ ,  $P < 0.001$ ). (n) *Celʃ* expression levels in *vGluT2*<sup>+</sup> neurons across the three major cerebellar nuclei ( $n = 3$ , one-way ANOVA  $P < 0.001$ ; Holm-Sidak's,  $P = 0.026$ ,  $P < 0.001$ ,  $P < 0.001$ ). (o-r) Quantification of *Spp1*<sup>+</sup> (o), *Celʃ*<sup>+</sup> (p), *Spp1*<sup>+</sup>*Celʃ*<sup>+</sup> (q) and *Spp1*<sup>-</sup>*Celʃ*<sup>-</sup> (r) *vGluT2*<sup>+</sup> neurons across the three major cerebellar nuclei ( $n = 3$ , one-way ANOVA (o)  $P = 0.002$ , (p)

$P < 0.001$ ; Holm-Sidak's, (o)  $P = 0.190$ ,  $P = 0.005$ ,  $P = 0.002$ , (p)  $P = 0.982$ ,  $P < 0.001$ ,  $P < 0.001$ , lateral versus interposed, lateral versus medial, and interposed versus medial, respectively). Data are expressed as mean  $\pm$  SEM, two-sided  $P$  values, post-hoc comparisons: \* $P < 0.05$ , \*\* $P < 0.01$ , \*\*\* $P < 0.001$ ; ANOVA interaction:  $\infty\infty\infty P < 0.001$ . Statistical analysis in [Supplementary Table 1](#)

[Source data](#).

## **Extended Data Fig. 8 Molecular and topographical distinctions of DCN neurons that respond to food intake.**

(a-f) Expression of activity-regulated transcript *Homer1a*<sup>63</sup> (red) in the three major cerebellar nuclei following food deprivation (a, c, e) or refeeding (b, d, f). (g-l) *Spp1* expression (green) in *vGluT2*<sup>+</sup> neurons (blue) (g, i, k), and colocalised *Spp1* (cyan, *Spp1*<sup>+</sup>*vGluT2*<sup>+</sup> neurons) (h, j, l) in the three major cerebellar nuclei. (m-r) *Celf4* expression (blue) in *vGluT2*<sup>+</sup> neurons (red) (m, o, q), and colocalised *Celf4* (magenta, *Celf4*<sup>+</sup>*vGluT2*<sup>+</sup> neurons) (n, p, r) in the three major cerebellar nuclei. Scale bar, 100  $\mu$ m. (s) Summary of the expression of *Spp1* and *Celf4* and the distribution of *Homer1a*<sup>+</sup> DCN neurons. (t) Schematic of fibre photometry system. (u-w) Fibre targeting aDCN-LAT glutamatergic neurons in *vGluT2::Cre* mouse (u), expression of GCaMP6s (green) and *vGluT2* (red) (v, w). Scale bar, 20  $\mu$ m. (x-z) Heatmaps depicting  $\Delta F/F$  of GCaMP6 signals in the aDCN-LAT glutamatergic neurons of *ad libitum* fed (x) and food-deprived (y) mice response to chow, and *ad libitum* fed mice response to non-food object (z, marble). Signals are aligned to the introduction of chow or non-food object (red line) ( $n = 7$  mice). (aa) Average  $\Delta F/F$  of GCaMP6 signals in the aDCN-LAT glutamatergic neurons (490 nm, green, and control 405 nm, magenta). Signals are aligned to the introduction of non-food object (red line). Dark line represents the mean and lighter shaded area represents SEMs ( $n = 7$ ). (bb-cc) Mean (bb) and max (cc)  $\Delta F/F$  GCaMP6s signals of aDCN-LAT glutamatergic neurons in response to chow, in *ad libitum* fed (grey) and food-deprived (red) mice, and response to non-food object in *ad libitum* fed mice ( $n=7$ , one-way ANOVA (bb)  $P < 0.001$ , (cc)  $P < 0.001$ ; Holm-Sidak's, (bb)  $P < 0.006$ ,  $P = 0.475$ ,  $P < 0.003$ , (cc)  $P < 0.009$ ,  $P = 0.651$ ,  $P = 0.011$ , *ad*

*libitum* fed chow versus food deprivation chow, *ad libitum* fed chow versus non-food, food deprivation chow versus non-food, respectively). Data are expressed as mean  $\pm$  SEM, two-sided *P* values, post-hoc comparisons: \**P* < 0.05, \*\**P* < 0.01. Statistical analysis in [Supplementary Table 1](#)

[Source data](#).

**Extended Data Fig. 9 Activation of arcuate AgRP neurons does not fully restore food intake suppression mediated by aDCN-LAT activation.**

(a) Schematic depicting hM3D(Gq) expression in the aDCN-LAT, ChR2 expression and fibre implant in the arcuate nucleus (ARC) of a *AgRP::Cre; Ai32* mouse for either individual or simultaneous activation.(b, c) ChR2-eYFP expression in AgRP ARC neurons (b) and hM3d(Gq) expression in the aDCN (c). Scale bar, 500  $\mu$ m in b, 1000  $\mu$ m in c. (d) Chow intake following AgRP neuron activation in *ad libitum* state (blue), aDCN neuron activation in food-deprived state (red), or AgRP and aDCN neuron activation in food-deprived state (pink) ( $n = 11$ , repeated measures one-way ANOVA, *P* = 0.001; Holm-Sidak's, *P* < 0.001, *P* < 0.001, *P* = 0.024). Data are expressed as mean  $\pm$  SEM, two-sided *P* values, post-hoc comparisons: \**P* < 0.05, \*\**P* < 0.01, \*\*\**P* < 0.001. Statistical analysis in [Supplementary Table 1](#)

[Source data](#).

**Extended Data Fig. 10 Activation of aDCN neurons robustly increases striatal dopamine signalling that correlates with reduced food intake.**

(a) Schematic depicting hM3D(Gq) expression in the DCN combined with GRAB<sup>DA</sup> expression<sup>41</sup> and fibre implant in the ventral striatum which receives projections from the ventral tegmental area (VTA) dopamine (DA) neurons<sup>64,65</sup>. (b) GRAB<sup>DA</sup> expression and fibre placement in the ventral striatum. Scale bar, 1000  $\mu$ m. (c, d) Average  $\Delta F/F$  of GRAB<sup>DA</sup> signals in the ventral striatum of food-deprived mCherry control (c) or aDCN-LAT

hM3D(Gq) (d) mice treated with vehicle or CNO. Signals are aligned to the vehicle or CNO injection (red line). Dark line represents the mean and lighter shaded area represents SEMs. Corresponding heatmaps (right) depict  $\Delta F/F$  of GRAB<sup>DA</sup> signals in each mouse ( $n = 6$  control mice, grey;  $n = 6$  hM3D(Gq) aDCN-LAT mice, green). (e) Average  $\Delta F/F$  of GRAB<sup>DA</sup> signals in 3-min bins ( $n = 6$  control mice, grey;  $n = 6$  hM3D(Gq) aDCN-LAT mice, repeated measures two-way ANOVA interaction  $P < 0.001$ , main effect  $P < 0.001$ ; Holm-Sidak's,  $P = 0.027/ = 0.397/ = 0.625$  (12-15 min),  $P < 0.001/ < 0.001/ < 0.001$  (15-18 min),  $P < 0.001/ < 0.001/ < 0.001$  (18-21 min),  $P < 0.001/ < 0.001/ < 0.001$  (21-24 min),  $P < 0.001/ < 0.001/ < 0.001$  (24-27 min),  $P < 0.001/ < 0.001/ < 0.001$  (27-30 min), hM3D(Gq) CNO to hM3D(Gq) vehicle/control CNO/control vehicle respectively). (f) Maximum  $\Delta F/F$  of GRAB<sup>DA</sup> signals in the ventral striatum of vehicle or CNO treated food-deprived mice with aDCN-LAT hM3D(Gq) ( $n = 6$ , paired t-test,  $P = 0.011$ ). (g) Mean  $\Delta F/F$  of GRAB<sup>DA</sup> signals in the ventral striatum ( $n = 6$ , paired t-test,  $P = 0.002$ ). (h) Maximum  $\Delta F/F$  of GRAB<sup>DA</sup> signals in the ventral striatum of vehicle or CNO treated food-deprived mice with aDCN mCherry control mice ( $n = 6$ , paired t-test,  $P = 0.242$ ). (i) Mean  $\Delta F/F$  of GRAB<sup>DA</sup> signals in the ventral striatum of vehicle or CNO treated food-deprived mice with aDCN mCherry control mice ( $n = 6$ , paired t-test,  $P = 0.418$ ). (j) Scatter plot comparing changes in GRAB<sup>DA</sup> signals to amount of chow consumed in 1 h following activation of the aDCN in hM3D(Gq)-expressing mice treated with CNO ( $n = 13$ , Pearson correlation). (k) Average  $\Delta F/F$  of GRAB<sup>DA</sup> signals in the ventral striatum of food-deprived aDCN-INT hM3D(Gq) mice treated with vehicle or CNO. Signals are aligned to the vehicle or CNO injection (red line). Dark line represents the mean and lighter shaded area represents SEMs. Corresponding heatmaps (right) depict  $\Delta F/F$  of GRAB<sup>DA</sup> signals in each mouse ( $n = 7$ ). (l) Average  $\Delta F/F$  of GRAB<sup>DA</sup> signals in 3-min bins following vehicle or CNO treatment of the aDCN-INT with hM3D(Gq) ( $n = 7$ , repeated measures two-way ANOVA interaction  $P = 0.301$ ). (m) Maximum  $\Delta F/F$  of GRAB<sup>DA</sup> signals in the ventral striatum of vehicle or CNO treated food-deprived mice with aDCN-INT hM3D(Gq) mice ( $n = 7$ , paired t-test,  $P = 0.410$ ). (n) Mean  $\Delta F/F$  of GRAB<sup>DA</sup> signals in the ventral striatum of vehicle or CNO treated food-deprived mice with aDCN-INT hM3D(Gq) mice ( $n = 7$ , paired t-test,  $P = 0.367$ ). Data are expressed as mean  $\pm$  SEM, two-sided  $P$  values, t-

tests and post-hoc comparisons:  $*P < 0.05$ ,  $**P < 0.01$ ,  $***P < 0.001$ ; ANOVA interaction:  $\infty\infty P < 0.001$ ; ANOVA main effect of group:  $\alpha\alpha\alpha P < 0.001$ . Statistical analysis in [Supplementary Table 1](#)

[Source data](#).

**Extended Data Fig. 11 Selective activation of glutamatergic aDCN neurons is sufficient to induce striatal dopamine surge and suppression of food intake.**

(a) Schematic depicting hM3D(Gq) expression in the DCN combined with GRAB<sup>DA</sup> expression and fibre implant in the striatum of a *vGluT2::Cre* mouse. (b-d) IHC analysis of Cre dependent hM3D(Gq) expression in the DCN of *vGluT2::Cre* mouse (green, vGluT2, red, hM3D(Gq), blue, DAPI). Scale bar, 25  $\mu$ m in b-d. (e) Average  $\Delta F/F$  of GRAB<sup>DA</sup> signals in the ventral striatum of food-deprived mice expressing hM3D(Gq) in glutamatergic neurons of the aDCN-LAT following vehicle or CNO injection. Signals are aligned to the vehicle or CNO injection (red line). Dark line represents the mean and lighter shaded area represents SEMs. Corresponding heatmaps (right) depict  $\Delta F/F$  of GRAB<sup>DA</sup> signals in each mouse ( $n = 7$ ). (f) Average  $\Delta F/F$  of GRAB<sup>DA</sup> signals in the ventral striatum of food-deprived mice expressing hM3D(Gq) in glutamatergic neurons of the aDCN-INT following vehicle or CNO injection. Signals are aligned to the vehicle or CNO injection (red line). Dark line represents the mean and lighter shaded area represents SEMs. Corresponding heatmaps (right) depict  $\Delta F/F$  of GRAB<sup>DA</sup> signals in each mouse ( $n = 6$ ). (g) Average  $\Delta F/F$  of GRAB<sup>DA</sup> signals in 3-min bins of food-deprived mice expressing hM3D(Gq) in glutamatergic neurons of the aDCN-INT or aDCN-LAT ( $n = 7$  *vGluT2* aDCN-LAT mice, green,  $n = 6$  *vGluT2* aDCN-INT mice, grey, two-way ANOVA, interaction  $P < 0.001$ , main effect  $P < 0.001$ ; Holm-Sidak's,  $P = 0.001/0.001/0.001$  (9-12 min),  $P < 0.001/0.001/0.001$  (12-15 min),  $P < 0.001/0.001/0.001$  (15-18 min),  $P < 0.001/0.001/0.001$  (18-21 min),  $P < 0.001/0.001/0.001$  (21-24 min),  $P < 0.001/0.001/0.001$  (24-27 min),  $P < 0.001/0.001/0.001$  (27-30 min), aDCN-LAT CNO to vehicle/aDCN-INT CNO/aDCN-INT vehicle respectively). (h) Maximum  $\Delta F/F$  GRAB<sup>DA</sup> signals in the ventral striatum

of food-deprived mice expressing hM3D(Gq) in glutamatergic neurons of the aDCN-LAT following vehicle or CNO treatment ( $n = 7$ , paired t-test,  $P < 0.001$ ). (i) Mean  $\Delta F/F$  GRAB<sup>DA</sup> signals in the ventral striatum of food-deprived mice expressing hM3D(Gq) in glutamatergic neurons of the aDCN-LAT following vehicle or CNO treatment ( $n = 7$ , paired t-test,  $P = 0.001$ ). (j) Maximum  $\Delta F/F$  GRAB<sup>DA</sup> signals in the ventral striatum of food-deprived mice expressing hM3D(Gq) in glutamatergic neurons of the aDCN-INT following vehicle or CNO treatment ( $n = 6$ , paired t-test,  $P = 0.644$ ). (k) Mean  $\Delta F/F$  GRAB<sup>DA</sup> signals in the ventral striatum of food-deprived mice expressing hM3D(Gq) in glutamatergic neurons of the aDCN-INT following vehicle or CNO treatment ( $n = 6$ , paired t-test,  $P = 0.367$ ). (l) Maximum  $\Delta F/F$  GRAB<sup>DA</sup> signals in the striatum following non-specific aDCN-LAT activation or vGluT2<sup>+</sup> aDCN-LAT neuron activation (aDCN-LAT:  $n = 6$  mice, vGluT2 aDCN-LAT:  $n = 7$ , unpaired t-test,  $P = 0.250$ ). (m) Mean  $\Delta F/F$  GRAB<sup>DA</sup> signals in the striatum of following non-specific aDCN-LAT activation or vGluT2<sup>+</sup> aDCN-LAT neuron activation (aDCN-LAT:  $n = 6$  mice, vGluT2 aDCN-LAT:  $n = 7$ , unpaired t-test,  $P = 0.323$ ). (n) Plot of GRAB<sup>DA</sup> signals and corresponding food intake in food-deprived mice treated following glutamatergic aDCN activation ( $n = 13$ , Pearson correlation). Solid line indicates the linear trend line fit to the data. Data are expressed as mean  $\pm$  SEM, two-sided  $P$  values, t-tests and post-hoc comparisons: \*\* $P < 0.01$ , \*\*\* $P < 0.001$ ; ANOVA interaction:  $\infty\infty\infty P < 0.001$ ; ANOVA main effect of group:  $\alpha\alpha\alpha P < 0.001$ . Statistical analysis in [Supplementary Table 1](#).

### [Source data](#)

### [\*\*Extended Data Fig. 12 Increased striatal dopamine suppresses food intake.\*\*](#)

(a) Schematic depicting hM3D(Gq) expression in the VTA of a *DAT::Cre* mouse, and GRAB<sup>DA</sup> expression and fibre implant in the ventral striatum. (b-c) Representative images of hM3D(Gq) expression in the VTA (b), and GRAB<sup>DA</sup> expression and fibre track in the ventral striatum (c) of a *DAT::Cre* mouse. Scale bar, 500  $\mu m$  in B, 200  $\mu m$  in C. (d) Average  $\Delta F/F$  of GRAB<sup>DA</sup> signals in 3-min bins following VTA neuron activation with

vehicle and varying concentrations of CNO (0.025 mg/Kg, 0.25 mg/Kg, 1 mg/Kg and 2.5 mg/Kg; n = 8 per group, repeated measures two-way ANOVA interaction  $P < 0.001$ , main effect  $P < 0.001$ ; Holm-Sidak's). (e) Net area under curve  $\Delta F/F$  of GRAB<sup>DA</sup> signals following VTA neuron activation with vehicle and varying concentrations of CNO (0.025 mg/Kg, 0.25 mg/Kg, 1 mg/Kg and 2.5 mg/Kg; n = 8 per group, repeated measures one-way ANOVA  $P < 0.001$ ; Holm-Sidak's,  $P = 0.012$  (vehicle versus 0.025 mg/Kg),  $P = 0.010$  (vehicle versus 0.25 mg/Kg),  $P = 0.023$  (vehicle versus 1.0 mg/Kg),  $P = 0.010$  (vehicle versus 2.5 mg/Kg)). (f) Food intake of food-deprived mice following VTA neuron activation with vehicle and varying concentrations of CNO (0.025 mg/Kg, 0.25 mg/Kg, 1 mg/Kg and 2.5 mg/Kg; n = 8 per group, repeated measures one-way ANOVA  $P < 0.001$ ; Holm-Sidak's,  $P < 0.001$  (vehicle versus 0.025 mg/Kg),  $P < 0.001$  (vehicle versus 0.25 mg/Kg),  $P < 0.001$  (vehicle versus 1.0 mg/Kg),  $P < 0.001$  (vehicle versus 2.5 mg/Kg)). (g) Plot of GRAB<sup>DA</sup> signals and corresponding food intake in food-deprived mice treated following VTA neuron activation (n = 8 per group, Pearson correlation). Solid line indicates the linear trend line fit to the data. (h) Average  $\Delta F/F$  of GRAB<sup>DA</sup> signals from 0 to 30 min following treatment with vehicle and varying concentrations of CNO (n = 8 per group, repeated measures one-way ANOVA  $P < 0.001$ ; Holm-Sidak's,  $P = 0.004$  (vehicle versus 0.025 mg/Kg),  $P = 0.004$  (vehicle versus 0.25 mg/Kg),  $P = 0.004$  (vehicle versus 1.0 mg/Kg),  $P = 0.004$  (vehicle versus 2.5 mg/Kg)). (i) Maximum  $\Delta F/F$  of GRAB<sup>DA</sup> signals following treatment with vehicle and varying concentrations of CNO (n = 8 per group, repeated measures one-way ANOVA  $P = 0.023$ ; Holm-Sidak's,  $P = 0.034$  (vehicle versus 2.5 mg/Kg)). (j) Average  $\Delta F/F$  of GRAB<sup>DA</sup> signals during presentation of food in fasted mice following treatment with vehicle and varying concentrations of CNO (0.025, 0.25, 1.0 and 2.5 mg/Kg). Signals are aligned to food presentation. Dark lines represent mean values and lighter shaded areas represent SEM (n = 8). (k) Heatmaps reporting  $\Delta F/F$  of GRAB<sup>DA</sup> signals in individual mice in (j) (n = 8). (l) Maximum  $\Delta F/F$  of GRAB<sup>DA</sup> signals during food presentation in mice following treatment with vehicle and varying concentrations of CNO (n = 8 per group, one-way ANOVA  $P = 0.0117$ ; Holm-Sidak's,  $P = 0.0389$  (vehicle versus 0.25 mg/Kg),  $P = 0.0056$  (vehicle versus 1.0 mg/Kg),  $P = 0.0121$  (vehicle versus 2.5 mg/Kg)). (m) Scatter plot

depicting the maximal  $\Delta F/F$  GRAB<sup>DA</sup> response to food following pre-stimulation of VTA DA neurons and the associated amount of food intake following pre-stimulation of VTA DA neurons ( $n = 8$  per group, Pearson correlation,  $P < 0.01$ ). Solid line shows the linear trend line fit to the data. (n-p) Images of hM4D(Gi) expression (red) in TH<sup>+</sup>, VTA neurons (green) of a *DAT*::Cre mouse (n). Higher magnification of white box (o-p). Scale bar, 500  $\mu\text{m}$  (n), 50  $\mu\text{m}$  (p). (q) Neurons transduced with hM4D(Gi) in the VTA and SNC ( $n = 3, 1047, 2745, 2710$  neurons each mouse, unpaired t-test,  $P = 0.02$ ). (r) Average  $\Delta F/F$  of DA signals in aDCN-LAT hM3D(Gq) mice and aDCN-LAT hM3D(Gq); VTA hM4D(Gi) mice ( $n = 6$  per group, unpaired t-test,  $P = 0.003$ ). (g) Distance travelled by aDCN-LAT hM3D(Gq) mice and aDCN-LAT hM3D(Gq); VTA hM4D(Gi) mice during a 10-min open field session ( $n = 6$  and 7, respectively, unpaired t-test,  $P = 0.382$ ). Data are expressed as mean  $\pm$  SEM, two-sided  $P$  values, t-tests and post-hoc comparisons: \* $P < 0.05$ , \*\* $P < 0.01$ , \*\*\* $P < 0.001$ ; ANOVA interaction:  $\infty\infty P < 0.001$ ; ANOVA main effect of group:  $\alpha\alpha\alpha P < 0.001$ . SNC, substantia nigra pars compacta; TH, tyrosine hydroxylase; VTA, ventral tegmental area. Statistical analysis in [Supplementary Table 1](#).

#### [Source data](#)

### [Extended Data Fig. 13 Proposed role of the cerebellum in feeding control.](#)

The cerebellum is well-positioned to integrate homeostatic satiation signals and is capable of orchestrating adaptive feeding responses by modulating motor, cognitive, affective and endocrine functions<sup>20,66,67,68,69,70,71,72,73,74,75</sup>. Visual, gustatory and olfactory inputs are all known to activate the cerebellum<sup>76,77,78</sup> which could provide salience update to control appetitive drive. It functions as a comparator of physiological nutrient state (interoception) and post-ingestion nutritional outcome (nutrient feedback) to fine-tune predictive reward signals (reward network)<sup>79</sup> and ultimately influence meal size (feeding network). While cerebellar output has been shown to influence VTA neuron activity<sup>12,80</sup>, our observed changes in DA signalling are tightly associated with decreases in food intake, suggesting a dedicated role of the cerebellum in regulating DA

circuits that influence feeding that is distinct from motor<sup>80</sup> or social<sup>12</sup> behaviours. Based on our mechanistic studies into the changes in the reward system mediated by the cerebellum, it is possible that previously discovered differences between PWS and control subjects arise because of cerebellar alterations<sup>8,81,82</sup>. In response to a predicted meal size (predicted nutritional reward outcome) by either food cues or food, cerebellar activity increases dopamine efflux that blunts dopamine transients. Consequently, the reward value of consuming food reduces and meals are terminated. In PWS patients<sup>8,81,82</sup>, food-dependent cerebellar activity is absent and thus, dopamine transients remain regardless of amount of food consumed, leading to excessive eating. Conversely, in dopamine-deficient animals, there is a complete absence of drive to eat<sup>14</sup>. A better understanding of the mechanisms and circuits underlying cerebellar-mediated behaviours can guide brain stimulation strategies to control food intake recently shown to have the capability of ameliorating symptoms for disorders associated with the cerebellum<sup>83,84,85,86</sup>.

## Supplementary information

### Supplementary Table 1

Details of statistics used and statistical results. Related to Figs. 1–4, and Extended Data Figs. 2–12.

### Reporting Summary

### Peer Review File

## Source data

### Source Data Fig. 1

### Source Data Fig. 2

### Source Data Fig. 3

[\*\*Source Data Fig. 4\*\*](#)

[\*\*Source Data Extended Data Fig. 2\*\*](#)

[\*\*Source Data Extended Data Fig. 3\*\*](#)

[\*\*Source Data Extended Data Fig. 4\*\*](#)

[\*\*Source Data Extended Data Fig. 5\*\*](#)

[\*\*Source Data Extended Data Fig. 6\*\*](#)

[\*\*Source Data Extended Data Fig. 7\*\*](#)

[\*\*Source Data Extended Data Fig. 8\*\*](#)

[\*\*Source Data Extended Data Fig. 9\*\*](#)

[\*\*Source Data Extended Data Fig. 10\*\*](#)

[\*\*Source Data Extended Data Fig. 11\*\*](#)

[\*\*Source Data Extended Data Fig. 12\*\*](#)

## Rights and permissions

[Reprints and Permissions](#)

## About this article

### Cite this article

Low, A.Y.T., Goldstein, N., Gaunt, J.R. *et al.* Reverse-translational identification of a cerebellar satiation network. *Nature* **600**, 269–273

(2021). <https://doi.org/10.1038/s41586-021-04143-5>

- Received: 14 March 2021
- Accepted: 14 October 2021
- Published: 17 November 2021
- Issue Date: 09 December 2021
- DOI: <https://doi.org/10.1038/s41586-021-04143-5>

## Share this article

Anyone you share the following link with will be able to read this content:

[Get shareable link](#)

Sorry, a shareable link is not currently available for this article.

[Copy to clipboard](#)

Provided by the Springer Nature SharedIt content-sharing initiative

## Further reading

- [\*\*Cerebellar neurons that curb food consumption\*\*](#)
  - Richard Simerly
  - Ralph DiLeone

*Nature* (2021)

## [\*\*Cerebellar neurons that curb food consumption\*\*](#)

- Richard Simerly
- Ralph DiLeone

# News & Views 17 Nov 2021

---

This article was downloaded by **calibre** from <https://www.nature.com/articles/s41586-021-04143-5>

| [Section menu](#) | [Main menu](#) |

- Article
- [Published: 10 November 2021](#)

# Allometric rules for mammalian cortical layer 5 neuron biophysics

- [Lou Beaulieu-Laroche](#)<sup>1</sup>,
- [Norma J. Brown](#)<sup>1</sup>,
- [Marissa Hansen](#)<sup>1</sup>,
- [Enrique H. S. Toloza](#)<sup>1,2,3</sup>,
- [Jitendra Sharma](#)<sup>4,5</sup>,
- [Ziv M. Williams](#) [ORCID: orcid.org/0000-0002-0017-0048](#)<sup>6</sup>,
- [Matthew P. Frosch](#)<sup>7</sup>,
- [Garth Rees Cosgrove](#)<sup>8</sup>,
- [Sydney S. Cash](#)<sup>9</sup> &
- [Mark T. Harnett](#) [ORCID: orcid.org/0000-0002-5301-1139](#)<sup>1</sup>

[Nature](#) volume 600, pages 274–278 (2021)

- 11k Accesses
- 532 Altmetric
- [Metrics details](#)

## Subjects

- [Evolution](#)
- [Ion channels in the nervous system](#)

## Abstract

The biophysical properties of neurons are the foundation for computation in the brain. Neuronal size is a key determinant of single neuron input–output features and varies substantially across species<sup>1,2,3</sup>. However, it is unknown whether different species adapt neuronal properties to conserve how single neurons process information<sup>4,5,6,7</sup>. Here we characterize layer 5 cortical pyramidal neurons across 10 mammalian species to identify the allometric relationships that govern how neuronal biophysics change with cell size. In 9 of the 10 species, we observe conserved rules that control the conductance of voltage-gated potassium and HCN channels. Species with larger neurons, and therefore a decreased surface-to-volume ratio, exhibit higher membrane ionic conductances. This relationship produces a conserved conductance per unit brain volume. These size-dependent rules result in large but predictable changes in somatic and dendritic integrative properties. Human neurons do not follow these allometric relationships, exhibiting much lower voltage-gated potassium and HCN conductances. Together, our results in layer 5 neurons identify conserved evolutionary principles for neuronal biophysics in mammals as well as notable features of the human cortex.

This is a preview of subscription content

## Access options

Subscribe to Journal

Get full journal access for 1 year

\$199.00

only \$3.90 per issue

[Subscribe](#)

All prices are NET prices.

VAT will be added later in the checkout.

Tax calculation will be finalised during checkout.

Rent or Buy article

Get time limited or full article access on ReadCube.

from \$8.99

[Rent or Buy](#)

All prices are NET prices.

### **Additional access options:**

- [Log in](#)
- [Learn about institutional subscriptions](#)

**Fig. 1: Highly variable neuron size and input–output properties across species.**

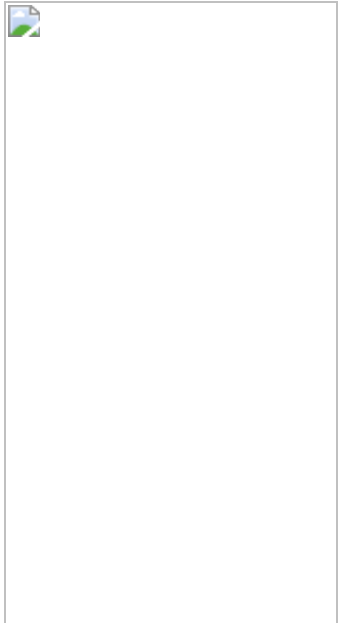


**Fig. 2: Dendritic input–output properties are not conserved across species.**

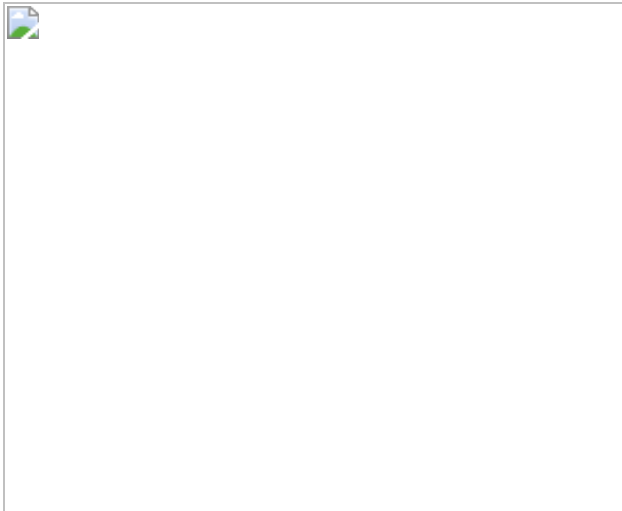
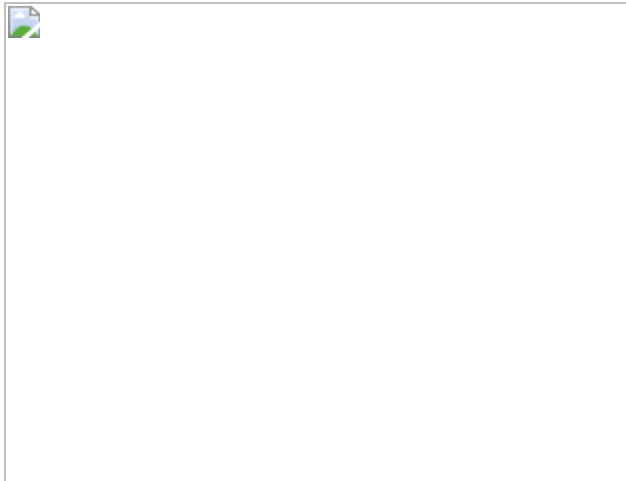


**Fig. 3: Ionic conductance increases with size except in human neurons.**



**Fig. 4: Humans are an exception to the allometric relationship that normalizes ionic conductance per brain volume.**



## Data availability

All data generated and supporting the findings of this study are presented in the paper. Additional information will be made available upon reasonable request.

## References

1. 1.

Elston, G. N., Benavides-Piccione, R. & DeFelipe, J. The pyramidal cell in cognition: a comparative study in human and monkey. *J. Neurosci.* **21**, RC163 (2001).

2. 2.

Mohan, H. et al. Dendritic and axonal architecture of individual pyramidal neurons across layers of adult human neocortex. *Cereb. Cortex* **25**, 4839–4853 (2015).

3. 3.

Jacobs, B. et al. Comparative morphology of gigantopyramidal neurons in primary motor cortex across mammals. *J. Comp. Neurol.* **526**, 496–536 (2018).

4. 4.

Beaulieu-Laroche, L. et al. Enhanced dendritic compartmentalization in human cortical neurons. *Cell* **175**, 643–651 (2018).

5. 5.

Gidon, A. et al. Dendritic action potentials and computation in human layer 2/3 cortical neurons. *Science* **367**, 83–87 (2020).

6. 6.

Kalmbach, B. E. et al. h-Channels contribute to divergent intrinsic membrane properties of supragranular pyramidal neurons in human versus mouse cerebral cortex. *Neuron* **100**, 1194–1208 (2018).

7. 7.

Verhoog, M. B. et al. Mechanisms underlying the rules for associative plasticity at adult human neocortical synapses. *J. Neurosci.* **33**, 17197–17208 (2013).

8. 8.

Hattox, A. M. & Nelson, S. B. Layer V neurons in mouse cortex projecting to different targets have distinct physiological properties. *J. Neurophysiol.* **98**, 3330–3340 (2007).

9. 9.

Dembrow, N. C., Chitwood, R. A. & Johnston, D. Projection-specific neuromodulation of medial prefrontal cortex neurons. *J. Neurosci.* **30**, 16922–16937 (2010).

10. 10.

Herculano-Houzel, S., Catania, K., Manger, P. R. & Kaas, J. H. Mammalian brains are made of these: a dataset of the numbers and densities of neuronal and nonneuronal cells in the brain of glires,

primates, scandentia, eulipotyphlans, afrotherians and artiodactyls, and their relationship with body mass. *Brain Behav. Evol.* **86**, 145–163 (2015).

11. 11.

Spruston, N. Pyramidal neurons: dendritic structure and synaptic integration. *Nat. Rev. Neurosci.* **9**, 206–221 (2008).

12. 12.

Larkum, M. E., Zhu, J. J. & Sakmann, B. Dendritic mechanisms underlying the coupling of the dendritic with the axonal action potential initiation zone of adult rat layer 5 pyramidal neurons. *J. Physiol.* **533**, 447–466 (2001).

13. 13.

Harnett, M. T., Xu, N. L., Magee, J. C. & Williams, S. R. Potassium channels control the interaction between active dendritic integration compartments in layer 5 cortical pyramidal neurons. *Neuron* **79**, 516–529 (2013).

14. 14.

Mainen, Z. F. & Sejnowski, T. J. Influence of dendritic structure on firing pattern in model neocortical neurons. *Nature* **382**, 363–366 (1996).

15. 15.

Harnett, M. T., Magee, J. C. & Williams, S. R. Distribution and function of HCN channels in the apical dendritic tuft of neocortical pyramidal neurons. *J. Neurosci.* **35**, 1024–1037 (2015).

16. 16.

Kole, M. H., Hallermann, S. & Stuart, G. J. Single  $I_h$  channels in pyramidal neuron dendrites: properties, distribution, and impact on action potential output. *J. Neurosci.* **26**, 1677–1687 (2006).

17. 17.

Vigneswaran, G., Kraskov, A. & Lemon, R. N. Large identified pyramidal cells in macaque motor and premotor cortex exhibit “thin spikes”: implications for cell type classification. *J. Neurosci.* **31**, 14235–14242 (2011).

18. 18.

Naumann, R. K., Anjum, F., Roth-Alpermann, C. & Brecht, M. Cytoarchitecture, areas, and neuron numbers of the Etruscan shrew cortex. *J. Comp. Neurol.* **520**, 2512–2530 (2012).

19. 19.

Paxinos G. & Watson C. *The Rat Brain in Stereotaxic Coordinates* 7th edn (Academic Press, 2013).

20. 20.

Hutchinson, E. B. et al. Population based MRI and DTI templates of the adult ferret brain and tools for voxelwise analysis. *Neuroimage* **152**, 575–589 (2017).

21. 21.

Muñoz-Moreno, E. et al. A magnetic resonance image based atlas of the rabbit brain for automatic parcellation. *PLoS ONE* **8**, e67418 (2013).

22. 22.

Yuasa, S., Nakamura, K. & Kohsaka, S. *Stereotaxic Atlas of the Marmoset Brain* (National Institute of Neuroscience (JP), 2010).

23. 23.

Paxinos, G., Petrides, M. & Evrard, H. *The Rhesus Monkey Brain in Stereotaxic Coordinates* 4th edn (Elsevier, 2021).

24. 24.

Bekkers, J. M. Properties of voltage-gated potassium currents in nucleated patches from large layer 5 cortical pyramidal neurons of the rat. *J. Physiol.* **525**, 593–609 (2000).

25. 25.

Ramaswamy, S. & Markram, H. Anatomy and physiology of the thick-tufted layer 5 pyramidal neuron. *Front. Cell. Neurosci.* **9**, 233 (2015).

26. 26.

Hay, E., Hill, S., Schurmann, F., Markram, H. & Segev, I. Models of neocortical layer 5b pyramidal cells capturing a wide range of dendritic and perisomatic active properties. *PLoS Comput. Biol.* **7**, e1002107 (2011).

27. 27.

Hodge, R. D. et al. Conserved cell types with divergent features in human versus mouse cortex. *Nature* **573**, 61–68 (2019).

28. 28.

Carnevale, N. T. & Hines, M. L. *The NEURON Book* (Cambridge University Press, 2006).

29. 29.

Larkum, M. E., Nevian, T., Sandler, M., Polsky, A. & Schiller, J. Synaptic integration in tuft dendrites of layer 5 pyramidal neurons: a new unifying principle. *Science* **325**, 756–760 (2009).

30. 30.

Miller, D. J., Balaram, P., Young, N. A. & Kaas, J. H. Three counting methods agree on cell and neuron number in chimpanzee primary visual cortex. *Front. Neuroanat.* **8**, 36 (2014).

31. 31.

Pilati, N., Barker, M., Pantelimonitis, S., Donga, R. & Hamann, M. A rapid method combining Golgi and Nissl staining to study neuronal morphology and cytoarchitecture. *J. Histochem. Cytochem.* **56**, 539–550 (2008).

32. 32.

Engel, D. & Jonas, P. Presynaptic action potential amplification by voltage-gated  $\text{Na}^+$  channels in hippocampal mossy fiber boutons. *Neuron* **45**, 405–417 (2005).

33. 33.

Herculano-Houzel, S. *The Human Advantage: A New Understanding of How Our Brain Became Remarkable* (MIT Press, 2016).

34. 34.

Jardim-Messeder, D. et al. Dogs have the most neurons, though not the largest brain: trade-off between body mass and number of neurons in the cerebral cortex of large carnivore species. *Front. Neuroanat.* **11**, 118 (2017).

## Acknowledgements

We thank M. Tadross, S. Herculano-Houzel, M. T. Do, A. Chang, C. Yaeger, V. Francioni and A. Landau for comments on the manuscript; M. Brecht for the gift of Etruscan shrews; J. Haupt for veterinary assistance with procedures; Z. Fu, G. Feng, R. Desimone, M. Jazayeri, E. Miller, M. De-Medonsa, M. Livingstone, M. Greenberg, G. Boulting, A. Chang, C.

Walsh and E. DeGennaro for their help with tissue acquisition; J. Fox and the division of comparative medicine (DCM) at MIT for expert care and supervision of animals; B. Coughlin for help with the epileptic rats; and A. O'Donnell, A. Paulk and Y. Chou for assistance in acquiring human tissue. L.B.-L. was supported by the Natural Sciences and Engineering Research Council of Canada (NSERC) (PGSD2-517068-2018) and a Friends of the McGovern Institute fellowship. E.H.S.T. was supported by the National Institute of General Medical Sciences (T32GM007753) and the Paul & Daisy Soros Fellowship. M.T.H. was supported by the Dana Foundation David Mahoney Neuroimaging Grant Program, the NIH (RO1NS106031) and the Harvard-MIT Joint Research Grants Program in Basic Neuroscience. M.T.H. is a Klingenstein-Simons Fellow, a Vallee Foundation Scholar and a McKnight Scholar.

## Author information

### Affiliations

1. McGovern Institute for Brain Research, Department of Brain and Cognitive Sciences, Massachusetts Institute of Technology, Cambridge, MA, USA

Lou Beaulieu-Laroche, Norma J. Brown, Marissa Hansen, Enrique H. S. Toloza & Mark T. Harnett

2. Department of Physics, Massachusetts Institute of Technology, Cambridge, MA, USA

Enrique H. S. Toloza

3. Harvard Medical School, Boston, MA, USA

Enrique H. S. Toloza

4. Picower Institute for Learning and Memory, Department of Brain and Cognitive Sciences, Massachusetts Institute of Technology, Cambridge, MA, USA

Jitendra Sharma

5. Martinos Center for Biomedical Imaging, Department of Radiology, Massachusetts General Hospital and Harvard Medical School, Boston, MA, USA

Jitendra Sharma

6. Department of Neurosurgery, Massachusetts General Hospital, Boston, MA, USA

Ziv M. Williams

7. C.S. Kubik Laboratory for Neuropathology, Massachusetts General Hospital, Boston, MA, USA

Matthew P. Frosch

8. Department of Neurosurgery, Brigham and Women's Hospital, Boston, MA, USA

Garth Rees Cosgrove

9. Department of Neurology, Harvard Medical School and Massachusetts General Hospital, Boston, MA, USA

Sydney S. Cash

## Contributions

L.B.-L. designed experiments, collected human brain samples, extracted animal brains, prepared slices, performed electrophysiological recordings, analysed data, prepared the figures and wrote the manuscript. N.J.B. performed and analysed electrophysiological recordings, prepared fixed tissues for histology, performed histological stainings and created illustrations for the figures. M.H. performed and analysed electrophysiological recordings. E.H.S.T. performed biophysical modelling. J.S. performed animal surgeries. Z.M.W. and G.R.C. performed the

surgeries that resulted in the human tissue. M.P.F. oversaw the removal and parcellation of that tissue as well as overall IRB aspects and regulatory aspects of the project with regard to human participants. S.S.C. helped in designing methods for acquiring human tissue and ensured that the tissue was collected. M.T.H supervised all aspects of the project.

## Corresponding author

Correspondence to [Mark T. Harnett](#).

## Ethics declarations

## Competing interests

The authors declare no competing interests.

## Additional information

**Peer review information** *Nature* thanks the anonymous reviewers for their contribution to the peer review of this work.

**Publisher's note** Springer Nature remains neutral with regard to jurisdictional claims in published maps and institutional affiliations.

## Extended data figures and tables

### [Extended Data Fig. 1 Histological identification of cortical layers. Related to Fig. 1.](#)

**a**, Nissl-stained brain slices from the 10 species with labelled cortical layers. Box plots on the right of individual slices denote the median and 25–75th percentiles of somatic depth for electrophysiological recordings (Etruscan shrew n = 39, mouse n = 162, gerbil n = 105, rat n = 215, ferret n = 31, guinea pig n = 118, rabbit n = 87, marmoset n = 41, macaque n = 34,

human n = 208). **b**, The shrew slice from a, expanded to show detail (n = 39).

### Extended Data Fig. 2 Somatic impedance profiles and voltage sag. Related to Fig. 1.

**a-d**, Somatic impedance profiles (Etruscan shrew n = 29, mouse n = 71, gerbil n = 39, rat n = 64, ferret n = 28, guinea pig n = 35, rabbit n = 37, marmoset n = 30, macaque n = 25, human n = 100). Pooled data represent mean  $\pm$  SEM for a-b. Box plots denote the median and 25–75th percentiles for c-d. **a**, Impedance profile in response to sinewaves of 50-100 pA injected at the indicated frequencies for 2 s. **b**, Phase offset between the voltage response and the injected current. **c**, Maximal impedance ( $p < 10^{-49}$  Kruskal-Wallis;  $\chi^2 = 259$  & 9 df). **d**, Resonance frequency ( $p < 10^{-13}$  Kruskal-Wallis;  $\chi^2 = 81$  & 9 df). Data points displayed as a beeswarm plot to show overlapping integers. **e**, Somatic voltage sag ( $p < 10^{-57}$  Kruskal-Wallis,  $\chi^2 = 298$  & 9 df; Etruscan shrew n = 39, mouse n = 85, gerbil n = 58, rat n = 117, ferret n = 31, guinea pig n = 47, rabbit n = 40, marmoset n = 41, macaque n = 34, human n = 126). Box plots denote the median and 25–75th percentiles.

### Extended Data Fig. 3 Somatic firing properties. Related to Fig. 1.

Somatic firing properties (Etruscan shrew n = 22, mouse n = 59, gerbil n = 46, rat n = 93, ferret n = 23, guinea pig n = 30, rabbit n = 33, marmoset n = 34, macaque n = 29, human n = 104). **a**, Firing rates as a function of injected current. The lines and shaded error bars represent population medians and 95% confidence intervals. **b-g**, Box plots denote the median and 25–75th percentiles. **b**, Rheobase ( $p < 10^{-47}$  Kruskal-Wallis,  $\chi^2 = 250$  & 9 df). Data points displayed as a beeswarm plot to show overlapping integers. **c**, Slope of firing rate-current relationship ( $p < 10^{-59}$  Kruskal-Wallis,  $\chi^2 = 304$  & 9 df). **d**, Maximal firing rate ( $p < 10^{-26}$  Kruskal-Wallis,  $\chi^2 = 146$  & 9 df). **e**, Maximal current eliciting action potentials before entering depolarization block ( $p < 10^{-54}$  Kruskal-Wallis,  $\chi^2 = 283$  & 9 df). **f**, Representative action potential waveforms. **g**, Width of first action potential at rheobase ( $p <$

$10^{-13}$  Kruskal-Wallis,  $\chi^2 = 86$  & 9 df). **h-j**, Correlation between action potential width (at rheobase) and other parameters for macaque L5 neurons of different somatic sizes (not restricted to large L5 with thick dendrites). **h**, Correlation with soma diameter ( $R^2 = 0.145$ ,  $p = 0.006$ , linear regression,  $F = 8.3$  & 49 df,  $n = 51$ ). **i**, Correlation with soma input resistance ( $R^2 = 0.596$ ,  $p < 10^{-13}$ , linear regression,  $F = 94.5$  & 64 df,  $n = 66$ ). **j**, Correlation with soma voltage sag ( $n = 66$ ;  $R^2 = 0.079$ ,  $p = 0.02$ , linear regression,  $F = 5.5$  & 64 df,  $n = 66$ ). **k-m**, Rat somatic firing properties of L5b neurons in TEA ( $n = 93$ ) versus M1 ( $n = 39$ ). Orange lines represent median L5 macaque data from Extended Data Fig. 3d,g. **k**, Firing rates as a function of injected current. The lines and shaded error bars represent population medians and 95% confidence intervals. **l**, Maximal firing rate ( $p < 10^{-8}$ , two-sided Wilcoxon rank sum,  $Z = -5.93$ ). **m**, Width of first action potential at rheobase ( $p < 10^{-3}$ , two-sided Wilcoxon rank sum,  $Z = 3.34$ ).

### Extended Data Fig. 4 Somatic bursting properties. Related to Fig. 1.

Somatic bursting properties (Etruscan shrew  $n = 22$ , mouse  $n = 59$ , gerbil  $n = 46$ , rat  $n = 93$ , ferret  $n = 23$ , guinea pig  $n = 30$ , rabbit  $n = 33$ , marmoset  $n = 34$ , macaque  $n = 29$ , human  $n = 104$ ). **a**, Minimum instantaneous interspike interval (ISI) on a log scale as a function of injected current above rheobase. The lines and shaded error bars represent population medians and 95% confidence intervals. **b**, Percentage of neurons exhibiting bursts with different frequency thresholds at rheobase. **c**, Same as b but at double the rheobase. **d-e**, Box plots denote the median and 25–75th percentiles. **d**, Maximal action potential amplitude reduction ( $p < 10^{-18}$  Kruskal-Wallis,  $\chi^2 = 107$  & 9 df). **e**, Maximal action potential  $dV/dt$  reduction ( $p < 10^{-15}$  Kruskal-Wallis,  $\chi^2 = 95$  & 9 df).

### Extended Data Fig. 5 Dendritic impedance profiles. Related to Fig. 2.

Dendritic impedance profiles (mouse  $n = 26$ , gerbil  $n = 19$ , rat  $n = 59$ , guinea pig  $n = 37$ , rabbit  $n = 23$ , human  $n = 25$ ). Pooled data represent mean  $\pm$  SEM for a-b. Box plots denote the median and 25–75th percentiles for d-

e. **a**, Impedance profile in response to sinewaves of 50-100 pA injected at the indicated frequencies for 2 s. **b**, Phase offset between the voltage response and the injected current. **c**, Mean data from b. **d**, Maximal impedance ( $p < 10^{-10}$  Kruskal-Wallis,  $\chi^2 = 59$  & 5 df). **e**, Resonance frequency ( $p < 10^{-6}$  Kruskal-Wallis,  $\chi^2 = 39$  & 5 df). Data points displayed as a beeswarm plot to show overlapping integers.

### [Extended Data Fig. 6 Additional dendritic properties. Related to Fig. 2.](#)

Voltage sag (mouse n = 76, gerbil n = 47, rat n = 108, guinea pig n = 71, rabbit n = 47, human n = 72), resting membrane potential (mouse n = 76, gerbil n = 47, rat n = 108, guinea pig n = 71, rabbit n = 47, human n = 72), and spike properties (mouse n = 51, gerbil n = 40, rat n = 65, guinea pig n = 45, rabbit n = 35, human n = 49) as a function of distance from the soma. Triangles are somatic medians. Lines are an exponential fit to the data or double exponential fit for spike dV/dt. Spike width and area are on a log scale.

### [Extended Data Fig. 7 Proximal dendritic properties and additional distal dendritic properties. Related to Fig. 2.](#)

**a**, Two-photon z-stack montage image of mouse neuron with a proximal patch-clamp electrode 63  $\mu$ m from soma. **b**, Proximal dendritic voltage in response to subthreshold (top) or threshold (bottom) step current injections. **c-d**, Subthreshold properties of proximal dendrites (mouse n = 31, gerbil n = 23, rat n = 19, guinea pig n = 28, rabbit n = 21, human n = 27). Box plots denote the median and 25–75th percentiles. **c**, Proximal input resistance ( $p < 10^{-18}$  Kruskal-Wallis,  $\chi^2 = 98$  & 5 df). **d**, Proximal voltage sag ( $p < 10^{-8}$  Kruskal-Wallis,  $\chi^2 = 47$  & 5 df). **e-i**, Suprathreshold properties of proximal dendrites (mouse n = 19, gerbil n = 20, rat n = 9, guinea pig n = 18, rabbit n = 12, human n = 15). Box plots denote the median and 25–75th percentiles. **e**, Proximal rheobase ( $p < 10^{-9}$  Kruskal-Wallis,  $\chi^2 = 51$  & 5 df). Data points displayed as a beeswarm plot to show overlapping integers. **f**, Proximal spike threshold ( $p < 10^{-4}$  Kruskal-Wallis,  $\chi^2 = 31$  & 5 df). **g**, Proximal spike area on a log scale ( $p < 10^{-6}$  Kruskal-Wallis,  $\chi^2 = 36$  & 5 df). **h**, Proximal

spike width on a log scale ( $p < 10^{-5}$  Kruskal-Wallis,  $\chi^2 = 36$  & 5 df). **i**, Proximal maximum spike  $dV/dt$  ( $p < 10^{-5}$  Kruskal-Wallis,  $\chi^2 = 35$  & 5 df). **j-m**, Additional suprathreshold properties of distal dendrites (mouse  $n = 18$ , gerbil  $n = 19$ , rat  $n = 47$ , guinea pig  $n = 25$ , rabbit  $n = 20$ , human  $n = 25$ ). Box plots denote the median and 25–75th percentiles. **j**, Distal rheobase ( $p < 10^{-4}$  Kruskal-Wallis,  $\chi^2 = 28$  & 5 df). Data points displayed as a beeswarm plot to show overlapping integers. **k**, Distal spike threshold ( $p < 10^{-11}$  Kruskal-Wallis,  $\chi^2 = 61$  & 5 df). **l**, Distal spike area on a log scale ( $p < 10^{-10}$  Kruskal-Wallis,  $\chi^2 = 58$  & 5 df). **m**, Maximum distal spike  $dV/dt$  ( $p < 10^{-13}$  Kruskal-Wallis,  $\chi^2 = 74$  & 5 df). **n-o**, Somatic outside-out currents in sclerosis ( $n = 44$ ), tumour ( $n = 30$ ) and others ( $n = 12$ ). Box plots denote the median and 25–75th percentiles. **n**, Somatic  $K_v$  peak currents ( $p = 0.39$  Kruskal-Wallis,  $\chi^2 = 1.90$  & 2 df). **o**, Somatic  $K_v$  plateau currents ( $p = 0.35$  Kruskal-Wallis,  $\chi^2 = 2.09$  & 2 df). **p**, Example EEG recording of epileptic seizure in rat kainic acid model. **q-r**, Somatic outside-out currents in control ( $n = 80$ ) and epileptic ( $n = 68$ ) rats. Box plots denote the median and 25–75th percentiles. **q**, Somatic  $K_v$  peak currents ( $p = 0.65$ , two-sided Wilcoxon rank sum,  $Z = 0.45$ ). **r**, Somatic  $K_v$  plateau currents ( $p = 0.525$ , two-sided Wilcoxon rank sum,  $Z = 0.64$ ).

## Extended Data Fig. 8 Additional conductance measurements.

### Related to Fig. 3.

**a**, Dendritic outside-out patches were pulled from proximal dendrites after obtaining whole-cell recordings. Top, HCN currents with the associated voltage-clamp protocol on the left. Bottom,  $K_v$  currents with the associated voltage-clamp protocol on the left. **b-g**, Box plots denote the median and 25–75th percentiles. **b**, Proximal  $K_v$  peak currents ( $p = 0.010$  Kruskal-Wallis,  $\chi^2 = 15$  & 5 df; mouse  $n = 32$ , gerbil  $n = 38$ , rat  $n = 38$ , guinea pig  $n = 37$ , rabbit  $n = 35$ , human  $n = 44$ ). **c**, Proximal HCN steady-state currents ( $p = 0.07$  Kruskal-Wallis,  $\chi^2 = 10$  & 5 df; mouse  $n = 29$ , gerbil  $n = 30$ , rat  $n = 38$ , guinea pig  $n = 30$ , rabbit  $n = 31$ , human  $n = 42$ ). **d**, Somatic  $K_v$  peak currents ( $p < 10^{-19}$  Kruskal-Wallis,  $\chi^2 = 115$  & 9 df; Etruscan shrew  $n = 59$ , mouse  $n = 56$ , gerbil  $n = 80$ , rat  $n = 80$ , ferret  $n = 80$ , guinea pig  $n = 70$ , rabbit  $n = 53$ , marmoset  $n = 63$ , macaque  $n = 87$ , human  $n = 86$ ). **e**, Somatic

$K_v$  plateau currents ( $p < 10^{-19}$  Kruskal-Wallis,  $\chi^2 = 115$  & 9 df; Etruscan shrew  $n = 59$ , mouse  $n = 56$ , gerbil  $n = 80$ , rat  $n = 80$ , ferret  $n = 80$ , guinea pig  $n = 70$ , rabbit  $n = 53$ , marmoset  $n = 63$ , macaque  $n = 87$ , human  $n = 86$ ). **f**, Proximal  $K_v$  plateau currents ( $p < 10^{-4}$  Kruskal-Wallis,  $\chi^2 = 29$  & 5 df; mouse  $n = 32$ , gerbil  $n = 38$ , rat  $n = 38$ , guinea pig  $n = 26$ , rabbit  $n = 35$ , human  $n = 44$ ). **g**, Distal  $K_v$  plateau currents ( $p = 0.00001$  Kruskal-Wallis,  $\chi^2 = 30$  & 5 df; mouse  $n = 35$ , gerbil  $n = 46$ , rat  $n = 59$ , guinea pig  $n = 58$ , rabbit  $n = 39$ , human  $n = 43$ ). **h-k**, Conductance as a function of neuron size. The lines and shaded error bars represent the fit and 95% confidence interval of an allometric relationship constructed excluding humans. **h**, Total  $K_v$  plateau conductance on a log-log scale (exponent  $1.24 \pm 0.09$ ,  $R^2 = 0.983$ ,  $p < 10^{-3}$ , linear regression on log-log scale,  $F = 176$  & 3 df,  $n = 5$  for mouse, gerbil, rat, guinea pig, and rabbit). **i**, Somatic  $K_v$  plateau conductance on a log-log scale (exponent  $1.98 \pm 0.15$ ,  $R^2 = 0.962$ ,  $p < 10^{-5}$ , linear regression on log-log scale,  $F = 175$  & 7 df,  $n = 9$  for shrew, mouse, gerbil, rat, ferret, guinea pig, rabbit, marmoset, and macaque). **j**, Normalized average of HCN,  $K_v$  peak and  $K_v$  plateau conductance (exponent  $1.43 \pm 0.15$ ,  $R^2 = 0.966$ ,  $p = 0.003$ , linear regression on log-log scale,  $F = 85.7$  & 3 df,  $n = 5$  for mouse, gerbil, rat, guinea pig, and rabbit). **k**, Normalized average of somatic  $K_v$  peak and  $K_v$  plateau conductance (exponent  $1.82 \pm 0.12$ ,  $R^2 = 0.968$ ,  $p < 10^{-5}$ , linear regression on log-log scale,  $F = 212$  & 7 df,  $n = 9$  for shrew, mouse, gerbil, rat, ferret, guinea pig, rabbit, marmoset and macaque). **l**, Relationship between somatic (normalized average of somatic  $K_v$  peak and  $K_v$  plateau conductance) and dendritic (normalized average of HCN,  $K_v$  peak and  $K_v$  plateau conductance) conductance ( $R^2 = 0.891$ ,  $p = 0.005$ , linear regression,  $F = 32.7$  & 4 df,  $n = 6$  for mouse, gerbil, rat, guinea pig, rabbit, and human). **m**, Soma volume as a function of neuronal density (Extended Data Table 1) on a log-log scale (exponent  $-0.74 \pm 0.10$ ,  $R^2 = 0.897$ ,  $p < 10^{-3}$ , linear regression,  $F = 52.3$  & 6 df,  $n = 8$  for shrew, mouse, rat, ferret, guinea pig, rabbit, marmoset, and macaque). The line and shaded error bars represent the fit and 95% confidence interval of an allometric relationship constructed excluding humans. **n-t**, Allometric relationship on a log-log scale. The lines and shaded error bars represent the fit and 95% confidence interval of the

relationship constructed excluding humans. **n-o**, Somatic  $K_v$  plateau conductance densities in volumes as in Fig. 4c. **n**, Membrane conductance density (exponent  $0.98 \pm 0.15$ ,  $R^2 = 0.860$ ,  $p < 10^{-3}$ , linear regression,  $F = 43.0$  & 7 df,  $n = 9$  for shrew, mouse, gerbil, rat, ferret, guinea pig, rabbit, marmoset, and macaque). **o**, Volume  $K_v$  peak conductance density where the volume is filled with somas (exponent  $0.53 \pm 0.15$ ,  $R^2 = 0.651$ ,  $p = 0.009$ , linear regression,  $F = 13.1$  & 7 df,  $n = 9$  for shrew, mouse, gerbil, rat, ferret, guinea pig, rabbit, marmoset, and macaque). **p-q**, Somatic  $K_v$  plateau conductance densities in volumes as in Fig. 4g. Gerbils were not included because the necessary information was not available in the literature (Extended Data Table 1). **p**, Cortex conductance density with accurate neuronal densities (exponent  $-0.27 \pm 0.34$ ,  $R^2 = 0.092$ ,  $p = 0.47$ , linear regression,  $F = 0.61$  & 6 df,  $n = 8$  for shrew, mouse, rat, ferret, guinea pig, rabbit, marmoset, and macaque). **q**, Total cortex conductance (exponent  $1.09 \pm 0.06$ ,  $R^2 = 0.985$ ,  $p < 10^{-5}$ , linear regression,  $F = 393$  & 6 df,  $n = 8$  for shrew, mouse, rat, ferret, guinea pig, rabbit, marmoset and macaque). **r-t**, Same analysis as in Fig. 4f, but including dendrites in the volume and conductance calculation. **r**, Volume  $K_v$  peak conductance density where the volume is filled with somas and dendrites (exponent  $0.05 \pm 0.10$ ,  $R^2 = 0.083$ ,  $p = 0.64$ , linear regression,  $F = 0.272$  & 3 df,  $n = 5$  for mouse, gerbil, rat, guinea pig, and rabbit). **s**, Volume  $K_v$  plateau conductance density where the volume is filled with somas and dendrites (exponent  $0.02 \pm 0.13$ ,  $R^2 = 0.006$ ,  $p = 0.90$ , linear regression,  $F = 0.02$  & 3 df,  $n = 5$  for mouse, gerbil, rat, guinea pig, and rabbit). **t**, Volume HCN conductance density where the volume is filled with somas and dendrites (exponent  $0.5 \pm 0.29$ ,  $R^2 = 0.500$ ,  $p = 0.18$ , linear regression,  $F = 2.99$  & 3 df,  $n = 5$  for mouse, gerbil, rat, guinea pig, and rabbit).

### [Extended Data Fig. 9 Outside-out patch size estimation.](#) [Related to Fig. 3.](#)

**a**, Rat dual nucleated patch recordings to test the efficacy of voltage-clamp under nucleated patch configuration. **b**, Voltage-clamp command action potential waveform (black) and independently observed waveform (grey) without compensation (left) or with series resistance and whole-cell

capacitance predicted and compensated >90% and lag <10  $\mu$ s (right). **c**, Percentage of command waveform amplitude observed with the independent electrode ( $n = 4$ ;  $p = 0.0045$ , two-sided paired t test,  $t = 4.41$  & 6 df). Pooled data represent mean  $\pm$  SEM. **d**, Rat nucleated patch recording with series resistance and whole-cell capacitance predicted and compensated >90% and lag <10  $\mu$ s. **e**,  $K_v$  currents from the recording in d. **f**, Rat  $K_v$  peak current density computed using the  $K_v$  currents and patch surface area ( $n = 22$ ). Pooled data represent mean  $\pm$  SEM. **g**, Rat  $K_v$  peak currents in somatic outside-out patch ( $n = 80$ ). Box plots denote the median and 25–75th percentiles. **h**, Outside-out patch surface area computed using the mean  $K_v$  peak current density in f and the median  $K_v$  peak current in g. **i-j**, Recapitulation of outside-out patch recordings in a compartmental model of rat L5 neuron. **i**, Model dendritic outside-out patches as spheres of 50  $\mu\text{m}^2$ . HCN (top) and  $K_v$  (bottom) currents (right) with associated voltage-clamp protocol (left). **j**, Model  $K_v$  currents in somatic outside-out patches. **k**, Morphology used in the model taken from (<https://senselab.med.yale.edu/ModelDB>ShowModel?model=124043#tabs-3>). **l**, Distal dendritic (520  $\mu\text{m}$  from soma) and somatic voltage in response to subthreshold step current injections in the model. **m**, Somatic and dendritic input resistance as a function of distance from the soma. Fit to experimental rat data in blue taken from Fig. 2d versus model data in black. **n**, Somatic and dendritic voltage sag as a function of distance from the soma. Fit to experimental rat data in blue taken from Extended Data Fig. 6 versus model data in black.

### **Extended Data Fig. 10 Only human neurons are consistent outliers in electrophysiological features. Related to Fig. 4.**

**a**, Explained variance of allometric relationship with (x-axis) versus without (y-axis) individual species for the same electrophysiological properties as in Fig. 4b. **b**, Calculation of outlier index. Positive outlier indices reflect cases in which a given species is an outlier and does not follow a conserved pattern observed in the other species. **c**, Percentage of features with substantial positive outlier indices (threshold at 0.2 or 0.4) for the different species.

**Extended Data Table 1 Species information**

**Extended Data Table 2 Breakdown of dataset of 2,257 recordings from temporal cortex**

**Extended Data Table 3 Information on patients with epilepsy (related to Methods)**

## Supplementary information

### [Reporting Summary](#)

### Rights and permissions

### [Reprints and Permissions](#)

### About this article

#### Cite this article

Beaulieu-Laroche, L., Brown, N.J., Hansen, M. *et al.* Allometric rules for mammalian cortical layer 5 neuron biophysics. *Nature* **600**, 274–278 (2021). <https://doi.org/10.1038/s41586-021-04072-3>

- Received: 08 August 2020
- Accepted: 29 September 2021
- Published: 10 November 2021
- Issue Date: 09 December 2021
- DOI: <https://doi.org/10.1038/s41586-021-04072-3>

#### Share this article

Anyone you share the following link with will be able to read this content:

[Get shareable link](#)

Sorry, a shareable link is not currently available for this article.

[Copy to clipboard](#)

Provided by the Springer Nature SharedIt content-sharing initiative

---

This article was downloaded by **calibre** from <https://www.nature.com/articles/s41586-021-04072-3>

| [Section menu](#) | [Main menu](#) |

- Article
- [Published: 26 November 2021](#)

# Multiview confocal super-resolution microscopy

- [Yicong Wu](#) [ORCID: orcid.org/0000-0002-8819-7527](#)<sup>1 na1</sup>,
- [Xiaofei Han](#)<sup>1,2 na1</sup>,
- [Yijun Su](#)<sup>1,3,4</sup>,
- [Melissa Glidewell](#)<sup>5</sup>,
- [Jonathan S. Daniels](#)<sup>5</sup>,
- [Jiamin Liu](#)<sup>6</sup>,
- [Titas Sengupta](#)<sup>7</sup>,
- [Ivan Rey-Suarez](#)<sup>8</sup>,
- [Robert Fischer](#)<sup>9</sup>,
- [Akshay Patel](#) [ORCID: orcid.org/0000-0001-6176-2496](#)<sup>10</sup>,
- [Christian Combs](#)<sup>11</sup>,
- [Junhui Sun](#)<sup>12</sup>,
- [Xufeng Wu](#)<sup>11</sup>,
- [Ryan Christensen](#)<sup>1</sup>,
- [Corey Smith](#)<sup>13</sup>,
- [Lingyu Bao](#)<sup>14</sup>,
- [Yilun Sun](#) [ORCID: orcid.org/0000-0002-6249-2704](#)<sup>15</sup>,
- [Leighton H. Duncan](#)<sup>7</sup>,
- [Jiji Chen](#) [ORCID: orcid.org/0000-0002-4426-3035](#)<sup>6</sup>,
- [Yves Pommier](#)<sup>15</sup>,
- [Yun-Bo Shi](#) [ORCID: orcid.org/0000-0002-6330-0639](#)<sup>14</sup>,
- [Elizabeth Murphy](#)<sup>12</sup>,
- [Sougata Roy](#) [ORCID: orcid.org/0000-0002-2236-9277](#)<sup>10</sup>,
- [Arpita Upadhyaya](#)<sup>8,16</sup>,

- [Daniel Colón-Ramos](#) ORCID: [orcid.org/0000-0003-0223-7717<sup>7,17,18</sup>](https://orcid.org/0000-0003-0223-7717),
- [Patrick La Riviere](#) ORCID: [orcid.org/0000-0003-3415-9864<sup>13,17</sup>](https://orcid.org/0000-0003-3415-9864) &
- [Hari Shroff](#)<sup>1,6,17</sup>

*Nature* volume 600, pages 279–284 (2021)

- 14k Accesses
- 232 Altmetric
- [Metrics details](#)

## Subjects

- [Fluorescence imaging](#)
- [Super-resolution microscopy](#)

## Abstract

Confocal microscopy<sup>1</sup> remains a major workhorse in biomedical optical microscopy owing to its reliability and flexibility in imaging various samples, but suffers from substantial point spread function anisotropy, diffraction-limited resolution, depth-dependent degradation in scattering samples and volumetric bleaching<sup>2</sup>. Here we address these problems, enhancing confocal microscopy performance from the sub-micrometre to millimetre spatial scale and the millisecond to hour temporal scale, improving both lateral and axial resolution more than twofold while simultaneously reducing phototoxicity. We achieve these gains using an integrated, four-pronged approach: (1) developing compact line scanners that enable sensitive, rapid, diffraction-limited imaging over large areas; (2) combining line-scanning with multiview imaging, developing reconstruction algorithms that improve resolution isotropy and recover signal otherwise lost to scattering; (3) adapting techniques from structured illumination microscopy, achieving super-resolution imaging in densely labelled, thick samples; (4) synergizing deep learning with these advances, further improving imaging speed, resolution and duration. We demonstrate these capabilities on more than 20 distinct fixed and live samples, including

protein distributions in single cells; nuclei and developing neurons in *Caenorhabditis elegans* embryos, larvae and adults; myoblasts in imaginal disks of *Drosophila* wings; and mouse renal, oesophageal, cardiac and brain tissues.

This is a preview of subscription content

## Access options

Subscribe to Journal

Get full journal access for 1 year

\$199.00

only \$3.90 per issue

[Subscribe](#)

All prices are NET prices.

VAT will be added later in the checkout.

Tax calculation will be finalised during checkout.

Rent or Buy article

Get time limited or full article access on ReadCube.

from \$8.99

[Rent or Buy](#)

All prices are NET prices.

### Additional access options:

- [Log in](#)
- [Learn about institutional subscriptions](#)

**Fig. 1: Multiview line confocal microscopy.**



**Fig. 2: Multiview confocal live imaging.**

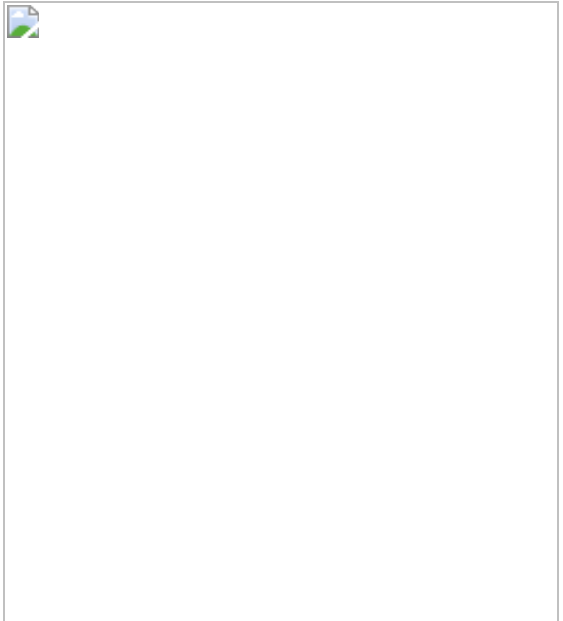


**Fig. 3: Multiview super-resolution microscopy.**

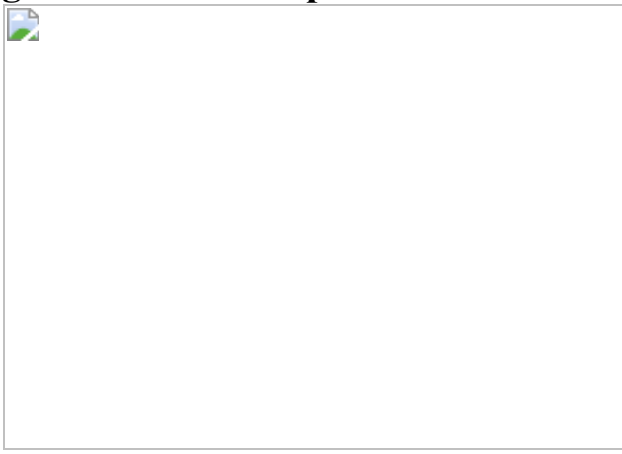
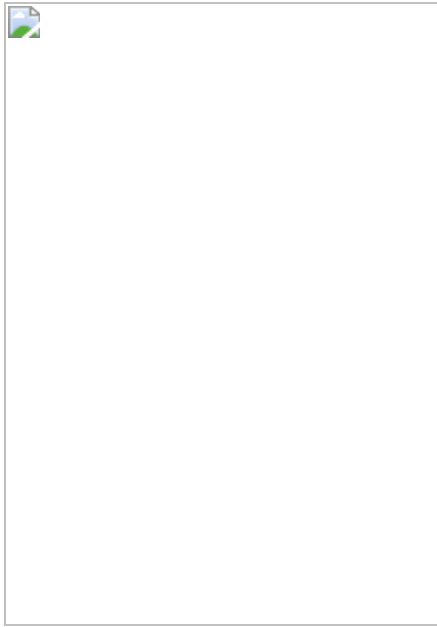


**Fig. 4: Deep learning enhances multiview super-resolution imaging.**



## Data availability

The data that support the findings of this study are included in Extended Data Figs. 1–18 and Supplementary Videos 1–8, and some representative source data for the figures (Figs. [1c](#), g, [2a](#), h, [3b](#), [4b](#), [i](#)) are publicly available at <https://zenodo.org/record/5495955#.YVIItPTHMJaS>. Other datasets are available from the corresponding author upon reasonable request. [Source data](#) are provided with this paper.

## Code availability

The custom codes used in this study are available upon request, with most software and test data publicly available at <https://github.com/hroi-aim/multiviewSR> and <https://github.com/AiviaCommunity/3D-RCAN>.

## References

1. 1.

Pawley, J. B. (ed.) *Handbook of Biological Confocal Microscopy* 3rd edn (Springer, 2006).

2. 2.

Laissue, P. P., Alghamdi, R. A., Tomancak, P., Reynaud, E. G., Shroff, H. Assessing phototoxicity in live fluorescence imaging. *Nat. Methods* **14**, 657–661 (2017).

3. 3.

Baumgart, E. & Kubitscheck, U. Scanned light sheet microscopy with confocal slit detection. *Opt. Express* **20**, 21805–21814 (2012).

4. 4.

Kumar, A. et al. Using stage- and slit-scanning to improve contrast and optical sectioning in dual-view inverted light-sheet microscopy (diSPIM). *Biol. Bull.* **231**, 26–39 (2016).

5. 5.

Guo, M. et al. Rapid image deconvolution and multiview fusion for optical microscopy. *Nat. Biotechnol.* **38**, 1337–1346 (2020).

6. 6.

Lucy, L. B. An iterative technique for the rectification of observed distributions. *Astron. J.* **79**, 745–754 (1974).

7. 7.

Richardson, W. H. Bayesian-based iterative method of image restoration. *J. Opt. Soc. Am.* **62**, 55–59 (1972).

8. 8.

Descloux, A., Grußmayer, K. S. & Radenovic, A. Parameter-free image resolution estimation based on decorrelation analysis. *Nat. Methods* **16**, 918–924 (2019).

9. 9.

Chen, F., Tillberg, P. & Boyden, E. S. Expansion microscopy. *Science* **347**, 543–548 (2015).

10. 10.

He, K., Gkioxari, G., Dollár, P. & Girshick, R. Mask R-CNN. In *2017 IEEE Conf Computer Vision (ICCV)* (eds Ikeuchi, K. et al.) 2980–2988 (2017).

11. 11.

Lin, T.-Y. et al. Microsoft COCO: common objects in context. In *Computer Vision – CV 2014* (eds Fleet, D. et al.) 740–755 (Springer, 2014).

12. 12.

Kosmach, A. et al. Monitoring mitochondrial calcium and metabolism in the beating MCU-KO heart. *Cell Rep.* **37**, 109846 (2021).

13. 13.

Wu, Y. et al. Inverted selective plane illumination microscopy (*i*SPIM) enables coupled cell identity lineage and neurodevelopmental imaging in *Caenorhabditis elegans*. *Proc. Natl Acad. Sci. USA* **108**, 17708–17713 (2011).

14. 14.

Weigert, M. et al. Content-aware image restoration: pushing the limits of fluorescence microscopy. *Nat. Methods* **15**, 1090–1097 (2018).

15. 15.

Sulston, J. E., Schierenberg, E., White, J. G. & Thomson, J. N. The embryonic cell lineage of the nematode *Caenorhabditis elegans*. *Dev. Biol.* **100**, 64–119 (1983).

16. 16.

Wu, Y. et al. Spatially isotropic four-dimensional imaging with dual-view plane illumination microscopy. *Nat. Biotechnol.* **31**, 1032–1038 (2013).

17. 17.

Kumar, A. et al. Dual-view plane illumination microscopy for rapid and spatially isotropic imaging. *Nat. Protoc.* **9**, 2555–2573 (2014).

18. 18.

Duncan, L. H. et al. Isotropic light-sheet microscopy and automated cell lineage analyses to catalogue *Caenorhabditis elegans* embryogenesis with subcellular resolution. *J. Vis. Exp.* **148**, e59533 (2019).

19. 19.

Towlson, E. K., Vértes, P. E., Ahnert, S. E., Schafer, W. R. & Bullmore, E. T. The rich club of the *C. elegans* neuronal connectome. *J. Neurosci.* **33**, 6380–6387 (2013).

20. 20.

White, J. G., Southgate, E., Thomson, J. N. & Brenner, S. The structure of the nervous system of the nematode *Caenorhabditis elegans*. *Phil. Trans. R. Soc. B* **314**, 1–340 (1986).

21. 21.

Armenti, S. T., Lohmer, L. L., Sherwood, D. R. & Nance, J. Repurposing an endogenous degradation system for rapid and targeted depletion of *C. elegans* proteins. *Development* **141**, 4640–4647 (2014).

22. 22.

Wu, Y. & Shroff, H. Faster, sharper, and deeper: structured illumination microscopy for biological imaging. *Nat. Methods* **15**, 1011–1019 (2018); correction **16**, 205 (2019).

23. 23.

Fischer, R. S., Gardel, M. L., Ma, X., Adelstein, R. S. & Waterman, C. M. Local cortical tension by myosin II guides 3D endothelial cell branching. *Curr Biol.* **19**, 260–265 (2009).

24. 24.

York, A. G. et al. Instant super-resolution imaging in live cells and embryos via analog image processing. *Nat. Methods* **10**, 1122–1126 (2013).

25. 25.

Gambarotto, D. et al. Imaging cellular ultrastructures using expansion microscopy (U-ExM). *Nat. Methods* **16**, 71–74 (2019).

26. 26.

Tabara, H., Motohashi, T. & Kohara, Y. A multi-well version of in situ hybridization on whole mount embryos of *Caenorhabditis elegans*. *Nucleic Acids Res.* **24**, 2119–2124 (1996).

27. 27.

Chen, J. et al. Three-dimensional residual channel attention networks denoise and sharpen fluorescence microscopy image volumes. *Nat. Methods* **18**, 678–687 (2020).

28. 28.

Wu, Y. et al. Simultaneous multiview capture and fusion improves spatial resolution in wide-field and light-sheet microscopy. *Optica* **3**, 897–910 (2016).

29. 29.

Barth, R., Bystricky, K. & Shaban, H. A. Coupling chromatin structure and dynamics by live super-resolution imaging. *Sci. Adv.*

<https://doi.org/10.1126/sciadv.aaz2196> (2020).

30. 30.

Han, X. et al. A polymer index-matched to water enables diverse applications in fluorescence microscopy. *Lab Chip* **21**, 1549–1562 (2021).

31. 31.

Chen, B.-C. et al. Lattice light-sheet microscopy: imaging molecules to embryos at high spatiotemporal resolution. *Science* **346**, 1257998 (2014).

32. 32.

Gustafsson, M. G. L. et al. Three-dimensional resolution doubling in wide-field fluorescence microscopy by structured illumination. *Biophys. J.* **94**, 4957–4970 (2008).

33. 33.

Rego, E. H. et al. Nonlinear structured-illumination microscopy with a photoswitchable protein reveals cellular structures at 50-nm resolution. *Proc. Natl Acad. Sci. USA* **109**, E135–E143 (2011).

34. 34.

Krüger, J.-R., Keller-Findeisen, J., Geisler, C. & Egner, A. Tomographic STED microscopy. *Biomed. Opt. Express* **11**, 3139–3163 (2020).

35. 35.

Wu, Y. et al. Reflective imaging improves spatiotemporal resolution and collection efficiency in light sheet microscopy. *Nat. Commun.* **8**, 1452 (2017).

36. 36.

Shroff, H., York, A., Giannini, J. P. & Kumar, A. Resolution enhancement for line scanning excitation microscopy systems and methods. US patent 10,247,930 (2019).

37. 37.

Wang, H. et al. Deep learning enables cross-modality super-resolution in fluorescence microscopy. *Nat. Methods* **16**, 103–110 (2019).

38. 38.

Ji, N. Adaptive optical fluorescence microscopy. *Nat. Methods* **14**, 374–380 (2017).

39. 39.

Royer, L. A. et al. Adaptive light-sheet microscopy for long-term, high-resolution imaging in live organisms. *Nat. Biotechnol.* **34**, 1267–1278 (2016).

40. 40.

Liu, T.-L. et al. Observing the cell in its native state: imaging subcellular dynamics in multicellular organisms. *Science* **360**, eaqq1392 (2018).

41. 41.

Zheng, W. et al. Adaptive optics improves multiphoton super-resolution imaging. *Nat. Methods* **14**, 869–872 (2017).

## Acknowledgements

We thank C. Liu and F. Zhang from the NHLBI Transgenic Core for making the TOMM20–mNeonGreen transgenic mouse line; E. Jorgensen, C. Frøkjær-Jensen and M. Rich for sharing the EG6994 *C. elegans* strain; L. Samelson for the gift of the Jurkat T cells; G. Patterson for the H2B–GFP plasmid; J. Hammer for the F-tractin–tdTomato plasmid; N. Koonce and L.

Shao for sharing images of larvae imaged with spinning-disk microscopy and iSIM; SVision LLC for maintaining and updating the 3D RCAN GitHub site; X. Li for assistance with imaging samples on the OMX 3D SIM; E. Tyler and A. Hoofring (NIH Medical Arts) for help with figure preparation; R. Leapman, H. Eden, S. Parekh and M. Guo for feedback on the manuscript; Q. Dai for supporting X.H.’s visit to H.S.’s lab; and C. Waterman for supporting R.F.’s participation in this project. We thank the Research Center for Minority Institutions programme, the Marine Biological Laboratories (MBL) and the Instituto de Neurobiología de la Universidad de Puerto Rico for providing meeting and brainstorming platforms. H.S., P.L.R. and D.C.-R. acknowledge the Whitman and Fellows programme at MBL for providing funding and space for discussions valuable to this work. Research in the D.C.-R. lab was supported by NIH grant no. R24-OD016474, NIH R01NS076558, DP1NS111778 and by an HHMI Scholar Award. X.H. was supported by an international exchange fellowship from the Chinese Scholar Council. This research was supported by the intramural research programmes of the National Institute of Biomedical Imaging and Bioengineering; National Institute of Heart, Lung, and Blood; Eunice Kennedy Shriver National Institute of Child Health and Human Development; and the National Cancer Institute within the National Institutes of Health. C.S. acknowledges funding from the National Institute of General Medical Sciences of the NIH under award number R25GM109439 (project title: University of Chicago Initiative for Maximizing Student Development (IMSD)) and NIBIB under grant number T32 EB002103. Y.P. and Y. Sun are supported by the Center for Cancer Research, the Intramural Program of the National Cancer Institute, NIH (Z01-BC 006150). This research is funded in part by the Gordon and Betty Moore Foundation. A.U. acknowledges support from NIH R01 GM131054. S.R. acknowledges support from NIH R35GM124878. This work utilized the computational resources of the NIH HPC Biowulf cluster (<http://hpc.nih.gov>), and we also thank the Office of Data Science Strategy, NIH, for providing a seed grant enabling us to train deep-learning models using cloud-based computational resources. The NIH and its staff do not recommend or endorse any company, product or service.

## Author information

## Author notes

1. These authors contributed equally: Yicong Wu, Xiaofei Han

## Affiliations

1. Laboratory of High Resolution Optical Imaging, National Institute of Biomedical Imaging and Bioengineering, National Institutes of Health, Bethesda, MD, USA

Yicong Wu, Xiaofei Han, Yijun Su, Ryan Christensen & Hari Shroff

2. Department of Automation, Tsinghua University, Beijing, China

Xiaofei Han

3. Leica Microsystems, Buffalo Grove, IL, USA

Yijun Su

4. SVision, Bellevue, WA, USA

Yijun Su

5. Applied Scientific Instrumentation, Eugene, OR, USA

Melissa Glidewell & Jonathan S. Daniels

6. Advanced Imaging and Microscopy Resource, National Institutes of Health, Bethesda, MD, USA

Jiamin Liu, Jiji Chen & Hari Shroff

7. Department of Neuroscience and Department of Cell Biology, Yale University School of Medicine, New Haven, CT, USA

Titas Sengupta, Leighton H. Duncan & Daniel Colón-Ramos

8. Institute for Physical Science and Technology, University of Maryland,  
College Park, MD, USA

Ivan Rey-Suarez & Arpita Upadhyaya

9. Cell and Developmental Biology Center, National Heart, Lung, and  
Blood Institute, National Institutes of Health, Bethesda, MD, USA

Robert Fischer

10. Department of Cell Biology and Molecular Genetics, University of  
Maryland, College Park, MD, USA

Akshay Patel & Sougata Roy

11. NHLBI Light Microscopy Facility, National Institutes of Health,  
Bethesda, MD, USA

Christian Combs & Xufeng Wu

12. Laboratory of Cardiac Physiology, National Heart, Lung, and Blood  
Institute, National Institutes of Health, Bethesda, MD, USA

Junhui Sun & Elizabeth Murphy

13. Department of Radiology, University of Chicago, Chicago, IL, USA

Corey Smith & Patrick La Riviere

14. Section on Molecular Morphogenesis, Eunice Kennedy Shriver  
National Institute of Child Health and Human Development (NICHD),  
National Institutes of Health (NIH), Bethesda, MD, USA

Lingyu Bao & Yun-Bo Shi

15. Laboratory of Molecular Pharmacology, Developmental Therapeutics  
Branch, Center for Cancer Research, National Institutes of Health,  
Bethesda, MD, USA

Yilun Sun & Yves Pommier

16. Department of Physics, University of Maryland, College Park, MD, USA

Arpita Upadhyaya

17. Marine Biological Laboratory, Woods Hole, MA, USA

Daniel Colón-Ramos, Patrick La Riviere & Hari Shroff

18. Instituto de Neurobiología, Recinto de Ciencias Médicas, Universidad de Puerto Rico, San Juan, Puerto Rico

Daniel Colón-Ramos

## Contributions

Conceived idea: Y.W., H.S. Designed and assembled line scanners: M.G., J.S.D. Tested line scanners: Y.W., X.H., M.G., J.S.D., H.S. Designed optical set-up: Y.W., X.H., H.S. Built optical set-up: Y.W., X.H. Designed reconstruction algorithms: Y.W., C.S., P.L.R., H.S. Wrote software: Y.W., X.H., J.L., C.S. Developed deep-learning nuclear segmentation pipeline: J.L. Developed cloud and local pipelines for deep learning: Y.W., J.L., J.C., H.S. Designed experiments: Y.W., X.H. Y. Su, T.S., I.R.-S., R.F., A.P., S.R., A.U., D.C.-R., H.S. Performed experiments: Y.W., X.H., Y. Su, T.S., I.R.-S., C.C., R.F., A.P., X.W. Prepared samples: Y.W., X.H., Y. Su, T.S., I.R.-S., R.F., A.P., C.C., J.S., R.C. Developed expansion microscopy procedures: Y. Su. Provided reagents or equipment: C.C., X.W., L.B., Y. Sun, L.H.D., Y.P., Y.-B.S. All authors analysed data. Wrote paper: Y.W., X.H., Y. Su, H.S., with input from all authors. Supervised research: Y.W., J.D., Y.P., Y.-B.S., E.M., S.R., A.U., D.C.-R., P.L.R., H.S. Directed research: H.S.

## Corresponding author

Correspondence to [Yicong Wu](#).

# Ethics declarations

## Competing interests

Y.W., X.H., P.L.R. and H.S. have filed invention disclosures covering aspects of this work (US patent application no. 63/001,672 and PCT application no. WO2021/202316). M.G. and J.S.D. are employees of Applied Scientific Instrumentation, which manufactures the line scanning units used in this work.

## Additional information

**Publisher's note** Springer Nature remains neutral with regard to jurisdictional claims in published maps and institutional affiliations.

## Extended data figures and tables

### Extended Data Fig. 1 Instrument overview.

- a) Photograph of instrument, highlighting objectives, cameras, sample area.
- b) CAD rendering of MEMS line scanner.
- c) Optical set-up. Diode lasers are combined and passed through an acousto-optic tunable filter (AOTF) for shuttering and power control, before being directed into broadband single-mode fibres. Galvanometric mirrors are used to direct beams into each fibre, and to adjust the power of the beams entering the fibre. Each fibre is then fed into a MEMS line scanner (purple dot-dashed line, here only one shown for clarity), with optics as indicated. The scanner serves to collimate the fibre output, focus it with a cylindrical lens, scan it with a MEMS mirror, and image the scanned output to a field stop at a conjugate sample plane. The beam is then relayed via lens L3 and the objective to the sample plane, after reflection from a dichroic mirror. Fluorescence is collected in epi-mode, transmitted through a dichroic mirror, and imaged via tube lens L4 onto a scientific CMOS camera where it is synchronized to the rolling shutter readout.
- d) Control waveforms issued to camera, MEMS scanner, objective piezo, and AOTF, used to acquire volumetric data. See

also [Supplementary Methods](#). **e**) Example line illumination at various lateral positions on camera chip, as imaged with fluorescent dye in lower view C. Excitation PSF measurements are taken at various positions in the field (see also Extended Data Fig. [2a, c](#)). Scale bar: 50  $\mu\text{m}$ . **f**) Example images acquired in *C. elegans* embryo expressing GFP-histones, as visualized in bottom view C with widefield mode (top) and line-scanning mode (slit width 0.58  $\mu\text{m}$ , bottom). Scale bar: 5  $\mu\text{m}$ .

### **Extended Data Fig. 2 Further characterization of imaging field.**

**a**)  $175 \times 175 \mu\text{m}^2$  imaging field, showing representative horizontal illumination lines across field, as measured in fluorescent dye. Also superimposed are example regions of interest (#1–#9) from a separate experiment, showing images of 100 nm fluorescent beads at different field locations. Scale bar: 20  $\mu\text{m}$ . **b**) Excitation uniformity measured along the long axis of illumination, from lines at top, middle, and bottom of imaging field, as marked in **a**). **c**) Full width at half maximum (FWHM) of short axis of illumination line, as measured at regions in **a**). FWHMs are estimated by scanning illumination relative to bead and recording intensity as a function of scan position. Means and standard deviations derived from 15 beads are reported at each location. **d**) As in **c**), but now reporting *x*, *y*, and *z* FWHMs derived from images of individual beads ( $n = 15$ ).

### **Extended Data Fig. 3 Resolution enhancement with triple-view confocal imaging.**

**a**) Lateral maximum intensity projection image of fixed U2OS cells immunolabelled with mouse-anti-alpha tubulin, anti-mouse-biotin, streptavidin Alexa Fluor 488, marking microtubules (fused result after registration and deconvolution of all three raw views). Height: colour bar. **b**) Raw and fused axial views along the dashed line in **a**). Fourier transforms of axial view are shown in last row, showing resolution enhancement after fusion. Orange oval:  $1/260 \text{ nm}^{-1}$  in half width and  $1/405 \text{ nm}^{-1}$  in half height. **c**) Triple-view reconstruction of whole fixed L1 stage larval worm, nuclei labelled with NucSpot 488. Two maximum intensity projections are shown, taken after rotating volume 220 degrees (top) and

300 degrees (bottom) about the *x* axis. **d**) Higher magnification lateral view 10  $\mu\text{m}$  from the beginning of the volume, corresponding to the yellow dashed region in **c**). **e**) Higher magnification axial views (single planes) corresponding to the red rectangular region in **c**), comparing single-view deconvolved result (left) to triple-view result (right). Magenta arrows highlight subnuclear structure better resolved in triple-view result. **f**) Line profiles corresponding to e1, e2 in **e**). Scale bars: **a, c**) 10  $\mu\text{m}$ ; **b, e**) 3  $\mu\text{m}$ .

#### **Extended Data Fig. 4 Contrast and resolution is enhanced after multiview fusion or SIM.**

**a)** Nanoscale imaging of organelles (mitochondrial outer membrane, cyan; and double stranded DNA, magenta) in expanded U2OS cells, to accompany Fig. [1f](#). Top: images, bottom: line profiles corresponding to a1–a3 at top. **b)** Neurons marked with membrane targeted GFP in living *C. elegans* embryos, to accompany Fig. [2i](#). Top: images; bottom: line profiles corresponding to b1–b4 at top,  $n = 5$  profiles at indicated positions were used to generate means  $\pm$  standard deviations for b1, b2. **c)** Stained actin in fixed B16F10 mouse melanoma cells embedded in collagen gels, to accompany Fig. [3c](#). Left: images; right: line profiles corresponding to c1–c4 at left. **d)** Neurons in fixed, expanded *C. elegans* embryos, to accompany Fig. [3e,f](#). Top: images; bottom: line profiles corresponding to d1–d6 at left,  $n = 7$  profiles at indicated positions were used to generate means  $\pm$  standard deviations for d1–d3. **e)** histone H2B puncta in live Jurkat T cells, to accompany Fig. [4c](#). Top: images; bottom: line profiles corresponding to e1–e3 at top,  $n = 10$  profiles at indicated positions were used to generate means  $\pm$  standard deviations for e1–e3. Scale bars: **a, d**) 2  $\mu\text{m}$ , **b, c, e**) 5  $\mu\text{m}$ .

#### **Extended Data Fig. 5 Triple-view comparisons in adult *C. elegans*.**

**a)** Axial views of whole fixed worm labelled with NucSpot Live 488, comparing raw views gathered by objectives A, B, C; triple-view reconstruction; and point-scanning confocal microscope. Arrows highlight example region with uniformly good quality in triple-view reconstruction, but showing attenuation either at bottom (Views A, B) or top (View C,

point-scanning confocal) of stack with other methods. See also Fig. 2g–j. **b)** Average attenuation measured through axial extent of the worm, as measured by raw views A, B C (top graph) and triple-view reconstruction and point-scanning confocal (bottom graph). Exponential fits to the data are also shown with dashed lines. See also [Supplementary Methods](#). **c–f)** Comparative higher magnification views of dashed red rectangular region in **a**), with bottom deconvolved view **c**), commercial Leica SP8 confocal microscope **e**), conventional triple-view deconvolution **d**), attenuation-compensated triple-view deconvolution **f**). Coloured arrows highlight comparisons, orange: single-view versus triple-view, magenta: deconvolution methods. Scale bar: **a)** 50  $\mu\text{m}$ , **c–f)** 10  $\mu\text{m}$ .

### [Extended Data Fig. 6 Triple-view comparisons in scattering tissue.](#)

**a)** Schematic of kidney: approximate region where tissue was extracted. **b)** Four colour triple-view reconstruction of mouse kidney slice. Lateral image at 4- $\mu\text{m}$  depth, highlighting glomerulus surrounded by convoluted tubules. Red: nuclei stained with DAPI, green: actin stained with phalloidin-Alexa Fluor 488; magenta: tubulin immunolabelled with mouse- $\alpha$ -Tubulin primary,  $\alpha$ -Mouse-JF549 secondary; yellow: CD31 immunolabelled with Goat- $\alpha$ -CD31 primary,  $\alpha$ -Goat AF647 secondary. Scale bar: 20  $\mu\text{m}$ . **c)** Comparative higher magnification of white rectangular region in **b**) at 28- $\mu\text{m}$  depth. Scale bar: 20  $\mu\text{m}$ . **d)** Comparative axial view along dashed line in **b**). White arrows: structures that are dim in single-view but restored in triple-view. Scale bar: 20  $\mu\text{m}$ . **e)** Triple-view reconstruction of mouse cardiac tissue ( $\sim 536 \times 536 \times 37 \mu\text{m}^3$  section, shown is a maximum intensity projection of axial slices from 10–30  $\mu\text{m}$ ). Magenta: Atto 647 NHS, nonspecifically marking proteins, cyan: NucSpot Live 488, marking nuclei. Scale bar: 50  $\mu\text{m}$ . **f)** Higher-magnification view of orange rectangular region in **e**), comparing raw View C (top) to triple-view reconstruction (bottom). Scale bar: 20  $\mu\text{m}$ . **g)** Labels as in **e**) but showing triple-view reconstruction of mouse brain tissue ( $\sim 536 \times 536 \times 25 \mu\text{m}^3$  section, shown is a maximum intensity projection of axial slices from 5–15  $\mu\text{m}$ ). Scale bar: 50  $\mu\text{m}$ . **h)** Axial maximum intensity projection computed over 120  $\mu\text{m}$  vertical extent of white rectangular region shown in **g**), comparing raw View C (top) to triple-view (bottom) result. Scale bar: 10  $\mu\text{m}$ . **i)** Mouse

cardiac tissue stained with Atto 647 NHS (same sample as **e**), nonspecifically marking proteins, as observed in lower view C (left), after triple-view deconvolution (middle), and triple-view deconvolution after flat-fielding (right). Scale bar: 20  $\mu\text{m}$ . **j**) Intensity profiles from **i**), created by averaging across vertical axis.

### Extended Data Fig. 7 Triple-view comparisons in *Drosophila* wing imaginal disks.

**a**) Schematic of larval wing disc, lateral (top) and axial (bottom) views, including adult muscle precursor myoblasts and notum. **b**) Lateral plane from triple-view reconstruction, 30  $\mu\text{m}$  from sample surface. Notum nuclei (NLS-mCherry, magenta) and myoblast membranes (CD2-GFP, cyan) labelled. **c**) Axial maximum intensity projection derived from 6- $\mu\text{m}$ -thick yellow rectangle in **b**). **d**) Higher magnification view of white dashed line/rectangle in **b**, **c**), comparing single view C deconvolution (left) to triple-view result (right). White arrows: membrane observed in triple-view but absent in single-view. **e**) Line profiles corresponding to d1, d2 in **d**). **f**) Lateral (left) and axial (right) maximum intensity projections of the larval wing disc. **g**) As in **f**) but showing another larval wing disc imaged with a spinning-disk confocal microscope with NA = 1.3. Scale bars: **b**, **c**) 20  $\mu\text{m}$ , **d**) 5  $\mu\text{m}$ , **f**, **g**) 15  $\mu\text{m}$ .

### Extended Data Fig. 8 Live triple-view confocal imaging of Cardiomyocytes.

**a**) Cardiomyocytes expressing EGFP-Tomm20, labelled with MitoTracker Red CMXRos, imaged with triple-view confocal microscopy in 2.03 s, every 20 s, for 100 time points. Lateral (top) and axial (bottom) maximum intensity projections shown at indicated times before and after registration/deconvolution. Scale bar: 10  $\mu\text{m}$ . **b**) Higher-magnification view of orange rectangular region in **a**), highlighting mitochondrial fluctuations (red arrows) over time. Scale bar: 3  $\mu\text{m}$ . See also Supplementary Video 3.

### Extended Data Fig. 9 Neural network schematics.

**a)** Workflow for two-step deep learning procedure used in Fig. 2e–i.

Denoising neural networks are trained for views A, B, C, by using matched high and low SNR volumes derived from embryos paralysed with sodium azide. The denoising output of each model are combined with joint deconvolution (triple-view decon) and are combined with the denoised view C output to train a second neural work (Decon model). In this manner, noisy raw data from View C can be transformed into a high SNR, high resolution prediction. **b)** Example data (lateral slice through GFP-histone expressing *C. elegans* embryo) from left to right: raw View C data; single neural-network prediction (raw input View C to high SNR, triple-view deconvolved result); two-step denoised and deconvolved prediction; high SNR denoised triple-view deconvolved result (i.e., ground truth used in training the second neural network in **a**). The two-step prediction is noticeably closer to the ground truth (red arrows highlight regions for comparison; 3D SSIM  $0.89 \pm 0.05$ , PSNR  $43.4 \pm 2.2$  (mean  $\pm$  standard deviation,  $n = 7$  embryos) than the single network (3D SSIM  $0.72 \pm 0.17$ , PSNR  $27.8 \pm 6.4$ ,  $n = 7$ ). Scale bar: 10  $\mu\text{m}$ . See also Fig. 2e. **c)** Example raw input (left), output of single neural network (middle), and two-step output (right) for AIB neuron. Axial views are shown, orange arrows that fine features are better preserved in two-step rather than one-step neural network. Scale bar: 5  $\mu\text{m}$ . See also Fig. 2h,i. **d)** Training and validation loss (left) and error (right) as a function of epoch number, for the second step in the neural network, i.e., denoised view C input and triple-view deconvolved output in **c**). MSE: mean square error. MAE: mean absolute error. **e)** Mask RCNN used for segmenting nuclear data in Figs. 1j, 2e. Key components of the Mask RCNN include a backbone network, region proposal network (RPN), object classification module, bounding box regression module, and mask segmentation module. The backbone network is a convolutional neural network that extracts features from the input image. The RPN scans the feature map to detect possible candidate areas that may contain objects (nuclei). For each bounding box containing an object, the object classification module (containing fully connected (FC) layers) classifies objects into specific object class(es) or a background class. The bounding box regression module refines the location of the box to better contain the object. Finally, the mask segmentation module takes the foreground regions selected by the object classification module and generates segmentation masks. **f)** Post processing after Mask-RCNN. Nuclei (here four are shown)

are often connected and need to be split. We apply the watershed algorithm to split the nuclei based on a distance transform. **g**) Number of nuclei segmented by two-step deep learning, raw single-view light-sheet imaging, and single-view light-sheet imaging passed through DenseDeconNet, a neural network designed to improve resolution isotropy. Means and standard deviations shown from 16 embryos. See also Fig. 2f. **h**) Higher magnification of neurites in Fig. 2i. Neurites straightened using ImageJ; corresponding neurite tip regions are indicated by red arrows in Fig. 2i. White arrowheads: varicosities evident in deep learning prediction (top) but obscured in the diSPIM data. Yellow dashed lines outline neurite. Scale bar: 2  $\mu\text{m}$ .

### **Extended Data Fig. 10 Triple-view 1D SIM methods.**

**a)** Workflow for a single scanning direction and extension for multiview 1D SIM. Five confocal images are acquired per plane, each with illumination structure shifted  $2\pi/5$  in phase relative to the previous position. Averaging produces diffraction-limited images. Detecting each illumination maximum and reassigning the fluorescence signal around it (photon reassignment) improves spatial resolution in the direction of the line scan. Combining image volumes acquired from multiple views further improves volumetric resolution. Images are of immunolabelled microtubules in fixed U2OS cells and corresponding Fourier transforms. Scale bar: 2  $\mu\text{m}$ . **b)** Simulated fluorescence patterns elicited by (top to bottom) 3, 4, 5, 6 phase illumination. Modulation contrast for each pattern is also indicated. Scale bar: 1  $\mu\text{m}$ . See also [Supplementary Methods](#). **c)** Raw data as excited with 3, 4, 5, 6 phase illumination. **d)** Corresponding deconvolved result after photon-reassignment. Scale bars in **c**, **d**): 3  $\mu\text{m}$ . **e)** Fourier transforms corresponding to **d**). Vertical/horizontal resolution improvement corresponding to red ellipse also indicated. **f)** Line profiles for 3, 4, 5, 6 phase illumination, corresponding to dotted red line in **b**). **g)** As in **f**) but corresponding to dotted line in **c**).

### **Extended Data Fig. 11 Triple-view 1D SIM of *C. elegans* embryo.**

**a)** Fixed *C. elegans* embryo (strain DCR6681) with tubulin immunolabelled with  $\alpha$ -alpha tubulin primary,  $\alpha$ -mouse-biotin, Streptavidin Alexa Fluor 568, imaged via lower View C (left) and triple-view 1D SIM mode (right). Lateral (left) and axial (right) maximum intensity projections are shown in each case. Scale bars: 5  $\mu\text{m}$ . Higher magnification lateral **b)** views and axial **c)** views of yellow and red rectangular regions in **a)** are also indicated, highlighting progressive improvement in resolution from view C (left), to triple-view diffraction-limited result (middle), to triple-view 1D SIM result (right). Scale bars: 2  $\mu\text{m}$ .

### Extended Data Fig. 12 Triple-view 1D SIM of cells.

**a, b)** Comparative triple-view SIM **a)** and instant SIM **b)** maximum intensity projections of the same fixed HEY-T30 cell embedded in collagen gel, labelled with MitoTracker Red CMXRos and Alexa Fluor 488 phalloidin. White and magenta arrows: the same features in lateral (left) and axial (right) projections. Insets are higher magnification axial views of dashed rectangular regions. **c)** Comparative raw single view C (left of dashed orange line) and triple-view SIM (right of dashed line) maximum intensity projections of fixed and 4 $\times$  expanded U2OS cell, immunolabelled with rabbit anti-Tomm20 primary, anti-rabbit-biotin, streptavidin Alexa Fluor 488 marking mitochondria (cyan) and mouse anti-alpha tubulin primary, anti-mouse JF 549, marking tubulin. Lateral (top) and axial (bottom) views are shown. **d)** Higher magnification views of white dashed region in **c**), comparing triple-view (left) and triple-view SIM (right) reconstructions. Bottom: sector-based decorrelation analysis to estimate spatial resolution in images at top. Resolution values for horizontal and vertical directions are indicated. Scale bars: **a–c)** 5  $\mu\text{m}$ , **d)** 1  $\mu\text{m}$ .

### Extended Data Fig. 13 Expansion workflow and imaging results for *C. elegans* embryos, related to Fig. 3d.

**a)** Immobilization, permeabilization, fixation, immunostaining, and expansion takes approximately four days. **b)** Overlay of embryo stained with DAPI before and after expansion after 12-degree affine registration (cyan: pre-expansion; magenta: post-expansion). The embryo was imaged with diSPIM. Single-view maximum intensity projection along *xy* and *xz*

views are shown for comparison. The registration results from 7 embryos (normalized cross-correlation:  $0.72 \pm 0.03$ ) show that the expansion factor for whole embryos is  $3.29 \pm 0.14$ , with nearly isotropic expansion ( $3.24 \pm 0.14$ ,  $3.39 \pm 0.14$ ,  $3.26 \pm 0.17$  for  $x$ ,  $y$  and  $z$  dimensions, respectively). Scale bar: 5  $\mu\text{m}$  in pre-expansion units. **c**) Magnified view of the rectangle shown in **b**), showing no obvious local distortions in nuclei shape during expansion. Scale bar: 2  $\mu\text{m}$  in pre-expansion units.

**Extended Data Fig. 14 Simulation of the deep-learning method for isotropic in-plane super-resolution imaging.**

**a)** An object (left column) consisting of lines and hollow spheres can be blurred to resemble diffraction-limited confocal input (middle column). Fourier transform of the raw input is shown (right column). **b)** Deep-learning 1D super-resolution output with no rotation (left column); deep learning output after rotating input by 30 degrees (middle column); deep learning output after rotating input by 60 degrees (right column). Fourier transforms in bottom row confirm 1D resolution enhancement regardless of rotation angle. **c)** Deep learning output after rotating input by 90 degrees (left column); outputs after deep learning and joint deconvolution of two orientations (middle column), or six orientations (right column) show progressive improvement in resolution isotropy (red arrows), confirmed with Fourier transforms of the images (bottom row). Ellipses bound decorrelation estimates of resolution (numerical values from ellipse boundary indicated in red text). Scale bar: 2  $\mu\text{m}$ .

**Extended Data Fig. 15 Isotropic in-plane super-resolution imaging of fixed cells.**

**a)** Immunolabelled microtubules in fixed U2OS cells, from the same sample shown in Fig. 4b. Shown are raw input (view C); 1D SIM output after physics-based reconstruction with five images; deep learning 1D super-resolution output after rotation at 0 degrees; deep learning 1D super-resolution output after rotation at 120 degrees and rotation back to the original frame. Scale bar: 10  $\mu\text{m}$ . Accompanying Fourier transforms are shown in bottom row. **b)** Higher magnification view of red dashed region in

**a**), comparing raw confocal input, 1D SIM output after deep learning and deconvolution, and 2D SIM output after deep learning and joint deconvolution after six rotations. Arrows highlight regions for comparison. **c**) Profiles along red line in **b**), comparing the resolution of two filaments in 2D SIM mode (red), 1D SIM mode (blue), and confocal input (black).

### Extended Data Fig. 16 Isotropic in-plane super-resolution imaging of living cells.

**a**) Lateral maximum intensity projections of Jurkat T cell expressing EMTB-3XGFP (yellow) and F-tractin-tdTomato (red), volumetrically imaged every 2 s, as imaged with raw line confocal input (view C, left) and 2D SIM output after deep learning and joint deconvolution with six rotations. Four time points from 150 volume series are shown; green arrows highlight features better resolved in 2D SIM output vs. raw input; white arrows indicate actin dynamics at cell periphery. Scale bar: 5  $\mu\text{m}$ . See also Supplementary Video 6. **b**) Imaris 3D renderings of Jurkat T cell (same sample as shown in Fig. 4c) with nucleus (histone H2B-GFP, cyan, top) and segmented centrosome (EMTB-mCherry, magenta, bottom) at indicated time points. The centrosome produces a concave nuclear deformation (red arrows), pulling and rotating the nucleus as it becomes docked at the immune synapse. Scale bar: 5  $\mu\text{m}$ . **c**) Maximum intensity projections over bottom half of EMTB-mCherry volumes at indicated times, showing coordinated movement of the microtubule cytoskeleton. Coloured arrowheads mark regions for comparison. See also Supplementary Video 6. Scale bar: 5  $\mu\text{m}$ .

### Extended Data Fig. 17 Multi-modality imaging enabled with the multiview line confocal system.

**a**) Different methods of combining data, enabling a highly versatile imaging platform. Left: Diffraction limited volumes acquired from views A (yellow), B (green), C (red) may be combined with joint deconvolution to yield triple-view diffraction-limited data (RYG arrows). Middle: Alternatively, 5 volumes per view may be collected and processed as in Extended Data Fig. 10 for 1D SIM, and the 3 1D SIM volumes combined

using joint deconvolution to reconstruct triple-view 1D SIM data. Right: Instead, confocal data from each view may be passed through 1D SIM networks, and the data combined via joint deconvolution. Combining 6 rotations (for clarity only two are shown in figure) from view C yields view C 2D SIM data. If the procedure is repeated for views A, B, and the data combined with joint deconvolution, triple-view 2D SIM data may be obtained.  $xz$  cross-sections through PSFs are shown in black boxes. Blue volumes are relative sizes of PSFs that result from each process. Scale bars: white: 500 nm, black: 200 nm. **b)** Applications include wide-field microscopy, single-view line confocal microscopy (from any of the views), single-view 1D SIM, triple-view diffraction limited imaging, and triple-view 1D SIM. With deep learning (red), triple-view line confocal volumes can be predicted from low SNR single-view input, 1D SIM can be predicted from diffraction-limited input, and combination with joint deconvolution allows further extension to single- and triple-view 2D SIM. Biological and imaging performance examples (resolution, imaging speed and duration) are also provided. Resolution values in line confocal microscopy, triple-view line confocal (without deep learning), and triple-view 1D-SIM (without deep learning) are estimated from immunostained microtubules in fixed U2OS cells. Deep learning resolution values are estimated from fine *C. elegans* embryo neurites (triple-view confocal) or actin fibres (single view 2D SIM, triple-view 2D SIM). See also Supplementary Table 1. **c)** Decorrelation resolution analysis from the images of worm L4 larval (strain DCR8528) expressing membrane targeted GFP primarily in the nervous system. See also Extended Data Fig. 18d and Fig. 4i–m. Data (mean  $\pm$  standard deviation) are derived from 45 measurements (3 animals, 15 planes per animal). Given the ~2.3-fold improvement laterally and ~2.6-fold improvement axially, the triple-view 2D SIM ( $253 \times 253 \times 322 \text{ nm}^3$ ) result offers a volume resolution improvement of ~13.8-fold over the raw view C data ( $601 \times 56 \times 836 \text{ nm}^3$ ). **d)** Apparent widths (open circles, mean  $\pm$  standard deviation) of 8 actin fibres from the cell presented in Fig. 4n–q, comparing lateral (left) and axial (right) full width at half maximum in different microscope modalities. Given the ~2.2-fold improvement laterally and ~2.4-fold improvement axially, the triple-view 2D SIM result offers a volume resolution improvement of ~11.6-fold over the raw view C data.

## Extended Data Fig. 18 Multiview super-resolution imaging of larval worm.

**a**) Maximum intensity projection of fixed L2 stage larval worm expressing membrane targeted GFP primarily in the nervous system, imaged in triple-view 2D SIM mode. Anatomy as highlighted. **b**) Higher magnification views (single slices 6  $\mu\text{m}$  into volume) of dashed green rectangle in **a**), highlighting VNC neurons as viewed in diffraction-limited View C (upper), triple-view 1D SIM obtained by processing 15 volumes (5 per view, middle), and triple-view 2D SIM mode (3 volumes, 1 per view, lower). **c**) Line profiles corresponding to b1–b3 in **b**). **d**) Lateral (upper) and axial (bottom) maximum intensity projections from anaesthetized L4 stage larval worm expressing the same marker, comparing dense nerve ring region imaged in diffraction-limited view C (left), view C 2D SIM mode (middle), and iSIM (right). Purple, red arrows highlight labelled cell bodies or membranous protrusions for comparison. See also Fig. 4i–m. **e**) Fixed *C. elegans* L2 larvae (strain DCR6681) expressing GFP-membrane marker imaged in commercial OMX 3D SIM system. A single slice  $\sim$ 2  $\mu\text{m}$  from the bottom surface of the worm is shown, derived from 5  $\mu\text{m}$  stack. Raw data (top) and reconstruction (bottom) are shown. No modulation is evident in raw data, and reconstruction shows obvious artifacts (red arrows). Scale bars: **a, d**) 10  $\mu\text{m}$ ; **b, e**) 5  $\mu\text{m}$ .

## Extended Data Table 1 Characterization of imaging field

## Supplementary information

### Supplementary Information

The Supplementary Information includes (1) legends for Supplementary Videos 1–8 (page 3); (2) Supplementary Methods (pages 4–23); and (3) Supplementary Table (pages 24–27).

### Reporting Summary

### Peer Review File

## **Supplementary Video 1**

See Supplementary Information for description.

## **Supplementary Video 2**

See Supplementary Information for description.

## **Supplementary Video 3**

See Supplementary Information for description.

## **Supplementary Video 4**

See Supplementary Information for description.

## **Supplementary Video 5**

See Supplementary Information for description.

## **Supplementary Video 6**

See Supplementary Information for description.

## **Supplementary Video 7**

See Supplementary Information for description.

## **Supplementary Video 8**

See Supplementary Information for description.

## **Source data**

### **Source Data Fig. 2**

# Rights and permissions

[Reprints and Permissions](#)

## About this article

### Cite this article

Wu, Y., Han, X., Su, Y. *et al.* Multiview confocal super-resolution microscopy. *Nature* **600**, 279–284 (2021). <https://doi.org/10.1038/s41586-021-04110-0>

- Received: 14 June 2021
- Accepted: 07 October 2021
- Published: 26 November 2021
- Issue Date: 09 December 2021
- DOI: <https://doi.org/10.1038/s41586-021-04110-0>

### Share this article

Anyone you share the following link with will be able to read this content:

[Get shareable link](#)

Sorry, a shareable link is not currently available for this article.

[Copy to clipboard](#)

Provided by the Springer Nature SharedIt content-sharing initiative

| [Section menu](#) | [Main menu](#) |

- Article
- [Published: 17 November 2021](#)

# Single-cell transcriptomic characterization of a gastrulating human embryo

- [Richard C. V. Tyser](#) [ORCID: orcid.org/0000-0001-7884-1756](#)<sup>1 na1</sup>,
- [Elmir Mahammadov](#) [ORCID: orcid.org/0000-0003-0008-1413](#)<sup>2,3,4 na1</sup>,
- [Shota Nakano](#)<sup>5</sup>,
- [Ludovic Vallier](#) [ORCID: orcid.org/0000-0002-3848-2602](#)<sup>5</sup>,
- [Antonio Scialdone](#) [ORCID: orcid.org/0000-0002-4956-2843](#)<sup>2,3,4 na2</sup>  
&
- [Shankar Srinivas](#) [ORCID: orcid.org/0000-0001-5726-7791](#)<sup>1 na2</sup>

[Nature](#) volume 600, pages 285–289 (2021)

- 13k Accesses
- 1 Citations
- 949 Altmetric
- [Metrics details](#)

## Subjects

- [Epithelial–mesenchymal transition](#)
- [Gastrulation](#)
- [Haematopoiesis](#)
- [Mesoderm](#)
- [Pluripotent stem cells](#)

# Abstract

Gastrulation is the fundamental process in all multicellular animals through which the basic body plan is first laid down<sup>1,2,3,4</sup>. It is pivotal in generating cellular diversity coordinated with spatial patterning. In humans, gastrulation occurs in the third week after fertilization. Our understanding of this process in humans is relatively limited and based primarily on historical specimens<sup>5,6,7,8</sup>, experimental models<sup>9,10,11,12</sup> or, more recently, in vitro cultured samples<sup>13,14,15,16</sup>. Here we characterize in a spatially resolved manner the single-cell transcriptional profile of an entire gastrulating human embryo, staged to be between 16 and 19 days after fertilization. We use these data to analyse the cell types present and to make comparisons with other model systems. In addition to pluripotent epiblast, we identified primordial germ cells, red blood cells and various mesodermal and endodermal cell types. This dataset offers a unique glimpse into a central but inaccessible stage of our development. This characterization provides new context for interpreting experiments in other model systems and represents a valuable resource for guiding directed differentiation of human cells in vitro.

This is a preview of subscription content

## Access options

Subscribe to Journal

Get full journal access for 1 year

\$199.00

only \$3.90 per issue

[Subscribe](#)

All prices are NET prices.

VAT will be added later in the checkout.

Tax calculation will be finalised during checkout.

Rent or Buy article

Get time limited or full article access on ReadCube.

from \$8.99

[Rent or Buy](#)

All prices are NET prices.

### **Additional access options:**

- [Log in](#)
- [Learn about institutional subscriptions](#)

**Fig. 1: Morphological and transcriptional characterization of a CS7 human gastrula.**

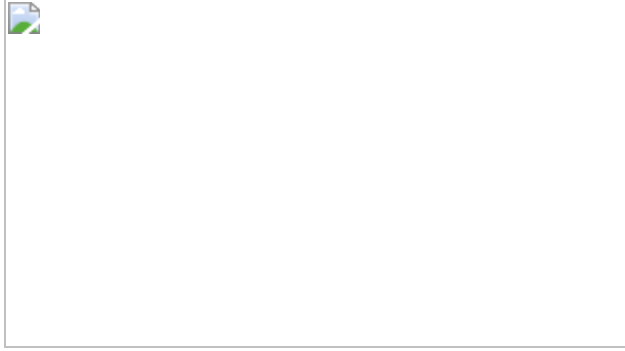


**Fig. 2: State transitions during gastrulation.**



**Fig. 3: Identification of cell subtypes.**

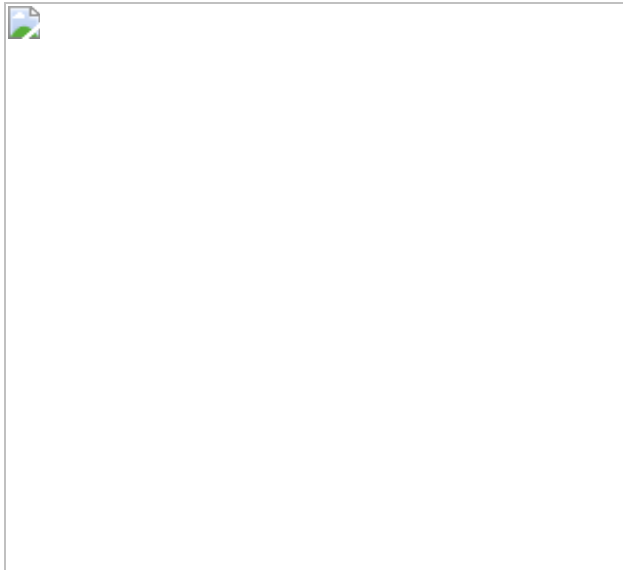


**Fig. 4: Identification of early blood progenitor types in the human.**



## Data availability

The raw data from our study can be downloaded from ArrayExpress under accession code [E-MTAB-9388](#). The processed data can be downloaded from <http://www.human-gastrula.net>. Datasets used as references include mouse gastrula data ([E-MTAB-6967](#)); pre-implantation embryo data: [E-MTAB-3929](#). [Source data](#) are provided with this paper.

## Code availability

All data were analysed with standard programs and packages, as detailed in Methods. The code used to create the human gastrula shiny app is available at <https://github.com/ScialdoneLab/human-gastrula-shiny>.

## References

1. 1.

Stern, C. D. *Gastrulation: From Cells to Embryo* (CSHL Press, 2004).

2. 2.

Tam, P. P. L. & Loebel, D. A. F. Gene function in mouse embryogenesis: get set for gastrulation. *Nat. Rev. Genet.* **8**, 368–381 (2007).

3. 3.

Bardot, E. S. & Hadjantonakis, A. K. Mouse gastrulation: coordination of tissue patterning, specification and diversification of cell fate. *Mech. Dev.* **163**, 103617 (2020).

4. 4.

Arnold, S. J. & Robertson, E. J. Making a commitment: cell lineage allocation and axis patterning in the early mouse embryo. *Nat. Rev. Mol. Cell Biol.* **10**, 91–103 (2009).

5. 5.

O’Rahilly, R. & Müller, F. Developmental stages in human embryos: Revised and new measurements. *Cells Tissues Organs* **192**, 73–84 (2010).

6. 6.

Yamaguchi, Y. & Yamada, S. The Kyoto collection of human embryos and fetuses: History and recent advancements in modern methods. *Cells Tissues Organs* **205**, 314–319 (2019).

7. 7.

Florian, J. & Hill, J. P. An early human embryo (no. 1285, Manchester Collection), with capsular attachment of the connecting stalk. *J. Anat.* **69**, 399–411 (1935).

8. 8.

De Bakker, B. S. et al. An interactive three-dimensional digital atlas and quantitative database of human development. *Science* **354**, aag0053 (2016).

9. 9.

Warmflash, A., Sorre, B., Etoc, F., Siggia, E. D. & Brivanlou, A. H. A method to recapitulate early embryonic spatial patterning in human embryonic stem cells. *Nat. Methods* **11**, 847–854 (2014).

10. 10.

Martyn, I., Kanno, T. Y., Ruzo, A., Siggia, E. D. & Brivanlou, A. H. Self-organization of a human organizer by combined Wnt and Nodal signaling. *Nature* **558**, 132–135 (2018).

11. 11.

Simunovic, M. et al. A 3D model of a human epiblast reveals BMP4-driven symmetry breaking. *Nat. Cell Biol.* **21**, 900–910 (2019).

12. 12.

Moris, N. et al. An in vitro model of early anteroposterior organization during human development. *Nature* **582**, 410–415 (2020).

13. 13.

Chen, D. et al. Human primordial germ cells are specified from lineage-primed progenitors. *Cell Rep.* **29**, 4568–4582.e5 (2019).

14. 14.

Molè, M. A. et al. A single cell characterisation of human embryogenesis identifies pluripotency transitions and putative anterior hypoblast centre. *Nat. Commun.* **12**, 3769 (2021).

15. 15.

Xiang, L. et al. A developmental landscape of 3D-cultured human pre-gastrulation embryos. *Nature* **577**, 537–542 (2020).

16. 16.

Zhou, F. et al. Reconstituting the transcriptome and DNA methylome landscapes of human implantation. *Nature* **572**, 660–664 (2019).

17. 17.

O’Rahilly, R. & Müller, F. eds. *Developmental Stages in Human Embryos*. (Carnegie Institute of Washington, 1987).

18. 18.

Pijuan-Sala, B. et al. A single-cell molecular map of mouse gastrulation and early organogenesis. *Nature* **566**, 490–495 (2019).

19. 19.

Ma, H. et al. In vitro culture of cynomolgus monkey embryos beyond early gastrulation. *Science* **366**, eaax7890 (2019).

20. 20.

Petropoulos, S. et al. Single-cell RNA-seq reveals lineage and X chromosome dynamics in human preimplantation embryos. *Cell* **165**, 1012–1026 (2016).

21. 21.

Messmer, T. et al. Transcriptional heterogeneity in naive and primed human pluripotent stem cells at single-cell resolution. *Cell Rep.* **26**, 815–824.e4 (2019).

22. 22.

Haghverdi, L., Büttner, M., Wolf, F. A., Buettner, F. & Theis, F. J. Diffusion pseudotime robustly reconstructs lineage branching. *Nat. Methods* **13**, 845–848 (2016).

23. 23.

La Manno, G. et al. RNA velocity of single cells. *Nature* **560**, 494–498 (2018).

24. 24.

Streit, A. The preplacodal region: an ectodermal domain with multipotential progenitors that contribute to sense organs and cranial sensory ganglia. *Int. J. Dev. Biol.* **51**, 447–461 (2007).

25. 25.

Trevors, K. E. et al. Neural induction by the node and placode induction by head mesoderm share an initial state resembling neural plate border and ES cells. *Proc. Natl Acad. Sci. USA* **115**, 355–360 (2017).

26. 26.

Delile, J. et al. Single cell transcriptomics reveals spatial and temporal dynamics of gene expression in the developing mouse spinal cord. *Development* **146**, dev1738078 (2019).

27. 27.

Yang, L. et al. An early phase of embryonic Dlx5 expression defines the rostral boundary of the neural plate. *J. Neurosci.* **18**, 8322–8330 (1998).

28. 28.

Roost, M. S. et al. KeyGenes, a tool to probe tissue differentiation using a human fetal transcriptional atlas. *Stem Cell Rep.* **4**, 1112–1124 (2015).

29. 29.

Chiquoine, A. D. The identification, origin, and migration of the primordial germ cells in the mouse embryo. *Anat. Rec.* **118**, 135–146 (1954).

30. 30.

Magnúsdóttir, E. & Surani, A. M. How to make a primordial germ cell. *Development* **141**, 245–252 (2014).

31. 31.

Sasaki, K. et al. The germ cell fate of cynomolgus monkeys is specified in the nascent amnion. *Dev. Cell* **39**, 169–185 (2016).

32. 32.

Picelli, S. et al. Full-length RNA-seq from single cells using Smart-seq2. *Nat. Protoc.* **9**, 171–181 (2014).

33. 33.

Patro, R., Duggal, G., Love, M. I., Irizarry, R. A. & Kingsford, C. Salmon provides fast and bias-aware quantification of transcript expression. *Nat. Methods* **14**, 417–419 (2017).

34. 34.

Lun, A. T. L., Bach, K. & Marioni, J. C. Pooling across cells to normalize single-cell RNA sequencing data with many zero counts. *Genome Biol.* **17**, 75 (2016).

35. 35.

Wolf, F. A., Angerer, P. & Theis, F. J. SCANPY: Large-scale single-cell gene expression data analysis. *Genome Biol.* **19**, 15 (2018).

36. 36.

McInnes, L., Healy, J., Saul, N. & Großberger, L. UMAP: uniform manifold approximation and projection. *J. Open Source Softw.* **3**, 861 (2018).

37. 37.

Traag, V. A., Waltman, L. & van Eck, N. J. From Louvain to Leiden: guaranteeing well-connected communities. *Sci. Rep.* **9**, 5233 (2019).

38. 38.

Patrick, E. A. Clustering using a similarity measure based on shared near neighbors. *IEEE Trans. C-22*, 1025–1034 (1973).

39. 39.

Froussios, K., Mourão, K., Simpson, G., Barton, G. & Schurch, N. Relative abundance of transcripts (RATs): identifying differential isoform abundance from RNA-seq. *F1000Research* **8**, 213 (2019).

40. 40.

Dobin, A. et al. STAR: Ultrafast universal RNA-seq aligner. *Bioinformatics* **29**, 15–21 (2013).

41. 41.

Bergen, V., Lange, M., Peidli, S., Wolf, F. A. & Theis, F. J. Generalizing RNA velocity to transient cell states through dynamical modeling. *Nat. Biotechnol.* **38**, 1408–1414 (2020).

42. 42.

Durinck, S., Spellman, P. T., Birney, E. & Huber, W. Mapping identifiers for the integration of genomic datasets with the R/Bioconductor package biomaRt. *Nat. Protoc.* **4**, 1184–1191 (2009).

43. 43.

Efremova, M., Vento-Tormo, M., Teichmann, S. A. & Vento-Tormo, R. CellPhoneDB: inferring cell–cell communication from combined expression of multi-subunit ligand–receptor complexes. *Nat. Protoc.* **15**, 1484–1506 (2020).

44. 44.

Kiselev, V. Y., Yiu, A. & Hemberg, M. scmap: Projection of single-cell RNA-seq data across data sets. *Nat. Methods* **15**, 359–362 (2018).

45. 45.

Grün, D. et al. Single-cell messenger RNA sequencing reveals rare intestinal cell types. *Nature* **525**, 251–255 (2015).

46. 46.

Subramanian, A. et al. Gene set enrichment analysis: a knowledge-based approach for interpreting genome-wide expression profiles. *Proc. Natl Acad. Sci. USA* **102**, 15545–15550 (2005).

47. 47.

Scialdone, A. et al. Computational assignment of cell-cycle stage from single-cell transcriptome data. *Methods* **85**, 54–61 (2015).

48. 48.

Leng, N. et al. Oscope identifies oscillatory genes in unsynchronized single-cell RNA-seq experiments. *Nat. Methods* **12**, 947–950 (2015).

49. 49.

Segal, J. M. et al. Single cell analysis of human foetal liver captures the transcriptional profile of hepatobiliary hybrid progenitors. *Nat. Commun.* **10**, 3350 (2019).

50. 50.

Li, H. Aligning sequence reads, clone sequences and assembly contigs with BWA-MEM. Preprint at <https://arxiv.org/abs/1303.3997> (2013).

51. 51.

Yang, R., Van Etten, J. L. & Dehm, S. M. Indel detection from DNA and RNA sequencing data with transIndel. *BMC Genomics* **19**, 270 (2018).

52. 52.

Love, M. I., Huber, W. & Anders, S. Moderated estimation of fold change and dispersion for RNA-seq data with DESeq2. *Genome Biol.* **15**, 550 (2014).

53. 53.

Stuart, T. et al. Comprehensive integration of single-cell data. *Cell* **177**, 1888–1902.e21 (2019).

54. 54.

Korsunsky, I. et al. Fast, sensitive and accurate integration of single-cell data with Harmony. *Nat. Methods* **16**, 1289–1296 (2019).

55. 55.

Chen, G. et al. Chemically defined conditions for human iPSC derivation and culture. *Nat. Methods* **8**, 424–429 (2011).

56. 56.

Johansson, B. M. & Wiles, M. V. Evidence for involvement of activin A and bone morphogenetic protein 4 in mammalian mesoderm and hematopoietic development. *Mol. Cell. Biol.* **15**, 141–151 (1995).

57. 57.

Choi, H. M. T. et al. Third-generation *in situ* hybridization chain reaction: multiplexed, quantitative, sensitive, versatile, robust. *Development* **145**, dev165753 (2018).

58. 58.

Tyser, R. C. V. et al. Characterization of a common progenitor pool of the epicardium and myocardium. *Science* **371**, eabb2986 (2021).

## Acknowledgements

Human embryonic material was provided by the MRC–Wellcome Trust funded (grant no. 099175/Z/12/Z and MR/R006237/1) Human Developmental Biology Resource ([www.hnbr.org](http://www.hnbr.org)). We thank N. Ashley (Oxford MRC single-cell facility) for help with sequencing, M. De Bruijn, B. Gottgens, J. Palis, L. Robertson, T. Rodriguez and M.-E. Torres-Padilla for helpful comments. This work was funded by British Heart Foundation Immediate Postdoctoral Basic Science Research Fellowship no. FS/18/24/33424 to R.C.V.T., JSPS Overseas Research Fellowship to S.N., European Research Council advanced grant ERC: 741707 to L.V., funding from the Helmholtz Association to A.S. and Wellcome Awards 105031/C/14/Z, 108438/Z/15/Z, 215116/Z/18/Z and 103788/Z/14/Z to S.S.

## Author information

### Author notes

1. These authors contributed equally: Richard C. V. Tyser, Elmir Mahammadov
2. These authors jointly supervised this work: Antonio Scialdone, Shankar Srinivas

## Affiliations

1. Department of Physiology, Anatomy and Genetics, South Parks Road,  
University of Oxford, Oxford, UK

Richard C. V. Tyser & Shankar Srinivas

2. Institute of Epigenetics and Stem Cells, Helmholtz Zentrum München–  
German Research Center for Environmental Health, Munich, Germany

Elmir Mahammadov & Antonio Scialdone

3. Institute of Functional Epigenetics, Helmholtz Zentrum München–  
German Research Center for Environmental Health, Neuherberg,  
Germany

Elmir Mahammadov & Antonio Scialdone

4. Institute of Computational Biology, Helmholtz Zentrum München–  
German Research Center for Environmental Health, Neuherberg,  
Germany

Elmir Mahammadov & Antonio Scialdone

5. Wellcome–MRC Cambridge Stem Cell Institute, Jeffrey Cheah  
Biomedical Centre, Cambridge, UK

Shota Nakano & Ludovic Vallier

## Contributions

Human gastrula processing: R.C.V.T. and S.S. Human ES cell in vitro experiments: S.N. Computational analyses of sequence data: E.M. and A.S. Gastrula single-cell annotation and analyses: R.C.V.T., E.M., A.S. and S.S. Human ES cell in vitro data analysis: R.C.V.T. and S.N. Preparation of illustrations and figures: R.C.V.T. Preparation of manuscript draft: R.C.V.T., E.M., S.N., A.S. and S.S. Editing and review of final manuscript: R.C.V.T., E.M., S.N., L.V., A.S. and S.S. Study coordination: A.S. and S.S.

## Corresponding authors

Correspondence to [Antonio Scialdone](#) or [Shankar Srinivas](#).

## Ethics declarations

### Competing interests

The authors declare no competing interests.

## Additional information

**Peer review information** *Nature* thanks Joshua Welch and the other, anonymous, reviewer(s) for their contribution to the peer review of this work.

**Publisher's note** Springer Nature remains neutral with regard to jurisdictional claims in published maps and institutional affiliations.

## Extended data figures and tables

### [Extended Data Fig. 1 Quality control of scRNA-seq dataset.](#)

**a**, Dorsal view of the dissected embryonic disk showing the primitive streak and node (Scale bar = 500 $\mu$ m; n = 1). **b**, Brightfield images showing embryo dissection with schematic diagrams highlighting the three anatomical regions collected (yolk sac, rostral and caudal regions of embryonic disk; Scale bar = 500 $\mu$ m; n = 1). **c**, Metrics used to assess the quality of the scRNA-seq libraries. From top to bottom the scatter plots show the number of detected genes, the fraction of reads mapped to the human genome, the fraction of reads mapped to mitochondrial genes and the fraction of reads mapped to ERCC spike-ins, all as a function of the total number of reads. Cells that passed quality control are marked by green circles, while black circles indicate cells that failed the quality control and were excluded from downstream analyses. **d**, The boxplots show the total log expression of normalized counts for XIST and Y-genes across all clusters. While XIST was mostly not detected, Y-chromosome genes had always non-zero counts;

this suggests that there is no contamination from maternal tissues in any of the clusters. n = 1195 cells were examined from a single embryo. Horizontal black lines denote median values and boxes cover the 25<sup>th</sup> and 75<sup>th</sup> percentiles range; whiskers extend to 1.5 × IQR. **e**, The stacked barplots indicate the percentages of cells from each cluster in the phase G1, S or G2/M of the cell cycle, as predicted from their transcriptomic profiles. **f**, Insertion-deletion length and size distribution of gastrula and fetal liver data. Y axis represents total number of indels on merged cells, while x axis represents indel length in base pairs. Hemato-Endothelial Progenitors (HEP), Endoderm (End), Advanced Mesoderm (AM), Primitive Streak (PS), Extraembryonic Mesoderm (ExM), Axial Mesoderm (AxM), Erythroblasts (Ery), Emergent Mesoderm (EM), Epiblast (Epi), Nascent Mesoderm (NM), Ectoderm (Amniotic/Embryonic (EAE)).

### **Extended Data Fig. 2 Characterisation and comparison of a CS7 human gastrula with Non-human primate and Mouse.**

**a**, Heatmap with the normalized log expression of well characterized marker genes for the identified cell types: Epiblast (Epi), Ectoderm (Amniotic/Embryonic (EAE)), Primitive Streak (PS), Nascent Mesoderm (NM), Emergent Mesoderm (EM), Advanced Mesoderm (AM), Extraembryonic Mesoderm (ExM), Axial Mesoderm (AxM), Endoderm (Endo), Hemato-Endothelial Progenitors (HEP), Erythroblasts (Ery). **b**, Stacked bar plots highlighting the anatomical region that cells were collected from and the percentage breakdown of each cluster. Numbers in brackets represent the total number of cells per cluster. **c**, Heatmap showing the fraction of human gastrula cells allocated to mouse cell types at E7.25 (data from<sup>18</sup>). **d**, Dendrogram showing hierarchical clustering of the transcriptomes of cell types from human gastrula and cultured cynomolgus macaque embryos at 16-day post-fertilization (from<sup>19</sup>). **e**, Top, UMAP plots showing the log expression of *MEST* and *GCNT2*. Bottom, violin plots showing the log expression of total transcripts (top row) and selected isoforms scaled by the maximum value in different cell types. Isoform names refer to Ensembl nomenclature.

### **Extended Data Fig. 3 In Vitro vs In Vivo comparisons.**

**a**, Dendrogram representation built on corrected expression values obtained with Seurat showing comparison of an *in vitro* model of pluripotency with *in vivo* data. **b**, Log-fold changes of expression levels of the genes between primed vs naïve hESC (y axis) and CS7 epiblast vs E6 data (x axis). Selected genes are highlighted in red; the blue line is obtained through a linear regression. A statistically significant positive correlation is found (Pearson's correlation coefficient ~0.63, p-value = 3e-107), indicating that the hESC resemble the *in vivo* primed and naïve states at the transcriptome-wide level. **c**, Heatmaps showing the correlations between the transcriptomic profiles of the human gastrula cell types (rows) and sections of human gastruloids taken at different positions along the rostral-caudal axis (columns) in two different replicates (Gastruloid 1 and Gastruloid 2). Only the values of the statistically significant correlations (p-value < 0.01; 2-tailed Pearson's correlation, see [Methods](#)) are reported, while all the non-significant correlations were set to 0. **d**, UMAP representation of the human gastrula data with the PGCs highlighted. **d**, Diffusion map of cells from all 11 clusters. The first three diffusion components (DC1, 2, 3) are plotted in different combinations. In the top panels, cells are coloured by the clusters they belong to, while in the bottom panels the colours indicate the region each cell was dissected from. Ectoderm (amniotic/embryonic) (EAE), Epiblast (Epi), Primitive Streak (PS), Axial Mesoderm (AxM), Nascent Mesoderm (NM), Emergent Mesoderm (EM), Advanced Mesoderm (AM), Erythroblasts (Ery), Hemato-Endothelial Progenitors (HEP), Endoderm (Endo), Extraembryonic Mesoderm (ExM).

#### [Extended Data Fig. 4 Rostral and Caudal differences in diversification of mesodermal subtypes.](#)

**a**, UMAP highlighting combinatorial gene expression. Individual gene expression (left) is reported as the log expression whilst combinatorial plots (right) show scaled log expression values. **b**, Diffusion map of cells from the 6 mesoderm related clusters (Primitive Streak, PS; Nascent Mesoderm, NM; Emergent Mesoderm, EM; Mesoderm, Meso; Axial Mesoderm, AxM; Extraembryonic Mesoderm, ExM), with the first and the second diffusion components plotted. **c**, Diffusion map of mesodermal showing the log expression levels of mesodermal markers genes. **d**, Differential gene expression between rostral and caudal advanced mesoderm cells.

Significantly upregulated in rostral (\*) or caudal (#) cells. **e-j**, Diffusion map of mesodermal clusters showing log expression levels of mesoderm subtype markers.

### Extended Data Fig. 5 Differentiation of the epiblast.

**a**, Diffusion map of cells from the Epiblast, Primitive Streak, Nascent Mesoderm and Ectoderm (amniotic/embryonic). The first two diffusion components are plotted (DC1 and DC2) and cells are colored by their cluster (top) or the anatomical region they were isolated from (bottom). **b** and **c**, Normalized log gene expression changes along a pseudotime coordinate (see Fig. 4a) running from 0 to 1 and spanning the Ectoderm (amniotic/embryonic) (EAE), the Epiblast (EPI), the Primitive Streak (PS) and the Nascent Mesoderm (NM), as depicted by the arrow on top. The selected genes highlight Primitive Streak and mesoderm formation (panel b) as well as ectoderm differentiation (panel c).

### Extended Data Fig. 6 Mesoderm formation in human and mouse.

**a**, Diffusion map with cells from the human (top two plots) or mouse (bottom two plots) Epiblast, Primitive Streak and Nascent Mesoderm clusters. Cells are colored based on their cluster of origin or on their diffusion pseudotime coordinate. **b**, Upset plot for the number of differentially expressed (DE) genes as a function of the diffusion pseudotime (dpt) shown in panel a in mouse (m) or human (h). Here, only genes that are differentially expressed in both species and with a log-fold change  $> 1$  along the trajectory are included. Genes are split according to their increasing (up) or decreasing (down) trend as a function of dpt. **c**, Comparison of pseudotime analysis during primitive streak and nascent mesoderm formation in human and mouse (data from<sup>18</sup>). Cells in epiblast (Epi), Primitive Streak (PS) and Nascent Mesoderm (NM) clusters from human and mouse embryos at matching stages (see [Methods](#)) were independently aligned along a differentiation trajectory and a diffusion pseudotime coordinate (dpt) was calculated for each (top). The expression pattern and standard error of the mean of selected genes along pseudotime is plotted for human (left, continuous lines) and mouse (right, dashed lines).

Both *SNAII* and *CDH1* showed comparable expression profiles during mesoderm formation in mouse and human whilst *MSGN1* was differently expressed between species.

### **Extended Data Fig. 7 Characterization of EMT during hESC mesoderm formation.**

**a**, Bright-field microscopy images of D0 hESC (left), D1 Meso (center) and D1 MEK Inhibition (right) ESC colonies (top panels). Fluorescence microscopy images of E-Cadherin staining (bottom panels). **b**, Quantification of transcript levels for selected pluripotent, EMT and mesendoderm genes across the three conditions PLU, ME, ME+PD. **c**, Quantification of transcript levels for selected non-neural ectoderm genes across the three conditions PLU, ME, ME+PD. (n = 6 from three different experiments. Center line, median; box limits, upper and lower quartiles; whiskers, minimum and maximum; dots, mean value per experiment. ns = p-value  $\geq 0.05$ ; \*\*\* = p-value  $< 0.001$ ; \*\*\*\* = p-value  $< 0.0001$  (Ordinary one-way ANOVA after passing a Shapiro-Wilk normality test. Kruskal-Wallis multiple comparison test used if Shapiro-Wilk normality test failed (*MSGN1*, *TDGF1*, *HAND1*, *DLX5*). House-keeping genes, HKGs. See SI Table 17 for source data and exact p-values

Source data.

### **Extended Data Fig. 8 Comparison of signaling during mesoderm formation in the human and mouse.**

Heatmap comparison of the z-score-normalized log expression values of components of FGF, TGF- $\beta$  and Wnt signaling pathways in the human gastrula, mouse embryos (E7.25 stage) and cultured cynomolgus macaque embryos (16 d.p.f stage). From human and mouse we considered the Epiblast (Epi), Primitive Streak (PS) and Nascent Mesoderm (NM) clusters; in the macaque, we used the clusters annotated as postL-Epi, L-Gast1 and L-Gast2.

### **Extended Data Fig. 9 Endoderm subcluster identification.**

**a**, Heatmap showing the scaled log expression levels of marker genes of the four endodermal subclusters. **b**, Percentage of cells dissected from the Caudal, Rostral or Yolk Sac portion of the embryo in the four endodermal subclusters. **c**, Percentage of cells based on their predicted cell-cycle phase of the four endodermal subclusters. **d**, Diffusion map of cells from the Endoderm cluster. The first two diffusion components (DC1 and DC2) are plotted and cells are coloured by the sub clusters (left), anatomical origin (central) or the predicted cell-cycle phase (right). Yolk Sac, YS; Definitive Endoderm (DE) 1 and 2. **e**, Diffusion map of cells from the Endoderm cluster with DC1 and DC3 plotted, showing log expression levels of Pan-endoderm, Yolk-sac endoderm and definitive endoderm markers. **f**, Log expression levels of Anterior Definitive Endoderm markers. These genes are more highly expressed in DE2. **g**, Log expression levels of Gut Endoderm markers, showing limited expression. **h**, Maximum intensity projection and mid-sagittal section (**h'**) of an E7.0 mouse embryo showing expression of *Gjb1* (yolk sac endoderm marker) as well as *Cer1* and *Hhex* (anterior definitive endoderm markers) using Hybridization Chain Reaction ( $n = 4$ ). *Cer1* and *Hhex* show greater expression in the anterior embryonic endoderm. Anterior, Ant; Posterior, Pos; Yolk-sac Endoderm, YSE. **i**, Violin plots showing the scaled log expression of total transcripts (top row) and individual isoforms in different endodermal subclusters. Isoform labels refer to Ensembl transcript numbers.

## Extended Data Fig. 10 Hemato-Endothelial Progenitors subclusters.

**a**, Boxplots showing the total log expression of normalized counts for XIST and Y-genes in Erythroblasts (Ery) and Hemato-Endothelial Progenitors (HEP), indicating no contamination from maternal tissue.  $n = 143$  cells were examined from a single embryo. Horizontal black lines denote median values and boxes cover the 25<sup>th</sup> and 75<sup>th</sup> percentiles range; whiskers extend to  $1.5 \times$  IQR. **b**, UMAP of HEP and Erythroblast clusters showing log expression of blood related marker genes. **c**, Heatmap showing the scaled log expression of well-characterized marker genes for both the Hemato-Endothelial Progenitors subclusters and Erythroblast cluster. **d**, Heatmap showing the normalized log expression levels of the top 5 marker genes of the four Hemato-Endothelial Progenitors subclusters. **e**, Diffusion maps of

HEP subclusters and Erythroblasts showing diffusion components (DC) 1, 2 and 3. **f**, Violin plots showing the scaled log expression of Globin genes in the five blood related clusters: Erythroblasts (Ery), Myeloid Progenitors (MP), Endothelium, Megakaryocyte-Erythroid Progenitors (MEP) and Erythro-Myeloid progenitors (EMP). Each grey dot represents a single cell. **g**, Heatmap showing the estimated mapping of human Erythroid and HEP subclusters to mouse blood-related clusters. Scalebar represents the fraction of human cells mapped to each category. **h**, Bar graph showing the number of cells present in the mouse scRNA-seq dataset<sup>18</sup> at different development timepoints.

## Supplementary information

### Supplementary Information

This file contains Supplementary Notes 1 – 4 and Supplementary References.

### Reporting Summary

### Supplementary Table 1

Human gastrula cluster marker genes. Table showing the marker genes ranked by statistical significance for the 11 different clusters identified, including: Epiblast (Epi), ectoderm (amniotic/embryonic) (EAE), primitive streak (PS), nascent mesoderm (NM), emergent mesoderm (EM), advanced mesoderm (AM), extraembryonic mesoderm (ExM), axial mesoderm (AxM), endoderm (Endo), HEP and erythroblasts (Ery).

### Supplementary Table 2

Cell origin per cluster. Table showing the percentage of cells from a specific anatomical region for each cluster.

### Supplementary Table 3

Transcript isoform differences for all clusters comparisons. Tables showing transcript isoform comparisons between clusters. Each worksheet refers to the comparison of a single cluster with every other cluster of cell types, and includes the names of the genes whose isoforms are differentially expressed with the relative *P* value. One-sided chi-square test. extraembryonic mesoderm (ExM), HEP, ectoderm (amniotic/embryonic) (EAE).

#### **Supplementary Table 4**

Top 30 genes with highest log-fold change in each quadrant of CS7 vs E6 embryos and naive vs primed human ES cell correlation. Table showing the top 30 genes with the highest  $\log_2$ -fold changes in each quadrant of the CS7 vs E6 embryos and naive vs primed human ES cell comparison (Fig. 3b). The numeric values in the table represent  $\log_2$ -fold changes in shown comparisons.

#### **Supplementary Table 5**

Differentially expressed genes along the epiblast to nascent mesoderm trajectory. List of differentially expressed genes and their trends during epiblast to nascent mesoderm transition in the human gastrula. The trends are ‘up’ or ‘down’ when there is an increasing or decreasing trend with a  $\log_2$ -fold change greater than 1 between the expression values at the beginning and at the end of the trajectory; ‘flat’ genes are those having a log fold change less than 1 between initial and final expression value.

#### **Supplementary Table 6**

Genes correlating with *TBXT* along the epiblast to nascent mesoderm trajectory. List of genes that correlate with *TBXT* along the epiblast to nascent mesoderm trajectory. Values represent correlation coefficient (coef), *P* value (p-val) and FDR. Two-sided Spearman’s rho test.

#### **Supplementary Table 7**

Differentially expressed genes in human and mouse during epiblast to nascent mesoderm differentiation. Comparison of differentially expressed genes in mouse and human along the epiblast to nascent mesoderm differentiation trajectory. Genes are marked by whether they are differentially expressed in mouse (DE mouse) or human (DE human), their expression trends in mouse and human and FDR in these species. The trends are ‘up’ or ‘down’ when there is an increasing or decreasing trend with a  $\log_2$  fold change greater than 1 between the expression values at the beginning and at the end of the trajectory; ‘flat’ genes are those having a log fold change less than 1 between initial and final expression value.

### Supplementary Table 8

Ectoderm (amniotic/embryonic) subcluster genes. Table of the top 50 marker genes for the ectoderm (amniotic/embryonic) subclusters (amnion and non-neural ectoderm (NNE)).

### Supplementary Table 9

Primordial germ cell primitive streak differentially expressed genes. List of top differentially expressed genes between PGC and primitive streak with FDR. Two-sided Wilcoxon rank-sum test.

### Supplementary Table 10

PGC cross-species gene-expression analysis. Table showing 50 shared and disparate genes when comparing human primordial germ cells to cynomolgus macaque and mouse. Only genes differentially expressed for PGCs in each species are shown.

### Supplementary Table 11

Endoderm subcluster marker genes. List of endoderm subcluster marker genes. Definitive endoderm, DE; yolk sac, YS.

### Supplementary Table 12

Transcript isoform differences for endoderm subclusters. Tables showing transcript isoform comparisons between endoderm subclusters. Each worksheet refers to the comparison of a single subcluster with every other endoderm subclusters, and includes the names of the genes whose isoforms are differentially expressed with the relative *P* value. Definitive endoderm, DE; yolk sac, YS. One-sided chi-square test.

### **Supplementary Table 13**

HEP subcluster genes. List of HEP subcluster marker genes and associated FDR.

### **Supplementary Table 14**

Transcript Isoform differences in HEP subclusters. Tables showing transcript isoform comparisons between HEP subclusters. Each worksheet refers to the comparison of a single subcluster with every other HEP subclusters, and includes the names of the genes whose isoforms are differentially expressed with the relative p-value. One-sided chi-square test.

### **Supplementary Table 15**

Real-time PCR primer details. List of real-time PCR primer sequences.

### **Supplementary Table 16**

Extraembryonic and advanced mesoderm differentially expressed genes. List of top 100 most differentially expressed genes between advanced mesoderm and extraembryonic (Exe) mesoderm.

### **Supplementary Table 17**

Source data for real-time PCR analysis.

## **Source data**

## [Source Data Fig. 2](#)

## [Source Data Extended Data Fig. 7](#)

## Rights and permissions

### [Reprints and Permissions](#)

## About this article

### Cite this article

Tyser, R.C.V., Mahammadov, E., Nakanoh, S. *et al.* Single-cell transcriptomic characterization of a gastrulating human embryo. *Nature* **600**, 285–289 (2021). <https://doi.org/10.1038/s41586-021-04158-y>

- Received: 28 July 2020
- Accepted: 05 October 2021
- Published: 17 November 2021
- Issue Date: 09 December 2021
- DOI: <https://doi.org/10.1038/s41586-021-04158-y>

## Share this article

Anyone you share the following link with will be able to read this content:

[Get shareable link](#)

Sorry, a shareable link is not currently available for this article.

[Copy to clipboard](#)

Provided by the Springer Nature SharedIt content-sharing initiative

# Further reading

- [A peek into the black box of human embryology](#)

- Alexander Goedel
- Fredrik Lanner

*Nature* (2021)

## [A peek into the black box of human embryology](#)

- Alexander Goedel
- Fredrik Lanner

News & Views 17 Nov 2021

---

This article was downloaded by **calibre** from <https://www.nature.com/articles/s41586-021-04158-y>.

| [Section menu](#) | [Main menu](#) |

- Article
- [Published: 17 November 2021](#)

# Observation of universal ageing dynamics in antibiotic persistence

- [Yoav Kaplan<sup>1</sup>](#),
- [Shaked Reich<sup>1</sup>](#),
- [Elyaqim Oster<sup>1</sup>](#),
- [Shani Maoz<sup>1</sup>](#),
- [Irit Levin-Reisman<sup>1</sup>](#),
- [Irine Ronin<sup>1</sup>](#),
- [Orit Gefen<sup>1</sup>](#),
- [Oded Agam](#) ORCID: [orcid.org/0000-0002-4118-8586<sup>1</sup>](https://orcid.org/0000-0002-4118-8586) &
- [Nathalie Q. Balaban](#) ORCID: [orcid.org/0000-0001-8018-0766<sup>1</sup>](https://orcid.org/0000-0001-8018-0766)

[Nature](#) volume **600**, pages 290–294 (2021)

- 6730 Accesses
- 1 Citations
- 110 Altmetric
- [Metrics details](#)

## Subjects

- [Dynamical systems](#)
- [Microbiology](#)

## Abstract

Stress responses allow cells to adapt to changes in external conditions by activating specific pathways<sup>1</sup>. Here we investigate the dynamics of single cells that were subjected to acute stress that is too strong for a regulated response but not lethal. We show that when the growth of bacteria is arrested by acute transient exposure to strong inhibitors, the statistics of their regrowth dynamics can be predicted by a model for the cellular network that ignores most of the details of the underlying molecular interactions. We observed that the same stress, applied either abruptly or gradually, can lead to totally different recovery dynamics. By measuring the regrowth dynamics after stress exposure on thousands of cells, we show that the model can predict the outcome of antibiotic persistence measurements. Our results may account for the ubiquitous antibiotic persistence phenotype<sup>2</sup>, as well as for the difficulty in attempts to link it to specific genes<sup>3</sup>. More generally, our approach suggests that two different cellular states can be observed under stress: a regulated state, which prepares cells for fast recovery, and a disrupted cellular state due to acute stress, with slow and heterogeneous recovery dynamics. The disrupted state may be described by general properties of large random networks rather than by specific pathway activation. Better understanding of the disrupted state could shed new light on the survival and evolution of cells under stress.

This is a preview of subscription content

## Access options

Subscribe to Journal

Get full journal access for 1 year

\$199.00

only \$3.90 per issue

[Subscribe](#)

All prices are NET prices.  
VAT will be added later in the checkout.  
Tax calculation will be finalised during checkout.

Rent or Buy article

Get time limited or full article access on ReadCube.

from \$8.99

[Rent or Buy](#)

All prices are NET prices.

### **Additional access options:**

- [Log in](#)
- [Learn about institutional subscriptions](#)

**Fig. 1: The tail of the lag time distribution correlates with survival under antibiotic treatment.**

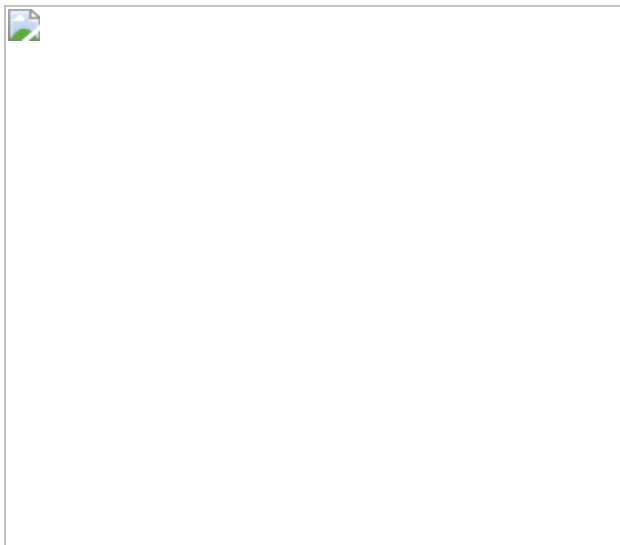


**Fig. 2: Distribution of the lag time following starvation for various durations  $T_w$  of exposure to SHX.**

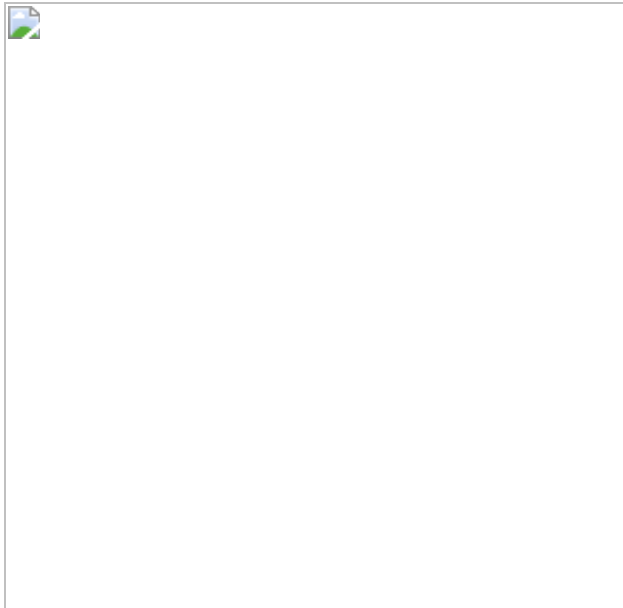


**Fig. 3: The RCCN model reproduces the ageing dynamics observed in the experiment.**

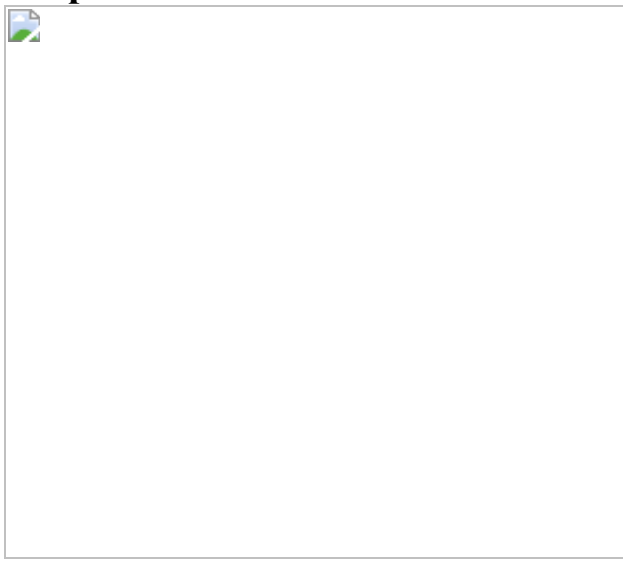
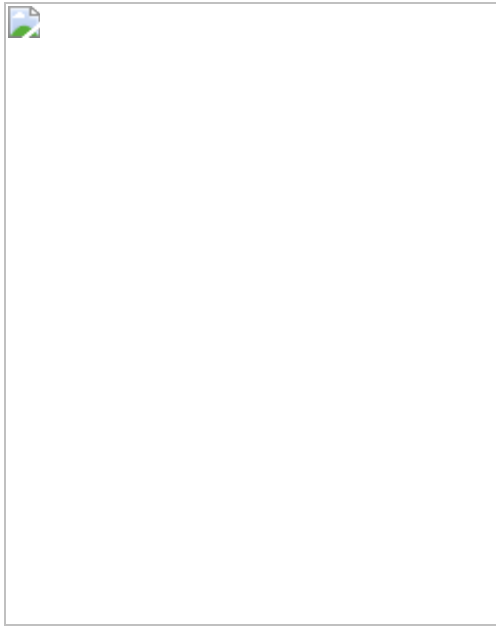


**Fig. 4: No ageing under gradual starvation.**



## Data availability

Source data for Figs. 1–4 are provided with the paper. [Source data](#) are provided with this paper.

## Code availability

All Matlab scripts for the simulation<sup>52</sup> are available through GitHub at the link: <https://github.com/NQBLab/RCCN>.

## References

1. 1.

Storz, G. & Hengge, R. *Bacterial Stress Responses* (ASM, 2011).

2. 2.

Balaban, N. Q. et al. Definitions and guidelines for research on antibiotic persistence. *Nat. Rev. Microbiol.* **17**, 441–448 (2019).

3. 3.

Levin, B. R., Concepcion-Acevedo, J. & Udekwu, K. I. Persistence: a copacetic and parsimonious hypothesis for the existence of non-inherited resistance to antibiotics. *Curr. Opin. Microbiol.* **21**, 18–21 (2014).

4. 4.

Balaban, N. Q., Merrin, J., Chait, R., Kowalik, L. & Leibler, S. Bacterial persistence as a phenotypic switch. *Science* **305**, 1622–1625 (2004).

5. 5.

Levin-Reisman, I. et al. Automated imaging with ScanLag reveals previously undetectable bacterial growth phenotypes. *Nat. Methods* **7**, 737–739 (2010).

6. 6.

Johnson, P. J. T. & Levin, B. R. Pharmacodynamics, population dynamics, and the evolution of persistence in *Staphylococcus aureus*. *PLoS Genet.* **9**, e1003123 (2013).

7. 7.

Fridman, O., Goldberg, A., Ronin, I., Shores, N. & Balaban, N. Q. Optimization of lag time underlies antibiotic tolerance in evolved bacterial populations. *Nature* **513**, 418–421 (2014).

8. 8.

Lewis, K. *Persister Cells and Infectious Disease* (Springer Nature, 2019).

9. 9.

Brauner, A., Fridman, O., Gefen, O. & Balaban, N. Q. Distinguishing between resistance, tolerance and persistence to antibiotic treatment. *Nat. Rev. Microbiol.* **14**, 320–330 (2016).

10. 10.

Luidalepp, H., Joers, A., Kaldalu, N. & Tenson, T. Age of inoculum strongly influences persister frequency and can mask effects of mutations implicated in altered persistence. *J. Bacteriol.* **193**, 3598–3605 (2011).

11. 11.

Pin, C. & Baranyi, J. Single-cell and population lag times as a function of cell age. *Appl. Environ. Microbiol.* **74**, 2534–2536 (2008).

12. 12.

Moreno-Gámez, S. et al. Wide lag time distributions break a trade-off between reproduction and survival in bacteria. *Proc. Natl Acad. Sci. USA* **117**, 18729–18736 (2020).

13. 13.

Potrykus, K. & Cashel, M. (p)ppGpp: still magical? *Annu. Rev. Microbiol.* **62**, 35–51 (2008).

14. 14.

Simsek, E. & Kim, M. Power-law tail in lag time distribution underlies bacterial persistence. *Proc. Natl Acad. Sci. USA* **116**, 17635–17640 (2019).

15. 15.

Potvin-Trottier, L., Luro, S. & Paulsson, J. Microfluidics and single-cell microscopy to study stochastic processes in bacteria. *Curr. Opin. Microbiol.* **43**, 186–192 (2018).

16. 16.

Amir, A., Oreg, Y. & Imry, Y. On relaxations and aging of various glasses. *Proc. Natl Acad. Sci. USA* **109**, 1850–1855 (2012).

17. 17.

Struik, L. in *Physical Aging in Amorphous Polymers and Other Materials* (Elsevier, 1978).

18. 18.

Hwa, T., Marinari, E., Sneppen, K. & Tang, L. H. Localization of denaturation bubbles in random DNA sequences. *Proc. Natl Acad. Sci. USA* **100**, 4411–4416 (2003).

19. 19.

Cugliandolo, L. F. & Kurchan, J. Analytical solution of the off-equilibrium dynamics of a long-range spin-glass model. *Phys. Rev. Lett.* **71**, 173–176 (1993).

20. 20.

Franz, S., Mezard, M., Parisi, G. & Peliti, L. Measuring equilibrium properties in aging systems. *Phys. Rev. Lett.* **81**, 1758–1761 (1998).

21. 21.

Bouchaud, J. P. Weak ergodicity breaking and aging in disordered-systems. *J. Phys. I* **2**, 1705–1713 (1992).

22. 22.

Ackermann, M., Chao, L., Bergstrom, C. T. & Doebeli, M. On the evolutionary origin of aging. *Aging Cell* **6**, 235–244 (2007).

23. 23.

Kirkpatrick, S. & Sherrington, D. Infinite-ranged models of spin-glasses. *Phys. Rev. B* **17**, 4384–4403 (1978).

24. 24.

Sompolinsky, H., Crisanti, A. & Sommers, H. J. Chaos in random neural networks. *Phys. Rev. Lett.* **61**, 259–262 (1988).

25. 25.

Gabalda-Sagarra, M., Carey, L. B. & Garcia-Ojalvo, J. Recurrence-based information processing in gene regulatory networks. *Chaos* **28**, 106313 (2018).

26. 26.

Ravasz, E., Somera, A. L., Mongru, D. A., Oltvai, Z. N. & Barabasi, A. L. Hierarchical organization of modularity in metabolic networks. *Science* **297**, 1551–1555 (2002).

27. 27.

Nagar, N. et al. Harnessing machine learning to unravel protein degradation in *Escherichia coli*. *mSystems* **6**, e01296-20 (2021).

28. 28.

Kauffman, S., Peterson, C., Samuelsson, B. & Troein, C. Random Boolean network models and the yeast transcriptional network. *Proc. Natl Acad. Sci. USA* **100**, 14796–14799 (2003).

29. 29.

Himeoka, Y. & Kaneko, K. Theory for transitions between exponential and stationary phases: universal laws for lag time. *Phys Rev X* **7**, 021049 (2017).

30. 30.

Nystrom, T. Conditional senescence in bacteria: death of the immortals. *Mol. Microbiol.* **48**, 17–23 (2003).

31. 31.

Schink, S. J., Biselli, E., Ammar, C. & Gerland, U. Death rate of *E. coli* during starvation is set by maintenance cost and biomass recycling. *Cell Syst.* **9**, 64–73.e3 (2019).

32. 32.

St John, A. C. & Goldberg, A. L. Effects of reduced energy production on protein degradation, guanosine tetraphosphate, and RNA synthesis in *Escherichia coli*. *J. Biol. Chem.* **253**, 2705–2711 (1978).

33. 33.

Sangurdekar, D. P., Srienc, F. & Khodursky, A. B. A classification based framework for quantitative description of large-scale microarray data. *Genome Biol.* **7**, R32 (2006).

34. 34.

Gurvich, Y., Leshkowitz, D. & Barkai, N. Dual role of starvation signaling in promoting growth and recovery. *PLoS Biol.* **15**, e2002039 (2017).

35. 35.

Link, H., Fuhrer, T., Gerosa, L., Zamboni, N. & Sauer, U. Real-time metabolome profiling of the metabolic switch between starvation and growth. *Nat. Methods* **12**, 1091–1097 (2015).

36. 36.

Erickson, D. W. et al. A global resource allocation strategy governs growth transition kinetics of *Escherichia coli*. *Nature* **551**, 119–123 (2017).

37. 37.

Koch, A. L. The adaptive responses of *Escherichia coli* to a feast and famine existence. *Adv. Microb. Physiol.* **6**, 147–217 (1971).

38. 38.

Braun, E. The unforeseen challenge: from genotype-to-phenotype in cell populations. *Rep. Prog. Phys.* **78**, 036602 (2015).

39. 39.

Tripathi, S., Kessler, D. A. & Levine, H. Biological networks regulating cell fate choice are minimally frustrated. *Phys. Rev. Lett.* **125**, 088101 (2020).

40. 40.

Radzikowski, J. L., Schramke, H. & Heinemann, M. Bacterial persistence from a system-level perspective. *Curr. Opin. Biotechnol.* **46**, 98–105 (2017).

41. 41.

Guo, Y. & Amir, A. Stability of gene regulatory networks. Preprint at arXiv <https://arxiv.org/abs/2006.00018v2> (2020).

42. 42.

Sekar, K. et al. Synthesis and degradation of FtsZ quantitatively predict the first cell division in starved bacteria. *Mol. Syst. Biol.* **14**, e8623 (2018).

43. 43.

Madar, D. et al. Promoter activity dynamics in the lag phase of *Escherichia coli*. *BMC Syst. Biol.* **7**, 136 (2013).

44. 44.

Shamir, M., Bar-On, Y., Phillips, R. & Milo, R. SnapShot: timescales in cell biology. *Cell* **164**, 1302–1302.e1 (2016).

45. 45.

Kaldalu, N. et al. In vitro studies of persister cells. *Microbiol. Mol. Biol. Rev.* **84**, e00070-20 (2020).

46. 46.

Craig, W. A. The post-antibiotic effect. *Clin. Microbiol. Newslett.* **13**, 121–128 (1991).

47. 47.

Holmquist, L. & Kjelleberg, S. Changes in viability, respiratory activity and morphology of the marine *Vibrio* Sp strain S14 during starvation of individual nutrients and subsequent recovery. *FEMS Microbiol. Ecol.* **12**, 215–224 (1993).

48. 48.

Lopatkin, A. J. & Collins, J. J. Predictive biology: modelling, understanding and harnessing microbial complexity. *Nat. Rev. Microbiol.* **18**, 507–520 (2020).

49. 49.

Imdahl, F., Vafadarnejad, E., Homberger, C., Saliba, A. E. & Vogel, J. Single-cell RNA-sequencing reports growth-condition-specific global transcriptomes of individual bacteria. *Nat. Microbiol.* **5**, 1202–1206 (2020).

50. 50.

Gefen, O., Fridman, O., Ronin, I. & Balaban, N. Q. Direct observation of single stationary-phase bacteria reveals a surprisingly long period of constant protein production activity. *Proc. Natl Acad. Sci. USA* **111**, 556–561 (2014).

51. 51.

Edelstein, A. D. et al. Advanced methods of microscope control using  $\mu$ Manager software. *J. Biol. Methods* 1, e10 (2014).

52. 52.

Kaplan, Y. et al. *Observation of Universal Ageing Dynamics in Antibiotic Persistence* <https://doi.org/10.5281/zenodo.5516475> (2021).

## Acknowledgements

We thank B. Seo and J. Paulsson for the microfluidic mother-machine templates; and N. Barkai, Y. Burak and A. Rotem for comments on the manuscript and for illuminating discussions. This work was supported by the European Research Council (consolidator grant no. 681819), the Israel Science Foundation (grant no. 597/20) and the Minerva Foundation.

## Author information

### Affiliations

1. Racah Institute of Physics, The Hebrew University of Jerusalem, Jerusalem, Israel

Yoav Kaplan, Shaked Reich, Elyaqim Oster, Shani Maoz, Irit Levin-Reisman, Irene Ronin, Orit Gefen, Oded Agam & Nathalie Q. Balaban

### Contributions

Y.K., E.O., O.G. and N.Q.B. designed, performed experiments and analysed the data. I.R. and I.L.-R. performed experiments and analysed the data. O.A., S.R., S.M., Y.K. and N.Q.B. provided theory. N.Q.B., Y.K. and O.A. wrote the manuscript.

### Corresponding authors

Correspondence to [Oded Agam](#) or [Nathalie Q. Balaban](#).

## Ethics declarations

### Competing interests

The authors declare no competing interests.

## Additional information

**Peer review information** *Nature* thanks Bruce Levin, Nozomu Yachie and the other, anonymous, reviewer(s) for their contribution to the peer review of this work. Peer reviewer reports are available.

**Publisher's note** Springer Nature remains neutral with regard to jurisdictional claims in published maps and institutional affiliations.

## Extended data figures and tables

### [Extended Data Fig. 1 Ageing under abrupt SHX exposure.](#)

**a**, Viability vs SHX exposure duration. The bars and error bars represent the mean and std ( $n=3$  biological replicates). Each time point was compared to  $t_0$  using two-sided Student's paired  $t$ -test. NS:  $p>0.05$ . **b**, Median time of the lag time distribution versus  $T_w$ . Colours indicate 3 biological replicates. Note that after about 1000 min, increasing the starvation duration does not increase the median lag time. **c**, To test whether long lagging colonies maintain this phenotype when regrown, a long lagging colony was isolated from a plate inoculated with an SHX-arrested culture. The appearance time of the isolated colony is indicated by the black arrow. **d**, Lag time distributions of the culture originating from the colony isolated in **c** shows the same aging phenotype under abrupt SHX exposure as the original culture, indicating that the long lag is not due to mutation.

### [Extended Data Fig. 2](#)

**Analogy between physical ageing in a spin network and ageing of bacteria under acute stress.**

**Extended Data Fig. 3 Correspondence between starvation and magnetic field ( $H$ ) in the Randomly Connected Cycles Network model.**

**a**, Schematic view of the time course of the simulation and experiments. First, no starvation ( $H=0$ ), then an abrupt starvation leads to a switch OFF of the spins (here  $H=0.8$ ). After a duration  $T_w$ , the conditions are returned back to  $H=0$ . **b**, Simulation (coloured lines) and analytical results according to Eq. S7 for the average magnetization (equal to twice the fraction of OFF nodes-1). Inset: An example for the simulation of one magnetization trace (linear scale) defined by Eq. S6, after the magnetic field is switched off. The lag time for each realization (bacterium) is defined by the first crossing of the magnetization back to zero.

**Extended Data Fig. 4 Ageing dynamics are robust to changes in the parameters of the model but depend on its architecture.**

**a–c**, Different random model connection architectures that do not display ageing. Asymmetric Sherrington-Kirkpatrick model (**a**). Erdős-Renyi connections with  $p=40\%$  (**b**). Rich-get-Richer connections (**c**). **d–i**, Variations in RCCN model parameters. Power law exponent,  $\alpha=1.1$  (**d**);  $\gamma=2$  (**e**); System size,  $N=2^{11}$  (solid lines),  $N=2^{12}$  (dotted lines) (**f**). Maximal cycle length,  $L_{max}=800$  (**g**). Magnetic field,  $H=0.3$  (**h**). Connections sparseness,  $p=10\%$  (**i**). Violet curves:  $T_w=20$ ; Yellow curves:  $T_w=3000$ . Other simulation parameters as in Supplementary Table 2.

**Extended Data Fig. 5 Powerlaw tail of lag time distribution after saturation of ageing.**

**a**, Experimental data of lag times after SHX exposure (green) plotted as (1-CDF). Inset of **a**: same data as **a** plotted on semilog shows that it cannot be fitted with an exponential function (dashed black line). **b**, Simulated lag

time distribution curve (solid black curve). Magenta curve: simulation with a different strength of magnetic field shows that the powerlaw behavior is an asymptotic behavior and here does not fit the  $t^{-2}$  dependence as well. The dashed red curves in **a** and **b** show the  $t^{-2}$  behavior. **c**, Simulation average over architecture sampling is equivalent to average over random connections. Black: average of different random cycles and connections. Red: fixed cycles architecture averaged over random connection strength (i.e.  $|J_i|$ ). Blue: same as the red curves, but for a different architecture sampled.

### Extended Data Fig. 6 Slow relaxation dynamics from stress exposure protects against subsequent ampicillin exposure.

Microfluidic experiment of bacteria MGY $\Delta motA$  exposed to sodium azide for a duration of  $T_w=1720$  min before the observations. Upon removal of sodium azide, ampicillin was added. Bacteria with a short lag were killed, whereas bacteria remaining at the lag phase during ampicillin treatment survived. The fate of 172 cells was followed. Death was determined by lysis. The probability for cells that grew (i.e. detectable increase in cell size) during the antibiotic die is 5.7 times that for cells that did not grow during the antibiotic.

### Extended Data Fig. 7 Ageing upon exposure to sodium azide in wild-type *E.coli* (MG1655/pZA21RmCherry).

**a**, Growth curve of cultures exposed to sodium azide during exponential growth (solid line) or unexposed (dashed line). The times at which the culture was sampled are marked in colours corresponding to the results shown in **b**. **b**, Experimental results for the distribution of lag times as measured after starvation under sodium azide. Distributions are plotted as 1-CDF (Cumulative Distribution Function). Note that the lag time distribution becomes independent of starvation duration for long enough starvation, as predicted by the RCCN model. Different colours represent different duration of exposure to sodium azide, as marked in **a**. **c**, Viability under sodium azide. Only after 2800 min viability decreased significantly. Error bars are the std ( $n=3$  biological replicates). Each time point was

compared to  $t_0$  using two-sided Student's paired *t*-test. 'NS', not significant; '\*\*',  $p=0.014$ . **d**, Bacteria were exposed to sodium azide for durations: 1454, 1546, 1644, and 2254 min. Upon removal of sodium azide, ampicillin was added. The survival fraction under 9.5 h ampicillin exposure was determined and plotted vs. the tail fraction measured in **b**. Dotted line: linear regression, two-sided Pearson's correlation: 0.98,  $p=0.024$ .

### [Extended Data Fig. 8 After gradual starvation in M9 the recovery is fast and not affected by SHX.](#)

**a**, Lag time distribution following gradual starvation in minimal medium reaching stationary phase (CASP - Constant Activity Stationary Phase)<sup>50</sup>. Adding SHX (solid line) or without SHX (dotted line) does not change the lag time distribution. For both curves SHX was maintained for  $T_w=1300$  min. **b**, Zoom on a gradually starved culture reaching stationary phase (CASP) exhibits exponential exit of lag (dashed black line). **c**, The distributions of lag times after gradual starvation is narrow compared to after abrupt starvation, as evident from the standard deviations (STD) and Fig. 4c & Extended Data Fig. 9. For the gradual starvation, the STD, the two-fold exponential decay time, and the liquid culture's doubling time are comparable. Abrupt starvation (EXP  $t_1$  and  $t_2$ ) results in large STD, even after shorter SHX duration.

[Source data](#)

### [Extended Data Fig. 9 Lag time distributions of biological replicates for all stress conditions tested.](#)

Different columns represent different biological replicates of the same experiment. Stresses from top to bottom: aging conditions: Abrupt SHX, sodium azide, CAM, LB KLY prolonged starvation. Broad and slow lag can be seen for the stresses leading to aging. Non-aging conditions: LB EPEC prolonged starvation, gradual starvation M9 (CASP), gradual SHX exposure, NaCl. Note that some of these replicates also appear in main figures and are added here for completeness. Viability: Abrupt SHX (Extended Data Fig. 1a), sodium azide (Extended Data Fig. 7c). Other plots:

Viability decrease compared to  $t_0$  non-significant ( $p>0.05$ ). Stress exposure durations (coloured lines) in data file.

## Extended Data Fig. 10 Quantification of ageing under various stress conditions.

Pink: acute stress (SHX, sodium azide, Cam, prolonged LB starvation-lab strain). Green: mild stress (gradual SHX, gradual starvation in M9, NaCl, LB starvation EPEC strain). **a**, **b**, Schematic Illustration of the measure of ageing. The times at which lag time survival functions intersect an arbitrary fraction,  $f L$ , are used to measure the change in the functions with  $T_w$ :  $dL$  (**a**). Then for each pair of successive functions,  $dL/dT_w$  is obtained in each experiment (**b**). **c**, The ageing measure,  $\max(dL/dT_w)$  was calculated for all conditions. Data include  $n=3$  biological replicates, except for LB KLY and NaCl, for which  $n=2$ . For different fractions (here  $f=10\%$ ), results are similar. Significance tests: Two-sided unpaired t-test was performed on the natural logarithm of the ageing measure, to compare different conditions. Comparisons between gradual SHX and some other conditions are marked by a horizontal line. ‘NS’: not significant. ‘\*\*’:  $p=0.00077$ ,  $0.00013$ ,  $0.00133$  for Abrupt-SHX, sodium azide, and CAM, respectively. The ageing conditions SHX/sodium azide/CAM are significantly different from the natural or gradual starvations: CASP, gradual SHX, and in rich medium. Similar results were obtained for different  $f$ .

## Supplementary information

### Supplementary Information

This file contains the Supplementary Methods and Supplementary Notes on the RCCN Model, Supplementary Tables 1–3 and Supplementary References.

### Reporting Summary

### Peer Review File

# Source data

[Source Data Fig. 1](#)

[Source Data Fig. 2](#)

[Source Data Fig. 3](#)

[Source Data Fig. 4](#)

[Source Data Extended Data Fig. 8](#)

# Rights and permissions

[Reprints and Permissions](#)

# About this article

## Cite this article

Kaplan, Y., Reich, S., Oster, E. *et al.* Observation of universal ageing dynamics in antibiotic persistence. *Nature* **600**, 290–294 (2021).  
<https://doi.org/10.1038/s41586-021-04114-w>

- Received: 16 July 2020
- Accepted: 08 October 2021
- Published: 17 November 2021
- Issue Date: 09 December 2021
- DOI: <https://doi.org/10.1038/s41586-021-04114-w>

## Share this article

Anyone you share the following link with will be able to read this content:

[Get shareable link](#)

Sorry, a shareable link is not currently available for this article.

[Copy to clipboard](#)

Provided by the Springer Nature SharedIt content-sharing initiative

## Further reading

- [\*\*Stress and disarray leading to persistence\*\*](#)
  - Ursula Hofer

*Nature Reviews Microbiology* (2021)

---

This article was downloaded by **calibre** from <https://www.nature.com/articles/s41586-021-04114-w>

| [Section menu](#) | [Main menu](#) |

- Article
- [Published: 25 October 2021](#)

# Untimely TGF $\beta$ responses in COVID-19 limit antiviral functions of NK cells

- [Mario Witkowski](#) [ORCID: orcid.org/0000-0002-8791-5558](#)<sup>1,2,3</sup> na1,
- [Caroline Tizian](#) [ORCID: orcid.org/0000-0002-6798-3406](#)<sup>1,2</sup> na1,
- [Marta Ferreira-Gomes](#) [ORCID: orcid.org/0000-0002-7171-7952](#)<sup>4</sup> na1,
- [Daniela Niemeyer](#) [ORCID: orcid.org/0000-0002-1897-6365](#)<sup>5,6</sup>,
- [Terry C. Jones](#) [ORCID: orcid.org/0000-0003-1120-9531](#)<sup>5,6,7</sup>,
- [Frederik Heinrich](#) [ORCID: orcid.org/0000-0001-6097-5422](#)<sup>4</sup>,
- [Stefan Frischbutter](#) [ORCID: orcid.org/0000-0003-3971-7343](#)<sup>8,9</sup>,
- [Stefan Angermair](#) [ORCID: orcid.org/0000-0002-5440-6968](#)<sup>10</sup>,
- [Thordis Hohnstein](#)<sup>1,2</sup>,
- [Irene Mattiola](#) [ORCID: orcid.org/0000-0002-2922-9947](#)<sup>1,2</sup>,
- [Philipp Nawrath](#)<sup>1,2</sup>,
- [Sophie McEwen](#)<sup>1,2</sup>,
- [Silvia Zocche](#)<sup>11</sup>,
- [Edoardo Viviano](#)<sup>12</sup>,
- [Gitta Anne Heinz](#) [ORCID: orcid.org/0000-0002-9330-3689](#)<sup>4</sup>,
- [Marcus Maurer](#) [ORCID: orcid.org/0000-0002-4121-481X](#)<sup>8,9</sup>,
- [Uwe Kölsch](#) [ORCID: orcid.org/0000-0001-5052-5049](#)<sup>13</sup>,
- [Robert Lorenz Chua](#)<sup>14</sup>,
- [Tom Aschman](#) [ORCID: orcid.org/0000-0002-2101-6146](#)<sup>15</sup>,
- [Christian Meisel](#) [ORCID: orcid.org/0000-0003-0222-991X](#)<sup>13,16</sup>,
- [Josefine Radke](#) [ORCID: orcid.org/0000-0001-9860-2007](#)<sup>15</sup>,
- [Birgit Sawitzki](#) [ORCID: orcid.org/0000-0001-8166-8579](#)<sup>16</sup>,
- [Jobst Roehmel](#) [ORCID: orcid.org/0000-0002-1535-8852](#)<sup>17</sup>,
- [Kristina Allers](#)<sup>18</sup>,
- [Verena Moos](#)<sup>18</sup>,
- [Thomas Schneider](#)<sup>18</sup>,
- [Leif Hanitsch](#)<sup>16</sup>,
- [Marcus A. Mall](#) [ORCID: orcid.org/0000-0002-4057-2199](#)<sup>17,19</sup>,
- [Christian Conrad](#)<sup>14</sup>,

- [Helena Radbruch](#) [ORCID: orcid.org/0000-0001-6941-3397<sup>15</sup>](#),
- [Claudia U. Duerr](#) [ORCID: orcid.org/0000-0002-5010-3994<sup>20</sup>](#),
- [Joseph A. Trapani<sup>21</sup>](#),
- [Emanuela Marcenaro](#) [ORCID: orcid.org/0000-0003-4103-7566<sup>22</sup>](#),
- [Tilmann Kallinich<sup>17,23</sup>](#),
- [Victor M. Corman](#) [ORCID: orcid.org/0000-0002-3605-0136<sup>5,6</sup>](#),
- [Florian Kurth](#) [ORCID: orcid.org/0000-0002-3807-473X<sup>24,25</sup>](#),
- [Leif Erik Sander](#) [ORCID: orcid.org/0000-0002-0476-9947<sup>24</sup>](#),
- [Christian Drosten](#) [ORCID: orcid.org/0000-0001-7923-0519<sup>5,6</sup>](#),
- [Sascha Treskatsch](#) [ORCID: orcid.org/0000-0002-0549-7680<sup>10</sup>](#),
- [Pawel Durek<sup>4</sup>](#),
- [Andrey Kruglov<sup>26,27,28</sup>](#),
- [Andreas Radbruch](#) [ORCID: orcid.org/0000-0001-5753-0000<sup>29</sup>](#),
- [Mir-Farzin Mashreghi](#) [ORCID: orcid.org/0000-0002-8015-6907<sup>4,30 na2</sup>](#) &
- [Andreas Diefenbach](#) [ORCID: orcid.org/0000-0002-9176-9530<sup>1,2,3 na2</sup>](#)

*Nature* volume 600, pages 295–301 (2021)

- 27k Accesses
- 1 Citations
- 238 Altmetric
- [Metrics details](#)

## Subjects

- [Infection](#)
- [Innate immunity](#)
- [Innate lymphoid cells](#)
- [SARS-CoV-2](#)

## Abstract

SARS-CoV-2 is a single-stranded RNA virus that causes COVID-19. Given its acute and often self-limiting course, it is likely that components of the innate immune system play a central part in controlling virus replication and determining clinical outcome. Natural killer (NK) cells are innate lymphocytes with notable activity against a broad range of viruses, including RNA viruses<sup>1,2</sup>. NK cell function may be altered during COVID-19 despite increased representation of NK cells with an activated and

adaptive phenotype<sup>3,4</sup>. Here we show that a decline in viral load in COVID-19 correlates with NK cell status and that NK cells can control SARS-CoV-2 replication by recognizing infected target cells. In severe COVID-19, NK cells show defects in virus control, cytokine production and cell-mediated cytotoxicity despite high expression of cytotoxic effector molecules. Single-cell RNA sequencing of NK cells over the time course of the COVID-19 disease spectrum reveals a distinct gene expression signature. Transcriptional networks of interferon-driven NK cell activation are superimposed by a dominant transforming growth factor-β (TGFβ) response signature, with reduced expression of genes related to cell–cell adhesion, granule exocytosis and cell-mediated cytotoxicity. In severe COVID-19, serum levels of TGFβ peak during the first two weeks of infection, and serum obtained from these patients severely inhibits NK cell function in a TGFβ-dependent manner. Our data reveal that an untimely production of TGFβ is a hallmark of severe COVID-19 and may inhibit NK cell function and early control of the virus.

[Download PDF](#)

## Main

The role of NK cells during SARS-CoV-2 infection remains unknown. We wondered whether we could find differences in the decline in SARS-CoV-2 load between patients admitted to hospital with normal ( $>40$  NK cells per  $\mu\text{l}$ ) or low ( $\leq 40$  NK cells per  $\mu\text{l}$ ) NK cell counts. There was an overall pattern of a faster decline in viral load in patients with normal NK cell counts (Fig. 1a,b) across patient groups with different overall clinical statuses (Extended Data Fig. 1a, Supplementary Table 3). Of note, such a negative correlation between NK cell counts (early during the infection) and viral load was not found for T cells or B cells (Extended Data Fig. 1a). Similarly, a more rapid decline in viral load over time was associated with a more rapid increase in NK cells and vice versa (Extended Data Fig. 1b). Overall, the availability of NK cells early during the course of COVID-19 correlated with a lower abundance of SARS-CoV-2 viral RNA.

**Fig. 1: NK cells from patients with severe COVID-19 fail to control SARS-CoV-2 replication.**

---

 **figure1**

**a, b,** Temporal viral load regression for patients with  $>40$  NK cells per  $\mu\text{l}$  (**a**;  $n = 183$ ) or  $\leq 40$  NK cells per  $\mu\text{l}$  (**b**;  $n = 23$ ) at first count (Methods). The  $x$ -axis indicates time since the first measurement. The analysis included 206 patients in the intensive care unit (ICU) (Extended Data Fig. 1), of which 47 patients had severe COVID-19

(highlighted in red; Supplementary Table 3). **c, d**, Vero E6 cells (**c**) or Calu-3 cells (**d**) were infected with SARS-CoV-2 (B.1 lineage). At 1 h after infection, NK cells from healthy donors activated for 24 h in vitro as indicated with interleukins were added. Viral replication was measured 12 h later as genome equivalents (GE) per ml (GE ml<sup>-1</sup>; target cells co-cultured with NK cells versus cultured alone (**c**) or versus NK cell:target cell ratio 1:3 (**d**),  $n = 4$  donors, no NK cells  $n = 5$  samples). **e, f**, Vero E6 cells (**e**) or Calu-3 cells (**f**) were infected with SARS-CoV-2 and co-cultured as described above with NK cells from either healthy donors ( $n = 8$  (**e**) or 6 (**f**)) or patients with severe COVID-19 ( $n = 6$  (**e**) or 4 (**f**)). Viral load as the fold-change of Vero E6 cells cultured alone versus co-cultured with NK cells was determined (**e**; pooled data from two independent experiments). For **f**, a 1:1 NK cell:target cell ratio was used. **g**, Calu-3 cells were infected and co-cultured as above with IL-12- and IL-15-activated NK cells in a 3:1 NK cell:target cell ratio. Before co-culture, NK cells were incubated with the indicated neutralizing receptor antibodies. Each filled dot represents viral replication of target cells co-cultured with NK cells from an individual donor (2B4  $n = 4$ , all others  $n = 6$ , no NK cells  $n = 8$  samples, indicated group versus NK cells only). Graphs display mean  $\pm$  s.e.m. Two-sided Mann–Whitney *U*-test (**f**,  $P = 0.038$ ; **g**,  $P = 0.041$  and  $P = 0.0043$ ). \* $P \leq 0.05$ , \*\* $P \leq 0.01$ , \*\*\* $P \leq 0.001$ , \*\*\*\* $P \leq 0.0001$ .

We investigated whether NK cells can directly control SARS-CoV-2 (B.1 lineage) replication in an infected human lung epithelial cell line (Calu-3) or in kidney epithelial cells (Vero E6). At the time of infection, highly purified NK cells from healthy donors were added to infected Calu-3 and Vero E6 cells and the intracellular viral load was measured. NK cells reduced viral replication in a dose-dependent manner (Fig. 1c, d), a finding that was confirmed with a second virus variant (B.1.351 lineage; Extended Data Fig. 1c). NK cells are often activated during viral infections<sup>5</sup>, but NK cells isolated from patients admitted to hospital with COVID-19 were significantly less effective in reducing the viral load compared with NK cells from healthy donors (Fig. 1e, f).

NK cell recognition of virus-infected cells is determined by interactions between activating and inhibitory NK cell receptors and their ligands on target cells<sup>6</sup>. The large reduction in viral replication induced by NK cells could not be further enhanced by HLA blockade, which suggests that infected Calu-3 cells do not appreciably inhibit NK cells through HLA-I-specific inhibitory receptors (Fig. 1g). Uninfected Calu-3 cells were poor targets of NK cells (Extended Data Fig. 1d). Blockade of single, activating NK cell receptors did not impair virus control, whereas simultaneous blockade of all three natural cytotoxicity receptors (NKp30, NKp44 and NKp46) or of 2B4, NKG2D and DNAM-1 led to a significant increase in virus replication (Fig. 1g). Collectively, our data demonstrate that NK-cell-mediated control of SARS-CoV-2 replication in infected target cells requires redundant recognition by activating NK cell

receptors. This process is impaired in infected cells treated with NK cells isolated from patients admitted to hospital with COVID-19.

## **Impaired NK cell function during COVID-19**

We set out to study NK cell effector functions in detail in patients with COVID-19 across the disease spectrum and time (Fig. 2a). Patients with non-COVID-19 flu-like illness (FLI), ambulant patients with COVID-19 and patients with moderate COVID-19 disease severity had normal frequencies of CD56<sup>dim</sup> NK cells. By contrast, patients with a severe course of COVID-19 had reduced frequencies of both CD56<sup>dim</sup> and CD56<sup>bright</sup> NK cells and of innate lymphoid cells during the first weeks after symptom onset (Extended Data Fig. 2).

**Fig. 2: Impaired NK-cell-mediated cytotoxicity during severe COVID-19.**

---

 **figure2**

**a**, Overview of the study design. **b, c**, Mean fluorescence intensity (MFI, median) of perforin (**b**) and granzyme B (**c**) in CD56<sup>dim</sup> NK cells. Independent measurements from 44 (**b**) or 50 (**c**) healthy donors, 9 patients with FLI, and patients with COVID-19 (24 ambulant,  $n = 56$ ; 17 moderate,  $n = 19$ ; 30 severe,  $n = 73$ ) obtained 1–8 weeks after

the onset of symptoms. **d**, Specific lysis (mean  $\pm$  s.e.m.) of K562 target cells by NK cells from the indicated donors obtained within the first 2 weeks after symptom onset was determined in a  $^{51}\text{Cr}$  release assay. Data represent pooled data of 12 independent experiments using 18 healthy donors ( $n = 38$  independent measurements), 8 patients with FLI ( $n = 8$ ) and 28 patients with COVID-19 (7 ambulant,  $n = 7$ ; 14 moderate,  $n = 15$ ; 10 severe,  $n = 10$ ). **e**, PBMCs from the indicated donor groups were co-cultured for 4 h with K562 cells and the percentage (median) of CD107a $^+$  NK cells was measured. Patients receiving corticosteroid treatment were excluded from the analysis. Data depict independent measurements across the disease course (29 healthy,  $n = 29$ ; 11 FLI,  $n = 11$ ; 21 ambulant COVID-19,  $n = 28$ ; 13 moderate COVID-19,  $n = 13$ ; 16 severe COVID-19,  $n = 22$ ). **f, g**, Quantification (**f**, mean) and representative flow cytometry plots (**g**) of conjugation of NK cells from healthy donors ( $n = 8$ ) and from patients with severe COVID-19 ( $n = 5$ ) with target cells. Numbers indicate the frequency in the percentage of NK cells conjugated to target cells out of all NK cells (pooled data from two independent experiments). For **b, c** and **e**, statistical analysis (indicated group versus healthy) was performed using one-way analysis of variance (ANOVA) followed by a two-sided Mann–Whitney *U*-test. The dashed line indicates median frequency or MFI of NK cells from healthy donors. For **d** and **f**, two-sided Mann–Whitney *U*-test was used (**f**,  $P = 0.03$ ).

Previous data regarding the expression profile of cytotoxic molecules in COVID-19 were inconclusive<sup>3,4,7,8</sup>. We found a significant and early upregulation of perforin and granzyme B both in ambulant patients and in hospitalized patients with COVID-19 (Fig. 2b, c, Extended Data Fig. 3a–c), which is an early sign of NK cell activation that is observed in the context of various other viral infections<sup>5,9,10,11</sup>. NK cells isolated during the first two weeks after symptom onset from hospitalized and, to a lesser extent, from ambulant patients with COVID-19 showed impairments in cell-mediated cytotoxicity despite the high levels of perforin and granzyme B expression (Fig. 2d). Such a reduced cytotoxic activity of NK cells was not found in patients with FLI. Given the apparent paradox of high levels of cytotoxic molecule expression and low cytotoxic function, we analysed the release of cytotoxic granules. NK cells from healthy donors, patients with FLI and ambulant patients with COVID-19 did not show differences in degranulation. By contrast, NK cells from hospitalized patients with COVID-19 showed impaired degranulation (Fig. 2e, Extended Data Fig. 3d). One of the first steps during interactions between cognate NK cells and target cells is the formation of cellular conjugates, and the establishment of such conjugates was reduced for NK cells from patients with severe COVID-19 (Fig. 2f, g). Of note, reduced cell–cell interactions and degranulation were not a consequence of a reduced expression of activating NK cell receptors in severe COVID-19 (Extended Data Fig. 3e, f).

NK cells from ambulant patients with COVID-19 showed an increased production of interferon- $\gamma$  (IFN $\gamma$ ), whereas NK cells from patients with severe COVID-19 produced only low levels of IFN $\gamma$  and tumour necrosis factor (TNF)<sup>12</sup> (Extended Data Fig. 3g, h). The T-box transcription factor T-bet coordinates NK cell effector programmes, including the expression of granzyme B, IFN $\gamma$  and perforin<sup>13</sup>. T-bet was upregulated in NK cells from patients with FLI and its expression was maintained in ambulant patients with COVID-19. By contrast, T-bet was substantially suppressed at all time points in NK cells from hospitalized patients with COVID-19 (Extended Data Fig. 3a, i). These data cannot be easily explained by differences in age because we did not find strong negative correlations between age and any of the NK cell readouts (Extended Data Fig. 4). Reductions in NK-cell-mediated cytotoxicity and effector programmes were also not caused by dexamethasone treatment, as comparable data were obtained for samples taken during the first wave of COVID-19 (March to April 2020), a period when dexamethasone was not administered to patients (Fig. 2e).

## Single-cell RNA sequencing atlas of NK cells

We used single-cell RNA sequencing (scRNA-seq) to generate a time-resolved, droplet-based single-cell transcriptomics atlas of peripheral blood NK cells from the following individuals: patients with severe COVID-19; outpatients with oligosymptomatic SARS-CoV-2 infection; and healthy donors (Fig. 3a). Using the gating strategy depicted in Extended Data Fig. 5a, 80,325 single NK cell transcriptomes were captured. Using uniform manifold approximation and projection for dimension reduction (UMAP), we identified seven transcriptionally distinct clusters of cells<sup>14</sup> (Fig. 3a). A small number (1,375 cells) of contaminating non-NK cells was found in cluster 6; therefore this cluster was excluded from further analysis. Cells in the remaining clusters (0–5) expressed genes that define conventional NK cells, including surface markers (Extended Data Fig. 5b), effector molecules, such as *PRF1*, *GNYL*, *GZMB*, *GZMH* and *GZMM*, and *TBX21* (which encodes T-bet)<sup>15,16</sup> (Extended Data Fig. 5b–f). Cluster 2 represented CD56<sup>bright</sup> NK cells characterized by high expression of *IL7R*, *SELL*, *XCL1*, *LTB* and *GZMK* and low expression of *CD160* (refs. 16,17) (Extended Data Fig. 5b, c). Cluster 0 contained cells with high expression of NK cell effector molecules and of *TBX21*, but with low expression of *NCAM1*, and we therefore identified these as a subset of CD56<sup>dim</sup> NK cells. Cluster 1 was closely related to cluster 0. Among the few differentially expressed genes were *CD96* and *KLRG1*, both of which have been linked to NK cell maturation and functional exhaustion<sup>18,19</sup>. In addition, they showed reduced expression of most NK effector genes, thus they demarcate late effector NK cells that may be reduced in function (Extended Data Fig. 5d). Within CD56<sup>dim</sup> NK cells, a third cluster (cluster 3) was discriminated with low expression of effector molecules (*GZMB*, *GZMH* and *GZMM*; Extended Data Fig. 5d). This NK cell subset may correspond to the previously

described 'terminally differentiated' CD56<sup>dim</sup> NK cells that are in a post-activation state<sup>16,20</sup>.

**Fig. 3: A TGFβ response signature is a hallmark of NK cells in severe COVID-19 but not in severe influenza.**

 figure3

**a–g**, scRNA-seq of highly purified peripheral blood NK cells of 5 healthy donors ( $n = 5$ ) and patients with COVID-19 from day 2 to day 68 after symptom onset (11 ambulant patients ( $n = 11$ ) and 13 patients with severe COVID-19 ( $n = 52$ ) (Supplementary Tables 1–3). The gating strategy is depicted in Extended Data Fig. 5a. **a**, UMAP representation of 80,325 sorted NK cells from all samples ( $n = 68$ ). Colours indicate unsupervised clustering. **b**, Percentage (median) of cells allocated to each cluster in the indicated groups. Each dot represents one sample subjected to scRNA-seq.  $P$  values determined by one-way ANOVA followed by two-sided Mann–Whitney  $U$ -test. **c**, **d**, Pseudotime trajectories (**c**) and representation of the individual NK cell clusters in trajectories (**d**) of 11,613 randomly selected NK cell transcriptomes from all groups. **e–g**, Single-cell GSEA of indicated gene sets was projected on the UMAP

analysis (clusters 0, 1 and 3 only). Single cells with enriched gene expression are displayed as red dots (left), cells with depletion of the genes are displayed as blue dots (right). All sequenced NK cells per group are displayed as grey dots in the background. **e**, Hallmark IFN $\alpha$  response GSEA. **f, g**, Enrichment of TGF $\beta$ -induced genes (**f**, left) and depletion of TGF $\beta$ -suppressed genes (**f**, right) in the indicated groups and across the course of severe COVID-19 (**g**; early:  $\leq$ day 14 after symptom onset; intermediate: days 15–28, late:  $>$ day 28). **h**, NK cells were extracted from a publicly available single-cell dataset of PBMCs from healthy donors and from patients with COVID-19 or with severe influenza<sup>30</sup> and a single-cell GSEA of the NK-cell-specific TGF $\beta$  response gene set was performed as described in **e**. GSEA *P* values were calculated using two-sided Fisher's exact test comparing the indicated groups with the left-sided (in **e**, early was compared to healthy). \**P* value describes a reduction in enrichment or depletion.

Similar to CD56<sup>bright</sup> NK cells, cells in cluster 4 were characterized by high expression of *IL7R* and *GZMK*, but expressed low levels of *XCL1* and *SELL* (Extended Data Fig. [5c](#)) and corresponded to “transitional NK cells”<sup>16</sup>. Cluster 4 also contained cells that express the activating NK cell receptor *KLRC2* (which encodes NKG2C; Extended Data Fig. [5e](#)). Low expression levels of NKG2A (encoded by *KLRC1*) and of the signalling adaptor molecule Fc $\epsilon$ R $\gamma$  (encoded by *FCER1G*) corroborated the enrichment of adaptive NK cells in cluster 4 (ref. [21](#)). Thus, cluster 4 is heterogenous and represents transitional and adaptive NK cells. Cluster 5 represented proliferating NK cells identified by the high expression of *MKI67* and of genes controlling the cell cycle (Extended Data Fig. [5e,g](#)).

An analysis of the representation of each NK cell cluster across COVID-19 disease states revealed dynamics in NK cell differentiation. In severe COVID-19, we observed a significant increase in proliferating (cluster 5) NK cells (Fig. [3b](#)), and this result was in line with flow cytometry data (Extended Data Fig. [5h](#)). Although the frequency of cells belonging to cluster 1 (late effector) NK cells was reduced in patients with severe COVID-19, these patients had increased levels of terminally differentiated cluster 3 NK cells (Fig. [3b](#)). Although not statistically significant, adaptive NK cells (cluster 4) were reproducibly increased in severe COVID-19, results that are in line with previous data<sup>3</sup>.

To investigate whether COVID-19 introduces changes in the dynamics of NK cell differentiation, we used monocle pseudotime trajectory analysis<sup>22</sup>, which connects related clusters to construct differentiation trajectories (Fig. [3c,d](#), Extended Data Fig. [6a-d](#)). We defined cluster 2 CD56<sup>bright</sup> NK cells as the root of the progression trajectory. The pseudotime model predicted that CD56<sup>bright</sup> NK cells (cluster 2)—through a proliferative state in the left leaf (cluster 5)—differentiate into effector NK cells (cluster 0: CD56<sup>dim</sup> NK effector I cells). Next, by gradually decreasing effector

molecule expression, the effector NK cells differentiate into cluster 1 CD56<sup>dim</sup> effector II cells until reaching the terminally differentiated state (cluster 3), which dominates the distal right leaf of the differentiation trajectory (Fig. 3c, d, Extended Data Fig. 6a, b). Along the pseudotime trajectory, major differentiation states were CD56<sup>bright</sup> NK cells (state 12: high expression of *IL7RA* and *GZMK*), proliferating NK cells (state 1: *MKI67* high), effector NK cells (states 2–7; with graded levels of effector genes such as *PRF1*) and finally terminally differentiated NK cells (states 8 and 9) (Extended Data Fig. 6c, d). This differentiation trajectory was generally conserved in patients with COVID-19. However, patients with particularly severe COVID-19 had increased levels of proliferating NK cells that fed into one root of the differentiation trajectory and had an accumulation of terminally differentiated NK cells at the distal end of the trajectory (Extended Data Fig. 6a–d).

## A TGF $\beta$ signature is a hallmark of severe COVID-19

We interrogated our dataset for enrichment of genes that may affect NK cell effector functions and applied gene set enrichment analysis (GSEA) to the effector NK cell clusters 0, 1 and 3. In patients with COVID-19, there was a significant enrichment of ‘Hallmark IFN $\alpha$  response genes’ (Fig. 3e) and ‘Hallmark IFN $\gamma$  response genes’ (Extended Data Fig. 6e) predominantly in the NK effector cluster 0. This result was in line with increased virus-induced type I and type II interferon levels observed in the serum of patients with COVID-19 (Extended Data Fig. 6f). We also confirmed<sup>3</sup> an increased expression of markers linked to NK cell activation and differentiation (for example, CD69 and CD57) in hospitalized patients with COVID-19 (Extended Data Fig. 6g–i). Among the enriched functional networks in NK cells isolated from patients with COVID-19 were several gene sets related to cellular metabolism and translation. Together, these results demonstrate that there are substantial changes in cellular activation in the context of SARS-CoV-2 infections (Extended Data Fig. 7a).

We next performed a Kyoto Encyclopedia of Genes and Genomes (KEGG) pathway analysis. We noted that among the transcriptional networks significantly enriched in effector NK cells from ambulant patients with COVID-19 and in particular from patients with severe COVID-19, was the pathway ‘intestinal immune network for IgA production’ (Extended Data Fig. 7b). IgA class switching is strictly controlled by TGF $\beta$ <sup>23,24</sup>, and many genes in this KEGG pathway are direct targets of TGF $\beta$  signalling, a cytokine that suppresses NK cell function<sup>25,26</sup>. Even terminally differentiated (cluster 3) NK cells, which were substantially depleted in gene sets regulated by IFN $\alpha$  or cellular metabolism (Extended Data Fig. 7a), were enriched for genes of this KEGG pathway (Extended Data Fig. 7b). Because the transcriptional changes instructed by TGF $\beta$  in NK cells are not known at single-cell resolution, we generated a scRNA-seq dataset of highly purified peripheral blood NK cells from

healthy donors cultured in the presence or absence of TGF $\beta$ . UMAP analysis of the two treatment groups showed a large effect of TGF $\beta$  on the transcriptional state of NK cells that was highly reproducible across individual donors (Extended Data Fig. 8a). An analysis of differentially expressed genes revealed that the majority of genes were negatively regulated by TGF $\beta$  in their expression, including *TBX21* and *STAT1* and several effector genes such as *PRF1* and granzyme family members (Extended Data Fig. 8b). The expression of a small group of genes was induced by exposure to TGF $\beta$ , including genes that encode the chemokine receptor CXCR4 or the transcription factor EOMES, which are both known TGF $\beta$  target genes (Extended Data Fig. 8b). Within the cells that were exposed to TGF $\beta$  (Extended Data Fig. 8c, red), we found that various pathways that are central to granule exocytosis<sup>27</sup> were negatively regulated by TGF $\beta$  (Extended Data Fig. 8d).

Using this established TGF $\beta$  signature, we interrogated the scRNA-seq dataset from patients with COVID-19 for changes in the expression of TGF $\beta$ -controlled genes. TGF $\beta$ -controlled genes were expressed at a low level in NK cells from healthy donors, but a substantial enrichment in TGF $\beta$  response genes was noted in effector NK cell clusters from patients with severe COVID-19 (Fig. 3f). Of note, changes in the expression of TGF $\beta$ -controlled genes were already detectable during the very early stages of COVID-19 and increased during the course of infection (Fig. 3g). Indeed, the expression of canonical TGF $\beta$  target genes such as *EOMES* and *ITGAE* was upregulated in NK cells from patients with severe COVID-19 (Extended Data Fig. 8e, f). Our data demonstrate that there is a progressive and long-lasting reprogramming of NK cells by TGF $\beta$  during COVID-19 that starts within the first days after symptom onset and is commensurate with disease severity.

In ambulant patients with COVID-19, gene sets associated with cell adhesion and NK cell cytotoxicity were slightly upregulated in some NK cells. However, substantial downregulation was found in most effector NK cells in severe COVID-19 (Extended Data Fig. 8g). Of note, among the genes substantially downregulated in patients with severe COVID-19 was *ITGB2*, which encodes the  $\beta_2$ -integrin (also known as CD18). This integrin associates with the  $\alpha$ -integrins CD11a to CD11d to generate functional integrin receptors (Extended Data Fig. 8h) and is involved in NK-cell-mediated cytotoxicity<sup>28,29</sup>. This may provide a molecular explanation for the substantial failure of NK cells from patients with severe COVID-19 to form conjugates with target cells. Collectively, NK cells from patients with severe COVID-19 show a gene signature characterized by IFN-controlled cell activation programmes (for example, upregulation of perforin, granzyme B and CD69) superimposed by strong and long-lasting TGF $\beta$ -controlled transcriptional reprogramming, in particular the downregulation of genes linked to NK-cell-mediated cytotoxicity.

We wondered whether reprogramming of NK cells by TGF $\beta$  is a common event in pneumonia. We extracted NK cell data from a previously published scRNA-seq dataset of peripheral blood mononuclear cells (PBMCs) from patients with COVID-19 and from patients with influenza pneumonia<sup>30</sup>. This analysis revealed a strong enrichment of TGF $\beta$ -controlled genes in NK cells from patients with COVID-19 but not from patients with influenza pneumonia (Fig. 3h). To explore whether TGF $\beta$  signatures can also be found in lung NK cells, we analysed a single-nucleus RNA-seq dataset of post-mortem lung tissue samples from patients with severe COVID-19 or with SARS-CoV-2-negative pneumonia<sup>31</sup>. The dataset enabled the analysis of single-cell transcriptomes of lung NK cells (Extended Data Fig. 9a–c). GSEA revealed that lung NK cells from patients with severe COVID-19 pneumonia but not those from patients with SARS-CoV-2-negative pneumonia were significantly enriched in TGF $\beta$ -controlled genes (Extended Data Fig. 9d).

## Untimely peak of serum TGF $\beta$ in severe COVID-19

Our transcriptional and functional data suggested that TGF $\beta$  is produced early in the phase of SARS-CoV-2 infection, particularly in the context of severe COVID-19. Patients with FLI and ambulant patients with COVID-19 did not show increased serum TGF $\beta$  within the first week after symptom onset, whereas hospitalized patients with COVID-19 had significantly increased TGF $\beta$  serum levels at week 1 that peaked at week 2 (Fig. 4a). Ambulant patients with COVID-19 showed only a small increment in serum TGF $\beta$  at later time points of the infection (>3 weeks after symptom onset). To obtain insights into the cellular sources of TGF $\beta$ , we analysed the lung single-nucleus RNA-seq dataset for *TGFB* transcripts and for transcripts associated with TGF $\beta$  bioactivity. In comparison to non-COVID-19 pneumonia illnesses, we observed a large increase in *TGFB1* and *TGFB2* expression in type 1 alveolar epithelial cells, fibroblasts, myofibroblasts, endothelial cells and myeloid cells (Extended Data Fig. 9e, g). Expression levels of various genes required for the bioactivity of TGF $\beta$  (such as *LTBP3*, *LAP3* and *MMP2*) were also increased in patients with COVID-19 (Extended Data Fig. 9f). Of note, some of the clusters with the highest expression of *TGFB1*, *LAP3* and *MMP28* contained SARS-CoV-2 transcripts (that is, were infected) (Extended Data Fig. 9h). Thus, the early TGF $\beta$  peak in hospitalized patients with COVID-19 is closely correlated to the early impairment of NK cell effector programmes.

**Fig. 4: Serum of patients with severe COVID-19 inhibits NK cell function in a TGF $\beta$ -dependent manner.**

---

 **figure4**

**a**, Serum levels of active TGF $\beta$ . Independent measurements (mean) from 13 patients with FLI ( $n = 13$ ) and 66 patients with COVID-19 (30 severe,  $n = 74$ ; 7 moderate,  $n = 12$ ; 39 ambulant,  $n = 53$ ) at indicated time points after symptom onset (group  $>3$  weeks contains samples from weeks 4 and 5). The dashed line indicates the median TGF $\beta$  serum level of 34 healthy donors. Patients receiving corticosteroids were excluded. **b**, NK cells from healthy donors were cultured in medium containing IL-12 and IL-15 with (green) or without TGF $\beta$  (blue) and co-cultured with SARS-CoV-2-infected Vero E6 cells. Viral load (mean  $\pm$  s.e.m.) was measured 12 h later. Each data point represents NK cells from one individual donor (E:T 9:1  $n = 3$ , all others  $n = 4$ , no NK cells  $n = 11$  samples). **c, d**, Sorted NK cells from 3–9 healthy donors were cultured in medium containing either serum from a healthy donor or serum from a patient with severe COVID-19 ( $n = 9$  (**c**) or 7 (**d**)) and the frequency of CD107a $^+$  NK cells (mean) after co-culture with K562 (**c**) or the MFI of T-bet (**d**, mean) was determined. Each dot represents NK cells of one healthy donor cultured with serum of another healthy donor (blue;  $n = 17$  (**c**) or 6 (**d**)) or of one patient with severe COVID-19 (red;  $n = 24$  (**c**) or 14 (**d**)). **e, f**, Sorted NK cells from 3–8 healthy donors were cultured in medium alone or with serum from patients with severe COVID-19. In a second condition, patient sera were pre-incubated with anti-TGF $\beta$  and then added as described

above. The frequency of CD107a<sup>+</sup> NK cells (**e**, mean,  $n = 14$ ) and the MFI of T-bet (**f**, mean,  $n = 32$ ) were determined. Shown is the fold-change frequency or MFI between NK cells cultured in sera from patients (with or without prior anti-TGFβ treatment) and NK cells cultured in medium alone. For **e**, **f**, two-sided Wilcoxon matched-pairs rank test was used. For **a–d**, two-sided Mann–Whitney *U*-test was used.

We wondered whether exposure of NK cells to TGFβ has any effect on their capacity to control viral replication. TGFβ completely abrogated the NK cell effector programme, that is, NK-cell-mediated control of SARS-CoV-2 replication in vitro (Fig. [4b](#)), cell-mediated cytotoxicity, degranulation in response to target cells and cytokine production (Extended Data Fig. [10a–d](#)). TGFβ treatment of stimulated NK cells also led to the downregulation of T-bet, whereas the canonical TGFβ target EOMES was upregulated (Extended Data Fig. [10e, f](#)).

NK cells from healthy donors that were exposed to serum from patients with severe COVID-19, obtained during the first weeks after symptom onset, significantly inhibited NK cell degranulation and T-bet expression (Fig. [4c, d](#)). This inhibitory effect was lost when sera was pretreated with a TGFβ-blocking antibody with activity against TGFβ1, TGFβ2 and TGFβ3 (Fig. [4e, f](#), Extended Data Fig. [10g–i](#)). By contrast, neutralization of interleukin-6 (IL-6), IL-10 or IL-15 did not restore NK cell degranulation or T-bet expression (Extended Data Fig. [10j–p](#)), even though these cytokines have been previously linked to severe COVID-19 (refs. [4,32](#)). Thus, the untimely expression of TGFβ leads to suppressed NK cell function, which may reduce virus control and be detrimental in severe COVID-19.

Although TGFβ is thought to curtail excessive immune responsiveness and to restore or maintain immune homeostasis<sup>[33](#)</sup>, we now demonstrate that an untimely early production of TGFβ and associated NK cell dysfunction is a hallmark of severe COVID-19. Multilevel proteomics data support a specific dysregulation of TGFβ signalling by the SARS-CoV-2 ORF8 protein<sup>[34](#)</sup> and we have previously shown that TGFβ impairs B-cell responses in the context of COVID-19 (ref. [35](#)). Two matrix metalloproteinase inhibitors (prinomastat and marimastat) that diminish TGFβ bioactivity strongly inhibited the replication of SARS-CoV-2 but not of SARS-CoV<sup>[34](#)</sup>. TGFβ-mediated impairment of NK cell function may also have an impact on other aspects of COVID-19. A dysregulated myeloid response is another hallmark of severe COVID-19 in which there is an inadequate production of inflammatory cytokines<sup>[36,37](#)</sup>. Lessons learnt from genetic syndromes of NK cell cytotoxic defects have implicated NK cells in the quality control of innate immune responses by curtailing excessive myeloid responses, thereby preventing immunopathology<sup>[27,38](#)</sup>. Another intriguing link is the role of NK cells in the control of fibrotic reprogramming and the elimination of pre-fibrotic cells that undergo a senescence programme<sup>[39](#)</sup>. Thus, the inhibition of

untimely TGF $\beta$  production and the promotion of NK cell function may positively affect SARS-CoV-2 control on multiple levels<sup>40</sup>.

## Methods

### Human participants

The recruitment of study participants was approved by the Institutional Review Board of Charité (EA2/066/20, EA2/072/20, EAEA4/014/20 and EA2/092/20). Written informed consent was provided by all patients or legal representatives for participation in the study. Forty-five ambulant patients with COVID-19 (World Health Organization (WHO) disease severity 1 and 2 according to the WHO clinical ordinal scale), 21 hospitalized patients (WHO 3–4) with moderate COVID-19 and 79 patients with severe COVID-19 who required ventilation (WHO 5–7, 52 of which fulfilled acute respiratory distress syndrome criteria according to the Berlin definition of this condition<sup>41</sup>) were enrolled in this study. All patients with COVID-19 were tested positive for SARS-CoV-2 RNA via nasopharyngeal swabs. Twenty patients who presented with influenza-like symptoms but were tested negative for SARS-CoV-2 (FLI) and a total of 96 healthy donors who did not present any clinical sign of viral infection were enrolled as controls. The clinical characteristics of all participants are summarized in Supplementary Tables 1–3. For autopsy, informed consent was given by the next of kin, and autopsies were performed on the legal basis of section 1 SRegG BE of the autopsy act of Berlin and section 25(4) of the German Infection Protection Act. The sequencing of the post-mortem tissue was approved by the Ethics Committee of the Charité (EA2/066/20, EA1/144/13 and EA1/075/19 to H.R.) and by the Charité-BIH COVID-19 research board and complied with the Declaration of Helsinki. Additional use of anonymized clinical data is covered by section 25 of the Berlin Hospital Law and did not require further ethical or legal clearance.

### Isolation of PBMCs and serum

Peripheral blood was drawn from each donor into EDTA collection tubes and, for selected samples (CD107a assay), into heparin tubes (BD Biosciences). PBMCs were separated from peripheral blood by Pancoll human (PAN-Biotech) density gradient centrifugation at room temperature. Cells were either used directly for analysis or stored in heat-inactivated fetal bovine serum (FCS; Pan-Biotech, P30-3602) with 10% dimethylsulfoxide at –80 °C before analysis. Serum samples were drawn from each donor into Vacutainer SSTTM tubes (BD Biosciences), centrifuged for 10 min at 2,000g and stored at –20 °C before analysis.

### Flow cytometry analysis

PBMCs were incubated with Fc blocking reagent (Miltenyi Biotec) according to the manufacturer's instructions. To exclude dead cells, the cells were stained using a Live/Dead (LD) Fixable Aqua Dead Cell staining kit (ThermoFisher, L34965). For surface antigen staining, the cells were incubated with monoclonal anti-human antibodies (Supplementary Table 4) for 20 min at 4 °C. The Foxp3 Transcription Factor Staining Buffer Set (eBioscience, 00-5523-00) was applied before intracellular staining of transcription factors, cytotoxic molecules and cytokines. The samples were analysed using a FACS Fortessa X20 (BD Biosciences). Data were analysed using FlowJo Software v.10.3 (Treestar). Mean fluorescent intensity (MFI) values of NK cell populations were normalized to the MFI of lineage-negative marker-negative cells<sup>42</sup>. For intracellular cytokine staining of IFN $\gamma$  (BioLegend, 502527) and TNF (BioLegend, 502908), NK cells were stimulated for 4 h at 37 °C in the presence of brefeldin A (Sigma-Aldrich) with phorbol 12-myristate 13-acetate (25 ng ml<sup>-1</sup>, Sigma-Aldrich) and ionomycin (500 ng ml<sup>-1</sup>, Sigma-Aldrich). Alternatively, NK cells were co-cultured with K562 target cells (American Type Culture Collection (ATCC) CCL-243, verified by ATCC) for 4 h at 37 °C in the presence of brefeldin A. In Supplementary Table 4, all antibodies are listed and assigned to staining panels A, B, C, D and E. Patient information and time point after onset of symptoms when the peripheral blood was obtained for each flow cytometry analysis are listed Supplementary Tables 1–3.

## In vitro culture of sorted NK cells

Frozen PBMCs were gradually thawed at 37 °C and resuspended in RPMI medium (Gibco, 31870074) supplemented with 20% heat-inactivated FCS (Pan-Biotech P30-3602), l-glutamine (200 mM, Gibco, 25030081), penicillin–streptomycin (10,000 U ml<sup>-1</sup>, Gibco, 5140122) and gentamicin (Lonza BioWhittaker, BW17-519L). Live cells were discriminated using a Live/Dead Fixable Aqua Dead Cell staining kit (ThermoFisher, L34965) and incubated in human Fc blocking reagent (Miltenyi Biotec) according to the manufacturer's instructions. The cells were stained with the following anti-human antibodies for 20 min at 4 °C: CD3 (eBioscience, 11-0039-42), CD4 (eBioscience, 11-0048-42), CD14 (BioLegend, 325604), CD19 (BioLegend, 363008), CD45 (BioLegend, 393409), CD7 (BioLegend, 343119) and CD56 (BioLegend, 362511). NK cells were sorted as LD<sup>-</sup>Lin<sup>-</sup> (CD3, CD4, CD14 and CD19) CD45<sup>+</sup>CD7<sup>+</sup>CD56<sup>+</sup> using a FACS Aria II Cell Sorter (BD Biosciences).

Sorted NK cells were cultured in RPMI containing rh-IL-12 (20 ng ml<sup>-1</sup>; PeproTech, 200-12H), rh-IL-15 (20 ng ml<sup>-1</sup>; PeproTech, 200-15), rh-TGF $\beta$  (10 ng ml<sup>-1</sup>; PeproTech, 100-21), rh-IFN $\alpha$  (10,000 U ml<sup>-1</sup>; R&D Systems, 11100-1) or rh-IFN $\beta$  (20 ng ml; R&D Systems, MAB1835-SP) and cultured for 2–4 days at 37 °C with 5% CO<sub>2</sub> as indicated.

## Chromium release assay

A chromium release assay was performed as previously described<sup>43</sup>. In brief, full PBMCs were cultured overnight in RPMI supplemented with rh-IL-12 and rh-IL-15. For selected analyses, rh-TGFβ was added. NK cell frequencies in the PBMC fraction were determined using flow cytometry. K562 target cells were radioactively labelled by incubating  $2 \times 10^6$  K562 cells in 450 µl RPMI with 50 µl of  $^{51}\text{Cr}$  (CR-RA-8, Cr51, 185 MBq, 5 mCi ml<sup>-1</sup>) for 2 h at 37 °C on a rotator. After labelling, target cells were washed twice with RPMI before adding PBMCs at the indicated NK cell:target cell ratios (9:1, 3:1, 1:1 or 1:3). Following a co-culture incubation of 4 h (37 °C with 5% CO<sub>2</sub>), the supernatant was collected and the  $^{51}\text{Cr}$  released was quantified using a Wallac Wizard 1470 gamma counter. To quantify the maximal  $^{51}\text{Cr}$  release for each experiment, the gamma count of the supernatant of target cells cultured without effector cells (spontaneous  $^{51}\text{Cr}$  release) was subtracted from the gamma signal of labelled target cells only. The percentage of specific lysis or the percentage of  $^{51}\text{Cr}$  release induced by NK cells from healthy donors in a 3:1 NK cell:target cell ratio (per cent of maximum  $^{51}\text{Cr}$  release) was calculated for each sample.

## Degranulation assay of NK cells

CD107a expression on NK cells of the PBMC fraction was measured as previously described<sup>44</sup> (protocol 2 of the consensus protocol). In brief, PBMCs were cultured at  $2 \times 10^6$  ml<sup>-1</sup> in RPMI overnight. NK cells were subsequently co-cultured for 2 h with K562 cells and stained for CD107a (eBioscience, 11-1079-42), CD56 (Beckman Coulter, A82943), CD8 (Beckman Coulter, IM2469), CD3 (Beckman Coulter, A94680) and CD45 (Beckman Coulter, B36294). The samples were analysed on a Navios-EX FACS (Beckman Coulter). Data were analysed using the Navios 2.0 software. CD107a mobilization of sorted NK cells (as described in the section ‘In vitro culture of sorted NK cells’) cultured in RPMI, supplemented with rh-IL-12, rh-IL-15 and rh-TGFβ as indicated, was analysed after co-culture with K562 cells at a 2:1 NK cell:target cell ratio for 4 h at 37 °C. Subsequently, cells were re-stained using a Live/Dead Fixable Aqua Dead Cell staining kit, human Fc blocking reagent and the following antibodies: CD3 (eBioscience, 11-0039-42), CD4 (eBioscience, 11-0048-42), CD14 (BioLegend, 325604), CD19 (BioLegend, 363008), CD45 (BioLegend, 393409), CD7 (BioLegend, 343119), CD107a (BD Bioscience, 562622) and CD56 (BioLegend, 362511). The frequency of CD107a expression was determined in LD<sup>-</sup> Lin<sup>-</sup> (CD3, CD4, CD14 and CD19) CD45<sup>+</sup>CD7<sup>+</sup>CD56<sup>+</sup> NK cells using a FACS Fortessa X20 (BD Biosciences).

## Conjugation assay

NK cell:target cell adhesion was assessed as previously described<sup>45</sup>. In brief, PBMCs were separated from peripheral blood by a density gradient as described above. Cells were enriched by negative selection using a NK cell isolation kit (Miltenyi Biotec) according to the manufacturer's instructions. After isolation, NK cells were labelled for 20 min using a Celltrace Far Red Cell Proliferation kit (Invitrogen, C34564) according to the manufacturer's instructions. K562 target cells were labelled for 10 min at 37 °C with cell proliferation dye (Invitrogen, 65-0842-85). After labelling, cells were washed with RPMI, mixed in a 1:4 NK cell: target cell ratio and centrifuged at 300g for 1 s. Cells were co-cultured for 1 h at 37 °C before conjugates were quantified by flow cytometry.

### Co-culture of NK cells with SARS-CoV-2-infected cells

PBMCs were separated from freshly drawn peripheral blood by a density gradient as described above. Cells were enriched by negative selection using a NK cell isolation kit (Miltenyi Biotec) according to the manufacturer's instructions. Enrichment was ensured by flow cytometry. After isolation, NK cells were stimulated for 24–48 h in RPMI 1640 supplemented with rh-IL-12 (PeproTech, 200-12H), rh-IL-15 (PeproTech, 200-15) and rh-TGFβ (PeproTech, 100-21) as indicated at 37 °C with 5% CO<sub>2</sub>. NK cells were washed with DMEM and co-cultured with SARS-CoV-2-infected Vero E6 cells (*Cercopithecus aethiops* kidney epithelial cells; ATCC CRL-1586, verified by ATCC) or Calu-3 cells (human bronchial epithelial cells; ATCC HTB-55, verified by ATCC) as indicated. Approximately 175,000 Vero E6 cells and 300,000 Calu-3 cells per well were seeded in 24-well plates 24 h before infection as indicated.

For masking experiments, NK cells were incubated with the neutralizing antibodies anti-NKp30 (clone F252), anti-NKp44 (clone KS38), anti-NKp46 (clone KL247), anti-NKG2D (clone BAT221 and clone ON72), anti-DNAM-1 (clone F5) and anti-2B4 (clone CO54) at room temperature 45 min before co-culture as indicated. For all blocking experiments, target cells were incubated with anti-HLA-I (clone A6/136). Monoclonal antibodies were provided by E. Marcenaro (University of Genova, Italy).

Cells were infected with the SARS-CoV-2/München 984 virus isolate (B.1 lineage, hCoV-19/Germany/BY-ChVir-984/2020, accession ID: EPI\_ISL\_406862; Pango lineage v.3.1.1, lineages v.2021-06-15) or the variant B.1.351 (hCoV-19/Germany/BW-ChVir22131/2021, accession ID: EPI\_ISL\_862149) at cell culture passage 2 (ref. <sup>46</sup>) with a multiplicity of infection (MOI) of 0.001 (Vero E6) or a MOI of 0.1 (Calu-3). Virus was diluted in OptiPro serum-free medium (Thermo Fisher). For infection, the supernatant was removed, cells were rinsed once with 0.5 ml PBS (Thermo Fisher) and 200 µl of virus-containing dilution was inoculated on the cells for 1 h at 37 °C. Next, 500 µl of NK cell suspension was added 12 h after infection as indicated. Adherent cells were collected 12 h (Vero E6) or 24 h (Calu-3) after NK cell

addition for isolation of viral RNA. For isolation of viral RNA, 35 µl of MagNA Pure 96 external lysis buffer (Roche) was added to the adherent cells. All samples were heat-inactivated for 10 min at 70 °C. Isolation and purification of viral RNA was performed using a MagNA Pure 96 System (Roche) according to the manufacturer's recommendations. Viral RNA was quantified using real-time PCR with reverse transcription (RT–PCR; E gene assay) as previously described<sup>47</sup>. All infection experiments were done under biosafety level 3 conditions with enhanced respiratory personal protection equipment.

## Viral load data analyses

Viral load (RNA copies per swab) measurements were obtained based on a calibrated curve of viral RNA copies and RT–PCR cycle threshold values as previously described<sup>48</sup>. For the examination of temporal viral load dynamics, patients with at least two viral load measurements and two immune cell count measurements were included, and a linear regression was calculated. A maximum offset for both parameters was set to 7 days, and only infections with a duration of less than 40 days were considered. Regression analysis was performed using the seaborn (regplot) package v.0.11.1 and the scipy (stats.linregress) package (v.1.6.0) running under Python 3.9.1. For indicated analyses, patients were categorized as having either low or normal absolute immune cell counts according to whether their first immune cell count had a value below or above a threshold value. The following thresholds were used: 40 NK cells per µl; 40 B cells per µl; 360 T cells per µl; 200 CD4<sup>+</sup> T cells per µl; 300 CD8<sup>+</sup> T cells per µl; 600 lymphocytes (CD45<sup>+</sup>CD14<sup>-</sup>) per µl. Analysis was performed on hospitalized patients who tested positive (through SARS-CoV-2 RT–PCR), including patients who tested positive in an intensive care unit ward at any point during their infection and including patients with severe COVID-19 of the study cohort (Extended Data Fig. 1, Supplementary Table 3).

## NK cell isolation from peripheral blood for single-cell sequencing

Frozen PBMCs from 13 patients with severe COVID-19 (52 samples), 11 ambulant patients with COVID-19 (11 samples) from day 2 to day 68 after onset of symptoms (Supplementary Tables 1–3) and 5 healthy donors (5 samples) were thawed in RPMI (Gibco, 31870074) supplemented with 20% heat-inactivated FCS and incubated with Fc blocking reagent (Miltenyi Biotec) following the manufacturer's instructions. Up to  $1 \times 10^7$  cells per 100 µl were stained with the following anti-human antibodies: CD3 (Miltenyi Biotec, 130-113-133), CD14 (Miltenyi Biotec, 130-113-152), CD19 (Miltenyi Biotec, 130-113-172), CD45 (BioLegend, 304008) and CD56 (Miltenyi Biotec, 130-113-305). To allow cell pooling, each sample was also incubated with one of eight different TotalSeq-C anti-human Hashtags (LNH-94;2M2, Barcoded, BioLegend, 394661, 394663, 394665, 394667, 394669, 394671, 394673 and 394675).

4,6-diamidino-2-phenylindole (DAPI) was added before sorting to enable exclusion of dead cells. NK cells were identified and sorted as DAPI<sup>-</sup>CD3<sup>-</sup>CD14<sup>-</sup>CD19<sup>-</sup>CD45<sup>+</sup>CD56<sup>+</sup>. All sortings used a MA900 Multi-Application Cell Sorter (Sony Biotechnology). Cell counting was performed using a MACSQuant flow cytometer (Miltenyi Biotec). Sorted NK cells were further processed for scRNA-seq.

For the generation of a NK cell-specific TGFβ-response dataset, live cells in thawed PBMCs were discriminated using a Live/Dead Fixable Aqua Dead Cell staining kit (ThermoFisher, L34965) and incubated in human Fc blocking reagent (Miltenyi Biotec) according to the manufacturer's instruction. The cells were stained with the following anti-human antibodies for 20 min at 4 °C: CD3 (eBioscience, 11-0039-42), CD4 (eBioscience, 11-0048-42), CD14 (BioLegend, 325604), CD19 (BioLegend, 363008), CD45 (BioLegend, 393409), CD7 (BioLegend, 343119) and CD56 (BioLegend, 362511). NK cells were sorted as LD<sup>-</sup>Lin<sup>-</sup> (CD3, CD4, CD14 and CD19) CD45<sup>+</sup>CD7<sup>+</sup>CD56<sup>+</sup> using a FACS Aria II Cell Sorter (BD Biosciences). Sorted NK cells were cultured in RPMI containing rh-IL-12 and rh-IL-15 with or without additional rh-TGFβ for 4 days at 37 °C with 5% CO<sub>2</sub> before scRNA-seq.

## scRNA library preparation and sequencing

The 10X Genomics workflow for cell capturing and scRNA gene expression (GEX) was applied to sorted NK cells using a Chromium Single Cell 5' Library & Gel Bead kit and a Single Cell 5' Feature Barcode Library kit (10X Genomics). Final GEX was obtained after fragmentation, adapter ligation and final index PCR using the Single Index Kit T Set A. A Qubit HS DNA assay kit (Life Technologies) was used for library quantification, and fragment sizes were determined using the Fragment Analyzer with the HS NGS Fragment kit (1–6,000 bp; Agilent). Sequencing was performed on a NextSeq500 device (Illumina) using High Output v2 kits (150 cycles) with the recommended sequencing conditions for 5' GEX libraries (read 1: 26 nt, read 2: 98 nt, index 1: 8 nt).

## Single-cell transcriptome analysis

Chromium single-cell data were processed using cellranger-3.1.0. The mkfastq and the count pipeline were used in default parameter settings for demultiplexing, alignment of reads to the Refdata-cellranger-hg19-1.2.0 genome, barcode and unique molecular identifier (UMI) counting, and calling of intact cells. The number of expected cells was set to 3,000. Further analysis was performed using the Seurat R-package (v.3.1.1)<sup>49</sup>. The pooled samples were separated using eight cite-seq hashtags (TotalSeq-C, BioLegend). Cells with more than 30% cite-seq reads for a particular hashtag were assumed as positively stained. Cells with no (undefined origin) or ambivalent assignments (doublets) were removed from further analysis. The resulting

transcriptome profiles of NK cells from healthy donors, ambulant patients with COVID-19 and patients with severe COVID-19 were normalized and integrated as previously described<sup>50</sup>. Variable genes were detected and scaled. Data were scaled and UMAP was performed in default parameter settings using Scale Data, RunPCA and RunUMAP with 30 principal components. Quality control was performed by visual inspection of the fraction of mitochondrial genes, the number of detected genes and UMI counts per cell. No notable abnormalities were observed. Transcriptionally similar cells were clustered using shared nearest neighbour (SNN) modularity optimization with a SNN resolution of 0.2. Marker genes for clusters were identified using FindAllGenes with a log fold-change of  $>2.5$  and a minimum of 0.1 expressing cells. The genes used for manual annotation of the function of the clusters was informed by previous publications<sup>16,20,51</sup>. One out of six clusters revealed B-cell-specific and monocyte-specific genes (*CD19*, *CD14*) and was excluded from further analysis.

Pseudotime trajectory analysis was performed using the monocle2 R package. Cells from each group (healthy, ambulant and severe COVID-19) were randomly downsampled to an equal depth of 3,871 cells. The overall 11,613 cells were used for the calculation in monocle2. The top 1,000 differentially expressed genes across the five clusters (ranked by lowest *q*-value) were used to order the cells. The BEAM method was used to identify genes that significantly differed in expression level across a branch point<sup>22</sup>.

Single-cell data derived from NK cells cultured in presence and absence of TGF $\beta$  were analysed using the analog workflow except for clustering and trajectory analysis steps. The TGF $\beta$  response signature was defined on the basis of differentially expressed genes between samples with and without TGF $\beta$  treatment. To compare samples, two-sided Mann–Whitney *U*-test was used on log-normalized counts. Differentially expressed genes were identified (adjusted *P*  $\leq 0.05$  and a log fold-change of  $>2.2$  for enrichment and  $<2.2$  for depletion). The heatmap of differentially expressed genes is based on *z*-transformed means of log-normalized counts. Hierarchical clustering was performed using Euclidian distances and WARD linkage criterium. All generated sequencing data were deposited into the NCBI Gene Expression Omnibus (accession number [GSE184329](#)).

## Analysis of peripheral blood NK cells from a publicly available dataset

NK cell data were extracted from a publicly available PBMC single-cell sequencing dataset ([GSE149689](#)) consisting of 4 samples from healthy participants, 11 samples from patients with COVID-19 and 5 samples from patients with severe influenza<sup>30</sup>. In the first step, the individual samples and 59,572 cells were integrated and subdivided into 10 clusters in a UMAP representation with a SNN resolution of 0.1. A heatmap of

cell-type-defining genes was used to identify 10,604 NK cells from the PBMCs. GSEA for TGF $\beta$ -induced and TGF $\beta$ -suppressed NK cell genes was performed as described below.

## Analysis of non-haematopoietic and haematopoietic cell populations from lung tissue

The publicly available lung single-nucleus dataset (European Genome–Phenome Archive reference ID: [EGAS00001004689](#)) consisting of three patients who died from pneumonia unrelated to COVID-19 (as controls) and seven patients who died from COVID-19-associated pneumonia<sup>31</sup> was aligned to a hg19 reference transcriptome that included the SARS-CoV-2 genome (NCBI reference sequence ID: [NC\\_045512](#)) using cellranger v3.0.1 (10X Genomics). Ambient RNA removal was performed with SoupX (v1.4.5)<sup>52</sup>. First, the 10 samples and 53,709 cells were integrated as previously described<sup>50</sup> for the NK cell single-cell sequencing dataset and subdivided into 33 clusters in a UMAP representation with a SNN resolution of 1. A heatmap of 13 genes was used to identify NK cells from the lung, and cluster 25 was defined as the NK-cell-specific cluster of 845 cells. The remaining cell populations were identified according to Gassen et al.<sup>31</sup>.

## GSEA

GSEA was performed for each cell on the basis of differences in log-normalized counts to the mean of all cells analysed using 1,000 randomizations (false discovery rate < 0.5 and normalized  $P < 0.2$ )<sup>53</sup>. For visualization, the normalized enrichment score per cell within the indicated gene set (upregulation or downregulation) was plotted. Gene sets (Hallmark, Reactome and KEGG) were obtained from the Molecular Signatures Database (MSigDB, v.6.2)<sup>54,55</sup>. The NK-cell-specific TGF $\beta$  response gene set was newly generated in this study. The GSEA-enrichment plot (score curve) of TGF $\beta$ -suppressed genes in lung-tissue-resident NK cells was performed on pre-ranked differences between medians of expressing cells in otherwise default parameter settings. Only genes expressed in at least one group were considered. The median was set to 0 if no expressing cells were found.

## In vitro NK cell exposure to patient serum

Sorted NK cells from healthy donors were cultured for 48 h in RPMI containing IL-12, IL-15 and IL-2 (25 ng ml<sup>-1</sup>; PeproTech, 212-12) as indicated and 20% of either serum from another healthy donor (Supplementary Table 1) or from a patient with severe COVID-19 (Supplementary Table 3). Unless stated otherwise, IL-12, IL-15 and serum were used. For indicated experiments, the patient sera were pre-incubated with

antibodies directed against TGF $\beta$ 1, TGF $\beta$ 2 and TGF $\beta$ 3 (R&D Systems, MAB1835-SP), anti-IL-6 (5  $\mu$ g ml $^{-1}$ ; R&D Systems, MAB206), anti-IL-10 (30  $\mu$ g ml; R&D Systems, MAB217) or anti-IL-15 (5  $\mu$ g ml; eBioscience, 16-0157-82) as indicated for 10 min before being added to the culture and using identical culture conditions. After 48 h, protein expression levels of T-bet were measured, the frequency of CD107a expression in NK cells was analysed after 4 h of co-culture with K562 cells using flow cytometry or viral replication was determined, as described above.

## Cytokine measurements

Cytokine levels were measured using a bead-based multiplex cytokine array (Human Cytokine 25-Plex ProcartaPlex Panel 1B, Thermo Fisher Scientific). Before the assay, serum samples were diluted 1:3 in dilution buffer provided with the kit. TGF $\beta$  was detected using a Human TGF $\beta$ 1 Simplex ProcartaPlex kit (Thermo Fisher Scientific). Before measuring serum TGF $\beta$ 1, the bioactive form of TGF $\beta$ 1 was generated by incubating the serum with 1 N HCl followed by neutralization with 1.2 N NaOH according to the manufacturer's instructions. The samples were incubated with antibody-coated magnetic beads for 30 min at room temperature with shaking, then incubated overnight at 4 °C followed by a 1-h incubation period at room temperature. All subsequent incubation steps were performed according to the manufacturer's instructions. The assay plates were read using a Luminex MAGPIX system and quantified using xPONENT analysis software (Luminex). IFN $\alpha$  serum concentration was analysed using a Simoa IFN $\alpha$  Advantage kit (Quanterix) according to the manufacturer's instructions.

## Statistical analysis and reproducibility

All statistical tests were performed with Graph Pad Prism V7 software as indicated for each analysis ( $*P \leq 0.05$ ,  $**P \leq 0.01$ ,  $***P \leq 0.001$  and  $****P \leq 0.0001$ ; NS, not significant). Representative data of at least three independent experiments are shown in Figs. 1d, e, g, 2f and 4c, f, and Extended Data Figs. 15a, b, c, d. Representative data of two independent experiments are shown in Extended Data Fig. 15j, k, n, o.

## Reporting summary

Further information on research design is available in the [Nature Research Reporting Summary](#) linked to this paper.

## Data availability

All generated sequencing data were deposited at NCBI Gene Expression Omnibus (accession number [GSE184329](#)).

## References

1. 1.

Diaz-Salazar, C. & Sun, J. C. Natural killer cell responses to emerging viruses of zoonotic origin. *Curr. Opin. Virol.* **44**, 97–111 (2020).

2. 2.

Vivier, E., Tomasello, E., Baratin, M., Walzer, T. & Ugolini, S. Functions of natural killer cells. *Nat. Immunol.* **9**, 503–510 (2008).

3. 3.

Maucourant, C. et al. Natural killer cell immunotypes related to COVID-19 disease severity. *Sci. Immunol.* **5**, eabd6832 (2020).

4. 4.

Mazzoni, A. et al. Impaired immune cell cytotoxicity in severe COVID-19 is IL-6 dependent. *J. Clin. Invest.* **130**, 4694–4703 (2020).

5. 5.

Lucas, M., Schachterle, W., Oberle, K., Aichele, P. & Diefenbach, A. Dendritic cells prime natural killer cells by trans-presenting interleukin 15. *Immunity* **26**, 503–517 (2007).

6. 6.

Diefenbach, A. & Raulet, D. H. Innate immune recognition by stimulatory immunoreceptors. *Curr. Opin. Immunol.* **15**, 37–44 (2003).

7. 7.

Zenarruzabeitia, O. et al. T cell activation, highly armed cytotoxic cells and a shift in monocytes CD300 receptors expression is characteristic of patients with severe COVID-19. *Front. Immunol* **12**, 655934 (2021).

8. 8.

Zheng, M. et al. Functional exhaustion of antiviral lymphocytes in COVID-19 patients. *Cell. Mol. Immunol.* **17**, 533–535 (2020).

9. 9.

Shellam, G., Allan, J., Papadimitriou, J. & Bancroft, G. Increased susceptibility to cytomegalovirus infection in beige mutant mice. *Proc. Natl Acad. Sci. USA* **78**, 5104–5108 (1981).

10. 10.

Trinchieri, G. Biology of natural killer cells. *Adv. Immunol.* **47**, 187–376 (1989).

11. 11.

Fehniger, T. A. et al. Acquisition of murine NK cell cytotoxicity requires the translation of a pre-existing pool of granzyme B and perforin mRNAs. *Immunity* **26**, 798–811 (2007).

12. 12.

Varchetta, S. et al. Unique immunological profile in patients with COVID-19. *Cell. Mol. Immunol.* **18**, 604–612 (2021).

13. 13.

Townsend, M. J. et al. T-bet regulates the terminal maturation and homeostasis of NK and V $\alpha$ 14*i* NKT cells. *Immunity* **20**, 477–494 (2004).

14. 14.

Becht, E. et al. Dimensionality reduction for visualizing single-cell data using UMAP. *Nat. Biotechnol.* **37**, 38–44 (2019).

15. 15.

Freud, A. G. et al. NKp80 defines a critical step during human natural killer cell development. *Cell Rep.* **16**, 379–391 (2016).

16. 16.

Yang, C. et al. Heterogeneity of human bone marrow and blood natural killer cells defined by single-cell transcriptome. *Nat. Commun.* **10**, 3931 (2019).

17. 17. Luetke-Eversloh, M., Killig, M. & Romagnani, C. Signatures of human NK cell development and terminal differentiation. *Front. Immunol.* **4**, 499 (2013).
18. 18. Huntington, N. D. et al. NK cell maturation and peripheral homeostasis is associated with KLRG1 up-regulation. *J. immunol.* **178**, 4764–4770 (2007).
19. 19. Sun, H. et al. Human CD96 correlates to natural killer cell exhaustion and predicts the prognosis of human hepatocellular carcinoma. *Hepatology* **70**, 168–183 (2019).
20. 20. Crinier, A. et al. High-dimensional single-cell analysis identifies organ-specific signatures and conserved NK cell subsets in humans and mice. *Immunity* **49**, 971–986.e5 (2018).
21. 21. Hammer, Q. et al. Peptide-specific recognition of human cytomegalovirus strains controls adaptive natural killer cells. *Nat. Immunol.* **19**, 453–463 (2018).
22. 22. Qiu, X. et al. Reversed graph embedding resolves complex single-cell trajectories. *Nat. Methods* **14**, 979–982 (2017).
23. 23. Coffman, R. L., Lebman, D. A. & Shrader, B. Transforming growth factor beta specifically enhances IgA production by lipopolysaccharide-stimulated murine B lymphocytes. *J. Exp. Med.* **170**, 1039–1044 (1989).
24. 24. Sonoda, E. et al. Transforming growth factor beta induces IgA production and acts additively with interleukin 5 for IgA production. *J. Exp. Med.* **170**, 1415–1420 (1989).

25. 25.

Viel, S. et al. TGF- $\beta$  inhibits the activation and functions of NK cells by repressing the mTOR pathway. *Sci Signal.* **9**, ra19 (2016).

26. 26.

Rook, A. H. et al. Effects of transforming growth factor beta on the functions of natural killer cells: depressed cytolytic activity and blunting of interferon responsiveness. *J. Immunol.* **136**, 3916–3920 (1986).

27. 27.

Pachlornik Schmid, J. et al. Inherited defects in lymphocyte cytotoxic activity. *Immunol. Rev.* **235**, 10–23 (2010).

28. 28.

Kohl, S., Springer, T. A., Schmalstieg, F. C., Loo, L. S. & Anderson, D. C. Defective natural killer cytotoxicity and polymorphonuclear leukocyte antibody-dependent cellular cytotoxicity in patients with LFA-1/OKM-1 deficiency. *J. Immunol.* **133**, 2972–2978 (1984).

29. 29.

Riteau, B., Barber, D. F. & Long, E. O. Vav1 phosphorylation is induced by  $\beta 2$  integrin engagement on natural killer cells upstream of actin cytoskeleton and lipid raft reorganization. *J. Exp. Med.* **198**, 469–474 (2003).

30. 30.

Lee, J. S. et al. Immunophenotyping of COVID-19 and influenza highlights the role of type I interferons in development of severe COVID-19. *Sci. Immunol.* **5**, eabd1554 (2020).

31. 31.

Gassen, N. C. et al. SARS-CoV-2-mediated dysregulation of metabolism and autophagy uncovers host-targeting antivirals. *Nat. Commun.* **12**, 3818 (2021).

32. 32.

Liu, C. et al. Time-resolved systems immunology reveals a late juncture linked to fatal COVID-19. *Cell* **184**, 1836–1857.e22 (2021).

33. 33.
- Travis, M. A. & Sheppard, D. TGF- $\beta$  activation and function in immunity. *Annu. Rev. Immunol.* **32**, 51–82 (2014).
34. 34.
- Stukalov, A. et al. Multilevel proteomics reveals host perturbations by SARS-CoV-2 and SARS-CoV. *Nature* **594**, 246–252 (2021).
35. 35.
- Ferreira-Gomes, M. et al. SARS-CoV-2 in severe COVID-19 induces a TGF- $\beta$ -dominated chronic immune response that does not target itself. *Nat. Comm.* **12**, 1961 (2021).
36. 36.
- Schulte-Schrepping, J. et al. Severe COVID-19 is marked by a dysregulated myeloid cell compartment. *Cell* **182**, 1419–1440.e23 (2020).
37. 37.
- Merad, M. & Martin, J. C. Pathological inflammation in patients with COVID-19: a key role for monocytes and macrophages. *Nat. Rev. Immunol.* **20**, 355–362 (2020).
38. 38.
- van Dommelen, S. L. et al. Perforin and granzymes have distinct roles in defensive immunity and immunopathology. *Immunity* **25**, 835–848 (2006).
39. 39.
- Krizhanovsky, V. et al. Senescence of activated stellate cells limits liver fibrosis. *Cell* **134**, 657–667 (2008).
40. 40.
- Chen, W. A potential treatment of COVID-19 with TGF- $\beta$  blockade. *Int. J. Biol. Sci.* **16**, 1954–1955 (2020).
41. 41.

Force, A. D. T. et al. Acute respiratory distress syndrome: the Berlin Definition. *JAMA* **307**, 2526–2533 (2012).

42. 42.

Cossarizza, A. et al. Guidelines for the use of flow cytometry and cell sorting in immunological studies (second edition). *Eur. J. Immunol.* **49**, 1457–1973 (2019).

43. 43.

Verneris, M. R., Karimi, M., Baker, J., Jayaswal, A. & Negrin, R. S. Role of NKG2D signaling in the cytotoxicity of activated and expanded CD8<sup>+</sup> T cells. *Blood* **103**, 3065–3072 (2004).

44. 44.

Bryceson, Y. T. et al. A prospective evaluation of degranulation assays in the rapid diagnosis of familial hemophagocytic syndromes. *Blood* **119**, 2754–2763 (2012).

45. 45.

Deguine, J., Breart, B., Lemaitre, F., Di Santo, J. P. & Bousso, P. Intravital imaging reveals distinct dynamics for natural killer and CD8<sup>+</sup> T cells during tumor regression. *Immunity* **33**, 632–644 (2010).

46. 46.

Wolfel, R. et al. Virological assessment of hospitalized patients with COVID-2019. *Nature* **581**, 465–469 (2020).

47. 47.

Corman, V. M. et al. Detection of 2019 novel coronavirus (2019-nCoV) by real-time RT-PCR. *Euro Surveill.* **25**, 2000045 (2020).

48. 48.

Jones, T. C. et al. Estimating infectiousness throughout SARS-CoV-2 infection course. *Science* **373**, eabi5273 (2021).

49. 49.

Butler, A., Hoffman, P., Smibert, P., Papalexi, E. & Satija, R. Integrating single-cell transcriptomic data across different conditions, technologies, and species. *Nat. Biotechnol.* **36**, 411–420 (2018).

50. 50.

Stuart, T. et al. Comprehensive integration of single-cell data. *Cell* **177**, 1888–1902.e21 (2019).

51. 51.

Smith, S. L. et al. Diversity of peripheral blood human NK cells identified by single-cell RNA sequencing. *Blood Adv.* **4**, 1388–1406 (2020).

52. 52.

Young, M. D. & Behjati, S. SoupX removes ambient RNA contamination from droplet-based single-cell RNA sequencing data. *Gigascience* **9**, giaa151 (2020).

53. 53.

Subramanian, A. et al. Gene set enrichment analysis: a knowledge-based approach for interpreting genome-wide expression profiles. *Proc. Natl Acad. Sci. USA* **102**, 15545–15550 (2005).

54. 54.

Li, S. et al. Molecular signatures of antibody responses derived from a systems biology study of five human vaccines. *Nat. Immunol.* **15**, 195–204 (2014).

55. 55.

Liberzon, A. et al. Molecular signatures database (MSigDB) 3.0. *Bioinformatics* **27**, 1739–1740 (2011).

56. 56.

Sivori, S. et al. Human NK cells: surface receptors, inhibitory checkpoints, and translational applications. *Cell. Mol. Immunol.* **16**, 430–441 (2019).

## Acknowledgements

The authors are most grateful to the patients for their consent in participating in this study. We thank members of the Diefenbach laboratory, the Mashreghi laboratory, the

Kruglov laboratory, the Klose laboratory and the Romagnani laboratory for valuable discussions on the manuscript. Masking antibodies against NKp30 (clone F252) and DNAM-1 (clone F5) were provided by D. Pende (IRCCS Ospedale Policlinico San Martino, 16132 Genoa, Italy) and NKp46 (clone KL247) and NKp44 (KS38) by S. Parolini (Sezione di Oncologia e Immunologia Sperimentale, Dipartimento di Medicina Molecolare e Traslazionale, Università di Brescia). We are grateful to the staff at the Benjamin Franklin Flow Cytometry (BFFC) Facility (M. Fernandes and A. Branco) and the DRFZ flow cytometry facility (J. Kirsch, A. C. Teichmuller and T. Kaiser) for support in cell sorting. The BFFC is supported by DFG Instrument grants INST 335/597-1 FUGG und INST 335/777-1 FUGG. We are indebted to K. Oberle, F. Egelhofer, J. Heinze and A. Sebastiampillai for technical assistance and advice. We thank A. Bayindir, F. Cicek and E. Daka for support in the management of patient material. This work was supported by the following entities: Deutsche Forschungsgemeinschaft (TR-SFB 84/A02 and A06, TR-SFB241/A01, SPP1937-DI764/7 to A.D.; TRR130/P16 and P17 to A.R. and H.R.; TR-SFB 84/A07 to C.D.; TRR241/A04 to A.K.; RA 2491/1-1 to H.R.; SFB-TR 84/B08, SFB 1449/Z02 to M.A.M); the European Research Council (ERC-2010-AdG 268978 to A.R.); the Einstein Foundation Berlin (Einstein Professorship to A.D. and M.A.M.); the state of Berlin and the “European Regional Development Fund” to M.-F.M. (ERDF 2014-2020, EFRE 1.8/11, Deutsches Rheuma-Forschungszentrum); the Berlin Institute of Health with the Starting Grant Multi-Omics Characterization of SARS-CoV-2 infection, Project 6 “Identifying immunological targets in COVID-19” to A.D. and M.-F.M.; the Russian Ministry of Science and Higher Education of the Russian Federation (grant 075-15-2019-1660) and the Russian Foundation for Basic Research (no. 17-00-00268 (<https://kias.rfbr.ru/index.php>)) to A.K; the Leibniz Association (Leibniz Collaborative Excellence, TargArt) to T.K. and M.-F.M.; the German Federal Ministry of Education and Research (BMBF) projects “NaFoUniMedCovid19” (FKZ: 01KX2021)—COVIM (AP-4) to V.M.C., L.E.S. and A.D.; RECAST (01KI20337) to B.S., V.M.C., L.E.S., J. Roehmel. and M.A.M.; 82DZL009B1 to M.A.M.; Fondazione AIRC per la Ricerca sul Cancro to E.M. T.C.J. is in part funded through the NIAID–NIH CEIRS contract HHSN272201400008C. C.U.D. acknowledges support by a Rahel Hirsch Habilitationsstipendium. The autopsies were facilitated by the Biobank of the Department of Neuropathology, Charité–Universitätsmedizin Berlin and supported by the BMBF (Organosrat, Defeat Pandemics).

# **Author information**

## **Author notes**

1. These authors contributed equally: Mario Witkowski, Caroline Tizian, Marta Ferreira-Gomes
2. These authors jointly supervised this work: Mir-Farzin Mashreghi, Andreas Diefenbach

## **Affiliations**

1. Laboratory of Innate Immunity, Institute of Microbiology, Infectious Diseases and Immunology, Charité - Universitätsmedizin Berlin, Corporate Member of Freie Universität Berlin and Humboldt-Universität zu Berlin, Campus Benjamin Franklin, Berlin, Germany

Mario Witkowski, Caroline Tizian, Thordis Hohnstein, Irene Mattiola, Philipp Nawrath, Sophie McEwen & Andreas Diefenbach

2. Mucosal and Developmental Immunology, Deutsches Rheuma-Forschungszentrum (DRFZ), an Institute of the Leibniz Association, Berlin, Germany

Mario Witkowski, Caroline Tizian, Thordis Hohnstein, Irene Mattiola, Philipp Nawrath, Sophie McEwen & Andreas Diefenbach

3. Department of Microbiology and Hygiene, Labor Berlin, Charité–Vivantes, Berlin, Germany

Mario Witkowski & Andreas Diefenbach

4. Therapeutic Gene Regulation, Deutsches Rheuma-Forschungszentrum (DRFZ), an Institute of the Leibniz Association, Berlin, Germany

Marta Ferreira-Gomes, Frederik Heinrich, Gitta Anne Heinz, Paweł Durek & Mir-Farzin Mashreghi

5. Institute of Virology, Charité - Universitätsmedizin Berlin, Corporate Member of Freie Universität Berlin and Humboldt-Universität zu Berlin, Campus Charité Mitte, Berlin, Germany

Daniela Niemeyer, Terry C. Jones, Victor M. Corman & Christian Drosten

6. German Center for Infection Research (DZIF), Partner Site Berlin, Berlin, Germany

Daniela Niemeyer, Terry C. Jones, Victor M. Corman & Christian Drosten

7. Centre for Pathogen Evolution, Department of Zoology, University of Cambridge, Cambridge, UK

Terry C. Jones

8. Dermatological Allergology, Allergie-Centrum-Charité, Department of Dermatology and Allergy, Charité–Universitätsmedizin Berlin, Corporate Member of Freie Universität Berlin and Humboldt–Universität zu Berlin, Campus Charité Mitte, Berlin, Germany

Stefan Frischbutter & Marcus Maurer

9. Fraunhofer Institute for Translational Medicine and Pharmacology (ITMP) Allergology and Immunology, Berlin, Germany

Stefan Frischbutter & Marcus Maurer

10. Department of Anesthesiology and Intensive Care Medicine, Charité - Universitätsmedizin Berlin, Corporate Member of Freie Universität Berlin and Humboldt-Universität zu Berlin, Campus Benjamin Franklin, Berlin, Germany

Stefan Angermair & Sascha Treskatsch

11. Department of Pediatric Gastroenterology, Nephrology and Metabolic Diseases, Charité - Universitätsmedizin Berlin, Corporate Member of

Freie Universität Berlin and Humboldt-Universität zu Berlin, Campus Virchow-Klinikum, Berlin, Germany

Silvia Zocche

12. Institute of Physiology, Center for Space Medicine and Extreme Environments Berlin, Charité–Universitätsmedizin Berlin, Corporate Member of Freie Universität Berlin and Humboldt-Universität zu Berlin, Berlin, Germany

Edoardo Viviano

13. Department of Immunology, Labor Berlin, Charité-Vivantes, Berlin, Germany

Uwe Kölsch & Christian Meisel

14. Center for Digital Health, Berlin Institute of Health (BIH) and Charité-Universitätsmedizin Berlin, Corporate Member of Freie Universität Berlin and Humboldt-Universität zu Berlin, Berlin, Germany

Robert Lorenz Chua & Christian Conrad

15. Department of Neuropathology, Charité-Universitätsmedizin Berlin, Corporate Member of Freie Universität Berlin and Humboldt-Universität zu Berlin, Berlin, Germany

Tom Aschman, Josefine Radke & Helena Radbruch

16. Institute of Medical Immunology, Charité - Universitätsmedizin Berlin, Corporate Member of Freie Universität Berlin and Humboldt-Universität zu Berlin, Campus Virchow-Klinikum, Berlin, Germany

Christian Meisel, Birgit Sawitzki & Leif Hanitsch

17. Department of Pediatric Respiratory Medicine, Immunology and Critical Care Medicine, Charité-Universitätsmedizin Berlin, Corporate Member of Freie Universität Berlin and Humboldt-Universität zu Berlin, Berlin, Germany

Jobst Roehmel, Marcus A. Mall & Tilmann Kallinich

18. Department of Medicine (Gastroenterology, Infectious Diseases, Rheumatology), Charité - Universitätsmedizin Berlin, Corporate Member of Freie Universität Berlin, Humboldt-Universität zu Berlin and Berlin Institute of Health, Campus Benjamin Franklin, Berlin, Germany

Kristina Allers, Verena Moos & Thomas Schneider

19. German Center for Lung Research (DZL), Associated Partner Berlin, Berlin, Germany

Marcus A. Mall

20. Laboratory of Mucosal Immunity, Institute of Microbiology, Infectious Diseases and Immunology, Charité – Universitätsmedizin Berlin, Corporate Member of Freie Universität Berlin and Humboldt-Universität zu Berlin, Campus Benjamin Franklin, Berlin, Germany

Claudia U. Duerr

21. Cancer Immunology Program, Peter MacCallum Cancer Centre, Melbourne, Victoria, Australia

Joseph A. Trapani

22. Department of Experimental Medicine, University of Genoa, Genoa, Italy

Emanuela Marcenaro

23. Chronic inflammation in Childhood, Deutsches Rheuma-Forschungszentrum (DRFZ), an Institute of the Leibniz Association, Berlin, Germany

Tilmann Kallinich

24. Department of Infectious Diseases and Respiratory Medicine, Charité - Universitätsmedizin Berlin, Corporate Member of Freie Universität Berlin and Humboldt-Universität zu Berlin, Berlin, Germany

Florian Kurth & Leif Erik Sander

25. Department of Tropical Medicine, Bernhard Nocht Institute for Tropical Medicine, and Department of Medicine I, University Medical Centre Hamburg-Eppendorf, Hamburg, Germany

Florian Kurth

26. Chronic Inflammation, Deutsches Rheuma-Forschungszentrum (DRFZ), an Institute of the Leibniz Association, Berlin, Germany

Andrey Kruglov

27. Belozersky Institute of Physico-Chemical Biology and Biological Faculty, M.V. Lomonosov Moscow State University, Moscow, Russia

Andrey Kruglov

28. Center for Precision Genome Editing and Genetic Technologies for Biomedicine, Engelhardt Institute of Molecular Biology, Russian Academy of Sciences, Moscow, Russia

Andrey Kruglov

29. Cell Biology, Deutsches Rheuma-Forschungszentrum (DRFZ), an Institute of the Leibniz Association, Berlin, Germany

Andreas Radbruch

30. BIH Center for Regenerative Therapies (BCRT), Charité Universitätsmedizin Berlin, Berlin, Germany

Mir-Farzin Mashreghi

## Contributions

M.W. and C.T. performed most of the experiments and analysed the data. M.F.-G. performed the flow cytometry-based sorting of NK cells and library preparation for scRNA sequencing. D.N. contributed to the experiments with SARS-CoV-2-infected cells. T.C.J. performed the viral load data analyses. T.H., P.N., S.M., I.M., U.K., C.M., C.D., A.K. and G.A.H., helped with experiments. F.H. and P.D. analysed the RNA-seq data. S.F. and M.M. performed the serum cytokine measurements. S.A., S.T., S.Z., E.V., F.K., L.E.S., L.H., M.A.M., V.M.C., R.L.C., T.A., B.S., J. Roehmel., T.S., C.C., H.R., J. Radke, T.K., V.M., K.A. and T.S. supported the management of patient samples and clinical data. J.A.T., E.M., I.M. and C.D. helped with the design of the in vitro experiments. M.W., C.T., M.F.-M. and A.R. contributed to the development of the study concept. A.D. and M.F.-M. designed, directed and supervised the study. A.D. wrote the manuscript with input from co-authors.

## Corresponding authors

Correspondence to [Mario Witkowski](#) or [Andreas Diefenbach](#).

## Ethics declarations

## Competing interests

The authors declare no competing interests.

## Additional information

**Peer review information** *Nature* thanks the anonymous reviewers for their contribution to the peer review of this work. Peer review reports are available.

**Publisher's note** Springer Nature remains neutral with regard to jurisdictional claims in published maps and institutional affiliations.

## Extended data figures and tables

## Extended Data Fig. 1 The temporal viral load decline is related to the NK cell status.

**(a)** Regressions for temporal viral load according to absolute peripheral blood immune cell count. The viral load trajectory was estimated by linear regression for COVID-19 patients with at least two viral load measurements each, and whose first absolute immune cell count was below or above the indicated threshold (see also [methods](#)). Analysis was performed on SARS-CoV-2 RNA-positive patients who were hospitalized, hospitalized and who tested positive on an ICU ward at any point during their infection (Intensive Care Unit group), and severe COVID-19 patients of the study cohort (Supplementary Table 3). The table lists the mean and median temporal viral load regression gradient, standard deviation (SD) and number of patients (n) per group. **(b)** The relationship between temporal gradient of  $\log_{10}$  viral load and NK cell count change. For each of 32 severe COVID-19 patients with at least two viral load measurements and at least two NK cell count measurements, a linear regression was calculated for each series and a dot corresponding to the two gradients was plotted (n = 32). The blue regression line in the center of the error band shows the correlation between temporal  $\log_{10}$  viral load gradient and NK cell count gradient, with the shaded region indicating the 95% confidence region. The overall regression slope has  $-1.33$  (standard error 0.9) and the correlation coefficient of the dots is  $-0.26$ . Two-sided Fisher's exact test p = 0.029; Two-sided Chi-square p = 0.018. **(c)** Vero E6 cells were infected with the B.1.351 variant of SARS-CoV-2. At 1h post infection, NK cells from healthy donors activated for 24h *in vitro* with IL-12/15 were added. Viral replication (mean  $\pm$  s.e.m.) was measured 12h later as genome equivalents (GE)/ml (NK cell:target cell ratio (NK:T) 1:3 n = 3 donors, all other NK:T ratios n = 4 donors, no NK cells n = 8 samples, two-sided Mann-Whitney U-test comparing NK:T ratios vs. no NK cells, NK:T 3:1; p = 0.004, NK:T 9:1; p = 0.004). **(d)** Quantification of CD107a expression (mean  $\pm$  s.e.m.) in NK cells from healthy donors co-cultured 4h with Calu-3 or K562 cells (n = 3 donors for Calu-3 cells and n = 4 donors for K562).

## Extended Data Fig. 2 Reduction of peripheral blood NK cells and ILC1-like cells during COVID-19.

**(a)** Gating strategy for the identification of CD56<sup>bright</sup> and CD56<sup>dim</sup> peripheral blood NK cells. **(b)** Continuation of the gating depicted in **(a)** and representative flow cytometry plots for the indicated markers in CD56<sup>dim</sup> NK cells of a healthy donor, patient with flu-like illness (FLI), ambulant patient with COVID-19, patient with moderate COVID-19 and a patient with severe COVID-19 **(b)**. **(c)** Frequency of CD56<sup>dim</sup> and CD56<sup>bright</sup> NK cells (median) in the peripheral blood of healthy donors and patients. Independent measurements of 53 healthy donors (n=53), 9 flu-like illness (FLI, n = 9), 29 ambulant COVID-19 (n=62), 17 moderate (n=19) and 45 severe COVID-19 patients (n = 133) between week 1 and week 11 after onset of symptoms. Statistical analysis was performed using a One-way ANOVA followed by a two-sided Mann-Whitney *U*-test comparing healthy vs. FLI or COVID-19 groups. The dashed line indicates the median frequency in healthy donors. **(d,e)** Identification of ILC subsets in 14 healthy donors (n = 14) and 8 patients with severe COVID-19 (n = 28 independent measurements). **(d)** Gating strategy for ILC with pre-gate set on live, CD45<sup>+</sup> single lymphocytes. **(e)** Frequencies (median) of indicated ILC subsets in both groups (independent measurements of two-sided Mann-Whitney *U*-test, ILCs; p=0.007, ‘ILC1’; p=0.09, ILC2; p=0.04, ILCp; p<0.0001) (\*; p ≤ 0.05, \*\*; p ≤ 0.01, \*\*\*; p ≤ 0.001, \*\*\*\*; p ≤ 0.0001).

### Extended Data Fig. 3 NK cells upregulate the expression of cytotoxic molecules but fail to express IFNy and TNF during severe COVID-19.

**(a)** Representative flow cytometry analysis showing the mean fluorescence intensity (MFI) of the indicated proteins in CD56<sup>dim</sup> NK cells from the indicated patient groups. **(b,c)** MFI (median) of perforin **(b)** and granzyme B **(c)** in CD56<sup>bright</sup> peripheral blood NK cells. Independent measurements from 44 (n=44 for perforin) or 50 healthy donors (n=50 for granzyme B), 9 patients with FLI (n=9), 24 ambulant COVID-19 (n=56), 17 moderate COVID-19 (n=19) and 30 severe COVID-19 patients (n=73) from week 1 to 6 after onset of symptoms. **(d)** Representative flow cytometry plots of cell surface CD107a expression by NK cells from indicated groups after 4h co-culture with K562 cells. Pre-gate was set on CD3<sup>-</sup> CD56<sup>+</sup> lymphocytes. **(e,f)** Frequency (median) of expressing NK cells **(e)** and MFI **(f)** of

indicated immunoreceptors on NK cells of 9 healthy donors (n=9 independent measurements), 6 patients with FLI (n=6), 7 ambulant (n=7) and severe 9 COVID-19 (n=10) (Frequency of NKp44<sup>+</sup> NK cells healthy vs. severe p=0.004, MFI of NKp44<sup>+</sup> NK cells healthy vs. severe p=0.022). (g,h) PBMC of healthy donors (n = 8), ambulant patients with COVID-19 (n=6) and patients with severe COVID-19 (n = 8) were stimulated with PMA/Ionomycin and the frequency (median) of IFN $\gamma$ <sup>+</sup> (g) and TNF<sup>+</sup> (h) NK cells was determined by flow cytometry. Statistical analysis was performed using the two-sided Mann-Whitney *U*-test (IFN $\gamma$ <sup>+</sup> NK cells ambulant vs. severe p=0.0007; TNF<sup>+</sup> NK cells ambulant vs. severe p=0.008). (i) Mean fluorescence intensity (MFI, median) of T-bet in CD56<sup>dim</sup> NK cells across the disease course. Independent measurements of 53 healthy donors (n=53), 9 patients with FLI (n=9), 29 ambulant (n = 62), 17 moderate (n=19) and 45 severe COVID-19 patients (n=133). For (b–c,e–f) and (i) statistical analysis was performed using a One-way ANOVA followed by a two-sided Mann-Whitney *U*-test comparing healthy vs. FLI or COVID-19 groups. The dashed line indicates the median MFI or frequency of healthy donors. (\*; p ≤ 0.05, \*\*; p ≤ 0.01, \*\*\*; p ≤ 0.001, \*\*\*\*; p ≤ 0.0001).

#### **Extended Data Fig. 4 Dysregulated NK cell function in severe COVID-19 does not correlate with age.**

(a–d) Two-tailed spearman correlation of age and  $^{51}\text{Cr}$  release in indicated NK cell: target cell ratios in a single experiment (a, n=9 donors), CD107a expression in NK cells (b, n=29) and expression of indicated markers measured by flow cytometry in CD56<sup>dim</sup> (c) and CD56<sup>bright</sup> (d) NK cells of healthy donors (n=44 for perforin and CD57, n=50 for granzyme B, n=53 for all others). Age in years is represented by the x-axis whilst the indicated read out is represented by the y-axis.

#### **Extended Data Fig. 5 Gene expression profile of individual NK cell clusters.**

(a) Gating strategy for FACS of peripheral blood NK cells subjected to single cell RNA sequencing. (b,c,e) UMAP representation depicting the

expression levels of indicated genes. (d,f) Dot plots depicting the expression of the indicated genes in the NK cell clusters. Dot size represents the frequency of cells expressing the indicated gene. Selection of genes for each group in (f) according to Sivori et al<sup>56</sup>. (g) Single cell gene set enrichment analysis for the indicated gene set in all samples. Single cells with enriched gene expression are displayed as red dots, cells with depletion of the genes are displayed as blue dots. (h) Frequency of Ki-67<sup>+</sup> CD56<sup>dim</sup> and CD56<sup>bright</sup> NK cells (median). Independent measurements of 53 healthy donors (n=53), 9 flu-like illness (FLI, n=9), 29 ambulant (n=62), 17 moderate (n=19) and 45 severe COVID-19 patients (n=133) between week 1 and week 11 following onset of symptoms. Statistical analysis was performed using a One-way ANOVA followed by a two-sided Mann-Whitney U-test comparing healthy *vs.* FLI or COVID-19 groups. The dashed line indicates the median frequency of Ki-67<sup>+</sup> NK cells in healthy donors.

### **Extended Data Fig. 6 Differentiation trajectories of NK cells towards terminally differentiated NK cells.**

(a–d) Pseudotime trajectories of a total of 11,613 randomly selected NK cell transcriptomes from all groups. (a) Isolated visualization of each NK cell cluster in the pseudotime trajectory analysis. (b) Expression of indicated genes in the pseudotime trajectories. (c) Cell states in the trajectory analysis. (d) Pie charts depicting the representation of each NK cell cluster in the different cell states. (e) Single cell gene set enrichment analysis (GSEA) of the indicated gene set in the differentiated NK cell clusters (clusters 0, 1 and 3) of all samples. Single cells with enriched gene expression are displayed as red dots and cells with depletion of the genes are displayed as blue dots. Significance of the enrichment or depletion was calculated using the two-sided Fisher’s exact test by comparing the indicated group with the group left-sided (ambulant *vs.* healthy and severe *vs.* ambulant, respectively). (f) Serum cytokine levels over the course of COVID-19. For IFN $\alpha$  data points represent independent measurements of 6 healthy donors (n = 6), 20 ambulant patients with COVID-19 (n = 27) and 17 patients with severe COVID-19 (n = 26) at the indicated time points after onset of symptoms. Group size of 4 to 10 samples for COVID-19

patients per timepoint. For all other cytokines, data points represent independent measurements from 33 healthy donors (n=33), 15 ambulant patients with COVID-19 (n=20) and 6 patients with severe COVID-19 (n=17) with a group size of 3 to 8 samples for COVID-19 patients. Patients receiving corticosteroid treatment were excluded from the analysis except for the IFN $\alpha$  serum measurements. Bars represent the mean  $\pm$  s.e.m. The dashed line indicates the mean serum concentration of the cytokine in healthy donors. Statistical analysis was performed using the two-sided Mann-Whitney *U*-test. (g,h) Frequency (median) of CD69 $^+$  CD56 $^{\text{dim}}$  (g) and CD56 $^{\text{bright}}$  NK cells (h). Independent measurements of 53 healthy donors (n = 53), 9 flu-like illness (FLI, n = 9), 29 ambulant (n = 62), 17 moderate (n = 19) and 45 severe COVID-19 patients (n = 133) between week 1 and week 11 after onset of symptoms. (i) Quantification of CD57 $^+$  CD56 $^{\text{dim}}$  NK cells (median). Independent measurements from 44 (n = 44) healthy donors, 9 patients with FLI (n = 9), 24 ambulant (n = 56), 17 moderate (n = 19) and 30 severe COVID-19 patients (n = 73) from week 1 to 8 after onset of symptoms. Statistical analysis in g–i was performed using a One-way ANOVA followed by a two-sided Mann-Whitney *U*-test comparing healthy *vs.* FLI or COVID-19 groups. The dashed line indicates the median frequency in healthy donors.

### **Extended Data Fig. 7 NK cells show profound changes in gene networks related to cellular metabolism and intestinal IgA production during COVID-19.**

(a,b) Single cell gene set enrichment analysis (GSEA) of the indicated gene sets in the differentiated NK cell clusters (clusters 0, 1 and 3) of all samples. Single cells with enriched gene expression are displayed as red dots and cells with depletion of the genes are displayed as blue dots. Significance of the enrichment or depletion was calculated using the two-sided Fisher's exact test by comparing the indicated group with the group left-sided (ambulant *vs.* healthy and severe *vs.* ambulant, respectively). P-value\* describes a reduction in enrichment or depletion.

### **Extended Data Fig. 8 Genes related to cell adhesion are suppressed in NK cells during severe COVID-19 and by *in vitro***

## exposure to TGF $\beta$ .

**(a,b)** Peripheral blood NK cells of 4 healthy donors were FACS-sorted and cultured *in vitro* in the presence of either IL-12, IL-15 and TGF $\beta$  or IL-12 and IL-15 alone and a total of 8137 single cell transcriptomes were generated. **(a)** UMAP representation of single cell transcriptomes of the four donors for both conditions. **(b)** Heatmap shows differentially expressed genes between both conditions. Upregulated genes are displayed in red, downregulated genes in blue. **(c,d)** Single cell GSEA of the NK cell-specific TGF $\beta$  response gene data set **(c)** or the indicated gene sets **(d)** projected on the UMAP of the scRNA-seq data obtained from NK cells cultured *in vitro* in the presence or absence of TGF $\beta$  as described above. Red dots represent cells with increased expression of the indicated gene set. Blue dots represent cells with a depletion of genes within the indicated gene set. Significance of the enrichment or depletion was calculated using the two-sided Fisher's exact test. **(e,h)** Violin Plot showing the median expression of the indicated genes in differentiated NK cell clusters (0,1 and 3) of healthy individuals and in ambulant and severe COVID-19 patients during the course of disease (Early:  $\leq$ day 14 after symptom onset, intermediate: day 15–28, late:  $>$  day 28, two-sided Mann-Whitney *U*-test, p-value adjusted for multiple comparisons). **(f)** MFI of Eomes (median) was measured in CD56<sup>dim</sup> NK cells from 9 healthy donors ( $n=9$  independent measurements), 6 patients with FLI ( $n=6$ ), 7 ambulant ( $n=7$ ) and 9 severe COVID-19 ( $n=10$ ). Statistical analysis was performed using a One-way ANOVA followed by a two-sided Mann-Whitney *U*-test comparing healthy *vs.* FLI or COVID-19 groups. **(g)** Single cell gene set enrichment analysis (GSEA) of the indicated gene sets in the differentiated NK cell clusters (clusters 0, 1 and 3) of all samples. Single cells with enriched gene expression are displayed as red dots and cells with depletion of the genes are displayed as blue dots. Significance of the enrichment or depletion was calculated using the two-sided Fisher's exact test by comparing the indicated group with the group left-sided (ambulant *vs.* healthy and severe *vs.* ambulant, respectively).

## Extended Data Fig. 9 TGF $\beta$ expression is induced in lung tissue hematopoietic and non-hematopoietic cell populations during

## COVID-19.

**(a–h)** Single-nucleus sequencing of lung tissue from patients with SARS-CoV-2-negative pneumonia (non-COVID-19) and severe COVID-19<sup>31</sup>. **(a)** UMAP visualization of single-nucleus transcriptomes (>52,000) and identification of cellular populations according to (ref. <sup>31</sup>). **(b)** Dot plot depicting the expression of the indicated genes in the various clusters. Dot size represents the frequency of cells expressing the indicated gene. **(c)** UMAPs showing the expression of the indicated genes in all cells. **(d)** GSEA of TGFβ-suppressed NK cells genes in lung tissue-resident NK cells extracted from the data set. **(e,f)** UMAP representation of indicated genes in all cells of non-COVID-19 and COVID-19 patients. **(g)** Quantification of the frequency of *TGFB1*<sup>+</sup> cells per cluster per patient in both groups. Only clusters represented by cells were included. Bars display mean ± s.e.m. (non-COVID-19: all n=3 patients, COVID-19: cluster 24; n=6, cluster 27; n=4, all other clusters n=7, p-value was determined by two-sided t-test). **(h)** Median expression level of indicated genes in *TGFB1*<sup>+</sup> SARS-CoV-2-negative cells and *TGFB1*<sup>+</sup> SARS-CoV-2-positive cells of all COVID-19 samples. Significance was calculated using the two-sided Mann-Whitney *U*-test.

## Extended Data Fig. 10 Serum from severe COVID-19 patients suppresses NK cells in a TGFβ-dependent manner.

**(a)** NK cells were cultured in medium with (green) or without TGFβ (blue). Specific lysis (mean ± s.e.m.; n=3 healthy donors) of K562 target cells was determined in a <sup>51</sup>Chromium release assay. Significance determined by two-sided unpaired t-test. **(b)** Sorted NK cells of healthy donors were cultured in medium containing the indicated cytokines with and without TGFβ. The frequency of CD107a<sup>+</sup> NK cells was analyzed after 4h co-culture with K562 cells (n=3 per group). **(c,d)** PBMC of healthy donors (n=6) were cultured for 4 days with the indicated cytokines and the frequency (mean) of IFNγ<sup>+</sup> **(c)** and TNF<sup>+</sup> NK cells **(d)** was determined after PMA/Iono stimulation. **(e,f)** Sorted NK cells of healthy donors were cultured for 4 days in medium containing the indicated cytokines. The MFI of T-bet **(e)** and Eomes **(f)** was measured by flow cytometry. The dashed line indicates

median MFI of NK cells cultured in medium only (RPMI and IL-12/15 in e n=5 donors, all others n=6). (g–p) Sorted NK cells from 3 to 4 healthy donors per experiment were cultured in medium containing the cytokines IL-2 and IL-12 (g,m), IL-12 and IL-15 (h–k, n–o) or IL-2 (l,p) either alone or with serum from 3 to 6 patients with severe COVID-19 per experiment. In a second condition, patient sera were pre-incubated as indicated with anti-TGF $\beta$ , anti-IL-6, anti-IL-10 or anti-IL-15 antibody before adding to the culture. The frequency of CD107a $^{+}$  NK cells (g,j–m), the frequency of IFN $\gamma$  $^{+}$ /TNF $^{+}$  NK cells after 4h co-culture with K562 cells (i), the viral load after co-culture with SARS-CoV-2-infected Vero E6 cells (h) and the MFI of T-bet (n–p) was determined. Fold change frequency or MFI was calculated between NK cells cultured in patients' sera (+/- prior anti-TGF $\beta$  treatment) and NK cells cultured in medium only. Each dot represents NK cells from one healthy donor cultured with severe COVID-19 serum (+/- prior anti-TGF $\beta$  treatment) (g; n=24, i; n=18, j–p; n=16, h; n=11 pooled samples derived from 3 patients, NK cell:target cell ratio 1:3, 1:1, 3:1, 9:1, bars represent mean). Statistical analysis was performed using two-sided paired t-test (b–f) or two-sided Wilcoxon matched-pairs rank test (g–p).

## Supplementary information

### Reporting Summary

### Peer Review File

### 41586\_2021\_4142\_MOESM3\_ESM.xlsx

Supplementary Table 1 Healthy donors. Characteristics and experiments performed with healthy donors included in this study. Antibodies of flow cytometry panels A, B, C, D, E and F are listed in Supplementary Table 4. CD107a: surface expression of CD107a;  $^{51}\text{Chromium}$ :  $^{51}\text{Chromium}$  release assay; conjugation: conjugation of NK cells with K562 cells; ICS: intracellular cytokine staining; serum experiment: NK cell culture in the presence of respective donor serum.

### 41586\_2021\_4142\_MOESM4\_ESM.xlsx

Supplementary Table 2 Outpatients with COVID-19 or FLI. Characteristics of ambulant patients with COVID-19 and patients with FLI tested negative for SARS-CoV-2. All analyses of peripheral blood NK cells are listed for each patient, including the time point after onset of symptoms of blood withdrawal in parenthesis. Antibodies of flow cytometry panels A, B, C, D and F are listed in Supplementary Table 4. Na, not available.

### [41586 2021 4142 MOESM5 ESM.xlsx](#)

Supplementary Table 3 Hospitalized patients with COVID-19. Characteristics of hospitalized patients with moderate or severe COVID-19. Listed are relevant comorbidities, mechanical ventilation, high-flow oxygen therapy (with or without noninvasive ventilation), diagnosis of ARDS (according to the Berlin definition of ARDS)<sup>40</sup> and relevant medication, including corticosteroids and biologicals (anakinra, tocilizumab). For corticosteroids and biologicals, the start of the treatment after onset of symptoms is listed in parentheses. All analyses of peripheral blood NK cells are listed for each patient, including the time point after onset of symptoms of blood withdrawal in parentheses. Antibodies of flow cytometry panels A, B, C, D, E and F are listed in Supplementary Table 4.

### [Supplementary Table 4 Antibodies for flow cytometry analysis.](#)

## Rights and permissions

### [Reprints and Permissions](#)

## About this article

### Cite this article

Witkowski, M., Tizian, C., Ferreira-Gomes, M. *et al.* Untimely TGF $\beta$  responses in COVID-19 limit antiviral functions of NK cells. *Nature* **600**, 295–301 (2021). <https://doi.org/10.1038/s41586-021-04142-6>

- Received: 30 March 2021

- Accepted: 14 October 2021
- Published: 25 October 2021
- Issue Date: 09 December 2021
- DOI: <https://doi.org/10.1038/s41586-021-04142-6>

## Share this article

Anyone you share the following link with will be able to read this content:

[Get shareable link](#)

Sorry, a shareable link is not currently available for this article.

[Copy to clipboard](#)

Provided by the Springer Nature SharedIt content-sharing initiative

## Further reading

- [\*\*Clues that natural killer cells help to control COVID\*\*](#)
  - Emilie Narni-Mancinelli
  - Eric Vivier

*Nature* (2021)

## [\*\*Clues that natural killer cells help to control COVID\*\*](#)

- Emilie Narni-Mancinelli
- Eric Vivier

News & Views 25 Oct 2021

| [Section menu](#) | [Main menu](#) |

- Article
- [Published: 10 November 2021](#)

# Host immunomodulatory lipids created by symbionts from dietary amino acids

- [Sungwhan F. Oh](#) ORCID: [orcid.org/0000-0002-0280-7903<sup>1,2</sup>](https://orcid.org/0000-0002-0280-7903) na1,
- [T. Praveena<sup>3</sup>](#) na1,
- [Heebum Song<sup>4</sup>](#),
- [Ji-Sun Yoo](#) ORCID: [orcid.org/0000-0003-3100-0794<sup>2</sup>](https://orcid.org/0000-0003-3100-0794),
- [Da-Jung Jung<sup>2</sup>](#),
- [Deniz Erturk-Hasdemir<sup>1</sup>](#),
- [Yoon Soo Hwang<sup>4</sup>](#),
- [ChangWon C. Lee](#) ORCID: [orcid.org/0000-0001-7534-0526<sup>1</sup>](https://orcid.org/0000-0001-7534-0526),
- [Jérôme Le Nours<sup>3</sup>](#),
- [Hyunsoo Kim<sup>4</sup>](#),
- [Jesang Lee<sup>4</sup>](#),
- [Richard S. Blumberg](#) ORCID: [orcid.org/0000-0002-9704-248X<sup>5</sup>](https://orcid.org/0000-0002-9704-248X),
- [Jamie Rossjohn](#) ORCID: [orcid.org/0000-0002-2020-7522<sup>3,6,7</sup>](https://orcid.org/0000-0002-2020-7522),
- [Seung Bum Park](#) ORCID: [orcid.org/0000-0003-1753-1433<sup>4</sup>](https://orcid.org/0000-0003-1753-1433) &
- [Dennis L. Kasper](#) ORCID: [orcid.org/0000-0001-8808-5333<sup>1</sup>](https://orcid.org/0000-0001-8808-5333)

[Nature](#) volume 600, pages 302–307 (2021)

- 9536 Accesses
- 122 Altmetric
- [Metrics details](#)

## Subjects

- [Mass spectrometry](#)
- [Microbiology](#)
- [Mucosal immunology](#)
- [Chemical synthesis](#)
- [X-ray crystallography](#)

## Abstract

Small molecules derived from symbiotic microbiota critically contribute to intestinal immune maturation and regulation<sup>1</sup>. However, little is known about the molecular mechanisms that control immune development in the host–microbiota environment. Here, using a targeted lipidomic analysis and synthetic approach, we carried out a multifaceted investigation of immunomodulatory α-galactosylceramides from the human symbiont *Bacteroides fragilis* (BfaGCs). The characteristic terminal branching of BfaGCs is the result of incorporation of branched-chain amino acids taken up in the host gut by *B. fragilis*. A *B. fragilis* knockout strain that cannot metabolize branched-chain amino acids showed reduced branching in BfaGCs, and mice monocolonized with this mutant strain had impaired colonic natural killer T (NKT) cell regulation, implying structure-specific immunomodulatory activity. The sphinganine chain branching of BfaGCs is a critical determinant of NKT cell activation, which induces specific immunomodulatory gene expression signatures and effector functions. Co-crystal structure and affinity analyses of CD1d–BfaGC–NKT cell receptor complexes confirmed the interaction of BfaGCs as CD1d-restricted ligands. We present a structural and molecular-level paradigm of immunomodulatory control by interactions of endobiotic metabolites with diet, microbiota and the immune system.

This is a preview of subscription content

## Access options

Subscribe to Journal

Get full journal access for 1 year

\$199.00

only \$3.90 per issue

[Subscribe](#)

All prices are NET prices.

VAT will be added later in the checkout.

Tax calculation will be finalised during checkout.

Rent or Buy article

Get time limited or full article access on ReadCube.

from \$8.99

[Rent or Buy](#)

All prices are NET prices.

### **Additional access options:**

- [Log in](#)
- [Learn about institutional subscriptions](#)

**Fig. 1: Chemical structure assignment of chain-length and branching variation in BfaGCs.**

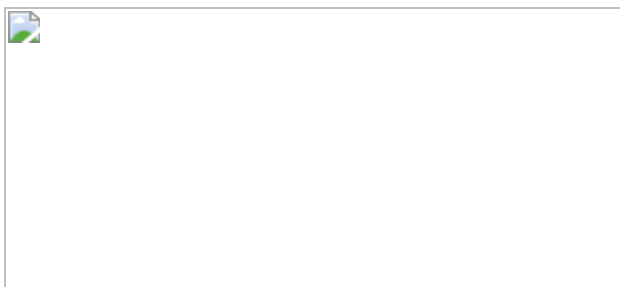


**Fig. 2: BfaGC branching is dictated by host dietary BCAAs, and loss of BCAA utilization in *B. fragilis* impairs its ability to modulate host colonic NKT cells.**



**Fig. 3: BfaGCs cause distinct immunomodulatory signalling and actions.**

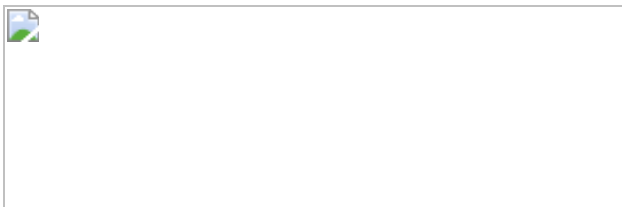
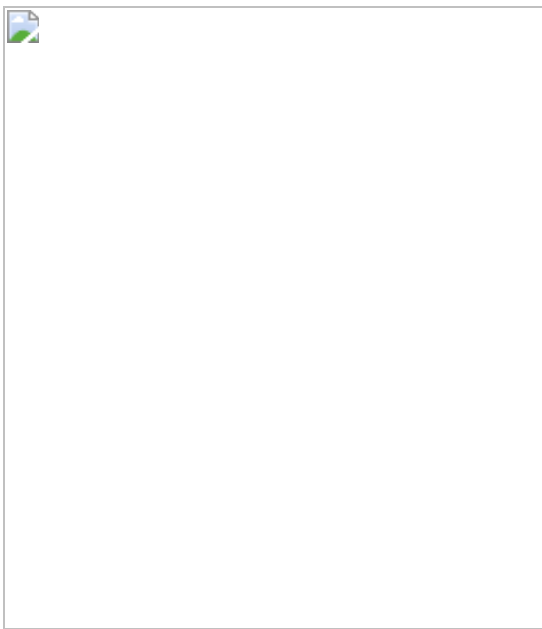


**Fig. 4: Crystal structure of 2C12 NKT cell receptor (TCR)–mCD1d–BfaGC ternary complexes showed conserved and distinct molecular interactions of BfaGCs with mCD1d and the 2C12 TCR.**



# Data availability

Raw data for NKT cell transcriptomic analysis was deposited in the NCBI Sequence Read Archive (SRA) with accession [PRJNA750126](#). The crystal structures of the 2C12 TCR–mCD1d–SB2217 and 2C12 TCR–mCD1d–SB2219 ternary complexes were deposited in the Protein Data Bank under accession numbers [7M72](#) and [6XNG](#), respectively. Lipidomic analysis data containing MS1 scans were deposited to Metabolomics Workbench study number ST001910.

# References

1. 1.

Surana, N. K. & Kasper, D. L. Deciphering the tête-à-tête between the microbiota and the immune system. *J. Clin. Invest.* **124**, 4197–4203 (2014).

2. 2.

Skelly, A. N., Sato, Y., Kearney, S. & Honda, K. Mining the microbiota for microbial and metabolite-based immunotherapies. *Nat. Rev. Immunol.* **19**, 305–323 (2019).

3. 3.

Surana, N. K. & Kasper, D. L. The yin yang of bacterial polysaccharides: lessons learned from *B. fragilis* PSA. *Immunol. Rev.* **245**, 13–26 (2012).

4. 4.

Erturk-Hasdemir, D. et al. Symbionts exploit complex signaling to educate the immune system. *Proc. Natl Acad. Sci. USA* **116**, 26157–26166 (2019).

5. 5.

Vatanen, T. et al. Variation in microbiome LPS immunogenicity contributes to autoimmunity in humans. *Cell* **165**, 842–853 (2016).

6. 6.

d’Hennezel, E., Abubucker, S., Murphy, L. O. & Cullen, T. W. Total lipopolysaccharide from the human gut microbiome silences Toll-like receptor signaling. *mSystems* **2**, (2017).

7. 7.

Kawahara, K., Tsukano, H., Watanabe, H., Lindner, B. & Matsuura, M. Modification of the structure and activity of lipid A in *Yersinia pestis* lipopolysaccharide by growth temperature. *Infect. Immun.* **70**, 4092–4098 (2002).

8. 8.

Erturk-Hasdemir, D. & Kasper, D. L. Finding a needle in a haystack: *Bacteroides fragilis* polysaccharide a as the archetypical symbiosis factor. *Ann. NY Acad. Sci.* **1417**, 116–129 (2018).

9. 9.

Wieland Brown, L. C. et al. Production of  $\alpha$ -galactosylceramide by a prominent member of the human gut microbiota. *PLoS Biol.* **11**, e1001610 (2013).

10. 10.

An, D. et al. Sphingolipids from a symbiotic microbe regulate homeostasis of host intestinal natural killer T cells. *Cell* **156**, 123–133 (2014).

11. 11.

Wingender, G. et al. Intestinal microbes affect phenotypes and functions of invariant natural killer T cells in mice. *Gastroenterology* **143**, 418–428 (2012).

12. 12.

Kinjo, Y. et al. Recognition of bacterial glycosphingolipids by natural killer T cells. *Nature* **434**, 520–525 (2005).

13. 13.

Brondz, I. & Olsen, I. Multivariate analyses of cellular fatty acids in *Bacteroides*, *Prevotella*, *Porphyromonas*, *Wolinella*, and *Campylobacter* spp. *J. Clin. Microbiol.* **29**, 183–189 (1991).

14. 14.

Miyagawa, E., Azuma, R., Suto, T. & Yano, I. Occurrence of free ceramides in *Bacteroides fragilis* NCTC 9343. *J. Biochem.* **86**, 311–320 (1979).

15. 15.

Leo, R. F. & Parker, P. L. Branched-chain fatty acids in sediments. *Science* **152**, 649–650 (1966).

16. 16.

Naik, D. N. & Kaneda, T. Biosynthesis of branched long-chain fatty acids by species of *Bacillus*: relative activity of three alpha-keto acid substrates and factors affecting chain length. *Can. J. Microbiol.* **20**, 1701–1708 (1974).

17. 17.

Beck, H. C. Branched-chain fatty acid biosynthesis in a branched-chain amino acid aminotransferase mutant of *Staphylococcus carnosus*. *FEMS Microbiol. Lett.* **243**, 37–44 (2005).

18. 18.

Kaneda, T. Iso-and anteiso-fatty acids in bacteria: biosynthesis, function, and taxonomic significance. *Microbiol. Rev.* **55**, 288–302

(1991).

19. 19.

Liberzon, A. et al. The Molecular Signatures Database Hallmark gene set collection. *Cell Syst.* **1**, 417–425 (2015).

20. 20.

Pellicci, D. G. et al. Differential recognition of CD1d- $\alpha$ -galactosyl ceramide by the V $\beta$ 8.2 and V $\beta$ 7 semi-invariant NKT T cell receptors. *Immunity* **31**, 47–59 (2009).

21. 21.

Girardi, E. & Zajonc, D. M. Molecular basis of lipid antigen presentation by CD1d and recognition by natural killer T cells. *Immunol. Rev.* **250**, 167–179 (2012).

22. 22.

Rossjohn, J., Pellicci, D. G., Patel, O., Gapin, L. & Godfrey, D. I. Recognition of CD1d-restricted antigens by natural killer T cells. *Nat. Rev. Immunol.* **12**, 845–857 (2012).

23. 23.

Chennamadhavuni, D. et al. Dual modifications of  $\alpha$ -galactosylceramide synergize to promote activation of human invariant natural killer T cells and stimulate anti-tumor immunity. *Cell Chem. Biol.* **25**, 571-584.e8 (2018).

24. 24.

Li, Y. et al. The V $\alpha$ 14 invariant natural killer T cell TCR forces microbial glycolipids and CD1d into a conserved binding mode. *J. Exp. Med.* **207**, 2383–2393 (2010).

25. 25.

Wun, K. S. et al. A molecular basis for the exquisite CD1d-restricted antigen specificity and functional responses of natural killer T cells. *Immunity* **34**, 327–339 (2011).

26. 26.

Natori, T., Koezuka, Y. & Higa, T. Agelasphins, novel  $\alpha$ -galactosylceramides from the marine sponge *Agelas mauritianus*. *Tetrahedron Lett.* **34**, 5591–5592 (1993).

27. 27.

Kobayashi, E. et al. Enhancing effects of agelasphin-11 on natural killer cell activities of normal and tumor-bearing mice. *Biol. Pharm. Bull.* **19**, 350–353 (1996).

28. 28.

Kobayashi, E., Motoki, K., Uchida, T., Fukushima, H. & Koezuka, Y. KRN7000, a novel immunomodulator, and its antitumor activities. *Oncol. Res.* **7**, 529–534 (1995).

29. 29.

Li, X. et al. Design of a potent CD1d-binding NKT cell ligand as a vaccine adjuvant. *Proc. Natl Acad. Sci. USA* **107**, 13010–13015 (2010).

30. 30.

Laurent, X. et al. Switching invariant natural killer T (iNKT) cell response from anticancerous to anti-inflammatory effect: molecular bases. *J. Med. Chem.* **57**, 5489–5508 (2014).

31. 31.

Sag, D., Krause, P., Hedrick, C. C., Kronenberg, M. & Wingender, G. IL-10-producing NKT10 cells are a distinct regulatory invariant NKT cell subset. *J. Clin. Invest.* **124**, 3725–3740 (2014).

32. 32.

Olszak, T. et al. Protective mucosal immunity mediated by epithelial CD1d and IL-10. *Nature* **509**, 497–502 (2014).

33. 33.

Brutkiewicz, R. R. CD1d ligands: the good, the bad, and the ugly. *J. Immunol.* **177**, 769–775 (2006).

34. 34.

Joyce, S., Girardi, E. & Zajonc, D. M. NKT cell ligand recognition logic: molecular basis for a synaptic duet and transmission of inflammatory effectors. *J. Immunol.* **187**, 1081–1089 (2011).

35. 35.

Chung, H. et al. Gut immune maturation depends on colonization with a host-specific microbiota. *Cell* **149**, 1578–1593 (2012).

36. 36.

Stewart, C. J. et al. Temporal development of the gut microbiome in early childhood from the TEDDY study. *Nature* **562**, 583–588 (2018).

37. 37.

Sefik, E. et al. Individual intestinal symbionts induce a distinct population of ROR $^+$  regulatory T cells. *Science* **349**, 993–997 (2015).

38. 38.

Varel, V. H. & Bryant, M. P. Nutritional features of *Bacteroides fragilis* subsp. *fragilis*. *Appl. Microbiol.* **28**, 251–257 (1974).

39. 39.

Matyash, V., Liebisch, G., Kurzchalia, T. V., Shevchenko, A. & Schwudke, D. Lipid extraction by methyl- *tert*-butyl ether for high-throughput lipidomics. *J. Lipid Res.* **49**, 1137–1146 (2008).

40. 40.

Comstock, L. E. et al. Analysis of a capsular polysaccharide biosynthesis locus of *Bacteroides fragilis*. *Infect. Immun.* **67**, 3525–3532 (1999).

41. 41.

Lim, B., Zimmermann, M., Barry, N. A. & Goodman, A. L. Engineered regulatory systems modulate gene expression of human commensals in the gut. *Cell* **169**, 547–558.e15 (2017).

42. 42.

Olszak, T. et al. Microbial exposure during early life has persistent effects on natural killer T cell function. *Science* **336**, 489–493 (2012).

43. 43.

Dobin, A. et al. STAR: ultrafast universal RNA-seq aligner. *Bioinformatics* **29**, 15–21 (2013).

44. 44.

Liao, Y., Smyth, G. K. & Shi, W. featureCounts: an efficient general purpose program for assigning sequence reads to genomic features. *Bioinformatics* **30**, 923–930 (2014).

45. 45.

Love, M. I., Huber, W. & Anders, S. Moderated estimation of fold change and dispersion for RNA-seq data with DESeq2. *Genome Biol.* **15**, 550 (2014).

46. 46.

Wickham, H. *ggplot2: elegant graphics for data analysis*. <https://ggplot2.tidyverse.org/> (accessed: 9 March 2021).

47. 47.

Korotkevich, G. et al. Fast gene set enrichment analysis. Preprint at <https://doi.org/10.1101/060012> (2016).

48. 48.

Matsuda, J. L. et al. Tracking the response of natural killer T cells to a glycolipid antigen using CD1d tetramers. *J. Exp. Med.* **192**, 741–754 (2000).

49. 49.

Kabsch, W. XDS. *Acta Crystallogr. D* **66**, 125–132 (2010).

50. 50.

Evans, P. Scaling and assessment of data quality. *Acta Crystallogr. D* **62**, 72–82 (2006).

51. 51.

Adams, P. D. et al. PHENIX: A comprehensive Python-based system for macromolecular structure solution. *Acta Crystallogr. D* **66**, 213–221 (2010).

52. 52.

Emsley, P., Lohkamp, B., Scott, W. G. & Cowtan, K. Features and development of Coot. *Acta Crystallogr. D* **66**, 486–501 (2010).

53. 53.

Bricogne G. et al. *BUSTER Version 2.10.3* (Global Phasing Ltd, 2017).

54. 54.

Tong, J., Liu, C., Summanen, P., Xu, H., Finegold, S. M. Application of quantitative real-time PCR for rapid identification of *Bacteroides fragilis* group and related organisms in human wound samples. *Anaerobe* **17**, 64–68 (2011).

55. 55.

Suzuki, M. T., Taylor, L. T. & DeLong, E. F. Quantitative analysis of small-subunit rRNA genes in mixed microbial populations via 5'-nuclease assays. *Appl. Environ. Microbiol.* **66**, 4605–4614 (2000).

## Acknowledgements

We thank J. McCoy and E. J. Paik for manuscript preparation, R. T. Bronson for histopathological scoring, S. Iyer, L. Gebremedhin, E. Choi and T. Yanostang for technical assistance, and the staff at the Australian Synchrotron for assistance with data collection. This work was supported by National Institutes of Health (K01-DK102771 and R01-AT010268 to S.F.O., and R01-DK044319 to R.S.B.), Department of Defense (W81XWH-19-1-0625 to D.L.K.), Brigham and Women's Hospital (Department of Anesthesiology, Perioperative and Pain Medicine Basic Science Grant to S.F.O.), the National Research Foundation of Korea (2014R1A3A2030423 and 2012M3A9C4048780 to S.B.P.), and the Australian Research Council (ARC) (CE140100011 and ARC Laureate Fellowship to J.R., and ARC Future Fellowship to J.L.N.). Graphical images used for the Fig. 2 were created with BioRender.com.

## Author information

### Author notes

1. These authors contributed equally: Sungwhan F. Oh, T. Praveena

## Affiliations

1. Department of Immunology, Blavatnik Institute of Harvard Medical School, Boston, MA, USA

Sungwhan F. Oh, Deniz Erturk-Hasdemir, ChangWon C. Lee & Dennis L. Kasper

2. Center for Experimental Therapeutics and Reperfusion Injury, Department of Anesthesiology, Perioperative and Pain Medicine, Brigham and Women's Hospital, Boston, MA, USA

Sungwhan F. Oh, Ji-Sun Yoo & Da-Jung Jung

3. Infection and Immunity Program & Department of Biochemistry and Molecular Biology, Biomedicine Discovery Institute, Monash University, Clayton, Victoria, Australia

T. Praveena, Jérôme Le Nours & Jamie Rossjohn

4. CRI Center for Chemical Proteomics, Department of Chemistry, Seoul National University, Seoul, Republic of Korea

Heebum Song, Yoon Soo Hwang, Hyunsoo Kim, Jesang Lee & Seung Bum Park

5. Division of Gastroenterology, Hepatology and Endoscopy, Department of Medicine, Brigham and Women's Hospital, Boston, MA, USA

Richard S. Blumberg

6. Australian Research Council Centre of Excellence in Advanced Molecular Imaging, Monash University, Clayton, Victoria, Australia

Jamie Rossjohn

7. Institute of Infection and Immunity, Cardiff University School of Medicine, Heath Park, Cardiff, UK

Jamie Rossjohn

## Contributions

S.F.O., D.L.K. and R.S.B. conceived the idea and designed the outline of the research. S.F.O., H.B.S. and S.B.P. designed the structures of synthetic BfaGCs; H.B.S., Y.S.H., H.K. and J.L. synthesized BfaGC molecules. T.P., J.L.N. and J.R. generated crystals of 2C12 TCR–CD1d–BfaGCs and carried out X-ray crystallography analysis as well as affinity measurements by SPR. S.F.O., J.-S.Y. and C.C.L. designed and carried out all experiments with microorganisms. S.F.O., D.-J.J. and D.E.-H. executed in vitro and in vivo cytokine assays. S.F.O. and D.-J.J. designed and carried out all animal experiments. J.-S.Y. carried out transcriptomic analysis. S.F.O., S.B.P., J.R. and D.L.K. wrote the manuscript, and all authors contributed to relevant discussions.

## Corresponding authors

Correspondence to [Sungwhan F. Oh](#), [Jamie Rossjohn](#), [Seung Bum Park](#) or [Dennis L. Kasper](#).

## Ethics declarations

## Competing interests

S.F.O., R.S.B. and D.L.K. have filed a patent on the functions of BfaGCs and related structures (US patent 10,329,315). S.F.O., S.B.P. and D.L.K. filed a patent on the functions of BfaGCs and related structures (under review).

## Additional information

**Peer review information** *Nature* thanks the anonymous reviewer(s) for their contribution to the peer review of this work.

**Publisher's note** Springer Nature remains neutral with regard to jurisdictional claims in published maps and institutional affiliations.

## Extended data figures and tables

Extended Data Fig. 1 Molecular structures of prototypic NKT agonist KRN7000, OCH and a representative *B. fragilis*-derived aGC (SB2217).

Extended Data Fig. 2 LC-MS profile of BfaGCs.

(A) Representative extracted ion chromatograms (XICs) of C<sub>32</sub>–C<sub>36</sub> BfaGCs. (B) C<sub>34</sub> BfaGCs are the major component of *B. fragilis* glycosphingolipids (N=5).

Extended Data Fig. 3 LC-MS/MS assignment of C<sub>34</sub> BfaGC structural variants.

(A) The MS/MS-XIC of total C<sub>34</sub> BfaGCs (762→698) shows that BfaGCs are isobaric mixtures separated by RP-HPLC. (B, C) MS/MS-XICs of C<sub>34</sub> BfaGCs reveal co-eluting chemical homologues. Two isobaric species with aliphatic chains of C<sub>17</sub>/C<sub>17</sub> (B) and C<sub>18</sub>/C<sub>16</sub> (C) were assigned MS/MS fingerprints of 490 and 504, respectively. (D) MS/MS fingerprints of three peaks show a distinct difference in relative intensity between MS/MS fragments of 490 (C<sub>17</sub>/C<sub>17</sub>) and 504 (C<sub>18</sub>/C<sub>16</sub>), implying that the latter two peaks are a mixture of chain-length homologues. Chromatograms and spectra represent triplicate observations. (E-H) MS/MS spectra of the most abundant peaks of (E) C<sub>32</sub>, (F) C<sub>33</sub>, (G) C<sub>35</sub> and (H) C<sub>36</sub> BfaGCs. MS/MS fingerprint of 462–518 indicates lengths of sphinganine and acyl chains. Spectra are representative of triplicate observation.

Extended Data Fig. 4 Chemical structures of 23 synthetic BfaGCs.

(SB2201–SB2223).

## Extended Data Fig. 5 BCAA dictates branching of BfaGCs by direct incorporation *in vivo*.

(A–E) Ratios among differently branched C<sub>34</sub> BfaGCs (MS1 XIC=762.57, as [M+HCOO<sup>-</sup>]) are clearly different for *B. fragilis* grown in rich medium (A) and *B. fragilis* grown in minimal medium (B). Supplementation with individual BCAAs (C–E) on defined medium increases production of branched-chain (both dibranched and monobranched) BfaGCs. (F–H) MS/MS fingerprints confirm the incorporation of leucine and isoleucine into the C<sub>17</sub>/C<sub>17</sub> ceramide backbone (via C5 branched acyl-CoA) and of valine into the C<sub>18</sub>/C<sub>16</sub> backbone (via C4 branched acyl-CoA).

Chromatograms and spectra are representative of triplicate observations. (I) An MS/MS-XIC of d<sub>3</sub>- and d<sub>6</sub>-C<sub>34</sub> BfaGC shows that deuterium-labeled leucine is actively incorporated into BfaGC. (J–K) MS/MS pattern shows distinctive differences between gut luminal BfaGC (M+3 isotopolog) in (J) presence or (K) absence of d3-leucine, showing MS2 fragments in presence of d3-leucine reflect inclusion of deuterium-labeled leucine in the structure. Chromatograms and spectra are representative results of four mice.

## Extended Data Fig. 6 Genetic study of *B. fragilis* Bcat orthologue (BF9343-3671).

(A) Confirmation of the target gene deletion by PCR. (B) The knockout strain (BF9343-Δ3671) shows comparable growth pattern to isogenic WT strain (grown in duplicate per group), and a complemented strain of KO strain with empty vector shows same pattern to BF9343-3671 complemented strain. (C) BF9343-Δ3671 complementation can recover the production of di-branched C17/C17 BfaGC production to wild-type level. (D) WT and mutant strain (N=5 for each group) can colonize mouse in comparable density. All results represent of two independent experiments with similar trend. For gel source data, see Supplementary Fig. 1.

## Extended Data Fig. 7 Structure-specific actions of BfaGCs.

(A) NKT cell–APC co-culture assays show that branching of sphinganine chain is, but 3'-OH group is not, critical for IL-2 inducing activity. Results

are shown in duplicate and represent three independent experiment sets with similar trend ( $p=0.017$  for 100nM and  $p=0.026$  for 1000nM). (B-C) When injected intraperitoneally ( $N=5$  per group, one sample in OCH group in panel C was lost), unlike Th1- or Th2-skewed prototypic ligands such as KRN7000 or OCH, SB2217 only weakly induce IFN- $\gamma$  and did not induce IL-4 *in vivo*. (D-F) SB2217 weakly induced expression of co-stimulatory molecules such as CD86, CD40 and CD80 in splenic DCs, where SB2219 did not ( $N=5$  per group).

### **Extended Data Fig. 8 Transcriptomic landscape of splenic NKT cells in responses to agonists.**

(A) A heatmap shown with the Euclidean distances between different treatment groups. (B) Transcriptomic profile comparison of SB2217, SB2219 and OCH. (C) Pathway enrichment analysis of SB2217 reveals increased expression of immunoregulatory pathways in NKT cells when compared to vehicle or SB2219.

### **Extended Data Fig. 9 Comparison between SB2217 and SB2219 in mCD1d-BfaGC-2C12 complexes.**

(A) 2Fo-Fc electron density map (in blue) contoured at a  $0.8\sigma$  level of the BfaGCs within each ternary complex. (B) Fo-Fc electron density map (in brown) contoured at a  $2.2\sigma$  level of the BfaGCs and spacer lipids within each ternary complex. SB2217 is shown as blue and SB2219 is shown as green; Spacer lipids are shown as black sticks. (C) Superimposition of the headgroups of BfaGCs and KRN7000 (PDB code: 6BNK). (D) 2C12 TCR molecular interactions with SB2217 (in blue). mCD1d and CDR loops are colored as in Fig. 4a. Hydrogen bonds are shown as red dashed lines. (E-F) The mCD1d–SB2217 complex shows higher affinity to 2C12 TCR than the mCD1d–SB2219 complex. (E) Each SPR datapoint is mean of technical duplicate and  $K_D$  values (mean $\pm$ SD) were calculated from two independent results, using a single-site binding model with  $K_D$  as a shared variable. (F) The sensorgrams are results of single experiment.

## Extended Data Fig. 10 BfaGC profile in human microbiota-associated mice.

(A) BfaGC and *B. fragilis* abundance shows positive correlation in *B. fragilis*-gavaged HMB mice. Results are from longitudinally collected samples (2, 3 and 7 days after *B. fragilis* oral introduction) from five mice (total N=15). (B) BfaGC ( $C_{17}/C_{17}$  dibranched and monobranched) are identified from neonatal (p14) GI contents. Chromatogram and spectrum represent seven samples.

## Supplementary information

### Supplementary Information

This file contains Supplementary Tables; Supplementary Figs. 1 (raw gel data) and 2 (FACS gating strategies for immune cell analysis); raw data (weight monitoring over disease time course) of in vivo experiment (oxazolone colitis); and total organic synthesis of BfaGC analogue (SB2201-SB2223) library.

### Reporting Summary

## Rights and permissions

### Reprints and Permissions

## About this article

### Cite this article

Oh, S.F., Praveena, T., Song, H. *et al.* Host immunomodulatory lipids created by symbionts from dietary amino acids. *Nature* **600**, 302–307 (2021). <https://doi.org/10.1038/s41586-021-04083-0>

- Received: 06 April 2021

- Accepted: 28 September 2021
- Published: 10 November 2021
- Issue Date: 09 December 2021
- DOI: <https://doi.org/10.1038/s41586-021-04083-0>

## Share this article

Anyone you share the following link with will be able to read this content:

[Get shareable link](#)

Sorry, a shareable link is not currently available for this article.

[Copy to clipboard](#)

Provided by the Springer Nature SharedIt content-sharing initiative

---

This article was downloaded by **calibre** from <https://www.nature.com/articles/s41586-021-04083-0>

| [Section menu](#) | [Main menu](#) |

- Article
- [Published: 18 November 2021](#)

# CRISPR screens unveil signal hubs for nutrient licensing of T cell immunity

- [Lingyun Long<sup>1</sup>](#),  
<sup>na1</sup>,
- [Jun Wei<sup>1</sup>](#),  
<sup>na1</sup>,
- [Seon Ah Lim<sup>1</sup>](#),
- [Jana L. Raynor<sup>1</sup>](#),
- [Hao Shi](#) [ORCID: orcid.org/0000-0002-2796-629X<sup>1</sup>](#),
- [Jon P. Connelly](#) [ORCID: orcid.org/0000-0002-5564-1775<sup>2</sup>](#),
- [Hong Wang](#) [ORCID: orcid.org/0000-0002-6215-6348<sup>3</sup>](#),
- [Cliff Guy<sup>1</sup>](#),
- [Boer Xie<sup>3</sup>](#),
- [Nicole M. Chapman<sup>1</sup>](#),
- [Guotong Fu<sup>1</sup>](#),
- [Yanyan Wang<sup>1</sup>](#),
- [Hongling Huang<sup>1</sup>](#),
- [Wei Su<sup>1</sup>](#),
- [Jordy Saravia](#) [ORCID: orcid.org/0000-0002-2691-501X<sup>1</sup>](#),
- [Isabel Risch](#) [ORCID: orcid.org/0000-0003-3356-0349<sup>1</sup>](#),
- [Yong-Dong Wang](#) [ORCID: orcid.org/0000-0001-8751-9216<sup>4</sup>](#),
- [Yuxin Li](#) [ORCID: orcid.org/0000-0001-9739-9860<sup>3</sup>](#),
- [Mingming Niu<sup>3</sup>](#),
- [Yogesh Dhungana<sup>1</sup>](#),
- [Anil KC<sup>1</sup>](#),
- [Peipei Zhou<sup>1</sup>](#),
- [Peter Vogel](#) [ORCID: orcid.org/0000-0002-7535-0545<sup>5</sup>](#),

- [Jiyang Yu](#) ORCID: [orcid.org/0000-0003-3629-4330<sup>6</sup>](https://orcid.org/0000-0003-3629-4330),
- [Shondra M. Pruett-Miller](#) ORCID: [orcid.org/0000-0002-3793-585X<sup>2</sup>](https://orcid.org/0000-0002-3793-585X),
- [Junmin Peng](#) ORCID: [orcid.org/0000-0003-0472-7648<sup>3,7,8</sup>](https://orcid.org/0000-0003-0472-7648) &
- [Hongbo Chi](#) ORCID: [orcid.org/0000-0002-9997-2496<sup>1</sup>](https://orcid.org/0000-0002-9997-2496)

*Nature* volume **600**, pages 308–313 (2021)

- 13k Accesses
- 79 Altmetric
- [Metrics details](#)

## Subjects

- [CD4-positive T cells](#)
- [Signal transduction](#)

## Abstract

Nutrients are emerging regulators of adaptive immunity<sup>1</sup>. Selective nutrients interplay with immunological signals to activate mechanistic target of rapamycin complex 1 (mTORC1), a key driver of cell metabolism<sup>2,3,4</sup>, but how these environmental signals are integrated for immune regulation remains unclear. Here we use genome-wide CRISPR screening combined with protein–protein interaction networks to identify regulatory modules that mediate immune receptor- and nutrient-dependent signalling to mTORC1 in mouse regulatory T ( $T_{reg}$ ) cells. SEC31A is identified to promote mTORC1 activation by interacting with the GATOR2 component SEC13 to protect it from SKP1-dependent proteasomal degradation. Accordingly, loss of SEC31A impairs T cell priming and  $T_{reg}$  suppressive function in mice. In addition, the SWI/SNF complex restricts expression of the amino acid sensor CASTOR1, thereby enhancing mTORC1 activation. Moreover, we reveal that the CCDC101-associated SAGA complex is a potent inhibitor of mTORC1, which limits the expression of glucose and amino acid transporters and maintains T cell

quiescence in vivo. Specific deletion of *Ccdc101* in mouse T<sub>reg</sub> cells results in uncontrolled inflammation but improved antitumour immunity. Collectively, our results establish epigenetic and post-translational mechanisms that underpin how nutrient transporters, sensors and transducers interplay with immune signals for three-tiered regulation of mTORC1 activity and identify their pivotal roles in licensing T cell immunity and immune tolerance.

This is a preview of subscription content

## Access options

Subscribe to Journal

Get full journal access for 1 year

\$199.00

only \$3.90 per issue

[Subscribe](#)

All prices are NET prices.

VAT will be added later in the checkout.

Tax calculation will be finalised during checkout.

Rent or Buy article

Get time limited or full article access on ReadCube.

from \$8.99

[Rent or Buy](#)

All prices are NET prices.

## Additional access options:

- [Log in](#)
- [Learn about institutional subscriptions](#)

**Fig. 1: Genome-wide CRISPR screening uncovers mTORC1 regulatory networks in T<sub>reg</sub> cells.**

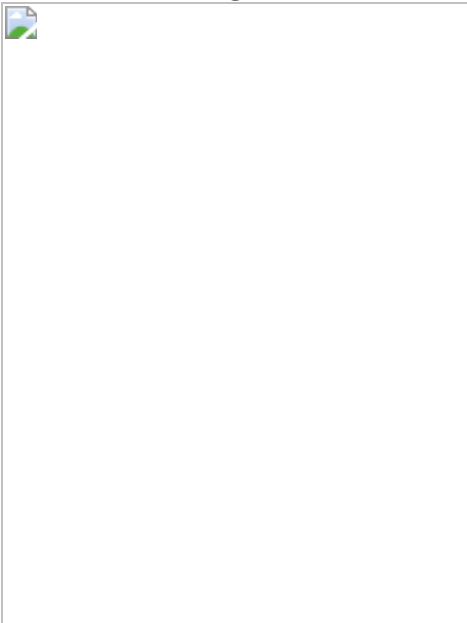


**Fig. 2: SEC31A is crucial for nutrient and GATOR2-dependent mTORC1 activation and the abundance of SEC13.**

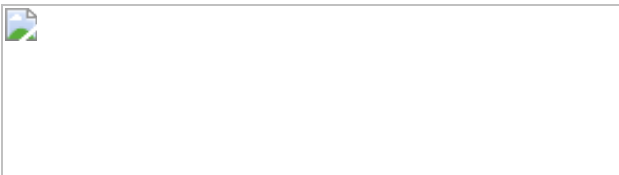


**Fig. 3: SEC31A protects SEC13 from SKP1-mediated proteasomal degradation.**

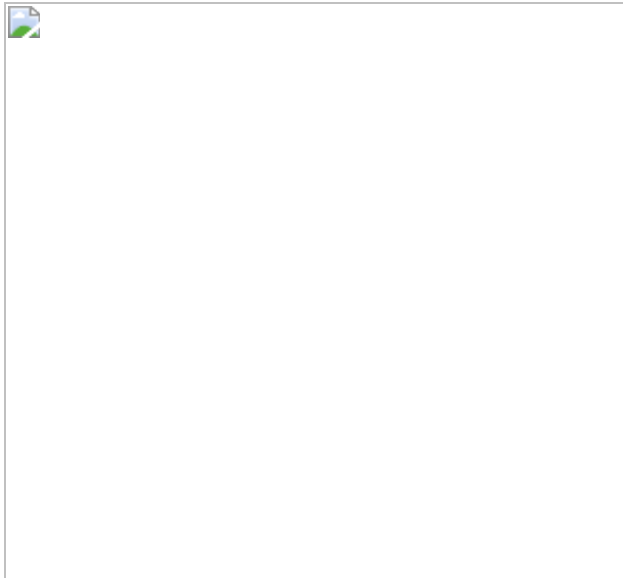
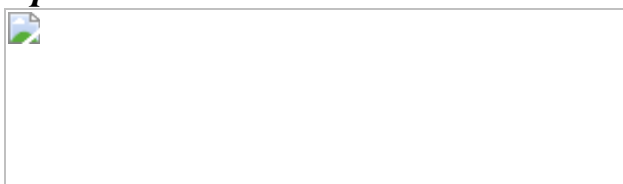


**Fig. 4: The SAGA complex suppresses nutrient transporter expression and mTORC1 activation.**



**Fig. 5: Steady state and tumour challenge phenotypes of *Foxp3*<sup>Cre</sup>*Ccdc10l*<sup>f/f</sup> mice.**



## Data availability

The authors declare that the data supporting the findings of this study are available within the paper and its [Supplementary Information](#). All microarray, ATAC-seq and scRNA-seq data described in the manuscript have been deposited in the NCBI Gene Expression Omnibus (GEO) database and are accessible through the GEO SuperSeries accession number [160598](#). Other resources: CRAPome database (<https://reprint-apms.org/>); Uniprot mouse database (<https://www.uniprot.org/>); STRING (v10) (<https://string-db.org/>); BioPlex (<https://bioplex.hms.harvard.edu/>). [Source data](#) are provided with this paper.

## References

1. 1.  
Chapman, N. M., Boothby, M. R. & Chi, H. Metabolic coordination of T cell quiescence and activation. *Nat. Rev. Immunol.* **20**, 55–70 (2020).
2. 2.  
Kim, J. & Guan, K. L. mTOR as a central hub of nutrient signalling and cell growth. *Nat. Cell Biol.* **21**, 63–71 (2019).
3. 3.  
Liu, G. Y. & Sabatini, D. M. mTOR at the nexus of nutrition, growth, ageing and disease. *Nat. Rev. Mol. Cell Biol.* **21**, 183–203 (2020).
4. 4.  
Huang, H., Long, L., Zhou, P., Chapman, N. M. & Chi, H. mTOR signaling at the crossroads of environmental signals and T-cell fate decisions. *Immunol. Rev.* **295**, 15–38 (2020).
5. 5.  
Shi, H. et al. Amino acids license kinase mTORC1 activity and T<sub>reg</sub> cell function via small G proteins Rag and Rheb. *Immunity* **51**, 1012–1027 (2019).

6. 6.

Doench, J. G. et al. Optimized sgRNA design to maximize activity and minimize off-target effects of CRISPR–Cas9. *Nat. Biotechnol.* **34**, 184–191 (2016).

7. 7.

Yang, K. et al. T cell exit from quiescence and differentiation into Th2 cells depend on Raptor–mTORC1-mediated metabolic reprogramming. *Immunity* **39**, 1043–1056 (2013).

8. 8.

Tan, H. et al. Integrative proteomics and phosphoproteomics profiling reveals dynamic signaling networks and bioenergetics pathways underlying T cell activation. *Immunity* **46**, 488–503 (2017).

9. 9.

Bai, B. et al. Deep multilayer brain proteomics identifies molecular networks in Alzheimer’s disease progression. *Neuron* **105**, 975–991 (2020).

10. 10.

Loo, C. S. et al. A genome-wide CRISPR screen reveals a role for the non-canonical nucleosome-remodeling BAF complex in FOXP3 expression and regulatory T cell function. *Immunity* **53**, 143–157 (2020).

11. 11.

Tang, B. L. et al. Mammalian homologues of yeast sec31p. An ubiquitously expressed form is localized to endoplasmic reticulum (ER) exit sites and is essential for ER–Golgi transport. *J. Biol. Chem.* **275**, 13597–13604 (2000).

12. 12.

Zeng, H. et al. mTORC1 couples immune signals and metabolic programming to establish T(reg)-cell function. *Nature* **499**, 485–490 (2013).

13. 13.

Zhou, P. Determining protein half-lives. *Methods Mol. Biol.* **284**, 67–77 (2004).

14. 14.

Shi, H. et al. Hippo kinases Mst1 and Mst2 sense and amplify IL-2R–STAT5 signaling in regulatory T cells to establish stable regulatory activity. *Immunity* **49**, 899–914 (2018).

15. 15.

Skaar, J. R., Pagan, J. K. & Pagano, M. SCF ubiquitin ligase-targeted therapies. *Nat. Rev. Drug Discov.* **13**, 889–903 (2014).

16. 16.

Cortez, J. T. et al. CRISPR screen in regulatory T cells reveals modulators of Foxp3. *Nature* **582**, 416–420 (2020).

17. 17.

Yang, K., Neale, G., Green, D. R., He, W. & Chi, H. The tumor suppressor Tsc1 enforces quiescence of naive T cells to promote immune homeostasis and function. *Nat. Immunol.* **12**, 888–897 (2011).

18. 18.

Wei, J. et al. Autophagy enforces functional integrity of regulatory T cells by coupling environmental cues and metabolic homeostasis. *Nat. Immunol.* **17**, 277–285 (2016).

19. 19.

Sakaguchi, S. et al. Regulatory T cells and human disease. *Annu. Rev. Immunol.* **38**, 541–566 (2020).

20. 20.

Overacre-Delgoffe, A. E. et al. Interferon- $\gamma$  drives  $T_{reg}$  fragility to promote anti-tumor immunity. *Cell* **169**, 1130–1141 (2017).

21. 21.

Su, W. et al. Protein prenylation drives discrete signaling programs for the differentiation and maintenance of effector  $T_{reg}$  cells. *Cell Metab.* **32**, 996–1011 (2020).

22. 22.

Mombaerts, P. et al. RAG-1-deficient mice have no mature B and T lymphocytes. *Cell* **68**, 869–877 (1992).

23. 23.

Lee, P. P. et al. A critical role for Dnmt1 and DNA methylation in T cell development, function, and survival. *Immunity* **15**, 763–774 (2001).

24. 24.

Rubtsov, Y. P. et al. Regulatory T cell-derived interleukin-10 limits inflammation at environmental interfaces. *Immunity* **28**, 546–558 (2008).

25. 25.

Oxenius, A., Bachmann, M. F., Zinkernagel, R. M. & Hengartner, H. Virus-specific MHC-class II-restricted TCR-transgenic mice: effects on humoral and cellular immune responses after viral infection. *Eur. J. Immunol.* **28**, 390–400 (1998).

26. 26.

Platt, R. J. et al. CRISPR–Cas9 knockin mice for genome editing and cancer modeling. *Cell* **159**, 440–455 (2014).

27. 27.

Wei, J. et al. Targeting REGNASE-1 programs long-lived effector T cells for cancer therapy. *Nature* **576**, 471–476 (2019).

28. 28.

Huang, H. et al. In vivo CRISPR screening reveals nutrient signaling processes underpinning CD8<sup>+</sup> T cell fate decisions. *Cell* **184**, 1245–1261 (2021).

29. 29.

Fu, G. et al. Metabolic control of T<sub>FH</sub> cells and humoral immunity by phosphatidylethanolamine. *Nature* **595**, 724–729 (2021).

30. 30.

Zeng, H. et al. mTORC1 and mTORC2 kinase signaling and glucose metabolism drive follicular helper T cell differentiation. *Immunity* **45**, 540–554 (2016).

31. 31.

Chen, R. et al. In vivo RNA interference screens identify regulators of antiviral CD4<sup>+</sup> and CD8<sup>+</sup> T cell differentiation. *Immunity* **41**, 325–338 (2014).

32. 32.

Parnas, O. et al. A genome-wide CRISPR screen in primary immune cells to dissect regulatory networks. *Cell* **162**, 675–686 (2015).

33. 33.

Yu, J., Silva, J. & Califano, A. ScreenBEAM: a novel meta-analysis algorithm for functional genomics screens via Bayesian hierarchical modeling. *Bioinformatics* **32**, 260–267 (2016).

34. 34.

Sanjana, N. E., Shalem, O. & Zhang, F. Improved vectors and genome-wide libraries for CRISPR screening. *Nat. Methods* **11**, 783–784 (2014).

35. 35.

Joung, J. et al. Genome-scale CRISPR–Cas9 knockout and transcriptional activation screening. *Nat. Protoc.* **12**, 828–863 (2017).

36. 36.

Karmaus, P. W. F. et al. Metabolic heterogeneity underlies reciprocal fates of T<sub>H</sub>17 cell stemness and plasticity. *Nature* **565**, 101–105 (2019).

37. 37.

Buenrostro, J. D., Giresi, P. G., Zaba, L. C., Chang, H. Y. & Greenleaf, W. J. Transposition of native chromatin for fast and sensitive epigenomic profiling of open chromatin, DNA-binding proteins and nucleosome position. *Nat. Methods* **10**, 1213–1218 (2013).

38. 38.

Bailey, T. L. et al. MEME SUITE: tools for motif discovery and searching. *Nucleic Acids Res.* **37**, W202–W208 (2009).

39. 39.

Li, Z. et al. Identification of transcription factor binding sites using ATAC-seq. *Genome Biol.* **20**, 45 (2019).

40. 40.

Lim, S. A. et al. Lipid signalling enforces functional specialization of T<sub>reg</sub> cells in tumours. *Nature* **591**, 306–311 (2021).

41. 41.

Zheng, G. X. Y. et al. Massively parallel digital transcriptional profiling of single cells. *Nat. Commun.* **8**, 14049 (2017).

42. 42.

Butler, A., Hoffman, P., Smibert, P., Papalexi, E., Satija, R. Integrating single-cell transcriptomic data across different conditions, technologies, and species. *Nat. Biotechnol.* **36**, 411–420 (2018).

43. 43.

Collison, L. W. et al. The inhibitory cytokine IL-35 contributes to regulatory T-cell function. *Nature* **450**, 566–569 (2007).

44. 44.

Stewart, E. et al. Identification of therapeutic targets in rhabdomyosarcoma through integrated genomic, epigenomic, and proteomic analyses. *Cancer Cell* **34**, 411–426 (2018).

45. 45.

Lim, K. L. et al. Parkin mediates nonclassical, proteasomal-independent ubiquitination of synphilin-1: implications for Lewy body formation. *J. Neurosci.* **25**, 2002–2009 (2005).

46. 46.

Wertz, I. E. et al. De-ubiquitination and ubiquitin ligase domains of A20 downregulate NF-κB signalling. *Nature* **430**, 694–699 (2004).

47. 47.

Wang, H. et al. Deep multiomics profiling of brain tumors identifies signaling networks downstream of cancer driver genes. *Nat. Commun.* **10**, 3718 (2019).

48. 48.

Wang, H. et al. Integrated analysis of ultra-deep proteomes in cortex, cerebrospinal fluid and serum reveals a mitochondrial signature in Alzheimer's disease. *Mol. Neurodegeneration* **15**, 43 (2020).

49. 49.

Wang, X. et al. JUMP: a tag-based database search tool for peptide identification with high sensitivity and accuracy. *Mol. Cell. Proteomics* **13**, 3663–3673 (2014).

50. 50.

Li, Y. et al. JUMPg: an integrative proteogenomics pipeline identifying unannotated proteins in human brain and cancer cells. *J. Proteome Res.* **15**, 2309–2320 (2016).

51. 51.

Mellacheruvu, D. et al. The CRApome: a contaminant repository for affinity purification-mass spectrometry data. *Nat. Methods* **10**, 730–736 (2013).

52. 52.

Szklarczyk, D. et al. STRING v10: protein–protein interaction networks, integrated over the tree of life. *Nucleic Acids Res.* **43**, D447–D452 (2015).

53. 53.

Hutlin, E. L. et al. The BioPlex Network: a systematic exploration of the human interactome. *Cell* **162**, 425–440 (2015).

54. 54.

Li, T. et al. A scored human protein–protein interaction network to catalyze genomic interpretation. *Nat. Methods* **14**, 61–64 (2017).

55. 55.

Barabasi, A. L. & Oltvai, Z. N. Network biology: understanding the cell’s functional organization. *Nat. Rev. Genet.* **5**, 101–113 (2004).

56. 56.

Shannon, P. et al. Cytoscape: a software environment for integrated models of biomolecular interaction networks. *Genome Res.* **13**, 2498–2504 (2003).

57. 57.

Bader, G. D. & Hogue, C. W. An automated method for finding molecular complexes in large protein interaction networks. *BMC Bioinformatics* **4**, 2 (2003).

58. 58.

Morris, J. H. et al. clusterMaker: a multi-algorithm clustering plugin for Cytoscape. *BMC Bioinformatics* **12**, 436 (2011).

## Acknowledgements

We acknowledge M. Hendren and S. Rankin for animal colony management; J. Wen for help with phenotypic studies; C. Li and S. Zhou for technical and scientific insights; G. Neale and S. Olsen for assistance with sequencing; the St. Jude Immunology FACS core facility for cell sorting; and the St. Jude Communications and Science/Medical Content Outreach for artwork. This work was supported by ALSAC and by US National Institutes of Health grants R01AG053987 (to J.P.) and AI105887, AI131703, AI140761, AI150241, AI150514, CA250533 and CA253188 (to

H.C.). The content is solely the responsibility of the authors and does not necessarily represent the official views of the National Institutes of Health.

## Author information

### Author notes

1. These authors contributed equally: Lingyun Long, Jun Wei

### Affiliations

1. Department of Immunology, St. Jude Children's Research Hospital, Memphis, TN, USA

Lingyun Long, Jun Wei, Seon Ah Lim, Jana L. Raynor, Hao Shi, Cliff Guy, Nicole M. Chapman, Guotong Fu, Yanyan Wang, Hongling Huang, Wei Su, Jordy Saravia, Isabel Risch, Yogesh Dhungana, Anil KC, Peipei Zhou & Hongbo Chi

2. Center for Advanced Genome Engineering, St. Jude Children's Research Hospital, Memphis, TN, USA

Jon P. Connelly & Shondra M. Pruett-Miller

3. Center for Proteomics and Metabolomics, St. Jude Children's Research Hospital, Memphis, TN, USA

Hong Wang, Boer Xie, Yuxin Li, Mingming Niu & Junmin Peng

4. Department of Cell and Molecular Biology, St. Jude Children's Research Hospital, Memphis, TN, USA

Yong-Dong Wang

5. Department of Pathology, St. Jude Children's Research Hospital, Memphis, TN, USA

Peter Vogel

6. Department of Computational Biology, St. Jude Children's Research Hospital, Memphis, TN, USA

Jiyang Yu

7. Department of Structural Biology, St. Jude Children's Research Hospital, Memphis, TN, USA

Junmin Peng

8. Department of Developmental Neurobiology, St. Jude Children's Research Hospital, Memphis, TN, USA

Junmin Peng

## Contributions

L.L. and J.W. conceived the project, designed and performed in vitro and in vivo experiments, analysed data and wrote the manuscript. S.A.L. performed tumour and scRNA-seq experiments. J.L.R. performed Seahorse experiments. H.S., I.R., Y.L. and Y.D. performed bioinformatic analyses. J.P.C. and S.M.P.-M. designed and generated the focused sgRNA library. H.W., B.X., M.N. and J.P. performed proteomics. C.G. performed imaging experiments. N.M.C., Y.W., H.H., W.S., A.K. and P.Z. helped with immunological experiments. G.F. performed LCMV infection experiments. J.S. helped with ATAC-seq sample preparation. Y.-D.W. and J.Y. analysed CRISPR–Cas9 screening data. P.V. provided histological analysis. H.C. helped to design experiments, co-wrote the manuscript, and provided overall direction.

## Corresponding author

Correspondence to [Hongbo Chi](#).

## Ethics declarations

## Competing interests

H.C. is a consultant for Kumquat Biosciences.

## Additional information

**Peer review information** *Nature* thanks Jeffrey Rathmell and the other, anonymous, reviewers for their contribution to the peer review of this work.

**Publisher's note** Springer Nature remains neutral with regard to jurisdictional claims in published maps and institutional affiliations.

## Extended data figures and tables

### [Extended Data Fig. 1 Two rounds of pooled CRISPR screening to identify novel regulators of nutrient and mTORC1 signalling.](#)

Related to Fig. 1. **(a)** Flow cytometry analysis of IFN $\gamma$ , IL-4, IL-17A or FOXP3 expression in cells cultured in T<sub>H</sub>0-, T<sub>H</sub>1-, T<sub>H</sub>2-, T<sub>H</sub>17- or induced T<sub>reg</sub>-polarizing condition ( $n = 3$  samples each group). **(b)** Flow cytometry analysis of pS6 in T<sub>H</sub>1 and T<sub>reg</sub> cells with TCR stimulation for 0 or 1 h ( $n = 3$  samples each group). **(c)** Induced T<sub>reg</sub> cells were stimulated with anti-CD3 and anti-CD28 in the presence or absence of amino acids (AA) or glucose for 3 h followed by flow cytometry analysis and quantification of pS6 level [based on mean fluorescence intensity (MFI)] ( $n = 3$  samples each group). **(d)** Induced T<sub>reg</sub> cells were labelled with CellTrace Violet (CTV) and stimulated with anti-CD3 and anti-CD28 in the presence or absence of AA or glucose for 3 d, followed by flow cytometry analysis of CTV dilution ( $n = 3$  samples each group). **(e)** Gating strategy used for sorting cells with the  $\geq 10\%$  highest (pS6<sup>hi</sup>) and  $\leq 10\%$  lowest (pS6<sup>lo</sup>) levels after stimulation with 0.25 or 4  $\mu\text{g}^{-1}$  of anti-CD3 for 3 h ( $n = 2$  samples each group). Mean  $\pm$  s.e.m. **(c)**. \*\*\* $P < 0.001$ ; one-way ANOVA **(c)**. Data are representative of two **(b–d)** or three **(a)** experiments.

[Source data](#)

## Extended Data Fig. 2 Validation of individual candidate mTORC1 regulators.

Related to Fig. 1. **(a)** Flow cytometry analysis and quantification of pS6 level [based on mean fluorescence intensity (MFI)] in naïve or activated WT and *Depdc5*-deficient CD4<sup>+</sup>Foxp3<sup>-</sup> T cells ( $n = 4$  samples each group). Naïve CD4<sup>+</sup> T cells among freshly isolated splenocytes from WT and *Cd4*<sup>Cre</sup>*Depdc5*<sup>f/f</sup> mice were gated (indicated as TCR 0 h), or naïve CD4<sup>+</sup> T cells were sorted and stimulated with anti-CD3 and anti-CD28 overnight for flow cytometry analysis of pS6 level. **(b)** Quantification of relative pS6 level in induced T<sub>reg</sub> cells transduced with sgNTC, sg*Sec13*, sg*Mios*, sg*Seh1l*, or sg*Wdr24* (all Ametrine<sup>+</sup>) were stimulated with TCR for 3 h ( $n = 3$  samples each group). **(c)** Diagram of dual-colour co-culture system to examine cell-intrinsic effects of deletion of a candidate gene on TCR-induced pS6, cell size and CD71 expression. Specifically, Cas9<sup>+</sup> cells transduced with sgNTC (mCherry<sup>+</sup> or GFP<sup>+</sup>; ‘spike’) were mixed with those transduced with those targeting a specific gene (Ametrine<sup>+</sup>), and stimulated with anti-CD3 for 3 h (for pS6) or with anti-CD3 and anti-CD28 for 20 h (for cell size and CD71). **(d)** Validation of dual-colour co-culture system by using two sgNTC-expressing vectors with different fluorophores. Cells transduced with sgNTC (GFP<sup>+</sup>; ‘spike’) were mixed with those transduced with sgNTC (Ametrine<sup>+</sup>), and stimulated with anti-CD3 for 3 h to examine pS6 (see phos-flow staining), or stimulated with anti-CD3 and anti-CD28 for 20 h ( $n = 3$  samples each group) to measure cell size and CD71 expression (see surface staining). **(e)** Heat map summary of log<sub>2</sub> (pS6<sup>hi</sup>/pS6<sup>lo</sup>) for individually validated candidate genes (63 positive and 21 negative regulators) including positive (*Rheb*, *Rptor*, *Lamtor3*, *Rraga* and *Mtor*) and negative (*Cd5*, *Nprl3*, *Nprl2* and *Tsc1*) control genes (2 sgRNAs for each candidate). Specifically, Cas9-expressing CD4<sup>+</sup> T cells transduced with sgRNA for target genes (Ametrine<sup>+</sup>) or non-targeting control sgRNA (sgNTC) (mCherry<sup>+</sup>; ‘spike’) were mixed and differentiated into induced T<sub>reg</sub> cells. These cells were then stimulated with anti-CD3 for 3 h ( $n = 3$  samples each group). Relative pS6 level (normalized to ‘spike’) was analysed by flow cytometry. **(f)** Analysis of protein–protein interaction (PPI) networks of high-confidence regulators. Specifically, 286 positive and

60 negative high-confidence hits were integrated with the composite PPI databases that encompass STRING, BioPlex and InWeb\_IM databases for the inference of functional modules. Red and blue circles represent genes the deletion of which represses and promotes mTORC1 activity, respectively. Mean  $\pm$  s.e.m. (a, b). \* $P < 0.05$ ; \*\* $P < 0.01$ ; \*\*\* $P < 0.001$ ; one-way ANOVA (a, b). Data are representative of one (f) or three (d, e), or pooled from two (a) or three (b) experiments.

[Source data](#)

**Extended Data Fig. 3 SWI/SNF complex represses expression of nutrient sensor CASTOR1 to support mTORC1 activation.**

Related to Fig. 1. (a) Quantification (normalized to ‘spike’) of relative pS6 level, cell size (FSC-A) and CD71 expression in induced T<sub>reg</sub> cells transduced with the indicated sgRNAs followed by stimulation with anti-CD3 for 3 h to measure pS6 level, or with anti-CD3 and anti-CD28 for 20 h to measure cell size (FSC-A) and CD71 expression by flow cytometry ( $n = 3$  samples each group). (b) Imaging analysis and quantification of lysosome-associated mTOR [based on mean fluorescence intensity (MFI)] in sgNTC- or sg*Smarcb1*-transduced cells that were stimulated with anti-CD3 for 3 h, starved of amino acids (AA), and refed AA for 20 min ( $n > 230$  cells per condition). Scale bars, 5  $\mu$ m. (c) Volcano plots of expression levels of transcripts, including *Castor1*, in sgNTC- or sg*Smarcb1* (both Ametrine<sup>+</sup>)-transduced cells that were stimulated with TCR for 3 h ( $n = 4$  samples each group). (d) *Castor1* mRNA expression in sgNTC- or sg*Smarcb1* (both Ametrine<sup>+</sup>)-transduced cells were stimulated with anti-CD3 for 3 h or with anti-CD3 and anti-CD28 for 20 h ( $n = 3$  samples per group). (e) sgNTC- or sg*Smarcb1* (both Ametrine<sup>+</sup>)-transduced cells were left unstimulated (indicated by 0 h) or stimulated with anti-CD3 for 3 h or anti-CD3 and anti-CD28 for 20 h. Immunoblot analysis and quantification of relative CASTOR1 expression ( $n = 3$  samples each group). (f) Immunoblot analysis and quantification of relative pS6K1 and pS6 levels in cells transduced with empty vector or vector expressing *Castor1*, followed by stimulation with anti-CD3 and anti-CD28 for 2 d ( $n = 3$  samples each group). Mean  $\pm$  s.e.m. (a, b, d–f). \*\* $P < 0.01$ ; \*\*\* $P < 0.001$ ; two-tailed

unpaired Student's *t*-test (**f**); one-way ANOVA (**a, b, d, e**). Data are representative of one (**c**) or two (**b**), or pooled from two (**d, e**) or three (**a, f**) experiments

[Source data](#).

## Extended Data Fig. 4 SEC31A is required for mTORC1 activation.

Related to Fig. 2. **(a)** Interaction of endogenous SEC13 with SEC31A in induced T<sub>reg</sub> cells as assessed by immunoprecipitation (IP)-immunoblot analysis. **(b, c)** sgNTC- or sg*Sec31a*-transduced cells were starved of and refed amino acids (AA, **b**) or glucose (**c**) for 20 min, followed by immunoblot analysis of SEC31A, pS6K1, pS6 and β-actin. Bottom, quantification of relative pS6K1 and pS6 levels (*n* = 3 samples each group). **(d)** Cells transduced with the indicated sgRNAs (all Ametrine<sup>+</sup>) were mixed with sgNTC (mCherry<sup>+</sup>; ‘spike’)-transduced cells, and stimulated with anti-CD3 for 3 h to measure pS6 level or with anti-CD3 and anti-CD28 for 20 h to measure cell size (FSC-A) and CD71 expression by flow cytometry (normalized to ‘spike’) (*n* = 3 samples each group). **(e–g)** sgNTC-, sg*Sec31a*- or sg*Sec13* (all Ametrine<sup>+</sup>)-transduced cells were co-transduced with constitutively active RAGA<sup>Q66L</sup> (CA-RAGA)-expressing retrovirus (GFP<sup>+</sup>) or sg*Nprl2* (GFP<sup>+</sup>), followed by stimulation with TCR for 3 h to examine relative pS6 level by flow cytometry (*n* = 3 samples each group) **(e)**, pS6K1 and pS6 levels by immunoblot analysis (*n* = 4 samples each group) **(f)**, or lysosomal localization of mTOR [based on mean fluorescence intensity (MFI)] (*n* > 700 cells per condition). Scale bars, 5 μm **(g)**. In **f**, two different exposures for pS6K1 were included to account for the differential intensities between mock and CA-RAGA or sg*Nprl2* conditions, and relative pS6K1 level was quantified from long exposure for mock and short exposure for CA-RAGA or sg*Nprl2* conditions (middle). Bottom, quantification of pS6 level. Mean ± s.e.m. **(b–g)**. NS, not significant; \*\**P* < 0.01; \*\*\**P* < 0.001; one-way ANOVA **(b–g)**. Data are representative of two **(e–g)** or four **(a)**, or pooled from three **(b–d)** experiments.

[Source data](#)

## Extended Data Fig. 5 SEC31A–SEC13 axis promotes mTORC1 activation and cell proliferation in vivo.

Related to Fig. 2. (a) Cells transduced with sgNTC or sg*Sec31a* (both Ametrine<sup>+</sup>) were labelled with CellTrace Violet (CTV) and transferred into *Rag1*<sup>−/−</sup> mice. Flow cytometry analysis of CTV dilution, and quantification of percentage of proliferated (CTV<sup>lo</sup>) cells at 7 d after transfer ( $n = 5$  samples each group). (b) WT, *Rptor*- and *Sec31a*-null T<sub>reg</sub> cells (all CD45.1<sup>+</sup> Ametrine<sup>+</sup>) were mixed with conventional CD4<sup>+</sup> T cells (T<sub>conv</sub>; CD45.2<sup>+</sup>) at a 1:4 ratio and transferred into *Rag1*<sup>−/−</sup> mice. Quantification of the accumulation of conventional T cells in the spleen at 7 d after transfer ( $n = 5$  samples each group). (c) Naïve CD4<sup>+</sup> T cells were stimulated with anti-CD3 and anti-CD28 for 0, 24, 48 or 72 h followed by immunoblot analysis of the indicated protein expression, and quantification of pS6K1, SEC13, SEC31A, and TSC2 ( $n = 3$  samples each group). (d) sgNTC-, sg*Sec31a*- and sg*Sec13*-transduced cells were sorted and lysed with CHAPS buffer for immunoprecipitation (IP) with an antibody against WDR24. The immunoprecipitated proteins were analysed by immunoblot for WDR24, WDR59, MIOS, SEH1L, SEC13, SEC31A, SEC23A and β-Actin. Mean ± s.e.m. (a–c). \*\* $P < 0.01$ ; \*\*\* $P < 0.001$ ; two-tailed unpaired Student's *t*-test (a); one-way ANOVA (b). Data are representative of one (a, b) or two (c, d) experiments.

### Source data

## Extended Data Fig. 6 SEC31A protects SEC13 from proteasomal degradation to sustain mTORC1 activation.

Related to Fig. 3. (a) *Sec13* mRNA expression in sgNTC- or sg*Sec31a*-transduced induced T<sub>reg</sub> cells ( $n = 3$  samples each group). (b) sgNTC- or sg*Sec31a*-transduced induced T<sub>reg</sub> cells were sorted and treated with cycloheximide (CHX) for the indicated times. Total protein extracts of cells transduced with sgNTC (5 µg) or sg*Sec31a* (12.5 µg; more protein was loaded to equalize basal SEC13 amount between these cells) were used for immunoblot analysis and quantification of relative SEC13 abundance ( $n = 4$

samples each group). (c) Naïve CD4<sup>+</sup> T cells were stimulated with anti-CD3 and anti-CD28 for 0, 24, or 48 h and then treated with DMSO or MG132 at 48–72 h of stimulation, followed by immunoblot analysis and quantification of SEC13 and SEC31A expression ( $n = 3$  samples each group). (d) HEK293T cells were transfected with HA-tagged SEC13 and 6× His-tagged WT-, K48R- or K63R-ubiquitin (Ub) and treated with MG132 for 6 h. Ni-nitrilotriacetic acid (Ni-NTA) bead-based pull-down and immunoblot analysis of HA-SEC13. Bottom, expression of indicated proteins in whole cell lysates (WCL). (e) sgNTC- or sg*Sec31a*-transduced HEK293T cells were transfected with HA-tagged SEC13 and 6× His-tagged WT ubiquitin (His-tagged Ub), and treated with MG132 for 6 h. Left, Ni-NTA bead-based pull-down of His-tagged Ub-labelled proteins followed by immunoblot analysis for HA-SEC13. Right, immunoblot analysis of WCL for expression of endogenous SEC31A or HA-SEC13, His-tagged Ub, and β-Actin. Mean ± s.e.m. (a–c). NS, not significant; \*\* $P < 0.01$ ; \*\*\* $P < 0.001$ ; two-tailed unpaired Student's *t*-test (a); two-way ANOVA (b); one-way ANOVA (c). Data are representative of two (d, e) or three (a), or pooled from two (b) or three (c) experiments.

#### Source data

#### Extended Data Fig. 7 SEC31A protects SEC13 from SKP1-mediated proteasomal degradation and supports T cell functional fitness.

Related to Fig. 3. (a) HA-tagged WT or the indicated lysine mutant constructs of SEC13 were transfected into HEK293T cells individually. Immunoblot analysis of HA and Hsp90. (b) HA-tagged WT or K260R mutant SEC13 was transfected into HEK293T cells together with the K48-only His-Ub followed by MG132 treatment and anti-HA immunoprecipitation (IP). Immunoblot analysis for HA, His-Ub and β-actin. WCL, whole cell lysate. (c) Cas9-expressing CD4<sup>+</sup> T cells were transduced with sgNTC or sg*Sec31a* retrovirus (Ametrine<sup>+</sup>) together with WT or K260R mutant SEC13-expressing retrovirus (GFP<sup>+</sup>). Ametrine<sup>+</sup>GFP<sup>lo</sup> cells (see gating on flow cytometry plot, top) were stimulated with TCR for 0 or 3 h. Immunoblot analysis and quantification

of relative SEC13 and pS6 levels ( $n = 4$  samples each group). (d) Volcano plot of proteins, including SKP1, that interact with HA-SEC13 in induced T<sub>reg</sub> cells as identified by mass spectrometry ( $n = 3$  samples each group). (e) Induced T<sub>reg</sub> cells transduced with HA-tagged-SEC13- or empty vector-expressing retrovirus were lysed with CHAPS buffer followed by anti-HA immunoprecipitation (IP) and immunoblot analysis of HA and SKP1. (f) Induced T<sub>reg</sub> cells were lysed with CHAPS buffer followed by immunoprecipitation of endogenous SKP1 and immunoblot analysis of SKP1 and SEC13. (g) Interaction of endogenous SKP1 with SEC13 in sgNTC- or sg*Sec31a*-transduced cells. (h) Naïve CD4<sup>+</sup> T cells were stimulated with anti-CD3 and anti-CD28 for 0, 24, 48 or 72 h. Immunoblot analysis of anti-SKP1 immunoprecipitants and WCL for SKP1, SEC13, and β-Actin ( $n = 2$  samples per group). (i) Immunoblot analysis and quantification of relative expression of indicated proteins in sgNTC- or sg*Skp1* (both Ametrine<sup>+</sup>)-transduced cells ( $n = 3$  samples per group). (j) The indicated sgRNA-transduced cells were labelled with CellTrace Violet (CTV), and stimulated with anti-CD3 and anti-CD28 for 72 h, followed by flow cytometry analysis and quantification of CTV dilution ( $n = 3$  samples each group). (k) Diagram of SMARTA T cell transfer and LCMV infection system. In brief, SMARTA–Cas9 CD4<sup>+</sup> T cells (CD45.1<sup>+</sup>) transduced with sgRNA for candidate genes (CD45.1<sup>+</sup>Ametrine<sup>+</sup>) and mixed with sgNTC (CD45.1<sup>+</sup>mCherry<sup>+</sup>; ‘spike’)-transduced cells at a 1:1 ratio, and adoptively transferred into naïve (unchallenged; CD45.2<sup>+</sup>) mice that were left uninfected (see l) or challenged with LCMV infection (see Fig. 3f). (l) Quantification of the relative proportion (normalized to ‘spike’) of donor-derived (CD45.1<sup>+</sup>) T cells in the spleen of uninfected mice at 7 d after transfer ( $n = 6$  mice per group). (m) Cells transduced with sgNTC (Ametrine<sup>+</sup>), sg*Sec31a* (Ametrine<sup>+</sup>) or sg*Sec31a/Skp1* (GFP<sup>+</sup> and Ametrine<sup>+</sup>) were sorted and stimulated with anti-CD3 and anti-CD28 for 20 h ( $n = 6$ -7 samples per group), followed by the measurement of extracellular acidification rate (ECAR). Oligo, oligomycin; FCCP, fluoro-carbonyl cyanide phenylhydrazone; Rot, rotenone. Mean ± s.e.m. (c, i, j, l, m). \*\* $P < 0.01$ ; \*\*\* $P < 0.001$ ; one-way ANOVA (c, i, j, l, m, right); two-way ANOVA (m, left). Data are representative of one (d, j, l, m) or two (a, b, e-h), or pooled from two (c) or three (i) experiments.

[Source data](#)

[Extended Data Fig. 8 The SAGA complex suppresses mTORC1 activation.](#)

Related to Fig. 4. **(a)** Quantification (normalized to ‘spike’) of relative pS6 level, cell size (FSC-A) and CD71 expression in induced  $T_{reg}$  cells transduced with sgRNA for *Ccdc101* or *Taf6l*, followed by stimulation with anti-CD3 for 3 h to measure pS6 level (left) or with anti-CD3 and anti-CD28 for 20 h to measure cell size (FSC-A; middle) and CD71 (right) expression by flow cytometry ( $n = 3$  samples each group). **(b)** Immunoblot analysis and quantification of relative pS6K1 and pS6 expression in sgNTC- or sg*Ccdc101*-transduced cells that were starved of and refed amino acids (AA) for 20 min ( $n = 4$  samples each group). Mean  $\pm$  s.e.m. **(a, b)**. \* $P < 0.05$ ; \*\* $P < 0.01$ ; \*\*\* $P < 0.001$ ; one-way ANOVA **(a, b)**. Data are representative of three **(a)**, or pooled from three **(b)** experiments.

[Source data](#)

[Extended Data Fig. 9 The SAGA complex represses the expression of nutrient transporters and mTORC1 activation.](#)

Related to Fig. 4. **(a)** Heat map of differentially expressed genes in *Ccdc101*-null  $T_{reg}$  cells stimulated with anti-CD3 and anti-CD28 for 0 ( $n = 3$  samples each group) or 20 h ( $n = 4$  samples each group). **(b)** *Slc2a1*, *Slc16a10* or *Slc43a1* mRNA expression in sgNTC- or sg*Ccdc101*-transduced cells at steady state ( $n = 3$  samples each group). **(c)** Immunoblot analysis and quantification of relative GLUT1 expression in sgNTC- or sg*Ccdc101*-transduced cells that were stimulated with anti-CD3 and anti-CD28 for 0 or 20 h ( $n = 3$  samples each group). **(d)** Flow cytometry analysis and quantification of 2-NBDG uptake in sgNTC- or sg*Ccdc101* (both Ametrine $^+$ )-transduced cells were stimulated with anti-CD3 and anti-CD28 for 20 h ( $n = 4$  samples each group). **(e, f)** Quantification of relative pS6 level in cells transduced with the indicated sgRNAs that were stimulated with TCR for 3 h ( $n = 3$  samples each group). **(g)** Principal component analysis (PCA) of ATAC-seq for cells transduced with sgNTC

( $n = 4$  samples) or sg*Ccdc101* (both Ametrine $^+$ ) ( $n = 3$  samples) and stimulated with anti-CD3 and anti-CD28 for 20 h. (h) Motif enrichment analysis of ATAC-seq of sgNTC- and sg*Ccdc101*-transduced cells ( $n = 4$  samples each group). (i) Footprinting analysis of *Sp3* binding in ATAC-seq. (j) Accessibility of the *Sp3* locus in sgNTC- and sg*Ccdc101*-transduced cells as identified by ATAC-seq. Highlighted peaks in the red box indicate differential accessible regions. (k) Immunoblot analysis of SP3 expression in sgNTC- or sg*Ccdc101* (both Ametrine $^+$ )-transduced cells. Mean  $\pm$  s.e.m. (b–f). \*\*\* $P < 0.001$ ; two-tailed unpaired Student's *t*-test (b, d); one-way ANOVA (c, e, f). Data are representative of one (a, g–j), two (b, e, f, k), or pooled from two (c, d) experiments.

### Source data

### Extended Data Fig. 10 The SAGA complex prevents mTORC1 hyperactivation to enforce immune homeostasis in vivo.

Related to Fig. 4. (a, b) Induced T<sub>reg</sub> cells transduced with the indicated sgRNAs were stimulated with anti-CD3 and anti-CD28 for 20 h ( $n = 3$  samples each group). Flow cytometry analysis and quantification of staining with active caspase-3 (a) and fixable viability dye (FVD, b) ( $n = 3$  per group). (c) Cells transduced with the indicated sgRNAs were stimulated with anti-CD3 and anti-CD28 for 20 h ( $n = 5$ –7 samples per group), followed by the measurement of extracellular acidification rate (ECAR). Oligo, oligomycin; FCCP, fluoro-carbonyl cyanide phenylhydrazone; Rot, rotenone. (d) Immunoblot analysis and quantification of CCDC101 expression in naïve CD4 $^+$  T cells from WT and *Cd4*<sup>Cre</sup>*Ccdc101* $^{fl/fl}$  mice ( $n = 3$  mice per group). (e) Quantification of CD71 expression on naïve or activated WT and *Ccdc101*-deficient CD4 $^+$  T cells. Naïve CD4 $^+$  T cells among freshly isolated splenocytes from WT and *Cd4*<sup>Cre</sup>*Ccdc101* $^{fl/fl}$  mice ( $n = 4$  mice per group) were gated (indicated as 0 h), or naïve CD4 $^+$  T cells were stimulated with anti-CD3 and anti-CD28 for 20 h. (f) Flow cytometry analysis and quantification of numbers of total, double-negative (DN), double-positive (DP), CD4 single-positive (CD4SP), and CD8 single-positive (CD8SP) thymocytes from WT and *Cd4*<sup>Cre</sup>*Ccdc101* $^{fl/fl}$  mice ( $n = 4$  mice each group). (g) Flow cytometry analysis and quantification of

proportions and numbers of splenic CD4<sup>+</sup> and CD8<sup>+</sup> T cells from WT and *Cd4*<sup>Cre</sup>*Ccdc101*<sup>f/f</sup> mice ( $n = 4$  mice each group). **(h)** Flow cytometry analysis and normalized ratio of CD122<sup>+</sup> versus CD122<sup>-</sup> cells among CD44<sup>hi</sup> populations (gated on splenic CD8<sup>+</sup> T cells) from indicated mice ( $n = 4$  mice each group). Mean  $\pm$  s.e.m. **(a–h)**. NS, not significant; \*\* $P < 0.01$ ; \*\*\* $P < 0.001$ ; two-tailed unpaired Student's *t*-test (**d–h**); one-way ANOVA (**a, b, c**, right); two-way ANOVA (**c**, left). Data are representative of one (**c**) or two (**a, b**), or pooled from three (**d–h**) experiments.

### Source data

### Extended Data Fig. 11 T<sub>reg</sub>-specific deletion of *Ccdc101* disrupts immune homeostasis and boosts antitumour response.

Related to Fig. 5. **(a)** Quantification of relative pS6 level in splenic CD4<sup>+</sup>FOXP3<sup>+</sup> cells from WT and *Foxp3*<sup>Cre</sup>*Ccdc101*<sup>f/f</sup> (around 8 weeks old) mice ( $n = 4$  mice per group). **(b)** Quantification of relative FOXP3 expression (gated on splenic FOXP3<sup>+</sup>CD4<sup>+</sup> T cells) from WT and *Foxp3*<sup>Cre</sup>*Ccdc101*<sup>f/f</sup> mice ( $n = 4$  mice per group). **(c)** Quantification of percentages of effector/memory (CD44<sup>hi</sup>CD62L<sup>lo</sup>) subsets in splenic CD4<sup>+</sup>FOXP3<sup>-</sup> and CD8<sup>+</sup> T cells from WT and *Foxp3*<sup>Cre</sup>*Ccdc101*<sup>f/f</sup> (around 8 weeks old) mice ( $n = 4$  mice each group). **(d)** Representative flow cytometry analysis of IL-2<sup>+</sup> or IFN $\gamma$ <sup>+</sup> population of splenic CD4<sup>+</sup>Foxp3<sup>-</sup> and CD8<sup>+</sup> T cells from WT and *Foxp3*<sup>Cre</sup>*Ccdc101*<sup>f/f</sup> (around 8 weeks old) mice. **(e–g)** WT and *Foxp3*<sup>Cre</sup>*Ccdc101*<sup>f/f</sup> mice were inoculated with MC38 colon adenocarcinoma cells. T<sub>reg</sub> cells (CD45<sup>+</sup>CD4<sup>+</sup>YFP<sup>+</sup>), non-T<sub>reg</sub> immune cells (CD45<sup>+</sup>YFP<sup>-</sup>CD11b<sup>-</sup>) and myeloid cells (CD45<sup>+</sup>CD11b<sup>+</sup>) were isolated and sorted from tumours, and mixed at a 1:2:1 ratio for scRNA-seq analysis (2 biological replicates, pooled from 3-4 mice each, per group) at 19 d after tumour inoculation. Dot plot showing the differentially expressed marker genes for 4 subclusters of CD8<sup>+</sup> T cells in the MC38 tumours (**e**; see [Methods](#) for details). UMAP embeddings of CD8<sup>+</sup> T cells grouped by genotype (**f**, left) and indicated subclusters (**f**, right). Frequencies of the indicated subclusters were quantified for each genotype (**g**). T<sub>eff</sub>-like, effector-like CD8<sup>+</sup> T cells; T<sub>ex</sub>-like, exhaustion-like

CD8<sup>+</sup> T cells; T<sub>cm</sub>-like, central memory-like CD8<sup>+</sup> T cells; T<sub>em</sub>-like, effector/memory-like CD8<sup>+</sup> T cells. (h) Flow cytometry analysis and quantification of the percentages of CD44<sup>hi</sup>CD62L<sup>lo</sup> intratumoral CD8<sup>+</sup> T cells from WT and *Foxp3*<sup>Cre</sup>*Ccdc101*<sup>f/f</sup> mice ( $n \geq 5$  per group). (i) Flow cytometry analysis and quantification of IFN $\gamma$ <sup>+</sup> and TNF<sup>+</sup> cells among intratumoral CD8<sup>+</sup> T cells from WT and *Foxp3*<sup>Cre</sup>*Ccdc101*<sup>f/f</sup> mice ( $n \geq 5$  per group). (j) Violin plots of scRNA-seq data depicting *Icos*, *Tnfrsf18*, *Ctla4* and *Ifng* expression in intratumoral T<sub>reg</sub> cells. (k) Flow cytometry analysis and quantification of ICOS, GITR and CTLA-4 for intratumoral T<sub>reg</sub> cells from WT and *Foxp3*<sup>Cre</sup>*Ccdc101*<sup>f/f</sup> mice ( $n \geq 5$  per group). (l) Flow cytometry analysis and quantification of IFN $\gamma$  expression in intratumoral T<sub>reg</sub> cells from WT and *Foxp3*<sup>Cre</sup>*Ccdc101*<sup>f/f</sup> mice ( $n \geq 5$  per group). Mean  $\pm$  s.e.m. (a–c, h, i, k, l). \* $P < 0.05$ ; \*\* $P < 0.01$ ; \*\*\* $P < 0.001$ ; two-tailed unpaired Student's *t*-test (a–c, h, i, k, l); two-sided Wilcoxon rank sum test in j. Data are representative of one (e–l) or two (d), or pooled from two (a–c) experiments.

[Source data](#)

[\*\*Extended Data Fig. 12 Schematic of applying CRISPR screening and integrative analyses to dissect nutrient and mTORC1 signalling in primary T cells.\*\*](#)

Related to Fig. 5. With two rounds of genome-wide and focused CRISPR screenings, we identify 346 high-confidence mTORC1 signalling factors, including many novel activators and inhibitors, as well as known regulators (identified in other systems) that have not been studied in primary T cells. Notably, using analysis of protein–protein interaction (PPI) networks and unbiased functional and proteomic approaches, we further establish the epigenetic and post-translational mechanisms underpinning the three-tier regulatory modules of nutrient signalling, composed of nutrient transporters (e.g. via affecting expression of GLUT1 and other transporters by SAGA complex), sensors (e.g. via epigenetic regulation of CASTOR1 expression by SWI/SNF complex) and transducers (e.g. via shaping GATOR2 complex stability by SEC31A; regulating SEC13 ubiquitination at lysine 260), which

transmit immunological and nutrient cues to mTORC1 signalling for proper regulation of T cell activity in vivo and in vitro.

## Supplementary information

### Supplementary Figure 1

This file contains Supplementary Fig. 1.

### Reporting Summary

### Data of the first-round genome-wide CRISPR screening via the Brie library

Supplementary Table 1 . This file contains the output of the analysis of the first-round genome-wide Brie library CRISPR screening data at the gene level analysed by pipeline 1 (Tab a) and pipeline 2 (Tab b), or at the sgRNA level analysed by pipeline 1 (Tab c) and pipeline 2 (Tab d). The comparison ( $pS6^{\text{high}}$  versus  $pS6^{\text{low}}$ ) for two stimulation conditions ( $0.25$  and  $4 \mu\text{g ml}^{-1}$  anti-CD3) is shown. Ranked by target gene symbol.

### List of sgRNA sequence information in the second-round focused CRISPR library

Supplementary Table 2 . This file contains the sgRNA sequences in the CRISPR sgRNA library used in the second-round focused CRISPR screening. Ranked by target gene symbol.

### Data of the second-round focused CRISPR library screening

Supplementary Table 3 . This file contains the output of the analysis of the second-round focused CRISPR library screening data at the gene level analysed by pipeline 1 (Tab a) and pipeline 2 (Tab b), or at the sgRNA level analysed by pipeline 1 (Tab c) and pipeline 2 (Tab d). The comparison

(pS6<sup>high</sup> versus pS6<sup>low</sup>) for two stimulation conditions (0.25 and 4 µg ml<sup>-1</sup> anti-CD3) is shown. Ranked by target gene symbol.

### List of sgRNA sequence information

Supplementary Table 4 . This file contains the sgRNA sequences used for validation in this study. Ranked by target gene symbol.

### Differentially expressed gene list in induced T

Supplementary Table 5 <sub>reg</sub> cells upon *Smarcb1* deletion. This file contains 2,023 differentially expressed ( $|\log_2 \text{FC}| > 0.55$ , FDR < 0.05) genes in *Smarcb1*-null versus control at 3 h [sg*Smarcb1*-3 h versus sgNTC-3 h (columns E and F)] or 20 h [sg*Smarcb1*-20 h versus sgNTC-20 h (columns G and H)] after TCR stimulation as profiled by microarray analysis.

### Differentially expressed gene list in induced T

Supplementary Table 6 <sub>reg</sub> cells upon *Ccdc101* deletion. This file contains 1,120 differentially expressed ( $|\log_2 \text{FC}| > 0.55$ , FDR < 0.05) genes of in *Ccdc101*-null versus control cells at 0 h [sg*Ccdc101*-0 h versus sgNTC-0 h (columns E and F)] or 20 h [sg*Ccdc101*-20 h versus sgNTC-20 h (columns G and H)] after TCR stimulation as profiled by microarray analysis.

### Primers used to generate SEC13 mutants

Supplementary Table 7 . This file contains the forward and reverse primer sequences used to generate the various single or double mutants of SEC13.

## Source data

### Source Data Fig. 1

### Source Data Fig. 2

[\*\*Source Data Fig. 3\*\*](#)

[\*\*Source Data Fig. 4\*\*](#)

[\*\*Source Data Fig. 5\*\*](#)

[\*\*Source Data Extended Data Fig. 1\*\*](#)

[\*\*Source Data Extended Data Fig. 2\*\*](#)

[\*\*Source Data Extended Data Fig. 3\*\*](#)

[\*\*Source Data Extended Data Fig. 4\*\*](#)

[\*\*Source Data Extended Data Fig. 5\*\*](#)

[\*\*Source Data Extended Data Fig. 6\*\*](#)

[\*\*Source Data Extended Data Fig. 7\*\*](#)

[\*\*Source Data Extended Data Fig. 8\*\*](#)

[\*\*Source Data Extended Data Fig. 9\*\*](#)

[\*\*Source Data Extended Data Fig. 10\*\*](#)

[\*\*Source Data Extended Data Fig. 11\*\*](#)

## Rights and permissions

[Reprints and Permissions](#)

## About this article

## Cite this article

Long, L., Wei, J., Lim, S.A. *et al.* CRISPR screens unveil signal hubs for nutrient licensing of T cell immunity. *Nature* **600**, 308–313 (2021).  
<https://doi.org/10.1038/s41586-021-04109-7>

- Received: 12 November 2020
- Accepted: 07 October 2021
- Published: 18 November 2021
- Issue Date: 09 December 2021
- DOI: <https://doi.org/10.1038/s41586-021-04109-7>

## Share this article

Anyone you share the following link with will be able to read this content:

[Get shareable link](#)

Sorry, a shareable link is not currently available for this article.

[Copy to clipboard](#)

Provided by the Springer Nature SharedIt content-sharing initiative

---

This article was downloaded by **calibre** from <https://www.nature.com/articles/s41586-021-04109-7>

- Article
- [Published: 24 November 2021](#)

# IL-27 signalling promotes adipocyte thermogenesis and energy expenditure

- [Qian Wang](#) ORCID: [orcid.org/0000-0003-4755-7001<sup>1,2 na1</sup>](https://orcid.org/0000-0003-4755-7001),
- [Dehai Li<sup>1,2 na1</sup>](#),
- [Guangchao Cao](#) ORCID: [orcid.org/0000-0003-2069-3396<sup>1,2 na1</sup>](https://orcid.org/0000-0003-2069-3396),
- [Qiping Shi<sup>3 na1</sup>](#),
- [Jing Zhu<sup>1,2</sup>](#),
- [Mingyue Zhang<sup>1,2</sup>](#),
- [Hao Cheng<sup>4</sup>](#),
- [Qiong Wen<sup>1,2</sup>](#),
- [Hao Xu<sup>5</sup>](#),
- [Leqing Zhu<sup>2,6</sup>](#),
- [Hua Zhang<sup>1,2</sup>](#),
- [Rachel J. Perry](#) ORCID: [orcid.org/0000-0003-0748-8064<sup>7,8</sup>](https://orcid.org/0000-0003-0748-8064),
- [Olga Spadaro<sup>5,9</sup>](#),
- [Yunfan Yang](#) ORCID: [orcid.org/0000-0002-5266-7208<sup>9</sup>](https://orcid.org/0000-0002-5266-7208),
- [Shengqi He<sup>10</sup>](#),
- [Yong Chen<sup>10</sup>](#),
- [Baocheng Wang<sup>11</sup>](#),
- [Guangqiang Li<sup>2,6</sup>](#),
- [Zonghua Liu<sup>1,2</sup>](#),
- [Caixian Yang<sup>12</sup>](#),
- [Xiaoli Wu<sup>13</sup>](#),
- [Libing Zhou<sup>14</sup>](#),
- [Qinghua Zhou<sup>1,2</sup>](#),

- [Zhenyu Ju](#) ORCID: orcid.org/0000-0002-9525-6521<sup>15</sup>,
- [Hongyun Lu](#)<sup>1</sup>,
- [Yongjie Xin](#)<sup>1</sup>,
- [Xiaoyong Yang](#) ORCID: orcid.org/0000-0002-5315-7285<sup>8,9</sup>,
- [Cunchuan Wang](#)<sup>16</sup>,
- [Yong Liu](#) ORCID: orcid.org/0000-0001-7771-4181<sup>10</sup>,
- [Gerald I. Shulman](#) ORCID: orcid.org/0000-0003-1529-5668<sup>7,8</sup>,
- [Vishwa Deep Dixit](#)<sup>5,9</sup>,
- [Ligong Lu](#) ORCID: orcid.org/0000-0002-0301-4454<sup>1 na2</sup>,
- [Hengwen Yang](#) ORCID: orcid.org/0000-0002-6418-1985<sup>1,2 na2</sup>,
- [Richard A. Flavell](#) ORCID: orcid.org/0000-0003-4461-0778<sup>5 na2</sup> &
- [Zhinan Yin](#) ORCID: orcid.org/0000-0001-6524-8777<sup>1,2 na2</sup>

*Nature* volume 600, pages 314–318 (2021)

- 13k Accesses
- 35 Altmetric
- [Metrics details](#)

## Subjects

- [Interleukins](#)
- [Metabolic syndrome](#)
- [Metabolism](#)

## Abstract

Thermogenesis in brown and beige adipose tissue has important roles in maintaining body temperature and countering the development of metabolic disorders such as obesity and type 2 diabetes<sup>1,2</sup>. Although much is known about commitment and activation of brown and beige adipose tissue, its multiple and abundant immunological factors have not been well characterized<sup>3,4,5,6</sup>. Here we define a critical role of IL-27–IL-27R $\alpha$  signalling in improving thermogenesis, protecting against diet-induced

obesity and ameliorating insulin resistance. Mechanistic studies demonstrate that IL-27 directly targets adipocytes, activating p38 MAPK–PGC-1 $\alpha$  signalling and stimulating the production of UCP1. Notably, therapeutic administration of IL-27 ameliorated metabolic morbidities in well-established mouse models of obesity. Consistently, individuals with obesity show significantly decreased levels of serum IL-27, which can be restored after bariatric surgery. Collectively, these findings show that IL-27 has an important role in orchestrating metabolic programs, and is a highly promising target for anti-obesity immunotherapy.

This is a preview of subscription content

## Access options

Subscribe to Journal

Get full journal access for 1 year

\$199.00

only \$3.90 per issue

[Subscribe](#)

All prices are NET prices.

VAT will be added later in the checkout.

Tax calculation will be finalised during checkout.

Rent or Buy article

Get time limited or full article access on ReadCube.

from \$8.99

[Rent or Buy](#)

All prices are NET prices.

## **Additional access options:**

- [Log in](#)
- [Learn about institutional subscriptions](#)

**Fig. 1: IL-27 restrains the development of obesity and insulin resistance.**



**Fig. 2: IL-27 signalling promotes thermogenesis and energy expenditure.**



**Fig. 3: IL-27 directly targets adipocytes to promote thermogenesis and combat obesity.**



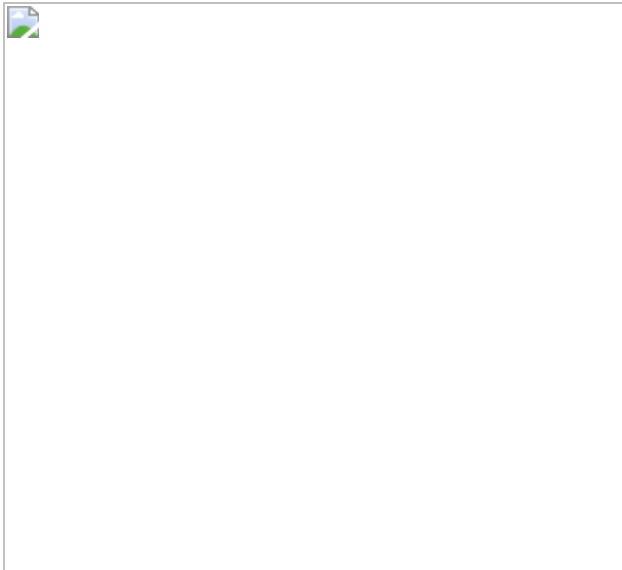
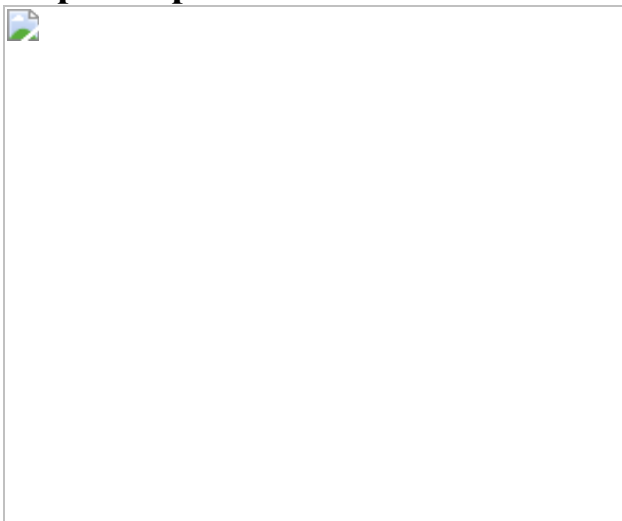


**Fig. 4: IL-27 promotes the activation of thermogenesis with promising therapeutic potential.**



## Data availability

Our RNA-seq data are available at the Sequence Read Archive (SRA) repository at NCBI under the accession numbers [SRX10969398](#)–[SRX10969403](#). [Source data](#) are provided with this paper.

## References

1. 1.

Betz, M. J. & Enerback, S. Human brown adipose tissue: what we have learned so far. *Diabetes* **64**, 2352–2360 (2015).

2. 2.

Bartelt, A. & Heeren, J. Adipose tissue browning and metabolic health. *Nat. Rev. Endocrinol.* **10**, 24–36 (2014).

3. 3.

Wang, W. & Seale, P. Control of brown and beige fat development. *Nat. Rev. Mol. Cell Biol.* **17**, 691–702 (2016).

4. 4.

Odegaard, J. I. et al. Perinatal licensing of thermogenesis by IL-33 and ST2. *Cell* **166**, 841–854 (2016).

5. 5.

Qiu, Y. et al. Eosinophils and type 2 cytokine signaling in macrophages orchestrate development of functional beige fat. *Cell* **157**, 1292–1308 (2014).

6. 6.

Camell, C. D. et al. Inflammasome-driven catecholamine catabolism in macrophages blunts lipolysis during ageing. *Nature* **550**, 119–123 (2017).

7. 7.

Reilly, S. M. & Saltiel, A. R. Adapting to obesity with adipose tissue inflammation. *Nat. Rev. Endocrinol.* **13**, 633–643 (2017).

8. 8.

Lackey, D. E. & Olefsky, J. M. Regulation of metabolism by the innate immune system. *Nat. Rev. Endocrinol.* **12**, 15–28 (2016).

9. 9.

Hoffmann, T. J. et al. A large multiethnic genome-wide association study of adult body mass index identifies novel loci. *Genetics* **210**, 499–515 (2018).

10. 10.

Vargas-Alarcon, G. et al. Interleukin 27 polymorphisms, their association with insulin resistance and their contribution to subclinical atherosclerosis. The GEA Mexican study. *Cytokine* **114**, 32–37 (2019).

11. 11.

Yoshida, H. & Hunter, C. A. The immunobiology of interleukin-27. *Ann. Rev. Immunol.* **33**, 417–443 (2015).

12. 12.

Yang, B. et al. IL-27 facilitates skin wound healing through induction of epidermal proliferation and host defense. *J. Invest. Dermatol.* **137**, 1166–1175 (2017).

13. 13.

Nam, H., Ferguson, B. S., Stephens, J. M. & Morrison, R. F. Modulation of IL-27 in adipocytes during inflammatory stress. *Obesity* **24**, 157–166 (2016).

14. 14.

Wolfrum, C. & Straub, L. G. Lessons from Cre-mice and indicator mice. *Handb. Exp. Pharmacol.* **251**, 37–54 (2019).

15. 15.

Kissig, M., Shapira, S. N. & Seale, P. SnapShot: brown and beige adipose thermogenesis. *Cell* **166**, 258–258 (2016).

16. 16.

Kajimura, S. & Saito, M. A new era in brown adipose tissue biology: molecular control of brown fat development and energy homeostasis. *Ann. Rev. Physiol.* **76**, 225–249 (2014).

17. 17.

Owaki, T., Asakawa, M., Fukai, F., Mizuguchi, J. & Yoshimoto, T. IL-27 induces Th1 differentiation via p38 MAPK/T-bet- and intercellular adhesion molecule-1/LFA-1/ERK1/2-dependent pathways. *J. Immunol.* **177**, 7579–7587 (2006).

18. 18.

Cao, W. et al. p38 mitogen-activated protein kinase is the central regulator of cyclic AMP-dependent transcription of the brown fat uncoupling protein 1 gene. *Mol. Cell. Biol.* **24**, 3057–3067 (2004).

19. 19.

Cao, W., Medvedev, A. V., Daniel, K. W. & Collins, S.  $\beta$ -Adrenergic activation of p38 MAP kinase in adipocytes: cAMP induction of the uncoupling protein 1 (UCP1) gene requires p38 MAP kinase. *J. Biol. Chem.* **276**, 27077–27082 (2001).

20. 20.

Pirzgalska, R. M. et al. Sympathetic neuron-associated macrophages contribute to obesity by importing and metabolizing norepinephrine. *Nat. Med.* **23**, 1309–1318 (2017).

21. 21.

Imai, T. et al. Identification and molecular characterization of fractalkine receptor CX3CR1, which mediates both leukocyte migration and adhesion. *Cell* **91**, 521–530 (1997).

22. 22.

Rosenwald, M., Perdikari, A., Rulicke, T. & Wolfrum, C. Bi-directional interconversion of brite and white adipocytes. *Nat. Cell Biol.* **15**, 659–667 (2013).

23. 23.

Zhang, S. et al. High susceptibility to liver injury in IL-27 p28 conditional knockout mice involves intrinsic interferon-gamma dysregulation of CD4<sup>+</sup> T cells. *Hepatology* **57**, 1620–1631 (2013).

## Acknowledgements

We thank A. Xu from Hongkong University, L. Ye from the Third Military Medical University, B. Li from Shanghai Jiao Tong University, Y. Qiu from Peking University, Y. Huo from Guangzhou Medical University and J. Chen from Sun Yat-Sen University for discussion, comments and technical guidance; and C. Cote for English language editing of this manuscript. This work is supported by the National Key Research and Development Program of China (no. 2020YFA0803502 to Z.Y.; no. 2017YFA0205200 to L.L.), the National Natural Science Foundation of China (nos 31830021, 32030036 and 31420103901 to Z.Y.; no. 81771957 to L.L.; no. 32070121 to H.Y.; no. 31800721 to Q. Wang; and no. 31500742 to Q.S.), the 111 Project (no. B16021 to Z.Y.), the Incubating Program from the Science and Technology Department of Guangdong Province of China (no. 2014A030308003 to Z.Y.), China Postdoctoral Science Foundation (nos 2018M633278 and 2020M683159 to Q. Wang; no. 2020M673045 to H.Z.).

## Author information

### Author notes

1. These authors contributed equally: Qian Wang, Dehai Li, Guangchao Cao, Qiping Shi
2. These authors jointly supervised this work: Ligong Lu, Hengwen Yang, Richard A. Flavell, Zhinan Yin

## Affiliations

1. Guangdong Provincial Key Laboratory of Tumor Interventional Diagnosis and Treatment, Zhuhai Institute of Translational Medicine, Zhuhai People's Hospital Affiliated with Jinan University, Jinan University, Zhuhai, China

Qian Wang, Dehai Li, Guangchao Cao, Jing Zhu, Mingyue Zhang, Qiong Wen, Hua Zhang, Zonghua Liu, Qinghua Zhou, Hongyun Lu, Yongjie Xin, Ligong Lu, Hengwen Yang & Zhinan Yin

2. The Biomedical Translational Research Institute, Faculty of Medical Science, Jinan University, Guangzhou, China

Qian Wang, Dehai Li, Guangchao Cao, Jing Zhu, Mingyue Zhang, Qiong Wen, Leqing Zhu, Hua Zhang, Guangqiang Li, Zonghua Liu, Qinghua Zhou, Hengwen Yang & Zhinan Yin

3. Department of Endocrine, The First Affiliated Hospital, Jinan University, Guangzhou, China

Qiping Shi

4. Key Laboratory for the Genetics of Developmental & Neuropsychiatric Disorders (Ministry of Education), Bio-X Institutes, Shanghai Jiao Tong University, Shanghai, China

Hao Cheng

5. Department of Immunobiology, School of Medicine, Yale University, New Haven, CT, USA

Hao Xu, Olga Spadaro, Vishwa Deep Dixit & Richard A. Flavell

6. The First Affiliated Hospital, Faculty of Medical Science, Jinan University, Guangzhou, China

Leqing Zhu & Guangqiang Li

7. Department of Medicine, School of Medicine, Yale University, New Haven, CT, USA

Rachel J. Perry & Gerald I. Shulman

8. Department of Cellular & Molecular Physiology, School of Medicine, Yale University, New Haven, CT, USA

Rachel J. Perry, Xiaoyong Yang & Gerald I. Shulman

9. Department of Comparative Medicine, School of Medicine, Yale University, New Haven, CT, USA

Olga Spadaro, Yunfan Yang, Xiaoyong Yang & Vishwa Deep Dixit

10. Hubei Key Laboratory of Cell Homeostasis, College of Life Sciences, Institute for Advanced Studies, Wuhan University, Wuhan, China

Shengqi He, Yong Chen & Yong Liu

11. Tsinghua Berkeley Shenzhen Institute (TBSI), Tsinghua University, Shenzhen, China

Baocheng Wang

12. Department of Endocrine, The Sixth Affiliated Hospital of Guangzhou Medical University, Qingyuan People's Hospital, Qingyuan, China

Caixian Yang

13. School of Life Sciences, Tianjin University, Tianjin, China

Xiaoli Wu

14. Guangdong-Hong Kong-Macau Institute of CNS Regeneration, Ministry of Education CNS Regeneration Collaborative Joint Laboratory, Jinan University, Guangzhou, China

Libing Zhou

15. Key Laboratory of Regenerative Medicine of Ministry of Education,  
Institute of Aging and Regenerative Medicine, Jinan University,  
Guangzhou, China

Zhenyu Ju

16. Department of Surgery, The First Affiliated Hospital of Jinan  
University, Guangzhou, China

Cunchuan Wang

## Contributions

Q. Wang, D.L., G.C. and Q.S. conceived this research. Q. Wang, D.L., J.Z., M.Z., H.C. and Q. Wen performed experiments and analysed data. Q.S., C.W. and C.Y. analysed the human samples. H.X. helped with HFD treatment. L. Zhu, H.Z., B.W. and G.L. facilitated in western blot experiments. R.J.P. carried out the metabolic cage experiments and O.S. assisted with cold challenge experiments. Y.Y., S.H. and Y.C. provided technical support for primary adipocyte culture. Z.L. helped in ordering reagents. X.W., Q.Z., Z.J., H.L. and Y.X. assisted in the revision of the manuscript. L. Zhou provided the cold room. C.W. carried out the gastric bypass surgery. X.Y., Y.L., G.I.S. and V.D.D. helped in conceiving the project and afforded guidance in discussions. Q. Wang, G.C. and Z.Y. wrote the manuscript with help from D.L., Q.S., J.Z. and M.Z. L.L., H.Y., R.A.F. and Z.Y. helped in conceiving the project, mentored and supervised its participants.

## Corresponding authors

Correspondence to [Ligong Lu](#), [Hengwen Yang](#), [Richard A. Flavell](#) or [Zhinan Yin](#).

## Ethics declarations

## Competing interests

Z.Y., Q. Wang and H.Y. have applied a patent with China National Intellectual Property Administration, with Jinan University as the applicant, Z.Y., Q. Wang and H.Y. as the inventors. The application number is 202110986914.X, and the patent covers the screening of IL-27R $\alpha$  agonists for promoting UCP1 production. The other authors (D.L., G.C., Q.S., J.Z., M.Z., H.C., Q. Wen, H.X., L. Zhu, H.Z., R.J.P., O.S., Y.Y., S.H., Y.C., B.W., G.L., Z.L., C.Y., X.W., L. Zhou, Q.Z., Z.J., H.L., Y.X., X.Y., C.W., Y.L., G.I.S., V.D.D., L.L. and R.A.F.) declare no competing interests.

## Additional information

**Peer review information** *Nature* thanks the anonymous reviewers for their contribution to the peer review of this paper.

**Publisher's note** Springer Nature remains neutral with regard to jurisdictional claims in published maps and institutional affiliations.

## Extended data figures and tables

### [Extended Data Fig. 1 Reduced serum IL-27 level in obese subjects.](#)

**a.** Serum from obese human subjects ( $n = 42$ ) and lean healthy controls ( $n = 26$ ) were used for detection of inflammatory factors by Bio-Rad Bio-Plex 200 Multiplexing Analyzer System. The body mass index (BMI) of individual subject was presented in the first panel. **b.** Serum IL-27 level in obese patients was detected by ELISA as in Figure 1a. Correlation of BMI and serum IL-27 level in obese subjects was analysed and shown ( $n = 32$ ). **c.** Correlation of fasting glucose and serum IL-27 level in type 2 diabetes (T2D) patients ( $n = 12$ ). Data are mean  $\pm$  s.d. of biologically independent samples. Two-tailed unpaired student's *t*-test (**a**); linear regression analysis (**b & c**). NS, not significant.

### [Source data](#)

## Extended Data Fig. 2 IL-27Ra deficiency aggravates HFD-induced obesity.

IL-27R $\alpha$  KO and WT mice at 8 weeks of age were fed on HFD or ND for 10 weeks (**a–f**). **a**. Histology (H&E) slides of epididymal white adipose tissue (eWAT), subcutaneous white adipose tissue (SCW) and brown adipose tissue (BAT). Scale bar = 50 $\mu$ m. **b**. Histology (H&E) and oil red O staining of liver from HFD treated mice. Scale bar = 100 $\mu$ m. Serum was collected after 10 weeks HFD treatment and triglyceride (**c**, n=6), (**d**) leptin (n = 5) and adiponectin (n = 4 for WT and n = 6 for KO) were detected. **e**. The infiltrated macrophages in the stromal vascular fraction (SVF) of epididymal fat were analysed by FACS, the statistical analysis of macrophage percentage in CD45+ is shown (n = 8 for WT and n = 11 for KO). **f**. Realtime PCR analysis of key cytokines in epididymal fat (eWAT) from mice fed on HFD for 10 weeks (n = 12 for WT-*Il4* and n = 10 for KO-*Il4*, n = 13-WT and n = 12-KO for the rest genes). **g**. C57BL/6J, IL-27R $\alpha$  KO and C57BL/6N mice were genotyped via *Nnt* gene PCR. **h–j**. IL-27R $\alpha$  KO and C57BL/6N mice at 8 weeks of age were fed on HFD for 10 weeks. **h**. Body weight was recorded each week (n = 14 for C57BL/6N and n = 10 for KO). **i**. Adipose tissues and livers were collected and weighted (n=5). **j**. GTT was performed (n = 14 for C57BL/6N and n = 10 for KO). **k**. The splenocytes were isolated from *Il27ra*+/-, *Il27ra*+- and *Il27ra*-/- mice and protein samples were used for immunoblotting analysis of IL-27R $\alpha$ . Each lane represents one biological independent sample. **l–n**. *Il27ra*+- and *Il27ra*++ mice at 8 weeks of age were fed on HFD for 10 weeks. **l**. Body weight was recorded each week (n = 10 for *Il27ra*++ and n = 5 for *Il27ra*+-). GTT (**m**, n = 3 for *Il27ra*++ and n = 6 for *Il27ra*+-) and ITT (**n**, n = 4 for *Il27ra*++ and n = 7 for *Il27ra*+-) were performed. **o**. IL-27R $\alpha$  KO (n = 18) and WT (n = 12) mice at 8 weeks of age were fed on HFD, GTT was performed after 4 weeks of HFD treatment. All experiments were repeated at least twice with similar results. Data are mean  $\pm$  s.e.m. of biologically independent samples. Two-tailed unpaired student's test (**c–f** & **i**); two-way ANOVA (**h**); two-way ANOVA with Sidak's multiple comparisons test (**j** & **l–o**). NS, not significant.

[Source data](#)

## Extended Data Fig. 3 Reduced energy expenditure and thermogenesis in IL-27 signalling deficient mice.

**a–c.** IL-27R $\alpha$  KO and WT mice at 8 weeks of age were placed in metabolic cages. The food intake (**a**, n = 8 for WT and n = 7 for KO), oxygen consumption (**b**, n = 8) and energy expenditure (**c**, n = 8) were shown. **d.** BAT and SCW tissues were isolated from WT-ND and IL-27R $\alpha$  KO-ND mice at 6–8 weeks of age, cut into small pieces (~0.003g for BAT and ~0.004g for SCW) and used for detection of basal oxygen consumption rate by Seahorse XF Analyzer (n = 5 mice per group, 18 pieces for WT-BAT, 23 pieces for KO-BAT and 17 pieces for SCW samples). **e & f.** IL-27R $\alpha$  KO and WT mice at 8 weeks of age were fed on HFD for 10 weeks, SCW were collected for RNA-seq analysis. **e.** Gene set enrichment analysis was performed for indicated pathways. Genes were ranked according to their expression. NES, normalized enrichment score; FDR, false discovery rate. **f.** Heat maps of differentially expressed genes in indicated pathway. **g.** Gene expression in SCW from IL-27R $\alpha$  KO and WT mice on normal diet were determined by real-time PCR (n = 9 for WT-*Ucp1*, WT-*Cidea*, WT-*Adipoq* and WT-*Retn*, n = 10 for WT-*Ppargc1a*, WT-*Ppara*, WT-*Cox8b*, WT-*Cox5a*, WT-*Prdm16* and WT-*Elovl3*, n = 11 for WT-*Pparg*, WT-*Fabp4* and WT-*Lep*, n = 8 for KO-*Ucp1*, n = 10 for KO-*Retn*, n = 11 for the rest KO mRNAs). **h.** Survival curve of IL-27R $\alpha$  KO and WT mice fed on ND in response to cold challenge (4 °C, n = 9 for WT and n = 11 for KO). **i.** Rectal temperature of mice fed on ND in response to cold challenge (4 °C, n = 9 for WT and n = 11 for KO). **j–l.** EBI-3 KO mice and WT controls fed on normal chow were challenged at 4 °C. The survival curve (**j**) and rectal temperature (**k**) were recorded and shown (n = 5 for WT and n = 6 for KO). After 12 hours of cold stimulation, BAT and SCW were collected, lysed and used for immunoblotting analysis of UCP1 (**l**). **m–p.** EBI-3 KO mice were i.p. injected with rmIL-27 (100 $\mu$ g/kg) or PBS every day for 7 days and then challenged at 4°C. **m.** Rectal temperature of mice in response to cold was shown (n = 6). **n.** Immunoblot analysis of protein extracts from SCW and BAT after 24 hours of cold challenge. UCP1 staining (**o**) and histology analysis (**p**) (Scale bar = 100 $\mu$ m). Representative sections were shown. (**l & n**) Each lane represents one biological independent sample and band densities were quantified with ImageJ, ratios of UCP1/HSP90 were normalized. All experiments were repeated at least twice with similar

results. Data are mean  $\pm$  s.e.m. Data represent biologically independent samples except for **d**. Two-tailed unpaired student's t-test (**d & g**); two-way ANOVA (**a–c**); two-way ANOVA with Sidak's multiple comparisons test (**i, k & m**); log-rank test (**h & j**); Gene Set Enrichment Analysis (**e**).

### Source data

### Extended Data Fig. 4 The counteracting obesity effects of IL-27Ra signalling was not through direct actions on CD2+ lymphoid or Lyz2+ myeloid cells.

**a.** Schematic model for the generation of *Il27ra*<sup>flx/flx</sup> mice. The *Il27ra* locus (top) was targeted by the targeting vector (second), which contains the homologous sequence of *Il27ra*, including two LoxP sites flanking exons 3&4, and a Neo selecting cassette. The linearized vector was subsequently delivered to embryonic stem cells (C57BL/6) via electroporation, followed by drug selection, PCR screening, and Southern Blot confirmation. Homologous recombination resulted in the floxed allele (Third). After confirming correctly targeted ES clones via Southern Blotting, selected clones were used for blastocyst microinjection to produce the F0 generation. The F1 were confirmed as germline-transmitted via crossbreeding F0 with Flp-deleter to delete Neo cassette (Fourth). After Cre recombination, the floxed *Il27ra* allele will results in the deletion of exons 3 and 4 (bottom). **b.** Genotyping of *Il27ra*<sup>ff</sup> mice. **c.** IL-27R $\alpha$  expression in spleen from *Il27ra*<sup>ff</sup> and WT mice were determined by Real-time PCR (n = 6, left) and Western Blot (right, each lane represents one biological independent sample). **d.** *Il27ra* gene expression in FACS sorted CD3+ T cells, CD45+ CD19+ B cells, CD45+ Lin- (CD3- CD4- CD8a- CD19- CD11b- Ly6c-) CD90.2+ CD127+ ILCs, CD45+ CD3- NK1.1+ NK cells from the spleen of *Il27ra*<sup>ff</sup> and *Cd2-Cre Il27ra*<sup>ff</sup> mice were determined by Real-time PCR (n = 6, left 4 panels). Thioglycollate was intraperitoneally injected into *Il27ra*<sup>ff</sup> and *Lyz2-Cre Il27ra*<sup>ff</sup> mice for 4 days, and then the peritoneal macrophages were collected for the detection of *Il27ra* gene expression by Real-time PCR (n = 6, last panel). **e-h.** *Il27ra*<sup>ff</sup>, *Cd2-Cre Il27ra*<sup>ff</sup> and *Lyz2-Cre Il27ra*<sup>ff</sup> mice at 8 weeks of age were fed on HFD for 10 weeks. **e.** Body weight was recorded each week (n = 21 for *Il27ra*<sup>ff</sup>,

n=11 for *Cd2-Cre Il27ra<sup>ff</sup>* and n = 18 for *Lyz2-Cre Il27ra<sup>ff</sup>*). GTT (**f**, n = 15 for *Il27ra<sup>ff</sup>*, n = 11 for *Cd2-Cre Il27ra<sup>ff</sup>* and n = 19 for *Lyz2-Cre Il27ra<sup>ff</sup>*) and ITT (**g**, n = 13 for *Il27ra<sup>ff</sup>*, n = 12 for *Cd2-Cre Il27ra<sup>ff</sup>* and n = 19 for *Lyz2-Cre Il27ra<sup>ff</sup>*) were performed after 10 weeks of HFD treatment. **h**. Adipose tissues were collected and weighted after 10 weeks of HFD treatment (n = 22 for *Il27ra<sup>ff</sup>*, n = 11 for *Cd2-Cre Il27ra<sup>ff</sup>* and n = 19 for *Lyz2-Cre Il27ra<sup>ff</sup>*). All experiments were repeated at least twice with similar results. Data are mean ± s.e.m. of biologically independent samples. Two-tailed unpaired student's test (**c**, **d**); two-way ANOVA (**e–g**); one-way ANOVA (**h**). NS, not significant.

### Source data

### Extended Data Fig. 5 The phenotypes of IL-27Ra KO and WT chimeras in HFD-induced obesity and adaptive thermogenesis.

**a.** Bone marrow cells from CD45.1 WT strain were transferred into irradiated CD45.2 IL-27Ra KO or CD45.2 WT hosts (1 x 10<sup>7</sup>cells/mouse) to generate chimera. Mice were housed for 8 weeks to reconstitute the immune system. Immune cells were isolated from different tissues as indicated, the percentages of donor (CD45.1+) and host (CD45.2+) cells in CD4+ T (top), CD19+ B (middle) or F4/80+ macrophages (bottom) were analysed via FACS (n = 3). **b–d.** Bone marrow chimeras were generated as in Fig. [3a](#) and fed on HFD. GTT (**b**, n = 13 for WT>WT, n = 11 for WT>KO, n = 12 for KO>WT and n = 10 for KO>KO) and ITT (**c**, n = 5 for WT>WT, n = 7 for WT>KO, n = 6 for KO>WT and n = 6 for KO>KO) were performed after 10 weeks of HFD treatment. **d.** Epididymal adipose (n = 6 for WT>WT, n = 4 for the rest groups), subcutaneous adipose, brown adipose tissue and liver (n = 6 for WT>WT, n = 5 for WT>KO, n = 5 for KO>WT and n = 4 for KO>KO) were collected and weighted after 10 weeks of HFD treatment. **e–g.** Chimeric mice fed on normal chow were challenged at 4 °C for 12 hours, SCW and BAT were collected for histology analysis (**e**, H&E, scale bar = 100μm) or immunohistochemical staining of UCP1 (**f**, scale bar = 100μm). Real-time PCR analysis of gene expression in SCW was also performed and shown (**g**, in WT>WT group, n = 15 for *Ucp1*, n=16 for *Cidea*, *Ppargc1a* and *Elovl3*, n = 17 for *Cox8b* and *Retn*,

n=18 for the rest genes; in WT>KO group, n = 11 for *Ucp1*, n = 12 for *Cidea*, *Ppargc1a*, *Ppara* and *Lep*, n=13 for *Cox8b*, *Prdm16* and *Retn*, n = 14 for *Cox5a* and *Fabp4*, n = 15 for *Elovl3*, *Pparg* and *Adipoq*). All experiments were repeated at least twice with similar results. Data are mean ± s.e.m. of biologically independent samples. Two-tailed unpaired student's t-test (**a & g**); one-way ANOVA (**d**); two-way ANOVA with Sidak's multiple comparisons test (**b & c**).

### [Source data](#)

### [Extended Data Fig. 6 \*Adipoq-Cre Il27ra<sup>ff</sup>\* mice were hypersensitive to HFD-induced obesity.](#)

- a.** Immunoblot analysis of IL-27R $\alpha$  expression in stromal vascular fraction (SVF) and adipocyte fraction of SCW and BAT from WT mice. **b.** Immunoblot analysis of IL-27R $\alpha$  during the primary beige adipocyte differentiation from SVF of WT SCW. **c.** IL-27R $\alpha$  expression in adipocyte fraction of eWAT / SCW or spleen from *Il27ra<sup>ff</sup>* and *Adipoq-Cre Il27ra<sup>ff</sup>* mice were determined by Real-time PCR (above; for *Il27ra<sup>ff</sup>* samples, n=6 for eWAT and spleen, n = 9 for SCW; for *Adipoq-Cre Il27ra<sup>ff</sup>* samples, n = 7 for eWAT, n = 10 for SCW and n = 5 for spleen) and Western Blot (below). **d.** Primary adipocytes were differentiated *in vitro* from SCW of *Il27ra<sup>ff</sup>* and *Adipoq-Cre Il27ra<sup>ff</sup>* mice. IL-27R $\alpha$  protein expression was detected by immunofluorescence. IL-27R $\alpha$  (Red), lipid droplet (Bodipy, Green) and cell nucleus (DAPI, Blue), scale bar = 20 $\mu$ m. **e-l.** *Adipoq-Cre Il27ra<sup>ff</sup>* mice and *Il27ra<sup>ff</sup>* controls at 8 weeks of age were fed on HFD for 10 weeks. **e.** Histology (H&E) staining of epididymal and subcutaneous fat tissue from HFD treated mice. Scale bar=100 $\mu$ m. GTT (**f**, n = 9 for *Il27ra<sup>ff</sup>* and n = 7 for *Adipoq-Cre Il27ra<sup>ff</sup>*), ITT (**g**, n=19 for *Il27ra<sup>ff</sup>* and n=14 for *Adipoq-Cre Il27ra<sup>ff</sup>*) and the weight of indicated tissues (**h**, n = 9 for *Il27ra<sup>ff</sup>* and n = 7 for *Adipoq-Cre Il27ra<sup>ff</sup>*) were detected after 10 weeks of HFD treatment. **i.** Histology (H&E) and oil red O staining of liver from HFD treated mice. Scale bar = 100 $\mu$ m. **j.** Serum cholesterol (CHOL, n = 8 for *Il27ra<sup>ff</sup>* and n = 7 for *Adipoq-Cre Il27ra<sup>ff</sup>*) and liver triglyceride (TG, n=9 for *Il27ra<sup>ff</sup>* and n=7 for *Adipoq-Cre Il27ra<sup>ff</sup>*) were detected. **k.** Realtime PCR analysis of inflammatory genes expression in eWAT (n = 9

for *Il27ra*<sup>ff</sup> samples, for *Adipoq-Cre Il27ra*<sup>ff</sup> group, n = 10 for *Il12b*, n=13 for *Il6* and n = 12 for the rest genes). **I.** Realtime PCR analysis of adipose related genes expression in SCW of mice housed at room temperature (for *Il27ra*<sup>ff</sup> samples, n = 9 for *Ucp1*, n = 10 for *Ppara*, *Elovl3* and *Retn*, n=12 for *Cox5a* and n = 11 for the rest genes; for *Adipoq-Cre Il27ra*<sup>ff</sup> group, n = 12 for *Cox5a* and *Elovl3*, n = 13 for the rest genes). **m.** *Adipoq-Cre Il27ra*<sup>ff</sup> and *Il27ra*<sup>ff</sup> mice fed on normal chow were challenged at 4 °C for 12 hours, SCW and BAT were collected for histology analysis (H&E). Scale bar = 50μm. All experiments were repeated at least twice with similar results. Data are mean ± s.e.m. of biologically independent samples. Two-tailed unpaired student's t-test (**c**, **h**, **j-l**); two-way ANOVA with Sidak's multiple comparisons test (**f** & **g**). NS, not significant.

### Source data

### Extended Data Fig. 7 IL-27 upregulates UCP1 and improves the browning of subcutaneous white adipose tissue.

**a.** *Il27ra*<sup>ff</sup> and *Ucp1-Cre-ER*<sup>T2</sup> *Il27ra*<sup>ff</sup> mice at 8 weeks of age were i.p. injected with tamoxifen (2mg/mouse) for 4 times in a period of 7days, after another 7 days, SCWs and BATs were collected and used for immunoblot analysis of IL-27Ra expression. **b&c.** *Il27ra*<sup>ff</sup>(n=10) and *Ucp1-Cre-ER*<sup>T2</sup> *Il27ra*<sup>ff</sup>(n = 12) mice at 8 weeks of age were pre-treated with tamoxifen and then fed on HFD for 10 weeks. GTT (**b**, n = 10 for *Il27ra*<sup>ff</sup> and n = 12 for *Ucp1-Cre-ER*<sup>T2</sup> *Il27ra*<sup>ff</sup>) and ITT (**c**, n = 9 for *Il27ra*<sup>ff</sup> and n = 12 for *Ucp1-Cre-ER*<sup>T2</sup> *Il27ra*<sup>ff</sup>) were performed after 10 weeks of HFD treatment. **d.** *Il27ra*<sup>ff</sup> and *Ucp1-Cre-ER*<sup>T2</sup> *Il27ra*<sup>ff</sup> mice fed on normal chow were pre-treated with tamoxifen and then challenged at 4 °C for 12 hours, SCW and BAT were collected for histology analysis (H&E). Scale bar = 200μm. **e.** Primary beige adipocytes were generated *in vitro* from the SVF of WT SCW and then treated with rmIL-27 (100ng/ml) or PBS for 24 hours. Cells were lysed and protein extracts were used for Immunoblot analysis (each lane represents one biological independent sample). BAT tissue from WT mice was set as positive control. **f.** Immunoblot analysis of STAT1 phosphorylation in extracts from WT primary beige adipocytes treated with rmIL-27 (100ng/ml) for indicated time. IFN-γ (10ng/ml, 30 min) treated

splenocytes were set as positive control (Con). **g–h.** Primary beige adipocytes from SCW of WT mice were generated *in vitro*. Two different p38 MAPK inhibitor (SB203580, 10μM and SB202190, 5μM) or three STAT3 inhibitor (C188-9, 10μM; stattic, 10μM or HO-3867, 20μM) were added into the culture medium 0.5 h before and in the duration of rmIL-27 treatment (100ng/ml for 12 h). The expression of UCP1 was detected via immunoblot. (**e, g & h**) Band densities were quantified with ImageJ and normalized. All experiments were repeated at least twice with similar results. Data are mean ± s.e.m. of biologically independent samples. Two-way ANOVA with Sidak's multiple comparisons test (**b & c**).

### Source data

### Extended Data Fig. 8 IL-27 promotes the activation of thermogenesis with promising therapeutic potential.

**a–i.** *Il27ra<sup>ff</sup>* and *Adipoq-Cre Il27ra<sup>ff</sup>* mice were fed on HFD for 32 weeks and then i.p. injected with rmIL-27 (100μg/kg) or PBS every other day for 15 days. **a.** Serum were collected and used for detection of inflammatory factors by Bio-Rad Bio-Plex 200 Multiplexing Analyzer System (n = 8 for *Il27ra<sup>ff</sup>*+ PBS, n=4 for *Adipoq-Cre Il27ra<sup>ff</sup>*+ PBS and all IL-27 treatment groups). **b.** Representative histological sections (H&E) of indicated tissues, scale bar = 500μm. **c.** The percentages of the infiltrating CD4 or CD8 T cells, and the cytokines production in CD4 T cells from liver were analysed by FACS (n = 8 for *Il27ra<sup>ff</sup>*+ PBS, n = 4 for *Adipoq-Cre Il27ra<sup>ff</sup>*+ PBS, n = 5 for IL-27 treatment groups). Body weight (**d**), GTT (**e**) and ITT (**f**) of *Il27ra<sup>ff</sup>* mice were detected and recorded (n = 8 for PBS and n=5 for IL-27). Body weight (**g**), GTT (**h**) and ITT (**i**) of *Adipoq-Cre Il27ra<sup>ff</sup>* mice were also detected and recorded (n = 4 for PBS and n=5 for IL-27). **j–l.** *Ucp1-Cre-ER<sup>T2</sup> Il27ra<sup>ff</sup>* mice were fed on HFD for 12 weeks, pretreated with tamoxifen and then i.p. injected with rmIL-27 (100μg/kg) or PBS every other day for 21 days. The body weight (**j**), glucose tolerance test (**k**) and insulin tolerance test (**l**) were detected and recorded (n = 5 for PBS and n = 6 for IL-27). **m–p.** UCP1 KO mice were fed on HFD for 20 weeks and then i.p. injected with rmIL-27 (100μg/kg) or PBS every other day for 15 days. **m.** Body weight was recorded at indicated time points (n=6). **n.** The

adipose tissues and livers were collected and weighted after 15 days of rmIL-27 treatment ( $n = 6$ ). GTT (**o**,  $n = 6$ ) and ITT (**p**,  $n = 4$ ) were performed after 15 days of rmIL-27 treatment. All experiments were repeated at least twice with similar results. Data are mean  $\pm$  s.e.m. of biologically independent samples. One-way ANOVA (**a & c**), two-way ANOVA (**d, g, j & m**); two-way ANOVA with Sidak's multiple comparisons test (**e, f, h, i, k, l, o & p**); two-tailed unpaired student's t-test (**n**).

### Source data

### Extended Data Fig. 9 CX3CR1<sup>+</sup> cells were an important source of IL-27 during HFD-induced obesity.

**a–c.** *Lyz2-Cre Il27p28<sup>ff</sup>* and *Il27p28<sup>ff</sup>* littermates at 8 weeks of age were treated with high fat diet (HFD) for 10 weeks. **a.** Body weight changes were recorded each week ( $n = 9$  for *Il27p28<sup>ff</sup>* and  $n = 6$  for *Lyz2-Cre Il27p28<sup>ff</sup>*). Intraperitoneal GTT (**b**) and ITT (**c**) were performed after 10 weeks of treatment ( $n = 7$  for *Il27p28<sup>ff</sup>* and  $n = 6$  for *Lyz2-Cre Il27p28<sup>ff</sup>*). **d–g.** *Itgax-Cre Il27p28<sup>ff</sup>* and *Il27p28<sup>ff</sup>* littermates at 8 weeks of age were fed on HFD for 10 weeks. Body weight changes were recorded each week (**d**,  $n = 8$  for *Il27p28<sup>ff</sup>* and  $n = 15$  for *Itgax-Cre Il27p28<sup>ff</sup>*). Intraperitoneal GTT (**e**,  $n = 8$  for *Il27p28<sup>ff</sup>* and  $n = 15$  for *Itgax-Cre Il27p28<sup>ff</sup>*) and ITT (**f**,  $n = 6$ ) was performed after 10 weeks of treatment. **g.** Adipose tissues were collected and weighted after 10 weeks of HFD treatment ( $n = 8$  for *Il27p28<sup>ff</sup>* and  $n = 15$  for *Itgax-Cre Il27p28<sup>ff</sup>*). **h&i.** *Adipoq-Cre Il27p28<sup>ff</sup>* and *Il27p28<sup>ff</sup>* littermates at 8 weeks of age were fed on HFD for 10 weeks. **h.** Body weight was recorded each week ( $n = 6$ ). **i.** Intraperitoneal GTT was performed after 10 weeks of treatment ( $n = 6$ ). **j–l.** *Cx3cr1-Cre Il27p28<sup>ff</sup>* and *Il27p28<sup>ff</sup>* littermates at 8 weeks of age were fed on HFD for 10 weeks. **j.** Body weight was recorded each week ( $n = 8$ ). Intraperitoneal GTT (**k**) and ITT (**l**) were performed after 10 weeks of treatment ( $n = 8$ ). All experiments were repeated at least twice with similar results. Data are mean  $\pm$  s.e.m. of biologically independent samples. Two-way ANOVA (**a, d & h**); two-way ANOVA with Sidak's multiple comparisons test (**b, c, e, f & i–l**); two-tailed unpaired student's t-test (**g**).

[Source data](#)

## Supplementary information

### [Supplementary Figures](#)

Supplementary Figure 1 contains the uncropped images of the western blot experiments and Supplementary Figure 2 shows the gating strategies for the FACS data in Extended Data Figure 2e.

### [Reporting Summary](#)

### [Supplementary Table 1](#)

Characteristics of human participants with obesity and control participants with a healthy BMI.

### [Supplementary Table 2](#)

Characteristics of the individuals with type 2 diabetes in Extended Data Fig. 1c.

### [Supplementary Table 3](#)

Characteristics of the human participants in Fig. 1b.

### [Supplementary Table 4](#)

Gene set enrichment analysis of *Il27ra*-KO HFD versus WT HFD for Extended Data Fig. 3e, f.

### [Supplementary Table 5](#)

Primer sequences for qPCR.

## **Source data**

[\*\*Source Data Fig. 1\*\*](#)

[\*\*Source Data Fig. 2\*\*](#)

[\*\*Source Data Fig. 3\*\*](#)

[\*\*Source Data Fig. 4\*\*](#)

[\*\*Source Data Extended Data Fig. 1\*\*](#)

[\*\*Source Data Extended Data Fig. 2\*\*](#)

[\*\*Source Data Extended Data Fig. 3\*\*](#)

[\*\*Source Data Extended Data Fig. 4\*\*](#)

[\*\*Source Data Extended Data Fig. 5\*\*](#)

[\*\*Source Data Extended Data Fig. 6\*\*](#)

[\*\*Source Data Extended Data Fig. 7\*\*](#)

[\*\*Source Data Extended Data Fig. 8\*\*](#)

[\*\*Source Data Extended Data Fig. 9\*\*](#)

## **Rights and permissions**

[\*\*Reprints and Permissions\*\*](#)

## **About this article**

## Cite this article

Wang, Q., Li, D., Cao, G. *et al.* IL-27 signalling promotes adipocyte thermogenesis and energy expenditure. *Nature* **600**, 314–318 (2021). <https://doi.org/10.1038/s41586-021-04127-5>

- Received: 03 December 2018
- Accepted: 13 October 2021
- Published: 24 November 2021
- Issue Date: 09 December 2021
- DOI: <https://doi.org/10.1038/s41586-021-04127-5>

## Share this article

Anyone you share the following link with will be able to read this content:

[Get shareable link](#)

Sorry, a shareable link is not currently available for this article.

[Copy to clipboard](#)

Provided by the Springer Nature SharedIt content-sharing initiative

---

This article was downloaded by **calibre** from <https://www.nature.com/articles/s41586-021-04127-5>

- Article
- [Published: 24 November 2021](#)

# The CLIP1–LTK fusion is an oncogenic driver in non-small-cell lung cancer

- [Hiroki Izumi<sup>1</sup>](#)<sup>na1</sup>,
- [Shingo Matsumoto<sup>1</sup>](#)<sup>na1</sup>,
- [Jie Liu<sup>2</sup>](#),
- [Kosuke Tanaka<sup>2</sup>](#),
- [Shunta Mori<sup>1</sup>](#),
- [Kumiko Hayashi<sup>3</sup>](#),
- [Shogo Kumagai<sup>4</sup>](#),
- [Yuji Shibata<sup>1</sup>](#),
- [Takuma Hayashida<sup>2,5</sup>](#),
- [Kana Watanabe<sup>6</sup>](#),
- [Tatsuro Fukuhara](#) ORCID: [orcid.org/0000-0003-0440-470X<sup>6</sup>](https://orcid.org/0000-0003-0440-470X),
- [Takaya Ikeda<sup>1</sup>](#),
- [Kiyotaka Yoh<sup>1</sup>](#),
- [Terufumi Kato<sup>7</sup>](#),
- [Kazumi Nishino<sup>8</sup>](#),
- [Atsushi Nakamura<sup>9</sup>](#),
- [Ichiro Nakachi<sup>10</sup>](#),
- [Shoichi Kuyama<sup>11</sup>](#),
- [Naoki Furuya](#) ORCID: [orcid.org/0000-0001-7162-5946<sup>12</sup>](https://orcid.org/0000-0001-7162-5946),
- [Jun Sakakibara-Konishi<sup>13</sup>](#),
- [Isamu Okamoto<sup>14</sup>](#),
- [Kageaki Taima<sup>15</sup>](#),
- [Noriyuki Ebi<sup>16</sup>](#),

- [Haruko Daga<sup>17</sup>](#),
- [Akira Yamasaki<sup>18</sup>](#),
- [Masahiro Kodani<sup>18</sup>](#),
- [Hibiki Udagawa<sup>1,2</sup>](#),
- [Keisuke Kirita<sup>1</sup>](#),
- [Yoshitaka Zenke<sup>1</sup>](#),
- [Kaname Nosaki<sup>1</sup>](#),
- [Eri Sugiyama<sup>1</sup>](#),
- [Tetsuya Sakai<sup>1</sup>](#),
- [Tokiko Nakai<sup>19</sup>](#),
- [Genichiro Ishii<sup>19</sup>](#),
- [Seiji Niho<sup>1</sup>](#),
- [Atsushi Ohtsu<sup>20</sup>](#),
- [Susumu S. Kobayashi](#)    ORCID: [orcid.org/0000-0003-2262-4001<sup>2,5,21</sup>](https://orcid.org/0000-0003-2262-4001)  
 &
- [Koichi Goto](#)    ORCID: [orcid.org/0000-0002-3023-2510<sup>1</sup>](https://orcid.org/0000-0002-3023-2510)

*Nature* volume 600, pages 319–323 (2021)

- 6708 Accesses
- 128 Altmetric
- [Metrics details](#)

## Subjects

- [Non-small-cell lung cancer](#)
- [Translational research](#)

## Abstract

Lung cancer is one of the most aggressive tumour types. Targeted therapies stratified by oncogenic drivers have substantially improved therapeutic outcomes in patients with non-small-cell lung cancer (NSCLC)<sup>1</sup>. However, such oncogenic drivers are not found in 25–40% of cases of lung

adenocarcinoma, the most common histological subtype of NSCLC<sup>2</sup>. Here we identify a novel fusion transcript of *CLIP1* and *LTK* using whole-transcriptome sequencing in a multi-institutional genome screening platform (LC-SCRUM-Asia, UMIN000036871). The *CLIP1–LTK* fusion was present in 0.4% of NSCLCs and was mutually exclusive with other known oncogenic drivers. We show that kinase activity of the *CLIP1–LTK* fusion protein is constitutively activated and has transformation potential. Treatment of Ba/F3 cells expressing *CLIP1–LTK* with lorlatinib, an ALK inhibitor, inhibited *CLIP1–LTK* kinase activity, suppressed proliferation and induced apoptosis. One patient with NSCLC harbouring the *CLIP1–LTK* fusion showed a good clinical response to lorlatinib treatment. To our knowledge, this is the first description of *LTK* alterations with oncogenic activity in cancers. These results identify the *CLIP1–LTK* fusion as a target in NSCLC that could be treated with lorlatinib.

This is a preview of subscription content

## Access options

Subscribe to Journal

Get full journal access for 1 year

\$199.00

only \$3.90 per issue

[Subscribe](#)

All prices are NET prices.

VAT will be added later in the checkout.

Tax calculation will be finalised during checkout.

Rent or Buy article

Get time limited or full article access on ReadCube.

from \$8.99

[Rent or Buy](#)

All prices are NET prices.

**Additional access options:**

- [Log in](#)
- [Learn about institutional subscriptions](#)

**Fig. 1: Identification of the *CLIP1–LTK* fusion.**

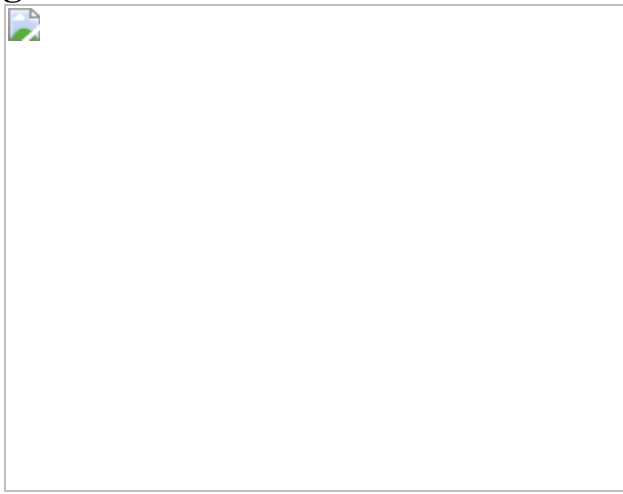
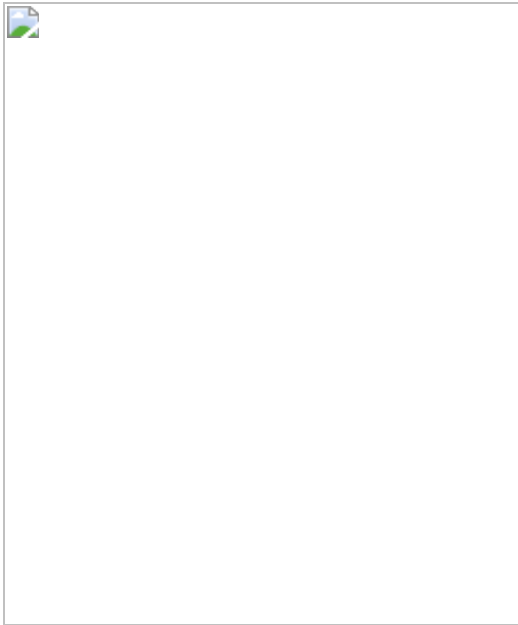


**Fig. 2: Transforming activity of the CLIP1-LTK fusion.**



**Fig. 3: Lorlatinib inhibits CLIP1-LTK kinase activity and suppresses tumour growth.**



## Data availability

The WTS data that support the findings of this study are not publicly available and restrictions apply to the availability of these data. Such WTS data are available through the corresponding authors for academic non-commercial research purposes upon reasonable request, and subject to review of a project proposal that will be evaluated by a LC-SCRUM-Asia data access committee, entering into an appropriate data access agreement and subject to any applicable ethical approvals. The presence of *LTK* fusion was explored in various types of cancer using publicly available data generated by TCGA consortium (<https://gdc.cancer.gov>), accessed through cBioPortal (<https://www.cbioportal.org/datasets>). Source data are provided with this paper.

## References

1. 1.

- Konig, D., Savic Prince, S. & Rothschild, S. I. Targeted therapy in advanced and metastatic non-small cell lung cancer. An update on treatment of the most important actionable oncogenic driver alterations. *Cancers* **13**, 713 (2021).

2. 2.

Saito, M. et al. Gene aberrations for precision medicine against lung adenocarcinoma. *Cancer Sci.* **107**, 713–720 (2016).

3. 3.

The Cancer Genome Atlas Research Network. Comprehensive molecular profiling of lung adenocarcinoma. *Nature* **511**, 543–550 (2014).

4. 4.

Fernandez-Cuesta, L. et al. CD74–NRG1 fusions in lung adenocarcinoma. *Cancer Discov.* **4**, 415–422 (2014).

5. 5.

Non-small cell lung cancer version 4.2021 *National Comprehensive Cancer Network*  
[https://www.nccn.org/professionals/physician\\_gls/pdf/nscl.pdf](https://www.nccn.org/professionals/physician_gls/pdf/nscl.pdf) (2021).

6. 6.

Roll, J. D. & Reuther, G. W. ALK-activating homologous mutations in LTK induce cellular transformation. *PLoS ONE* **7**, e31733 (2012).

7. 7.

Scheel, J. et al. Purification and analysis of authentic CLIP-170 and recombinant fragments. *J. Biol. Chem.* **274**, 25883–25891 (1999).

8. 8.

Grigoryan, G. & Keating, A. E. Structural specificity in coiled-coil interactions. *Curr. Opin. Struct. Biol.* **18**, 477–483 (2008).

9. 9.

Varmus, H. E. The molecular genetics of cellular oncogenes. *Annu. Rev. Genet.* **18**, 553–612 (1984).

10. 10.

Warmuth, M., Kim, S., Gu, X. J., Xia, G. & Adrián, F. Ba/F3 cells and their use in kinase drug discovery. *Curr. Opin. Oncol.* **19**, 55–60 (2007).

11. 11.

Soda, M. et al. Identification of the transforming EML4–ALK fusion gene in non-small-cell lung cancer. *Nature* **448**, 561–566 (2007).

12. 12.

Greulich, H. et al. Oncogenic transformation by inhibitor-sensitive and -resistant EGFR mutants. *PLoS Med.* **2**, e313 (2005).

13. 13.

Kobayashi, S. et al. An alternative inhibitor overcomes resistance caused by a mutation of the epidermal growth factor receptor. *Cancer Res.* **65**, 7096–7101 (2005).

14. 14.

Yasuda, H. et al. Structural, biochemical, and clinical characterization of epidermal growth factor receptor (EGFR) exon 20 insertion mutations in lung cancer. *Sci. Transl. Med.* **5**, 216ra177 (2013).

15. 15.

Zou, H. Y. et al. PF-06463922, an ALK/ROS1 inhibitor, overcomes resistance to first and second generation ALK inhibitors in preclinical models. *Cancer Cell* **28**, 70–81 (2015).

16. 16.

Yamada, S. et al. Expression of a chimeric CSF1R–LTK mediates ligand-dependent neurite outgrowth. *Neuroreport* **19**, 1733–1738 (2008).

17. 17.

Bruno, R. & Fontanini, G. Next generation sequencing for gene fusion analysis in lung cancer: a literature review. *Diagnostics* **10**, 521 (2020).

18. 18.

Kohno, T. et al. Beyond ALK–RET, ROS1 and other oncogene fusions in lung cancer. *Transl. Lung Cancer Res.* **4**, 156–164 (2015).

19. 19.

The Cancer Genome Atlas Research Network. Integrated genomic characterization of papillary thyroid carcinoma. *Cell* **159**, 676–690 (2014).

20. 20.

Yoshihara, K. et al. The landscape and therapeutic relevance of cancer-associated transcript fusions. *Oncogene* **34**, 4845–4854 (2015).

21. 21.

Muller-Tidow, C. et al. High-throughput analysis of genome-wide receptor tyrosine kinase expression in human cancers identifies potential novel drug targets. *Clin. Cancer Res.* **10**, 1241–1249 (2004).

22. 22.

Carvalho, P., Gupta, M. L., Jr., Hoyt, M. A. & Pellman, D. Cell cycle control of kinesin-mediated transport of Bik1 (CLIP-170) regulates microtubule stability and dynein activation. *Dev. Cell* **6**, 815–829 (2004).

23. 23.

Drilon, A. et al. Cabozantinib in patients with advanced RET-rearranged non-small-cell lung cancer: an open-label, single-centre, phase 2, single-arm trial. *Lancet Oncol.* **17**, 1653–1660 (2016).

24. 24.

Kuroda, N. et al. ALK rearranged renal cell carcinoma (ALK-RCC): a multi-institutional study of twelve cases with identification of novel partner genes CLIP1, KIF5B and KIAA1217. *Mod. Pathol.* **33**, 2564–2579 (2020).

25. 25.

Pinsolle, J. et al. A rare fusion of CLIP1 and ALK in a case of non-small-cell lung cancer with neuroendocrine features. *Clin. Lung Cancer* **20**, e535–e540 (2019).

26. 26.

Yeh, I. et al. Clinical, histopathologic, and genomic features of Spitz tumors with ALK fusions. *Am. J. Surg. Pathol.* **39**, 581–591 (2015).

27. 27.

Gainor, J. F. et al. Molecular mechanisms of resistance to first- and second-generation ALK inhibitors in ALK-rearranged lung cancer. *Cancer Discov.* **6**, 1118–1133 (2016).

28. 28.

Haas, B. J. et al. Accuracy assessment of fusion transcript detection via read-mapping and de novo fusion transcript assembly-based methods. *Genome Biol.* **20**, 213 (2019).

29. 29.

Pear, W. S. et al. Efficient and rapid induction of a chronic myelogenous leukemia-like myeloproliferative disease in mice receiving P210 bcr/abl-transduced bone marrow. *Blood* **92**, 3780–3792 (1998).

30. 30.

Borowicz, S. et al. The soft agar colony formation assay. *J. Vis. Exp.* **(92)**, e51998 (2014).

31. 31.

Tomayko, M. M. & Reynolds, C. P. Determination of subcutaneous tumor size in athymic (nude) mice. *Cancer Chemother. Pharmacol.* **24**, 148–154 (1989).

## Acknowledgements

We thank Y. Murata and PREMIA for administrative assistance with managing clinical samples, molecular screening and the clinico-genomic database in LC-SCRUM-Asia; and T. Y. Morita for assistance with flow cytometry analyses. This work was supported by the Princess Takamatsu Cancer Research Fund 18-250 (S.S.K.), JSPS KAKENHI Grant Number JP20K17215 (H.I.), JP16K21746 (S.S.K.) and JP21K15541 (K. Tanaka.), the National Cancer Center Research and Development Fund 31-A-5 (A.O.), 31-A-6 (S.S.K) and 28-A-6 (K.G.), and AMED Grant Number JP21ck0106289 (K.G.), JP21ck0106294 (K.Y.), JP21ck0106483 (K. Nosaki), JP21ck0106568 (K.G.), JP20ck0106411 (S. Matsumoto), JP20ck0106449 (I.O.), JP20ck0106450 (S.N.), JP20ak0101050 (K. Tsuchihara), JP18Ik0201056 (A.O.), JP18kk0205004 (H. Nakagama), JP17Ack0106148 (K.G.), JP17Ack0106147 (S. Yano), and JP16ck0106041 (K.G.). Molecular screening in LC-SCRUM-Asia was supported by Amgen, Astellas, AstraZeneca, Boehringer Ingelheim, Bristol-Myers Squibb, Chugai, Daiichi sankyo, Eisai, Janssen, Kyowa kirin, Merck, Medical & Biological Laboratories, MSD, Novartis, Ono, Pfizer, Sumitomo Dainippon, Taiho and Takeda. WTS was supported by Merus.

# **Author information**

## Author notes

1. These authors contributed equally: Hiroki Izumi and Shingo Matsumoto

## Affiliations

1. Department of Thoracic Oncology, National Cancer Center Hospital East, Kashiwa, Japan

Hiroki Izumi, Shingo Matsumoto, Shunta Mori, Yuji Shibata, Takaya Ikeda, Kiyotaka Yoh, Hibiki Udagawa, Keisuke Kirita, Yoshitaka Zenke, Kaname Nosaki, Eri Sugiyama, Tetsuya Sakai, Seiji Niho & Koichi Goto

2. Division of Translational Genomics, Exploratory Oncology Research and Clinical Trial Center, National Cancer Center, Kashiwa, Japan

Jie Liu, Kosuke Tanaka, Takuma Hayashida, Hibiki Udagawa & Susumu S. Kobayashi

3. LSI Medience Corporation Central Laboratory, Itabashi-ku, Japan

Kumiko Hayashi

4. Division of Cancer Immunology, Research Institute/Exploratory Oncology Research and Clinical Trial Center, National Cancer Center, Kashiwa, Japan

Shogo Kumagai

5. Department of Integrated Biosciences, Graduate School of Frontier Sciences, The University of Tokyo, Kashiwa, Japan

Takuma Hayashida & Susumu S. Kobayashi

6. Department of Respiratory Medicine, Miyagi Cancer Center, Natori, Japan

Kana Watanabe & Tatsuro Fukuhara

7. Department of Thoracic Oncology, Kanagawa Cancer Center, Yokohama, Japan

Terufumi Kato

8. Department of Thoracic Oncology, Osaka International Cancer Institute, Osaka, Japan

Kazumi Nishino

9. Department of Pulmonary Medicine, Sendai Kousei Hospital, Sendai, Japan

Atsushi Nakamura

10. Pulmonary Division, Department of Internal Medicine, Saiseikai Utsunomiya Hospital, Utsunomiya, Japan

Ichiro Nakachi

11. Department of Respiratory Medicine, National Hospital Organization Iwakuni Clinical Center, Iwakuni, Japan

Shoichi Kuyama

12. Division of Respiratory Medicine, Department of Internal Medicine, St Marianna University School of Medicine, Kawasaki, Japan

Naoki Furuya

13. First Department of Medicine, Hokkaido University Hospital, Sapporo, Japan

Jun Sakakibara-Konishi

14. Research Institute for Diseases of the Chest, Graduate School of Medical Sciences, Kyushu University, Fukuoka, Japan

Isamu Okamoto

15. Department of Respiratory Medicine, Hirosaki University Graduate School of Medicine, Hirosaki, Japan

Kageaki Taima

16. Department of Respiratory Medicine, Iizuka Hospital, Iizuka, Japan

Noriyuki Ebi

17. Department of Medical Oncology, Osaka City General Hospital, Osaka, Japan

Haruko Daga

18. Division of Respiratory Medicine and Rheumatology, Department of Multidisciplinary Internal Medicine, Faculty of Medicine, Tottori University, Yonago, Japan

Akira Yamasaki & Masahiro Kodani

19. Department of Pathology and Clinical Laboratories, National Cancer Center, Kashiwa, Japan

Tokiko Nakai & Genichiro Ishii

20. Department of Gastroenterology and Gastrointestinal Oncology, National Cancer Center Hospital East, Kashiwa, Japan

Atsushi Ohtsu

21. Department of Medicine, Beth Israel Deaconess Medical Center, Harvard Medical School, Boston, MA, USA

Susumu S. Kobayashi

## **Contributions**

H.I., S. Matsumoto, S.S.K. and K.G. conceived the idea and designed the experiments. H.I., S. Mori, S. Matsumoto, K.W., T.F., K.Y., A.O. and K.G. treated patients and interpreted data. H.I. performed cloning and mutagenesis of expression constructs for in vitro analysis, J.L., S. Kumagai and S.S.K. generated stable cell lines. H.I., J.L., K. Tanaka., S. Mori, T.H. and S.S.K. carried out biochemical analysis. K.H. performed FISH analysis. H.I., S. Matsumoto, Y.S., S. Mori, K.W., T.F., T.I., K.Y., T.K., K. Nishino, A.N., I.N., S. Kuyama, N.F., J.S.-K., I.O., K. Taima., N.E., H.D., A.Y., M.K., H.U., K.K., Y.Z., K. Nosaki, E.S., T.S., S.N. and K.G. planned and performed screening for the gene fusion in LC-SCRUM-Asia cohorts. T.N. and G.I. performed pathological evaluation. S.S.K. and K.G. supervised the project. H.I., S. Matsumoto, K.Y., S.S.K. and K.G. wrote the manuscript with input from all authors.

## **Corresponding authors**

Correspondence to [Susumu S. Kobayashi](#) or [Koichi Goto](#).

## **Ethics declarations**

## **Competing interests**

H.I. reports research support from Amgen and personal fees (honoraria) from Ono. S. Matsumoto reports research support from Chugai, Novartis, Eli Lilly, Merck and MSD, and personal fees (honoraria) from AstraZeneca, Chugai, Novartis, Pfizer and Eli Lilly. Y.S. reports research support from MSD, and personal fees (honoraria) from Ono, Pfizer, Chugai, Novartis, Bristol-Myers Squibb, AstraZeneca and Taiho Pharmaceutical Co. T.F. reports research support from Pfizer, Chgai, Novartis and AstraZeneca. K. Y. reports research support from AstraZeneca, Eli Lilly, Pfizer, Daiichi sankyo, Abbvie, Taiho, Bayer, Takeda and MSD, and personal fees (honoraria) from AstraZeneca, Bristol-Myers Squibb, Chugai, Daiichi sankyo, Janssen, Eli Lilly, Taiho, Novartis, Kyowa kirin and Boehringer Ingelheim. T.K. reports research support from Pfizer, Chugai, Takeda,

Novartis, Turning Point Therapeutics and AstraZeneca, and personal fees (honoraria) from Pfizer, Chugai, Takeda, Novartis and AstraZeneca. K. Nishino reports research support from Pfizer and personal fees (honoraria) from Pfizer, Chugai, Takeda, Novartis and AstraZeneca. A.N. reports personal fees (honoraria) from Chugai and Novartis. S. Kuyama reports personal fees (honoraria) from Pfizer, Chugai and AstraZeneca. N.F. reports personal fees (honoraria) from Pfizer, Chugai, Novartis and AstraZeneca. I.O. reports research support from Chugai, Takeda and Novartis, and personal fees (honoraria) from Pfizer, Chugai, Novartis and AstraZeneca. K. Taima. reports personal fees (honoraria) from Chugai, Novartis and AstraZeneca. H.D. reports research support from Pfizer, Chugai and Takeda, and personal fees from Chugai. A.Y. reports personal fees (honoraria) from Takeda. K.K. reports personal fees (honoraria) from Pfizer, Chugai, Novartis and AstraZeneca. Y.Z. reports research support from AstraZeneca and personal fees (honoraria) from Pfizer, Chugai, Takeda and AstraZeneca. K. Nosaki reports research support from Chugai and Takeda, and personal fees (honoraria) from Pfizer, Chugai, Takeda, Novartis and AstraZeneca. T.S. reports personal fees (honoraria) from Chugai and AstraZeneca. G.I. reports research support from Takeda and personal fees (honoraria) from Pfizer, Chugai, Takeda, Novartis and AstraZeneca. S.N. reports research support from Pfizer, Chugai, Takeda and AstraZeneca, and personal fees (honoraria) from Pfizer, Chugai, Takeda, Novartis and AstraZeneca. A.O. reports personal fees (honoraria) from Chugai. S.S.K. reports research support from Boehringer Ingelheim, MiNA Therapeutics and Taiho Therapeutics, as well as personal fees (honoraria) from Boehringer Ingelheim, Bristol Meyers Squibb, AstraZeneca, Chugai Pharmaceutical and Takeda Pharmaceuticals, all outside of the submitted work. K.G. reports research support from Boehringer Ingelheim, Bristol-Myers Squibb, Chugai, Daiichi sankyo, Eisai, Eli Lilly, Guardant Health, Janssen, Kyowa Kirin, Life Technologies Japan, MSD, Novartis, Ono, Otsuka, Pfizer, Taiho and Takeda, and personal fees (honoraria) from Bristol-Myers Squibb, Chugai, Daiichi sankyo, Eisai, Eli Lilly, Haihe Biopharma, Ignyta, Janssen, KISSEI, Kyowa Kirin, LOXO Oncology, Medical & Biological Laboratories, Merck Biopharma, Merus, MSD, Ono, Pfizer, Sumitomo Dainippon Pharma, Shanghai Haihe, Sysmex Corporation, Taiho, Takeda, and Xcoo. The authors report no other competing interests.

## Additional information

**Publisher's note** Springer Nature remains neutral with regard to jurisdictional claims in published maps and institutional affiliations.

## Extended data figures and tables

### [Extended Data Fig. 1 Electropherogram showing Sanger sequencing of the CLIP1-LTK fusion transcript.](#)

cDNAs were generated from RNAs isolated from patient tumours and amplified by RT-PCR with CLIP1-LTK F3 and R3 primers. PCR products were directly sequenced using respective primers.

### [Extended Data Fig. 2 LTK break-apart FISH assay.](#)

Non-tumour cells from Patient #1 showed orange (5')-green (3') fused signals (yellow arrows), while 82% (41/50) of scored tumour cells showed one fused (yellow arrows) and at least one green (3') signals (white arrows), which indicates the presence of *LTK* rearrangement. Bars = 10  $\mu$ m.

### [Extended Data Fig. 3 Histological findings of tumours positive for the CLIP1-LTK fusion.](#)

**a**, Hematoxylin and eosin (H&E) stained images. Samples from Patient #1 and #3 were diagnosed with adenocarcinoma morphologically. Samples from Patient #2 was diagnosed with NSCLC. Bars = 100  $\mu$ m. **b**, Immunohistochemical analysis of samples from Patient #2. TTF-1 positive (upper panel) and p40 negative (lower panel) staining supported the diagnosis of NSCLC favor adenocarcinoma. Bars = 100  $\mu$ m.

### [Extended Data Fig. 4 Analysis of Ba/F3 \(a\) and NIH3T3 \(b\) cells stably transduced using MIGR1 IRES-GFP vectors harboring indicated constructs.](#)

GFP-positive cells were sorted and expanded and then cell extracts were immunoblotted with antibodies indicated at the left side of each graph.

**Extended Data Fig. 5 Cellular localization of LTK and CLIP1-LTK.**

**a**, NIH3T3-Mock NIH3T3-LTK, or NIH3T3-CLIP1-LTK cells were stained with primary antibody specific for LTK, conjugated with Alexa Fluor 488, and subjected to flow cytometry analysis. Viable cells were gated as shown in Supplementary Information Figure 2. **b**, NIH3T3-Mock NIH3T3-LTK, or NIH3T3-CLIP1-LTK cells were fixed, permeabilized, and stained with anti-DDDDK-tag antibody conjugated to Alexa Fluor 594. Cells were subjected to immunofluorescence analysis.

**Extended Data Fig. 6 Light microscopy images of indicated stably-transduced NIH3T3 cells.**

**a**, Cells were plated in 10 cm plates at  $2 \times 10^5$  cells/ml and cultured in DMEM supplemented with 10% FBS and P/S for 2–3 days until cells reached 100% confluence. Bars = 100  $\mu$ m. **b**, Cells were plated in 6-well plates at  $1 \times 10^4$  cells/ml and cultured in a soft agar medium for 14 days. Bars = 100  $\mu$ m.

**Extended Data Fig. 7 Analysis of viability of Ba/F3-CLIP1-LTK cells.**

Ba/F3-CLIP1-LTK cells were treated with various concentrations of lorlatinib in the presence of 5% WEHI medium as a source of IL-3. Results are shown as an average  $\pm$  standard deviation from three independent experiments.

[Source data](#)

**Extended Data Fig. 8 Lorlatinib suppresses anchorage-independent growth of NIH3T3-CLIP1-LTK cell colonies.**

Colony diameters were measured in lorlatinib- versus vehicle (DMSO)-treated cells and shown as average  $\pm$  standard deviation from three independent experiments.

## [Source data](#)

**Extended Data Table. 1 Extended Data Table 1: Characteristics of patients subjected to WTS (n=75)**

**Extended Data Table. 2 Characteristics of lung cancer patients with the CLIP1-LTK fusion**

# **Supplementary information**

## [Supplementary Information](#)

This file contains Supplementary Figures 1 and 2 and their accompanying legends.

## [Reporting Summary](#)

## [Supplementary Information Table 1](#)

: Oligonucleotides used in this study.

## [Supplementary Information Table 2](#)

: Antibodies used in this study

## **Source data**

## [Source Data Fig. 2](#)

## [Source Data Fig. 3](#)

## [Source Data Extended Data Fig. 7](#)

## Source Data Extended Data Fig. 8

## Rights and permissions

### Reprints and Permissions

## About this article

### Cite this article

Izumi, H., Matsumoto, S., Liu, J. *et al.* The CLIP1–LTK fusion is an oncogenic driver in non-small-cell lung cancer. *Nature* **600**, 319–323 (2021). <https://doi.org/10.1038/s41586-021-04135-5>

- Received: 27 May 2021
- Accepted: 13 October 2021
- Published: 24 November 2021
- Issue Date: 09 December 2021
- DOI: <https://doi.org/10.1038/s41586-021-04135-5>

## Share this article

Anyone you share the following link with will be able to read this content:

[Get shareable link](#)

Sorry, a shareable link is not currently available for this article.

[Copy to clipboard](#)

Provided by the Springer Nature SharedIt content-sharing initiative

---

This article was downloaded by **calibre** from <https://www.nature.com/articles/s41586-021-04135-5>

| [Section menu](#) | [Main menu](#) |

- Article
- [Published: 24 November 2021](#)

# FAM72A antagonizes UNG2 to promote mutagenic repair during antibody maturation

- [Yuqing Feng](#)<sup>1</sup> na1,
- [Conglei Li](#)<sup>1</sup> na1 nAff13,
- [Jessica A. Stewart](#)<sup>2</sup>,
- [Philip Barbulescu](#)<sup>1</sup>,
- [Noé Seija Desivo](#)<sup>3,4</sup>,
- [Alejandro Álvarez-Quilón](#) ORCID: [orcid.org/0000-0001-9330-6823](https://orcid.org/0000-0001-9330-6823)<sup>5,6</sup>,
- [Rossanna C. Pezo](#)<sup>7,8</sup>,
- [Madusha L. W. Perera](#)<sup>2</sup>,
- [Katherine Chan](#)<sup>9</sup>,
- [Amy Hin Yan Tong](#)<sup>9</sup>,
- [Rukshana Mohamad-Ramshan](#)<sup>2</sup>,
- [Maribel Berru](#)<sup>1</sup>,
- [Diana Nakib](#) ORCID: [orcid.org/0000-0002-4046-2109](https://orcid.org/0000-0002-4046-2109)<sup>1</sup>,
- [Gavin Li](#)<sup>1</sup>,
- [Gholam Ali Kardar](#)<sup>10</sup>,
- [James R. Carlyle](#)<sup>1</sup>,
- [Jason Moffat](#) ORCID: [orcid.org/0000-0002-5663-8586](https://orcid.org/0000-0002-5663-8586)<sup>5,9,11</sup>,
- [Daniel Durocher](#) ORCID: [orcid.org/0000-0003-3863-8635](https://orcid.org/0000-0003-3863-8635)<sup>5,6</sup>,
- [Javier M. Di Noia](#) ORCID: [orcid.org/0000-0003-2896-0321](https://orcid.org/0000-0003-2896-0321)<sup>3,4</sup>,
- [Ashok S. Bhagwat](#) ORCID: [orcid.org/0000-0003-1188-0579](https://orcid.org/0000-0003-1188-0579)<sup>2,12</sup> &
- [Alberto Martin](#) ORCID: [orcid.org/0000-0002-1260-7710](https://orcid.org/0000-0002-1260-7710)<sup>1</sup>

[Nature](#) volume **600**, pages 324–328 (2021)

- 3298 Accesses
- 138 Altmetric
- [Metrics details](#)

## Subjects

- [Base excision repair](#)
- [Class switch recombination](#)

## Abstract

Activation-induced cytidine deaminase (AID) catalyses the deamination of deoxycytidines to deoxyuracils within immunoglobulin genes to induce somatic hypermutation and class-switch recombination<sup>1,2</sup>. AID-generated deoxyuracils are recognized and processed by subverted base-excision and mismatch repair pathways that ensure a mutagenic outcome in B cells<sup>3,4,5,6</sup>. However, why these DNA repair pathways do not accurately repair AID-induced lesions remains unknown. Here, using a genome-wide CRISPR screen, we show that FAM72A is a major determinant for the error-prone processing of deoxyuracils. *Fam72a*-deficient CH12F3-2 B cells and primary B cells from *Fam72a*<sup>-/-</sup> mice exhibit reduced class-switch recombination and somatic hypermutation frequencies at immunoglobulin and *Bcl6* genes, and reduced genome-wide deoxyuracils. The somatic hypermutation spectrum in B cells from *Fam72a*<sup>-/-</sup> mice is opposite to that observed in mice deficient in uracil DNA glycosylase 2 (UNG2)<sup>7</sup>, which suggests that UNG2 is hyperactive in FAM72A-deficient cells. Indeed, FAM72A binds to UNG2, resulting in reduced levels of UNG2 protein in the G1 phase of the cell cycle, coinciding with peak AID activity. FAM72A therefore causes U·G mispairs to persist into S phase, leading to error-prone processing by mismatch repair. By disabling the DNA repair pathways that normally efficiently remove deoxyuracils from DNA, FAM72A enables AID to exert its full effects on antibody maturation. This work has

implications in cancer, as the overexpression of FAM72A that is observed in many cancers<sup>8</sup> could promote mutagenesis.

This is a preview of subscription content

## Access options

Subscribe to Journal

Get full journal access for 1 year

\$199.00

only \$3.90 per issue

[Subscribe](#)

All prices are NET prices.

VAT will be added later in the checkout.

Tax calculation will be finalised during checkout.

Rent or Buy article

Get time limited or full article access on ReadCube.

from \$8.99

[Rent or Buy](#)

All prices are NET prices.

### Additional access options:

- [Log in](#)
- [Learn about institutional subscriptions](#)

**Fig. 1: Whole-genome CRISPR screen identified FAM72A as a factor required for CSR.**

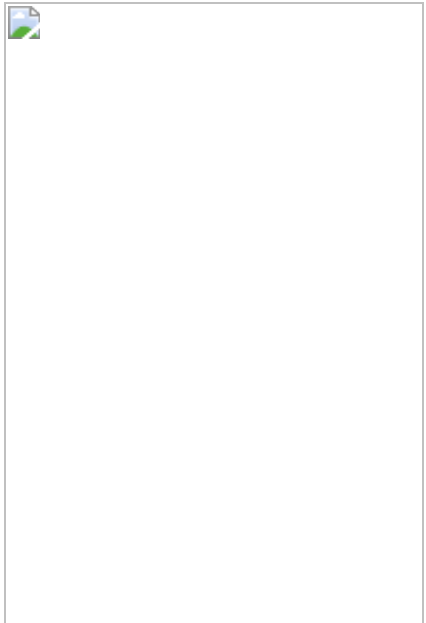


**Fig. 2:** *Fam72a*<sup>-/-</sup> mice exhibit defects in CSR and SHM.

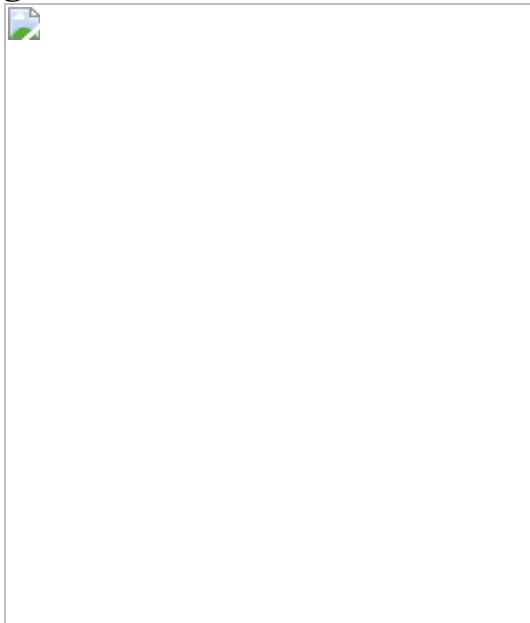


**Fig. 3:** FAM72A is epistatic with UNG and MMR during CSR.

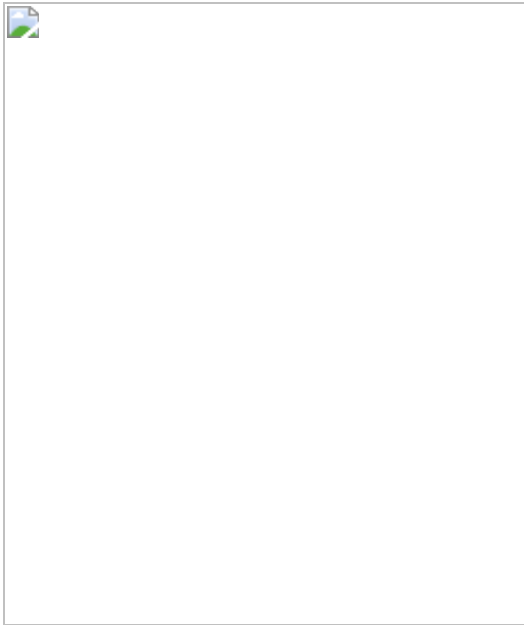
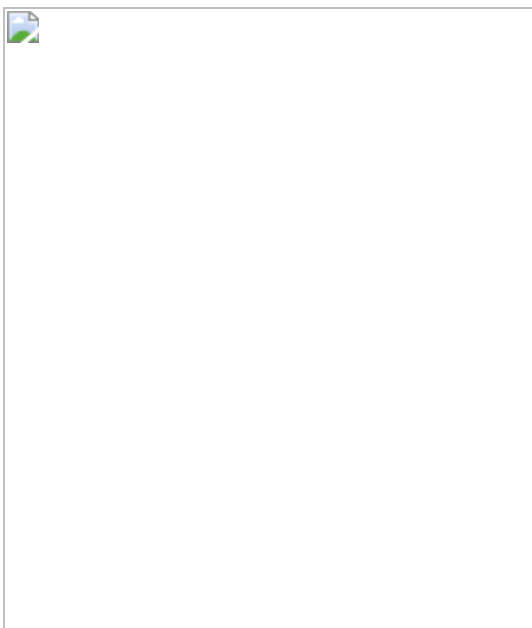


**Fig. 4: FAM72A binds to UNG2 and leads to reduced UNG2 protein levels.**



## Data availability

The raw sequence reads from CRISPR screening have been deposited in the NCBI Gene Expression Omnibus under accession number [GSE183706](#). [Source data](#) are provided with this paper.

# References

1. 1.

Muramatsu, M. et al. Class switch recombination and hypermutation require activation-induced cytidine deaminase (AID), a potential RNA editing enzyme. *Cell* **102**, 553–563 (2000).

2. 2.

Feng, Y., Seija, N., JM, D. I. N. & Martin, A. AID in antibody diversification: there and back again. *Trends Immunol.* **41**, 586–600 (2020).

3. 3.

Cascalho, M., Wong, J., Steinberg, C. & Wabl, M. Mismatch repair co-opted by hypermutation. *Science* **279**, 1207–1210 (1998).

4. 4.

Di Noia, J. & Neuberger, M. S. Altering the pathway of immunoglobulin hypermutation by inhibiting uracil-DNA glycosylase. *Nature* **419**, 43–48 (2002).

5. 5.

Wiesendanger, M., Kneitz, B., Edelmann, W. & Scharff, M. D. Somatic hypermutation in MutS homologue (MSH)3-, MSH6-, and MSH3/MSH6-deficient mice reveals a role for the MSH2-MSH6 heterodimer in modulating the base substitution pattern. *J. Exp. Med.* **191**, 579–584 (2000).

6. 6.

Rada, C., Di Noia, J. M. & Neuberger, M. S. Mismatch recognition and uracil excision provide complementary paths to both Ig switching

and the A/T-focused phase of somatic mutation. *Mol. Cell* **16**, 163–171 (2004).

7. 7.

Rada, C. et al. Immunoglobulin isotype switching is inhibited and somatic hypermutation perturbed in UNG-deficient mice. *Curr. Biol.* **12**, 1748–1755 (2002).

8. 8.

Guo, C. et al. Ugene, a newly identified protein that is commonly overexpressed in cancer and binds uracil DNA glycosylase. *Cancer Res.* **68**, 6118–6126 (2008).

9. 9.

Muramatsu, M. et al. Specific expression of activation-induced cytidine deaminase (AID), a novel member of the RNA-editing deaminase family in germinal center B cells. *J. Biol. Chem.* **274**, 18470–18476 (1999).

10. 10.

Lawson, K. A. et al. Functional genomic landscape of cancer-intrinsic evasion of killing by T cells. *Nature* **586**, 120–126 (2020).

11. 11.

Pan-Hammarstrom, Q. et al. Impact of DNA ligase IV on nonhomologous end joining pathways during class switch recombination in human cells. *J. Exp. Med.* **201**, 189–194 (2005).

12. 12.

Ward, I. M. et al. 53BP1 is required for class switch recombination. *J. Cell Biol.* **165**, 459–464 (2004).

13. 13.

Yan, C. T. et al. IgH class switching and translocations use a robust non-classical end-joining pathway. *Nature* **449**, 478–482 (2007).

14. 14.

Perez-Duran, P. et al. UNG shapes the specificity of AID-induced somatic hypermutation. *J. Exp. Med.* **209**, 1379–1389 (2012).

15. 15.

Frieder, D., Larijani, M., Collins, C., Shulman, M. & Martin, A. The concerted action of Msh2 and UNG stimulates somatic hypermutation at A.T base pairs. *Mol. Cell. Biol.* **29**, 5148–5157 (2009).

16. 16.

Thientosapol, E. S. et al. Proximity to AGCT sequences dictates MMR-independent versus MMR-dependent mechanisms for AID-induced mutation via UNG2. *Nucleic Acids Res.* **45**, 3146–3157 (2017).

17. 17.

Martin, A. et al. Msh2 ATPase activity is essential for somatic hypermutation at a-T basepairs and for efficient class switch recombination. *J. Exp. Med.* **198**, 1171–1178 (2003).

18. 18.

Phung, Q. H. et al. Increased hypermutation at G and C nucleotides in immunoglobulin variable genes from mice deficient in the MSH2 mismatch repair protein. *J. Exp. Med.* **187**, 1745–1751 (1998).

19. 19.

Delbos, F., Aoufouchi, S., Faili, A., Weill, J. C. & Reynaud, C. A. DNA polymerase eta is the sole contributor of A/T modifications during immunoglobulin gene hypermutation in the mouse. *J. Exp. Med.* **204**, 17–23 (2007).

20. 20.

Arakawa, H., Saribasak, H. & Buerstedde, J. M. Activation-induced cytidine deaminase initiates immunoglobulin gene conversion and hypermutation by a common intermediate. *PLoS Biol.* **2**, E179 (2004).

21. 21.

Di Noia, J. M. & Neuberger, M. S. Immunoglobulin gene conversion in chicken DT40 cells largely proceeds through an abasic site intermediate generated by excision of the uracil produced by AID-mediated deoxycytidine deamination. *Eur. J. Immunol.* **34**, 504–508 (2004).

22. 22.

Campo, V. A. et al. MSH6- or PMS2-deficiency causes re-replication in DT40 B cells, but it has little effect on immunoglobulin gene conversion or on repair of AID-generated uracils. *Nucleic Acids Res.* **41**, 3032–3046 (2013).

23. 23.

Di Noia, J. M., Rada, C. & Neuberger, M. S. SMUG1 is able to excise uracil from immunoglobulin genes: insight into mutation versus repair. *EMBO J.* **25**, 585–595 (2006).

24. 24.

Wang, Q. et al. The cell cycle restricts activation-induced cytidine deaminase activity to early G1. *J. Exp. Med.* **214**, 49–58 (2017).

25. 25.

Cappelli, E. et al. Rates of base excision repair are not solely dependent on levels of initiating enzymes. *Carcinogenesis* **22**, 387–393 (2001).

26. 26.

Krusong, K., Carpenter, E. P., Bellamy, S. R., Savva, R. & Baldwin, G. S. A comparative study of uracil-DNA glycosylases from human and herpes simplex virus type 1. *J. Biol. Chem.* **281**, 4983–4992 (2006).

27. 27.

Krokan, H. E. et al. Error-free versus mutagenic processing of genomic uracil—relevance to cancer. *DNA Repair* **19**, 38–47 (2014).

28. 28.

Zeng, X. et al. DNA polymerase eta is an A–T mutator in somatic hypermutation of immunoglobulin variable genes. *Nat. Immunol.* **2**, 537–541 (2001).

29. 29.

Belcheva, A. et al. Gut microbial metabolism drives transformation of MSH2-deficient colon epithelial cells. *Cell* **158**, 288–299 (2014).

30. 30.

Ramachandran, S. et al. The SAGA deubiquitination module promotes DNA repair and class switch recombination through ATM and DNAPK-mediated γH2AX formation. *Cell Rep.* **15**, 1554–1565 (2016).

31. 31.

Aregger, M., Chandrashekhar, M., Tong, A. H. Y., Chan, K. & Moffat, J. Pooled lentiviral CRISPR–Cas9 screens for functional genomics in mammalian cells. *Methods Mol. Biol.* **1869**, 169–188 (2019).

32. 32.

Sarno, A. et al. Uracil–DNA glycosylase UNG1 isoform variant supports class switch recombination and repairs nuclear genomic uracil. *Nucleic Acids Res.* **47**, 4569–4585 (2019).

33. 33.

Li, C. et al. The H2B deubiquitinase Usp22 promotes antibody class switch recombination by facilitating non-homologous end joining. *Nat. Commun.* **9**, 1006 (2018).

34. 34.

Li, C. et al. Early-life programming of mesenteric lymph node stromal cell identity by the lymphotoxin pathway regulates adult mucosal immunity. *Sci. Immunol.* **4**, aax1027 (2019).

35. 35.

Liu, M. et al. Two levels of protection for the B cell genome during somatic hypermutation. *Nature* **451**, 841–845 (2008).

36. 36.

Siriwardena, S. U., Perera, M. L. W., Senevirathne, V., Stewart, J. & Bhagwat, A. S. A tumor-promoting phorbol ester causes a large increase in APOBEC3A expression and a moderate increase in APOBEC3B expression in a normal human keratinocyte cell line without increasing genomic uracils. *Mol. Cell. Biol.* **39**, e00238-18 (2019).

37. 37.

So, C. C., Ramachandran, S. & Martin, A. E3 ubiquitin ligases RNF20 and RNF40 are required for double-stranded break (DSB) repair: evidence for monoubiquitination of histone H2B lysine 120 as a novel axis of DSB signaling and repair. *Mol. Cell. Biol.* **39**, e00488-18 (2019).

38. 38.

Boulianne, B. et al. AID-expressing germinal center B cells cluster normally within lymph node follicles in the absence of FDC<sup>-</sup>M1<sup>+</sup>

CD35<sup>+</sup> follicular dendritic cells but dissipate prematurely. *J. Immunol.* **191**, 4521–4530 (2013).

## Acknowledgements

We thank P. Poussier and M. Shulman for critical review of the manuscript. Y.F., C.L. and A.A.-Q. are recipients of the Canadian Institutes of Health Research Postdoctoral Fellowship. N.S.D. is the recipient of a doctoral award from the FRQ-S (Fonds de recherche Santé Québec). J.A.S. was supported by a competitive graduate research assistantship from the Wayne State University and R.M.-R. was supported by a Thomas C. Rumble fellowship. J.M.D.N. is a Merit scholar from the Fonds de recherche de Quebec–Santé and is supported by CIHR (PJT-155944). J.M. is supported from a CIHR project grant (CBT-438323) and holds a Canada Research Chair in Functional Genomics. D.D. is a Canada Research Chair (Tier I) and work in the D.D. laboratory was supported by a grant from the CIHR (FDN143343). A.S.B. was supported by a National Institutes of Health grant (1R21AI144708) and Bridge Funding grant from Wayne State University. A.M. is supported by grants from the CIHR (PJT-153307 and PJT-156330).

## Author information

### Author notes

1. Conglei Li

Present address: School of Medicine, The Chinese University of Hong Kong, Shenzhen, China

2. These authors contributed equally: Yuqing Feng, Conglei Li

## Affiliations

1. Department of Immunology, University of Toronto, Toronto, Ontario, Canada

Yuqing Feng, Conglei Li, Philip Barbulescu, Maribel Berru, Diana Nakib, Gavin Li, James R. Carlyle & Alberto Martin

2. Department of Chemistry, Wayne State University, Detroit, MI, USA

Jessica A. Stewart, Madusha L. W. Perera, Rukshana Mohamad-Ramshan & Ashok S. Bhagwat

3. Institut de recherches cliniques de Montréal, Montreal, Quebec, Canada

Noé Seija Desivo & Javier M. Di Noia

4. Molecular Biology Programs, Department of Medicine, University of Montreal, Montreal, Quebec, Canada

Noé Seija Desivo & Javier M. Di Noia

5. Department of Molecular Genetics, University of Toronto, Toronto, Ontario, Canada

Alejandro Álvarez-Quilón, Jason Moffat & Daniel Durocher

6. Lunenfeld–Tanenbaum Research Institute, Sinai Health System, Toronto, Ontario, Canada

Alejandro Álvarez-Quilón & Daniel Durocher

7. Sunnybrook Health Sciences Center, Toronto, Ontario, Canada

Rossanna C. Pezo

8. Department of Medicine, University of Toronto, Toronto, Ontario, Canada

Rossanna C. Pezo

9. Donnelly Centre, University of Toronto, Toronto, Ontario, Canada

Katherine Chan, Amy Hin Yan Tong & Jason Moffat

10. Immunology, Asthma and Allergy Research Institute, Tehran University of Medical Sciences, Tehran, Iran

Gholam Ali Kardar

11. Institute for Biomedical Engineering, University of Toronto, Toronto, Ontario, Canada

Jason Moffat

12. Department of Biochemistry, Microbiology and Immunology, Wayne State University School of Medicine, Detroit, MI, USA

Ashok S. Bhagwat

## Contributions

Y.F. performed the CRISPR screen in collaboration with K.C., A.H.Y.T. and J.M., and characterized *Fam72a*<sup>-/-</sup> CH12 clones. C.L. characterized *Fam72a*<sup>-/-</sup> mice and performed drug inhibitor-treated CH12 assays. J.A.S. performed protein purification and in vitro biochemical assays. P.B. generated knockout clones in CH12 cells and performed repair substrate assays. N.S.D. characterized DT40 *Fam72a*<sup>-/-</sup> clones. A.A.-Q. conducted Bio-ID experiments. R.C.P. performed immunofluorescence analysis. M.L.W.P. performed uracil quantification experiments. M.B. helped with minipreps and maintain colonies for animal work. D.N. and G.A.K. helped generate knockout clones in cell culture. G.L. conducted western blotting in cell culture. Y.F., C.L., J.A.S., N.S.D. and A.A.-Q. performed experiments, analysed data and wrote the manuscript. P.B., R.C.P., M.L.W.P., K.C., A.H.Y.T., R.M.-R., M.B., D.N., G.L., G.A.K. and J.R.C. performed experiments. J.R.C., J.M., D.D., J.M.D.N., A.S.B. and A.M. analysed the data and wrote the manuscript. A.M. conceived, designed and supervised the study.

## Corresponding author

Correspondence to [Alberto Martin](#).

## Ethics declarations

### Competing interests

The authors declare no competing interests.

## Additional information

**Peer review information** *Nature* thanks Uttiya Basu and the other, anonymous, reviewer(s) for their contribution to the peer review of this work. Peer reviewer reports are available.

**Publisher's note** Springer Nature remains neutral with regard to jurisdictional claims in published maps and institutional affiliations.

## Extended data figures and tables

### [Extended Data Fig. 1 Validating the role of FAM72A during CSR in CH12 cells.](#)

**(a)** Western blot analysis to identify Cas9-expressing CH12 cell subclones after transduction with a lentiviral vector expressing Cas9. Experiment was repeated 2 times independently with similar results. **(b)** Schematic of the CRISPR/Cas9 sorting screen in CH12 cells. CH12 cells stably expressing Cas9 were transduced with a mouse gRNA library that contains ~5 gRNA per gene. Transduced populations were treated with CIT cocktail (CD40 ligand, IL4, TGF $\beta$ ) to induce CSR from IgM to IgA, followed FACS sorting to separate the switched (IgA $^+$ ) *versus* the unswitched (IgA $^-$ ) population. Genomic DNA from the initially transduced cells (T0), and from unsorted, IgA $^-$ , IgA $^+$  population was isolated, and sequenced. **(c)** gRNA was ranked using a NormZ plot (standard deviations from the mean) comparing IgA $^-$  cells to the unsorted population. **(d)** Guide RNA (gRNA) targeting strategy against mouse *Aicda* and *Fam72a* genes to validate the role of FAM72A in

CSR in bulk CH12 cells expressing Cas9. (e) Quantification of *Fam72a* mRNA relative to HPRT in wild-type (WT) and *Fam72a*<sup>-/-</sup> CH12 clones by qPCR. (f) Sequenced *Fam72a*, *Msh2*, *Ung*, and *ligase4* alleles in *Fam72a*<sup>-/-</sup>, *Ung*<sup>-/-</sup>, *Fam72a*<sup>-/-</sup>*Ung*<sup>-/-</sup>, *Msh2*<sup>-/-</sup>, *Fam72a*<sup>-/-</sup>*Msh2*<sup>-/-</sup>, and *Ligase 4*<sup>-/-</sup> CH12 clones generated using CRISPR/Cas9. Underlined sequence denotes gRNA target sequence, with the wildtype amino acid sequence indicated at the bottom. (g) Assessing the role of FAM72A in DNA double-strand break repair pathways. WT, *Fam72a*<sup>-/-</sup> and *Ligase 4*<sup>-/-</sup> CH12 clones stably expressing EJ5-GPF, EJ2-GFP, and DR-GFP substrates that measure non-homologous end joining (NHEJ), alternative end joining (A-EJ), and homologous recombination (HR), respectively. Cells were mock transfected or transfected with yeast endonuclease I-SceI expressing vector, pCBA-SceI. GFP expression was monitored by flow cytometry three days post-transfection. Data were presented as mean ± SEM and were analyzed using two-tailed unpaired Student t test. Left panel: p=0.028 for the comparison between WT clone 1 and *Lig4*<sup>-/-</sup> clone; middle panel: p=0.014 for the comparison between WT clone I and *Fam72a*<sup>-/-</sup> clone 1; p=0.0003 for the comparison between WT clone I and *Lig4*<sup>-/-</sup> clone; ns: not significant. Data are representative of 3 independent experiments.

[Source data](#)

[Extended Data Fig. 2 Generation of \*Fam72a\*<sup>-/-</sup> mice.](#)

(a) Schematic representation of *Fam72a* gene disruption strategy. The whole coding sequence of *Fam72a* was replaced with a LacZ/neo cassette by homologous recombination using a bacterial artificial chromosome (BAC)-based targeting vector. The floxed neo cassette was removed by further breeding to a ubiquitous Cre mouse strain. Strain development was done at MMRRC (UC, Davis). PCR genotyping primer sequence can be found in Supplementary Table 2. (b) qPCR analysis of *Fam72a* mRNA from resting spleen B cells or spleen B cells that were *ex vivo* stimulated with LPS for 3 days (n= 4 mice per group). Data were presented as mean ± SEM and were analyzed using two-tailed unpaired Student t test (p= 0.0006 for the comparison in the left panel). Data are representative of 2 independent experiments.

[Source data](#)

**Extended Data Fig. 3 Comparable B cell profiles in the bone marrow of *Fam72a*<sup>-/-</sup> and *Fam72a*<sup>+/+</sup> littermate mice.**

(a) Representative FACS plots of B cells derived from the bone marrow of *Fam72a*<sup>-/-</sup> or *Fam72a*<sup>+/+</sup> littermate mice. (b) Full minus one (FMO)-derived background staining for B220, CD43, BP-1, CD24 and IgM, respectively. (c) The frequencies of indicated B cell fractions in the bone marrow of *Fam72a*<sup>-/-</sup> or *Fam72a*<sup>+/+</sup> littermates (n= 4 mice per group). Data were presented as mean ± SEM and were analyzed using two-tailed unpaired Student t test (ns: not significant). Data are representative of 2 independent experiments. (d) Same as c except that total cell numbers were reported.

[Source data](#)

**Extended Data Fig. 4 Comparable B cell profiles in the spleen of *Fam72a*<sup>-/-</sup> and *Fam72a*<sup>+/+</sup> littermates.**

(a) Representative FACS plots of B cells in the spleen of *Fam72a*<sup>-/-</sup> or *Fam72a*<sup>+/+</sup> littermate mice. (b) FMO-derived background staining for B220, CD93, CD23 and IgM, respectively. (c) The frequencies of indicated B cell subsets in the spleen of *Fam72a*<sup>-/-</sup> or *Fam72a*<sup>+/+</sup> littermates (n= 4 mice per group). Data were presented as mean ± SEM and were analyzed using two-tailed unpaired Student t test (ns: not significant). Data are representative of 2 independent experiments. MZ: marginal zone B cells; FO: follicular B cells. (d) Same as c except that total cell numbers were reported.

[Source data](#)

**Extended Data Fig. 5 CSR and germinal center formation analysis from *Fam72a*<sup>-/-</sup> *Fam72a*<sup>+/+</sup> and WT mice and CH12 clones, as well as AID and germline transcripts, cell proliferation and cell cycle profile of splenic B cells.**

**(a)** Analysis of *ex vivo* CSR in splenic B cells from *Fam72a*<sup>+/+</sup>, *Fam72a*<sup>+-</sup>, and *Fam72a*<sup>-/-</sup> mice (n=2 mice per group; duplicate assays per mouse). For IgG1 panel, p= 0.0014 for the comparison between *Fam72a*<sup>+/+</sup> and *Fam72a*<sup>-/-</sup> group; for IgG2b panel, p= 0.0005 for the comparison between *Fam72a*<sup>+/+</sup> and *Fam72a*<sup>-/-</sup> group; for IgG3 panel, p= 0.0143 for the comparison between *Fam72a*<sup>+/+</sup> and *Fam72a*<sup>+-</sup> group; for IgA panel, p= 0.0002 for the comparison between *Fam72a*<sup>+/+</sup> and *Fam72a*<sup>-/-</sup> group, and p= 0.0074 for the comparison between *Fam72a*<sup>+/+</sup> and *Fam72a*<sup>+-</sup> group.

**(b)** CH12 clones of indicated genotype were treated with CIT for 2 days and analyzed for CSR to IgA. Data are representative of 3 independent experiments. **(c)** Characterization of the humoral response in NP-CGG immunized WT and *Fam72a*<sup>-/-</sup> mice. Splenic germinal center (GC) B cell analysis in WT and *Fam72a*<sup>-/-</sup> mice after NP-CGG immunization for 8 days. Y-axis in the left panel shows the frequency of GC (GL-7<sup>+</sup>Fas<sup>+</sup>) among live CD45<sup>+</sup>CD4<sup>+</sup>CD8<sup>-</sup>CD11c<sup>-</sup>F4/80<sup>-</sup>CD19<sup>+</sup>IgD<sup>-</sup> splenic cells(n= 3-5 mice per group). For the left panel, p= 0.0059 for the comparison between naïve and d8-immunized *Fam72a*<sup>+/+</sup> group, and p= 0.0308 for the comparison between d8-immunized *Fam72a*<sup>+/+</sup> and *Fam72a*<sup>-/-</sup> group; for the right panel, p= 0.0176 for the comparison between naïve and d8-immunized *Fam72a*<sup>+/+</sup> group. **(d)** Same as (c), except that follicular helper T (Tfh) cells were examined. Y-axis in the left panel shows the frequency of CXCR5<sup>+</sup>PD-1<sup>+</sup> among live CD4<sup>+</sup>B220<sup>-</sup> splenic cells (n= 3-5 mice per group). For the left panel, p= 0.0123 for the comparison between naïve and d8-immunized *Fam72a*<sup>+/+</sup> group; for the right panel, p= 0.0254 for the comparison between naïve and d8-immunized *Fam72a*<sup>+/+</sup> group. **(e)** Representative immunofluorescence analysis of splenic GCs post NP immunization in WT and *Fam72a*<sup>-/-</sup> mice. Magnification 20x. Spleens were collected day 8 post immunization. Cryosection were stained with PNA-FITC and IgD-PE. Right panel: The average GC size for each mouse is reported, in which ~2-6 individual GCs were analyzed per mouse (n=4 mice per group). **(f)** qPCR analysis of AID mRNA, I $\mu$ -C $\mu$  and I $\gamma$ 3-C $\gamma$ 3 germline transcripts of d3-LPS stimulated splenic B cells, as well as I $\alpha$ -C $\alpha$  germline transcripts of splenic B cells stimulated to switch to IgA from *Fam72a*<sup>-/-</sup> or *Fam72a*<sup>+/+</sup> littermate mice (n= 3-4 mice per group). Data are representative of 2 independent experiments. **(g)** Evaluation of cell proliferation of LPS-

stimulated splenic B cells from *Fam72a*<sup>-/-</sup> or *Fam72a*<sup>+/+</sup> littermate mice (n=4 mice per group), and data was tested by two-way ANOVA and representative of 2 independent experiments (left panel). Proliferation was also assessed by CFSE dilution (Middle panel), and apoptosis by Annexin V-staining (right panel; n=3-4 mice per group; p= 0.0341). **(h)** Gating strategy for cell cycle analysis. **(i)** The compiled cell cycle analysis of *Fam72a*<sup>-/-</sup> or *Fam72a*<sup>+/+</sup> splenic B cells that were stimulated by LPS for 3 days (n= 4 mice per group). Data are representative of 2 independent experiments. Data were presented as mean ± SEM and were analyzed using two-tailed unpaired Student t test (ns: not significant).

[Source data](#)

**Extended Data Fig. 6 Analysis of germinal center B cells and mutations from Peyer's patches.**

**(a)** Gating strategy used to sort germinal center B cells from Peyer's patches for *J<sub>H</sub>4* region and *Bcl6* gene sequencing. **(b)** The frequencies of germinal center B cells in Peyer's patches from naïve *Fam72a*<sup>+/+</sup>, *Fam72a*<sup>-/-</sup> or *Aicda*<sup>-/-</sup> mice (n= 3 mice per group). Data are representative of 2 independent experiments. Data were presented as mean ± SEM and were analyzed using two-tailed unpaired Student t test (ns: not significant). **(c)** The compiled spectrum of unique top-strand (coding-strand) mutations shown as mutation frequencies (top panel) and percentage of total mutations (bottom panel). These two panels represented the pooled data from 4 *Fam72a*<sup>+/+</sup> and 4 *Fam72a*<sup>-/-</sup> mice, respectively. Data shown in the upper panels showing mutation frequencies for each individual mutation type were analyzed using a Mann-Whitney test, and all types of mutations were significantly reduced in the *Fam72a*<sup>-/-</sup> mice, except for C to A mutations. **(d)** Analysis of SHM in the *J<sub>H</sub>4* region of germinal center B cells for each *Fam72a*<sup>+/+</sup> or *Fam72a*<sup>-/-</sup> mouse. **(e)** Size of insertion in the *J<sub>H</sub>4* region is shown (n= 4 mice per group). In addition, there was also no statistical significance in the frequency of insertions between *Fam72a*<sup>+/+</sup> and *Fam72a*<sup>-/-</sup> mice (data not shown). **(f)** Size of deletions in the *J<sub>H</sub>4* region is shown (n= 4 mice per group). In addition, there was also no statistical

significance in the frequency of deletions between *Fam72a*<sup>+/+</sup> and *Fam72a*<sup>-/-</sup> mice (data not shown).

Source data

**Extended Data Fig. 7 Characterizing the effect of FAM72A-deficiency on mutations.**

**(a)** Mutation characteristics at the 5' S $\mu$  region was analyzed in WT, *Fam72a*<sup>-/-</sup>, *Ung*<sup>-/-</sup>, and *Ung*<sup>-/-</sup> *Fam72a*<sup>-/-</sup> CH12 clones after 5 days of CIT treatment. Mutations at WRC and GYW motifs are considered AID hotspot mutation, where W=A/T, R=A/G, and Y=C/T. Mutation frequency was calculated from total mutations pooled from three independent experiment divided by total number of nucleotide sequenced. Data is summarized in Fig. 3a. **(b)** Distribution of mutations at the 5'  $\mu$  switch region in CH12 cells of the indicated genotype after 5 days of CIT stimulation. **(c)** AID expression levels of WT, *Fam72a*<sup>-/-</sup>, *Ung*<sup>-/-</sup>, and *Fam72a*<sup>-/-</sup>*Ung*<sup>-/-</sup> CH12 cells as assessed by Western blot analysis.  $\beta$ -ACTIN was used as loading control. Experiment was repeated 3 times independently with similar results. **(d)** S $\mu$  germline transcripts ( $\mu$ GLT) and S $\alpha$  germline transcript ( $\alpha$ GLT) of the indicated CH12 clones before and after stimulation with CIT for 2 days. Data are representative of 3 independent experiments. **(e)** Analysis of *ex vivo* CSR to IgG2b, IgG3, IgA and IgE using splenic B cells from WT, *Fam72a*<sup>-/-</sup>, *Msh2*<sup>-/-</sup>, or *Fam72a*<sup>-/-</sup>*Msh2*<sup>-/-</sup> littermate mice (n=2 mice per group; duplicate assays per mouse). Data are representative of 2 independent experiments. For IgG3 panel, p= 0.0004 for the comparison between WT and *Fam72a*<sup>-/-</sup> group, p= 0.011 for the comparison between *Fam72a*<sup>-/-</sup> and *Msh2*<sup>-/-</sup> group, and p= 0.005 for the comparison between *Fam72a*<sup>-/-</sup> and *Fam72a*<sup>-/-</sup>*Msh2*<sup>-/-</sup> group; for IgG2b panel, p= 0.0003 for the comparison between WT and *Fam72a*<sup>-/-</sup> group, p= 0.0024 for the comparison between *Fam72a*<sup>-/-</sup> and *Msh2*<sup>-/-</sup> group, and p= 0.0059 for the comparison between *Fam72a*<sup>-/-</sup> and *Fam72a*<sup>-/-</sup>*Msh2*<sup>-/-</sup> group; for IgE panel, p= 0.0184 for the comparison between WT and *Fam72a*<sup>-/-</sup> group, p= 0.0326 for the comparison between *Fam72a*<sup>-/-</sup> and *Msh2*<sup>-/-</sup> group, and p= 0.0005 for the comparison between *Fam72a*<sup>-/-</sup> and *Fam72a*<sup>-/-</sup>*Msh2*<sup>-/-</sup> group. **(f)** The compiled spectrum of unique top-strand (coding-strand) mutations shown

as mutation frequencies per 10, 000bp. The data were pooled from 4 WT mice, 3 *Fam72a*<sup>-/-</sup>, 2 *Msh2*<sup>-/-</sup>, or 3 *Fam72a*<sup>-/-</sup>*Msh2*<sup>-/-</sup> littermate mice, respectively. **(g)** The frequency of A or T mutations in the *J<sub>H</sub>4* region of WT, *Fam72a*<sup>-/-</sup>, *Msh2*<sup>-/-</sup>, or *Fam72a*<sup>-/-</sup>*Msh2*<sup>-/-</sup> littermate mice (n=2-4 mice per group). **(h)** Western blots measuring for UNG expression level in *ex vivo* LPS-activated spleen B cells from WT, *Fam72a*<sup>-/-</sup>, *Msh2*<sup>-/-</sup>, and *Fam72a*<sup>-/-</sup>*Msh2*<sup>-/-</sup> mice. Experiment was repeated 2 times independently with similar results.

[Source data](#)

**Extended Data Fig. 8 Characterization of chicken DT40 *Fam72a*<sup>-/-</sup> clones.**

**(a)** *Fam72a*<sup>-/-</sup> DT40 clones were generated using CRISPR/Cas9. Depletion of *Fam72a* was confirmed at the genomic DNA and mRNA level in 6 different DT40 clones. All the clones were mostly IgM<sup>-</sup> as assessed by flow cytometry and only 4 clones (renames K01-04) were picked for fluctuation analysis. *Prmt5* was used as a control for mRNA extraction. **(b)** Growth curve analysis in WT and *Fam72a*<sup>-/-</sup> DT40 cells. The average doubling time (DT) of WT and *Fam72a*<sup>-/-</sup> clones in cultures for each individual clone is shown in the bottom panel and revealed reduced growth kinetics for all *Fam72a*<sup>-/-</sup> clones **(c)** Fluctuation analysis for gene conversion in WT and *Fam72a*<sup>-/-</sup> DT40 cells based on same number of cell divisions. Data are representative of 3 independent experiments. **(d)** Western blots for UNG were carried out on the indicated clones.

[Source data](#)

**Extended Data Fig. 9 FAM72A binds to and inhibits UNG2, leading to reduced UNG2 protein level.**

**(a)** Streptavidin affinity purification from 293T cell lysates expressing N-terminal 3xFLAG-miniTURBO tagged FAM72A upon proximity biotinylation. FLAG-miniTURBO-SV40-NLS (NLS) was used as control.

Strepavidin bound proteins and whole-cell extracts (WCEs) were immunoblotted with the indicated antibodies. **(b)** Purified mFAM72A and UNG2 proteins were electrophoresed on an SDS-PAGE gel and stained with Coomassie Brilliant Blue dye. The 6XHis-mFAM72A (20 kDa), mUNG2-polyGly-FLAG (35kDa), and hUNG2 (35kDa) are seen next to the precision plus protein standard (Bio-Rad). **(c)** Murine UNG2 and FAM72A proteins were mixed in equal molar amounts and pulled-down using polyHis-tag or FLAG-tag on mFAM72A and mUNG2 proteins, respectively. The input and elutions were analyzed by Western blot using anti-His tag or anti-FLAG tag antibodies. Cross-species pull-down of mFAM72A with hUNG2 is also shown: the hUNG2 protein was detected using anti-UDG antibody. **(d)** Purified murine UNG2 and Fam72A proteins were pre-incubated at a 1:5 molar ratio, respectively, then reacted with either a single-stranded uracil substrate (ssU) or double-stranded uracil substrates with either U:G or U:A pairs. Reaction products were separated on a denaturing polyacrylamide gel. **(e)** Quantification of three independent experiments of the type shown in Extended Data Fig. [9d](#) using 0:1, 1:1 or 5:1 molar ratios of mFAM72A to mUNG2. **(f)** Inhibition of hUNG2, but not *E. coli* UNG by mFAM72A. Purified *E. coli* UNG or hUNG2 proteins were pre-incubated with a five-fold molar excess of mFAM72A and then reacted with a double-stranded DNA substrate, with uracils at position 9 and 33 in a 55 bp DNA. Both the ends of the uracil-containing oligomer are labeled with 6-FAM (shown as stars). Consequently, two major excision products (U9 and U33) are observed. Uracil glycosylase inhibitor (Ugi) was used in one of the reactions. **(g)** The mRNAs for *Aicda*, *Ung2*, and *Fam72a* genes were quantified from WT (clone 1) and *Fam72a*<sup>-/-</sup> (clone 1) cell lines that had been stimulated with the CIT cocktail (+CIT) or untreated (-CIT). Mean values and standard deviations of three independent qRT-PCR reactions are shown for each treatment. The expression was normalized to the reference gene *TBP*. *Ung* transcript levels were also quantified in resting primary mouse B cells by qRT-PCR (bottom right panel; n=4 per group). Data were presented as mean ± SEM and were analyzed using two-tailed unpaired Student t test (ns: not significant). **(h)** Western blots for UNG, MSH2, and β-ACTIN (as control) in CIT-stimulated CH12 clones of the indicated genotype. UNG1 and UNG2 are indicated on the gel. Experiment was repeated 3 times independently with similar results. **(i)** Western blot analysis for UNG in WT CH12 cells expressing the empty

vector or overexpressing FAM72A. Experiment was repeated 3 times independently with similar results. (j) WT CH12 clone#1 and *Fam72<sup>-/-</sup>* CH12 clone#1 were treated with CHX or CHX plus MG132 for the indicated time, and lysates were probed with anti-UNG or anti-β-actin antibodies. Data are representative of 3 independent experiments. (k) Lysates from G<sub>1</sub>-synchronized *Fam72a<sup>-/-</sup>* CH12 cells were diluted to determine the level of increase of UNG2 protein compared to undiluted WT CH12 cells, then probed for UNG protein by western blot. These blots suggest a 3-4 fold increase in UNG2 protein in *Fam72a<sup>-/-</sup>* CH12 cells compared to controls. Data are representative of 3 independent experiments.

#### [Source data](#)

#### [Extended Data Fig. 10 Model for the role of FAM72A in SHM and CSR.](#)

FAM72A antagonizes UNG2 in the G<sub>1</sub> phase of the cell cycle, leading to reduced processing of the AID-induced dU in *Ig* genes, which leads to increased G:U mismatches. The increased G:U lesions can either be replicated to produce transition mutations at G:C basepairs, or can engage the mismatch repair system to enhance mutagenesis, or provide DNA lesions, in collaboration with UNG2 that are required for CSR. In the absence of FAM72A, the protein expression and enzymatic activity of UNG2 are enhanced, resulting in increased excision of dU, which favors faithful repair by base excision repair pathway, as evidenced by diminished mutation frequencies in both μ switch region and J<sub>H</sub>4 region. Furthermore, the accelerated removal of dU in the context of FAM72A deficiency fails to recruit the mismatch repair system in the G<sub>1</sub> or S phase, which is required for both CSR and SHM. One question that arises, is why doesn't CSR increase with increased UNG2 protein/activity in *Fam72a<sup>-/-</sup>* B cells? The key is the engagement of the MMR system by FAM72A to induce CSR. First, deleting FAM72A in *Msh2<sup>-/-</sup>* CH12 cells and *Msh2<sup>-/-</sup>* spleen B cells moderately increases CSR (Fig. 3d, f) consistent with an increased UNG2 level and activity inducing larger number of breaks to facilitate CSR. Importantly, CSR is not increased to WT levels. For SHM, the increased UNG2 activity in *Fam72a<sup>-/-</sup>* B cells would cause an increase in ssDNA

breaks in the V-region, but ultimately lead to faithful repair of the dUs, thereby erasing many AID-induced uracil lesions. Second, removal of either *Ung* or *Msh2* leads to a defect in CSR that is not additive suggesting an interaction between these two proteins during CSR (Fig. [3c, d](#)). For SHM, UNG and MMR pathways converge to induce error-prone repair. The exact mechanism likely involves the interruption of faithful MMR repair by uracil excision by UNG2. The interaction between these both pathways has not been formally shown in CSR, although there was evidence for this notion in the literature (e.g. see figure 3d in [6](#)). As to how MMR and UNG2 work together to induce CSR is not clear, and requires more work, but the mechanism might be similar to that hypothesized to what occurs during SHM. For CSR, we therefore hypothesize that FAM72A antagonizes UNG2, leading to the accumulation of U:G mispairs that can be engaged by the MMR system to induce CSR.

## Supplementary information

### Supplementary Information

This file contains Supplementary Tables 1, 2 and Supplementary Figs 1, 2.

### Reporting Summary

### Peer Review File

## Source data

### Source Data Fig. 1

### Source Data Fig. 2

### Source Data Fig. 3

### Source Data Fig. 4

[\*\*Source Data Extended Data Fig. 1\*\*](#)

[\*\*Source Data Extended Data Fig. 2\*\*](#)

[\*\*Source Data Extended Data Fig. 3\*\*](#)

[\*\*Source Data Extended Data Fig. 4\*\*](#)

[\*\*Source Data Extended Data Fig. 5\*\*](#)

[\*\*Source Data Extended Data Fig. 6\*\*](#)

[\*\*Source Data Extended Data Fig. 7\*\*](#)

[\*\*Source Data Extended Data Fig. 8\*\*](#)

[\*\*Source Data Extended Data Fig. 9\*\*](#)

## Rights and permissions

[Reprints and Permissions](#)

## About this article

### Cite this article

Feng, Y., Li, C., Stewart, J.A. *et al.* FAM72A antagonizes UNG2 to promote mutagenic repair during antibody maturation. *Nature* **600**, 324–328 (2021). <https://doi.org/10.1038/s41586-021-04144-4>

- Received: 16 December 2020
- Accepted: 14 October 2021
- Published: 24 November 2021

- Issue Date: 09 December 2021
- DOI: <https://doi.org/10.1038/s41586-021-04144-4>

## Share this article

Anyone you share the following link with will be able to read this content:

[Get shareable link](#)

Sorry, a shareable link is not currently available for this article.

[Copy to clipboard](#)

Provided by the Springer Nature SharedIt content-sharing initiative

---

This article was downloaded by **calibre** from <https://www.nature.com/articles/s41586-021-04144-4>

| [Section menu](#) | [Main menu](#) |

- Article
- [Published: 24 November 2021](#)

# *Fam72a* enforces error-prone DNA repair during antibody diversification

- [Mélanie Rogier](#) ORCID: [orcid.org/0000-0002-0522-8931](https://orcid.org/0000-0002-0522-8931)<sup>1,2,3,4 na1</sup>,
- [Jacques Moritz](#)<sup>1,2,3,4 na1</sup>,
- [Isabelle Robert](#) ORCID: [orcid.org/0000-0001-6533-8297](https://orcid.org/0000-0001-6533-8297)<sup>1,2,3,4</sup>,
- [Chloé Lescalle](#) ORCID: [orcid.org/0000-0003-0622-1149](https://orcid.org/0000-0003-0622-1149)<sup>5</sup>,
- [Vincent Heyer](#)<sup>1,2,3,4</sup>,
- [Arthur Abello](#)<sup>1,2,3,4</sup>,
- [Ophélie Martin](#)<sup>6</sup>,
- [Katia Capitani](#)<sup>7,8</sup>,
- [Morgane Thomas](#)<sup>9</sup>,
- [Anne-Sophie Thomas-Claudepierre](#)<sup>1,2,3,4</sup>,
- [Brice Laffleur](#)<sup>10</sup>,
- [Florence Jouan](#)<sup>10</sup>,
- [Eric Pinaud](#) ORCID: [orcid.org/0000-0001-7405-9273](https://orcid.org/0000-0001-7405-9273)<sup>9</sup>,
- [Karin Tarte](#) ORCID: [orcid.org/0000-0002-6809-917X](https://orcid.org/0000-0002-6809-917X)<sup>10</sup>,
- [Michel Cogné](#)<sup>9,10</sup>,
- [Silvestro G. Conticello](#) ORCID: [orcid.org/0000-0002-4244-1846](https://orcid.org/0000-0002-4244-1846)<sup>7,11</sup>,
- [Evi Soutoglou](#)<sup>6</sup>,
- [Ludovic Deriano](#) ORCID: [orcid.org/0000-0002-9673-9525](https://orcid.org/0000-0002-9673-9525)<sup>5</sup> &
- [Bernardo Reina-San-Martin](#) ORCID: [orcid.org/0000-0003-2083-6166](https://orcid.org/0000-0003-2083-6166)<sup>1,2,3,4</sup>

[Nature](#) volume 600, pages 329–333 (2021)

- 2999 Accesses
- 41 Altmetric
- [Metrics details](#)

## Subjects

- [Class switch recombination](#)
- [Somatic hypermutation](#)

## Abstract

Efficient humoral responses rely on DNA damage, mutagenesis and error-prone DNA repair. Diversification of B cell receptors through somatic hypermutation and class-switch recombination are initiated by cytidine deamination in DNA mediated by activation-induced cytidine deaminase (AID)<sup>1</sup> and by the subsequent excision of the resulting uracils by uracil DNA glycosylase (UNG) and by mismatch repair proteins<sup>1,2,3</sup>. Although uracils arising in DNA are accurately repaired<sup>1,2,3,4</sup>, how these pathways are co-opted to generate mutations and double-strand DNA breaks in the context of somatic hypermutation and class-switch recombination is unknown<sup>1,2,3</sup>. Here we performed a genome-wide CRISPR–Cas9 knockout screen for genes involved in class-switch recombination and identified FAM72A, a protein that interacts with the nuclear isoform of UNG (UNG2)<sup>5</sup> and is overexpressed in several cancers<sup>5</sup>. We show that the FAM72A–UNG2 interaction controls the levels of UNG2 and that class-switch recombination is defective in *Fam72a*<sup>-/-</sup> B cells due to the upregulation of UNG2. Moreover, we show that somatic hypermutation is reduced in *Fam72a*<sup>-/-</sup> B cells and that its pattern is skewed upon upregulation of UNG2. Our results are consistent with a model in which FAM72A interacts with UNG2 to control its physiological level by triggering its degradation, regulating the level of uracil excision and thus the balance between error-prone and error-free DNA repair. Our findings have potential implications for tumorigenesis, as reduced levels of UNG2 mediated by overexpression of *Fam72a* would shift the balance

towards mutagenic DNA repair, rendering cells more prone to acquire mutations.

This is a preview of subscription content

## Access options

Subscribe to Journal

Get full journal access for 1 year

\$199.00

only \$3.90 per issue

[Subscribe](#)

All prices are NET prices.

VAT will be added later in the checkout.

Tax calculation will be finalised during checkout.

Rent or Buy article

Get time limited or full article access on ReadCube.

from \$8.99

[Rent or Buy](#)

All prices are NET prices.

## Additional access options:

- [Log in](#)
- [Learn about institutional subscriptions](#)

**Fig. 1: A genome-wide CRISPR–Cas9 knockout screen for genes involved in CSR identifies *Fam72a*.**

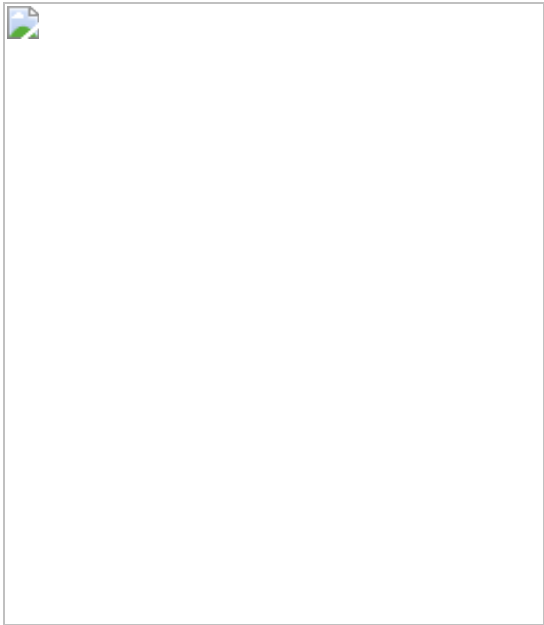


**Fig. 2: CSR is defective in B cells from *Fam72a*<sup>-/-</sup> mice.**

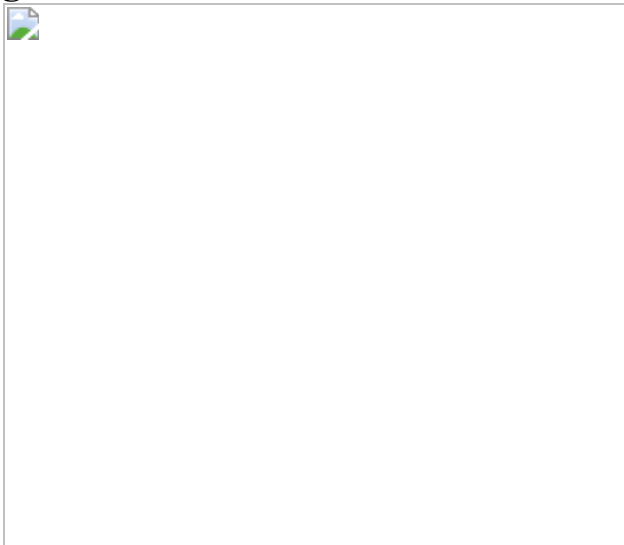


**Fig. 3: The CSR defect in *Fam72a*<sup>-/-</sup> B cells is due to the specific upregulation of UNG2.**

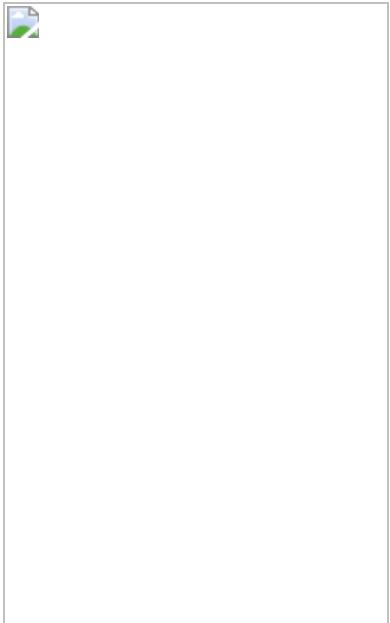


**Fig. 4: Deficiency in *Fam72a* shifts the balance towards error-free DNA repair.**



## Data availability

The CRISPR–Cas9 screen high-throughput sequencing data are available at the Gene Expression Omnibus ([GSE184145](#)). Source data for Figs. 1–4 can be found in [Supplementary Information](#). [Source data](#) are provided with this paper.

# References

1. 1.

Feng, Y., Seija, N., Di Noia, J. M. & Martin, A. AID in antibody diversification: there and back again. *Trends Immunol.* **41**, 586–600 (2020).

2. 2.

Methot, S. P. & Di Noia, J. M. Molecular mechanisms of somatic hypermutation and class switch recombination. *Adv. Immunol.* **133**, 37–87 (2017).

3. 3.

Stratigopoulou, M., van Dam, T. P. & Guikema, J. E. J. Base excision repair in the immune system: small DNA lesions with big consequences. *Front. Immunol.* **11**, 1084 (2020).

4. 4.

Krokan, H. E. et al. Error-free versus mutagenic processing of genomic uracil—relevance to cancer. *DNA Repair* **19**, 38–47 (2014).

5. 5.

Guo, C. et al. Ugene, a newly identified protein that is commonly overexpressed in cancer and binds uracil DNA glycosylase. *Cancer Res.* **68**, 6118–6126 (2008).

6. 6.

Rada, C. et al. Immunoglobulin isotype switching is inhibited and somatic hypermutation perturbed in UNG-deficient mice. *Curr. Biol.* **12**, 1748–1755 (2002).

7. 7.

Zanotti, K. J. & Gearhart, P. J. Antibody diversification caused by disrupted mismatch repair and promiscuous DNA polymerases. *DNA Repair* **38**, 110–116 (2016).

8. 8.

Nakamura, M. et al. High frequency class switching of an IgM<sup>+</sup> B lymphoma clone CH12F3 to IgA<sup>+</sup> cells. *Int. Immunol.* **8**, 193–201 (1996).

9. 9.

Doench, J. G. et al. Optimized sgRNA design to maximize activity and minimize off-target effects of CRISPR–Cas9. *Nat. Biotechnol.* **34**, 184–191 (2016).

10. 10.

Joung, J. et al. Genome-scale CRISPR–Cas9 knockout and transcriptional activation screening. *Nat. Protoc.* **12**, 828–863 (2017).

11. 11.

KOMP strain detail sheet. *MMRRC*  
[<https://www.mmrrc.org/catalog/sds.php?mmrcc\\_id=47653>](https://www.mmrrc.org/catalog/sds.php?mmrcc_id=47653)

12. 12.

Sarno, A. et al. Uracil-DNA glycosylase UNG1 isoform variant supports class switch recombination and repairs nuclear genomic uracil. *Nucleic Acids Res.* **47**, 4569–4585 (2019).

13. 13.

Begum, N. A. et al. Uracil DNA glycosylase activity is dispensable for immunoglobulin class switch. *Science* **305**, 1160–1163 (2004).

14. 14.

Di Noia, J. M. et al. Dependence of antibody gene diversification on uracil excision. *J. Exp. Med.* **204**, 3209–3219 (2007).

15. 15.

Yousif, A. S., Stanlie, A., Mondal, S., Honjo, T. & Begum, N. A. Differential regulation of S-region hypermutation and class-switch recombination by noncanonical functions of uracil DNA glycosylase. *Proc. Natl Acad. Sci. USA* **111**, E1016–E1024 (2014).

16. 16.

Eldin, P. et al. Impact of HIV-1 Vpr manipulation of the DNA repair enzyme UNG2 on B lymphocyte class switch recombination. *J. Transl. Med.* **18**, 310 (2020).

17. 17.

Holland, A. J., Fachinetti, D., Han, J. S. & Cleveland, D. W. Inducible, reversible system for the rapid and complete degradation of proteins in mammalian cells. *Proc. Natl Acad. Sci. USA* **109**, E3350–E3357 (2012).

18. 18.

Arakawa, H., Saribasak, H. & Buerstedde, J. M. Activation-induced cytidine deaminase initiates immunoglobulin gene conversion and hypermutation by a common intermediate. *PLoS Biol.* **2**, E179 (2004).

19. 19.

Martin, O. A. et al. Detecting rare AID-induced mutations in B-lineage oncogenes from high-throughput sequencing data using the detection of minor variants by error correction method. *J. Immunol.* **201**, 950–956 (2018).

20. 20.

Dev, H. et al. Shieldin complex promotes DNA end-joining and counters homologous recombination in BRCA1-null cells. *Nat. Cell Biol.* **20**, 954–965 (2018).

21. 21.

Yan, C. T. et al. IgH class switching and translocations use a robust non-classical end-joining pathway. *Nature* **449**, 478–482 (2007).

22. 22.

Krokan, H. E. & Bjoras, M. Base excision repair. *Cold Spring Harb. Perspect. Biol.* **5**, a012583 (2013).

23. 23.

Krokan, H. E., Drablos, F. & Slupphaug, G. Uracil in DNA—occurrence, consequences and repair. *Oncogene* **21**, 8935–8948 (2002).

24. 24.

Wu, X. & Stavnezer, J. DNA polymerase beta is able to repair breaks in switch regions and plays an inhibitory role during immunoglobulin class switch recombination. *J. Exp. Med.* **204**, 1677–1689 (2007).

25. 25.

Schrader, C. E., Guikema, J. E., Wu, X. & Stavnezer, J. The roles of APE1, APE2, DNA polymerase  $\beta$  and mismatch repair in creating S region DNA breaks during antibody class switch. *Phil. Trans. R. Soc. B* **364**, 645–652 (2009).

26. 26.

Nilsen, H. et al. Gene-targeted mice lacking the Ung uracil-DNA glycosylase develop B-cell lymphomas. *Oncogene* **22**, 5381–5386 (2003).

27. 27.

Andersen, S. et al. Monoclonal B-cell hyperplasia and leukocyte imbalance precede development of B-cell malignancies in uracil-DNA glycosylase deficient mice. *DNA Repair* **4**, 1432–1441 (2005).

28. 28.

Nilsen, H., An, Q. & Lindahl, T. Mutation frequencies and AID activation state in B-cell lymphomas from Ung-deficient mice. *Oncogene* **24**, 3063–3066 (2005).

29. 29.

Li, W. et al. MAGeCK enables robust identification of essential genes from genome-scale CRISPR/Cas9 knockout screens. *Genome Biol.* **15**, 554 (2014).

30. 30.

Kleinstiver, B. P. et al. High-fidelity CRISPR–Cas9 nucleases with no detectable genome-wide off-target effects. *Nature* **529**, 490–495 (2016).

31. 31.

Miyazaki, K. MEGAWHOP cloning: a method of creating random mutagenesis libraries via megaprimer PCR of whole plasmids. *Methods Enzymol.* **498**, 399–406 (2011).

32. 32.

MacCarthy, T., Roa, S., Scharff, M. D. & Bergman, A. SHMTool: a webserver for comparative analysis of somatic hypermutation datasets. *DNA Repair* **8**, 137–141 (2009).

33. 33.

Engler, C., Gruetzner, R., Kandzia, R. & Marillonnet, S. Golden gate shuffling: a one-pot DNA shuffling method based on type II restriction enzymes. *PLoS ONE* **4**, e5553 (2009).

34. 34.

Motohashi, K. A simple and efficient seamless DNA cloning method using SLiCE from *Escherichia coli* laboratory strains and its application to SLiP site-directed mutagenesis. *BMC Biotechnol.* **15**, 47 (2015).

35. 35.

Lescalle, C. et al. RAG2 and XLF/Cernunnos interplay reveals a novel role for the RAG complex in DNA repair. *Nat. Commun.* **7**, 10529 (2016).

36. 36.

Jeevan-Raj, B. P. et al. Epigenetic tethering of AID to the donor switch region during immunoglobulin class switch recombination. *J. Exp. Med.* **208**, 1649–1660 (2011).

37. 37.

Holden, P. & Horton, W. A. Crude subcellular fractionation of cultured mammalian cell lines. *BMC Res. Notes* **2**, 243 (2009).

## Acknowledgements

We thank A. Frey for help with gRNA library subcloning and the CRISPR–Cas9 screen; B. Kavli for the anti-UNG1/2 antibody; L. Brino for help with gRNA library subcloning and CRISPR–Cas9 screen analysis; B. Jost, C. Thibault-Carpentier and D. Plassard for gRNA high-throughput sequencing on the GenomEast platform of IGBMC; D. Dembele, S. Sarnataro and N. Molina for help with Python scripts and gRNA extraction and counting; B. Heller for cell culture; C. Ebel and M. Philipps for cell sorting in the FlowCytometry Facility of IGBMC; M. Li for the GL-7 antibody, M.

Selloum, D. Ali-Hadji and I. Gonçalves Da Cruz for animal care; W. Yu for generating *Xrcc4*<sup>-/-</sup> CH12 cells; and C. Goujon for the HIV1-VPR cDNA. J.M. and M.T. were supported by the Ministère de l'Enseignement Supérieur et de la Recherche, France, and the Fondation ARC. M.R. was supported by La Ligue Contre le Cancer. This study was supported by grants from the Fondation Recherche Médicale (Equipe FRM EQU201903007818 to B.R.-S.-M.), Institut National du Cancer (INCa\_13852 to L.D. and B.R.-S.-M.), Fondation ARC (ARCPJA32020060002061 to B.R.-S.-M.), the Ligue Nationale contre le Cancer (Equipe labellisée to L.D.) and by the grant ANR-10-LABX-0030-INRT, a French state fund managed by the Agence Nationale de la Recherche under the program Investissements d'Avenir labelled ANR-10-IDEX-0002-02.

## Author information

### Author notes

1. These authors contributed equally: Mélanie Rogier, Jacques Moritz

## Affiliations

1. Institut de Génétique et de Biologie Moléculaire et Cellulaire (IGBMC), Illkirch, France

Mélanie Rogier, Jacques Moritz, Isabelle Robert, Vincent Heyer, Arthur Abello, Anne-Sophie Thomas-Claudepierre & Bernardo Reina-San-Martin

2. Institut National de la Santé et de la Recherche Médicale (INSERM), U1258, Illkirch, France

Mélanie Rogier, Jacques Moritz, Isabelle Robert, Vincent Heyer, Arthur Abello, Anne-Sophie Thomas-Claudepierre & Bernardo Reina-San-Martin

3. Centre National de la Recherche Scientifique (CNRS), UMR7104,  
Illkirch, France

Mélanie Rogier, Jacques Moritz, Isabelle Robert, Vincent  
Heyer, Arthur Abello, Anne-Sophie Thomas-Claudepierre & Bernardo  
Reina-San-Martin

4. Université de Strasbourg, Illkirch, France

Mélanie Rogier, Jacques Moritz, Isabelle Robert, Vincent  
Heyer, Arthur Abello, Anne-Sophie Thomas-Claudepierre & Bernardo  
Reina-San-Martin

5. Genome Integrity, Immunity and Cancer Unit, Equipe Labellisée  
Ligue Contre Le Cancer, INSERM U1223, Institut Pasteur, Paris,  
France

Chloé Lescalle & Ludovic Deriano

6. Genome Damage and Stability Centre, School of Life Sciences,  
University of Sussex, Brighton, UK

Ophélie Martin & Evi Soutoglou

7. Core Research Laboratory, ISPRO, Firenze, Italy

Katia Capitani & Silvestro G. Conticello

8. Department of Medical Biotechnologies, University of Siena, Siena,  
Italy

Katia Capitani

9. Centre National de la Recherche Scientifique (CNRS), UMR7276,  
Institut National de la Santé et de la Recherche Médicale (INSERM),  
UMR1262-Contrôle de la Réponse Immune B et  
Lymphoproliférations, Université de Limoges, Limoges, France

Morgane Thomas, Eric Pinaud & Michel Cogné

10. Institut national de la santé et de la recherche médicale (INSERM),  
UMR1236, Université Rennes 1, Etablissement Français du Sang  
Bretagne, Rennes, France

Brice Laffleur, Florence Jouan, Karin Tarte & Michel Cogné

11. Institute of Clinical Physiology, National Research Council, Pisa, Italy

Silvestro G. Conticello

## Contributions

B.R.-S.-M. conceived and designed the study. M.R. generated CH12<sup>Cas9</sup> cells, subcloned the gRNA library and performed the CRISPR–Cas9 screen with I.R. Screen data were analysed by B.R.-S.-M. and M.R. All CH12 knockout cell lines were generated and characterized by M.R. and J.M. with the help of A.A. The majority of experiments in CH12 cells and in *Fam72a*<sup>-/-</sup> mice were performed by M.R. and J.M. *Igh* FISH experiments were performed and analysed by C.L. All constructs were cloned by M.R. and J.M., with help from V.H. V.H. performed the nuclear/chromatin fractionations and provided assistance for western blot analysis. M.R. and J.M. performed the SHM experiments in CH12 cells with the help of V.H. M.R. and J.M. performed SHM analysis in germinal centre B cells, with the help of A.A. O.M. generated the AID off-target high-throughput sequencing libraries, which were sequenced and analysed by M.T. and E.P. K.C. performed and analysed SHM in DT40 cells. A.-S.T.-C. performed mRNA sequencing and analysed the data. B.L. generated VPR lentiviral particles. F.J. performed immunohistochemistry on spleen sections. E.P., K.T., M.C., S.G.C. and E.S. oversaw experiments. M.R., J.M., E.S. and B.R.-S.-M. wrote the manuscript. M.R., J.M., C.L., E.S., L.D. and B.R.-S.-M. edited the manuscript. The overall research was directed by L.D. and B.R.-S.-M.

## Corresponding author

Correspondence to [Bernardo Reina-San-Martin](#).

## Ethics declarations

## Competing interests

The authors declare no competing interests.

## Additional information

**Peer review information** *Nature* thanks Uttiya Basu and the other, anonymous, reviewer(s) for their contribution to the peer review of this work. Peer reviewer reports are available.

**Publisher's note** Springer Nature remains neutral with regard to jurisdictional claims in published maps and institutional affiliations.

## Extended data figures and tables

### [Extended Data Fig. 1 Setting up the CRISPR/Cas9 genome-wide knock-out screen.](#)

**a**, Generation and validation of Cas9-expressing (CH12<sup>Cas9</sup>) cells. Clones were verified by Western blot for Cas9 expression, by PCR for Cas9-induced deletion of the enhancer γ1 (γ1E) and by flow cytometry for CSR. Clone #11 was chosen for the screen. Blots and data of CSR assay are representative of 3 experiments. **b**, The U6-gRNA sequence was amplified by PCR from the mBrie library and subcloned into pMX-28 using BamHI and NotI restriction enzymes to generate the pMX-mBrie gRNA library. gRNA representation was analyzed by high-throughput sequencing. **c**, Purity of IgM+ and IgA+ sorted populations was verified by flow cytometry. **d**, Number of reads at the *Aicda* and *Fam72a* genes in wild-type splenic B cells before and after 48h in culture with LPS and IL-4, as determined by mRNA-Seq. For gel source data, see Supplementary Fig. 1

### [Source data](#)

### [Extended Data Fig. 2 FAM72A interacts with UNG2 and Fam72a<sup>-/-</sup> CH12 cells have no defects in proliferation, AID](#)

## expression or switch region transcription.

**a**, Western blot analysis for Flag, UNG (UNG1 and UNG2) and β-Actin in wildtype and *Fam72a*<sup>-/-</sup> CH12 cells transduced with a retrovirus expressing FAM72A-Flag or FAM72A<sup>W125A</sup>-Flag before (Input) or after immunoprecipitation with a Flag-specific antibody (Pulldown). **b**, Schematic representation of the murine *Fam72a* locus and location of the gRNAs used to generate *Fam72a*<sup>-/-</sup> clones using CRISPR/Cas9-HF1. **c**, RT-PCR analysis for *Fam72a* and *Igβ* in *Fam72a*<sup>+/+</sup> and *Fam72a*<sup>-/-</sup> CH12 cells cultured or not for 3 days with TGFβ, anti-CD40 antibody and IL-4 (CIT). Data are representative of three experiments. **d**, Western blot analysis for AID and β-actin in wild-type (pCH12) and *Fam72a*<sup>-/-</sup> CH12 cells cultured or not for 3 days with TGFβ, anti-CD40 antibody and IL-4 (CIT). **e**, CFSE dye-dilution analysis by flow cytometry in *Fam72a*<sup>+/+</sup> and two independent *Fam72a*<sup>-/-</sup> CH12 cell clones cultured for 3 days with TGFβ, IL-4 and anti-CD40 antibody. Data are representative of three experiments. **f**, RT-qPCR analysis for GLTμ and GLTα in *Fam72a*<sup>+/+</sup> and *Fam72a*<sup>-/-</sup> CH12 cells cultured for 3 days with TGFβ, IL-4 and anti-CD40 antibody. Triplicates were normalized to the abundance of *Igβ* and are expressed relative to *Fam72a*<sup>+/+</sup>, set as 1. Statistical significance was determined by a two-tailed Student's *t*-test. Data are presented as mean ± s.d. and are representative of 3 experiments. For gel source data, see Supplementary Fig. 1

Source data.

## Extended Data Fig. 3 Robust B cell development and switch region transcription in *Fam72a*<sup>-/-</sup> mice.

**a**, Schematic representation of the murine *Fam72a* locus and strategy for the generation of *Fam72a*<sup>-/-</sup> mouse model. **b**, **c**, Flow cytometry and cellular analysis of B cell populations in the bone marrow (**b**) or the spleen (**c**) from *Fam72a*<sup>+/+</sup> and *Fam72a*<sup>-/-</sup> mice, using the indicated cell surface markers. The data are representative of 5 mice per genotype. Horizontal line: mean values. **d**, Real-time qPCR analysis for germline transcripts at donor (GLTμ) and acceptor switch regions (GLTγ3, GLTγ1, GLTγ2b, GLTγ2a and

GLT $\alpha$ ) in *Fam72a*<sup>+/+</sup> and *Fam72a*<sup>-/-</sup> splenic B cells cultured for 96h as in **c**. Expression is normalized to Ig $\beta$  and is presented relative to expression in *Fam72a*<sup>+/+</sup> B cells, set as 1. Mean of three mice per genotype + SEM were calculated following the rules for error propagation while calculating a ratio. Statistical analysis was performed using two-tailed Student's *t*-test

[Source data.](#)

**Extended Data Fig. 4 FAM72A specifically controls UNG2 protein levels and its accession to chromatin via a proteasome-dependent mechanism.**

**a**, RT-PCR analysis for *Fam72a* and *Ig $\beta$*  in *Fam72a*<sup>+/+</sup> and *Fam72a*<sup>-/-</sup> CH12 cells transduced (or not) with a retrovirus expressing FAM72A, FAM72A<sup>W125R</sup> or FAM72A<sup>W125A</sup>. Data are representative of three experiments. **b**, Flow cytometry analysis of IgA expression in *Fam72a*<sup>+/+</sup> and *Fam72a*<sup>-/-</sup> CH12 cells expressing (or not) an UNG inhibitor (Ugi) and cultured for 3 days with TGF $\beta$ , anti-CD40 antibody and IL-4. Representative plots are shown. The percentage of IgA-expressing cells is indicated. **c**, Schematic representation of the murine *Ung* locus and location of the gRNAs targeting *Ung2* (exon 1a; blue), *Ung1* (exon 1b; purple) or *Ung1/2* (exon4; black) used to generate *Ung1*<sup>-/-</sup>, *Ung2*<sup>-/-</sup>, *Ung1*<sup>-/-</sup> *Ung2*<sup>-/-</sup>, *Fam72a*<sup>-/-</sup> *Ung1*<sup>-/-</sup> and *Fam72a*<sup>-/-</sup> *Ung2*<sup>-/-</sup> CH12 cell clones using CRISPR/Cas9-HF1. Note, the gRNAs used to generate *Ung1/2*<sup>-/-</sup> CH12 cells target the same exon, which was deleted in *Ung1/2*-deficient mice. **d**, Western blot analysis for UNG (UNG1 and UNG2) and  $\beta$ -actin in wild-type, *Fam72a*<sup>-/-</sup>, *Ung1/2*<sup>-/-</sup>, *Ung1*<sup>-/-</sup>, *Ung2*<sup>-/-</sup>, *Fam72a*<sup>-/-</sup> *Ung1*<sup>-/-</sup> and *Fam72a*<sup>-/-</sup> *Ung2*<sup>-/-</sup> CH12 cells. Blots are representative of 3 experiments. **e**, Flow cytometry analysis of IgA expression in additional independent wildtype, *Ung1*<sup>-/-</sup>, *Ung2*<sup>-/-</sup>, *Fam72a*<sup>-/-</sup> *Ung1*<sup>-/-</sup> and *Fam72a*<sup>-/-</sup> *Ung2*<sup>-/-</sup> CH12 cells cultured for 72 h with TGF $\beta$ , IL-4 and anti-CD40 antibody. **f**, Western blot analysis for UNG (UNG1 and UNG2), NBS1 and Histone H3 on nuclear and chromatin fractions prepared from CH12 cells (pCH12) and *Fam72a*<sup>-/-</sup> CH12 cells expressing FAM72A or FAM72A<sup>W125R</sup>. Representative blots of 2 experiments. **g**, RT-qPCR analysis for *Ung1*, *Ung2* and *Ig $\beta$*  in *Fam72a*<sup>+/+</sup> and *Fam72a*<sup>-/-</sup> splenic B cells cultured for 4

days with LPS, IL-4 and anti-IgD-Dextran. Triplicates were normalized to the abundance of Ig $\beta$  and are expressed relative to *Fam72a*<sup>+/+</sup> B cells, set as 1. Data are presented as mean of five mice per genotype  $\pm$  s.d. Statistical analysis was performed using two-tailed Student's *t*-test. **h**, Western blot analysis for UNG (UNG1 and UNG2) and  $\beta$ -Actin in wild-type and *Fam72a*<sup>-/-</sup> CH12 cells cultured in the presence of cycloheximide (CHX) and MG132. **i**, Quantification of the protein level of UNG2, relative to time point zero from 3 independent experiments. Data are presented as mean  $\pm$  s.d. Statistical analysis was performed using two-tailed Student's *t* test. For gel source data, see Supplementary Fig. 1

[Source data.](#)

[Extended Data Fig. 5 UNG2 protein levels correlate with the efficiency of CSR.](#)

**a**, Western blot analysis for UNG (UNG1 and UNG2) and  $\beta$ -Actin protein levels in wild-type CH12 cells and primary B cells transduced with a retrovirus expressing FAM72A, FAM72A<sup>W125A</sup> or UNG2 and cultured with TGF $\beta$ , IL-4 and anti-CD40 antibody or LPS + IL-4 + anti-IgD-Dextran, respectively. **b**, Western blot analysis for UNG (UNG1 and UNG2) and  $\beta$ -actin in *Fam72a*<sup>-/-</sup> CH12 cells transduced with a retrovirus expressing HIV1-VPR (pMX-VPR), FAM72A and/or FAM72A<sup>W125A</sup>. **c**, Flow cytometry analysis of IgA expression in *Fam72a*<sup>-/-</sup> CH12 cells transduced with a retrovirus expressing HIV1-VPR (pMX-VPR), FAM72A and/or FAM72A<sup>W125A</sup>. Representative plots of three experiments are shown and quantified on the right. P values were determined using two-tailed Student's *t*-test; see Statistics and Reproducibility section in Methods. n.s: not significant; \*\*<0.01; \*\*\*<0.001. Horizontal line: mean values. **d**, Flow cytometry analysis of IgA expression in wild-type, *Fam72a*<sup>-/-</sup> and *Ung1/2*<sup>-/-</sup> CH12 cells transduced (or not) with a retrovirus expressing UNG2<sup>Degron</sup> and TIR1 and cultured for 72 h with TGF $\beta$ , IL-4 and anti-CD40 antibody in the presence or absence of auxin (IAA). Quantification is shown on the right. P-values were determined using two-tailed Student's *t*-test; see Statistics and Reproducibility section in Methods. \*<0.05; \*\*<0.005; \*\*\*<0.0005. Horizontal line: mean values. Data are from three experiments. **e**,

Western blot analysis for UNG (UNG1 and UNG2) and β-Actin in wild-type, *Fam72a*<sup>-/-</sup>, and *Ung1/2*<sup>-/-</sup>, transduced (or not) with a retrovirus expressing UNG2<sup>Degron</sup> and Tir1 and cultured in the presence or absence of auxin (IAA). Blots **a**, **b** and **e** are representative of 3 independent experiments. For gel source data, see Supplementary Fig. 1

[Source data](#).

### Extended Data Fig. 6 Somatic hypermutation at the J<sub>H</sub>4 intron (J<sub>H</sub>4i).

**a**, Flow cytometry analysis of germinal center B cells (B220+ Fas+ GL-7+) isolated from the Peyer's patches of unimmunized *Fam72a*<sup>+/+</sup> and *Fam72a*<sup>-/-</sup> mice. Plots are gated on B220+ cells. **b**, Distribution of mutations at the J<sub>H</sub>4 intron (J<sub>H</sub>4i) in *Fam72a*<sup>+/+</sup> (top) and *Fam72a*<sup>-/-</sup> (bottom) sequences obtained from germinal center B cells (B220+ Fas+ GL-7+) isolated from the Peyer's patches (PPs) of unimmunized *Fam72a*<sup>+/+</sup> and *Fam72a*<sup>-/-</sup> mice. **c**, Mean frequencies (at JH4i) of transition and transversion mutations at G/C and A/T base pairs, per sequence for each individual mouse analyzed. Data come from 5 mice of each genotype. p-value was determined using two-tailed Student's *t*-test. Horizontal line: mean values

[Source data](#).

### Extended Data Fig. 7 Somatic hypermutation at AID off-targets and *Igh* FISH strategy.

**a**, Tables depicting the mutation profiles observed for *Bcl6*, *Cd83* and *Pim1* in germinal center B cells (B220+ Fas+ GL-7+) isolated from the Peyer's patches (PPs) of unimmunized *Fam72a*<sup>+/+</sup> and *Fam72a*<sup>-/-</sup> mice. The respective number of nucleotides sequenced for each gene is also indicated. Data are from five mice per genotype. **b**, Schematic representation of the *Igh* locus with positions of the BACs used for generation of DNA FISH probes. Lower panel: DNA-FISH on representative metaphases from day 2

stimulated *Fam72a*<sup>-/-</sup> cells complemented with FAM72A or FAM72A<sup>W125A</sup> using the *Igh C* BAC probe (red) combined with *Igh V* BAC probe (green) and chromosome 12 paint (white). Yellow arrowheads point to broken or translocated chromosome 12

[Source data](#).

### **Extended Data Fig. 8 Working model for SHM and CSR in the presence or absence of FAM72A.**

Immunoglobulin genes are diversified through Somatic Hypermutation (SHM) and Class Switch Recombination (CSR). They are both initiated by the deamination of cytosines in DNA induced by Activation Induced Cytidine Deaminase (AID). The resulting uracils are processed, mainly by the nuclear isoform of Uracil DNA Glycosylase (UNG2), and by proteins of the Base Excision Repair (BER) and Mismatch Repair (MMR) pathways to introduce mutations or double-stranded DNA breaks (DSBS) during SHM (left panel) or CSR (right panel). FAM72A interacts with UNG2 to control its physiological level by triggering its degradation and to enforce error-prone DNA repair. Consequently, deficiency in *Fam72a* leads to the specific upregulation of UNG2 and its accumulation on chromatin. This would enhance uracil excision, resulting in a reduction in the efficiency of SHM and CSR and enforced error-free DNA repair. Therefore, FAM72A controls the balance between error-prone and error-free DNA repair during antibody diversification.

## **Supplementary information**

### **Supplementary Information**

This file contains Supplementary Figures 1 and 2.

### **Reporting Summary**

### **Peer Review File**

## **Supplementary Table 1**

CRISPR–Cas9 screen results.

## **Supplementary Table 2**

Igh FISH data.

## **Supplementary Table 3**

Primers and gRNAs.

## **Source data**

[\*\*Source Data Fig. 1\*\*](#)

[\*\*Source Data Fig. 2\*\*](#)

[\*\*Source Data Fig. 3\*\*](#)

[\*\*Source Data Fig. 4\*\*](#)

[\*\*Source Data Extended Data Fig. 1\*\*](#)

[\*\*Source Data Extended Data Fig. 2\*\*](#)

[\*\*Source Data Extended Data Fig. 3\*\*](#)

[\*\*Source Data Extended Data Fig. 4\*\*](#)

[\*\*Source Data Extended Data Fig. 5\*\*](#)

[\*\*Source Data Extended Data Fig. 6\*\*](#)

## Source Data Extended Data Fig. 7

## Rights and permissions

### Reprints and Permissions

## About this article

### Cite this article

Rogier, M., Moritz, J., Robert, I. *et al.* *Fam72a* enforces error-prone DNA repair during antibody diversification. *Nature* **600**, 329–333 (2021).  
<https://doi.org/10.1038/s41586-021-04093-y>

- Received: 17 December 2020
- Accepted: 04 October 2021
- Published: 24 November 2021
- Issue Date: 09 December 2021
- DOI: <https://doi.org/10.1038/s41586-021-04093-y>

## Share this article

Anyone you share the following link with will be able to read this content:

[Get shareable link](#)

Sorry, a shareable link is not currently available for this article.

[Copy to clipboard](#)

Provided by the Springer Nature SharedIt content-sharing initiative

---

This article was downloaded by **calibre** from <https://www.nature.com/articles/s41586-021-04093-y>.

| [Section menu](#) | [Main menu](#) |

- Article
- [Published: 17 November 2021](#)

# Structural insights into Ubr1-mediated N-degron polyubiquitination

- [Man Pan](#) ORCID: [orcid.org/0000-0001-7216-8193<sup>1 na1</sup>](https://orcid.org/0000-0001-7216-8193),
- [Qingyun Zheng](#)<sup>2,3 na1</sup>,
- [Tian Wang](#)<sup>2 na1</sup>,
- [Lujun Liang](#)<sup>2 na1</sup>,
- [Junxiong Mao](#)<sup>2</sup>,
- [Chong Zuo](#)<sup>2</sup>,
- [Ruichao Ding](#)<sup>2</sup>,
- [Huasong Ai](#)<sup>2</sup>,
- [Yuan Xie](#) ORCID: [orcid.org/0000-0001-5105-7136<sup>1</sup>](https://orcid.org/0000-0001-5105-7136),
- [Dong Si](#) ORCID: [orcid.org/0000-0001-7039-2589<sup>4</sup>](https://orcid.org/0000-0001-7039-2589),
- [Yuanyuan Yu](#) ORCID: [orcid.org/0000-0002-5379-5148<sup>1,3</sup>](https://orcid.org/0000-0002-5379-5148),
- [Lei Liu](#) ORCID: [orcid.org/0000-0001-6290-8602<sup>2</sup>](https://orcid.org/0000-0001-6290-8602) &
- [Minglei Zhao](#) ORCID: [orcid.org/0000-0001-5832-6060<sup>1</sup>](https://orcid.org/0000-0001-5832-6060)

*Nature* volume 600, pages 334–338 (2021)

- 4589 Accesses
- 92 Altmetric
- [Metrics details](#)

## Subjects

- [Cryoelectron microscopy](#)
- [Enzyme mechanisms](#)
- [Ubiquitin ligases](#)
- [Ubiquitylation](#)

## Abstract

The N-degron pathway targets proteins that bear a destabilizing residue at the N terminus for proteasome-dependent degradation<sup>1</sup>. In yeast, Ubr1—a single-subunit E3 ligase—is responsible for the Arg/N-degron pathway<sup>2</sup>. How Ubr1 mediates the initiation of ubiquitination and the elongation of the ubiquitin chain in a linkage-specific manner through a single E2 ubiquitin-conjugating enzyme (Ubc2) remains unknown. Here we developed chemical strategies to mimic the reaction intermediates of the first and second ubiquitin transfer steps, and determined the cryo-electron microscopy structures of Ubr1 in complex with Ubc2, ubiquitin and two N-degron peptides, representing the initiation and elongation steps of ubiquitination. Key structural elements, including a Ubc2-binding region and an acceptor ubiquitin-binding loop on Ubr1, were identified and characterized. These structures provide mechanistic insights into the initiation and elongation of ubiquitination catalysed by Ubr1.

This is a preview of subscription content

## Access options

Subscribe to Journal

Get full journal access for 1 year

\$199.00

only \$3.90 per issue

[Subscribe](#)

All prices are NET prices.  
VAT will be added later in the checkout.  
Tax calculation will be finalised during checkout.

Rent or Buy article

Get time limited or full article access on ReadCube.

from \$8.99

[Rent or Buy](#)

All prices are NET prices.

### **Additional access options:**

- [Log in](#)
- [Learn about institutional subscriptions](#)

**Fig. 1: The structure of the initiation complex.**



**Fig. 2: The structure of the elongation complex.**

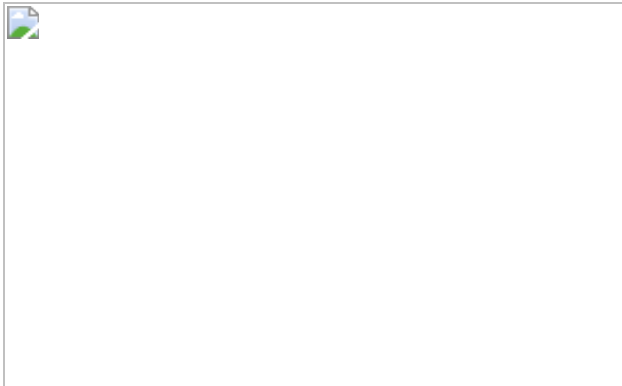


**Fig. 3: Analyses of the interactions between Ubc2 and Ubr1.**

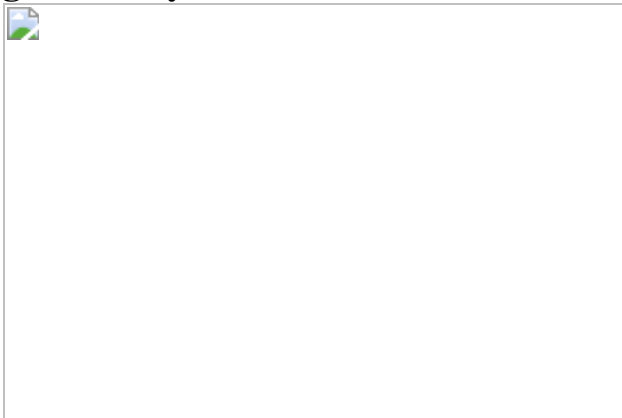


**Fig. 4: A model of Ubr1-mediated polyubiquitination.**

## Data availability

Cryo-EM maps have been deposited in the Electron Microscopy Data Bank (EMDB, [www.ebi.ac.uk/pdbe/emdb/](http://www.ebi.ac.uk/pdbe/emdb/)) under accession codes [EMDB-23806](#) (initiation complex), [EMDB-23807](#) (elongation complex), [EMDB-24935](#) (pre-elongation complex) and [EMDB-24936](#) (apo Ubr1). The atomic models have been deposited in the Protein Data Bank (PDB, [www.rcsb.org](http://www.rcsb.org))

under the accession codes [7MEX](#) (initiation complex) and [7MEY](#) (elongation complex). The atomic model of UbcH5 and the RING finger domain of TRIM25 is available under PDB accession code [5FER](#). Uncropped gels and blots source data are provided in Supplementary Fig. [7](#). Owing to the large file size, raw electron microscopy data are available from the corresponding authors on request. [Source data](#) are provided with this paper.

## References

1. 1.

Chau, V. et al. A multiubiquitin chain is confined to specific lysine in a targeted short-lived protein. *Science* **243**, 1576–1583 (1989).

2. 2.

Bartel, B., Wunning, I. & Varshavsky, A. The recognition component of the N-end rule pathway. *EMBO J.* **9**, 3179–3189 (1990).

3. 3.

Komander, D. & Rape, M. The ubiquitin code. *Annu. Rev. Biochem.* **81**, 203–229 (2012).

4. 4.

Chen, S. J., Wu, X., Wadas, B., Oh, J. H. & Varshavsky, A. An N-end rule pathway that recognizes proline and destroys gluconeogenic enzymes. *Science* **355**, eaal3655 (2017).

5. 5.

Kim, J. M. et al. Formyl-methionine as an N-degron of a eukaryotic N-end rule pathway. *Science* **362**, eaat0174 (2018).

6. 6.

Tasaki, T., Sriram, S. M., Park, K. S. & Kwon, Y. T. The N-end rule pathway. *Annu. Rev. Biochem.* **81**, 261–289 (2012).

7. 7.

Varshavsky, A. The N-end rule pathway and regulation by proteolysis. *Protein Sci.* **20**, 1298–1345 (2011).

8. 8.

Zenker, M. et al. Deficiency of UBR1, a ubiquitin ligase of the N-end rule pathway, causes pancreatic dysfunction, malformations and mental retardation (Johanson-Blizzard syndrome). *Nat. Genet.* **37**, 1345–1350 (2005).

9. 9.

Bodnar, N. O. & Rapoport, T. A. Molecular mechanism of substrate processing by the Cdc48 ATPase complex. *Cell* **169**, 722–735 (2017).

10. 10.

Petroski, M. D. & Deshaies, R. J. Mechanism of lysine 48-linked ubiquitin-chain synthesis by the cullin-RING ubiquitin-ligase complex SCF-Cdc34. *Cell* **123**, 1107–1120 (2005).

11. 11.

Saha, A. & Deshaies, R. J. Multimodal activation of the ubiquitin ligase SCF by Nedd8 conjugation. *Mol. Cell* **32**, 21–31 (2008).

12. 12.

Tasaki, T. et al. The substrate recognition domains of the N-end rule pathway. *J. Biol. Chem.* **284**, 1884–1895 (2009).

13. 13.

Baek, K. et al. NEDD8 nucleates a multivalent cullin-RING-UBE2D ubiquitin ligation assembly. *Nature* **578**, 461–466 (2020).

14. 14.

Horn-Ghetko, D. et al. A Ubiquitin ligation to F-box protein targets by SCF-RBR E3-E3 super-assembly. *Nature* **590**, 671–676 (2021).

15. 15.

Rusnac, D. V. & Zheng, N. Structural biology of CRL ubiquitin ligases. *Adv. Exp. Med. Biol.* **1217**, 9–31 (2020).

16. 16.

Matta-Camacho, E., Kozlov, G., Li, F. F. & Gehring, K. Structural basis of substrate recognition and specificity in the N-end rule pathway. *Nat. Struct. Mol. Biol.* **17**, 1182–1187 (2010).

17. 17.

Choi, W. S. et al. Structural basis for the recognition of N-end rule substrates by the UBR box of ubiquitin ligases. *Nat. Struct. Mol. Biol.* **17**, 1175–1181 (2010).

18. 18.

Du, F. Y., Navarro-Garcia, F., Xia, Z. X., Tasaki, T. & Varshavsky, A. Pairs of dipeptides synergistically activate the binding of substrate by ubiquitin ligase through dissociation of its autoinhibitory domain. *Proc. Natl Acad. Sci. USA* **99**, 14110–14115 (2002).

19. 19.

Roman-Hernandez, G., Grant, R. A., Sauer, R. T. & Baker, T. A. Molecular basis of substrate selection by the N-end rule adaptor protein ClpS. *Proc. Natl Acad. Sci. USA* **106**, 8888–8893 (2009).

20. 20.

AhYoung, A. P., Koehl, A., Vizcarra, C. L., Cascio, D. & Egea, P. F. Structure of a putative ClpS N-end rule adaptor protein from the malaria pathogen *Plasmodium falciparum*. *Protein Sci.* **25**, 689–701 (2016).

21. 21.

Kim, L. et al. Structural basis for the N-degron specificity of ClpS1 from *Arabidopsis thaliana*. *Protein Sci.* **30**, 700–708 (2021).

22. 22.

Das, R. et al. Allosteric activation of E2-RING finger-mediated ubiquitylation by a structurally defined specific E2-binding region of gp78. *Mol. Cell* **34**, 674–685 (2009).

23. 23.

Metzger, M. B. et al. A Structurally unique E2-binding domain activates ubiquitination by the ERAD E2, Ubc7p, through multiple mechanisms. *Mol. Cell* **50**, 516–527 (2013).

24. 24.

Koliopoulos, M. G., Esposito, D., Christodoulou, E., Taylor, I. A. & Rittinger, K. Functional role of TRIM E3 ligase oligomerization and regulation of catalytic activity. *EMBO J.* **35**, 1204–1218 (2016).

25. 25.

Plechanovova, A., Jaffray, E. G., Tatham, M. H., Naismith, J. H. & Hay, R. T. Structure of a RING E3 ligase and ubiquitin-loaded E2 primed for catalysis. *Nature* **489**, 115–120 (2012).

26. 26.

Zheng, Q. et al. An E1-catalyzed chemoenzymatic strategy to isopeptide-*N*-ethylated deubiquitylase-resistant ubiquitin probes. *Angew. Chem. Int. Ed. Engl.* **59**, 13496–13501 (2020).

27. 27.

Liu, Y. J. et al. Degradation of the separase-cleaved Rec8, a meiotic cohesin subunit, by the N-end rule pathway. *J. Biol. Chem.* **291**, 7426–7438 (2016).

28. 28.

Degroot, R. J., Rumenapf, T., Kuhn, R. J., Strauss, E. G. & Strauss, J. H. Sindbis virus-RNA polymerase is degraded by the N-end rule pathway. *Proc. Natl Acad. Sci. USA* **88**, 8967–8971 (1991).

29. 29.

Rao, H., Uhlmann, F., Nasmyth, K. & Varshavsky, A. Degradation of a cohesin subunit by the N-end rule pathway is essential for chromosome stability. *Nature* **410**, 955–959 (2001).

30. 30.

Szoradi, T. et al. SHRED is a regulatory cascade that reprograms Ubr1 substrate specificity for enhanced protein quality control during stress. *Mol. Cell* **70**, 1025–1037 (2018).

31. 31.

Streich, F. C., Jr & Lima, C. D. Capturing a substrate in an activated RING E3/E2-SUMO complex. *Nature* **536**, 304–308 (2016).

32. 32.

Xia, Z. et al. Substrate-binding sites of UBR1, the ubiquitin ligase of the N-end rule pathway. *J. Biol. Chem.* **283**, 24011–24028 (2008).

33. 33.

Pan, M. et al. Chemical protein synthesis enabled mechanistic studies on the molecular recognition of K27-linked ubiquitin chains. *Angew. Chem. Int. Ed. Engl.* **58**, 2627–2631 (2019).

34. 34.

Pan, M. et al. Quasi-racemic X-ray structures of K27-linked ubiquitin chains prepared by total chemical synthesis. *J. Am. Chem. Soc.* **138**, 7429–7435 (2016).

35. 35.

Qu, Q. et al. A highly efficient synthesis of polyubiquitin chains. *Adv. Sci.* **5**, 1800234 (2018).

36. 36.

Zheng, S. Q. et al. MotionCor2: anisotropic correction of beam-induced motion for improved cryo-electron microscopy. *Nat. Methods* **14**, 331–332 (2017).

37. 37.

Mindell, J. A. & Grigorieff, N. Accurate determination of local defocus and specimen tilt in electron microscopy. *J. Struct. Biol.* **142**, 334–347 (2003).

38. 38.

Zivanov, J. et al. New tools for automated high-resolution cryo-EM structure determination in RELION-3. *eLife* **7**, e42166 (2018).

39. 39.

Pfab, J., Phan, N. M. & Si, D. DeepTracer for fast de novo cryo-EM protein structure modeling and special studies on CoV-related complexes. *Proc. Natl Acad. Sci. USA* **118**, e2017525118 (2021).

40. 40.

Adams, P. D. et al. PHENIX: a comprehensive Python-based system for macromolecular structure solution. *Acta. Crystallogr. D* **66**, 213–221 (2010).

41. 41.

Emsley, P. & Cowtan, K. Coot: model-building tools for molecular graphics. *Acta Crystallogr D* **60**, 2126–2132 (2004).

42. 42.

Croll, T. I. ISOLDE: a physically realistic environment for model building into low-resolution electron-density maps. *Acta Crystallogr D* **74**, 519–530 (2018).

43. 43.

Pettersen, E. F. et al. UCSF ChimeraX: structure visualization for researchers, educators, and developers. *Protein Sci.* **30**, 70–82 (2021).

44. 44.

Krissinel, E. & Henrick, K. Inference of macromolecular assemblies from crystalline state. *J. Mol. Biol.* **372**, 774–797 (2007).

45. 45.

Holm, L. DALI and the persistence of protein shape. *Protein Sci.* **29**, 128–140 (2020).

46. 46.

Waterhouse, A. et al. SWISS-MODEL: homology modelling of protein structures and complexes. *Nucleic Acids Res.* **46**, W296–W303 (2018).

## Acknowledgements

We thank the staff at the National Cryo-Electron Microscopy Facility at the Frederick National Laboratory and the Advanced Electron Microscopy Facility at the University of Chicago for the help with cryo-EM data collection; H. Rao (Southern University of Science and Technology) and R. Hu (University of Chinese Academy of Sciences) for their help in yeast

related experiments. Funding for this work was in part provided by the Catalyst Award C-086 to M.Z. from the Chicago Biomedical Consortium. M.Z. is supported by National Institute of General Medical Sciences of the National Institutes of Health (NIH) under award number R35GM143052. We thank the National Key R&D Program of China (no. 2017YFA0505200) and NSFC (nos 91753205, 81621002, 21621003) for financial support; the National Postdoctoral Program for Innovative Talents (BX2021143), Shuimu Tsinghua Scholar Program (2021SM067) for financial support. This research was in part supported by the National Cancer Institute's National Cryo-EM Facility at the Frederick National Laboratory for Cancer Research under contract HSSN261200800001E. This research is based on work supported by the National Science Foundation under grant no. 2030381, the graduate research award of Computing and Software Systems division and the start-up fund 74–0525 at University of Washington Bothell to D.S. Any opinions, findings, and conclusions or recommendations expressed in this paper are those of the authors and do not necessarily reflect the views of the National Science Foundation. Molecular graphics and analyses were performed using UCSF ChimeraX, developed by the Resource for Biocomputing, Visualization, and Informatics at the University of California, San Francisco, with support from NIH R01GM129325 and the Office of Cyber Infrastructure and Computational Biology, National Institute of Allergy and Infectious Diseases.

## Author information

### Author notes

1. These authors contributed equally: Man Pan, Qingyun Zheng, Tian Wang, Lujun Liang

## Affiliations

1. Department of Biochemistry and Molecular Biology, The University of Chicago, Chicago, IL, USA

Man Pan, Yuan Xie, Yuanyuan Yu & Minglei Zhao

2. Tsinghua-Peking Center for Life Sciences, Department of Chemistry,  
Tsinghua University, Beijing, China

Qingyun Zheng, Tian Wang, Lujun Liang, Junxiong Mao, Chong  
Zuo, Ruichao Ding, Huasong Ai & Lei Liu

3. School of Medicine, Institute of Translational Medicine, Shanghai  
University, Shanghai, China

Qingyun Zheng & Yuanyuan Yu

4. Division of Computing and Software Systems, University of  
Washington Bothell, Bothell, WA, USA

Dong Si

## Contributions

M.P., M.Z., L. Liu and Y.Y. designed all of the experiments and interpreted the results. M.P., Q.Z. and L. Liu designed the synthetic route for chemically synthesized ubiquitination initiation and elongation intermediate mimics. T.W. synthesized the fluorescently labelled Ub–Degron and the elongation intermediate mimic. L. Liang synthesized the fluorescently labelled Degron and the initiation intermediate mimic. M.P., Y.Y., D.S. and M.Z. performed cryo-EM data collection and processing. J.M. performed the in vitro ubiquitination assays with Ubr1 and Ubc2 mutants. Q.Z. performed characterization of the U2BR peptide on the enzymatic properties of Ubc2. T.W., Y.Y., C.Z., R.D., J.M., H.A. and Y.X. cloned, expressed and purified Ubr1, Ubc2 and their mutants. M.Z., M.P. and L. Liu wrote the paper. M.Z., L. Liu, Y.Y. and M.P. supervised the project.

## Corresponding authors

Correspondence to [Man Pan](#), [Yuanyuan Yu](#), [Lei Liu](#) or [Minglei Zhao](#).

## Ethics declarations

## Competing interests

The authors declare no competing interests.

## Additional information

**Peer review information** *Nature* thanks Yong Tae Kwon and the other, anonymous, reviewer(s) for their contribution to the peer review of this work. Peer reviewer reports are available.

**Publisher's note** Springer Nature remains neutral with regard to jurisdictional claims in published maps and institutional affiliations.

## Extended data figures and tables

### [Extended Data Fig. 1 Ubr1-mediated Lys48-linked polyubiquitination of degron peptides.](#)

**a**, The amino acid sequence of the degron peptide (Degrон). SPPS: solid-phase peptide synthesis. **b**, The synthetic route of the monoubiquitinated degron peptide (Ub-Degrон). **c–d**, Fluorescent labelling of Degrон (**c**) and Ub-Degrон (**d**). An additional C-terminal cysteine was introduced for the labelling of fluorescein-5-maleimide. **e**, In vitro Ubr1-dependent ubiquitination assays using fluorescent Degrон (top) and Ub-Degrон (bottom) as substrates. Gel images are representative of independent biological replicates ( $n = 2$ ). **f–g**, Quantitative evaluations of the kinetics of Ubr1-mediated ubiquitination initiation (**f**) and the first step of elongation (**g**). Averages of two independent experiments were plotted and fitted to the Michaelis–Menten model to estimate the  $K_m$  and  $K_{cat}$ . Gel images are representative of independent biological replicates ( $n = 2$ ).

### [Extended Data Fig. 2 Analyses of ubiquitin chain linkage generated by Ubr1 and Ubc2.](#)

**a**, In vitro Ubr1-dependent ubiquitination on fluorescently labelled K<sup>17only</sup>Degron using wild-type Ub (left) and Ub<sup>K48R</sup> (right). Gel images are representative of independent biological replicates (n = 2). Gel slices in box b and c were cut and digested, followed by LC-MS/MS analyses. **b**, Identification of Ub chain linkages in box b. **c**, Identification of Ub chain linkages in box c. # PSMs: Number of peptide spectrum matches.

[Source data](#)

**Extended Data Fig. 3 Design and purification of the stable intermediate structures.**

**a**, A schematic representation of the transition state of the initiation step. The side chain of a Lys residue on Degron attacks the thioester bond of Ubc2–Ub. The inset shows the designed intermediate structure mimicking the transition state of the initiation step. **b**, A schematic representation of the transition state of the elongation step. The side chain of Lys48 on Ub-Degron attacks the thioester bond of Ubc2–Ub. The inset shows the designed intermediate structure mimicking the transition state of the elongation step. **c**, A brief synthetic route of the intermediate structure mimicking the transition state of the elongation step. **d**, A gel filtration chromatogram of Ubr1 (left) and an SDS–PAGE gel of purified Ubr1 and designed stable intermediate structures Ubc2-Ub-Degron and Ubc2-Ub-Ub-Degron (right).

**Extended Data Fig. 4 Cryo-EM density of the initiation and elongation complexes.**

**a**, Individual domains of Ubr1 in the initiation complex. **b**, Ubc2 and Ub in the initiation complex. **c**, Ubc2, donor Ub and acceptor Ub in the elongation complex. Maps in **a** and **b** were sharpened using a *B* factor of  $-96.5 \text{ \AA}^2$  and contoured at a level of 0.030. Maps in **c** were sharpened using a *B* factor of  $-96.7 \text{ \AA}^2$  and contoured at a level of 0.022. **d**, Degron recognition site of the initiation complex. **e**, Active site of the initiation complex. **f**, Three-domain junction of the initiation complex. **g**, Active site of the elongation complex. **h**, Acceptor Ub and Ubr1 binding interface in the elongation

complex. **i**, Acceptor Ub and Ubc2 binding interface in the elongation complex. Dotted circles in **d** and **e** mark the unmodelled densities corresponding to the Degron peptide which are only visible at the lower contour levels. Atomic models could not be reliably built into the densities.

### **Extended Data Fig. 5 Molecular structures of Ubr1 complex and interfaces between Ubr1 and Ub.**

**a**, The helical scaffold of Ubr1 consists of four separate regions. **b**, The three domains located around the helical scaffold, Ubr-Box1 (Ubox1, purple), Ubr-Box2 (Ubox2, light blue) and WHD (dark blue). **c**, The three domains above the helical scaffold, the RING finger domain (cyan), CHD (pink) and UBLC domain (yellow). The RING finger domain is sandwiched between the CHD and UBLC domain. An additional zinc finger motif (ZNF) in UBLC is labelled. **d**, U2BR (forest green), Ubc2 (magenta)–Ub (lime) and the RING finger domain form the catalytic module of Ubr1 complex. Two zinc finger motifs (ZNF) in the RING finger domain are labelled. **e**, Additional binding interfaces between the donor Ub and Ubr1 in the initiation complex, including K965 in WHD, E1436 and Q1437 in CHD. R1783 in UBLC domain is the key residue to stabilize the loop of WHD. **f**, Additional binding interfaces between the acceptor Ub and Ubr1 in the elongation complex. **g**, In vitro Ubr1-dependent ubiquitination assay. A quadruple mutant (H161A, Y933A, D1175A, and H1763A, DHHY) of the residues involved in the interface between Ubox1, WHD, and UBLC (three-domain junction, shown in Fig. [1e](#)) was tested. Gel images are representative of independent biological replicates ( $n = 2$ ). **h**, In vitro Ubr1-dependent ubiquitination assay. Mutants of Ubr1 including K965A, E1436A/Q1437A, R1783A and K965A/E1436A/Q1437A/R1783A (KREQ) involved in the interfaces mentioned in **e** were tested. Gel images are representative of independent biological replicates ( $n = 2$ ).

### **Extended Data Fig. 6 Characterization of N-degron recognition domains on Ubr1.**

**a**, A sequence alignment of Ubr-box1 in yeast and human Ubr1 and human Ubr2. The negatively charged pocket involved in the recognition of the

Arg/N-end is highlighted in light purple. **b**, A close-up view of substrate-engaged Ubr-box1. **c**, In vitro Ubr1-dependent ubiquitination assay on fluorescently labelled Arg/N-end degron (Degrон) and Met/N-end degron (Degrон with the first amino acid changed to methionine). Gel images are representative of independent biological replicates ( $n = 2$ ). **d**, A structure alignment of yeast Ubr-box2 determined in this study with substrate loaded ClpS (*Caulobacter crescentus*, 3GQ1) and substrate free ClpS (*Plasmodium falciparum*, 4O2X). Root-mean-square deviation (RMSD) of backbone atoms are indicated. Substrate peptide from ClpS (*Caulobacter crescentus*, 3GQ1) is coloured in dark blue. **e**, A structure alignment of Ubr-box2 determined in this study with substrate loaded ClpS (*Caulobacter crescentus*, 3GQ1) in the context of Ubr1. The C-terminus of type-1 (this study) and type-2 (from 3GQ1) substrates are highlighted using red and blue arrows, respectively, pointing to the active site of Ubr1. **f**, A sequence alignment of yeast Ubr-box2 with ClpS from *Caulobacter crescentus* (3GQ1) and *Plasmodium falciparum* (4O2X). The substrate binding pocket is highlighted in yellow.

### Extended Data Fig. 7 Characterization of the interfaces between Ubr1, Ubc2 and Ub.

**a–b**, In vitro Ubr1-dependent ubiquitination assays. Mutations of the Ub binding loop on Ubr1 (H678A/V679A/L680A/H681A, named UBLM mutant, **a**) and Ubc2 (N123A/V124A, **b**) were tested. Gel images are representative of independent biological replicates ( $n = 2$ ). Red boxes highlight the difference of UBLM mutant in initiation and elongation. **c**, Single-turnover ubiquitination assay of wild-type Ubr1 and UBLM mutant using Ubc2 charged with either wild-type Ub or Ub<sup>K0</sup> (all Lysine residues mutated to Arginine). Red boxes highlight the defect of UBLM mutant in elongation. Gel images are representative of independent biological replicates ( $n = 2$ ). **d**, Side views of the initiation and elongation complexes showing the displacement of U2BR, Ubc2, and Ub. **e**, An alignment of Ubr1 structures in the initiation and elongation complexes. **f–g**, In vitro Ubr1-dependent ubiquitination assays. Gel images are representative of independent biological replicates ( $n = 2$ ). **f**, Ubr1 (F1190A/Q1186A/F1183A/H1175A, named FQFH mutant) and Ubc2 mutants at the interface shown in Fig. 3b were tested. **g**, The inhibition of

Ubr1-dependent ubiquitination in the presence of increasing concentrations of a synthetic U2BR peptide. **h**, The accessibility of the catalytic cysteine (Cys88) of Ubc2 was tested using fluorescein-5-maleimide, a bulky fluorescent alkylation reagent (BFAR), in the presence or absence of the synthetic U2BR peptide. The average fluorescence from two independent biological replicates was plotted ( $n = 2$ ). **i**, A sequence alignment of multiple E2 enzymes, including yeast and human Ubc2 (also known as Rad6b in human). Two regions involved in the interaction with the RING finger domain are shown. **j**, In vitro Ubr1-dependent ubiquitination assays were performed to examine the role of Asn65 of Ubc2 in the interaction with the RING finger domain of Ubr1. Gel images are representative of independent biological replicates ( $n = 2$ ).

### **Extended Data Fig. 8 Characterization of the interactions between U2BR and Ubc2.**

**a**, ITC measurement of the binding between Ubc2 and the synthetic U2BR peptide. **b**, The formation of E1-dependent Ubc2–Ub thioester in the presence of the synthetic U2BR peptide. Gel images are representative of independent biological replicates ( $n = 2$ ). **c**, Quantitative evaluations of the inhibitory effect of the synthetic U2BR peptide on E1-dependent Ubc2–Ub thioester formation. Averages of three independent biological replicates ( $n = 3$ ) were plotted and fit to estimate the IC<sub>50</sub> of the synthetic U2BR peptide. The curves are presented as mean values  $\pm$  s.d. **d–e**, In vitro Ubr1-dependent ubiquitination assay. Increasing doses of catalytically inactive Ubc2-C88S (**d**) and non-hydrolysable Ubc2-Ub (**e**) up to 12.5  $\mu$ M were pre-mixed with Ubr1, followed by adding wild-type Ubc2 at 4  $\mu$ M. Gel images are representative of independent biological replicates ( $n = 2$ ).

### **Extended Data Fig. 9 The structure of the pre-elongation complex and validation of the structural mechanism.**

**a**, A comparison of initiation, pre-elongation and elongation complex in the same orientation showing the movement of ubiquitin. The colour code of Ubr1 is the same as that in Fig. [1b](#). Sharpened map of the pre-elongation complex is shown at a contour level of 0.011. **b**, In vitro ubiquitination

assay on fluorescently labelled Hs-Type-1 Degron (derived from human protein Rec8) with wild-type Ubr1 and Ubr1 mutants, UBLM, DHHY and FQFH. Gel images are representative of independent biological replicates ( $n = 2$ ). **c**, In vitro ubiquitination assay on fluorescently labelled Type-2 Degron (derived from Sindbis virus polymerase nsP4) with wild-type Ubr1 and Ubr1 mutants, UBLM, DHHY and FQFH. Gel images are representative of independent biological replicates ( $n = 2$ ). **d**, In vitro ubiquitination assay on truncated protein substrates ROQ1 (22-104) and Scc1 (268-384) with wild-type Ubr1 and Ubr1 mutants, UBLM, DHHY and FQFH. Gel images are representative of independent biological replicates ( $n = 2$ ). **e**, The design of the yeast-growth assay. Endogenous deubiquitinating enzymes (DUB) cleave the construct co-translationally and produce Scc1 fragment (R-Scc1<sup>269–566</sup>) which has an N-terminal arginine residue and is toxic to the yeast strain deficient of Ubr1 ( $\Delta UBR1$ ). If wild-type Ubr1 is supplemented, R-Scc1<sup>269–566</sup> will be rapidly polyubiquitinated and degraded, reversing the growth defect. **f**, Yeast strains carrying wild-type Ubr1 or Ubr1 mutants (FQFH, UBLM and DHHY) were streaked either on dextrose-containing (SD) plates (right) where all strains grew without the expression of Scc1 fragment and Ubr1 variants, or on galactose containing (SG) plates (left), where all strains grew with the induced gene expression of Scc1 fragment and Ubr1 variants. In addition to R-Scc1<sup>269–566</sup>, M-Scc1<sup>269–566</sup> which has an N-terminal methionine residue was also tested. The plates were incubated at 30 °C for 3 d.

### **Extended Data Table 1 Cryo-EM data collection, refinement and validation statistics**

## **Supplementary information**

### **Supplementary Information**

Supplementary Figs. 1–7.

### **Reporting Summary**

### **Peer Review File**

# Source data

## [Source Data Extended Data Fig. 2](#)

# Rights and permissions

## [Reprints and Permissions](#)

# About this article

## Cite this article

Pan, M., Zheng, Q., Wang, T. *et al.* Structural insights into Ubrl-mediated N-degron polyubiquitination. *Nature* **600**, 334–338 (2021).  
<https://doi.org/10.1038/s41586-021-04097-8>

- Received: 15 April 2021
- Accepted: 06 October 2021
- Published: 17 November 2021
- Issue Date: 09 December 2021
- DOI: <https://doi.org/10.1038/s41586-021-04097-8>

## Share this article

Anyone you share the following link with will be able to read this content:

[Get shareable link](#)

Sorry, a shareable link is not currently available for this article.

[Copy to clipboard](#)

Provided by the Springer Nature SharedIt content-sharing initiative

---

This article was downloaded by **calibre** from <https://www.nature.com/articles/s41586-021-04097-8>

| [Section menu](#) | [Main menu](#) |

- Article
- [Published: 10 November 2021](#)

# Structures of the HER2–HER3–NRG1 $\beta$ complex reveal a dynamic dimer interface

- [Devan Diwanji](#)<sup>1,2</sup> na1,
- [Raphael Trenker](#) [ORCID: orcid.org/0000-0003-1748-0517](#)<sup>1</sup> na1,
- [Tarjani M. Thaker](#)<sup>1,3</sup>,
- [Feng Wang](#)<sup>4</sup>,
- [David A. Agard](#) [ORCID: orcid.org/0000-0003-3512-695X](#)<sup>4</sup>,
- [Kliment A. Verba](#) [ORCID: orcid.org/0000-0002-2238-8590](#)<sup>5,6</sup> &
- [Natalia Jura](#) [ORCID: orcid.org/0000-0001-5129-641X](#)<sup>1,7</sup>

[Nature](#) volume **600**, pages 339–343 (2021)

- 5902 Accesses
- 53 Altmetric
- [Metrics details](#)

## Subjects

- [Breast cancer](#)
- [Cryoelectron microscopy](#)

## Abstract

Human epidermal growth factor receptor 2 (HER2) and HER3 form a potent pro-oncogenic heterocomplex<sup>1,2,3</sup> upon binding of growth factor neuregulin-1β (NRG1β). The mechanism by which HER2 and HER3 interact remains unknown in the absence of any structures of the complex. Here we isolated the NRG1β-bound near full-length HER2–HER3 dimer and, using cryo-electron microscopy, reconstructed the extracellular domain module, revealing unexpected dynamics at the HER2–HER3 dimerization interface. We show that the dimerization arm of NRG1β-bound HER3 is unresolved because the apo HER2 monomer does not undergo a ligand-induced conformational change needed to establish a HER3 dimerization arm-binding pocket. In a structure of the oncogenic extracellular domain mutant HER2(S310F), we observe a compensatory interaction with the HER3 dimerization arm that stabilizes the dimerization interface. Both HER2–HER3 and HER2(S310F)–HER3 retain the capacity to bind to the HER2-directed therapeutic antibody trastuzumab, but the mutant complex does not bind to pertuzumab. Our structure of the HER2(S310F)–HER3–NRG1β–trastuzumab Fab complex reveals that the receptor dimer undergoes a conformational change to accommodate trastuzumab. Thus, similar to oncogenic mutations, therapeutic agents exploit the intrinsic dynamics of the HER2–HER3 heterodimer. The unique features of a singly liganded HER2–HER3 heterodimer underscore the allosteric sensing of ligand occupancy by the dimerization interface and explain why extracellular domains of HER2 do not homo-associate via a canonical active dimer interface.

This is a preview of subscription content

## Access options

Subscribe to Journal

Get full journal access for 1 year

\$199.00

only \$3.90 per issue

## Subscribe

All prices are NET prices.

VAT will be added later in the checkout.

Tax calculation will be finalised during checkout.

Rent or Buy article

Get time limited or full article access on ReadCube.

from \$8.99

## Rent or Buy

All prices are NET prices.

### **Additional access options:**

- [Log in](#)
- [Learn about institutional subscriptions](#)

**Fig. 1: Overall structure of the HER2–HER3–NRG1 $\beta$  extracellular domain dimer complex.**

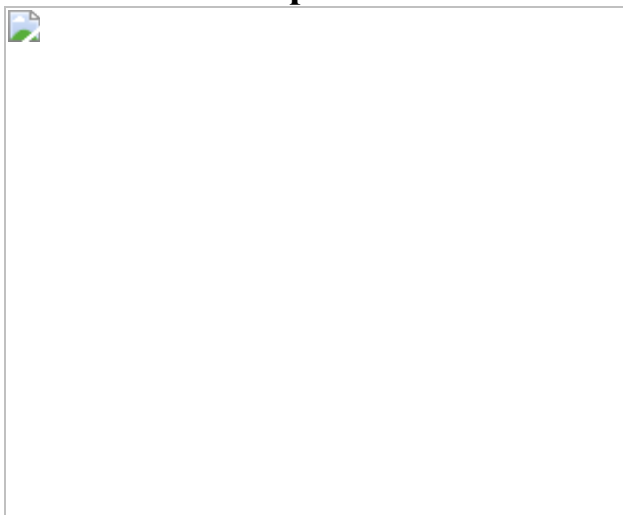


**Fig. 2: Analysis of liganded HER receptor states reveals an allosteric mechanism of dimerization arm engagement.**

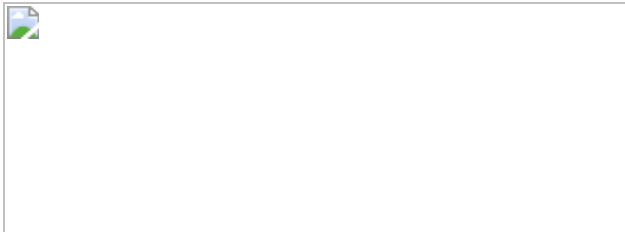


**Fig. 3: The HER2 oncogenic mutation S310F stabilizes the dimerization arm of HER3.**

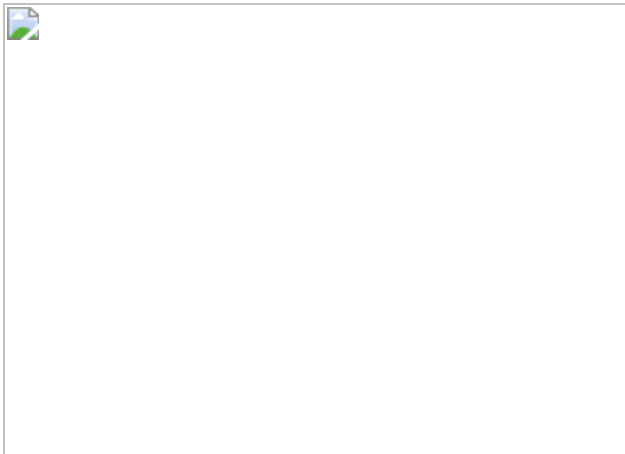
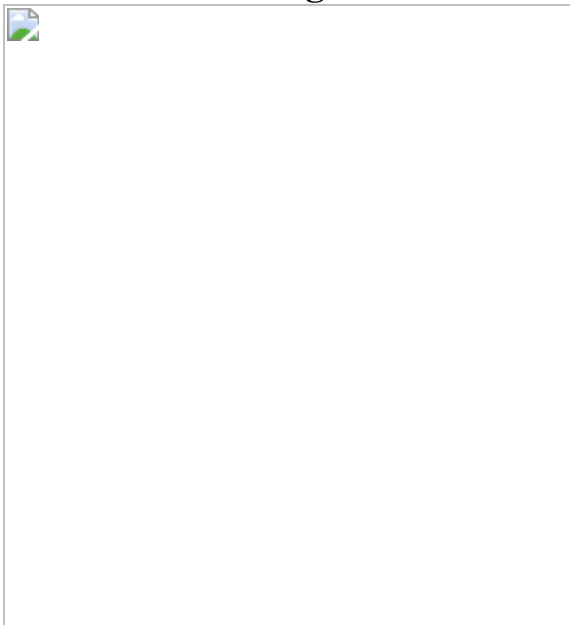


**Fig. 4: The HER2–HER3–NRG1 $\beta$  structure accommodates trastuzumab binding.**



## Data availability

Three-dimensional cryo-EM density maps have been deposited in the Electron Microscopy Data Bank under the accession numbers [EMD-23916](#) (HER2–HER3–NRG1b), [EMD-23917](#) (HER2(S310F)–HER3–NRG1b) and [EMD-23918](#) (HER2(S310F)–HER3–NRG1b–herceptin Fab). Atomic coordinates for the atomic models have been deposited in the RCSB Protein Data Bank under the accession numbers [7MN5](#) (HER2–HER3–NRG1b), [7MN6](#) (HER2(S310F)–HER3–NRG1b) and [7MN8](#) (HER2(S310F)–HER3–NRG1b–herceptin Fab). [Source data](#) are provided with this paper.

## References

1. 1.

Sliwkowski, M. X. et al. Coexpression of erbB2 and erbB3 proteins reconstitutes a high affinity receptor for heregulin. *J. Biol. Chem.* **269**, 14661–14665 (1994).

2. 2.

Wallasch, C. et al. Heregulin-dependent regulation of HER2/neu oncogenic signaling by heterodimerization with HER3. *EMBO J.* **14**, 4267–4275 (1995).

3. 3.

Moasser, M. M. The oncogene HER2: its signaling and transforming functions and its role in human cancer pathogenesis. *Oncogene* **26**, 6469–6487 (2007).

4. 4.

Sierke, S. L., Cheng, K., Kim, H. & Koland, J. G. Biochemical characterization of the protein tyrosine kinase domain of the ErbB3 (HER3) receptor protein. *Biochem. J.* **322**, 757–763 (1997).

5. 5.

Jura, N., Shan, Y., Cao, X., Shaw, D. E. & Kuriyan, J. Structural analysis of the catalytically inactive kinase domain of the human EGF receptor 3. *Proc. Natl Acad. Sci. USA* **106**, 21608–21613 (2009).

6. 6.

Zhang, X., Gureasko, J., Shen, K., Cole, P. A. & Kuriyan, J. An allosteric mechanism for activation of the kinase domain of epidermal growth factor receptor. *Cell* **125**, 1137–1149 (2006).

7. 7.

Littlefield, P. et al. Structural analysis of the EGFR/HER3 heterodimer reveals the molecular basis for activating HER3 mutations. *Sci. Signal.* **7**, ra114 (2015).

8. 8.

Ferguson, K. et al. EGF activates its receptor by removing interactions with autoinhibit ectodomain dimerization. *Mol. Cell* **11**, 507–517 (2003).

9. 9.

Bouyain, S., Longo, P. A., Li, S., Ferguson, K. M. & Leahy, D. J. The extracellular region of ErbB4 adopts a tethered conformation in the absence of ligand. *Proc. Natl Acad. Sci. USA* **102**, 15024–15029 (2005).

10. 10.

Cho, H.-S. & Leahy, D. J. Structure of the extracellular region of HER3 reveals an interdomain tether. *Science* **297**, 1330–1333 (2002).

11. 11.

Garrett, J. T. et al. Crystal structure of a truncated epidermal growth factor receptor extracellular domain bound to transforming growth factor  $\alpha$ . *Cell* **110**, 763–773 (2002).

12. 12.

Ogiso, H. et al. Crystal structure of the complex of human epidermal growth factor and receptor extracellular domains. *Cell* **110**, 775–787 (2002).

13. 13.

Liu, P. et al. A single ligand is sufficient to activate EGFR dimers. *Proc. Natl Acad. Sci. USA* **109**, 10861–10866 (2012).

14. 14.

Cho, H.-S. et al. Structure of the extracellular region of HER2 alone and in complex with the Herceptin Fab. *Nature* **421**, 756–760, (2003).

15. 15.

Hao, Y., Yu, X., Bai, Y., McBride, H. J. & Huang, X. Cryo-EM Structure of HER2–trastuzumab–pertuzumab complex. *PLoS ONE* **14**, e0216095 (2019).

16. 16.

Alvarado, D., Klein, D. E. & Lemmon, M. A. ErbB2 resembles an autoinhibited invertebrate epidermal growth factor receptor. *Nature* **461**, 287–291 (2009).

17. 17.

Ferguson, K. M., Darling, P. J., Mohan, M. J., Macatee, T. L. & Lemmon, M. A. Extracellular domains drive homo- but not heterodimerization of erbB receptors. *EMBO J.* **19**, 4632–4643 (2000).

18. 18.

Hanker, A. B. et al. Co-occurring gain-of-function mutations in HER2 and HER3 modulate HER2/HER3 activation, oncogenesis, and HER2 inhibitor sensitivity. *Cancer Cell*, **39**, 1099–1114.e8 (2021).

19. 19.

Freed, D. M. et al. EGFR ligands differentially stabilize receptor dimers to specify signaling kinetics. *Cell* **171**, 683–695 e618 (2017).

20. 20.

Lu, C. et al. Structural evidence for loose linkage between ligand binding and kinase activation in the epidermal growth factor receptor. *Mol. Cell. Biol.* **30**, 5432–5443, (2010).

21. 21.

Huang, Y. et al. A molecular mechanism for the generation of ligand-dependent differential outputs by the epidermal growth factor receptor. Preprint at <https://doi.org/10.1101/2020.12.08.417006> (2021).

22. 22.

Greulich, H. et al. Functional analysis of receptor tyrosine kinase mutations in lung cancer identifies oncogenic extracellular domain mutations of ERBB2. *Proc. Natl Acad. Sci. USA* **109**, 14476–14481 (2012).

23. 23.

Wang, T. et al. HER2 somatic mutations are associated with poor survival in HER2-negative breast cancers. *Cancer Sci.* **108**, 671–677 (2017).

24. 24.

The Cancer Genome Atlas Network. Comprehensive molecular portraits for human breast tumours. *Nature* **490**, 61–70 (2012).

25. 25.

Franklin, M. C. et al. Insights into ErbB signaling from the structure of the ErbB2–pertuzumab complex. *Cancer Cell* **5**, 317–328 (2004).

26. 26.

Alvarado, D., Klein, D. E. & Lemmon, M. A. Structural basis for negative cooperativity in growth factor binding to an EGF receptor. *Cell* **142**, 568–579 (2010).

27. 27.

Arkhipov, A., Shan, Y., Kim, E. T., Dror, R. O. & Shaw, D. E. Her2 activation mechanism reflects evolutionary preservation of asymmetric ectodomain dimers in the human EGFR family. *eLife* **2**, e00708 (2013).

28. 28.

Garrett, J. T. et al. The crystal structure of a truncated ErbB2 ectodomain reveals an active conformation, poised to interact with other ErbB receptors. *Mol. Cell* **11**, 495–505 (2003).

29. 29.

Xu, W. et al. Surface charge and hydrophobicity determine ErbB2 binding to the Hsp90 chaperone complex. *Nat. Struct. Mol. Biol.* **12**, 120–126 (2005).

30. 30.

Jaiswal, B. S. et al. Oncogenic ERBB3 mutations in human cancers. *Cancer Cell* **23**, 603–617 (2013).

31. 31.

Palovcak, E. et al. A simple and robust procedure for preparing graphene-oxide cryo-EM grids. *J. Struct. Biol.* **204**, 80–84 (2018).

32. 32.

Wang, F. et al. General and robust covalently linked graphene oxide affinity grids for high-resolution cryo-EM. *Proc. Natl Acad. Sci. USA*

**117**, 24269–24273 (2020).

33. 33.

Mastronarde, D. N. Automated electron microscope tomography using robust prediction of specimen movements. *J. Struct. Biol.* **152**, 36–51 (2005).

34. 34.

de la Rosa-Trevin, J. M. et al. Scipion: A software framework toward integration, reproducibility and validation in 3D electron microscopy. *J. Struct. Biol.* **195**, 93–99 (2016).

35. 35.

Zheng, S. Q. et al. MotionCor2: anisotropic correction of beam-induced motion for improved cryo-electron microscopy. *Nat. Methods* **14**, 331–332 (2017).

36. 36.

Rohou, A. & Grigorieff, N. CTFFIND4: Fast and accurate defocus estimation from electron micrographs. *J. Struct. Biol.* **192**, 216–221 (2015).

37. 37.

Punjani, A., Rubinstein, J. L., Fleet, D. J. & Brubaker, M. A. cryoSPARC: algorithms for rapid unsupervised cryo-EM structure determination. *Nat. Methods* **14**, 290–296 (2017).

38. 38.

Scheres, S. H. RELION: implementation of a Bayesian approach to cryo-EM structure determination. *J. Struct. Biol.* **180**, 519–530 (2012).

39. 39.

Kucukelbir, A., Sigworth, F. & Tagare, H. Quantifying the local resolution of cryo-EM density maps. *Nature Methods* **11**, 63–65 (2014).

40. 40.

Tan, Y. Z. et al. Addressing preferred specimen orientation in single-particle cryo-EM through tilting. *Nat. Methods* **14**, 793–796 (2017).

41. 41.

Asarnow, D., Palovcak, E. & Cheng, Y. UCSF pyem v0.5. *Zenodo* (2019).

42. 42.

DiMaio, F. et al. Atomic-accuracy models from 4.5-A cryo-electron microscopy data with density-guided iterative local refinement. *Nat. Methods* **12**, 361–365 (2015).

43. 43.

Emsley, P., Lohkamp, B., Scott, W. G. & Cowtan, K. Features and development of Coot. *Acta Crystallogr. D* **66**, 486–501 (2010).

44. 44.

Croll, T. I. ISOLDE: a physically realistic environment for model building into low-resolution electron-density maps. *Acta Crystallogr. D* **74**, 519–530 (2018).

45. 45.

Frenz, B. et al. Automatically fixing errors in glycoprotein structures with Rosetta. *Structure* **27**, 134–139.e133 (2019).

46. 46.

Adams, P. D. et al. PHENIX: a comprehensive Python-based system for macromolecular structure solution. *Acta Crystallogr. D* **66**, 213–221 (2010).

47. 47.

Agirre, J. et al. Privateer: software for the conformational validation of carbohydrate structures. *Nat. Struct. Mol. Biol.* **22**, 833–834 (2015).

## Acknowledgements

We thank A. Manglik for advice on receptor expression; D. Bulkley, G. Gilbert, E. Tse and Z. Yu from the UCSF EM facility; members of the Verba and Jura laboratories for their helpful discussions; E. Linossi and H. Torosyan for critical comments on the manuscript; and D. Suveges for his experimental contributions to the generation of our first HER expression constructs. This work was funded through UCSF Program for Breakthrough Biomedical Research to K.A.V. and N.J., NIH/NIGMS R35-GM139636 to N.J., Genentech research grant to N.J., NIH/NCI U54-CA209891 to N.J. and D.A.A., NIH/NIGMS R35-GM118099 to D.A.A., DFG German Research Foundation GZ: TR 1668/1-1 to R.T. and NIH/NCI 1F30CA247147 to D.D.

## Author information

### Author notes

1. These authors contributed equally: Devan Diwanji, Raphael Trenker

## Affiliations

1. Cardiovascular Research Institute, University of California San Francisco, San Francisco, CA, USA

Devan Diwanji, Raphael Trenker, Tarjani M. Thaker & Natalia Jura

2. Medical Scientist Training Program, University of California San Francisco, San Francisco, CA, USA

Devan Diwanji

3. Department of Chemistry and Biochemistry, The University of Arizona, Tucson, AZ, USA

Tarjani M. Thaker

4. Department of Biochemistry and Biophysics, University of California San Francisco, San Francisco, CA, USA

Feng Wang & David A. Agard

5. Quantitative Biosciences Institute (QBI), University of California San Francisco, San Francisco, CA, USA

Kliment A. Verba

6. Department of Pharmaceutical Chemistry, University of California San Francisco, San Francisco, CA, USA

Kliment A. Verba

7. Department of Cellular and Molecular Pharmacology, University of California San Francisco, San Francisco, CA, USA

Natalia Jura

## Contributions

N.J. conceived the project and D.D., R.T., K.A.V. and N.J. designed the research approach. D.D. and R.T. performed all expression and purification, electron microscopy imaging and processing, structural modelling and in vitro experiments. T.M.T. provided initial receptor expression constructs. F.W. and D.A.A. provided holey carbon graphene-oxide grids for cryo-EM. D.D., R.T., K.A.V. and N.J. wrote the manuscript.

## Corresponding authors

Correspondence to [Kliment A. Verba](#) or [Natalia Jura](#).

## Ethics declarations

### Competing interests

N.J. is a member of the Scientific Advisory Board and a shareholder of Turning Point Therapeutics, SUDO Biosciences and Type6 Therapeutics. The Jura laboratory has received sponsored research support from Genentech. The other authors declare no competing interests.

## Additional information

**Peer review information** *Nature* thanks Michael Eck, Stevan Hubbard, Zhi-Jie Liu and the other, anonymous, reviewer(s) for their contribution to the peer review of this work. Peer reviewer reports are available.

**Publisher's note** Springer Nature remains neutral with regard to jurisdictional claims in published maps and institutional affiliations.

## Extended data figures and tables

### [Extended Data Fig. 1 Purification, characterization, and reconstruction of the near full-length HER2/HER3/NRG1 \$\beta\$ heterocomplex.](#)

**a**, Schematic summary of the HER2/HER3/NRG1 $\beta$  complex purification strategy. **b**, A representative Coomassie-stained SDS-PAGE gel analysis of the HER2/HER3/NRG1 $\beta$  complex after purification showing bands corresponding to the HER2 and HER3 receptors. The gel is representative of three independent experiments. **c**, Representative size exclusion chromatography profile of the HER2/HER3/NRG1 $\beta$  complex resolved on a Superose6 10/300 Increase column (GE Healthcare). The major peak at ~14

ml elution volume is marked grey and corresponds to the fractions used for structural studies. We routinely obtained a 1-2 mA units peaks for the complex preparations from 120 ml of mammalian culture, which was sufficient for the structural studies. **d**, Mass photometry of the peak sample indicates that the majority of particles have an average mass of ~326 kDa with a standard deviation of 17 kDa. The mass is consistent with that of the HER2/HER3/NRG1 $\beta$  complex (predicted ~280 kDa without accounting for micelle mass, ~340 kDa assuming a ~60 kDa DDM micelle mass). **e**, Representative negative stain electron microscopy 2D class averages of sample from HER2/HER3/NRG1 $\beta$  complex fractions (ECDs (extracellular domains), ICDs (intracellular domains)). **f**, Near full-length reconstruction of HER2-S310F/HER3/NRG1 $\beta$  after particle recentering with center of mass at the micelle in RELION from a ~45,000 particle stack. Rod-shaped density consistent with the asymmetric kinase domain dimer is visible below the micelle. **g**, The reconstruction accommodates models of the HER2-S310F/HER3/NRG1 $\beta$  extracellular domains from this study, two helical transmembrane domains and juxtamembrane-A (JM-A) segments from HER2 (PDB ID 2N2A), and kinases arranged in the asymmetric dimer (homology model generated based on structures of the EGFR kinase from PDB ID 3KEX and PDB ID 3PP0). HER2 is colored in blue, HER3 in golden yellow, and NRG1 $\beta$  in teal.

### **Extended Data Fig. 2 Resolution estimation, map quality and the workflow for processing of the HER2/HER3/NRG1 $\beta$ dataset.**

**a**, Representative micrograph of the HER2/HER3/NRG1 $\beta$  sample on graphene oxide grids, from a dataset with 2035 GO-containing micrographs. The scale bar corresponds to 0.5  $\mu$ m. **b**, Example 2D cryo-EM class averages. **c**, Local resolution estimation from ResMap. **d**, Gold Standard Fourier Shell Correlation (GSFSC) of the final map used for model building from CryoSPARC2 with a reported resolution of 2.93  $\text{\AA}$ . **e**, Directional FSCs calculated by 3DFSC server. Map sphericity was calculated to be 0.927. **f**, Workflow for processing the HER2/HER3/NRG1 $\beta$  dataset. Blue box indicates model and associated particle stack used for downstream processing. The final model is indicated with a red box. The map in the yellow box represents a slightly different low-occupancy

species. The insets show that the HER3 dimerization arm is still poorly resolved in that class.

**Extended Data Fig. 3 Q-score analysis of the cryo-EM maps and a structural comparison of the HER2/HER3/NRG1 $\beta$  heterocomplex with crystal structures of previously reported HER receptor structures.**

**a**, Zoomed-in view of the cryo-EM density and model of WT HER2/HER3 (residues 63-150 of HER3) showing features appropriate for the reported resolution. **b**, WT HER2/HER3 model colored by estimated per residue Q-score ranging from 0 (red) to 0.75 (blue). The color bar shows corresponding estimated resolution in Å for each Q-score. Expected Q-score for 2.9Å map is 0.604. **c**, Zoomed-in view of the cryo-EM density and model of HER2 S310F/HER3 (residues 63-150 of HER3) showing features appropriate for the reported resolution. **d**, HER2-S310F/HER3 model colored by estimated Q-score with the same scale as in **b**. Expected Q-score for 3.1Å structure is 0.569. **e**, Overlay of the HER2/HER3/NRG1 $\beta$  heterocomplexes with symmetric structures of EGFR/EGF (PDB ID 3NJP), EGFR/TGF $\alpha$  (PDB ID 1MOX) and HER4/NRG1 $\beta$  (PDB ID 3U7U). **f**, Overlay of the HER2/HER3/NRG1 $\beta$  heterocomplexes with asymmetric structures of EGFR/EREG (PDB ID 5WB7), doubly liganded dEGFR/SPITZ (PDB ID 3LTF) and singly liganded dEGFR/SPITZ (PDB ID 3LTG). All structures were aligned on HER3. Differences between the heterodimer and the homodimers are primarily appreciated in overlays on the HER2 monomer. The heterodimer more closely resembles asymmetric homodimers than symmetric homodimers but reflects a unique conformation that is not seen in previous structures.

**Extended Data Fig. 4 Comparison of the domain II dimerization interface between HER2/HER3/NRG1 $\beta$  complex domain with crystal structures of previously reported HER receptor homodimers.**

**a–e**, The domain II interfaces of select HER receptor dimers are shown with the number of hydrogen bonds and the total buried surface area between

domains I-III indicated below. Domain IV was excluded from this analysis because it is not resolved in all structures. Hydrogen bonds are shown as red dotted lines, highlighting more substantial interfaces for symmetric homodimers (EGFR/EGF (PDB ID 3NJP), HER4/NRG1 $\beta$  (PDB ID 3U7U) than asymmetric dimers (HER2/HER3/NRG1 $\beta$ , EGFR/EREG (PDB ID 5WB7)), with the exception of the mutant HER2-S310F/HER3/NRG1 $\beta$  heterocomplex in which the mutation stabilizes the domain II interface. All interface hydrogen bonds are formed within domain II, except for an additional hydrogen bond in EGFR with domain III which is not shown here and marked (\*) in table.

**Extended Data Fig. 5 In-depth structural and functional analysis of the NRG1 $\beta$  binding-site and the HER2/HER3 dimerization interface.**

**a**, Left, HER4 bound to NRG1 $\beta$  (PDB ID 3U7U) with salt-bridge interactions highlighted. Middle, HER3 bound to NRG1 $\beta$  in our structure with salt bridge interactions highlighted. NRG1 $\beta$  engages with HER3 primarily through an extensive interaction network at its C-terminus (total buried surface area: 2,803 Å<sup>2</sup>) stabilized by salt bridges between R207 (NRG1 $\beta$ ) and D112 in HER3 domain I, and R220 (NRG1 $\beta$ ) and D371 in HER3 domain III, bringing domains I and III into close proximity. Right, overlay between the two structures shows that the overall orientation of the ligand and some salt-bridge interactions are shared between HER3 and HER4, but overall HER3 forms fewer salt bridges with NRG1 $\beta$  than HER4.

**b**, Structure of HER2 in our HER2/HER3/NRG1 $\beta$  dimer structure is overlayed with the crystal structure of the HER2 extracellular domain bound to trastuzumab Fab (PDB ID 1N8Z), the cryo-EM structure of the HER2 extracellular domain bound to pertuzumab and trastuzumab Fabs (PDB ID 6OGE) and the crystal structure of the rat HER2 extracellular domain (PDB ID 1N8Y). The structures are almost identical with root mean squared deviations (RMSDs) as following: 1.01 Å (1N8Z), 0.74 Å (1N8Y), 0.97 Å (6OGE). Minor conformational changes are observed in the dimerization arm and domain IV. **c**, Detailed view of the dimerization interface between domains II of HER2 and HER3 in the HER2/HER3/NRG1 $\beta$  structure with all polar contacts between receptors highlighted in the boxes to the left and to the right. **d**, Calculated buried

surface area at the dimerization interface for HER2/HER3/NRG1 $\beta$  complex and the known structures of the dimeric HER extracellular domain complexes. The following structures were used for the analysis: EGFR/EGF (PDB ID 3NJP), EGFR/EREG (PDB ID 5WB7), HER4/NRG1 $\beta$  (PDB ID 3U7U). **e**, Representative Western Blot analysis of the HER2 and HER3 (wild-type HER3 and HER3 GS-arm) constructs co-transfected in the EXPI293 cells and pulled-down via NRG1 $\beta$  immobilized on FLAG beads. TS – Twin Strep tag (present on both HER2 and HER3). Receptors were detected with the Strep-Tactin® HRP conjugate (anti-TS). For gel source data, see Supplementary Figure 1. **f**, Quantification of data shown in panel e. Values are presented as mean values  $\pm$  SD of mean intensity ratios of HER2 over HER3 for each blot in n = 3 independent biological replicates. The HER2/HER3 pulldown ratios are 0.18  $\pm$  0.06 for HER3-WT and 0.22  $\pm$  0.07 for HER3-GS-Arm complexes. Significance was determined via unpaired, two-tailed t-test via GraphPad Prism. p = 0.5463, t = 0.6582, df = 4. **g**, Anti-phospho-HER3 (pHER3, Y1289), anti-HER3 and anti-HER2 Western Blot analysis of lysates from COS7 cells transfected with indicated full-length receptors (wild type or carrying the indicated mutations), serum-starved and stimulated with 10 nM NRG1 $\beta$  for 10 min. HER3-V945R is a negative control due to the presence of mutation in the active kinase dimer interface. For gel source data, see Supplementary Figure 1. **h**, Quantification of data shown in panel g. Values are presented as mean values  $\pm$  SD of pHER3 intensities of the mutant relative to wild-type HER3 for each blot in n = 5 independent biological replicates. The mean intensity values are 0.90  $\pm$  0.19 for the HER3-GS-Arm and 0.13  $\pm$  0.04 for HER3-V945R relative to the WT with defined values of 1. Significance was determined via unpaired, two-tailed t-test via GraphPad Prism. HER3 GS-arm vs HER3: p = 0.2887, t = 1.136, df = 8, HER3 vs HER3 V945R: p < 0.0001, t = 43.89, df = 8.

[Source data](#)

[Extended Data Fig. 6 The oncogenic HER2-S310F/Y mutations increase the yields of the HER2/HER3/NRG1 \$\beta\$  complex purification.](#)

**a**, Representative Western Blot analysis of the HER2 (wild type, S310F or S310F mutant) and HER3 constructs co-transfected in the EXPI293 cells, and pulled-down via NRG1 $\beta$  immobilized on FLAG beads. TS – Twin Strep tag (present on both HER2 and HER3). Receptors were detected with the Strep-Tactin® HRP conjugate (anti-TS). For gel source data, see Supplementary Figure 1. **b**, Densitometry analysis of blots for data shown in panel a. Values are presented as mean values  $\pm$  SD of mean intensity ratios of HER2 over HER3 for each blot in n=3 independent biological replicates. The HER2/HER3 pulldown ratios are 0.09  $\pm$  0.04 for HER2-WT, 0.20  $\pm$  0.06 for HER2-S310F and 0.35  $\pm$  0.09 for HER2-S310Y complexes. Significance was determined via unpaired, two-tailed t-test via GraphPad Prism. WT vs S310F: p = 0.0605, t = 2.592, df = 4. WT vs. S310Y: p = 0.0107, t = 4.516, df = 4. **c**, Overlay of representative size exclusion chromatogram profiles from a Superose6 10/300 Increase column (GE Healthcare) of WT and oncogenic HER2-S310F heterocomplexes. Heterodimer peaks are denoted by asterisks. **d**, Cartoon representation of the cryo-EM structure of HER2-S310F/HER3/NRG1 $\beta$  complex overlayed on HER2/HER3/NRG1 $\beta$ . The HER2-S310F mutation is shown in red.

[Source data](#)

[\*\*Extended Data Fig. 7 Resolution estimation, map quality and the workflow for processing of the HER2-S310F/HER3/NRG1 \$\beta\$  and HER2-S310F/HER3/NRG1 \$\beta\$  trastuzumab datasets.\*\*](#)

**a**, Cryo-EM map colored by local resolution as estimated from ResMap. **b**, Gold Standard Fourier Shell Correlation (GSFSC) of the final map used for model building from CryoSPARC2 with a reported resolution of 3.10 Å. **c**, Directional FSCs calculated by 3DFSC server. Map sphericity was calculated to be 0.949. **d**, Workflow for processing the HER2/HER3/NRG1 $\beta$ /trastuzumab dataset. The final model is indicated with a red box. **e**, Cryo-EM map colored by local resolution as estimated from ResMap. **f**, Gold Standard Fourier Shell Correlation (GSFSC) of the final map used for model building from CryoSPARC2 with a reported resolution of 3.45 Å. **g**, Directional FSCs calculated by 3DFSC server. Map sphericity was calculated to be 0.941.

## Extended Data Fig. 8 Functional and structural analysis of interactions between the therapeutic Fabs and HER receptors in the HER2/HER3/NRG1 $\beta$ complex.

**a**, Overlay of the HER2/trastuzumab structure (PDB ID 6OGE) with the HER2-S310F/HER3/NRG1 $\beta$  structure reveals a steric clash between the Fab light chain constant domain and HER3 domain III. **b**, Left, overlay of the trastuzumab Fab variable domains in the HER2/trastuzumab structure (PDB ID 1N8Z) with the trastuzumab Fab in the HER2/HER3/NRG1 $\beta$  complex (HER2 domain IV in blue, trastuzumab Fab variable domains in magenta). The structures were aligned on HER2 domains I-III. Right, the HER2 domain IV bound to Fab variable domain from each structure was overlaid (RMSD: 1.569 Å) demonstrating that a Fab-binding epitope on HER2 is the same. Trastuzumab therefore avoids a steric clash with HER3 by inducing a rigid body rotation of HER2 domain IV relative to HER3. **c**, Overlay of the HER2/pertuzumab structure (PDB: 6OGE) with the HER2-S310F/HER3/NRG1 $\beta$  structure reveals a steric clash between the Fab variable domains, the HER3 dimerization arm, and HER3 domain II. **d**, Anti-phospho-HER3 (pHER3, Y1289), anti-HER3 and anti-HER2 Western Blot analysis of lysates from COS7 cells transfected with indicated full-length wild-type or mutant receptors. Cells were serum-starved, pre-incubated with pertuzumab or trastuzumab for 1h, as indicated, and then stimulated with 10 nM NRG1 $\beta$ . HER3-EGQR is HER3-E928G/Q809R. Representative Western Blot is shown, n=3. For gel source data, see Supplementary Figure 1. **e**, D31 of the pertuzumab variable light chain forms a polar contact with HER2 S310. **f**, HER2-S310F removes the polar contact with D31 and introduces a steric clash with T30 of the pertuzumab variable light chain. The predicted net effect of the oncogenic HER2-S310F mutation would be a decrease in pertuzumab affinity for HER2 (PDB ID 6OGE).

## **Extended Data Table 1 Cryo-EM data collection, refinement and validation statistics**

## **Supplementary information**

## **Supplementary Figure 1**

Unprocessed and uncropped gel images for Fig. 4a, Extended Data Figs. 5e, g, 6a, 8d. Dotted boxes indicate where the gels were cropped. Fig. 4a blot was processed on film, and the position of the molecular weight marker was manually marked on the film by overlay with the blot. For Extended Data Figs. 5e, g, 6a, 8d, blots were imaged using BioRad Imager. A colour image for each blot was obtained using a separate channel, and overlaid on the chemiluminescent image to obtain exact position of the molecular weight marker. The overlays are presented in their uncropped versions.

## **Reporting Summary**

## **Peer Review File**

## **Source data**

### **Source Data Extended Data Fig. 5**

### **Source Data Extended Data Fig. 6**

## **Rights and permissions**

### **Reprints and Permissions**

## **About this article**

### **Cite this article**

Diwanji, D., Trenker, R., Thaker, T.M. *et al.* Structures of the HER2–HER3–NRG1 $\beta$  complex reveal a dynamic dimer interface. *Nature* **600**, 339–343 (2021). <https://doi.org/10.1038/s41586-021-04084-z>

- Received: 13 April 2021

- Accepted: 29 September 2021
- Published: 10 November 2021
- Issue Date: 09 December 2021
- DOI: <https://doi.org/10.1038/s41586-021-04084-z>

## Share this article

Anyone you share the following link with will be able to read this content:

[Get shareable link](#)

Sorry, a shareable link is not currently available for this article.

[Copy to clipboard](#)

Provided by the Springer Nature SharedIt content-sharing initiative

---

This article was downloaded by **calibre** from <https://www.nature.com/articles/s41586-021-04084-z>

| [Section menu](#) | [Main menu](#) |

# Nature Index